Università degli studi di Napoli Federico II

DOTTORATO DI RICERCA IN FISICA

Ciclo XXX

Coordinatore: Prof. Salvatore Capozziello

Measurement of the antineutrino flux and cross section at the near detector of the T2K experiment

Settore Scientifico Disciplinare FIS/01

Dottorando
Ciro Riccio

Tutore
Prof. Vittorio Palladino
Dott.ssa Gianfranca de Rosa

Anni 2014/2017

université PARIS-SACLAY

NNT : Not available yet

Thèse de doctorat

université PARIS-SACLAY | ÉCOLE DOCTORALE PHENIICS

Mesure du flux et de la section efficace du antineutrino dans le dètecteur proche de l'expérience T2K

Thèse de doctorat de l'Université de Naples et de l'Université Paris-Saclay,
préparée au Commissariat à l'énergie atomique et aux énergies alternatives

Ecole doctorale n576
Particules, Hadrons, Energie, Noyau, Instrumentation, Imagerie, Cosmos et Simulation (PHENIICS)
Specialite de doctorat: Physique des particules

Thèse présentée et soutenue à Naples de soutenance, le 15 Janvier 2018, par

Ciro Riccio

Composition du Jury :

Giovanni la Rana, Professeur, Université de Naples Federico II	Président
Vincenzo Berardi, Professeur, Politecnique de Bari	Rapporteur
Francesco Cappuzzello, Professeur, Université de Catania	Rapporteur
David Verney, Chercheur, Institut de Physique Nucléaire d'Orsay	Examinateur
Gianfranca de Rosa, Chercheur, Université de Naples Federico II	Directeur de thèse
Marco Zito, CEAE06, IRFU, CEA Saclay,	Directeur de thèse

Introduction

T2K (Tokai to Kamioka) is a long-baseline neutrino oscillation experiment installed in Japan and designed to measure neutrino flavor oscillations using an off-axis neutrino beam produced at the J-PARC accelerator facility in Tokai, on the east cost of Japan. The neutrino beam travels toward the far detector Super-Kamiokande, located in the Mozumi mine, 295 km far from the neutrino production point. A near detector complex is located 280 m far from the beam target and it is used to measure the unoscillated flux and the neutrino cross-sections. The near detector complex consist of two detectors: one on the same axis of the beam, called INGRID and the other off-axis, called ND280. Since its discovery of electron neutrino appearance in 2013 excluding $\theta_{13} = 0$ with a significance of 7.3σ, T2K has switched its beam magnet polarities to run in antineutrino beam mode in order to enhance its sensitivity to the charge-parity violation in the leptonic sector. The beam is dominated by muon antineutrinos, but it also contains a sizeable contamination of muon neutrinos. The analysis of both neutrino and antineutrino charged-current interactions in the off-axis near detector ND280, provides a significant reduction of the flux prediction and cross-section modelling systematic uncertainties in the oscillation analysis. ND280 data also gives us the opportunity to measure antineutrino cross-sections at the energy around 600 MeV.

Information on (anti)neutrino scattering is vital for the interpretation of neutrino oscillation. Many theoretical models have been developed to describe the nuclear effects in (anti)neutrino scattering, but a consistent picture has yet to emerge. In particular, various measurements of charged-current cross-section without production of pions in the final state have suggested the presence of another channel where neutrinos interact with pairs of correlated nucleons and more than one nucleon is knocked-out from the nucleus (multinucleon knock out). Various models have proposed different estimations of such process and a precise and unambiguous measurement is not yet available.

This thesis work is focused on three different arguments. First the selections of CC interactions of muon neutrinos in antineutrino beam in the off-axis near detector. In a first iteration this sample has been divided into two sub-sample based on the track multiplicity, then with more statistic a separation into three sub-samples based on the pion content in

each event was possible. The second argument is the simultaneous measurement of the double-differential muon neutrino and antineutrino charged-current cross-section without pions in the final state using the off-axis near detector. The neutrino and antineutrino cross-sections will be simultaneously extracted as a function of muon momentum and angle with a likelihood fit, including proper estimation of the correlations, allowing the evaluation of the sum, difference and asymmetry between the two cross-sections. The sum isolates the axial-vector interference term of the cross-section, and the difference enhances the sensitivity to the multinucleon component. The asymmetry is a direct estimation on any possible bias due to mismodelling of (anti)neutrino interactions on the measurement of the CP violation phase in neutrino oscillation. The last topic concerns the proposal of the multi-PMT technology as detector for Hyper-Kamiokande, the upgrade of Super-Kamiokande, and the intermediate water Čerenkov proposed to study the neutrino flux at $\sim$1–2 km from the beam production point. A multi-PMT is a plastic sphere filled with 26 photomultiplier tube that could improve the efficiency of the Čerenkov detectors foreseen in the future.

This dissertation is organized in the following way: in Chapter 1 and Chapter 2 an introduction to neutrino oscillation physics and interaction is given to put in context the work, then in Chapter 3 the T2K experimental set-up is presented, Chapter 4 show the measurement of the intrinsic muon neutrino component in the antineutrino beam, in Chapter 5 the results of the measurement of muon neutrino and antineutrino cross sections without pions in the final state are discussed and in conclusion Chapter 6 is dedicated to the discussion of the future experiments, T2K phase two and Hyper-Kamiokande, and the multi-PMT proposal.

Résumé

T2K (Tokai to Kamioka) est une expérience d'oscillation de neutrinos muoniques sur une longue ligne de base, située au Japon. Elle est conçue pour mesurer le changement de saveur des neutrinos d'un faisceau produit à l'aide d'un accélérateur au laboratoire J-PARC de Tokai. Les détecteurs proche et lointain sont placés légèrement hors axe par rapport au faisceau. Depuis la découverte en 2013 de l'apparition de neutrinos électroniques excluant, T2K a inversé la polarité des cornes magnétiques intervenant dans la production du faisceau, afin de produire un faisceau d'antineutrinos et d'augmenter la sensibilité de l'expérience à la violation de la charge-parité dans le secteur leptonique. Le faisceau produit est alors dominé par les antineutrinos muoniques avec une composante mesurable de neutrinos muoniques. L'analyse simultanée, dans les données prises avec le faisceau de neutrinos et le faisceau d'antineutrinos, des interactions par courant chargé dans le détecteur proche ND280, permet de réduire l'impact sur les analyses d'oscillation des incertitudes liées au flux de (anti)neutrinos et à leur section efficace d'interaction. Les données de ND280 permettent également de mesurer les sections efficaces d'interaction des antineutrinos d'énergie proche de 600 MeV.

La bonne connaissance du processus d'interaction des (anti)neutrinos avec les noyaux atomiques est cruciale pour interpréter les résultats de l'expérience en termes d'oscillations. De nombreux modèles théoriques ont été développés pour décrire les effets nucléaires lors des interactions des (anti)neutrinos, mais une vison globale cohérente n'a pas encore émergé. En particulier, des mesures variées de section efficace d'interaction par courant chargé sans production de pion dans l'état final suggèrent la possibilité pour les neutrinos d'interagir avec des paires de nucléons corrélés, entrainant l'éjection de plus d'un nucleon hors du noyau (composante dite "multi-nucléon"). Divers modèles ont proposé des estimations différentes de ce processus et une mesure précise et sans ambiguité n'est pas encore disponible.

Ce travail de thèse se concentre sur trois études. La première détaille la sélection des interactions de neutrinos muoniques par courant chargé dans le détecteur proche hors axe. Dans un premier temps l'échantillon de données était divisé en deux selon le nombre de traces chargées de l'événement, puis l'accumulation de davantage de données a

permis la séparation de l'échantillon en trois lots selon le contenu en pions de l'événement. La seconde étude consiste en la mesure simultanée de la section efficace d'interaction des neutrinos et des antineutrinos muoniques par courant chargé, conduisant à un état final sans pion mesuré dans le détecteur ND280. Ces sections efficaces sont extraites en fonction de l'impulsion et de l'angle du muon issu de l'interaction, permettant ainsi d'évaluer la somme, la différence et l'asymétrie entre les sections efficaces des neutrinos et des antineutrinos. La somme permet d'isoler la composante d'interférence vecteur-axial de la section efficace, et la différence est sensible à la composante multi-nucléons. L'asymétrie permet d'estimer directement le biais éventuel sur la mesure de la phase de violation de CP dû à la modélisation des sections efficaces, dans l'analyse d'oscillation de neutrinos. La dernière partie de la thèse étudie la proposition d'utiliser la technologie dite de multi-PMT pour le detector Hyper-Kamiokande, version à plus grande échelle de Super-Kamiokande, ainsi que la possibilité d'étudier le flux de neutrinos avec un détecteur basé sur le rayonnement Cherenkov dans l'eau, et placé à environ 2 km de l'origine du faisceau de neutrinos. Un multi-PMT est une sphère de plastique contenant 26 tubes photomultiplicateurs, qui pourrait améliorer l'efficacité des futurs détecteurs basés sur le rayonnement Cherenkov dans l'eau.

Introduzione

T2K (Tokai to Kamioka) è un esperimento giapponese che studia il fenomeno delle oscillazione di neutrino usando un fascio di neutrini prodotto dal complesso di acceleratori di J-PARC, situato a Tokai. Il fascio di neutrini viaggia verso il rivelatore Super-Kamiokande, installato nella miniera di Mozumi a 295 km di distanza dal punto di produzione del fascio. Un complesso di rivelatori posizionati a 280 m studia le proprietà del fascio prima che il fenomeno di oscillazione abbia inizio. Tale complesso consiste di due rivelatori: uno sulla stessa direzione del fascio,chiamato INGRID, e l'altro situatio ad un angolo di 2.5° rispetto alla direzione del fascio, chiamato ND280. Dopo la scoperta del fenomeno di apparizione di neutrini elettotronici in un fascio di neutrini muorici nel 2013, che ha escluso un valore non nullo di uno dei parametri di oscillazione, θ_{13}, a 7.3σ, T2K ha cambiato la corrente dei focalizzatori degli adroni prodotti dalle collisioni di protoni con la targhetta di grafite, per prendere dati usando un fascio di antineutrini. Questa strategia permette di aumentare la sensitività dell'esperimento alla violazione della simmetria CP nel settore leptonico, misurando la differenza delle probabilità di oscillazione $\nu_\mu \to \nu_e$ e $\bar{\nu}_\mu \to \bar{\nu}_e$. Il fascio è dominato da antineutrini muonici, ma contiene anche una alta contaminazione di neutrini muonici. L'analisi delle interazioni di corrente carica prodotte da entrambe le componenti nel rivelatore vicino dell'esperimento T2K (ND280) permettono di ridurre le incertezze sistematiche legate al flusso e alla modellizzazione della sezione d'urto di neutrino. ND280 da anche la possibilità di misurare la sezione d'urto di (anti)neutrino ad energie intorno ad 1 GeV.

La conoscenza della diffusione di (anti)neutrino è vitale per una misura sempre più precisa dei parametri che governano il fenomeno delle oscillazioni. Molti modelli teorici sono stati sviluppati per descrivere gli effetti nucleari che entrano in gioco nella diffusione di neutrino nel caso in cui il bersaglio sia un nucleo più complesso, ma un quadro consistente non è ancora emerso. In particolare, varie misure di sezioni d'urto di corrente carica senza pioni nello stato finale suggeriscono la presenza di altri canali dove il neutrino interagisce con una coppia di nucleoni correlati e viene emesso più di un nucleone. Vari modelli hanno proposto differenti stime di questo tipo di processo, ma una misura precisa e non ambigua non è ancora disponibile.

Questo lavoro di tesi si focalizza su tre diversi argomenti. Prima viene discussa la selezione di interazioni di corrente carica prodotte dalla componente di neutrino muonico presente nel fascio di antineutrini. In una prima iterazione l'insieme delle interazioni di corrente carica selezionate sono state divise in due sottoinsiemi in base al numero di tracce: eventi con una traccia e eventi con più di una traccia nello stato finale. Successivamente, grazie ad un incremento della statistica, è stato possibile separare in tre l'insieme delle interazioni di corrente carica in base al numero di pioni nello stato finale.
Il secondo argomento trattato è la misura simultanea della sezione d'urto doppio differenziale dei processi di corrente carica senza pione nello stato finale prodotti da interazioni di neutrino e antineutrino muonico. Le sezioni d'urto sono estratte simultaneamente in funzione del momento e dell'angolo del muone usando un fit di likelihood e includendo le correlazione tra i neutrino e antineutrino, in modo da poter poi calcolare la somma, la differenza e l'asimmetria tra le due sezioni d'urto. La somma isola il termine di interferenza vettoriale-assiale della sezione d'urto e la differenza potrebbe aumentare la sensitività alla componente della sezione d'urto che prevede l'emissione di più di un nucleone. L'asimmetria è una stima diretta di ogni possibile bias dovuto ad una non corretta modellizzazione della sezione d'urto di neutrino.
L'ultimo argomento riguarda la proposta di utilizzare una sfera di materiale plastico riempita con un totale di 26 fotomoltiplicatori come rivelatore per i futuri rivelatori Čerenkov ad acqua legati al programma giapponese di studio del fenomeno delle oscillazioni di neutrino.

Contents

1 Neutrino physics and oscillation **1**
1.1 Neutrino in the Standard Model . . . 1
1.1.1 The neutrino mass problem . . . 4
1.1.2 The weak interaction . . . 5
1.2 Neutrino oscillations . . . 6
1.2.1 Neutrino oscillations in vacuum . . . 7
1.2.2 Oscillation in matter . . . 10
1.3 Neutrino oscillation experiments . . . 12
1.3.1 Solar neutrinos experiments . . . 13
1.3.2 Atmospheric neutrino experiments . . . 18
1.3.3 Reactor neutrino experiments . . . 21
1.3.4 Accelerator neutrino experiments . . . 22
1.4 Current knowledge of neutrino oscillation parameters . . . 26

2 Neutrino scattering **29**
2.1 Neutrino-nucleons scattering . . . 29
2.1.1 Charged-Current Quasi-Elastic scattering . . . 31
2.1.2 Resonant pion production . . . 33
2.1.3 Deep Inelastic scattering . . . 34
2.2 Neutrino-nucleus scattering . . . 35
2.2.1 Nuclear models . . . 36
2.2.2 Final State Interactions . . . 38
2.2.3 Neutrino-nucleus exclusive channels . . . 39
2.3 Neutrino event generators . . . 41
2.4 Experimental status of neutrino scattering . . . 45

3 T2K experimental setup **48**
3.1 Physics motivations . . . 49
3.2 The neutrino beam . . . 51
3.2.1 The J-PARC complex . . . 51
3.3 The neutrino beamline . . . 52

3.3.1 The Muon Monitor . . . 55
3.3.2 The off-axis straregy . . . 55
3.3.3 Neutrino flux prediction . . . 57
3.4 The near detector complex . . . 59
3.4.1 The on-axis detector . . . 59
3.4.2 The off-axis detector . . . 60
3.4.3 The magnet . . . 61
3.4.4 The Side Muon Range Detector . . . 62
3.4.5 The π^0 Detector . . . 63
3.4.6 The Time Projection Chambers . . . 64
3.4.7 The Fine-Grained Detector . . . 66
3.4.8 The Electromagnetic Calorimeter . . . 68
3.5 The far detector: Super-Kamiokande . . . 69

4 Measurement of the intrinsic muon neutrino component in the antineutrino beam 72
4.1 The data sets . . . 73
4.2 ν_μ CC event selection in $\bar{\nu}$-mode . . . 74
4.3 ν_μ CC Multiple track selection in $\bar{\nu}$-mode . . . 80
4.4 ν_μ CC Multiple pion selection in $\bar{\nu}$-mode . . . 83
4.5 Detector systematics . . . 90
4.6 Latest T2K oscillation results . . . 92
4.7 Conclusions and future outlook . . . 99

5 Measurement of muon neutrino and antineutrino cross sections without pions in the final state 100
5.1 Introduction . . . 100
5.2 Analysis Strategy . . . 102
5.2.1 Cross-section and signal definition . . . 102
5.2.2 Cross-section extraction method: binned likelihood fit . . . 103
5.3 Input for the cross sections extraction . . . 105
5.3.1 The data sets . . . 105
5.3.2 Event Selections . . . 106
5.3.3 Sidebands . . . 112
5.3.4 Analysis binning . . . 114
5.3.5 Efficiency . . . 120
5.3.6 Integrated flux . . . 121
5.3.7 Number of Targets . . . 122
5.4 Uncertainties evaluation . . . 125
5.4.1 Data statistical uncertainty . . . 126
5.4.2 Flux systematic uncertainty . . . 127
5.4.3 Detector systematic uncertainty . . . 130
5.4.4 Systematic uncertainty on number of targets . . . 134
5.4.5 Signal and background modelling systematic uncertainty . . . 135
5.4.6 Pion final state interaction systematic uncertainty . . . 139
5.4.7 Summary of all the uncertainties . . . 140

5.5 Fit results . . . 142
5.5.1 Fit results as function of reconstructed muon kinematics . . . 142
5.5.2 Cross section measurements . . . 142
5.6 Conclusions and future outlook . . . 164

6 Future perspectives: T2K-II and Hyper-Kamiokande 165
6.1 T2K phase II . . . 166
6.1.1 Beamline Upgrade . . . 166
6.1.2 Near Detector plan . . . 166
6.1.3 T2K-II expected physics outcomes . . . 169
6.2 Hyper-Kamiokande . . . 174
6.3 Physics capabilities . . . 175
6.4 Multi-PMT optical module . . . 178
6.4.1 The Multi-PMT Reference Design . . . 179
6.4.2 The mPMT Prototype . . . 180
6.5 Conclusions and future outlook . . . 183

Conclusions 185

Acknowledgments 187

Appendices 188

A Two neutrino mixing 189

B Oscillation in matter 191

C Fit validation 194
C.0.1 Pull studies . . . 194
C.0.2 Bias study . . . 197
C.0.3 Fake data studies . . . 197

List of Figures

1.1 A graphical representation of the Standard Model particles and interaction mediators along with their properties. The numbers in the green, red and orange boxes beside the particle symbols indicate the corresponding charges under the gauge group: electric charge, colour and isospin respectively. 2

1.2 Feynman diagram of (anti)neutrino interaction vertex in the case of CC (left) and NC (right) interactions. In then first case the outgoing lepton is positive if the interaction involve antineutrino or is negative in the other case. The exchanged W boson in negative antineutrino interaction. 6

1.3 The two possible neutrino mass hierarchies. The colours represent the approximate flavour admixtures present in each mass eigenstate. In the normal case, the masses exhibit a hierarchical pattern, and the lightest neutrino has the largest admixture of electron flavour. Figure taken from [35]. 10

1.4 Feynman diagrams of the CC (left) and NC (right) elastic scattering processes in matter. 10

1.5 The left figure shows the three principal cycles comprising the pp-chain (ppI, ppII, and ppIII), the associated neutrinos that tag each of the three branches, and the theoretical branching percentages. The right figure shows the CNO cycle. Figure taken from [43]. 14

1.6 Solar neutrino spectrum along with the SSM uncertainties. Units for continuous spectra are $cm^{-2}s^{-1}MeV^{-}1$. Figure taken from [44]. 15

1.7 Schematic overview of the SNO experiment. Figure taken from [29]. . . 18

1.8 Schematic overview of the SK experiment. Figure taken from [29]. . . . 19

1.9 Zenith angle distributions of μ-like and e-like events for sub-GeV and multi-GeV data sets. Upward-going particles have $\cos\Theta < 0$ and downward-going particles have $\cos\Theta > 0$. The hatched region shows the Monte Carlo expectation for no oscillations. The bold line is the best-fit expectation for $\nu_\mu \leftrightarrow \nu_\tau$ oscillations with the overall flux normalization fitted as a free parameter. Figure taken from [26]. 20

1.10 Ratio of measured neutrinos over expected $\bar{\nu}_e$ versus the distance of different reactor antineutrino experiments. The solid dot is the KamLAND point plotted at a flux-weighted average distance (the dot size is indicative of the spread in reactor distances). The shaded region indicates the range of flux predictions corresponding to the 95% C.L. LMA region found in a global analysis of the solar neutrino data. The dotted curve corresponds to $\sin^2 2\theta = 0.883$ and $\Delta m^2 = 5.5 \times 10^{-5}\, eV^2$ and is representative of recent best-fit LMA predictions while the dashed curve shows the case of small mixing angles (or no oscillation). Figure taken from [82]. 23

1.11 Regions of δ_{CP} versus $\sin^2\theta_{23}$ parameter space consistent with the observed spectrum of ν_e candidates and the ν_μ disappearance data. The top panel corresponds to normal mass hierarchy and the bottom panel to inverted hierarchy. The color intensity indicates the confidence level at which particular parameter combinations are allowed. Figure taken from [98]. 26

1.12 Feldman-Cousins significance at which each value of δ_{CP} is disfavoured for each of the four possible combinations of mass hierarchy: normal (blue) or inverted (red), and θ_{23} octant: lower (solid) or upper (dashed), by the combination of ν_e appearance and ν_μ disappearance measurement. Figure taken from [98]. 26

1.13 Global 3ν oscillation analysis. Projections of the χ^2 function onto the parameters δm^2, $|\Delta m^2|$, $\sin^2\theta_{ij}$, and δ, for NO (blue) and IO (red). In each panel, all the undisplayed parameters are marginalized, and the offset $\Delta\chi^2_{\mathrm{IO-NO}} = 3.6$ is included. Figure taken from [101]. 28

2.1 Feynman diagram of CC neutrino (left) and antineutrino (right) interaction. 30

2.2 Feynman diagram of CCQE neutrino (left) and antineutrino (right) interaction. 32

2.3 Feynman diagram of one of the possible CC RES neutrino (left) and antineutrino (right) interaction. 33

2.4 Feynman diagram of CC DIS neutrino (left) and antineutrino (right) interaction. 34

2.5 Sketch of the proton and neutron potentials and states in the Fermi gas model (B′ stands for the binding energy). Figure taken from [118]. . . . 36

2.6 Probability distribution for initial state nucleon as a function of the magnitude of the nucleon momentum in SF model. Figure taken from [121]. 37

2.7 Schematic representation of the IA, in which the nuclear cross section is replaced by the incoherent sum of cross sections describing scattering off individual nucleons, with the recoiling (A-1)–nucleon system acting as a spectator. Figure taken from [122]. 38

2.8 Schematic representation of the possible pion FSI interaction in the nuclear matter. 38

2.9 Flux-unfolded MiniBooNE ν_μ CCQE cross section per neutron as a function of neutrino energy. In (a), shape errors are shown as shaded boxes along with the total errors as bars. In (b), a larger energy range is shown along with results from the LSND [132] and NOMAD [131] experiments. The prediction has been obtained using the RFG model with two different value for the axial mass M_A. Figure taken from [130]. . . . 40

2.10 Pictorial representation of a genuine CCQE (left) and 2p2h (right) process. 40

2.11 Inclusive cross section for scattering of electrons on carbon at 560 MeV and 60 Deg ($Q^2 = 0.24\,GeV^2$ at the QE peak), obtained with a free Δ spectral function. The left dashed curve gives the contribution from true QE scattering, the dash-dotted curve that from 2p-2h processes, the dashed-dotted-dotted curve that from Δ excitation and the dotted curve that from pion background terms. Figure taken from from [135]. . 41

2.12 MiniBooNE flux-integrated CCQE-like ν_μ-^{12}C double differential cross section per neutron for several values of muon kinetic energy as a function of the scattering angle. Dashed curve: pure CCQE cross section calculated using RPA correction; solid curve: with the inclusion of np-nh component. The figure is taken from [136]. 41

2.13 Double-differential cross section as function of the available energy and the 3-momentum transfer compared to the GENIE model with reduced pion production (small dot line), the same with RPA suppression (long-dashed), and then combined with a QE-like 2p2h component (solid). The 2p2h component is shown separately as a shaded region. Figure taken from [154]. 46

2.14 Results of CC-0π measurement from T2K compared with the Martini and Nieves models (top raw) and with the model from Martini with and without 2p2h contribution (bottom raw). Figures taken from [155] . . . 47

2.15 T2K measurement of CC1π^+ cross section as a function of pion momentum (left) and angle (right), compared to NEUT and GENIE simulation. Figure taken from [158]. 47

3.1 A schematic of a neutrino journey from the neutrino beamline at J-PARC, through the near detectors which are used to determine the properties of the neutrino beam before the oscillation, to Super-Kamiokande located 295 km west of the beam source, 1000 m deep underground. . . 48

3.2 Muon neutrino (left) and antineutrino (right) CC cross-section measurements and predictions as a function of neutrino or antineutrino energy. Data are from different experiment and are represented by different colours and marker symbols. The dominant contributing process at the T2K peak energy is CCQE (dashed) scattering, with contributions from RES (dot-dashed) and DIS (dotted) in the high-energy tail of the neutrino spectrum. Figure taken from [102]. 49
3.3 Oscillation probabilities as a function of the neutrino energy for $\nu_\mu \to \nu_e$ (left) and $\bar{\nu}_\mu \to \bar{\nu}_e$ (right) transitions with L=295 km and $\sin^2 2\theta_{13} = 0.1$. Black, red, green, and blue lines correspond to $\delta_{CP} = 0, \frac{1}{2}\pi, \pi$, and $-\frac{1}{2}\pi$, respectively. Solid (dashed) line represents the case for a normal (inverted) mass hierarchy. Figure taken from [160]. 50
3.4 The difference between the energy reconstructed at T2K assuming CCQE kinematics and the true energy for events with no pions in the final state. Black are the NEUT simulation of CCQE events and red are the NEUT simulation of resonant production where the Δ is absorbed. The blue is the from the two-body current calculation of Nieves model. Figure taken from [160]. 51
3.5 Overview of the J-PARC accelerators. 52
3.6 Overview of the T2K beamlines. Figure taken from [159]. 53
3.7 Side view of the secondary beamline. The length of the decay volume is $\sim$96 m. Figure taken from [159]. 53
3.8 The T2K target station. 54
3.9 Schematic representation of the off-axis configuration. 55
3.10 Muon neutrino disappearance (top figure) and electron neutrino appearance (middle figure) probability at 295 km compared to the neutrino fluxes for different off-axis angles. The neutrino beam at SK has a peak energy at about 0.6 GeV maximizing the effect of the neutrino oscillations at 295 km. 56
3.11 Expected neutrino energy as a function of the parent pion energy for different values of the off-axis angle. 57
3.12 INGRID on-axis detector. Figure taken from [159]. 60
3.13 The left image shows the tracking planes (blue) and iron plates of an INGRID module. The image in the middle shows veto planes in black of an INGRID module. The image on the right shows the proton module which is similar to the INGRID modules, but with finer grain scintillator and without the iron plates. Figure taken from [159]. 60
3.14 A schematic view of the ND280 off-axis detector. 61
3.15 Event display of a muon track entering via the front face of the PØD detector, continuing to the TPCs and FGDs and producing secondary particles on the way. The secondary particles are then stopped in the ECal detectors. 61
3.16 View of SMRD scintillator counter components prior to assembly. Figure taken from [159]. 63

3.17 A schematic view of the pi-zero detector. The beam is coming from the left and going right. Insets show details of the Water Target super-PØDule layers and Central ECal layers. Figure taken from [159]. 64
3.18 Simplified cut-away drawing showing the main aspects of the TPC design. The outer dimensions of the TPC are approximately 2.3×2.4×1.0 m^3. Figure taken from [171]. 65
3.19 Distribution of the energy loss as a function of the momentum for negatively (left) and positively (right) charged particles produced in neutrino interactions, compared to the expected curves for muons, electrons, protons, and pions. Figure taken from [171]. 66
3.20 View of an FGD with the front cover removed. XY scintillator modules (green) hang perpendicular to the direction of the neutrino beam. Along the top, six mini-crates with electronics can be seen without their cooling lines, while on the right side the cooling lids covering the mini-crates are shown. Figure taken from [159]. 67
3.21 Reconstructed energy depositions as a function of the track lenght for muons, pions and protons in FGD1 (left) and FGD2 (right). 68
3.22 External view of one ECal module. The scintillator bars run horizontally inside the module as shown. The readout electronics, signal and power cables, and cooling pipes can be seen mounted on the aluminium plates on the sides of the module. The gray surface at the top is the carbon fiber sandwich front plate, which in the final module position is facing towards the inner subdetectors (PØD, FGDs and TPCs). Figure taken from [159]. 69
3.23 Diagram of the Super-Kamiokande Detector. It is mainly comprised of two segments, the inner and outer detectors. The boundary between the two segments is defined by a cylindrical scaffold used to mount photomultiplier tubes and optically separate the segments. Figure taken from [159]. 70
3.24 Example of reconstructed T2K events in Super-Kamiokande for (a) a muon-like ring and (b) an electron-like ring. Each colored point represents a PMT, with the color corresponding to the amount of charge, and the reconstructed cone is shown as a white line. The second figure in the upper right corner shows the same hit map for the OD. The white crosses indicate the location of the reconstructed vertex. 71

4.1 The T2K unoscillated flux prediction at ND280 (top) and SK (bottom) for neutrino (left) and antineutrino (right) modes. 73
4.2 Schematic view of the FGD1 (left) and FGD2 (right) FV. 75
4.3 MIP likelihood on the left and muon likelihood on the right. The arrows indicate the cut used. Different colours indicate different final state particles. 77
4.4 Muon likelihood versus the reconstructed muon momentum. Different colours indicate different final state particles following the same legend of Fig. 4.3. 77

4.5 Distribution of events with vertex in **FGD1 FV** as function of the reconstructed muon momentum (left) and scattering angle (right) for the **CC-Inclusive** sample. Different colours indicate different particle. MC is scaled to POT in data. 79
4.6 Distribution of events with vertex in **FGD2 FV** as function of the reconstructed muon momentum (left) and scattering angle (right) for the **CC-Inclusive** sample. Different colours indicate different particle. MC is scaled to POT in data. 79
4.7 Distribution of events with vertex in **FGD1 FV** as function of the reconstructed muon momentum (left) and scattering angle (right) for the **CC-1-Track** sample. Different colours indicate different topologies. MC is scaled to POT in data. 81
4.8 Distribution of events with vertex in **FGD1 FV** as function of the reconstructed muon momentum (left) and scattering angle (right) for the **CC-N-Tracks** sample. Different colours indicate different topologies. MC is scaled to POT in data. 81
4.9 Distribution of events with vertex in **FGD2 FV** as function of the reconstructed muon momentum (left) and scattering angle (right) for the **CC-1-Track** sample. Different colours indicate different topologies. MC is scaled to POT in data. 82
4.10 Distribution of events with vertex in **FGD2 FV** as function of the reconstructed muon momentum (left) and scattering angle (right) for the **CC-N-Tracks** sample. Different colours indicate different topologies. MC is scaled to POT in data. 82
4.11 Number of Michel electron in **CC-Inclusive** sample for events with reconstructed vertex in **FGD1 FV** (top left) and **FGD2 FV** (top right). On the bottom the same figures zoomed to better display events with more than one Michel electron. Colors indicate different topologies. The MC is normalized to the POT in data. 84
4.12 Distribution of events with vertex in **FGD1 FV** as function of the reconstructed muon momentum (left) and scattering angle (right) for the **CC-0π-like** sample. Different colours indicate different topologies. MC is scaled to POT in data. 85
4.13 Distribution of events with vertex in **FGD1 FV** as function of the reconstructed muon momentum (left) and scattering angle (right) for the **CC-1π^+-like** sample. Different colours indicate different topologies. MC is scaled to POT in data. 86
4.14 Distribution of events with vertex in **FGD1 FV** as function of the reconstructed muon momentum (left) and scattering angle (right) for the **CC-Other-like** sample. Different colours indicate different topologies. MC is scaled to POT in data. 86
4.15 Distribution of events with vertex in **FGD2 FV** as function of the reconstructed muon momentum (left) and scattering angle (right) for the **CC-0π-like** sample. Different colours indicate different topologies. MC is scaled to POT in data. 86

4.16 Distribution of events with vertex in **FGD2 FV** as function of the reconstructed muon momentum (left) and scattering angle (right) for the **CC-1π^+-like** sample. Different colours indicate different topologies. MC is scaled to POT in data. 87

4.17 Distribution of events with vertex in **FGD2 FV** as function of the reconstructed muon momentum (left) and scattering angle (right) for the **CC-Other-like** sample. Different colours indicate different topologies. MC is scaled to POT in data. 87

4.18 The SK flux parameters for the ν_μ (top left) in ν-mode, $\bar{\nu}_\mu$ (top right) and ν_μ (bottom) in $\bar{\nu}$-mode, shown as a fraction of the nominal value. The bands indicate the 1σ uncertainty on the parameters before (solid, red) and after (hatched, blue) the near detector fit. Figure taken from [176]. 94

4.19 Cross-section parameters before (solid, red) and after (hatched, blue) the near detector fit, shown as a fraction of the nominal value. The colored band shows the 1σ uncertainty. Figure taken from [176]. 94

4.20 Total error envelopes for the reconstructed energy distributions of ν_μ CC (left) and ν_e CC (right) candidate events, using typical oscillation parameter values, with and without the ND280 constraint applied. . . . 96

4.21 Contours in the $\sin^2\theta_{13}$–δ_{CP} plane using T2K-only data, obtained by analysing either the ν- or $\bar{\nu}$-mode appearance datasets which are compared for both orderings. The yellow band corresponds to the reactor value on $\sin^2\theta_{13}$ from the PDG 2015 [182]. Figure taken from [176]. . . 97

4.22 Comparison of two-dimensional constant $\Delta\chi^2$ contours in the δ_{CP}–$\sin^2\theta_{13}$ plane using T2K data with the reactor constraint, for both four-sample (red) and five-sample (black) analyses with normal (left) and inverted (right) mass ordering hypotheses. The contours are produced by marginalizing the likelihood with respect to all parameters other than the parameters of interest. Figure taken from [176]. 98

4.23 One dimensional $\Delta\chi^2$ surfaces for δ_{CP} using T2K data with the reactor constraint. The critical $\Delta\chi^2$ values obtained with the Feldman-Cousins method are used to evaluate the 90% confidence level. Figure taken from [176]. 98

5.1 On the left: ν_μ (upper panel) and $\bar{\nu}_\mu$ (lower panel) - ^{12}C CCQE per neutron and per proton with and without the multinucleon component as a function of neutrino energy. The experimental points are taken from [184]. On the right: ratio of multinucleon component of CCQE cross section on ^{12}C to the single nucleon one for ν_μ and $\bar{\nu}_\mu$ as a function of neutrino energy. Both figures are taken from [188]. 101

5.2 Distribution of ν_μ events in the different signal regions as function of the reconstructed muon momentum (left column) and scattering angle (right column). Different colors indicate different topologies. The legend show also the purity for each true topology. 108

5.3 Distribution of $\bar{\nu}_\mu$ events in the different signal regions as function of the reconstructed muon momentum (left column) and scattering angle (right column). Different colors indicate different topologies. The MC is normalized for POT in data. The legend show also the purity for each true topology. 111
5.4 Distribution of ν_μ events in the different sideband regions as function of the reconstructed muon momentum (left column) and scattering angle (right column) for the CC-1π^+-like (top row) and CC-Other-like (bottom row) samples. Different colors indicate different topologies. The MC is normalized for POT in data. The legend show also the purity for each true topology. 112
5.5 Distribution of $\bar{\nu}_\mu$ events in the different sideband regions as function of the reconstructed muon momentum (left column) and scattering angle (right column) for the CC-1π^--like (top row) and CC-Other-like (bottom row) samples. Different colors indicate different topologies. The MC is normalized for POT in data. The legend show also the purity for each true topology. 113
5.6 Cosine theta resolution for each bin for ν_μ (left) $\bar{\nu}_\mu$ (right) CC-0π events. 115
5.7 Transfer matrix (left) and normalized transfer matrix (right) for angular bins obtained from nominal MC summing the contribution from all the samples for ν_μ CC-0π events. Each row/column corresponds to an angular bin going from $0 = [-1, 0.2]$ to $7 = [0.98, 1]$. 115
5.8 Transfer matrix (left) and normalized transfer matrix (right) for angular bins obtained from nominal MC summing the contribution from all the samples for $\bar{\nu}_\mu$ CC-0π events. Each row/column corresponds to an angular bin going from $0 = [-1, 0.2]$ to $7 = [0.98, 1]$. 116
5.9 Momentum resolution for each true angular and momentum bin for ν_μ CC-0π events. 117
5.10 Momentum resolution for each true angular and momentum bin for $\bar{\nu}_\mu$ CC-0π events. 117
5.11 Transfer matrix (left) and normalized transfer matrix (right) for angular bins obtained from nominal MC summing the contribution from all the samples for ν_μ CC-0π events. Dashed lines indicate the angular boundaries. Each row/column corresponds to a bin going from $0 = [-1 \leqslant \cos\theta_\mu^{\text{true}} \leqslant 0.2,\ 0\,GeV/c \leqslant p_\mu^{\text{true}} \leqslant 30\,GeV/c]$ to $57 = [0.98 \leqslant \cos\theta_\mu^{\text{true}} \leqslant 1,\ 0\,GeV/c \leqslant p_\mu^{\text{true}} \leqslant 30\,GeV/c]$. 118
5.12 Transfer matrix (left) and normalized transfer matrix (right) for angular bins obtained from nominal MC summing the contribution from all the samples for $\bar{\nu}_\mu$ CC-0π events. Dashed lines indicate the angular boundaries. Each row/column corresponds to a bin going from $0 = [-1 \leqslant \cos\theta_\mu^{\text{true}} \leqslant 0.2,\ 0\,GeV/c \leqslant p_\mu^{\text{true}} \leqslant 30\,GeV/c]$ to $57 = [0.98 \leqslant \cos\theta_\mu^{\text{true}} \leqslant 1,\ 0\,GeV/c \leqslant p_\mu^{\text{true}} \leqslant 30\,GeV/c]$. 118
5.13 True (solid line) and reconstructed (dots) signal and background of the ν_μ sample as function of the muon kinematics using the optimized binning. The bin entries are not divided by the bin width. 119

5.14 True (solid line) and reconstructed (dots) signal and background of the $\bar{\nu}_\mu$ sample as function of the muon kinematics using the optimized binning. The bin entries are not divided by the bin width. 119

5.15 Efficiency versus the true muon momentum (left) and true muon cosine theta (right) for ν_μ CC-0π events. The different colours show the efficiency for each signal region. 120

5.16 Efficiency versus the true muon momentum (left) and true muon cosine theta (right) for $\bar{\nu}_\mu$ CC-0π events. The different colours show the efficiency for each signal region. 121

5.17 Efficiency as function of the double differential binning reported in Tab. XXIII. 121

5.18 FGD1 fiducial volume definition in orange used for this analysis on the top, and scintillator layers scheme on the bottom. Picture taken from [192]. 124

5.19 Relative uncertainty due to data statistics for ν_μ (red) and $\bar{\nu}_\mu$ (dark cyan) CC-0π cross section in bins of true muon kinematics. 126

5.20 Flux covariance (left) and correlation (right) matrices. The bin number correspond to the parameter number in Tab. XXVI. 127

5.21 Relative uncertainty due to flux systematic for ν_μ (red) and $\bar{\nu}_\mu$ (dark cyan) CC-0π cross section in bins of true muon kinematics. Solid line show the fractional uncertainty when the detector parameter are fitted, while the dashed line when they are not fitted. 129

5.22 Relative uncertainty due to flux systematic for ν_μ (red) and $\bar{\nu}_\mu$ (dark cyan) CC-0π cross section in bins of true muon kinematics. 129

5.23 Normalized detector covariance (left) and correlation (right) matrix according to the binning used for the cross section extraction reported in Tab. XXIII. Each bin represents the relative uncertainty in the number of selected events in bins of reconstructed muon kinematics. The dotted lines divided the contribution from each samples, which is, going from left to the right: ν_μ signal region, the first and second ν_μ sideband, the $\bar{\nu}_\mu$ signal region and the two $\bar{\nu}_\mu$ sideband. The bins within each sample are ordered in increasing momentum intervals, each containing all angular bins from $0 = [-1 \leqslant \cos\,\theta_\mu^{\text{true}} \leqslant 0.2,\ 0\,GeV/c \leqslant p_\mu^{\text{true}} \leqslant 30\,GeV/c]$ to $57 = [0.98 \leqslant \cos\,\theta_\mu^{\text{true}} \leqslant 1,\ 0\,GeV/c \leqslant p_\mu^{\text{true}} \leqslant 30\,GeV/c]$. 130

5.24 Normalized detector covariance (left) and correlation (right) matrix according to the averaged binning reported in Tab. XXVII. Each bin represents the relative uncertainty in the number of selected events in bins of reconstructed muon kinematics. The dotted lines divided the contribution from each samples, which is, going from left to the right: ν_μ signal region, the first and second ν_μ sideband, the $\bar{\nu}_\mu$ signal region and the two $\bar{\nu}_\mu$ sidebands. The bins within each sample are ordered in increasing momentum intervals, each containing all angular bins from $0 = [-1 \leqslant \cos\,\theta_\mu^{\text{true}} \leqslant 0.2,\ 0\,GeV/c \leqslant p_\mu^{\text{true}} \leqslant 30\,GeV/c]$ to $57 = [0.98 \leqslant \cos\,\theta_\mu^{\text{true}} \leqslant 1,\ 0\,GeV/c \leqslant p_\mu^{\text{true}} \leqslant 30\,GeV/c]$. 131

5.25 Relative uncertainty due to detector systematic for ν_μ (red) and $\bar{\nu}_\mu$ (dark cyan) CC-0π cross section in bins of true muon kinematics. Solid line show the fractional uncertainty when the detector parameter are fitted, while the dashed line when they are not fitted. 132

5.26 Relative uncertainty due to detector systematic for ν_μ (red) and $\bar{\nu}_\mu$ (dark cyan) CC-0π cross section in bins of true muon kinematics. 133

5.27 Covariance matrix of the elements composing FGD1. 134

5.28 Number of targets for 10^4 toys. The distribution is produced varying the areal density of the elements composing the FGD1 fiducial volume following the covariance matrix from Fig. 5.27. 135

5.29 Covariance matrix of the signal and background modelling. The bin number correspond to the order in Tab. XXVIII. The displayed values are the uncertainties divided by the means. 136

5.30 Relative uncertainty due to signal modelling systematic for ν_μ (red) and $\bar{\nu}_\mu$ (dark cyan) CC-0π cross section in bins of true muon kinematics. . . 138

5.31 Relative uncertainty due to background modelling systematic for ν_μ (red) and $\bar{\nu}_\mu$ (dark cyan) CC-0π cross section in bins of true muon kinematics. 138

5.32 Pion FSI covariance matrix.The bin number correspond to the order in Tab. XXIX. The displayed values are the uncertainties divided by the means and the off-diagonal terms reflect the correlations between the different parameters. 139

5.33 Relative uncertainty due to pion FSI modelling systematic for ν_μ (red) and $\bar{\nu}_\mu$ (dark cyan) CC-0π cross section in bins of true muon kinematics. 140

5.34 Summary of all the uncertainties on the ν_μ CC-0π cross section in bins of true muon kinematics. 141

5.35 Summary of all the uncertainties on the $\bar{\nu}_\mu$ CC-0π cross section in bins of true muon kinematics. 141

5.36 $\bar{\nu}_\mu$ CC-0π number of events as a function of reconstructed muon kinematics. The red solid lines shown the fit results with systematics uncertainties, the dots shows the data with statistical uncertainties, finally the blue dotted line show the nominal NEUT MC used as prior in the fit. 143

5.37 ν_μ CC-0π number of events as a function of reconstructed muon kinematics. The red solid lines shown the fit results with systematics uncertainties, the dots shows the data with statistical uncertainties, finally the blue dotted line show the nominal NEUT MC used as prior in the fit. 144

5.38 Distribution of ν_μ events in the different sideband regions as function of the reconstructed muon momentum (left column) and scattering angle (right column) for the CC-1π^+-like (top row) and CC-Other-like (bottom row) samples. The legend is the same as in Fig. 5.36: the red solid lines shown the fit results with systematics uncertainties, the dots shows the data with statistical uncertainties, finally the blue dotted line show the nominal NEUT MC used as prior in the fit. 145

5.39 Distribution of $\bar{\nu}_\mu$ events in the different sideband regions as function of the reconstructed muon momentum (left column) and scattering angle (right column) for the CC-1π^--like (top row) and CC-Other-like (bottom row) samples. The legend is the same as in Fig. 5.36: the red solid lines shown the fit results with systematics uncertainties, the dots shows the data with statistical uncertainties, finally the blue dotted line show the nominal NEUT MC used as prior in the fit. 146

5.40 Measured $\bar{\nu}_\mu$ CC-0π cross section in bins of true muon kinematics with shape uncertainty (error band) and fully correlated normalization uncertainty (red band). The result is compared with the NEUT prediction for CC-0π (blue line), CC-0π without 2p2h (orange line), CCQE (pink line) and 2p2h (green line). The last bin, up to 30 GeV/c is not displayed. 149

5.41 Measured ν_μ CC-0π cross section in bins of true muon kinematics with shape uncertainty (error band) and fully correlated normalization uncertainty (red band).The result is compared with the NEUT prediction for CC-0π (blue line), CC-0π without 2p2h (orange line), CCQE (pink line) and 2p2h (green line). The last bin, up to 30 GeV/c is not displayed. 150

5.42 Measured cross sections sum in bins of true muon kinematics with shape uncertainty (error band) and fully correlated normalization uncertainty (red band). The result is compared with the NEUT prediction for CC-0π (blue line), CC-0π without 2p2h (orange line), CCQE (pink line) and 2p2h (green line). The last bin, up to 30 GeV/c is not displayed. 151

5.43 Measured cross sections difference in bins of true muon kinematics with shape uncertainty (error band) and fully correlated normalization uncertainty (red band). The result is compared with the NEUT prediction for CC-0π (blue line), CC-0π without 2p2h (orange line), CCQE (pink line) and 2p2h (green line). The last bin, up to 30 GeV/c is not displayed. 152

5.44 Measured cross sections asymmetry in bins of true muon kinematics with shape uncertainty (error band) and fully correlated normalization uncertainty (red band). The result is compared with the NEUT prediction for CC-0π (blue line), CC-0π without 2p2h (orange line), CCQE (pink line) and 2p2h (green line). The last bin, up to 30 GeV/c is not displayed. 153

5.45 Measured $\bar{\nu}_\mu$ CC-0π cross section in bins of true muon kinematics with shape uncertainty (error band) and fully correlated normalization uncertainty (red band). The result is compared with the CC-0π NEUT (blue line) and GENIE (dotted green line) prediction. The last bin, up to 30 GeV/c is not displayed. 154

5.46 Measured ν_μ CC-0π cross section in bins of true muon kinematics with shape uncertainty (error band) and fully correlated normalization uncertainty (red band). The result is compared with the CC-0π NEUT (blue line) and GENIE (dotted green line) prediction. The last bin, up to 30 GeV/c is not displayed. 155

5.47 Measured cross sections sum in bins of true muon kinematics with shape uncertainty (error band) and fully correlated normalization uncertainty (red band). The result is compared with the CC-0π NEUT (blue line) and GENIE (dotted green line) prediction. The last bin, up to 30 GeV/c is not displayed. 156

5.48 Measured cross sections difference in bins of true muon kinematics with shape uncertainty (error band) and fully correlated normalization uncertainty (red band). The result is compared with the CC-0π NEUT (blue line) and GENIE (dotted green line) prediction. The last bin, up to 30 GeV/c is not displayed. 157

5.49 Measured cross sections asymmetry in bins of true muon kinematics with shape uncertainty (error band) and fully correlated normalization uncertainty (red band). The result is compared with the CC-0π NEUT (blue line) and GENIE (dotted green line) prediction. The last bin, up to 30 GeV/c is not displayed. 158

5.50 Measured $\bar{\nu}_\mu$ CC-0π cross section in bins of true muon kinematics with shape uncertainty (error band) and fully correlated normalization uncertainty (red band). The result is compared with the model by Martini et al. without (blue dotted line) and with 2p2h (solid line) prediction. The first angle bin ($-1 < \cos\theta < 0.2$) and the last bin, up to 30 GeV/c, are not displayed. In the last angle bin the momentum bin between 3.0 and 5.0 GeV/c is not displayed, since the Martini model predicts the cross section up to 3 GeV/c. 159

5.51 Measured ν_μ CC-0π cross section in bins of true muon kinematics with shape uncertainty (error band) and fully correlated normalization uncertainty (red band). The result is compared with the Martini model without (blue dotted line) and with 2p2h (solid line) prediction. The first angle bin ($-1 < \cos\theta < 0.2$) and the last bin, up to 30 GeV/c, are not displayed. In the last angle bin the momentum bin between 3.0 and 5.0 GeV/c is not displayed, since the Martini model predicts the cross section up to 3 GeV/c. 160

5.52 Measured cross sections sum in bins of true muon kinematics with shape uncertainty (error band) and fully correlated normalization uncertainty (red band). The result is compared with the Martini model without (blue dotted line) and with 2p2h (solid line) prediction. The first angle bin ($-1 < \cos\theta < 0.2$) and the last bin, up to 30 GeV/c, are not displayed. In the last angle bin the momentum bin between 3.0 and 5.0 GeV/c is not displayed, since the Martini model predicts the cross section momentum up to 3 GeV/c. 161

5.53 Measured cross sections difference in bins of true muon kinematics with shape uncertainty (error band) and fully correlated normalization uncertainty (red band). The result is compared with the Martini model without (blue dotted line) and with 2p2h (solid line) prediction. The first angle bin ($-1 < \cos\theta < 0.2$) and the last bin, up to 30 GeV/c, are not displayed. In the last angle bin the momentum bin between 3.0 and 5.0 GeV/c is not displayed, since the Martini model predicts the cross section up to 3 GeV/c. 162

5.54 Measured cross sections asymmetry in bins of true muon kinematics with shape uncertainty (error band) and fully correlated normalization uncertainty (red band). The result is compared with the Martini model without (blue dotted line) and with 2p2h (solid line) prediction. The first angle bin ($-1 < \cos\theta < 0.2$) and the last bin, up to 30 GeV/c, are not displayed. In the last angle bin the momentum bin between 3.0 and 5.0 GeV/c is not displayed, since the Martini model predicts the cross section up to 3 GeV/c. 163

6.1 Beam power and POT accumulation plan as function of calendar year. . 166

6.2 A schematic view of the upgraded ND280 detector. In place of the PØD there is a target sandwiched between two horizontal TPCs. 167

6.3 A schematic view of the SuperFGD. 167

6.4 Schematic view of 3D grid-like structure of plastic scintillator bars inside the WAGASCI detector. Figure taken from [100]. 168

6.5 ν_e CC inclusive differential cross-sections as a function of p_e (left), $\cos\theta_e$ (right). The inner (outer) error bars show the statistical (total) uncertainty on the data. The dashed (solid) line shows the NEUT (GENIE) prediction. Overflow (underflow) bins are indicated by $>$ ($<$) labels, and are normalized to the width shown. 170

6.6 Distribution of CCQE and 2p2h contributions as a function of muon momentum in the angular range $\cos\theta = [0.7, 0.8]$ at ND280 (left) and Super-K (right) as predicted in the Martini (continuous line) and Nieves (histogram) models. 171

6.7 Sensitivity as a function of true δ_{CP} (left) and accumulated POT (right) with three values of $\sin^2\theta_{23}$ (0.43, 0.50, 0.60) and normal hierarchy. For the full T2K-II exposure of 20×10^{21} POT with a reduction of the systematic error to 2/3 of the present T2K uncertainties compared with the present sensitivity. Figure taken from [183]. 172

6.8 Expected 90% C.L. sensitivity to Δm^2_{32} and $\sin^2\theta_{23}$ with the current T2K systematic error. For the T2K-II exposure of 20×10^{21} POT, a 50% increase in effective statistics is assumed. Top left plot has been obtained with true $\sin^2\theta_{23} = 0.43$, top right with true $\sin^2\theta_{23} = 0.6$ and the plot on the bottom with true $\sin^2\theta_{23} = 0.5$. Figure taken from [183]. 173

6.9 Schematic view of one HK detector. Figure take from [100]. 174

6.10 Sensitivity to exclude $\sin\delta_{CP} = 0$ for normal mass hierarchy (left) and expected 68% C.L. uncertainty of δ_{CP} as a function of running time. . . 176

6.11 Neutrino oscillation sensitivities from combined analysis of atmospheric neutrino and accelerator data at HK. The left (middle) panel illustrates the expected hierarchy (octant) sensitivity as a function of true value of $\sin^2\theta_{23}$ for three exposures: 1 year (grey), 5 years (blue), 10 years (orange). Figure taken from [100]. 177

6.12 Multi-PMT conceptual drawing for IWCD with 7.7 cm PMTs as ID detectors and the OD detectors on the other half. Each small PMT has a reflector cone. An 50 cm acrylic covers on an aluminium cylinder is used as pressure vessel. Readout electronics and calibration sources are placed inside the vessel. 180

6.13 Transmittance (left) and reflectance (right) as function of the wavelength for different acrylics. 181

6.14 Preliminary design of the mPMT vessel with its cooling system in the equator of the sphere. 182

6.15 ADC output of one channel of CITIROC. Input signal of 1 Hz and voltage 5 mV. 183

6.16 A schematic view of the Multi-PMT design. 184

C.1 Mean and width of the pulls distributions defined in Eq. C.3 for the parameters of interest for neutrino on the left and antineutrino on the right. 195

C.2 Mean and width of the pulls distributions defined in Eq. C.4 for the flux (top left), background cross section modelling (top right) and pion FSI (bottom) parameters. 196

C.3 Mean of the bias ($p_{Fit} - p_{Thrown}$) for the flux (left), background cross section modelling (center) and pion FSI (right) parameters. 196

C.4 Mean of the bias distribution defined in Eq. C.5 generated by applying fluctuation due to either systematic and statistical uncertainties (left) or only systematics uncertainties (right). The legend indicates if the bias is computed for the neutrino or antineutrino sample. 197

C.5 Fractional bias in case of asimov fit for the ν_μ (left) and $\bar{\nu}_\mu$ CC-0π cross section (right) in bins of true muon kinematics. 198

C.6 ν_μ CC-0π cross section in bins of true muon kinematics obtained with an asimov fit with shape uncertainty (error band) and fully correlated normalization uncertainty (red band). The result is compared with the NEUT prediction for CC-0π (blue line), CCQE (pink line) and CCQE plus pion absorption(cyan line). The NEUT prediction for 2p2h is displayed as well. The last bin, up to 30 GeV/c, is not displayed. 199

C.7 $\bar{\nu}_\mu$ CC-0π cross section in bins of true muon kinematics obtained with an asimov fit with shape uncertainty (error band) and fully correlated normalization uncertainty (red band). The result is compared with the NEUT prediction for CC-0π (blue line), CCQE (pink line) and CCQE plus pion absorption(cyan line). The NEUT prediction for 2p2h is displayed as well. The last bin, up to 30 GeV/c, is not displayed. 200

C.8 Cross sections sum in bins of true muon kinematics obtained with an asimov fit with shape uncertainty (error band) and fully correlated normalization uncertainty (red band). The result is compared with the NEUT prediction for CC-0π (blue line), CCQE (pink line) and CCQE plus pion absorption(cyan line). The NEUT prediction for 2p2h is displayed as well. The last bin, up to 30 GeV/c, is not displayed. 201

C.9 Cross sections difference in bins of true muon kinematics obtained with an asimov fit with shape uncertainty (error band) and fully correlated normalization uncertainty (red band). The result is compared with the NEUT prediction for CC-0π (blue line), CCQE (pink line) and CCQE plus pion absorption(cyan line). The NEUT prediction for 2p2h is displayed as well. The last bin, up to 30 GeV/c, is not displayed. 202

C.10 Cross sections asymmetry in bins of true muon kinematics obtained with an asimov fit with shape uncertainty (error band) and fully correlated normalization uncertainty (red band). The result is compared with the NEUT prediction for CC-0π (blue line), CCQE (pink line) and CCQE plus pion absorption(cyan line). The NEUT prediction for 2p2h is displayed as well. The last bin, up to 30 GeV/c, is not displayed. . . . 203

C.11 Fractional bias between the result of the fit and the fake data for the ν_μ (left) and $\bar{\nu}_\mu$ CC-0π cross section (right) in bins of true muon kinematics. The fake data used is NUET with RFG+RPA as nuclear model and 2p2h increased by a factor of two. 204

C.12 $\bar{\nu}_\mu$ CC-0π cross section in bins of true muon kinematics obtained using NEUT prediction with RFG+RPA as nuclear model and 2p2h increased by a factor of two as fake data and NEUT as nominal. The result is compared with the nominal and fake data prediction. The error bars stand for the shape uncertainty while the red band are the fully correlated normalization uncertainty. The last bin, up to 30 GeV/c, is not displayed. 205

C.13 $\bar{\nu}_\mu$ CC-0π cross section in bins of true muon kinematics obtained using NEUT prediction with RFG+RPA as nuclear model and 2p2h increased by a factor of two as fake data and NEUT as nominal. The result is compared with the nominal and fake data prediction. The error bars stand for the shape uncertainty while the red band are the fully correlated normalization uncertainty. The last bin, up to 30 GeV/c, is not displayed. 206

C.14 Sum of the cross sections in bins of true muon kinematics obtained using NEUT prediction with RFG+RPA as nuclear model and the 2p2h component increased by a factor of two as fake data and NEUT as nominal. The result is compared with the nominal and fake data prediction. The error bars stand for the shape uncertainty while the red band are the fully correlated normalization uncertainty. The last bin, up to 30 GeV/c, is not displayed. 207

C.15 Difference of the cross sections in bins of true muon kinematics obtained using NEUT prediction with RFG+RPA as nuclear model and the 2p2h component increased by a factor of two as fake data and NEUT as nominal. The result is compared with the nominal and fake data prediction. The error bars stand for the shape uncertainty while the red band are the fully correlated normalization uncertainty. The last bin, up to 30 GeV/c, is not displayed. 208

C.16 Asymmetry of the cross sections in bins of true muon kinematics obtained using NEUT prediction with RFG+RPA as nuclear model and the 2p2h component increased by a factor of two as fake data and NEUT as nominal. The result is compared with the nominal and fake data prediction. The error bars stand for the shape uncertainty while the red band are the fully correlated normalization uncertainty. The last bin, up to 30 GeV/c, is not displayed. 209

C.17 Fractional bias between the result of the fit and the fake data for the ν_μ (left) and $\bar{\nu}_\mu$ CC-0π cross section (right) in bins of true muon kinematics. The fake data used is NEUT with 2p2h increased by a factor of two. . . 211

C.18 Fractional bias between the result of the fit and the fake data for the ν_μ (left) and $\bar{\nu}_\mu$ CC-0π cross section (right) in bins of true muon kinematics. The fake data used is NEUT prediction without 2p2h. 211

C.19 ν_μ CC-0π cross section in bins of true muon kinematics obtained using NEUT prediction with 2p2h increased by a factor of two as fake data and NEUT as nominal. The result is compared with the nominal and fake data prediction. The error bars stand for the shape uncertainty while the red band are the fully correlated normalization uncertainty. The last bin, up to 30 GeV/c, is not displayed. 212

C.20 $\bar{\nu}_\mu$ CC-0π cross section in bins of true muon kinematics obtained using NEUT prediction with 2p2h increased by a factor of two as fake data and NEUT as nominal. The result is compared with the nominal and fake data prediction. The error bars stand for the shape uncertainty while the red band are the fully correlated normalization uncertainty. The last bin, up to 30 GeV/c, is not displayed. 213

C.21 Sum of the cross sections in bins of true muon kinematics obtained using NEUT prediction with 2p2h increased by a factor of two as fake data and NEUT as nominal. The result is compared with the nominal and fake data prediction. The error bars stand for the shape uncertainty while the red band are the fully correlated normalization uncertainty. The last bin, up to 30 GeV/c, is not displayed. 214

C.22 Difference of the cross sections in bins of true muon kinematics obtained using NEUT prediction with 2p2h increased by a factor of two as fake data and NEUT as nominal. The result is compared with the nominal and fake data prediction. The error bars stand for the shape uncertainty while the red band are the fully correlated normalization uncertainty. The last bin, up to 30 GeV/c, is not displayed. 215

C.23 Asymmetry of the cross sections in bins of true muon kinematics obtained using NEUT prediction with 2p2h increased by a factor of two as fake data and NEUT as nominal. The result is compared with the nominal and fake data prediction. The error bars stand for the shape uncertainty while the red band are the fully correlated normalization uncertainty. The last bin, up to 30 GeV/c, is not displayed. 216
C.24 ν_μ CC-0π cross section in bins of true muon kinematics obtained using NEUT prediction without 2p2h as fake data and NEUT as nominal. The result is compared with the nominal and fake data prediction. The error bars stand for the shape uncertainty while the red band are the fully correlated normalization uncertainty. The last bin, up to 30 GeV/c, is not displayed. 217
C.25 $\bar{\nu}_\mu$ CC-0π cross section in bins of true muon kinematics obtained using NEUT prediction without 2p2h as fake data and NEUT as nominal. The result is compared with the nominal and fake data prediction. The error bars stand for the shape uncertainty while the red band are the fully correlated normalization uncertainty. The last bin, up to 30 GeV/c, is not displayed. 218
C.26 Sum of the cross sections in bins of true muon kinematics obtained using NEUT prediction without 2p2h as fake data and NEUT as nominal. The result is compared with the nominal and fake data prediction. The error bars stand for the shape uncertainty while the red band are the fully correlated normalization uncertainty. The last bin, up to 30 GeV/c, is not displayed. 219
C.27 Difference of the cross sections in bins of true muon kinematics obtained using NEUT prediction without 2p2h as fake data and NEUT as nominal. The result is compared with the nominal and fake data prediction. The error bars stand for the shape uncertainty while the red band are the fully correlated normalization uncertainty. The last bin, up to 30 GeV/c, is not displayed. 220
C.28 Asymmetry of the cross sections in bins of true muon kinematics obtained using NEUT prediction without 2p2h as fake data and NEUT as nominal. The result is compared with the nominal and fake data prediction. The error bars stand for the shape uncertainty while the red band are the fully correlated normalization uncertainty. The last bin, up to 30 GeV/c, is not displayed. 221
C.29 Fractional bias between the result of the fit and the fake data for the ν_μ (left) and $\bar{\nu}_\mu$ CC-0π cross section (right) in bins of true muon kinematics. The fake data used is NEUT prediction with a lower "wrong sign" component in the different beams. 222
C.30 ν_μ CC-0π cross section in bins of true muon kinematics obtained using NEUT prediction with a lower "wrong sign" component in the different beams as fake data and NEUT as nominal. The result is compared with the nominal and fake data prediction. The error bars stand for the shape uncertainty while the red band are the fully correlated normalization uncertainty. The last bin, up to 30 GeV/c, is not displayed. 223

C.31 $\bar{\nu}_\mu$ CC-0π cross section in bins of true muon kinematics obtained using NEUT prediction with a lower "wrong sign" component in the different beams as fake data and NEUT as nominal. The result is compared with the nominal and fake data prediction. The error bars stand for the shape uncertainty while the red band are the fully correlated normalization uncertainty. The last bin, up to 30 GeV/c, is not displayed. 224

C.32 Sum of the cross sections in bins of true muon kinematics obtained using NEUT prediction with a lower "wrong sign" component in the different beams as fake data and NEUT as nominal. The result is compared with the nominal and fake data prediction. The error bars stand for the shape uncertainty while the red band are the fully correlated normalization uncertainty. The last bin, up to 30 GeV/c, is not displayed. 225

C.33 Difference of the cross sections in bins of true muon kinematics obtained using NEUT prediction with a lower "wrong sign" component in the different beams as fake data and NEUT as nominal. The result is compared with the nominal and fake data prediction. The error bars stand for the shape uncertainty while the red band are the fully correlated normalization uncertainty. The last bin, up to 30 GeV/c, is not displayed. 226

C.34 Asymmetry of the cross sections in bins of true muon kinematics obtained using NEUT prediction with a lower "wrong sign" component in the different beams as fake data and NEUT as nominal. The result is compared with the nominal and fake data prediction. The error bars stand for the shape uncertainty while the red band are the fully correlated normalization uncertainty. The last bin, up to 30 GeV/c, is not displayed. 227

C.35 Fractional bias between the result of the fit and the fake data for the ν_μ (left) and $\bar{\nu}_\mu$ CC-0π cross section (right) in bins of true muon kinematics. The fake data used is NEUT prediction with biased background. 228

C.36 ν_μ CC-0π cross section in bins of true muon kinematics obtained using NEUT prediction with biased background as fake data and NEUT as nominal. The result is compared with the nominal and fake data prediction. The error bars stand for the shape uncertainty while the red band are the fully correlated normalization uncertainty. The last bin, up to 30 GeV/c, is not displayed. 229

C.37 $\bar{\nu}_\mu$ CC-0π cross section in bins of true muon kinematics obtained using NEUT prediction with biased background as fake data and NEUT as nominal. The result is compared with the nominal and fake data prediction. The error bars stand for the shape uncertainty while the red band are the fully correlated normalization uncertainty. The last bin, up to 30 GeV/c, is not displayed. 230

C.38 Sum of the cross sections in bins of true muon kinematics obtained using NEUT prediction with biased background as fake data and NEUT as nominal. The result is compared with the nominal and fake data prediction. The error bars stand for the shape uncertainty while the red band are the fully correlated normalization uncertainty. The last bin, up to 30 GeV/c, is not displayed. 231
C.39 Difference of the cross sections in bins of true muon kinematics obtained using NEUT prediction with biased background as fake data and NEUT as nominal. The result is compared with the nominal and fake data prediction. The error bars stand for the shape uncertainty while the red band are the fully correlated normalization uncertainty. The last bin, up to 30 GeV/c, is not displayed. 232
C.40 Asymmetry of the cross sections in bins of true muon kinematics obtained using NEUT prediction with biased background as fake data and NEUT as nominal. The result is compared with the nominal and fake data prediction. The error bars stand for the shape uncertainty while the red band are the fully correlated normalization uncertainty. The last bin, up to 30 GeV/c, is not displayed. 233

List of Tables

I Summary table of the types of neutrino oscillation experiments with their typical source-detector distance, energy and sensitivity to Δm^2. . . 14

II Results of the global 3ν oscillation analysis, in terms of best-fit values for the mass-mixing parameters and associated $n\sigma$ ranges ($n = 1, 2, 3$), defined by $\chi^2 - \chi^2_{\text{min}} = n^2$ with respect to the separate minima in each mass ordering (NO, IO) and to the absolute minimum in any ordering. Remind that Δm^2 is defined herein as $m^2_3 - (m^2_1 + m^2_2)/2$, and that δ is taken in the (cyclic) interval $\delta/\pi \in [0, 2]$. Table taken from [101]. 27

III Summary table of the models used in NEUT v5.3.2 and GENIE v2.8.0 to simulate the CC interactions. 44

IV List of the main design parameters of the MR accelerator for the proton fast extraction at J-PARC. 52

V Neutrino-producing decay modes considered in T2K neutrino flux prediction and their branching ratio in percentage. The same branching ratios are obtained for antineutrino by conjugating the charge. The π^-, K^- and μ^- modes are charge conjugates of the π^+, K^+ and μ^+ modes, respectively. 58

VI Fraction (in %) of neutrino mode flux for each final hadron in the interaction chain. 58

VII Fraction (in %) of antineutrino mode flux for each final hadron in the interaction chain. 59

VIII Flavour composition (in %) of ν and $\bar{\nu}$ beam. 59

IX T2K data-taking periods in antineutrino mode and the proton on target used in this analysis for data and MC. 74

X Summary table of the selection criteria applied in the ν_μ analysis. 78

XI MC composition (in %) in term of **particles type** which contribute to the selected ν_μ CC events with reconstructed vertex in **FGD1 FV** and **FGD2 FV**. 79

XII MC composition (in %) in term of **topologies** for the ν_μ **CC-1-Track** and **CC-N-Tracks** samples obtained selecting events with vertex in **FGD1 FV** and **FGD2 FV**. . . . 82
XIII MC composition (in %) in term of **topologies** for the ν_μ **CC-0π-like**, **CC-1π^+-like** and **CC-Other-like** samples obtained selecting CC events with vertex in **FGD1 FV** and **FGD2 FV**. . . . 88
XIV MC composition (in %) in term of **reactions** for the ν_μ **CC-0π-like**, **CC-1π^+-like** and **CC-Other-like** samples obtained selecting CC events with vertex in **FGD1 FV** and **FGD2 FV**. . . . 89
XV Summary of the systematic error source and the way they are propagated. 93
XVI Effect of 1σ variation of the systematic uncertainties on the predicted event rates of the ν-mode samples. . . . 95
XVII Effect of 1σ variation of the systematic uncertainties on the predicted event rates of the $\bar{\nu}$- mode samples. . . . 96
XVIII T2K data-taking periods and collected POT used in the last published oscillation analysis. . . . 97
XIX Best-fit results and the 68% confidence interval of the T2K data fit with the reactor constraint with normal and inverted hypotheses. Value taken from [176] . . . 97

XX T2K data-taking periods in ν-mode and the POT used in this analysis for data and MC. . . . 105
XXI T2K data-taking periods in $\bar{\nu}$-mode and the POT used in this analysis for data and MC. . . . 106
XXII Summary of the selection criteria. . . . 109
XXIII Binning used for the fit to the $p_\mu, \cos\theta_\mu$ distribution and for the definition of the data/MC corrections c_i. . . . 116
XXIV Thickness and density of each component in each layer of the FGD1. . . . 122
XXV Information used to compute the total number of nucleons for each element of the FGD1 FV. . . . 123
XXVI Binning used for the flux. . . . 128
XXVII Binning used for the fit of the nuisance parameters correcting for the detector systematics. . . . 131
XXVIII Cross-section modelling parameters used in this analysis along with their type, prior, uncertainty and validity range. . . . 136
XXIX Pion FSI parameters used in this analysis along with their type, prior, uncertainty and validity range. . . . 139

XXX Parameters of past (KamiokaNDE), running (SK), and future (HK) water Čerenkov detectors. Table taken form [100]. . . . 175

XXXI Summary table of the χ^2 GOF computed using the total covariance matrix (statistical and systematic uncertainties). . . . 198
XXXII Summary table of the χ^2 GOF computed using the total covariance matrix (statistical plus systematic uncertainties). The fake data tested is NEUT with RFG+RPA as nuclear model and 2p2h increased by a factor of two. . . . 204

XXXIII Summary table of the χ^2 GOF computed using the total covariance matrix (statistical plus systematic uncertainties). The fake data tested is NEUT with the double of 2p2h events. 210
XXXIV Summary table of the χ^2 GOF computed using the total covariance matrix (statistical plus systematic uncertainties). The fake data tested is NEUT without 2p2h events. 210
XXXV Summary table of the χ^2 GOF computed using the total covariance matrix (statistical plus systematic uncertainties). 222
XXXVI Summary table of the χ^2 GOF computed using the total covariance matrix (statistical plus systematic uncertainties). 228

Chapter 1

Neutrino physics and oscillation

In a famous letter dated 4 December 1930, W. Pauli introduced a neutral particle in order to explain the problem of the energy missed in beta decay [1]. He called this particle "neutron", a combination of the root of the word "neutral" with the suffix "-on". However another neutral but heavier particle was discovered in 1932 by J. Chadwick and called with the same name [2]. In 1933, E. Fermi changed Pauli's suffix to the Italian diminutive "-ino". It took about 26 years to prove its existence. Indeed only in 1956, C. Cowan and F. Reines observed neutrinos, with a revolutionary experiment, using the beta decays from the Savannah River nuclear reactor in South Carolina [3]. For this discovery Reines won the Nobel Prize in Physics in 1995 [4].
In 1959, B. Pontecorvo suggested to investigate if the neutrino emitted together with a muon in pion decay is the same emitted with the electron in β-decay [5]. In 1962 an experiment at the Alternating Gradient Synchrotron (AGS) at Brookhaven National Laboratory (BNL), led by L. M. Lederman, M. Schwartz and J. Steinberger, identified another distinct type: the muon neutrino [6]. In 1988 "for the neutrino beam method and the demonstration of the doublet structure of the leptons through the discovery of the muon neutrino", the three physicists have been awarded the Nobel Prize in Physics [7]. The last piece of the puzzle, the tau neutrino, was observed only in 2000 by the DONuT (Direct Observation of Nu Tau) experiment at Fermilab [8].
In this Chapter neutrinos physics and oscillations will be discussed as well as the status of the current oscillation experiments to put in place the work described in this dissertation.

1.1 Neutrino in the Standard Model

The Standard Model of particle physics (SM) is a relativistic quantum field theory based on the local gauge group $SU(3)_C \otimes SU(2)_L \otimes U(1)_Y$, which describes the electromagnetic, weak, and strong interactions between elementary particles [9–11]. $SU(3)_C$ is the *color*

group of quantum chromodynamics (QCD), $SU(2)_L$ is the *weak isospin group* and $U(1)_Y$ the *hypercharge group*. There are two kinds of particles in the SM: *fermions* and *gauge bosons*. Fermions are particles of spin 1/2 that can be further divided into two families: *quarks*, the constituents of all the hadrons, which interact via strong and electroweak interactions, and *leptons*, which interact via electroweak interactions. Each fermion has a corresponding anti-particle with the same mass and opposites quantum numbers. Bosons have integer spin and mediate the strong, weak and electromagnetic forces. Their number corresponds to the generators of each gauge group: for the $SU(3)_C$ there are eight generators that correspond to eight massless *gluons*; other three massive ($W^{\pm}$ and Z), corresponding to the three generators of $SU(2)_L$ and one massless of $U(1)_Y$ (*photon*, γ), responsible for the electroweak interactions. An overview of the main properties of all SM particles is shown in Fig. 1.1.

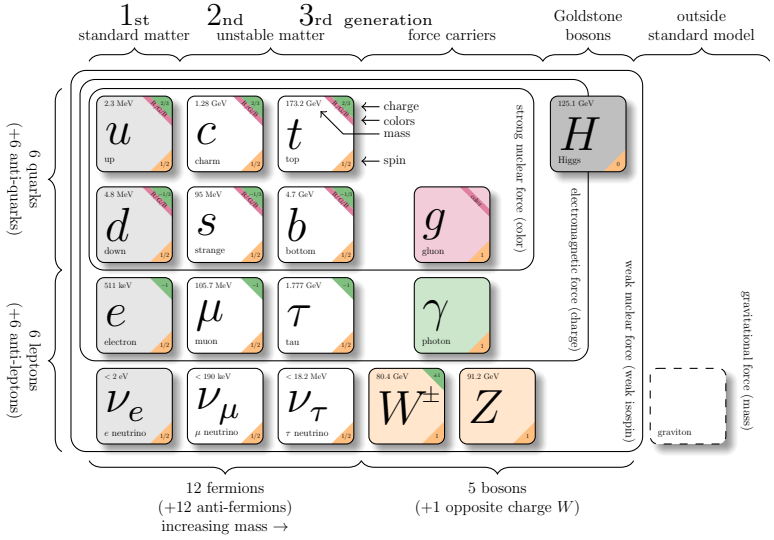

Figure 1.1. A graphical representation of the Standard Model particles and interaction mediators along with their properties. The numbers in the green, red and orange boxes beside the particle symbols indicate the corresponding charges under the gauge group: electric charge, colour and isospin respectively.

In this paragraph is briefly presented the electroweak part of the SM, which determines the interactions of neutrinos. This part is based on the symmetry group $SU(2)_L \otimes U(1)_Y$ and can be studied separately from strong interactions, because the symmetry under the color group $SU(3)_C$ is unbroken and there is no mixing between the $SU(3)_C$ and $SU(2)_L \times U(1)_Y$ sectors.

The electroweak Lagrangian can be written as the sum of three terms:

$$\mathscr{L}_{\text{EW}} = \mathscr{L}_{\text{YM}} + \mathscr{L}_{\text{Higgs}} + \mathscr{L}_{\text{Yukawa}} \tag{1.1}$$

where $\mathscr{L}_{\text{YM}}$ is the Yang–Mills Lagrangian for the gauge group $SU(2)_L \otimes U(1)_Y$, while the other terms are the Higgs and the Yukawa Lagrangian, respectively.

The first term can be written as:

$$\begin{aligned}\mathscr{L}_{\rm YM} &= -\frac{1}{4}\sum_{i=1}^{3} F^i_{\mu\nu}F^{i\mu\nu} - \frac{1}{4}B_{\mu\nu}B^{\mu\nu} + \bar{\psi}_L i\gamma^\mu D_\mu \psi_L \\ &\quad + \bar{\psi}_R i\gamma^\mu D_\mu \psi_R \ . \end{aligned} \tag{1.2}$$

where

$$B_{\mu\nu} = \partial_\mu B_\nu - \partial_\nu B_\mu \quad \text{and} \quad F^A_{\mu\nu} = \partial_\mu W^i_\nu - \partial_\nu W^i_\mu - g\epsilon_{ijk}\, W^j_\mu W^k_\nu \tag{1.3}$$

are the gauge antisymmetric tensors constructed out of the gauge field B_μ associated with $U(1)_L$, and W^i_μ corresponding to the three $SU(2)_L$ generators; ϵ_{ijk} are the group structure constants which, for $SU(2)_L$, coincide with the totally antisymmetric Levi-Civita tensor. The fermion fields are described through their left-hand and right-hand components:

$$\psi_{L,R} = \left[\frac{1 \mp \gamma_5}{2}\right]\psi, \quad \bar{\psi}_{L,R} = \bar{\psi}\left[\frac{1 \pm \gamma_5}{2}\right] \ . \tag{1.4}$$

In the standard electroweak theory ψ_L and ψ_R behave differently under the gauge group. In particular, all ψ_R are singlets and all ψ_L are doublets in the minimal SM. Thus, mass terms for fermions are forbidden in the symmetric limit. Fermion masses are introduced by the mechanism of symmetry breaking. The covariant derivatives $D_\mu\psi_{L,R}$ are given by

$$D_\mu \psi_{L,R} = \left[\partial_\mu + ig\sum_{i=1}^{3} \tau^i_{L,R} W^i_\mu + ig'\frac{1}{2}Y_{L,R}B_\mu\right]\psi_{L,R} \ , \tag{1.5}$$

where $\tau^i_{L,R}$ and $\frac{1}{2}Y_{L,R}$ are the $SU(2)_L$ and $U(1)_Y$ generators. The electric charge generator Q is given by the Gell–Mann–Nishijima relation:

$$Q = \tau^3_L + \frac{1}{2}\, Y_L = \tau^3_R + \frac{1}{2}\, Y_R \ . \tag{1.6}$$

The Higgs Lagrangian, specified by the gauge principle and the requirement to be renormalizable, is

$$\mathscr{L}_{\rm Higgs} = (D_\mu\phi)^\dagger (D^\mu\phi) - V(\phi^\dagger\phi) \ , \tag{1.7}$$

where ϕ is a column vector including all Higgs scalar fields and the potential $V(\phi^\dagger\phi)$, symmetric under $SU(2)_L \otimes U(1)_Y$, contains quartic terms in ϕ so that the theory is renormalizable:

$$V(\phi^\dagger\phi) = \mu^2\phi^\dagger\phi + \lambda(\phi^\dagger\phi)^2 \tag{1.8}$$

Spontaneous symmetry breaking is induced if the minimum of V is obtained for non-vanishing ϕ values. Defining with v the following quantity:

$$v \equiv \sqrt{\frac{-\mu^2}{\lambda}} \tag{1.9}$$

and neglecting an irrelevant constant term $v^4/4$, the Higgs potential in Eq. 1.8 can be written as:

$$V(\phi^\dagger\phi) = \lambda\left(\phi^\dagger\phi - \frac{v^2}{2}\right)^2 \tag{1.10}$$

From the above expression it is clear that the potential is minimum for

$$\phi^\dagger\phi = \frac{v^2}{2}. \tag{1.11}$$

The minimum of the potential corresponds to the vacuum, which is the lowest energy state, and the quantized excitations of each field above the vacuum correspond to particle states.

The electroweak SM Lagrangian is then

$$\begin{aligned}\mathscr{L}_{\rm EW} &= -\frac{1}{4}\sum_{i=1}^{3} F^i_{\mu\nu}F^{i\mu\nu} - \frac{1}{4}B_{\mu\nu}B^{\mu\nu} \\ &+\bar{\psi}_L i\gamma^\mu D_\mu \psi_L + \bar{\psi}_R i\gamma^\mu D_\mu \psi_R \\ &+(D_\mu\phi)^\dagger(D^\mu\phi) - \mu^2\phi^\dagger\phi - \lambda(\phi^\dagger\phi)^2 \\ &-y^j\left(\bar{\psi}_L\phi\psi_R + \bar{\psi}_R\phi^\dagger\psi_L\right)\end{aligned} \tag{1.12}$$

The terms proportional to y^j with $j = l, q$, that indicate lepton and quarks, is the so called Yukawa coupling, is responsible for the generation of the lepton and quark masses after the spontaneous symmetry breaking [12–14]. The fermions mass arises from the Higgs mechanism and Yukawa coupling, which applies to all quarks and charged lepton and in the SM is typically written as the Dirac mass term:

$$\mathscr{L}_{\rm Dirac} = \left(m\bar{\psi}_L\psi_R + m\bar{\psi}_R\psi_L\right) \tag{1.13}$$

here $m = \frac{v}{\sqrt{2}}\, y$, where v is *vacuum expectation value* of the Higgs field and y are the Yukawa coupling, different per each fermion.

1.1.1 The neutrino mass problem

As stated before neutrino are massless in the SM because their fields do not have the right-handed component as the discovery of the parity violation in 1957 by Wu et al. [15] and Lederman et al. [16] has demonstrated. Anyway their massless nature has been refuted by neutrino oscillation experimental data which can be explained only if neutrinos are massive and can mix violating lepton flavour conservation.

One possible extension of the SM foreseen the introduction of the right-handed component of the neutrino fields. In such a model, called the *minimally extended Standard Model*, neutrino mass can be generated with the same Higgs mechanism that gives masses to quarks and charged leptons in the SM. The Lagrangian is a Dirac mass term:

$$\mathscr{L}_\nu = i\bar{\psi}_\nu\gamma_\mu D_\mu\psi_\nu \tag{1.14}$$

that includes a kinetic term plus the gauge interaction with the massive vector bosons.

The alternative approach is to extend the SM introducing a completely different type of neutrino called the Majorana neutrino which is identical to its own antiparticle (the

concept was formally introduced by Majorana in 1937 [17]). However, by assuming the neutrino is the same as antineutrino, the Majorana mass term violates the lepton number conservation and changes it by two units, which is not allowed in the SM. The mass term in this scenario is the following:

$$\mathscr{L}_{\text{Majorana}} = \frac{1}{2}\left(m\bar{\psi}_L\psi_R^C + m\bar{\psi}_R^C\psi_L\right) = \frac{1}{2}\left(m\bar{\psi}_L C\psi_L^T + m\bar{\psi}_L^T C^\dagger\psi_L\right) \tag{1.15}$$

where ψ represents the neutrino, C is the charge conjugation matrix.
Right-handed neutrino fields are called sterile since they do not interact neither weakly or via strong and electromagnetic interactions. Different possibilities can be considered in the case of Dirac and Majorana mass term. The most popular are the following:

- transitions into sterile states: if the number of light Majorana neutrinos is larger than three, transitions of flavour neutrinos into sterile become possible;
- see-saw mechanism of the neutrino mass generation: if in the spectrum of masses of the Majorana particles there are three light and three heavy neutrino, it is possible to explain the small neutrino masses with respect to leptons and quarks.

The Dirac or Majorana nature of the neutrino is not yet definitely settled. Only the detection of neutrino–less double beta decay would provide the unique experimental test that neutrinos are Majorana particles [18–20].

1.1.2 The weak interaction

In the SM, neutrinos only interact with matter via the weak interaction by exchanging a $W^\pm$ boson (charged-current interactions) or a Z^0 (neutral current) boson. In charged-current (CC) processes a neutrino (antineutrino) in the initial state converts into a charged lepton in the final state. Therefore the flavour of the outgoing lepton give the flavour of the incoming neutrino, and its charge determines if it is a neutrino or an antineutrino. The neutral current (NC) mediated processes present both an incoming and an outgoing neutrino (antineutrino). In Fig. 1.2 are reported the Feynman diagram of (anti)neutrino interaction vertex in the case of CC (left) and NC (right) interactions.

The CC and NC Lagrangians are

$$\begin{aligned}\mathscr{L}_{\text{CC}} &= \frac{g}{\sqrt{2}}(j_W^\alpha W_\alpha + j_W^{\alpha,\dagger} W_\alpha^\dagger) \\ \mathscr{L}_{\text{NC}} &= \frac{g}{\cos\theta_W} j_Z^\alpha Z_\alpha\end{aligned} \tag{1.16}$$

Here, W_μ and Z_μ represent the heavy gauge boson fields, g is the weak coupling constant while θ_W is the weak mixing angle. The leptonic charged weak current, j_W^μ, is defined as

$$j_W^\alpha = \sum_{i=\text{e},\mu,\tau} \bar{\nu}_{iL}\gamma^\alpha l_{iL}. \tag{1.17}$$

where $\nu_{\alpha L(R)}$ and $l_{\alpha L(R)}$ correspond to the left (right) neutral and charged leptonic fields. The leptonic neutral current term, j_Z^μ, is defined as

$$j_Z^\alpha = \sum_{i=\text{e},\mu,\tau} g_L^\nu \bar{\nu}_{iL}\gamma^\alpha \nu_{iL} + g_L^l \bar{l}_{iL}\gamma^\alpha l_{iL} + g_R^l \bar{l}_{iR}\gamma^\alpha l_{iR} \tag{1.18}$$

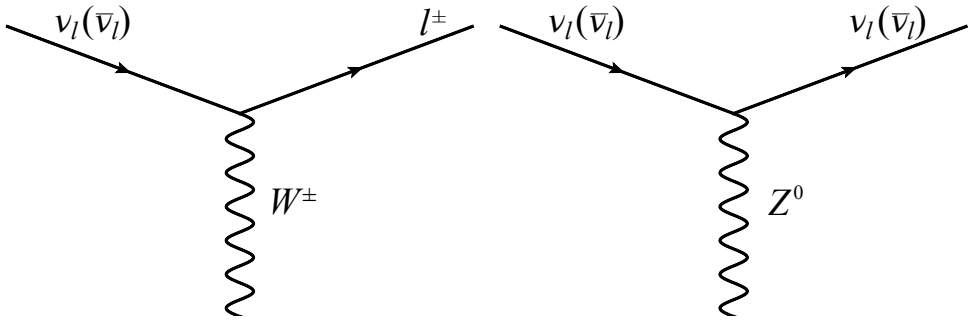

Figure 1.2. Feynman diagram of (anti)neutrino interaction vertex in the case of CC (left) and NC (right) interactions. In then first case the outgoing lepton is positive if the interaction involve antineutrino or is negative in the other case. The exchanged W boson in negative antineutrino interaction.

where $g_L^{\nu} = 1/2$, $g_L^l = -1/2 + \sin^2\theta_W$ and $g_R^l = \sin^2\theta_W$ represent the neutrino left and the charged lepton left and right–handed couplings.

1.2 Neutrino oscillations

In 1957, when the second neutrino family had not yet been discovered, Pontecorvo suggested the possibility of having neutrino/antineutrino oscillations of the type $\nu \leftrightarrow \bar{\nu}$ [21, 22] in analogy with $K^0 - \bar{K}^0$ oscillations. After the discovery of a second neutrino family, Z. Maki, M. Nagakawa and S. Sakata considered the possibility of having oscillations of neutrinos among the different types [23]. In 1967 Pontecorvo predicted the transition of electron neutrinos emitted by the Sun in muon neutrinos [24], even before the first measurement of the deficit in solar electron neutrino flux by the Homestake experiment in 1968 [25] headed by R. Davis, known as *solar neutrino problem*. In the second half of the 1980s measurements of atmospheric neutrinos flux showed a deficit, called the *atmospheric neutrino anomaly*. These measurements remained controversial for several years and they have been commonly accepted only when Super-Kamiokande [26] and SNO [27, 28] confirmed the oscillation hypothesis for atmospheric neutrinos and solar neutrino respectively. T. Kajita (Super-Kamiokande Collaboration) and A. B. McDonald (SNO Collaboration) have been awarded of the Nobel prize in Physics 2015 "for the discovery of neutrino oscillations, which shows that neutrinos have mass" [29–31].

From a theoretical point of view the neutrino oscillation is described by a neutrino mixing matrix with six free parameters: three mixing angles, a CP violating phase, δ_{CP} and two independent differences of the squared neutrino masses Δm^2. It is worth noting that neutrino oscillation experiments are not sensitive to the nature of the neutrinos: if they are Majorana particles, to completely describe them two more parameters called *Majorana phases* are needed.

1.2.1 Neutrino oscillations in vacuum

In the standard theory of neutrino oscillations [32–34] the flavour eigenstates $|\nu_\alpha\rangle$ can be expressed as linear superposition of the mass eigenstates, $|\nu_k\rangle$:

$$|\nu_\alpha\rangle = \sum_k U^*_{\alpha k}|\nu_k\rangle \tag{1.19}$$

where $\alpha = e, \mu, \tau$ and $k = 1, 2, 3$ while U^* is the unitary mixing matrix. The massive neutrino states $|\nu_k\rangle$ are eigenvectors of the following Hamiltonian:

$$\mathscr{H}|\nu_k\rangle = E_k|\nu_k\rangle \tag{1.20}$$

with the energy eigenvalues

$$E_k = \sqrt{\vec{p}^2 - m_k^2}. \tag{1.21}$$

Considering now a neutrino flavour state $|\nu_\alpha(t)\rangle$, which describes a neutrino created at time $t = 0$, then the time evolution of this state is:

$$|\nu_\alpha(t)\rangle = \sum_k U^*_{\alpha k} e^{-iE_k t}|\nu_k\rangle \tag{1.22}$$

such that $|\nu_\alpha(t = 0)\rangle = |\nu_\alpha\rangle$. Using the unitarity of the mixing matrix the massive neutrino states are

$$|\nu_k\rangle = \sum_\alpha U_{\alpha k}|\nu_\alpha\rangle. \tag{1.23}$$

Then the Eq. 1.22 become:

$$|\nu_\alpha(t)\rangle = \sum_\beta \left(\sum_k U^*_{\alpha k} e^{-iE_k t} U_{\beta k} \right) |\nu_\beta\rangle \tag{1.24}$$

Hence, the superposition of the neutrino state, which is the pure flavour state at $t = 0$, becomes a superposition of different flavour states at $t > 0$.
The time-dependent transition amplitude for a flavour conversion $\nu_\alpha \to \nu_\beta$ is then given by

$$A(\nu_\alpha \to \nu_\beta)(t) = \langle \nu_\beta | \nu(t) \rangle = \sum_k U^*_{\alpha k} U_{\beta k} e^{-iE_k t}. \tag{1.25}$$

Therefore the transition probability is

$$P(\nu_\alpha \to \nu_\beta) \;=\; |A(\nu_\alpha \to \nu_\beta)|^2 = \sum_{k,j} U^*_{\alpha k} U_{\beta k} U_{\alpha j} U^*_{\beta j} e^{-i(E_k - E_j)t} \tag{1.26}$$

An important feature necessary for the derivation of a simple and general expression for the probability of neutrino oscillations is that neutrinos in oscillation experiments are ultra-relativistic, since neutrino masses are smaller than about one eV and only neutrinos with energy larger than about 100 keV can be detected. Then the energy can be approximated:

$$E_k = E + \frac{m_k^2}{2E} \tag{1.27}$$

where $E = |\vec{p}|$ is the neutrino energy, neglecting the mass contribution. Then the difference $E_k - E_j$ become:

$$E_k - E_j = \frac{\Delta m^2_{kj}}{2E}, \tag{1.28}$$

Therefore, the transition probability in Eq. 1.29 can be approximated by:

$$P(\nu_\alpha \to \nu_\beta) = \sum_{k,j} U^*_{\alpha k} U_{\beta k} U_{\alpha j} U^*_{\beta j} \exp\left(-i\frac{\Delta m^2_{kj} L}{2E}\right). \tag{1.29}$$

This relation shows that the source-detector distance L, the neutrino energy E and the squared-mass differences determine the phases of neutrino oscillations

$$\Phi_{kj} = -\frac{\Delta m^2_{kj} L}{2E}. \tag{1.30}$$

Obviously the survival probability of finding the original flavour is

$$P(\nu_\alpha \to \nu_\alpha) = 1 - \sum_{\alpha \neq \beta} P(\nu_\alpha \to \nu_\beta). \tag{1.31}$$

Three neutrino mixing

In the case of three neutrino families, the mixing matrix can be written as a product of 3 matrices:

$$U = \begin{pmatrix} 1 & 0 & 0 \\ 0 & c_{23} & s_{23} \\ 0 & -s_{23} & c_{23} \end{pmatrix} \begin{pmatrix} c_{13} & 0 & s_{13}e^{-i\delta_{CP}} \\ 0 & 1 & 0 \\ -s_{13}e^{i\delta_{CP}} & 0 & c_{13} \end{pmatrix} \begin{pmatrix} c_{12} & s_{12} & 0 \\ -s_{12} & c_{12} & 0 \\ 0 & 0 & 1 \end{pmatrix}$$

where $c_{ij} = \cos\theta_{ij}$ and $s_{ij} = \sin\theta_{ij}$. This matrix is often called the Pontecorvo-Maki-Nakagawa-Sakata (PMNS) matrix. In this case the parameters describing the mixing are four, three angles, θ_{12}, θ_{23} and θ_{13}, and the CP violating phase δ_{CP}. The first matrix describes the oscillation of atmospheric neutrino and the third of solar neutrino. The PMNS matrix is also multiplied by the so called Majorana phase matrix which does not enter into oscillation phenomena:

$$\begin{pmatrix} e^{i\alpha} & 0 & 0 \\ 0 & e^{i\beta} & 0 \\ 0 & 0 & 1 \end{pmatrix}$$

The transition probability Eq. 1.29 can be also written as

$$\begin{aligned} P(\nu_\alpha \to \nu_\beta) &= \delta_{\alpha\beta} - 4\sum_{k>l=1}^{3} \Re\left(U_{\alpha k} U^*_{\beta k} U^*_{\alpha l} U_{\beta l}\right) \sin^2\left(\frac{\Delta m^2_{kl} L}{4E}\right) \\ &+ 4\sum_{k>l=1}^{3} \Im\left(U_{\alpha k} U^*_{\beta k} U^*_{\alpha l} U_{\beta l}\right) \sin\left(\frac{\Delta m^2_{kl} L}{4E}\right) \cos\left(\frac{\Delta m^2_{kl} L}{4E}\right) \end{aligned} \tag{1.32}$$

For antineutrino oscillations, U must be replaced by U^* in the last equation, which change the sign of the last term. The oscillation probability depends on the three mixing angles (θ_{12}, θ_{23}, θ_{13}) and on two independent squared-mass differences (Δm^2_{21} and Δm^2_{31}). Δm^2_{32} is determined by the relation $\Delta m^2_{32} = \Delta m^2_{31} - \Delta m^2_{21}$), since the sum of the three squared-mass differences is zero. Oscillations depend also on the "Dirac" CP violation phase $\delta_{\rm CP}$, but not on the "Majorana phases". Another possible observation is that CP violation is possible only in neutrino appearance, but not in disappearance, since the survival probability is the same for neutrinos and antineutrinos.

Even if a detailed description of neutrino oscillations is given by Eq. 1.32, subleading terms and CP-violation effects can be neglected in many experimental situations, using the two-flavour oscillation formula. While a detailed computation of the two-flavour oscillation probability is reported in Appendix A, here it is important to stress that the two-flavour oscillation framework has been used for decades, before oscillation experiments became sensitive to subdominant effects. In particular, the oscillations of solar and atmospheric neutrinos are well described in this framework with parameters ($\Delta m^2_{\rm sol}$, $\theta_{\rm sol}$) and ($\Delta m^2_{\rm atm}$, $\theta_{\rm atm}$), respectively, such that $\Delta m^2_{\rm sol} \ll \Delta m^2_{\rm atm}$ and both $\theta_{\rm sol}$ and $\theta_{\rm atm}$ are large. In the framework of three-flavour oscillations, instead, the solar and atmospheric neutrino oscillation can be interpret in the following way: $\Delta m^2_{\rm sol}$ is identified with the squared-mass splitting between ν_1 and ν_2 which are labelled in such a way that $m_2 > m_1$, i.e. $\Delta m^2_{21} = \Delta m^2_{\rm sol} > 0$. Then $\Delta m^2_{\rm atm}$ must be identified with $|\Delta m^2_{31}|$ or $|\Delta m^2_{32}|$. Therefore, being $\Delta m^2_{\rm sol} \ll \Delta m^2_{\rm atm}$, results

$$\Delta m^2_{\rm sol} = \Delta m^2_{21} \ll |\Delta m^2_{31}| \simeq |\Delta m^2_{32}| \simeq \Delta m^2_{\rm atm} \,. \tag{1.33}$$

This means that the mass spectrum is composed of two close mass states and another which is more separated in mass. However the mass hierarchy of those states is not completely known: if $m_3 > m_2 > m_1$ it is called *normal hierarchy*, while *inverted hierarchy* if $m_3 < m_1 < m_2$ as depicted in Fig. 1.3. The mass squared difference defines the value of L/E at which neutrino oscillations occur as well as the frequency of the oscillations.

The magnitude of the CP violation in neutrino oscillation can be characterized by the difference of the probabilities between neutrino and antineutrino appearance channels: $\Delta P_{\alpha\beta} \equiv P(\nu_\alpha \to \nu_\beta) - P(\bar{\nu}_\alpha \to \bar{\nu}_\beta)$, which is nothing but twice the CP-odd part in of Eq. 1.32. It can be expressed as [36]:

$$\Delta P_{\alpha\beta} = \pm 16 J \sin\left(\frac{\Delta m^2_{21} L}{4E}\right) \sin\left(\frac{\Delta m^2_{31} L}{4E}\right) \sin\left(\frac{\Delta m^2_{32} L}{4E}\right), \qquad J \equiv \mathrm{Im}\left[U_{e1} U^*_{\mu 1} U^*_{e2} U_{\mu 2}\right], \tag{1.34}$$

with a + sign when (α, β, γ) (with $\gamma \neq \alpha, \beta$) is an even permutation of (e, μ, τ), and a − when is an odd permutation. The quantity J is called *Jarlskog invariant* [37, 38]. It can be written as

$$J = \frac{1}{8} \cos\theta_{13} \sin 2\theta_{12} \sin 2\theta_{13} \sin 2\theta_{23} \sin\delta_{\rm CP} \,. \tag{1.35}$$

This implies that a necessary condition for CP violation in neutrino oscillations is that all three mixing angles θ_{ij} are nonzero and that the phase $\delta_{\rm CP}$ is different from 0 and π.

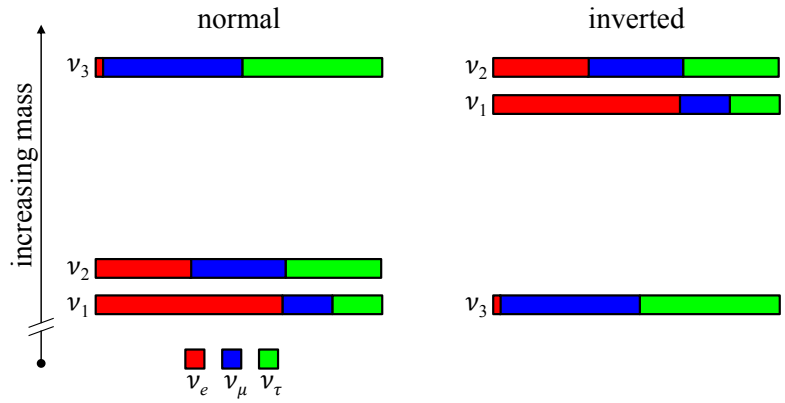

Figure 1.3. The two possible neutrino mass hierarchies. The colours represent the approximate flavour admixtures present in each mass eigenstate. In the normal case, the masses exhibit a hierarchical pattern, and the lightest neutrino has the largest admixture of electron flavour. Figure taken from [35].

1.2.2 Oscillation in matter

The probabilities shown in the previous section were obtained assuming that neutrinos propagate in vacuum. Indeed, in this case, the mixing behaviour is modified as neutrinos can interact with matter. In particular in matter ν_e can have both NC and CC interactions because of the existence of electrons, while for ν_μ and ν_τ only NC reactions are possible (Fig. 1.4). This results in a modification of the oscillation probability and is known as the Mikheyev-Smirnov-Wolfenstein (MSW) effect [39–41]. The matter effect on neutrino oscillation is detailed in Appendix B.

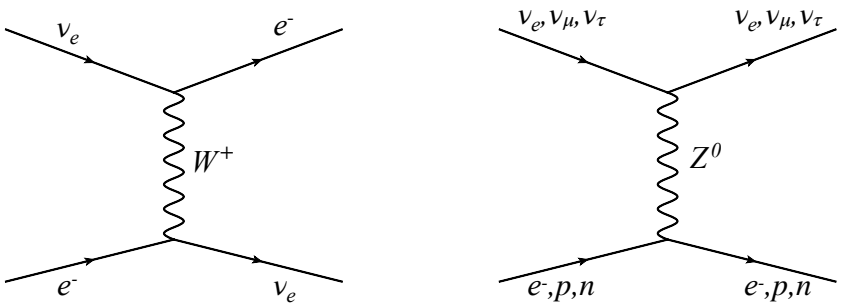

Figure 1.4. Feynman diagrams of the CC (left) and NC (right) elastic scattering processes in matter.

The oscillation probability from ν_μ to ν_e in vacuum is expressed as follows:

$$\begin{aligned} P(\nu_\mu \to \nu_e) &= 4c_{13}^2 s_{13}^2 s_{23}^2 \sin^2\Phi_{31} \\ &+ 8c_{13}^2 s_{12}s_{13}s_{23}\left(c_{12}c_{23}\cos\delta_{CP} - s_{12}s_{13}s_{23}\right)\cos\Phi_{32}\sin\Phi_{31}\sin\Phi_{21} \\ &- 8c_{13}^2 c_{12}c_{23}s_{12}s_{13}s_{23}\sin\delta_{CP}\sin\Phi_{32}\sin\Phi_{31}\sin\Phi_{21} \\ &+ 4s_{12}c_{13}(c_{12}c_{23} + s_{12}s_{23}s_{13} - 2c_{12}c_{23}s_{12}s_{23}s_{13}\cos\delta_{CP})\sin^2\Phi_{21} \end{aligned} \tag{1.36}$$

where $\Phi_{ij} \equiv \frac{\Delta m_{ij} L}{4E}$. In order to include the matter effect, to Eq. 1.36 must be added the following term:

$$\begin{aligned} &-8\frac{aL}{4E}\; c_{13}^2\; s_{13}^2\; s_{23}^2(1-2s_{13}^2)\cos\Phi_{32}\;\sin\Phi_{31} \\ &+8\frac{a}{\Delta m_{31}^2}\; c_{13}^2\; s_{13}^2\; s_{23}^2(1-2s_{13}^2)\sin\Phi_{31} \end{aligned} \tag{1.37}$$

where $a[\mathrm{eV}^2] = 7.56\times10^{-5}\times\rho[\mathrm{g/cm}^3]\times E_\nu[\mathrm{GeV}]$ is a function of the matter density, of the neutrino energy and mass differences. In this formula the matter effects are calculated in the approximation of constant density. These two terms, due to the matter effect caused by coherent forward scattering in matter, produce an asymmetry between neutrinos and antineutrinos in addition to the asymmetry due to CP violation. From the definition of a, the amount of asymmetry due to the matter effect is proportional to the neutrino energy at a fixed value of L/E.

The survival probability, $P(\nu_\mu \to \nu_\mu)$, can be computed using Eq. 1.31. For accelerator-based neutrino experiments is given by the following expression:

$$\begin{aligned} P(\nu_\mu \to \nu_\mu) &= 1 - \sin^2 2\theta_{23}\sin^2\Delta + \alpha c_{12}^2\Delta\sin 2\Delta - \alpha^2\sin^2 2\theta_{12}c_{23}^2\frac{\sin^2 A\Delta}{A^2} \\ &- \alpha^2 c_{12}^4\sin^2 2\theta_{23}\Delta^2\cos 2\Delta - 4s_{13}^2 s_{23}^2\frac{\sin^2(A-1)\Delta}{(A-1)^2} \\ &+ \frac{1}{2A}\alpha^2\sin^2 2\theta_{12}\sin^2 2\theta_{23}\left(\sin\Delta\frac{\sin A\Delta}{A}\cos(A-1)\Delta - \frac{\Delta}{2}\sin 2\Delta\right) \\ &- \frac{2}{A-1}s_{13}^2\sin^2 2\theta_{23}\left(\sin\Delta\cos A\Delta\frac{\sin(A-1)\Delta}{(A-1)} - \frac{A}{2}\Delta\sin 2\Delta\right) \\ &- 2\alpha s_{13}\sin 2\theta_{12}\sin 2\theta_{23}\cos\delta_{CP}\frac{\sin A\Delta}{A}\frac{\sin(A-1)\Delta}{(A-1)} \\ &+ \frac{2}{A-1}\alpha s_{13}\sin 2\theta_{12}\sin 2\theta_{23}\cos 2\theta_{23}\cos\delta_{CP} \\ &\quad \sin\Delta\left(A\sin\Delta - \frac{\sin A\Delta}{A}\cos(A-1)\Delta\right) \end{aligned} \tag{1.38}$$

where

$$\Delta = \frac{\Delta m_{13}^2 L}{4E} \qquad A = \frac{a}{\Delta m_{13}^2} \qquad \alpha = \frac{\Delta m_{21}^2}{\Delta m_{31}^2}. \tag{1.39}$$

1.3 Neutrino oscillation experiments

Neutrino oscillation experiments can be classified as:

- **Appearance experiments:** measure transitions between different neutrino flavours. If the background is very small, i.e. if the final flavour to be searched for is a low component of the initial beam. In this case, an experiment is sensitive to the mixing angles and the CP violation phase. Indeed CP violation is possible only in appearance channels, since survival probability is the same for neutrinos and antineutrinos.

- **Disappearance experiments:** measure the survival probability of a neutrino flavour by counting the number of interactions in the detector and comparing it with the expectation. This kind of experiment are only sensitive to the mixing angles.

As stated before the value of the mass squared difference defines the value of L/E at which neutrino oscillations occur. Therefore different experiments can be designed to be sensitive to different values of Δm^2 choosing appropriate values of the ratio L/E. The sensitivity to Δm^2 of an experiment is the value for which

$$\frac{\Delta m^2\, L}{2E} \sim 1 \tag{1.40}$$

Then neutrino oscillation experiments can be further classified depending on the average value of L/E:

Solar neutrino experiments. In the core of the Sun the thermonuclear reactions produce neutrinos which can be detected on earth. Since the Sun–Earth distance is around $1.5 \times 10^{11}\, m$ and the energy of detectable solar neutrinos is in the range $4.2 - 15\, MeV$, then the range of L/E and the sensitivity to Δm^2 in this kind of experiments are:

$$\frac{L}{E} \sim 10^{12} m/MeV \Longrightarrow \Delta m^2 \sim 10^{-12} eV^2 \tag{1.41}$$

Therefore, solar neutrino experiments are sensitive to small values of Δm^2.

Atmospheric neutrino experiments. They detect neutrinos produced by the decay of pions and kaons in the atmosphere which, in turn, are produced in the interaction of the primary cosmic rays with the upper layers of the atmosphere. The muons produce along with the neutrinos, further decay into electrons and neutrinos before hitting the ground. Their energy range go from about $500\, MeV$ to $100\, GeV$. The source-detector distance ranges from about $20\, km$ for neutrinos coming from the atmosphere, to about $1.3 \times 10^4\, km$ for neutrinos produced on the other side of the Earth. Hence, typical values of L/E and the sensitivity to Δm^2 are

$$\frac{L}{E} \sim 10^{4} km/GeV \Longrightarrow \Delta m^2 \sim 10^{-4} eV^2 \tag{1.42}$$

Reactor neutrino experiments. Large isotropic fluxes of electron antineutrinos are produced in nuclear reactors by β^--decays of four isotopes: ^{235}U ($\sim$ 56%), ^{238}U ($\sim$ 8%), $^{239}\,Pu$ ($\sim$ 30%) and ^{241}Pu ($\sim$ 6%). According to the distance between the source and the detector they are divided in Short BaseLine (SBL) and Long BaseLine (LBL) experiments. The first have a typical neutrino energy around few MeV and the source-detector distance is about 1 km, thus the range of L/E and the sensitivity to Δm^2 are:

$$\frac{L}{E} \sim 10^3\, m/MeV \Longrightarrow \Delta m^2 \sim 10^{-3}\, eV^2 \tag{1.43}$$

The LBL, with a distance of 100 km and same neutrino energy, cover this range:

$$\frac{L}{E} \sim 10^5 m/MeV \Longrightarrow \Delta m^2 \sim 10^{-5}\, eV^2 \tag{1.44}$$

Accelerator neutrino experiments. They utilize beams of neutrinos produced by decay of pions, kaons, and muons created by a proton beam hitting a target. They can be divided in SBL and LBL. The first have a neutrino energy between tens of MeV and hundred of GeV, according with the three different beam production techniques used (more detail in Sec. 1.3.4) and typical source-detector distance between 10 m and 1 km, thus the range of L/E and the sensitivity to Δm^2 are:

$$\tfrac{L}{E} \sim 10^{-2}\, m/MeV \Longrightarrow \Delta m^2 \sim 10^2\, eV^2 \tag{1.45}$$
$$\tfrac{L}{E} \sim 1\, m/MeV \Longrightarrow \Delta m^2 \sim 1\, eV^2 \tag{1.46}$$
$$\tfrac{L}{E} \sim 1\, km/GeV \Longrightarrow \Delta m^2 \sim 1\, eV^2 \tag{1.47}$$

The LBL experiments, with energy around or greater than 1 GeV and distance of $10^2 - 10^3\, km$, are characterized by the following range of L/E and Δm^2:

$$\frac{L}{E} \lesssim 10^3\, km/GeV \Longrightarrow \Delta m^2 \gtrsim 10^{-3}\, eV^2 \tag{1.48}$$

A summary of all the type of experiments along with their typical source-detector distance, energy and sensitivity to Δm^2 is shown in Tab. I.

1.3.1 Solar neutrinos experiments

The thermonuclear fusion in the solar core makes the Sun a powerful source of electron neutrinos with energy of the order of 1 MeV. Since neutrino interacts weakly with matter, all the neutrinos produced pass undisturbed through the solar matter. The solar neutrino flux on the Earth is about $6\times10^{10} cm^{-2} s^{-1}$ and is predicted by the so called Solar Standard Model (SSM) developed by John N. Bahcall in 1963 [42].
The Sun produces 99% of its energy through the so called pp-chain and the remaining 1% by the CNO cycle. The two chains are schematically shown in Fig.1.5. The result of the pp-chain is the fusion of four protons into a helium nucleus along with the release of two electrons plus two electron neutrinos:

$$4p + 2e^- \rightarrow 4^H e + 2\nu_e + 26.731\ MeV. \tag{1.49}$$

Type of experiment	L	E	Δm^2 sensitivity
Solar	$\sim 10^{11}\ km$	$0.2 - 15\ MeV$	$\sim 10^{-12}\ eV^2$
Atmospheric	$\sim 20 - 10^4\ km$	$0.5 - 10^2\ GeV$	$\sim 10^{-4}\ eV^2$
Reactor SBL	$\sim 10\ m$	$\sim 1 MeV$	$\sim 0.1\ eV^2$
Reactor LBL	$\sim 1\ km$	$\sim 1 MeV$	$\sim 10^{-3}\ eV^2$
Accelerator SBL	$\sim 10^{-2} - 1\ km$	$10^{-2} - 10^2\ GeV$	$\sim 1 - 10^2\ eV^2$
Accelerator LBL	$\sim 10^3\ km$	$\gtrsim 1\ GeV$	$\gtrsim 10^{-3}\ eV^2$

TABLE I. Summary table of the types of neutrino oscillation experiments with their typical source-detector distance, energy and sensitivity to Δm^2.

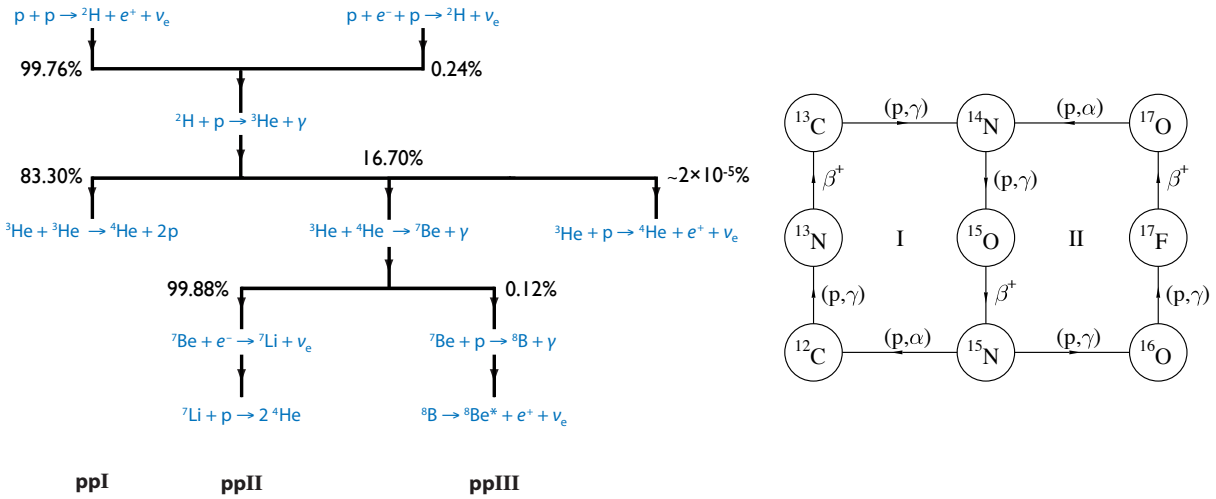

Figure 1.5. The left figure shows the three principal cycles comprising the pp-chain (ppI, ppII, and ppIII), the associated neutrinos that tag each of the three branches, and the theoretical branching percentages. The right figure shows the CNO cycle. Figure taken from [43].

In the subdominant CNO cycle the heavier elements present inside the star, such as C, N and O act only as catalyzers of nuclear reactions. The solar neutrino spectrum along with the SSM uncertainties is shown in Fig. 1.6.

Even if the flux is extremely large, the solar neutrinos experiments require large detectors because of the small neutrino interaction cross-section. Furthermore they must be placed underground in order to be shielded from cosmic rays which are a background for solar neutrinos.

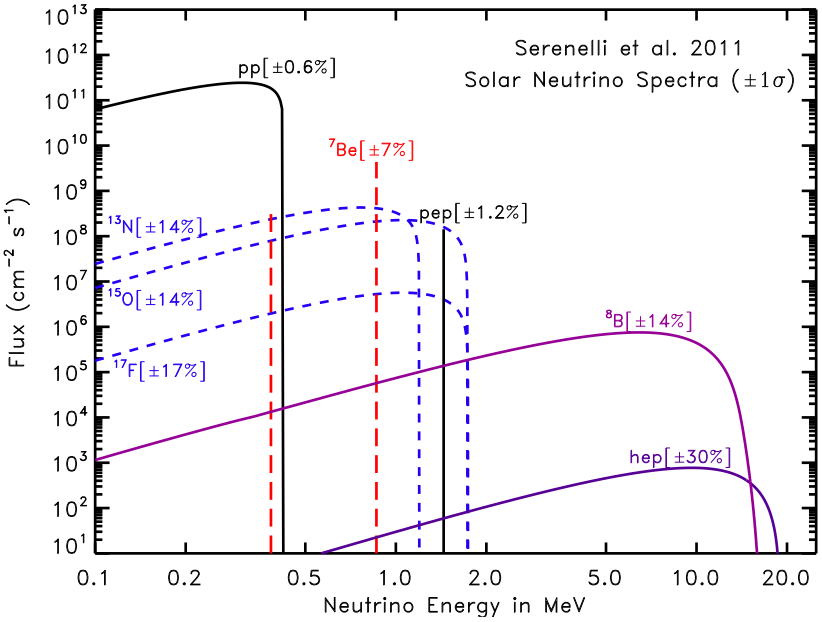

Figure 1.6. Solar neutrino spectrum along with the SSM uncertainties. Units for continuous spectra are $cm^{-2}s^{-1}MeV^{-}1$. Figure taken from [44].

The direct study of solar neutrinos began in the late 1960's with the pioneering radiochemical experiment in the Homestake Gold Mine in South Dakota (USA) headed by R. Davis Jr [45]. The Homestake Solar Neutrino Observatory used a tank placed at a depth of 1478 m, necessary to shield the cosmic rays background, filled with 615 *ton* of tetrachlorethylene C_2Cl_4. The exploited reaction was the Pontecorvo–Alvarez inverse β-decay Cl-Ar [46, 47]:

$$\nu_e + {}^{37}Cl \rightarrow {}^{37}Ar + e^- \tag{1.50}$$

with an energy threshold of 814 keV. Therefore the experiment was not able to detect all the solar neutrinos, but only those from reaction of the ^{8}B and ^{7}Be. The measurement was done through the counting of the number of ^{37}Ar atoms produced inside the detector. Since the ^{37}Ar atoms decay back to ^{37}Cl with a half-life of ∼35 days, the total number of ^{37}Ar atoms in the tank grows up to saturation, where the production rate is equal to the decay rate. The first data indicated that the solar neutrino flux was less than 3 SNU[1] [48], well below the rate predicted by the SSM. After more than 20 years of data taking the average solar neutrino rate was found to be [45]

$$R_{^{37}Cl} = 2.56 \pm 0.16\,(stat.) \pm 0.16\,(syst.)\,\text{SNU} \tag{1.51}$$

which has to be compared with the solar model predictions for the chlorine detector of 9.3 ± 1.3 SNU [45]. Thus the measured solar neutrino rate was about one-third of the SSM prediction with a discrepancy of about 5σ. This deficit has been called "the solar-neutrino problem".
In subsequent years other experiments have been performed to measure the solar neutrino flux. The GALLium EXperiment (GALLEX) [49] and the Soviet–American Gallium

[1] 1 SNU (Solar Neutrino Units) = capture of a neutrino per second on a target of 10^{36} atoms.

Experiment (SAGE) [50] have been radiochemical experiments based on the inverse beta decay of ^{71}Ga:

$$\nu_e + ^{71}Ga \rightarrow ^{71}Ge + e^- \tag{1.52}$$

The threshold of this reaction is 233 keV, thus gallium based experiments can detect also the low-energy pp neutrinos. Gallex and his successor GNO measured an interaction rate of $69.3 \pm 4.1(stat.) \pm 3.6(sys.)$ SNU [51]. The SAGE result on the flux was $65.4 \pm 2.7(stat.) \pm 2.7(syst.)$ SNU [52], in agreement with the Gallex/GNO result. The measured solar neutrino rate had a discrepancy of more than 5σ compared to the SSM prediction of 128^{+9}_{-7} SNU [53].

The water Čerenkov detectors have played a decisive role. They detect particle using the light produced by their passage in water: if the energy of the lepton generated by the neutrino interaction is above the energy threshold for the Čerenkov effect (few MeV for electrons and hundreds MeV for muons), a cone of light is generated with the axis corresponding with the lepton trajectory. Then if the lepton stops inside the detector, the amount of Čerenkov light is used to determine the energy of the lepton, and hence of its neutrino parent. Moreover muons and electrons can be separated by the shape of their Čerenkov rings, giving in this way also the flavour of the primary neutrino. A typical Čerenkov detector is arranged as a huge tank of water equipped with an array of photomultipliers tubes (PMTs) on the inside walls used to record the Čerenkov light.
KamiokaNDE, acronym of *Kamioka Nucleon Decay Experiment, was an experiment of this kind located 1000 m underground in the Kamioka mine in Japan.* It had a water mass of 3000 ton, looked by 1000 20-inch PMTs, contained in a cylindrical tank of 15.6 m diameter and 16 m height. It measured the solar neutrino flux via the elastic scattering reaction

$$\nu_\alpha + e \rightarrow \nu_\alpha + e. \tag{1.53}$$

The recoil electron has a sharp forward peak, which allows to distinguish solar neutrino events from the isotropic background measuring the scattering angle of the recoil electron with respect the direction of the Sun. The average ^8B neutrino flux measured with an energy threshold of 7.75 MeV, is [54]

$$\Phi^{Kam} = 2.80 \pm 0.19(stat.) \pm 0.33(syst.) \times 10^6\, cm^{-2} s^{-1} \tag{1.54}$$

which result to be about half of the SSM prediction, with a discrepancy of more than 2σ.

The upgrade of this experiment, Super-Kamiokande (SK) is a large water Čerenkov detector located 1,000 m deep in the Mozumi mine. It is a tank 41.4 m high and with a diameter of 39.3 m containing 50 kt of ultra-pure water. The detection volume is divided in an outer part, equipped with 1,885 8-inch PMTs, and an inner part with 11,146 20-inch PMTs. Super-Kamiokande, with a threshold of 7 MeV initially and 3.5 MeV today confirmed the KamiokaNDE result with increased precision, measuring a ^8B neutrino flux of [55]

$$\Phi^{SK} = 2.31 \pm 0.02(stat.) \pm 0.04(syst.) \times 10^6\, cm^{-2} s^{-1} \tag{1.55}$$

SK has recently observed for the first time a day-night effect for solar neutrinos, giving

alsot the first indication of Earth matter effects on neutrino propagation. The day-night asymmetry is defined as $A_{DN} = \frac{2(r_D - r_N)}{r_D + r_N}$, where r_D is the day event rate, while r_N is the night event rate. The asymmetry was measured to be:

$$A_{DN} = (-3.2 \pm 1.1(stat.) \pm 0.5(syst))\% \tag{1.56}$$

deviating from zero by 2.7σ [56].

The final answer to the solar neutrino problem was established in 2002 by the SNO (Sudbury Neutrino Observatory) experiment [27], able to proof that the total neutrino flux from the chain of ^{8}B is conserved. This experiment used 1000 tons of ultra-pure heavy water (D_2O) contained in a spherical acrylic vessel surrounded by an ultra-pure H_2O shield Čerenkov detector. SNO was able to detect not only CC ν_e interactions, but also NC with the deuterium nuclei that involve any neutrino flavour and neutrino-electron elastic scattering (ES):

$$CC: \quad \nu_e + d \rightarrow p + p + e^- \tag{1.57}$$

$$NC: \quad \nu_\alpha + d \rightarrow p + n + \nu_\alpha \tag{1.58}$$

$$ES: \quad \nu_\alpha + e^- \rightarrow \nu_\alpha + e^- \tag{1.59}$$

The CC reaction has been used to measure the flux of ^{8}B solar neutrinos being the energy threshold 6.9 MeV. The NC reaction on deuterium has been important to check the neutrino oscillation hypothesis as solution of the solar neutrino problem, since, being sensitive to all active neutrinos, can measure the total flux coming from the Sun. The ES reaction is the same as that of KamiokaNDE and SK and can only measure the flux of ^{8}B solar neutrinos. It is mainly sensitive to ν_e as $\sigma_{ES}(\nu_e) \backsimeq 6\sigma_{ES}(\nu_\mu, \nu_\tau)$ [36]. The period in which the experiment was in operation can be divided in three phases: the first (SNO-I) in which only D_2O has been used as target and detector, the second (SNO-II) where $NaCl$ has been added to improve the detection of the NC reaction and the third (SNO-III) in which SNO collaboration hung in a grid within the heavy water three hundred ^{3}He proportional counter tubes to improve the neutron capture. The results of this experiment are the following [57]:

$$\Phi_{CC} = 1.68 \pm 0.06(stat.)^{+0.08}_{-0.09}(syst.) \times 10^6 \frac{\nu}{cm^2 s} \tag{1.60}$$

$$\Phi_{NC} = 4.94 \pm 0.21(stat.)^{+0.38}_{-0.34}(syst.) \times 10^6 \frac{\nu}{cm^2 s} \tag{1.61}$$

$$\Phi_{ES} = 2.35 \pm 0.22(stat.) \pm 0.15(syst.) \times 10^6 \frac{\nu}{cm^2 s} \tag{1.62}$$

This results is in a good agreement with the expectation of the SSM and the fact that Φ_{CC} is only about one-third of Φ_{NC} can now be completely understood as the effect of neutrino oscillations. The energy spectrum of SNO CC events show that the data are compatible with the SSM prediction and with the Mikheyev- Smirnov-Wolfenstein Large-Mixing-Angle (MSW–LMA) solution of the solar neutrino problem (see App. B for an explanation of the LMA solution).

Most recent experiments are scintillator based: Borexino located in the Laboratori Nazionali del Gran Sasso (LNGS) in Italy and Kamioka Liquid Scintillator Antineutrino

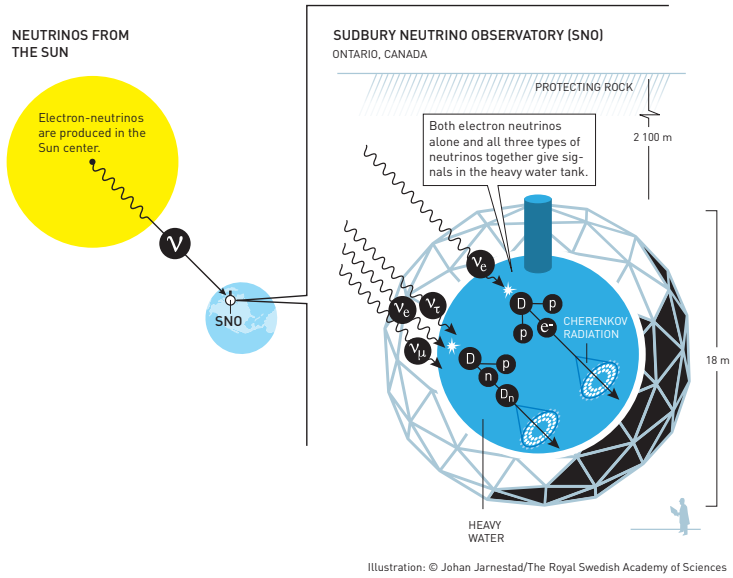

Figure 1.7. Schematic overview of the SNO experiment. Figure taken from [29].

Detector (KamLAND) located in Japan in the Kamioka mine in place of KamiokaNDE. The former measured pp neutrinos [58], ^{7}Be [59] and ^{8}B [60] flux and, a first evidence of pep neutrinos [61] flux. The latter provided a measurement of the ^{7}Be [62] and ^{8}B [63] flux.

1.3.2 Atmospheric neutrino experiments

Atmospheric neutrinos are produced in the upper layers of atmosphere by the interactions with nuclei of primary cosmic rays, mainly composed of protons. These interactions generate secondary cosmic rays, which include mainly pions, that decay in flight via the reaction

$$\pi^{\pm} \rightarrow \mu^{\pm} + \nu_{\mu}(\bar{\nu}_{\mu}) \tag{1.63}$$

The produced muons again decay generating electrons, electron neutrinos, and muon neutrinos:

$$\mu^{\pm} \rightarrow e^{\pm} + \nu_{e}(\bar{\nu}_{e}) + \bar{\nu}_{\mu}(\nu_{\mu}) \tag{1.64}$$

From the multiplicities of neutrinos in these processes it is clear that the ratio of neutrino fluxes is the following

$$\frac{\Phi_{\nu_{\mu}} + \Phi_{\bar{\nu}_{\mu}}}{\Phi_{\nu_{e}} + \Phi_{\bar{\nu}_{e}}} \approx 2 \tag{1.65}$$

which is valid at energies below 1 GeV, while it increases at higher energies leading to an increase of the flavour ratio [64].

In the second half of the 1980s, with the advent of large underground detectors to search for nucleon decay, measure the atmospheric neutrinos flux became important since they constitute a background for such a search. Both water-Čerenkov and fine-grained

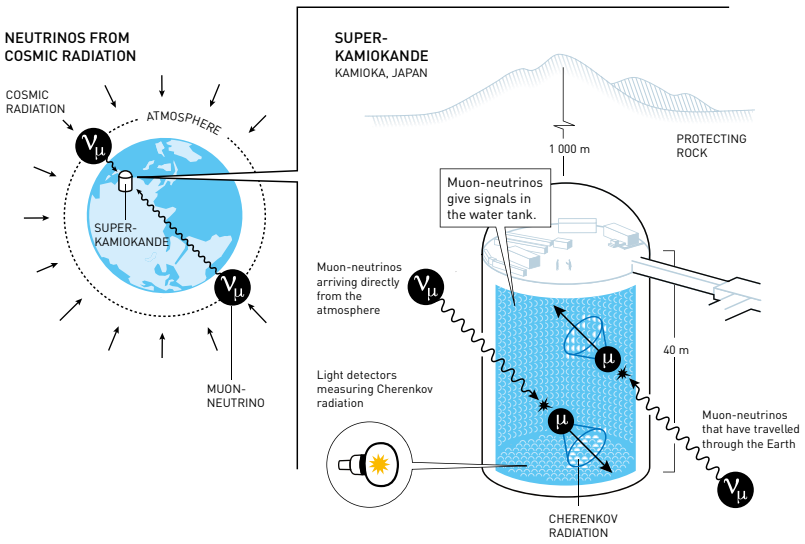

Figure 1.8. Schematic overview of the SK experiment. Figure taken from [29].

iron tracking detectors have been used. In the first the flavour ratio cannot be measured directly, because what is seen is the Čerenkov light produced by the charged leptons. Furthermore muons and electrons have different cross-sections, detection efficiencies and selection criteria. Hence experimental data are reported in terms of e-like and μ-like events and the ratio used to reveal an anomaly is the ratio-of-ratios

$$R_{\mu/e} = \frac{\left(N_{\mu-like}/N_{e-\text{like}}\right)_{\text{data}}}{\left(N_{\mu-\text{like}}/N_{e-\text{like}}\right)_{\text{MC}}} \tag{1.66}$$

where $\mathrm{N}_{\mu-\text{like}}$ and $\mathrm{N}_{e-\text{like}}$ are the numbers of μ-like and e-like events respectively and, the numerator is the measured ratio while at the denominator is calculated with Monte Carlo (MC). A measurement of a ratio-of-ratios different from unity is evidence of an anomaly.

The first hint of ratio-of-ratios lower than the expectation came from the KamiokaNDE experiment [65]. The collaboration reported the final results for two kind of events: sub-GeV events, which are characterized by a total visual energy E_{vis} below 1.33 GeV and multi-GeV with $E_{vis} > 1.33 GeV$ [66, 67]:

$$R_{\mu/e}^{sub-\text{GeV}} = 0.60^{+0.07}_{-0.06} \pm 0.05 \tag{1.67}$$

$$R_{\mu/e}^{multi-\text{GeV}} = 0.57^{+0.08}_{-0.07} \pm 0.07 \tag{1.68}$$

The IMB (Irvine–Michigan–Brookhaven) experiment, a Čerenkov detector filled with about 8 kton of water and located deep underground in the Morton Thiokol salt mine near Cleveland, Ohio (USA), found an anomaly compatible with KamiokaNDE with a significance of 2.5σ [68]. This observed deficit was commonly called the atmospheric neutrino anomaly, and remain controversial for many year, since two experiments, NUSEX and Fréjus, did not observe any anomalies [69, 70]. The first evidence in support of the

neutrino oscillation as explanation of the atmospheric neutrino anomaly was presented by the SK experiment in 1998 [26]. A schematic overview of SK is reported in Fig. 1.8 and a detailed description will be given in the Sec. 3.5. The zenith-angle distributions of the μ-like events showed a clear deficit for muons compared to the non-oscillation expectation. Neutrino events having their vertex in the fiducial volume in SK are classified into fully contained (FC) events and partially contained (PC) events. Single-ring events have only one charged lepton which radiates Čerenkov light in the final state and the particle identification is particularly clean. A ring produced by an e-like particle exhibits a more diffuse pattern than that produced by a μ-like particle, since the first produces an electromagnetic shower and low-energy electrons suffer considerable multiple Coulomb scattering. The experiment counts ν_e and ν_μ in bins of the zenith angle θ ($\cos\Theta = 1$ for the neutrinos coming from the zenith and $\cos\Theta = -1$ if they come from the nadir). Events included in Fig. 1.9 are single-ring FC events subdivided into sub-GeV

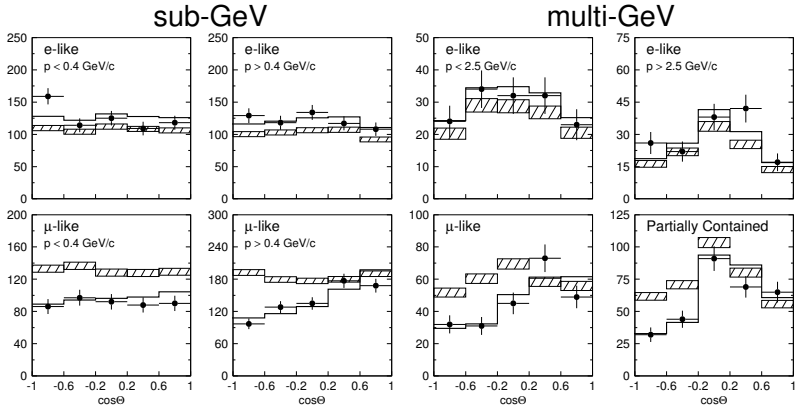

Figure 1.9. Zenith angle distributions of μ-like and e-like events for sub-GeV and multi-GeV data sets. Upward-going particles have $\cos\Theta < 0$ and downward-going particles have $\cos\Theta > 0$. The hatched region shows the Monte Carlo expectation for no oscillations. The bold line is the best-fit expectation for $\nu_\mu \leftrightarrow \nu_\tau$ oscillations with the overall flux normalization fitted as a free parameter. Figure taken from [26].

and multi-GeV events. The zenith-angle distribution of the multi-GeV μ-like events is shown combined with that of the PC events. The final-state leptons in these events have good directional correlation with the parent neutrinos. The zenith-angle distribution of the μ-like events shows a strong deviation from non-oscillation hypothesis. On the other hand, the zenith-angle distribution of the e-like events is consistent with the expectation. This characteristic may be interpreted if muon neutrinos coming from the opposite side of the Earth's atmosphere oscillate into other neutrinos and disappear. Disappeared muon neutrinos must have oscillated into tau neutrinos because there is no indication of electron neutrino appearance.
SK oscillation results has been confirmed by MACRO (Monopole Astrophysics and Cosmic Ray Observatory) experiment [71, 72] and Soudan 2 [73] and, more recently, by the large neutrino telescopes ANTARES (Astronomy with a Neutrino Telescope and Abyss environmental RESearch) [74] and IceCube [75].

1.3.3 Reactor neutrino experiments

Nuclear reactors provide a high intensity source of electron antineutrinos produced by the β^- decay of the fission products. Approximately six β decays occur for each fission event. On average, each fission produces about 200 MeV, with the release of about six electron antineutrinos, thus their yield is about $2 \times 10^{20} \nu_e \; s^{-1}$ for each GW_{th} of thermal power emitted in a 4π solid angle. Typical modern nuclear power plants have several reactor cores, each with a thermal power of the order of 3 GW_{th}. Thus, the total rate of antineutrino production of a typical nuclear power plant is very high ($\sim 10^{21}$ per second). On the other hand the antineutrino flux is isotropic, thus it decreases rapidly with distance. This problem is partially compensated by the low-energy of the produced electron antineutrinos (few MeV) which implies a relatively short oscillation length. Such a low energy implies that only $\bar{\nu}_e$ disappearance can be investigated in reactor experiments, since the energy is not sufficient to produce, in a detector, muons or taus. Reactor electron antineutrinos are detected through the inverse β-decay (IBD):

$$\bar{\nu}_e + p \rightarrow n + e^+ \tag{1.69}$$

Using the same experimental method of Reines and Cowan in first neutrino detection, antineutrino events are distinguished from the background by the coincidence of the prompt positron signal with the delayed signal produced by the nuclear capture of the neutron. As already mention, reactor neutrino experiment are divided in SBL with L$\sim$ 1 km and LBL with L$\sim$ 200 km.

An example of SBL experiment was CHOOZ in France. It used antineutrinos coming from two pressurized water reactors with a total thermal power of 8.5 GW_{th} and was designed to search $\bar{\nu}_e$ disappearance due to the atmospheric mass difference of the order of 10^{-3}. The detector therefore was roughly 1 km from the reactor. Neutrinos were observed via inverse β-decay in a detector divided in three regions. The inner most region was in a plexiglas container transparent to the scintillation light and was composed of 5 tons of scintillator doped with Gadolinium (Gd)[2], then there was a region composed of 17 tons of undoped scintillators that is used to capture the electromagnetic energy from the inverse beta decay and the photons from the neutron capture in the Gd. The outer surface of this region contained 192 inward facing photomultiplier tubes (PMT) held in an opaque plastic structure. Finally the outer region contained ninety tons of the same undoped scintillator as region 2 and vetoed cosmic ray events using 48 PMTs. The CHOOZ experiment took data from April 1997 to July 1998 and found no evidence for $\bar{\nu}_e$ disappearance [76]. In 2012, however three reactor neutrino experiments Double Chooz, Daya Bay and RENO reported their first results on reactor $\bar{\nu}_e$ disappearance. The Double Chooz experiment is the upgrade of CHOOZ and it a near and a far detector situated 400 m from the CHOOZ reactors. The RENO (Reactor Experiment for Neutrino Oscillations) experiment is located near the Hanbit nuclear power plant in Yongg-wang in South Korea. The plant consists of six reactors linearly aligned with equal distance of about 260 m. One detector is located at 294 m from the center of the six reactors, while another detector is located at 1383 m. Daya Bay is situated at approximately 52 km north-east of Hong Kong. The experiment consists of eight detectors, clustered in three

[2]Gadolinium has an high neutron-capture cross section.

locations within 1.9 km of six nuclear reactors. In 2012 both collaborations published the evidence at 5σ of non-zero θ_{13} [77, 78]. The latest results from the three collaborations are [79–81]:

$$\sin^2 2\theta_{13|DayaBay} = 0.084 \pm 0.005(stat + syst.) \tag{1.70}$$

$$\sin^2 2\theta_{13|RENO} = 0.082 \pm 0.009(stat.) \pm 0.006(syst.) \tag{1.71}$$

$$\sin^2 2\theta_{13|DoubleChooz} = 0.088 \pm 0.033(stat. + syst.) \tag{1.72}$$

The Kamioka Liquid Anti-Neutrino Detector (KamLAND) is a 1 kton ultra-pure liquid scintillator detector located at the old KamiokaNDE site in Japan, and detects $\bar{\nu}_e$ coming from 16 reactors located at an average distance of 160 km. The experiment consists of a stainless steel spherical vessel with a diameter of 18 m with 1879 PMTs of 20-inch and fast time response mounted on the inner surface. Inside the sphere is a 13 m diameter nylon balloon filled with liquid scintillator. Outside of it, non-scintillating, highly purified oil provides buoyancy for the balloon and shields the external radiation. The stainless steel vessel is surrounded by a water Čerenkov detector, which allows to reject any external background. This experiment had a sensitive Δm^2 range down to $\sim 10^{-5} eV^2$. The first KamLAND results was published in 2002 (see Fig. 1.10) showing that the ratio of observed to expected (assuming no $\bar{\nu}_e$ oscillations) number of events was [82]:

$$\frac{N_{obs} - N_{BG}}{N_{NoOsc}} = 0.611 \pm 0.085(stat.) \pm 0.041(syst.) \tag{1.73}$$

The probability to be consistent with no disappearance hypothesis was less than 0.05%, showing clear evidence of the event deficit expected from neutrino oscillations.
KamLAND updated results has been reported in [83] along with a combined analysis with solar neutrino data. The data set benefits of an increased exposure and of a lower background due to a radiopurity upgrade of the liquid scintillator.

JUNO (Jiangmen Underground Neutrino Observatory) is a multi-purpose underground reactor antineutrino experiment, under construction in the South of China. The primary goal of JUNO is the investigating of the mass hierarchy. Anyway the foreseen level of the energy resolution and the large fiducial volume of the detector offer exciting opportunities for addressing also many other important topics in neutrino and astroparticle physics [84].

1.3.4 Accelerator neutrino experiments

Another way to study neutrino oscillations, in particular those due to the Δm^2_{23} mass difference, is given by accelerator neutrino experiments. The neutrinos beam can be produced using three different strategy:

Pion Decay In Flight (DIF) where the beam is produced by the decay of pions and kaons produced in turn by a proton beam hitting a target.

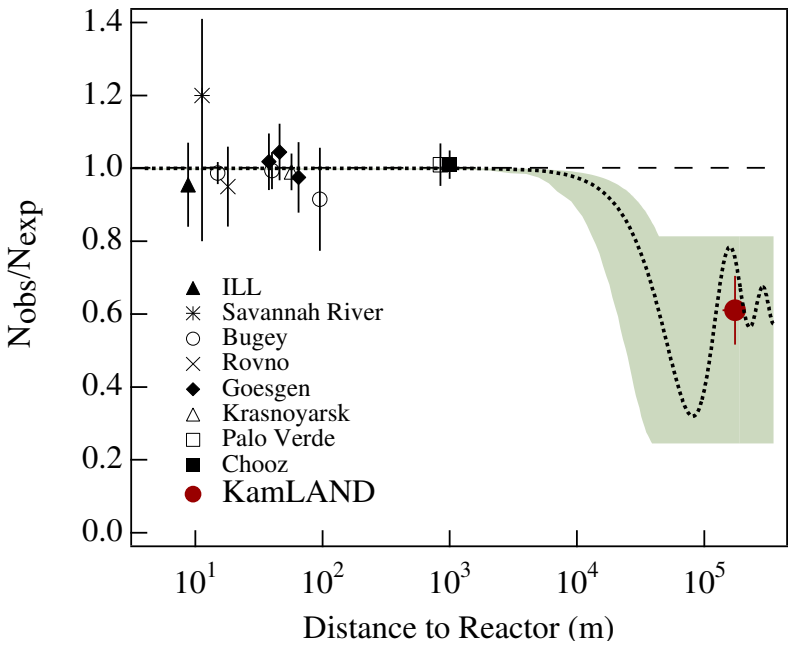

Figure 1.10. Ratio of measured neutrinos over expected $\bar{\nu}_e$ versus the distance of different reactor antineutrino experiments. The solid dot is the KamLAND point plotted at a flux-weighted average distance (the dot size is indicative of the spread in reactor distances). The shaded region indicates the range of flux predictions corresponding to the 95% C.L. LMA region found in a global analysis of the solar neutrino data. The dotted curve corresponds to $\sin^2 2\theta = 0.883$ and $\Delta m^2 = 5.5 \times 10^{-5}\, eV^2$ and is representative of recent best-fit LMA predictions while the dashed curve shows the case of small mixing angles (or no oscillation). Figure taken from [82].

Muon Decay at Rest (DAR) where the beam is characterized by a low energy and it is made of muon neutrinos coming from the muon decay.

Beam Dump where the beam have an energy of the order of $10^2\, GeV$ and is produced by a proton beam with very high energy which impinges a target producing charmed heavy hadrons that promptly decay in electrons and muons and again in electron and muon neutrinos.

Neutrino beams generated by DIF can be further classified in three categories:

Wide Band (WB) beam characterized by a high-intensity neutrino beam with a wide energy spectrum which can span one or two order of magnitude. This feature allows them to investigate a wide range of values of Δm^2.

Narrow Band (NB) beam where the narrow energy spectrum is obtained with the selection neutrino parents (pions and kaons) momenta. The resulting intensity of the neutrino flux of a NB beam is reduced compared with a WB beam obtained from the same proton beam. These beams are useful for measure precisely Δm^2.

Off Axis (OA) beam where the near and far detectors are shifted by a small angle from the axis of the beam resulting in an almost monochromatic and narrow beam.

As mentioned before, accelerator neutrino experiments can be classified by the average value of the parameter L/E: SBL with $L \sim 10\,m - 1\,km$ and LBL with $L \sim 10^2 - 10^3\,km$ accelerator neutrino experiments.

SBL accelerator neutrino experiments description is out of the scope of this dissertation, but it is important to mention that they did not find any indication of neutrino oscillations, except for the LSND experiment, which found a signal in the $\bar{\nu}_\mu \to \bar{\nu}_e$ channel [85] and a weaker signal in $\nu_\mu \to \nu_e$ [86] that could require an extension of the three–neutrino mixing scheme.

The LBL accelerator neutrino experiments measure the oscillation parameters Δm^2_{23}, θ_{23}, also measured by atmospheric neutrino experiment, θ_{13}, measured by reactor experiment as well, and the CP violation phase δ_{CP}. Usually, the neutrino beam is measured, before the oscillation, in a near detector and than again, after the oscillation, in a far detector. The past and present LBL experiments are: K2K and T2K in Japan, MINOS and NOνA in USA and OPERA in Italy.

The K2K (KEK to Kamioka) was the first LBL accelerator-based experiment and it had as goal the confirmation of atmospheric ν_μ disappearance observed at SK. A horn-focused wide–band muon neutrino beam with an average energy of about 1.3 GeV was directed toward the far detector SK, located 250 km far from the neutrino production point. The spectrum and profile of the neutrino beam were measured by a near detector system located 300 m downstream from the production target. The K2K experiment started data-taking in 1999 and was completed in 2004. It observed 112 FC events in the 22.5 kton fiducial volume of SK, compared with an expectation of $158.1^{+9.2}_{-8.6}$ events without oscillation. This discrepancy of about 4.3σ indicated the muon neutrino disappearance, excluding other interpretations of the atmospheric neutrino anomaly [87]. K2K also investigated the possibility of the $\nu_\mu \to \nu_e$ oscillation reporting no events above the expected background [88].

In the MINOS experiment (Main Injector Neutrino Oscillations) the beam was produced by the NuMI facility (Neutrinos at the Main Injector) using protons accelerated up to 120 GeV by the Fermilab Main Injector. The far detector was a 5.4 kton (total mass) iron-scintillator tracking calorimeter with toroidal magnetic field, located underground in the Soudan mine at a distance to the source of 735 km. It is also equipped with a near detector which is a 0.98 kton iron-scintillator tracking calorimeter. MINOS started the neutrino-beam run in 2005 searching for ν_μ disappearance and ν_e appearance. The combined analysis of the ν_μ disappearance and ν_e appearance data along with atmospheric neutrino data reported $|\Delta m^2_{32}| = [2.28 - 2.46] \times 10^{-3}\,\mathrm{eV}^2$ (68% C.L.) and $\sin^2\theta_{23} = 0.35 - 0.65$ (90% C.L.) in the normal hierarchy, and $|\Delta m^2_{32}| = [2.32 - 2.53] \times 10^{-3}\,\mathrm{eV}^2$ (68% C.L.) and $\sin^2\theta_{23} = 0.34 - 0.67$ (90% C.L.) in the inverted hierarchy [89]. The collaboration reported also the measurements of oscillation parameters from ν_μ and $\bar{\nu}_\mu$ disappearance using beam and atmospheric data. Assuming identical ν and $\bar{\nu}$ oscillation parameters $|\Delta m^2| = 2.41^{+0.09}_{-0.10} \times 10^{-3}\,eV^2$ and $\sin^2 2\theta = 0.950^{+0.035}_{-0.036}$. Instead allowing independent ν and $\bar{\nu}$ oscillations $|\Delta \bar{m}^2| = 2.50^{+0.23}_{-0.25} \times 10^{-3}\,eV^2$ and $\sin^2 2\bar{\theta} = 0.97^{+0.03}_{-0.08}$ [90].

OPERA (Oscillation Project with Emulsion-tRacking Apparatus) was a combination of the "Emulsion Cloud Chambers" and magnetized spectrometers. It had its neutrino source at CERN and a target detector mass of 1290 tons at Gran Sasso with the baseline distance of 730 km. The CNGS (CERN Neutrinos to Gran Sasso) neutrino beam with $E_\nu = 17 GeV$ was produced by high-energy protons from the CERN SPS. The experiment reported discovery of ν_τ appearance with a 5σ significance observing five ν_τ candidate and confirming the atmospheric ν_μ oscillation into ν_τ [91].

T2K (Tokai to Kamioka) is, with NOνA, a running LBL oscillation experiment. The work describer in this dissertation has been developed within the T2K Collaboration, thus the experimental setup and the oscillation analysis will be extensively described in the subsequent Chapters. It is important to mention here that T2K was the first to find an indication of electron neutrino appearance from an accelerator-produced off-axis neutrino beam [92]. Then it found the evidence using only $\sim 8.2\%$ of the total approved data [93] and the muon neutrino disappearance setting the world best measurement of $\sin^2\theta_{23}$ [94]. Recently started to take data also with an antineutrino beam in order to enhance its sensitivity to δ_{CP}.

NOνA (NuMI Off-Axis ν_e Appearance) started taking data in 2013. This experiment consists of a fully active liquid scintillator tracking detector and it has as goals the measurement of θ_{13}, study CP violation and the neutrino mass hierarchy. The beam is produced by the NuMI (Neutrinos at the Main Injector) facility and it has an average energy of 2 GeV. The far detector is located 810 km downstream from the target and 14.6 $mrad$ off-axis. It use also a near detector which is located about 100 m underground, 1 km from the target and 14.6 $mrad$ off-axis. Recently the collaboration reported results on ν_μ disappearance and ν_e appearance. In an exposure equivalent to 2.74×10^{20} protons-on-target at the NuMI beam at Fermilab, they observed 6 ν_e events at the far detector compared to a background expectation of 0.99 ± 0.11 (syst.) events. A secondary analysis observes 11 events with a background of 1.07 ± 0.14 (syst) [95]. With more statistics the Collaboration updated the first ν_μ disappearance measurement reported in 2016 [96]. Assuming the normal mass hierarchy $\Delta m^2_{32} = (2.67 \pm 0.11)\times10^{-3}\ eV^2$ and $\sin^2 2\theta_{23}$ at the two degenerate values $0.404^{+0.030}_{-0.022}$ and $0.624^{+0.022}_{-0.030}$, both at the 68% C.L., disfavouring the maximal mixing scenario with 2.6σ significance [97]. The ν_μ disappearance and ν_e appearance data has been also analysed together using also the reactor constraints and the results have been reported in [98]. Fig. 1.11 shows the regions of ($\sin^2\theta_{23}$, δ_{CP}) space allowed at various confidence levels. There are two degenerate best fit points in the normal hierarchy: $\sin^2\theta_{23} = 0.404$, $\delta_{CP} = 1.48\pi$ and $\sin^2\theta_{23} = 0.623$, $\delta_{CP} = 0.74\pi$. In inverted hierarchy the best-fit point occurs near $\delta_{CP} = 3\pi/2$. In Fig. 1.12 shows the significance at which values of δ_{CP} are disfavoured for each hierarchy and octant combination. Inverted hierarchy in lower octant is disfavoured at more than 93% C.L. for all values of δ_{CP} and excluded at greater than 3σ significance outside the range $0.97\pi < \delta_{CP} < 1.94\pi$.

The two next generation LBL experiments are the Deep Underground Neutrino Experiment (DUNE) [99] in the US and the Hyper-Kamiokande experiment [100] in Japan. Hyper-Kamiokande will be described in Chap. 6. DUNE will use four Liquid Argon time projection chambers, of 10 $kton$ each, as target of neutrino interactions, performing a

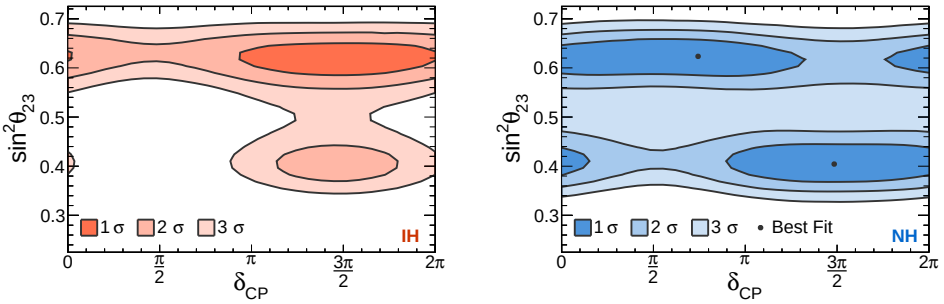

Figure 1.11. Regions of δ_{CP} versus $\sin^2\theta_{23}$ parameter space consistent with the observed spectrum of ν_e candidates and the ν_μ disappearance data. The top panel corresponds to normal mass hierarchy and the bottom panel to inverted hierarchy. The color intensity indicates the confidence level at which particular parameter combinations are allowed. Figure taken from [98].

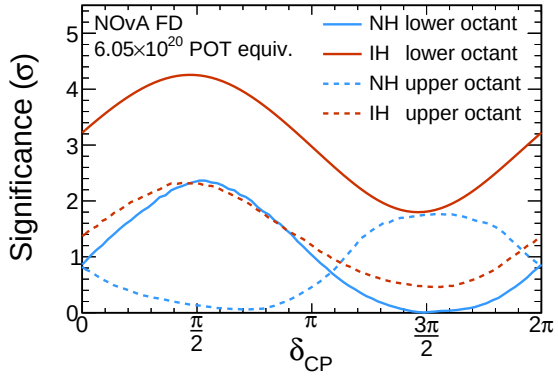

Figure 1.12. Feldman-Cousins significance at which each value of δ_{CP} is disfavoured for each of the four possible combinations of mass hierarchy: normal (blue) or inverted (red), and θ_{23} octant: lower (solid) or upper (dashed), by the combination of ν_e appearance and ν_μ disappearance measurement. Figure taken from [98].

calorimetric measurement of the particles produced in neutrino interactions. The neutrino beam will be produced at Fermilab, and will be sent 1,300 km away, to the Sanford Underground Research Facility (SURF) in South Dakota. The strategy of the experiment is to collect neutrino and anti-neutrino data and to measure $\nu_\mu/\bar{\nu}_\mu$ disappearance and $\nu_e/\bar{\nu}_e$ appearance probabilities. The combination of these four measurements will allow a clean measurement of the mass ordering and of δ_{CP}.

1.4 Current knowledge of neutrino oscillation parameters

Within the standard three-neutrino framework, the absolute neutrino masses and their ordering are currently unknown. Anyway a global fit of current data coming from oscillation experiments can provide interesting constraints for such parameters. The analysis

presented in [101] combined the results from oscillation experiments reported above. The extracted bounds on the mass-mixing parameters are expressed in terms of $\Delta\chi^2$ differences with respect to a minimum χ^2 value. The authors use the following $\Delta\chi^2$ difference $\Delta\chi^2_{\rm IO-NO} = \chi^2_{\rm min,IO} - \chi^2_{\rm min,NO}$ to assess the two mass-ordering hypotheses. In Tab II are reported the best-fit values and parameter ranges in normal (NO), inverted (IO) and any ordering. δm^2 and Δm^2 are defined in the following way:

$$\delta m^2 = m_2^2 - m_1^2 > 0 \ , \tag{1.74}$$

$$\Delta m^2 = m_3^2 - (m_2^2 + m_1^2)/2 \ , \tag{1.75}$$

where Δm^2 can be either positive or negative according to the NO or IO for the neutrino mass spectrum, respectively.

Parameter	Ordering	Best fit	1σ range	2σ range	3σ range
$\delta m^2/10^{-5}$ eV^2	NO, IO, Any	7.37	7.21 – 7.54	7.07 – 7.73	6.93 – 7.96
$\sin^2\theta_{12}/10^{-1}$	NO, IO, Any	2.97	2.81 – 3.14	2.65 – 3.34	2.50 – 3.54
$\lvert\Delta m^2\rvert/10^{-3}$ eV^2	NO	2.525	2.495 – 2.567	2.454 – 2.606	2.411 – 2.646
	IO	2.505	2.473 – 2.539	2.430 – 2.582	2.390 – 2.624
	Any	2.525	2.495 – 2.567	2.454 – 2.606	2.411 – 2.646
$\sin^2\theta_{13}/10^{-2}$	NO	2.15	2.08 – 2.22	1.99 – 2.31	1.90 – 2.40
	IO	2.16	2.07 – 2.24	1.98 – 2.33	1.90 – 2.42
	Any	2.15	2.08 – 2.22	1.99 – 2.31	1.90 – 2.40
$\sin^2\theta_{23}/10^{-1}$	NO	4.25	4.10 – 4.46	3.95 – 4.70	3.81 – 6.15
	IO	5.89	4.17 – 4.48 $\oplus$ 5.67 – 6.05	3.99 – 4.83 $\oplus$ 5.33 – 6.21	3.84 – 6.36
	Any	4.25	4.10 – 4.46	3.95 – 4.70 $\oplus$ 5.75 – 6.00	3.81 – 6.26
δ/π	NO	1.38	1.18 – 1.61	1.00 – 1.90	0 – 0.17 $\oplus$ 0.76 – 2
	IO	1.31	1.12 – 1.62	0.92 – 1.88	0 – 0.15 $\oplus$ 0.69 – 2
	Any	1.38	1.18 – 1.61	1.00 – 1.90	0 – 0.17 $\oplus$ 0.76 – 2

TABLE II. Results of the global 3ν oscillation analysis, in terms of best-fit values for the mass-mixing parameters and associated $n\sigma$ ranges ($n = 1, 2, 3$), defined by $\chi^2 - \chi^2_{\rm min} = n^2$ with respect to the separate minima in each mass ordering (NO, IO) and to the absolute minimum in any ordering. Remind that Δm^2 is defined herein as $m_3^2 - (m_1^2 + m_2^2)/2$, and that δ is taken in the (cyclic) interval $\delta/\pi \in [0, 2]$. Table taken from [101].

Fig. 1.13 shows the χ^2 curves in terms of the six oscillation parameters (δm^2, Δm^2, $\sin^2\theta_{12}$, $\sin^2\theta_{13}$, $\sin^2\theta_{23}$, δ), for both NO (blue) and IO (red). The author find an overall preference for NO, quantified by the χ^2 difference $\Delta\chi^2_{\rm IO-NO} = 3.6$.

The combination of various oscillation data starts to show some sensitivity to the sign of Δm^2 and a possible CP-violating phase δ.

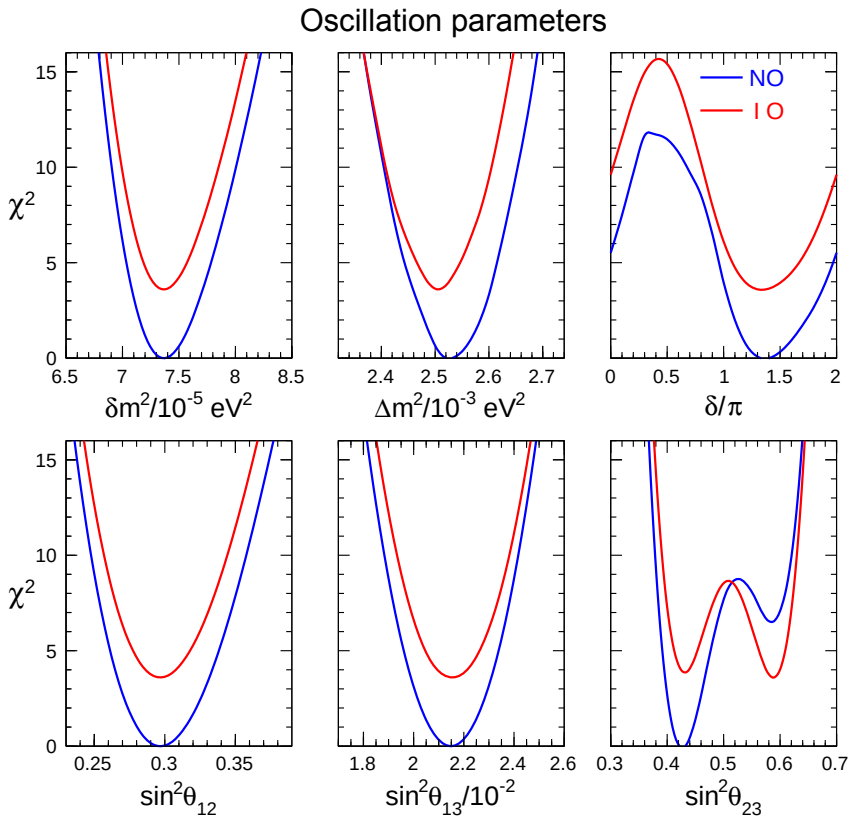

Figure 1.13. Global 3ν oscillation analysis. Projections of the χ^2 function onto the parameters δm^2, $|\Delta m^2|$, $\sin^2\theta_{ij}$, and δ, for NO (blue) and IO (red). In each panel, all the undisplayed parameters are marginalized, and the offset $\Delta\chi^2_{\mathrm{IO-NO}} = 3.6$ is included. Figure taken from [101].

Chapter 2

Neutrino scattering

Early neutrino scattering experiments, in the 1970's and 1980's, were conducted using either bubble chambers or spark chambers detectors and collected relatively small data samples. In earlier times, the focus was on confirming the V-A nature of the weak interaction and in measuring the axial-vector form factor of the nucleon [102]. Modern neutrino oscillation experiment use complex nuclei as target (carbon, oxygen). Thus it is crucial to understand the neutrino-nucleus scattering since it affects the background estimation and energy reconstruction. Driven by this motivation, in the last decade there has been considerable theoretical and experimental activity in the investigation of neutrino-nucleus cross sections in the few GeV energy region, where the flux of the contemporary long and short baseline experiments are peaked. The aim of this chapter is to discuss the neutrino scattering physics, giving the essential details to put in context future chapters, as well as the present theoretical and experimental status.

2.1 Neutrino-nucleons scattering

This dissertation focuses on the (anti)neutrino-nucleus CC interactions, but in order to define the formalism and terminology, it is useful to describe first the (anti)neutrino-nucleon CC scattering.

The most natural starting point is the definition of the formalism for the inclusive neutrino and antineutrino nucleon scattering for which the reactions are the following:

$$\nu_l + n \rightarrow l^- + X \tag{2.1}$$
$$\bar{\nu}_l + p \rightarrow l^+ + X \tag{2.2}$$

where $l^\pm$ is an arbitrary lepton and X is the hadronic debris produced in the scattering. It

is important to stess the analogy with the electron-nucleon scattering which is extensively used in used in this field.

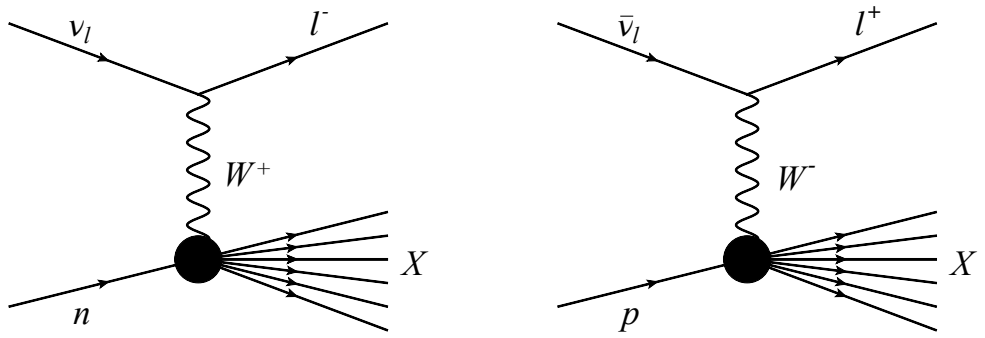

Figure 2.1. Feynman diagram of CC neutrino (left) and antineutrino (right) interaction.

The associated differential cross section as function of the energy of the outgoing lepton E_l and its angle with respect to the incoming neutrino θ_l, can be expressed as follows:

$$\frac{d^2\sigma}{dE_l d\cos\theta_l} = \frac{1}{32\pi^2 m_N}\frac{|\vec{p}_l|}{E_\nu}|\mathcal{M}|^2 \prod_X \frac{d^3\vec{p}_X}{(2\pi)^3 2E_X}(2\pi)^4\delta^4\left(\sum_X p_X - p_l - p_N - p_\nu\right) \quad (2.3)$$

$\mathcal{M}$ is invariant matrix element that, in the Born approximation, for neutrino CC interactions can be written as:

$$\mathcal{M} = \left(\frac{g}{2\sqrt{2}}\right)^2 \bar{l}_L(k')\gamma_\alpha(1-\gamma_5)\nu_L(k)\frac{i}{q^2 - M_W^2}\left(-g_{\alpha\beta} + \frac{q^\alpha q^\beta}{M_W^2}\right)\left\langle X(p')|j_\beta|N(p)\right\rangle \quad (2.4)$$

If the square of the 4-momentum transferred to the nucleon is much smaller than the intermediate vector boson mass squared, then the spin averaged matrix element is given by

$$|\mathcal{M}|^2 = \frac{G_F}{2}L_{\alpha\beta}W^{\alpha\beta} \qquad \text{with} \qquad \frac{G_F}{\sqrt{2}} = \frac{g^2}{8M_W^2} \quad (2.5)$$

where $L_{\alpha\beta}$ and $W^{\alpha\beta}$ are the leptonic and hadronic tensor respectively. Then the cross section is given by

$$\frac{d^2\sigma}{dE_l d\Omega_l} = \frac{G_F^2}{4\pi^2}\frac{|\vec{k}|}{|\vec{k}'|}L_{\alpha\beta}W^{\alpha\beta} \quad d\Omega_l = d\cos\theta_l d\phi_l \quad (2.6)$$

The leptonic tensor can be written in the following way

$$L_{\alpha\beta} = k_\alpha k'_\beta + k'_\alpha k_\beta - g_{\alpha\beta}k\cdot k' \pm i\epsilon_{\alpha\beta\sigma\delta}k'^\sigma k^\delta \quad (2.7)$$

where the metric is $g_{\alpha\beta} = (+;-;-;-)$ and the convention for the fully anti-symmetric Levi–Civita tensor is $\epsilon_{0123} = +1$. The $+$ is valid for ν while $-$ for $\bar{\nu}$ interactions. The

hadronic tensor, representing the structure of the nucleon, is completely determined by six independent structure functions [103]:

$$W^{\alpha\beta} = -g^{\alpha\beta}W_1 + \frac{p^\alpha p^\beta}{M^2}W_2 + \frac{i\epsilon^{\alpha\beta\rho\sigma}p_\rho p_\sigma}{2M^2}W_3 + \frac{q^\alpha q^\beta}{M^2}W_4 \tag{2.8}$$

$$+\frac{p^\alpha q^\beta - q^\alpha p^\beta}{M^2}W_5 + \frac{i(p^\alpha q^\beta - q^\alpha p^\beta)}{M^2}W_6 \tag{2.9}$$

The functions W_i are real functions of $\nu = p\cdot q$ and the square momentum transferred Q^2. Contracting the two tensors and the CC (anti)neutrino scattering cross section is

$$\begin{aligned}\frac{d^2\sigma}{dE_l d\Omega_l} &= \frac{|\vec{k'}|E_l M G_F^2}{\pi^2}\left\{2W_1\sin^2\frac{\theta_l}{2} + W_2\cos^2\frac{\theta_l}{2} \mp W_3\frac{E_\nu + E_l}{M}\sin^2\frac{\theta_l}{2}\right.\\ &+ \frac{m_l^2}{E_l(E_l+|\vec{k'}|)}\left[W_1\cos\theta_l - \frac{W_2}{2}\cos\theta_l \pm \frac{W_3}{2}\left(\frac{E_l+|\vec{k'}|}{M} - \frac{E_\nu+E_l}{M}\cos\theta_l\right)\right.\\ &+ \left.\left.\frac{W_4}{2}\left(\frac{m_l^2}{M^2}\cos\theta_l + \frac{2E_l(E_l+|\vec{k'}|)}{M^2}\sin^2\theta_l\right) - W_5\frac{E_l+|\vec{k'}|}{2M}\right]\right\}\end{aligned} \tag{2.10}$$

where the second sign specified, stand for the antineutrino cross-section, M is the mass of the nucleon, θ_l is the scattering angle of the outgoing lepton, $\vec{k'}$ is its momentum and $E_{\nu(l)}$ is the neutrino (lepton) energy[1]. It is important to stress that expression 2.10 is general since it has been computed without making assumptions on the hadronic system, essential instead to describe the exclusive processes which can be classified in three channels: charged-current quasi-elastic (CCQE), resonant pion production (RES) and deep inelastic scattering (DIS).

2.1.1 Charged-Current Quasi-Elastic scattering

The neutrino and antineutrino CCQE nucleon scattering are given by the following reactions:

$$\nu_l + n \rightarrow l^- + p \tag{2.11}$$

$$\bar{\nu}_l + p \rightarrow l^+ + n \tag{2.12}$$

where the incoming nucleon changes its identity (Fig. 2.2).

The CCQE differential cross section as detailed in [104] can be expressed as

$$\frac{d\sigma}{dQ^2} = \frac{G_F^2 M^2\cos^2\theta_C}{8\pi E_\nu^2}\left[A(Q^2) \pm \frac{(s-u)}{M^2}B(Q^2) + \frac{(s-u)^2}{M^4}C(Q^2)\right] \tag{2.13}$$

where $\pm$ refers to (anti)neutrino, s and u are the Mandelstam variables ($s-u = 4ME_\nu - Q^2 - m_l^2$, with m_l lepton mass) and θ_C is the Cabibbo angle. The factors $A(Q^2)$, $B(Q^2)$,

[1]The terms proportional to W_6 do not survive to the tensors contraction.

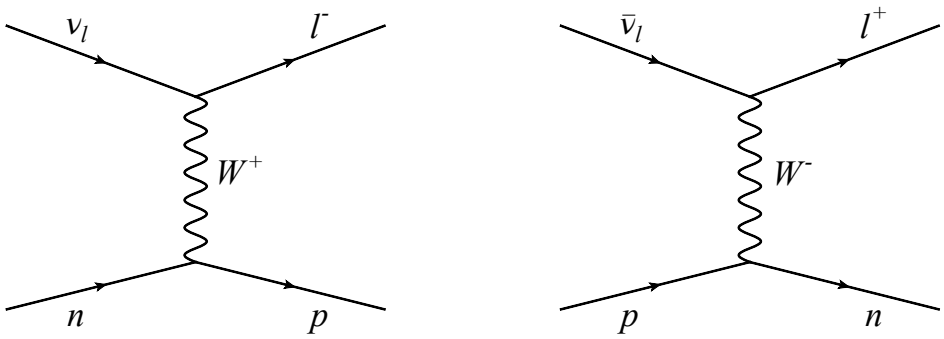

Figure 2.2. Feynman diagram of CCQE neutrino (left) and antineutrino (right) interaction.

and $C(Q^2)$ are form factors of the nucleon:

$$\begin{aligned} A(Q^2) &= \frac{(m_l^2+Q^2)}{M^2}\left[(1+\eta)\,F_A^2-(1-\eta)\,F_1^2\right. \\ &\quad +\eta\,(1-\eta)\,F_2^2+4\eta F_1F_2 \\ &\quad -\frac{m^2}{4M^2}\left((F_1+F_2)^2+(F_A+2F_P)^2\right. \\ &\quad \left.\left.-\left(\frac{Q^2}{M^2}+4\right)F_P^2\right)\right] \end{aligned} \tag{2.14}$$

$$B(Q^2) = \frac{Q^2}{M^2}F_A(F_1+F_2) \tag{2.15}$$

$$C(Q^2) = \frac{1}{4}\left(F_A^2+F_1^2+\eta F_2^2\right) \tag{2.16}$$

where $\eta=\frac{Q^2}{4M^2}$, F_1 and F_2 are the vector form factors and F_A is the axial form factors of the nucleon. It is important to note that $B(Q^2)$ contains the interference between the axial and vector currents, and it is responsible for the Q^2 dependent difference between ν and $\bar{\nu}$ cross sections. Moreover at $Q^2=0$ there is no difference between the two cross sections. Using conserved vector current (CVC), the vector form factors can be obtained from electron scattering, thus leaving the neutrino experiments to measure the axial-vector form factor of the nucleon. For this form factor a dipole form has been commonly assumed:

$$F_A(Q^2) = \frac{g_A}{\left(1+\frac{Q^2}{M_A^2}\right)^2} \tag{2.17}$$

which depends on two empirical parameters: the value of the axial-vector form factor at $Q^2=0$, $g_A=F_A(0)=1.2694\pm0.0028$ [105], determined from nuclear beta decay and, the "axial mass" M_A. Since the vector form factors and g_A were measured with high precision, measurement of M_A became the focus of the earliest measurements of neutrino QE scattering. A value of $M_A=1.026\pm0.021\ GeV$ has been obtained from a global

fit to the deuterium data [106] taken by bubble chamber experiments [107–110], while a consistent value of $M_A = 0.999 \pm 0.011\, GeV$ is obtained in Ref. [111] from a fit that additionally includes some of the early heavy target data.

2.1.2 Resonant pion production

The resonant channel can be accessed when the center–of–mass energy of a neutrino-nucleon interaction exceeds the mass of a delta baryon, leading to the production of a real pion[2]. Neutrino and antineutrino CC RES processes are:

$$\nu_l + p \rightarrow l^- + p + \pi^+, \qquad \bar{\nu}_l + p \rightarrow l^+ + p + \pi^- \tag{2.18}$$
$$\nu_l + n \rightarrow l^- + p + \pi^0, \qquad \bar{\nu}_l + p \rightarrow l^+ + n + \pi^0 \tag{2.19}$$
$$\nu_l + n \rightarrow l^- + n + \pi^+, \qquad \bar{\nu}_l + n \rightarrow l^+ + n + \pi^- \tag{2.20}$$

and two possible Feynman diagram are shown in Fig. 2.3.

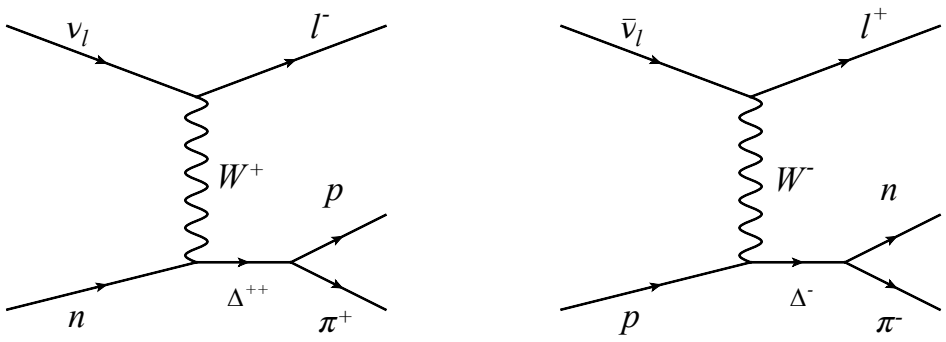

Figure 2.3. Feynman diagram of one of the possible CC RES neutrino (left) and antineutrino (right) interaction.

The resonant pion production cross section has been first performed by Rein and Sehgal [112]. In the computation are included 18 resonances with invariant mass $W \leq 2$ GeV and the interference terms between them, as well as non-resonant background. The contribution to the resonant pion production cross section from different resonances can be obtained multiplying the resonance formation cross section with the branching ratio for decay into the πN channels [113]:

$$\frac{d\sigma}{dQ^2 d\cos\theta_l d\Omega_\pi^{CM}} = \frac{1}{4\pi}\frac{d\sigma}{dQ^2 d\cos\theta_l}\frac{\Gamma_{R\rightarrow N\pi}}{\Gamma_{Total}} \tag{2.21}$$

where Q^2 is the energy transferred, $\cos\theta_l$ is the scattering angle of the outgoing lepton and Ω_π^{CM} is the solid angle between the outgoing lepton and the pion in the center–of–mass frame. Then the resonance formation cross section can be expressed as function of the lepton and hadronic tensors. As for CCQE, the structure of hadronic tensor can be

[2] As the neutrino energy increases, further resonances become available. These can produce kaons, photons or multiple particles.

written as a function of vector $C^V(Q^2)$ and axial $C^A(Q^2)$ form factors. The first can be measured by electron scattering experiment while the other can be constrained only using neutrino-nucleon scattering. Furthermore the axial part can be parametrised using two parameters: the axial mass for resonance interactions M_A^{RES} and the axial form factor $C_5^A(0)$.

2.1.3 Deep Inelastic scattering

Deep-inelastic scattering (DIS) on the nucleon is possible if the incident neutrino has enough energy to resolve the individual quarks in the nucleon. Then the knocked out quarks give rise to an hadronization process where a jet of particles is produced. Neutrino and antineutrino CC DIS reaction are:

$$\nu + N \rightarrow l^- + X \quad N = p, n \tag{2.22}$$
$$\bar{\nu} + N \rightarrow l^+ + X \tag{2.23}$$

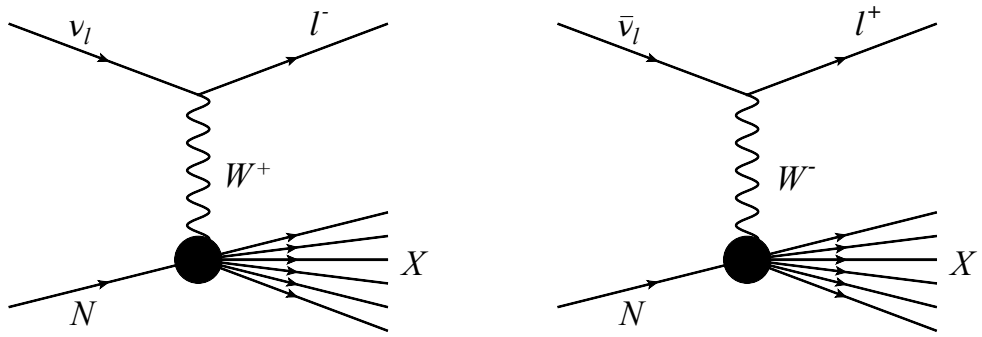

Figure 2.4. Feynman diagram of CC DIS neutrino (left) and antineutrino (right) interaction.

DIS processes can be completely described in terms of three dimensionless kinematic invariants: the inelasticity (y), the 4-momentum transfer ($Q^2 = -q^2$) and the Bjorken scaling variable x:

$$y = \frac{E_{had}}{E_\nu} \tag{2.24}$$
$$Q^2 = -m_l^2 + 2E_\nu(E_l - p_l \cos\theta_l) \tag{2.25}$$
$$x = \frac{Q^2}{2ME_\nu y} \tag{2.26}$$

where E_ν is the incident neutrino energy, M is the nucleon mass, $\nu = E_{had}$ is the energy of the hadronic system, and E_l, p_l, and $\cos\theta_l$ are the energy, momentum, and scattering angle of the outgoing lepton in the laboratory frame.
Then, using these three variables, the (anti)neutrino-nucleon DIS cross section scattering

can be written as:

$$\frac{d^2\sigma}{dx\,dy} = \frac{G_F^2 M E_\nu}{\pi\left(1+\frac{Q^2}{M_W^2}\right)^2}\left\{\frac{y^2}{2}2xF_1(x,Q^2) + \left(1-y-\frac{Mxy}{2E}\right)F_2(x,Q^2) \right. \\ \left. \pm y\left(1-\frac{y}{2}\right)xF_3(x,Q^2)\right\} \tag{2.27}$$

where M_W is the mass of the W and the $\pm$ refers to neutrino (antineutrino) interactions. The $F_i(x,Q^2)$ are the dimensionless nucleon structure functions that contain the underlying structure of the nucleon. Such factors can be related to the W functions introduced before in the following way:

$$F_1(x,Q^2) = MW_1(\nu,Q^2) \tag{2.28}$$
$$F_2(x,Q^2) = \nu W_2(\nu,Q^2) \tag{2.29}$$
$$F_3(x,Q^2) = \nu W_3(\nu,Q^2) \tag{2.30}$$

Assuming the nucleon is composed by point-like structures, then at very high Q^2 the factors F_i only depend on x. This behaviour goes under the name Bjorken scaling.

2.2 Neutrino-nucleus scattering

Theoretical modelling of the neutrino-nucleus scattering face many complications. The first is the initial state of the nucleons inside a nucleus. They are indeed constantly moving around inside the nuclear potential, changing their momentum and direction in relation to an incoming neutrino, which affects both the kinematics and the cross-section. Unfortunately the initial momentum spectra of nucleons is not well known, and can vary significantly even between similar mass nuclei. An additional complication is that the neutrino can interact not only with individual nucleons, but the interaction can include correlated nucleon pairs or any combination of nucleons in a quasi-bound state. After the final-state particles have been created from an interaction, they need to propagate out through the nucleus. During the propagation they can interact with the other nucleons inside the nucleus. These processes, called "final state interactions" (FSI), can alter the particles type and number.

In case of CC inclusive neutrino-nucleus scattering, the cross-section has the same expression of the neutrino-nucleon cross-section. The only difference is in the hadronic tensor, that can be written in the following way [114]:

$$W^{\alpha\beta} = W_s^{\alpha\beta} + iW_a^{\alpha\beta} \tag{2.31}$$

with W_s (W_a) the symmetric (antisymmetric) tensor. It can be expressed in terms of the polarization propagator

$$W_{(s,a)}^{\alpha\beta} = -\frac{1}{\pi}\,\mathrm{Im}\,\Pi_{(s,a)}^{\alpha\beta}\,. \tag{2.32}$$

This is a well known result obtained for the response of many-body systems to external probes [115]. The polarization propagator is the place where the different nuclear models enter in the cross section modelling. The commonly used are: *Relativistic global Fermi Gas* (RFG), *Relativistic local Fermi Gas* (LFG) and *Spectral Function* (SF).

2.2.1 Nuclear models

The simplest nuclear model, present in most event generators, is the Relativistic global Fermi Gas (also called Relativistic Fermi Gas, RFG) [116]. The nuclear ground state is modelled by a gas of non-interacting nucleons with a global Fermi momentum p_F and a constant binding energy E_B. Integrating over the spherical nucleus, the distribution of initial nucleon momentum result to be quadratic, as shown in Fig 2.5. Since the nucleons obey the Pauli exclusion principle, the scattered nucleons cannot end up in a state which is already occupied by another nucleon reducing the available phase space and hence the cross-section. Thus, this model can be described using two parameters that determine the probability distribution for the momentum and energy of the nucleons which can be expressed as follows:

$$P(E, \mathbf{p}) = \theta(p_F - |\vec{p}|)\delta(E + \sqrt{m_N^2 + |\vec{p}|^2} - E_B) \tag{2.33}$$

where θ is the step function and M_N is the nucleon mass. The values for p_F and E_B are obtained through fits to electron scattering data [117]. In this model the density of the nuclear matter is supposed to be constant which is the simplest approximation, valid for an infinite system.

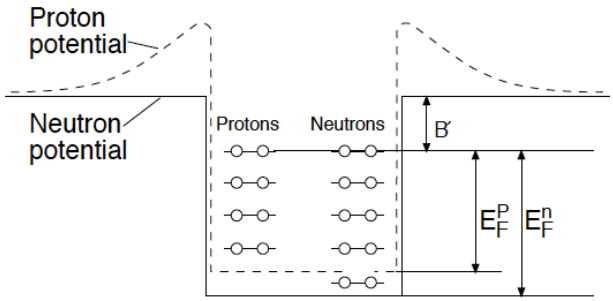

Figure 2.5. Sketch of the proton and neutron potentials and states in the Fermi gas model (B′ stands for the binding energy). Figure taken from [118].

An improvement of the RFG is the so called relativistic local Fermi Gas (LFG), where finite effects of the nucleus size are included, and the Fermi momentum is fixed according to the local density of protons and neutrons $\rho_{p,n}(r)$

$$p_F^{p,n}(r) = \left[3\pi^2 \rho_{p,n}(r)\right]^{1/3} . \tag{2.34}$$

where r is the nucleon distance from the center of the nucleus.

A more sophisticated model which avoid the discontinuity due the Fermi momentum in the RFG model is called *Spectral function* (SF) [119, 120]. In this case the probability distribution for the momentum and energy of the nucleons is made of two terms: a mean-field term for single particles, and a term which describes the interactions of correlated

pairs of nucleons

$$P(E, \mathbf{p}) = P_{MF}(E, \mathbf{p}) + P_{corr}(E, \mathbf{p}) \tag{2.35}$$

The correlation term leads to a very long tail in both momentum and binding energy (see Fig. 2.6), and accounts for roughly 20% of the total SF. These initial-state correlations lead to the ejection of a second nucleon. The SF in turn suppress the cross-section for small transferred energy, providing a total integrated cross-section which is suppressed by 5-10% with respect to Fermi gas. Also the SF are computed for each nucleus and are tuned using electron scattering data with $e^- + p$ final states.

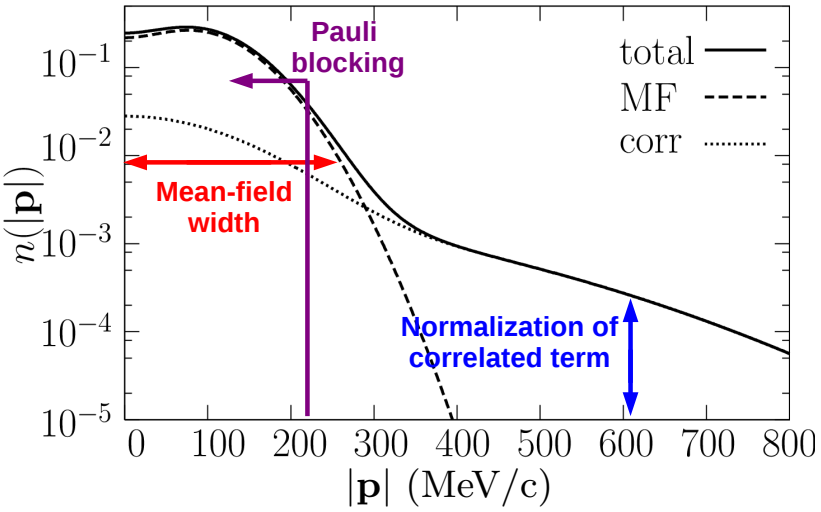

Figure 2.6. Probability distribution for initial state nucleon as a function of the magnitude of the nucleon momentum in SF model. Figure taken from [121].

These models assume the validity of the impulse approximation (IA) where (anti)neutrino interacts with a single nucleon in the nucleus and the remaining A-1 particles act as spectators. Then the cross section with a nucleus is described as an incoherent sum of processes only involving one nucleon (see Fig. 2.7).
However, when the momentum transferred to the target is small one should not expect this approximation to hold. Collective effects can be handled within the Random Phase Approximation (RPA) which is a non-perturbative method to describe microscopic quantum mechanical interactions in many body systems. It was introduced originally to describe the interaction between electrons in the theory of matter [123–125] and it has been adapted in recent model of neutrino-nucleus interactions to describe the collective effects due to the interactions and correlations of the nucleons inside the nucleus [126, 127]. In neutrino-nucleus scattering RPA is a nuclear screening effect used as a correction to the model based on RFG to account for medium and long-range correlations: at very low Q^2 the cross section is suppressed, while at medium values it is enhanced and at large values the effect disappear converging asymptotically into the IA prediction.

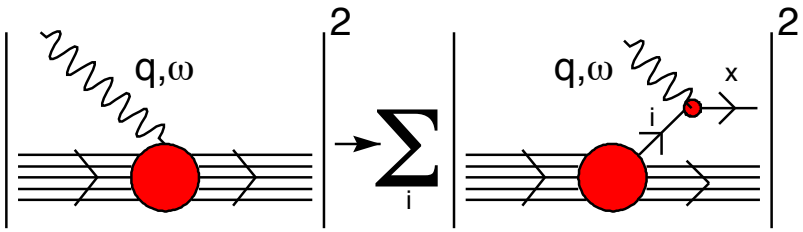

Figure 2.7. Schematic representation of the IA, in which the nuclear cross section is replaced by the incoherent sum of cross sections describing scattering off individual nucleons, with the recoiling (A-1)–nucleon system acting as a spectator. Figure taken from [122].

2.2.2 Final State Interactions

After the final-state hadrons have been created in a neutrino-nucleus interaction, they need to propagate out through the nucleus. Since these particles interact via the strong force, there is a significant probability of re-interaction within the nucleus before escape. These processes, called "final state interactions" (FSI), can alter the particles type and number via particle absorption, scattering and production as illustrated in Fig. 2.8. These kind of interactions are then not negligible for relatively heavy nuclei since they may lead to a misidentification of the reaction type.

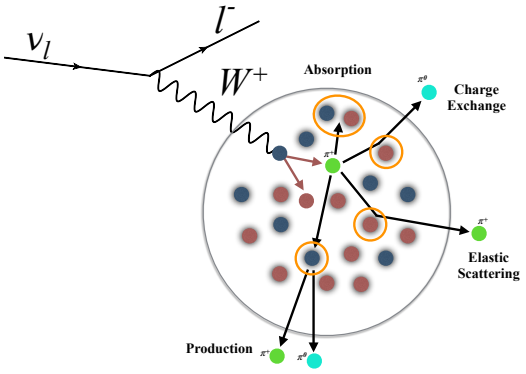

Figure 2.8. Schematic representation of the possible pion FSI interaction in the nuclear matter.

The most relevant process at GeV scale is the absorption of the pion in the nuclear medium. In all the other cases the kinematics of outgoing pion can be affected, changing the efficiency of pion identification. Finally charge-exchange processes affect the rate of π^0 production, which is an important background for ν_e appearance. Therefore, an accurate model of hadron interactions is required for precise cross sections and oscillation parameters measurements. In case of protons an important quantity is the nuclear transparency T which is the probability for a proton to escape the nucleus unchanged. Electron-scattering data on different nuclei show that T does not depend on the transferred momentum Q^2, but decreases as the nucleus become heavier [128].

2.2.3 Neutrino-nucleus exclusive channels

The polarization propagator can be decomposed as sum of the exclusive processes [114, 129]. The formalism introduced in the previous paragraph for the QE, resonant and DIS channels is still valid for neutrino-nucleus scattering. Anyway the interaction of a neutrino with a nucleus add more channels compared to the neutrino-nucleon interaction: the so-called multinucleon knock-out and the coherent pion production (COH)[3].

In the discussion of the multinucleon emission the MiniBooNE ν_μ CCQE measurement [130] plays a central role. The collaboration published the first double differential ν_μ CCQE cross section on ^{12}C extracted as a function of the energy and angle of the outgoing muon, reporting a cross section per nucleon ~ 20 % higher than expected from bubble chamber data. In this analysis the CCQE signal events were defined as the processes in which only a muon is detected in the final state, but no pions. This definition has been chosen by the Collaboration since MiniBooNE was a liquid scintillator Čerenkov detector, and if the proton is under the Čerenkov threshold it cannot be detected. The MiniBooNE analysis took also into account the possibility that in the neutrino interaction, a pion produced via the excitation of the Δ resonance escapes detection, for instance because it is reabsorbed in the nucleus, mimicking a CCQE process. The size of the cross section was found to be well described by the RFG model with an axial mass of $M_A = 1.35 \pm 0.17\, GeV$, which is in contradiction not only with the bubble chambers, but also with the NOMAD data, an higher-energy experiment on carbon that found a value of $M_A = 1.05 \pm 0.02 \pm 0.06 GeV/c^2$ [131] (see Fig. 2.9).
The origin of this disagreement, called the *CCQE puzzle*, has been extensively debated. A possible solution was suggested by Martini *et al.* [126] (in the following referred as Martini model). The interaction with a single nucleon which is knocked out (the genuine CCQE scattering) is not the only possible. In addition one must consider the interaction with a correlated pair of nucleus (NN correlations) that lead to two nucleon excitation (2p-2h) as pictorially represented in Fig. 2.10. Anyway 3p-3h excitation are also possible. Together they are called np-nh (or multinucleon) excitation. Historically, multinucleon emission hypothesis was firstly proposed to explain the dip between the QE and Δ excitations [133, 134] observed in electron scattering measurements as shown in Fig. 2.11 that reports the inclusive cross section for scattering of electrons on carbon at 560 MeV and 60 Deg.

The addition of this channel to the genuine CCQE contribution leads to an agreement with the MiniBooNE data without any increase of the axial mass as it is shown in Fig. 2.12. Nowadays processes in which only a final charged lepton is detected, hence including multinucleon excitations, but when the pion absorption contribution is subtracted, are usually called **CCQE-like**. Thus, what MiniBooNE published was not CCQE data, but CCQE-like data. To avoid the confusion of the signal definition, it is increasingly more popular to present the data in terms of the final state particles, such as "1 muon and 0 pion, with any number of protons", called **CC-0π**. This corresponds to the processes in which only a final charged lepton is detected and the pion absorption contribution is not subtracted.

[3] A detailed discussion of the coherent pion production is beyond the scope of this thesis. It is important to mention that in the coherent pion production the neutrino scatters on the whole nucleus which stays unchanged.

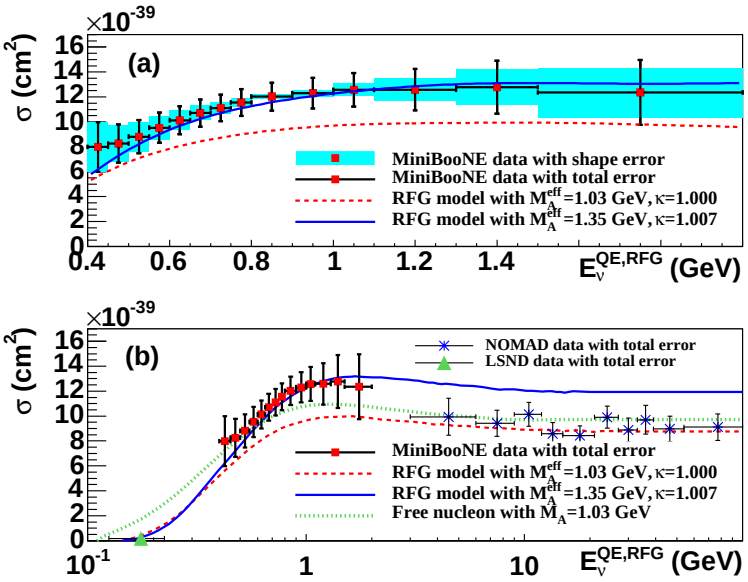

Figure 2.9. Flux-unfolded MiniBooNE ν_μ CCQE cross section per neutron as a function of neutrino energy. In (a), shape errors are shown as shaded boxes along with the total errors as bars. In (b), a larger energy range is shown along with results from the LSND [132] and NOMAD [131] experiments. The prediction has been obtained using the RFG model with two different value for the axial mass M_A. Figure taken from [130].

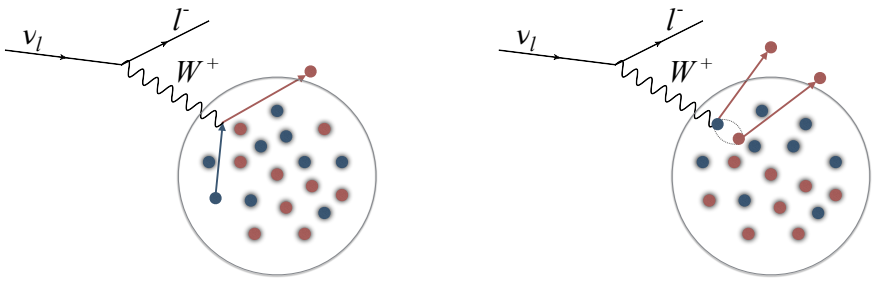

Figure 2.10. Pictorial representation of a genuine CCQE (left) and 2p2h (right) process.

After the suggestion of the inclusion of multinucleon knok-out as explanation of the MiniBooNE anomaly, the interest on this channel rapidly increased and nowadays several models agree on the crucial role of the multinucleon excitation in order to explain the experimental cross section. The theoretical approaches most discussed in this dissertation are the already mentioned Martini model and the one from Nieves *et al.* [127] (in the following referred as Nieves model). The two models are quite similar: they start from a LFG as nuclear model and consider medium polarization and collective effects through RPA.

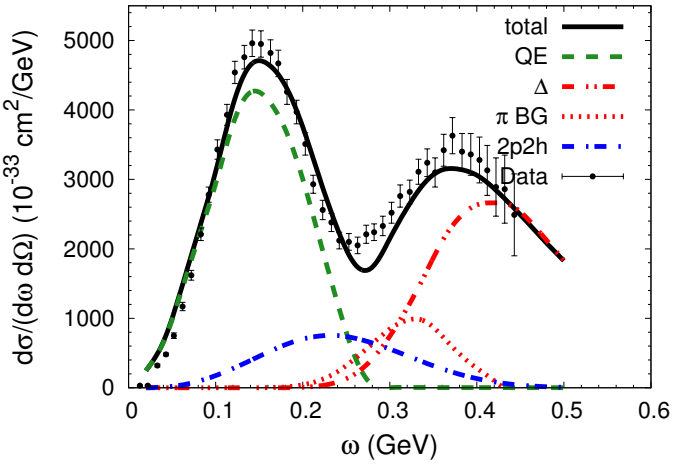

Figure 2.11. Inclusive cross section for scattering of electrons on carbon at 560 MeV and 60 Deg ($Q^2 = 0.24\,GeV^2$ at the QE peak), obtained with a free Δ spectral function. The left dashed curve gives the contribution from true QE scattering, the dash-dotted curve that from 2p-2h processes, the dashed-dotted-dotted curve that from Δ excitation and the dotted curve that from pion background terms. Figure taken from from [135].

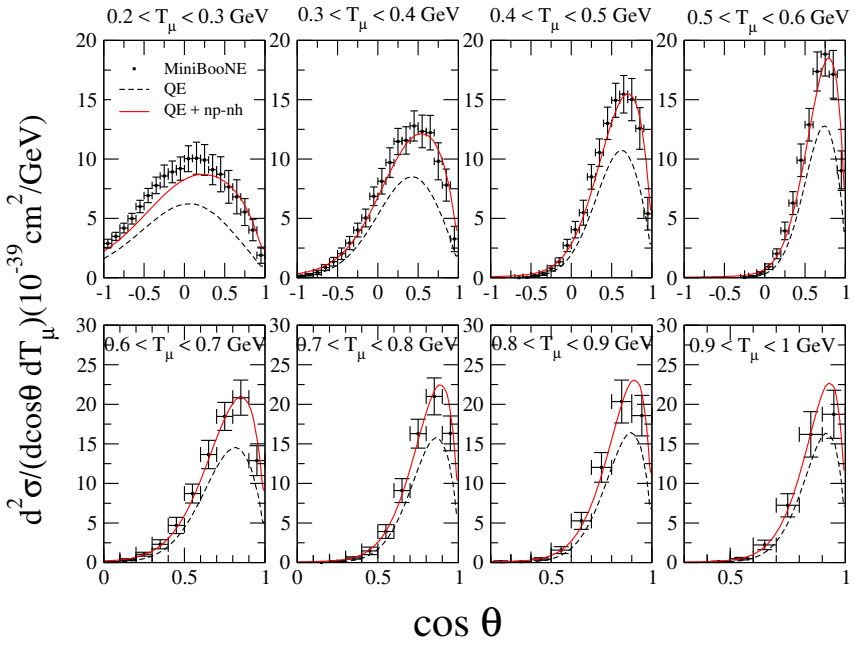

Figure 2.12. MiniBooNE flux-integrated CCQE-like ν_μ-^{12}C double differential cross section per neutron for several values of muon kinetic energy as a function of the scattering angle. Dashed curve: pure CCQE cross section calculated using RPA correction; solid curve: with the inclusion of np-nh component. The figure is taken from [136].

2.3 Neutrino event generators

Accelerator-based oscillation and scattering neutrino experiments use Monte Carlo (MC) event generators to simulate the processes discussed in the previous paragraphs. They

play a crucial rule since, in these experiments, it is necessary to identify the flavor of the interacting neutrino[4] and reconstruct its energy from the particles observed in the detectors. Thus a detailed knowledge of the final state after the interaction is essential to analyse and interpret the data, and to evaluate the efficiency and purity of the selected samples.

A neutrino event generator must provide:

- the inclusive cross sections and the contributions of each interaction mode;
- the energy and direction of all the produced particles, taking into account the possible re-interactions inside the target nucleus.

Usually the events simulation can be separated into several steps:

1. The target nucleus and the neutrino energy are selected according to the total cross section for each material and the spectrum of the neutrino beam.
2. The initial four–momentum of the target nucleon and the position inside the nucleus where the neutrino interaction takes place are chosen. The first quantity is selected using a probability density profile given by the different nuclear model implemented in the generator.
3. The type of interaction is selected taking into account the probabilities for the corresponding neutrino energy.
4. At this step the neutrino-nucleon interaction is simulated and the four–momenta of the outgoing lepton, nucleon(s) and other particles are fixed by the differential cross section of the interaction considered.
5. The possible interaction of the produced nucleons and mesons in their path through the nucleus are also simulated.

An important aspect for the neutrino events generators is their reproducibility. They are tuned and validated against a wide variety of data, taken by photon, electron, hadron and neutrino scattering experiments. Furthermore the results of the external data tuning are important for experiments as they quantify the uncertainty on model parameters, needed in the evaluation of generator-related systematic uncertainties. Electron scattering data plays an important role in determining the vector contribution to the form factors and in evaluating specific aspects of the nuclear model. Hadron scattering data are used in validating the nuclear model, in particular the modelling of final state interactions. Tuning of neutrino-nucleon scattering relies heavily on the previous generation of high energy neutrino scattering which used hydrogen and deuterium as target, and on more recent data [105].

The most common generators used by the accelerator-based oscillation and scattering neutrino experiments are: GENIE [137], NEUT [138], GiBUU [139] and NuWro [140].

[4]Neutrino beams are not mono–energetic and contain several flavors.

Since the neutrino events generators used to perform the work described in this dissertation are NEUT (version 5.3.2) and GENIE (version 2.8.0), the discussion will be limited only to them. For neutrino-nucleon and neutrino-nucleus interaction the two generators distinguish between the following interaction channels:

Quasi-Elastic Scattering: it is modelled in both generators using an implementation of the Llewellyn-Smith model [104] and the same parametrization for the vector form factors (called BBBA05) [141]. However, they use a different value for the axial mass M_A: 1.21 GeV/c^2 (value extracted from the K2K experiment and reported in Ref. [142]) and 0.99 GeV/c^2.

Multinucleon knock-out (usually indicated as 2p2h): NEUT uses the model developed by Nieves *et al.* [127], while GENIE does not include this interaction[5].

Resonance Production: use the calculation of Rein-Sehgal [112] with different cut-off on the invariant mass of the resonance. NEUT takes into account 18 resonances as well as their interferences and the lepton mass. The default values for the axial mass and the form factor are $M_A^{RES} = 0.95\, GeV/c^2$ and $C_A^5(Q^2 = 0) = 1.01$ respectively [144]. The normalization of the non-resonant background is set to 1.30. GENIE incorporates 16 resonances without including interference terms and neglecting the lepton mass. The default value used for the axial mass is 1.12 GeV/c^2 [145]. The Δ width is modified for in-medium effects and it is assumed that inside the nucleus 20% of Δ decays are pion-less.

Coherent scattering: in both generators this channel follow the model of Rein and Sehgal [146], which is based on the hypothesis of partially conserved axial current (PCAC).

Deep Inelastic Scattering: in both NEUT and GENIE this channel is modelled using the PDF parametrization (called GRV98) described in [147] which include a modification that describe scattering at low momentum transferred.

The nuclear effects are treated differently by both generators:

Nuclear model: NEUT use the SF model by Benhar *et al.* [119] as default. GENIE uses the RFG by Bodek and Ritchie implementation [148], in which a high-momentum tail is included to account for nucleon-nucleon correlations as those predicted by the SF model. In NEUT it is also possible to reweight the prediction obtained using the SF model in order to move on a model with RFG plus RPA correction.

Hadronization: for hadrons produced via baryonic resonances, the amplitudes and resonance branching fractions fully characterize the hadronic system. For non-resonant production, a hadronization model is required. In NEUT, for low invariant mass region, Koba-Nielsen-Olesen (KNO) scaling [149] is used, while for high invariant mass is used PYTHIA/JETSET model [150]. In GENIE three different invariant mass regions are taken into account. It uses the Andreopoulos-Gallagher-Kehayias-Yang (AGKY) model [151] for low invariant mass, which includes a phenomenological description of the low invariant mass region based on Koba-Nielsen-Olesen

[5] In the most recent versions of GENIE this interaction has been implemented [143].

(KNO) scaling. For the intermediate invariant mass region it uses AGKY and PYTHIA/JETSET.

FSI: in both NEUT and GENIE the transport in the nucleus of the particle produced in a neutrino interactions is simulated according to an intranuclear cascade [147] using the Woods-Saxon distribution to model the nuclear density [152]. The simulation relies on stepping the particles through the nucleus and allowing them to interact according to the mean free path for each interaction type. This heavily relies on data from pion-nucleus and proton-nucleus scattering experiments to predict the probabilities for various interaction types.

A summary of the different models for CC interaction channels implemented in the version of NEUT and GENIE used in the work described in this dissertation is reported in Tab. III.

Reaction type	NEUT v5.3.2	GENIE v2.8.0
CCQE scattering	SF [119] or RFG [116] and RPA [127]	RFG [148]
	BBBA05 [141]	BBBA05
	$M_A^{QE} = 1.21\ GeV/c^2$	$M_A^{QE} = 0.99\ GeV/c^2$
	$p_F^{^{12}C} = 217\ MeV/c\ p_F^{^{16}O} = 225\ MeV/c$	$p_F^{^{12}C} = 221\ MeV/c\ p_F^{^{16}O} = 225\ MeV/c$
	$E_B^{^{12}C} = 25\ MeV/c\ E_B^{^{16}O} = 27\ MeV/c$	$E_B^{^{12}C} = 25\ MeV/c\ E_B^{^{16}O} = 27\ MeV/c$
Multinucleon knock-out	Nieves model [127]	Not included
CC-RES π production	Rein-Sehgal model [112] ($W < 2\,GeV$)	Rein-Sehgal model ($W < 1.7\,GeV$)
	Form factor from [144]	Form factor from [145]
CC-DIS	GRV98 PDF [147]	GRV98 PDF
	Bodek-Yang corrections at low Q2 [153]	Bodek-Yang corrections at low Q2
Hadronization	KNO scaling [149] ($W < 2\,GeV$)	AGKY [151] ($W < 2.3\,GeV$)
	PYTHIA/JETSET [150] ($W > 2\,GeV$)	AGKY+PYTHIA/JETSET ($2.3 < W < 3\,GeV$)
		PYTHIA/JETSET ($W > 3\,GeV$)
FSI	Intra-nuclear cascade	Intra-nuclear cascade

TABLE III. Summary table of the models used in NEUT v5.3.2 and GENIE v2.8.0 to simulate the CC interactions.

Events generator provide also reweighting tools for systematic error evaluation. To each input physical parameter P is associated a systematic parameter x_P. Tweaking this systematic parameter modifies the corresponding physics parameter P as follows:

$$P \to P' = P\left(1 + x_P \frac{\delta P}{P}\right) \tag{2.36}$$

where δP is the estimated standard deviation of P. Thus tweaking the systematic parameter by ± 1 modifies the corresponding physics quantity P by δP. Usually the systematic parameters are estimated using external data such electron and hadron scattering.

2.4 Experimental status of neutrino scattering

In light of the above discussion, make precision (anti)neutrino-nucleus measurements is challenging due to the presence of nuclear effects. They modify the processes mentioned above and, being the neutrino beam not mono-chromatic, our source is not narrow enough to resolve multiple, competing effects within a given process. In addition also the detector effect play a role. For instance in a CC resonant pion production event the pion can be undetected and it is identified as CCQE event. Therefore it is better to define more inclusive reactions which reflect the experimental signature: the already mention CC-0π and the CC-1π instead of the CC resonant pion production.

In order to solve these issues the models of these processes are tested against a wide variety of experimental data. The MINERνA and T2K experiments include data on a wide range of target materials. This gives the possibility to perform cross section measurements changing the target material, but using the same probe, that can provides a constraint on nuclear effects. The second possible test of the available models is the comparisons of neutrino and antineutrino beams on the same target material. For instance the 2p2h component of the cross section have a different impact on the antineutrino cross section, thus a comparison against the neutrino data could shed light on the multinucleon emission process.

Attempt to probe the presence of nuclear effects in neutrino carbon interactions has been performed by the MINERνA collaboration directly through the extraction of both the 3-momentum transfer ($q_3 = |\vec{q}|$) and hadronic recoil energy for a given event [154]. They introduced the variable "energy available" (E_{avail}) which is defined as the sum of kinetic energy of protons and charged pions, and the total energy of neutral pions, electrons and photons leaving the nucleus. The result shows that the relative strength of 2p2h needs to be adjusted (Fig. 2.13); a similar approach was taken by NOνA, leading to the same result.

The 2p2h channel has been further studied and a recent result have been published by T2K [155] which is characterized by a beam peaked around 600 MeV, close to the MiniBooNE flux which was centered around 800 MeV. The measurement of the CC-0π ν_μ cross section has been performed at the T2K near detector (ND280) and the result has been presented as flux-integrated double-differential cross section as a function of

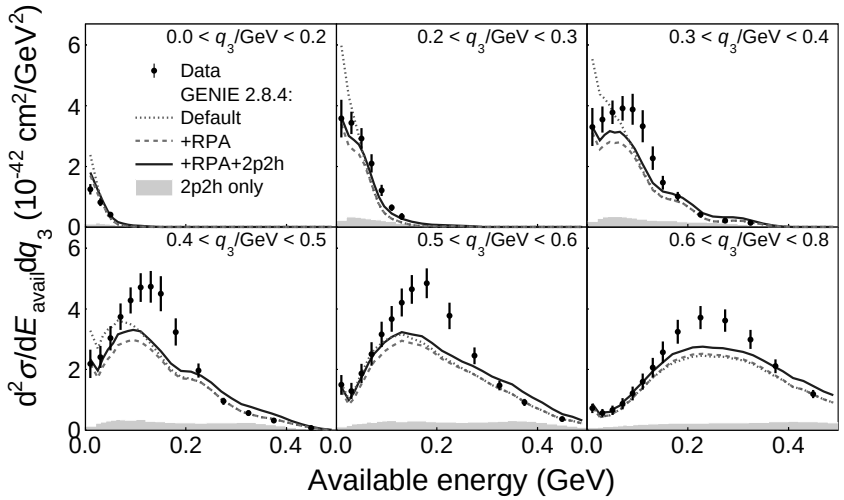

Figure 2.13. Double-differential cross section as function of the available energy and the 3-momentum transfer compared to the GENIE model with reduced pion production (small dot line), the same with RPA suppression (long-dashed), and then combined with a QE-like 2p2h component (solid). The 2p2h component is shown separately as a shaded region. Figure taken from [154].

muon momentum and angle. The analysis has been designed to be as much as possible model-independent. The selection requires events with only one reconstructed muon or a muon and a proton, the background prediction is tuned using two control regions with a consistent component of resonant pion production and DIS events. A second analysis, based on different selection and cross section extraction method, has also been performed. The results from the two analysis are in agreement proving the robustness of the measurement against the effects due to signal and background modelling. The results are compared in Fig.2.14 to the predictions from Martini and Nieves models, with and without including multinucleons effects. The data prefer the presence of 2p2h contribution with respect the genuine CCQE with RPA corrections but the level of precision is not enough low to distinguish between different models.

The production of single pion is mainly due to Δ resonance decay. MiniBooNE [156] and MINERνA [157] results are in disagreement: the differences between the two experiments in the shape of the differential cross section as a function of the outgoing pion energy cannot be described by any model. T2K has new results for CC-1π^+ on water using the near detector data. The signal includes events with only one pion and with positive charge. The results are shown in Fig.2.15: GENIE tends to overestimate the overall rate while NEUT is in good agreement with the data.

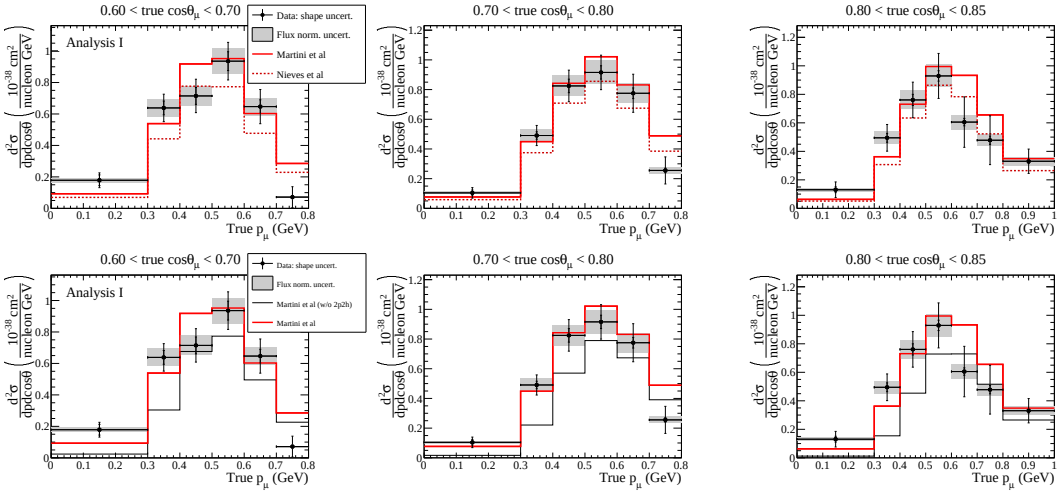

Figure 2.14. Results of CC-0π measurement from T2K compared with the Martini and Nieves models (top raw) and with the model from Martini with and without 2p2h contribution (bottom raw). Figures taken from [155]

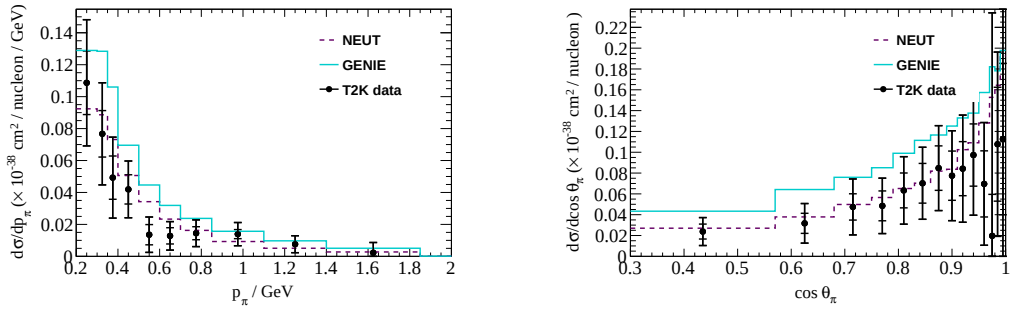

Figure 2.15. T2K measurement of CC1π^+ cross section as a function of pion momentum (left) and angle (right), compared to NEUT and GENIE simulation. Figure taken from [158].

In conclusion neutrino interaction physics has undergone a fast development in the last decades driven by the necessity of a reduction of systematic errors on the oscillation parameters. In the few-GeV energy region, the neutrino-nucleus cross sections are known with a precision not exceeding 20%, hence are one of the most important sources of systematic uncertainties. Indeed the oscillation experiments measure the neutrino interactions rate, which is the convolution of three factors: the neutrino flux, the interaction cross section and the detector efficiency. In view of the poor knowledge of the nuclear effects, it is particular important to design analyses as much as possible model-independent. Furthermore, to reach a detailed understanding will be crucial to compare measurements from different interaction processes, at different neutrino energies, on different nuclear targets and for different neutrino species.

Chapter 3

T2K experimental setup

T2K (Tokai-to-Kamioka) is a long baseline neutrino oscillation experiment located in Japan [159]. It started its first operation in March 2010 and its aims is to measure the parameters of the PMNS matrix and to look for the first indication of CP violation in the leptonic sector. It uses a (anti)neutrino beam produced impinging on a graphite target a proton beam accelerated up to 30 GeV by the accelerator complex of J-PARC (Japan Proton Accelerator Research Complex), located in Tokai, about 100 km north-west of Tokyo. Neutrinos are detected first in a near detector complex at 280 m from their production point and then travel 295 km toward the far detector, Super-Kamiokande (SK).

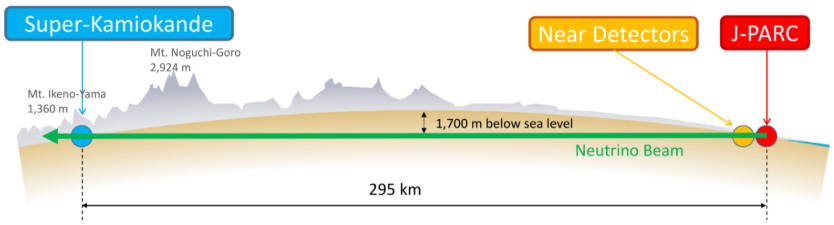

Figure 3.1. A schematic of a neutrino journey from the neutrino beamline at J-PARC, through the near detectors which are used to determine the properties of the neutrino beam before the oscillation, to Super-Kamiokande located 295 km west of the beam source, 1000 m deep underground.

In these years of operation T2K has already reached many achievements. In 2011 it observed for the first time a non-zero value for θ_{13} with a significance of about 3σ [92], then the evidence with a significance of 7.3σ with only $\sim 8.2\%$ of the total approved data [93], which correspond to an exposure of 7.8×10^{21} proton on target (POT), and the world best measurement of $\sin^2 \theta_{23}$ [94]. The measurement of non-zero values for all three

mixing angles opened the possibility to measure the CP violation in the leptonic sector. The future goals of T2K are the improvement of the measurement of the atmospheric oscillation parameters, the first observation of $\bar{\nu}_\mu \to \bar{\nu}_e$ appearance as well as search first hint of CP violation and searches for exotic physics, like sterile neutrinos.

3.1 Physics motivations

T2K was designed to study the neutrino ν_μ disappearance and ν_e appearance in a neutrino beam. In order to achieve these goals a near and a far detectors are exposed to a neutrino beam with an energy peaked around 0.6 GeV. Below 1 GeV, the dominant contribution to (anti)neutrino cross section is due to CCQE interactions as shown in Fig. 3.2. In this case the reconstructed neutrino energy, that enter in the oscillation probabilities (Eqs. 1.36 and 1.38), is given by:

$$E_\nu^{CCQE} = \frac{m_f^2 - (m_i')^2 - m_l^2 + 2m_i' E_l}{2(m_i' - E_l + p_l \cos\theta_l)} \tag{3.1}$$

where m_i and m_f are the initial and final nucleon masses respectively, $m_i' = m_i - E_B$, where $E_B = 27\ MeV$ is the binding energy of a nucleon inside oxygen, and E_l, p_l and θ_l are the lepton energy, momentum and angle with respect to the incident neutrino angle respectively.

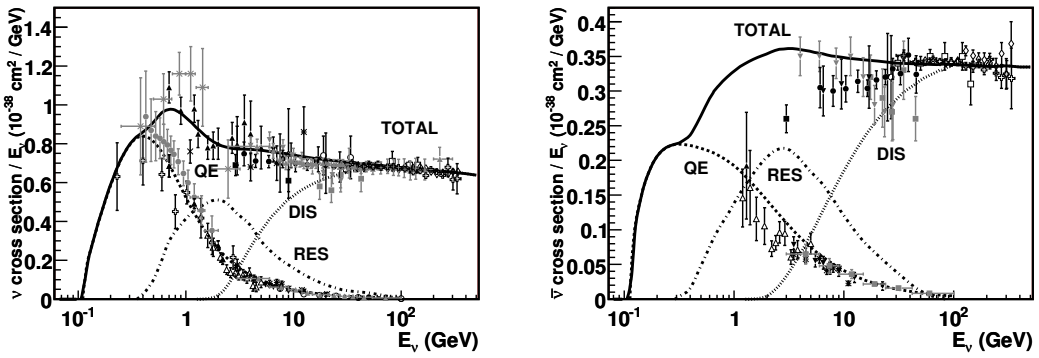

Figure 3.2. Muon neutrino (left) and antineutrino (right) CC cross-section measurements and predictions as a function of neutrino or antineutrino energy. Data are from different experiment and are represented by different colours and marker symbols. The dominant contributing process at the T2K peak energy is CCQE (dashed) scattering, with contributions from RES (dot-dashed) and DIS (dotted) in the high-energy tail of the neutrino spectrum. Figure taken from [102].

As already introduced T2K started to search hint of CP violation in the leptonic sector which can shed light on the matter/antimatter asymmetry in the universe. This phase introduces a difference in the appearance probability between neutrinos and antineutrinos. A direct measurement of CP violation can then be achieved comparing $\nu_\mu \to \nu_e$ and $\bar{\nu}_\mu \to \bar{\nu}_e$ channels. Fig. 3.3 shows $\nu_\mu \to \nu_e$ and $\bar{\nu}_\mu \to \bar{\nu}_e$ oscillation probabilities as a function of the true neutrino energy and for different value of δ_{CP}, $(0, \frac{\pi}{2}, \pi$ and $-\frac{\pi}{2})$ for

the T2K baseline. Also shown are the case of normal mass hierarchy ($\Delta m^2_{32} > 0$) with solid lines and inverted mass hierarchy ($\Delta m^2_{32} < 0$) with dashed lines. The oscillation probabilities depend on the value of δ_{CP}, and by comparing the neutrinos and antineutrinos, one can see the effect of CP violation. There are sets of different mass hierarchy and values of δ_{CP} which give similar oscillation probabilities. Therefore the measurement of $P(\nu_\mu \to \nu_e)$ and $P(\bar{\nu}_\mu \to \bar{\nu}_e)$ lead to multiple ambiguities due to three independent parameter degeneracies: (δ, θ_{13}), the sign of Δm^2_{31} and $(\theta_{23}, \pi/2 - \theta_{23})$ [36]. The first degeneracy is solved by precision measurements of θ_{13} by reactor experiments, while the second is solved comparing results from different LBL experiments. The T2K experiment, after taking data with a beam predominantly composed of muon neutrinos, in May 2014 switched the horn polarity and started taking data with an antineutrino beam in order to enhance its sensitivity to δ_{CP}. The main physics goals of the experiment are an Initial measurement of CP violation up to 2.5σ level of significance, observation of $\bar{\nu}_e$ appearance up to 3σ level of significance and more precision measurement of θ_{23} and Δm^2_{23}.

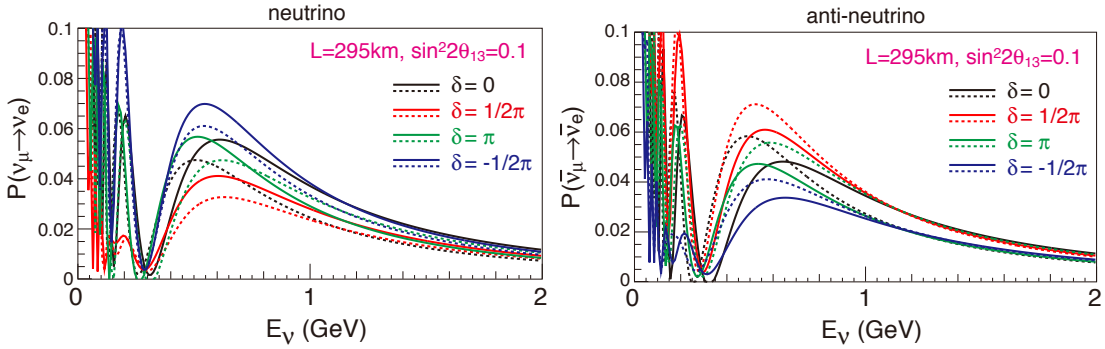

Figure 3.3. Oscillation probabilities as a function of the neutrino energy for $\nu_\mu \to \nu_e$ (left) and $\bar{\nu}_\mu \to \bar{\nu}_e$ (right) transitions with L=295 km and $\sin^2 2\theta_{13} = 0.1$. Black, red, green, and blue lines correspond to $\delta_{CP} = 0, \frac{1}{2}\pi, \pi$, and $-\frac{1}{2}\pi$, respectively. Solid (dashed) line represents the case for a normal (inverted) mass hierarchy. Figure taken from [160].

T2K has also a program of neutrino-nucleus cross section measurements at the near detector complex. As already discussed in the previous Chapter, precise knowledge of the cross sections is not only interesting by itself but are vital for the oscillation analysis. Indeed, neutrino oscillation experiments measure the number of CC event which is a convolution of the neutrino flux, cross-section and detector efficiency:

$$N(\vec{x}) = \Phi(E_\nu) \times \sigma_i(E_\nu, \vec{x}) \times \epsilon(\vec{x}) \times T \times P(\nu_\alpha \to \nu_\beta) \tag{3.2}$$

where $N(\vec{x})$ is the number of events as function of the kinematic of the outgoing particles $(\vec{x})$, $\Phi(E_\nu)$ is the neutrino flux that depends on neutrino energy E_ν, $\sigma_i(E_\nu, \vec{x})$ is the cross section,$\epsilon(\vec{x})$ describes the detector response and T_j is the number of targets. The poor knowledge of the nuclear effects increase the uncertainty on the cross section, therefore a precision knowledge of neutrinos interaction is extremely important for T2K and LBL experiments in general. Furthermore the presence of additional interaction channels that mimic CCQE processes, like 2p2h and pion-less delta decay, lead to a bias in the neutrino energy reconstruction, as shown in Fig. 3.4.

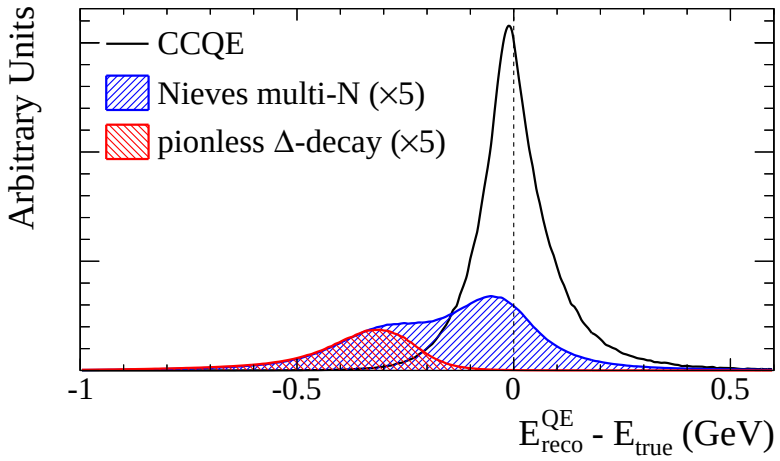

Figure 3.4. The difference between the energy reconstructed at T2K assuming CCQE kinematics and the true energy for events with no pions in the final state. Black are the NEUT simulation of CCQE events and red are the NEUT simulation of resonant production where the Δ is absorbed. The blue is the from the two-body current calculation of Nieves model. Figure taken from [160].

3.2 The neutrino beam

3.2.1 The J-PARC complex

Neutrinos in accelerator-based oscillation experiments are produced via the decay of pions and kaons generated from the collision of an high intensity proton beam on a target. The proton beam for T2K experiment is provided by the J-PARC complex using three accelerators:

The linear accelerator (LINAC). Here a beam of H^- is accelerated up to 400 MeV.

The rapid-cycling synchrotron (RCS). The beam of H^- is converted to an H^+ beam by charge-stripping foils at the RCS injection. It is then accelerated up to 3 GeV by the RCS with a 25 Hz cycle. The harmonic number of the RCS is two, and there are two bunches in a cycle.

The main ring (MR) synchrotron . The proton beam injected into the MR is accelerated up to 30 GeV. The harmonic number of the MR is nine, and the number of bunches in the MR is eight. There are two extraction points in the MR: slow extraction for the hadron beamline and fast extraction for the neutrino beamline. In the fast extraction mode, the eight circulating proton bunches are extracted within a single turn by a set of five kicker magnets. The time structure of the extracted proton beam is key to discriminating various backgrounds, including cosmic rays, in the various neutrino detectors. The parameters of the J-PARC MR for the fast extraction are listed in Tab. IV.

Circumference	1567 m
Beam Power	750 kW
Beam kinematic energy	$30GeV$
Beam intensity	$\sim 3 \times 10^{14}$ protons/spill
Number of kicker magnets	5
Spill cycle	$\sim 0.5\,Hz$
Number of bunches	8/spill
RF frequency	$1.67 - 1.72\,MHz$
Spill width	5.6 μs
Bunch width	58 ns

TABLE IV. List of the main design parameters of the MR accelerator for the proton fast extraction at J-PARC.

Figure 3.5. Overview of the J-PARC accelerators.

3.3 The neutrino beamline

Each proton beam spill consists of eight proton bunches extracted from the MR and is send to the T2K neutrino beamline which is composed of primary and secondary beamlines.

The primary beamline consists of:

1. **The preparation section**: a series of conducting magnet and collimators long 54 m that are used to adjust the beam for the transportation in the arc section;

2. **The arc section**: here the beam is bent toward the direction of Kamioka by 80.7°, with a 104 m radius of curvature, using 14 doublets of superconducting combined function magnets (SCFMs). There are also three pairs of horizontal and vertical superconducting steering magnets to correct the beam orbit. Its total length is 147 m;

3. **The final focusing section**: long 37 m, it is composed of dipoles and quadrupoles that make the beam parallel and adjust its direction to properly hit the target.

The proton beam needs to be well-tuned to ensure a stable neutrino beam production

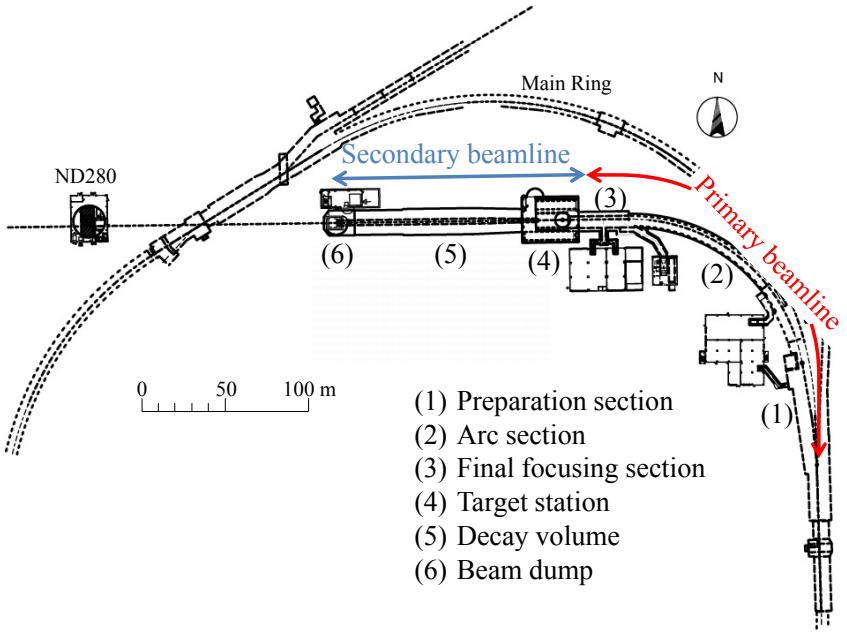

Figure 3.6. Overview of the T2K beamlines. Figure taken from [159].

and is therefore equipped with a series of beam quality monitors.

The secondary beamline, shown in Fig. 3.7, is placed in a volume of $1.5 \times 10^3\, m^3$ filled with helium gas ($1 atm$) and consist of three section: the target station, the decay volume, and a beam dump.

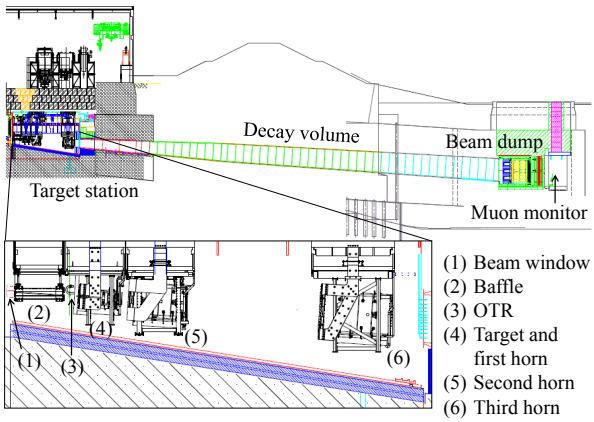

Figure 3.7. Side view of the secondary beamline. The length of the decay volume is ∼96 m. Figure taken from [159].

The target station. It is located 12 m underground and contains a baffle which is a collimator to protect the magnetic horns; an optical transition radiation monitor (OTR) to monitor the proton beam profile just upstream of the target [161].
The T2K target core is a 1.9 interaction length (91.4 cm long), 2.6 cm diameter and 1.8 g/cm^3 graphite rod. In the target ∼80% of protons interact generating

pions and kaons that will decay into neutrinos. The graphite was chosen because the intensity of the beam is so high that the target temperature immediately rises due to the energy deposited by the protons and materials with higher Z would be strongly damaged. Moreover it is stable and easy to handle. The cooling system consists of a co-axial double layer cooling pipe that maintains the target independent from the horn and uses the flow of gaseous helium to cool the target and keep its temperature between 400 and 800°C where the radiation damage for the graphite is minimum. The hadrons generated in the proton-target interactions are focused by three magnetic horns. They are excited by a $\pm 250\ kA$ current pulse. Using the positive or negative value for the current they can focus hadrons with a positive or negative charge producing a neutrino or an antineutrino beam respectively. When the protons arrive, the very intense pulsed current circulate into the horns producing a magnetic field of the order of few Tesla that is able to deviate the hadrons produced in the interaction between the protons and the target. The target is inside the first horn and it collects together the produced hadrons, the second and third horns focus these hadrons into a beam.

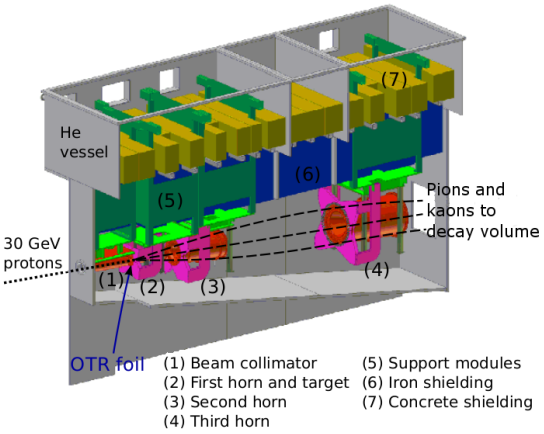

Figure 3.8. The T2K target station.

The decay volume. The focused hadrons, then, enter in a decay tunnel. It is a ∼96 m long tunnel. The length of the decay tunnel depends on the energy of the pions and is also a compromise between the need to have a tunnel long enough to let as many hadrons as possible decay and increasing the intensity of the neutrino beam, and the need to limit the muons coming from pions decay producing undesired background (ν_e and $\bar{\nu}_\mu$). The cross section is 1.4 m wide and 1.7 m high at the upstream end, and 3.0 m wide and 5.0 m high at the downstream end. The decay volume is surrounded by 6 m thick reinforced concrete shielding. Along the beam axis, 40 plate coils are welded on the steel wall, whose thickness is 16 mm, to cool the wall and concrete to below 100°C using water.

The beam dump. All the hadrons, as well as muons below ∼5 GeV/c, are stopped by the beam dump at the end of the decay volume. The neutrinos pass through the beam dump and are used for physics experiments. The distance between the center of the target and the upstream surface of the beam dump along the neutrino beam

direction for the off-axis angle of 2.5° is 109 m. The core of the beam dump is made of 75 $tons$ of graphite (1.7 g/cm^3), and is 3.174×1.94×4.69 m (length×width×height). Fifteen iron plates are placed outside the vessel and two inside, at the downstream end of the graphite core, to give a total iron thickness of 2.40 m. Only muons above ∼5 GeV/c pass through the beam dump and are detected by the Muon Monitor (MUMON).

3.3.1 The Muon Monitor

The neutrino beam intensity and direction can be monitored on a bunch-by-bunch basis by measuring the distribution profile of muons, since muons are mainly produced along with neutrinos from the two-body decay of pions. The neutrino beam direction is determined to be the direction from the target to the center of the muon profile. The Muon Monitor system (MUMON) is placed after the beam dump to detect muons with an energy larger than 5 GeV that are not stopped by the beam dump. The MUMON is formed by an array of ionization chambers and an array of semiconductor detectors. The first is a simple device to monitor the beam for a long run period and it covers the large area of the beam profile. Semiconductor detectors are also used to measure the neutrino beam direction with a precision better than 0.25 $mrad$, which corresponds to a 3 cm precision of the muon profile center. It is also required to monitor the stability of the neutrino beam intensity with a precision better than 3%. A detector made of nuclear emulsion is installed just downstream of the muon monitor to measure the absolute flux and momentum distribution of muons.

3.3.2 The off-axis straregy

The beam of the T2K experiment is sent to the near detector and to the far detector that are along a line at an angle of 2.5° respect to the beam as shown in Fig. 3.9.

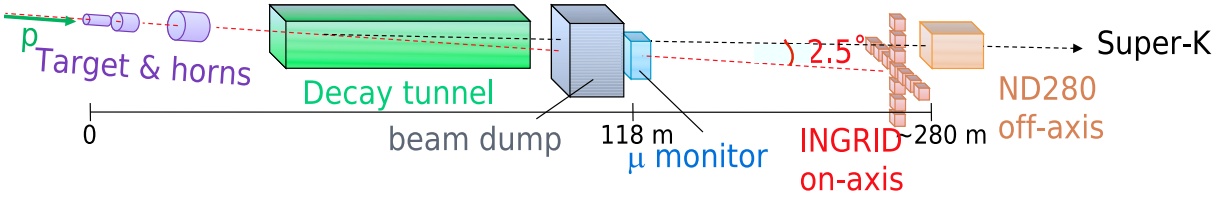

Figure 3.9. Schematic representation of the off-axis configuration.

T2K was the first experiment using an off-axis neutrino beam, a technique that allows the production of an almost monochromatic neutrino beam. Its mean energy maximize the oscillation probability, as shown in Fig. 3.10, where the the energy peak is compared with the disappearance and appearance probability for the T2K baseline. In addition to this advantage, the method also cuts the high energy tail present in the neutrino beam to remove the background to the oscillation signal.

To understand the off-axis method, let consider the ideal case where is possible to obtain a pure π^+ beam, produced by interactions of a proton beam with a graphite target. The pions decay, with a branching ratio ∼99%, following the reaction:

$$\pi^+ \rightarrow \mu^+ + \nu_\mu \tag{3.3}$$

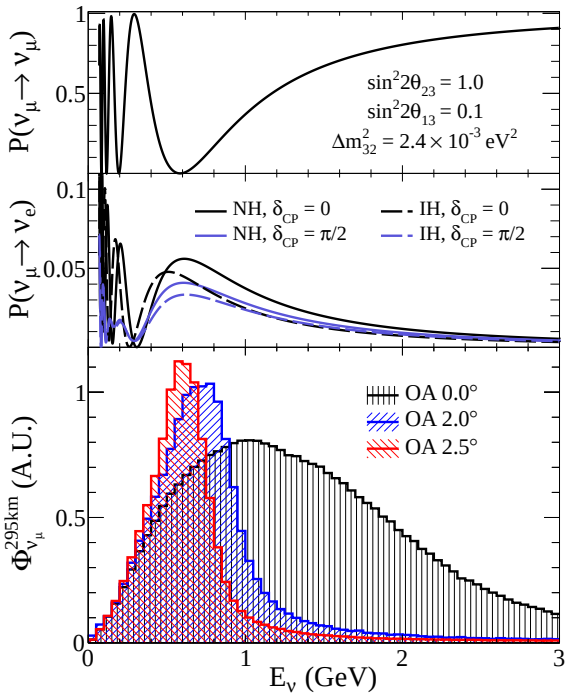

Figure 3.10. Muon neutrino disappearance (top figure) and electron neutrino appearance (middle figure) probability at 295 km compared to the neutrino fluxes for different off-axis angles. The neutrino beam at SK has a peak energy at about 0.6 GeV maximizing the effect of the neutrino oscillations at 295 km.

In the pion rest frame, according to the two body decays kinematics, the neutrino has a maximal energy:

$$E^*_{\nu,Max} = \frac{m_\pi^2 - m_\mu^2}{2m_\pi} = 29.8MeV \tag{3.4}$$

where asterisk indicates quantities in the pion rest frame. The neutrino four momentum for $|\vec{p_\nu}| \gg m_\nu$ will be in the pion rest frame:

$$p_\nu = (E_\nu, E_\nu \sin\theta, 0, E_\nu \cos\theta) \tag{3.5}$$

where θ is the angle of the neutrino relative to the direction of pion and E_ν is the neutrino energy. If now we use the Lorentz boost $\gamma_\pi = E_\pi/m_\pi$, in the laboratory frame, the neutrino four momentum is then:

$$p_\nu = (\gamma_\pi E^*_\nu(1 + \beta_\pi \cos\theta^*), E^*_\nu \sin\theta^*, 0, \gamma_\pi E^*_\nu(\beta_\pi + \cos\theta)) \tag{3.6}$$

The pion has spin zero, so the decay is isotropic in pion rest frame and a relation for the angle θ between the neutrino and the pion can be obtained from 3.5 and 3.6 and considering $\beta \sim 1$

$$\tan\theta \sim \frac{E^*_\nu \sin\theta^*}{\gamma_\pi E^*_\nu(1 + \cos\theta^*)} \sim \frac{E^*_\nu \sin\theta^*}{E_\nu} \tag{3.7}$$

Since $\sin\theta^* \ll 1$, in the laboratory frame there is a maximum angle at which the neutrino of energy E_ν can be emitted. Using Eq. 3.6 the maximum angle is

$$\theta_{max} \sim \frac{E^*_\nu}{E_\nu} \sim \frac{30MeV}{E_\nu} \tag{3.8}$$

Eq. 3.7 can be rewritten as a function of the angle θ, in the form

$$E_\nu \sim \frac{E^*_\nu \sin\theta^*}{\tan\theta} \leq \frac{E^*_\nu}{\tan\theta} \tag{3.9}$$

thus for a given angle $\theta \neq 0$ there is a maximum energy at which neutrinos can be emitted, while for $\theta = 0$ the energy of the neutrino is proportional to the energy of the parent pion. For $\theta = 2.5^\circ$, this correspond to $E_\nu \leq 682\ MeV$ in the laboratory frame. A similar calculation can be applied to neutrinos coming from two body decay of kaons.

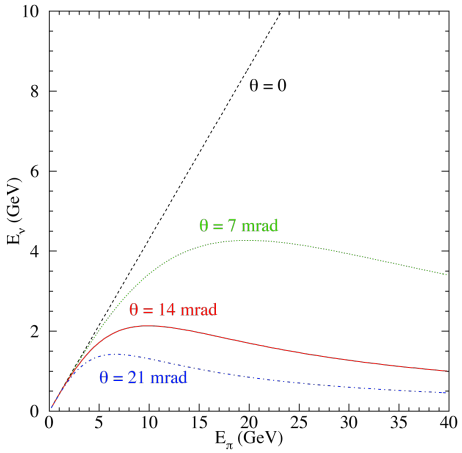

Figure 3.11. Expected neutrino energy as a function of the parent pion energy for different values of the off-axis angle.

Another advantage of the off-axis beam is that it reduces the ν_e contamination in the beam. This contamination, is one of two main backgrounds to the ν_e appearance signal. It comes from decays of muons and kaons (the so-called Ke3 decay, that has a branching ratio of 5%) in the decay tunnel according to reactions:

$$\mu^\pm \rightarrow e^\pm + \bar{\nu}_\mu(\nu_\mu) + \nu_e(\bar{\nu}_e) \tag{3.10}$$

$$K^+ \rightarrow \pi^0 + e^+ + \nu_e \tag{3.11}$$

These are both 3 body decays, while the off-axis strategy enhances the number of neutrinos coming from a two body decay. An off-axis neutrino spectrum will be less affected by the ν_e contamination.

3.3.3 Neutrino flux prediction

Protons interactions with the graphite target produce hadrons that decay into neutrinos through the reactions shown in Tab. V. Each hadron contribute to the neutrino (antineutrino) flux according with the fraction reported in Tab. VI(VII). The flavour composition of each neutrino and antineutrino beam is reported in Tab. VII.

The prediction of the flux and spectrum of neutrinos is based on a simulation that begins with the primary proton beam and ends with the decay of hadrons or muons that produce neutrinos [162]. The hadronic interactions in the target and baffle where the

Particle	Decay Products	Branching Fraction (%)
π^+	$\rightarrow \mu^+\nu_\mu$	99.9877
	$\rightarrow e^+\nu_e$	1.23×10^{-4}
K^+	$\rightarrow \mu^+\nu_\mu$	63.55
	$\rightarrow \pi^0\mu^+\nu_\mu$	3.353
	$\rightarrow \pi^0 e^+\nu_e$	5.07
K^0_L	$\rightarrow \pi^-\mu^+\nu_\mu$	27.04
	$\rightarrow \pi^- e^+\nu_e$	40.55
μ^+	$\rightarrow e^+\bar{\nu}_\mu\nu_e$	100

TABLE V. Neutrino-producing decay modes considered in T2K neutrino flux prediction and their branching ratio in percentage. The same branching ratios are obtained for antineutrino by conjugating the charge. The π^-, K^- and μ^- modes are charge conjugates of the π^+, K^+ and μ^+ modes, respectively.

Parents	ν_μ	$\bar{\nu}_\mu$	ν_e	$\bar{\nu}_e$
$\pi^\pm$	93.53	85.20	1.09	0.36
$K^\pm$	2.38	4.34	26.96	17.39
K^L_0	0.08	1.24	11.16	73.25
μ	0.01	9.22	61.06	9.00

TABLE VI. Fraction (in %) of neutrino mode flux for each final hadron in the interaction chain.

primary proton beam first interacts and produces the majority of the secondary pions are simulated using FLUKA [163]. The kinematic of the particles emitted from the target is saved and transferred to the JNUBEAM simulation [159], a GEANT3-based [164] MC simulation of the baffle, target, horn magnets, helium vessel, decay volume, beam dump, and muon monitor. Hadronic interactions in JNUBEAM are modelled by GCALOR model [165]. In this software, the particles are propagated through the horn magnetic field and may interact with the horn material. Then they are propagated through the decay volume until they interact or decay. The simulation and uncertainties associated are driven by the measurement of the proton beam profile, of the horns' magnetic fields, and hadron production data. A dedicated hadron production experiment at CERN, NA61/SHINE, studies the particles produced by the a proton beam of 30 GeV which interacts with a graphite target to improve the knowledge of the T2K neutrino flux [166, 167]. Currently the T2K flux prediction is tuned with data collected using a target of 2 cm. Anyway data has been taken with a replica T2K target and will be used soon into the flux prediction.

Parents	ν_μ	$\bar{\nu}_\mu$	ν_e	$\bar{\nu}_e$
$\pi^\pm$	83.67	98.64	0.32	1.21
$K^\pm$	8.81	1.24	35.23	14.81
K_0^L	1.02	0.10	56.35	14.76
μ	6.50	0.02	8.10	69.30

TABLE VII. Fraction (in %) of antineutrino mode flux for each final hadron in the interaction chain.

mode	ν_μ	$\bar{\nu}_\mu$	ν_e	$\bar{\nu}_e$
ν	92.63	6.24	0.98	0.15
$\bar{\nu}$	8.89	90.02	0.23	0.87

TABLE VIII. Flavour composition (in %) of ν and $\bar{\nu}$ beam.

3.4 The near detector complex

The near detector complex is located at a distance of 280 m from the target. The near detectors are used to measure the properties of the un-oscillated beam and to predict the neutrino interactions at the far detector. The complex consists of two detectors: the on-axis detector INGRID (Interactive Neutrino GRID) and the off-axis detector ND280.

3.4.1 The on-axis detector

The on-axis neutrino detector is used to monitor the neutrino beam observing particles produced by neutrino interactions. Being on-axis INGRID is sensitive to a large portion of the neutrino spectrum.
INGRID consists of 14 identical units, arranged to form a cross of two identical groups along the horizontal and vertical axis and two separate modules located at off-axis locations outside the main cross, as shown in Fig. 3.12. The purpose of the two off-axis modules is to check the axial symmetry of the neutrino beam. The 16 INGRID modules consist of a sandwich structure of 9 iron plates and 11 tracking scintillator planes (see Fig. 3.13). Each of this latter consists of 24 scintillator bars, in the horizontal direction glued to 24 perpendicular bars. A surrounding scintillator plane is used as a veto to reject interactions outside the module. The total iron mass of the neutrino target is 7.1 tons per module. The dimensions of the scintillator bars used for the tracking planes are 1.0 cm×5.0 cm×120.3 cm. The modules cover a beam area of 5 m^2 and the neutrino beam direction is measured with an accuracy better than 0.4 mrad [168].
The Proton Module, right image in Fig. 3.13, is an extra module different from the other that has been added in order to detect the proton produced with the muon in neutrino interactions with good efficiency. It consists of scintillator planes surrounded by veto planes. A different size scintillator bar was used to improve tracking capabilities. It is placed in the center of the INGRID cross between the standard vertical and horizontal central modules.

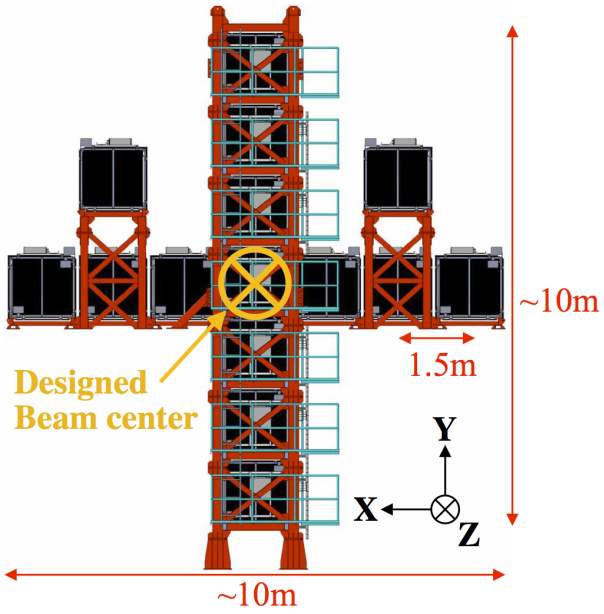

Figure 3.12. INGRID on-axis detector. Figure taken from [159].

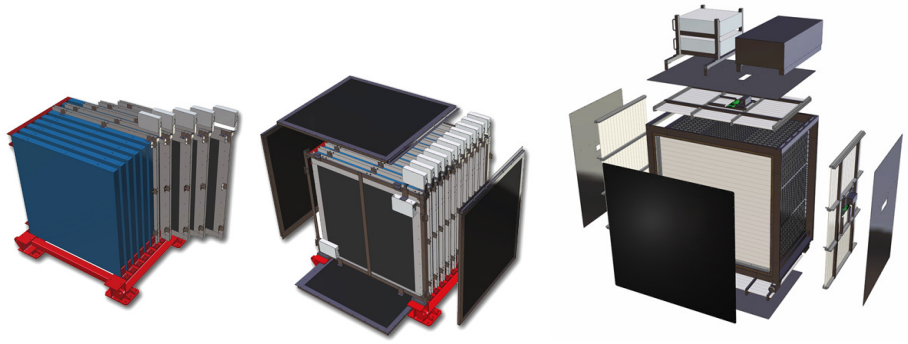

Figure 3.13. The left image shows the tracking planes (blue) and iron plates of an INGRID module. The image in the middle shows veto planes in black of an INGRID module. The image on the right shows the proton module which is similar to the INGRID modules, but with finer grain scintillator and without the iron plates. Figure taken from [159].

3.4.2 The off-axis detector

ND280 serves to measure the flux, energy spectrum and beam contaminations in the direction of the far detector, along with measuring rates for exclusive neutrino reactions, in order to characterize signals and backgrounds in the far detector. It must satisfy several requirements:

- It must provide information to determine the ν_μ (or $\bar{\nu}_\mu$) flux at SK.
- The content of the beam must be measured as a function of neutrino energy. The intrinsic beam background creates a significant non-removable background for the oscillation analysis.
- Precise measurements of ν_μ, $\bar{\nu}_\mu$ and ν_e cross-sections.

To meet these goals the ND280 must have the capability to reconstruct exclusive events and should measure inclusive event rates.

The off-axis detector (see Fig. 3.14) consists of: the π^0 detector (PØD), three Time Projection Chambers (TPC), two Fine Grained Detectors (FGDs), placed inside of a metal frame container, called the "basket"; an Electromagnetic Calorimeter (ECal) that surrounds the basket; and the refurbished UA1/NOMAD magnet instrumented with scintillator to perform as a muon range detector (SMRD). The basket has dimensions of 6.5 $\times$ 2.6 $\times$ 2.5 m^3 (length $\times$ width $\times$ height). The region covered by the TPCs and FGDs is called "tracker volume".

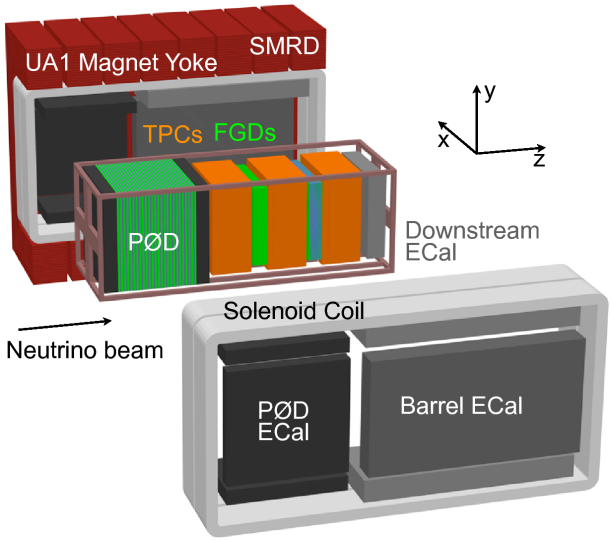

Figure 3.14. A schematic view of the ND280 off-axis detector.

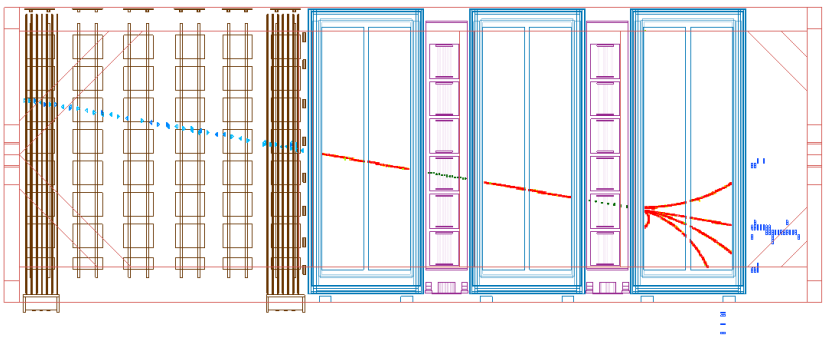

Figure 3.15. Event display of a muon track entering via the front face of the PØD detector, continuing to the TPCs and FGDs and producing secondary particles on the way. The secondary particles are then stopped in the ECal detectors.

3.4.3 The magnet

The ND280 uses the refurbished UA1/NOMAD magnet that provide a dipole magnetic field of 0.2 T, perpendicular to the neutrino beam direction. The curvature induced by the

magnet is used to measure the momenta of charged particles produced by neutrino interactions in the detector. The dimension of the inner volume of the magnet are 3.5×3.6×7.0 m^3, while the external dimensions are 7.6×5.6×6.1 m^3 and the total weight of the yoke is 850 *tons*. The magnet consists of two symmetric halves and each half consists of 8 C-shaped flux return yokes made of low-carbon steel plates. The magnetic field is produced by water-cooled aluminium coils that operate at a current of 3 kA. The coils are made of aluminium bars with 5.45×5.45 cm^2 square cross sections, with a central 23 mm diameter bore for water to flow. According to measurement the field is quite uniform in intensity and direction, with transverse components exceeding 1% only in regions close to the coils. The uncertainty on the magnetic field map is of 2 G. This very precise knowledge of the magnetic field map, especially for the transverse field components, helps to reduce the systematic uncertainty of the momentum determination, which is intended to be below 10% for charged particles around 1 GeV/c.

3.4.4 The Side Muon Range Detector

The SMRD performs multiple functions:

- It rejects cosmic ray muons that enter or penetrate the ND280 detector;
- It detects muons escaping at large angles with respect to the beam direction and measures their momentum;
- It helps identify beam-related event interactions in the surrounding cavity walls and the iron of the magnet.

The SMRD consists of a total of 440 scintillator modules inserted in the air gaps of 1.7 cm between 4.8 cm thick steel plates which make up the UA1/NOMAD magnet flux return yokes. It consists of 3 layers of scintillator modules on the top and bottom for all yokes. All of the SMRD modules populate the innermost gaps so as to be able to detect particles escaping the inner detectors. Due to the differently sized spaces for horizontal and vertical gaps, horizontal modules are composed of four scintillation counters and vertical modules consist of five scintillation counters. They are made of extruded polystyrene and dimethylacetamide with admixtures of POPOP and para-terphenyl [169]. The surface of each scintillator counter features a white diffuse layer which acts as a reflector. A 1 mm diameter Kuraray Y11 double-clad wavelength shifter fiber (WLS) exits both sides of the scintillator through a ferrule which is part of an endcap. The Multi-Pixel Photon Counters (MPPCs) are coupled to the polished WLS fiber ends through a snap-on mechanism. There are 4016 MPPCs connected to a miniature printed circuit (PCB). The miniature PCBs couple the MPPC signals into mini-coaxial cables, which lead the signal to the custom-designed Trip-T front-end boards (TFBs) mounted on the vertical sections of the magnet yokes.

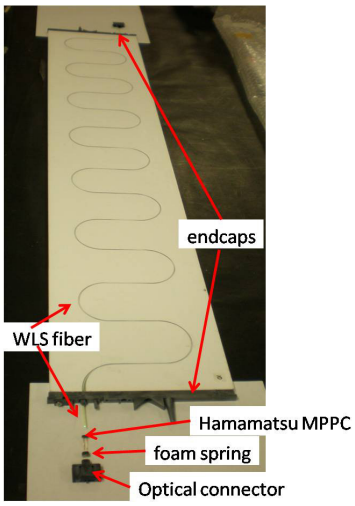

Figure 3.16. View of SMRD scintillator counter components prior to assembly. Figure taken from [159].

3.4.5 The π^0 Detector

The primary goal of the PØD is to measure the neutral current process:

$$\nu_\mu + N \rightarrow \nu_\mu + N + \pi^0 + X \tag{3.12}$$

on a water (H_2O) target so to be able to predict the amount of this background (in fact the decay of π^0 into two photon can mimic an e-like event) expected at SK. This is a crucial measurement since the two photons emitted in the π^0 decay can mimic an electron-like ring. These objectives were realized by a design using x and y planes of scintillator bars, as shown in Fig. 3.17. The planes of scintillator bars are interleaved with fillable water target bags and lead and brass sheets. This arrangement forms a neutrino target where the PØD operates with the water target bags filled or emptied, enabling a subtraction method to determine the water target cross sections. The scintillator bars provide sufficiently fine segmentation to reconstruct charged particle tracks (muons and pions) and electromagnetic showers.

The main features of the PØD design are shown in Fig. 3.17. The central section, composed of the "upstream water target" and "central water target", uses alternating scintillator planes, water bags and brass sheets. The front and rear sections, the "upstream ECal" and "central ECal", use alternating scintillator planes and lead sheets. This arrangement improves the containment of electromagnetic showers and provides a veto region before and after the water target region to provide effective rejection of particles entering from interactions outside the PØD. There are a total of 40 scintillator modules in the PØD. Each PØD module, or PØDule, has two perpendicular arrays of triangular scintillator bars. There are 134 vertical bars (2200 mm long) and 126 horizontal bars (2340 mm long) in each PØDule. Each bar has a single hole filled with a WLS fiber (Kuraray double-clad Y11 of 1 mm diameter). Each fiber is mirrored on one end and the other end is optically read out using a MPPC. The PØDules were formed into four "super-groups" called super-PØDules. The two ECal super-PØDules are a sandwich of seven PØDules alternating with seven stainless steel clad lead sheets (4 mm thick). The

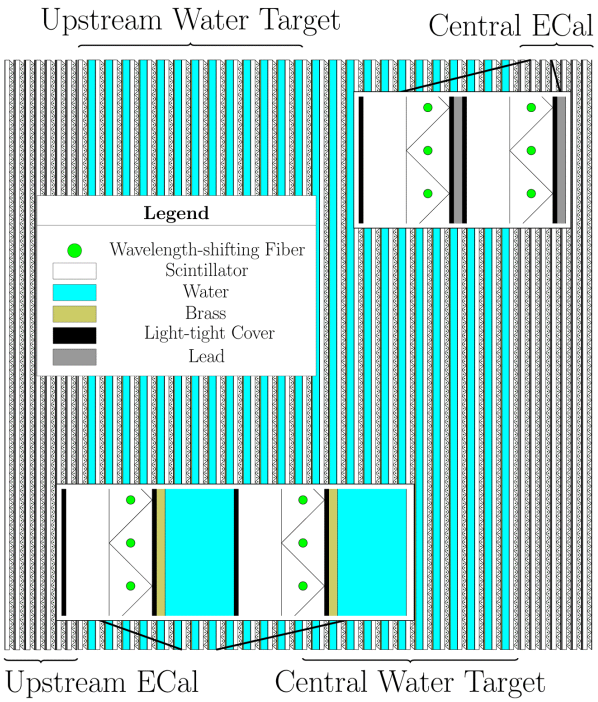

Figure 3.17. A schematic view of the pi-zero detector. The beam is coming from the left and going right. Insets show details of the Water Target super-PØDule layers and Central ECal layers. Figure taken from [159].

upstream (central) water target super-PØDule is a sandwich of 13 PØDules alternating with 13 (12) water bag layers (each 28 *mm* thick), and 13 (12) brass sheets (each 1.5 *mm* thick). The water target layers have two bags, for a total of 50 in the PØD detector, each with dimensions of 1006×2062×28 mm^3. The dimensions of the active target of the entire PØD are 2103×2239×2400 mm^3 and the mass of the detector is 16.1 tons with water and 13.3 tons without water. The detector was calibrated with minimum ionizing particles from cosmic ray muons. An average of 19 photoelectrons was obtained for the scintillator plane and 38 photoelectrons per x/y layer. The average attenuation of the pulse height in the scintillator bars from opposite ends is approximately 30%. The internal alignment of scintillator bars was checked using through-going muons with the magnet field off, and was determined to be approximately 3 *mm* [170].

3.4.6 The Time Projection Chambers

The TPCs fulfill three key functions in the near detector:

- measurement of the momentum of the charged particles since they operate in a magnetic field;
- 3-dimensional reconstruction of charged particles crossing the detector;
- particle identification using the amount of ionization left by each charged particle combined with the measured momentum.

These three functions allow to select high purity samples of different types of neutrino interactions, compute event rates as a function of neutrino energy for the neutrino beam before oscillation and determine the relative abundance of electron neutrinos in the beam. There are three TPCs installed inside the magnet. Each TPC consists of an inner box that holds an argon-based drift gas, contained within an outer box that holds CO_2 as an insulating gas. The inner (outer) walls are made from composite panels with copper-clad G10 (aluminium) skins. The inner box panels were precisely machined to form an 11.5 mm pitch copper strip pattern. The TPCs are separated into two sides by a central cathode. The voltage on each strips and on the cathode is set in order to have an uniform electric field in the active drift volume of the TPC, roughly aligned with the magnetic field provided by the near detector magnet. A simplified drawing of the TPC design is shown in Fig. 3.18. At each side of the TPCs, 12 bulk MicroMegas (micro-mesh

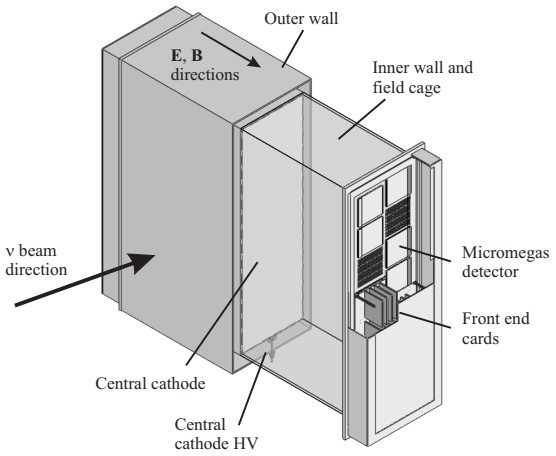

Figure 3.18. Simplified cut-away drawing showing the main aspects of the TPC design. The outer dimensions of the TPC are approximately 2.3×2.4×1.0 m^3. Figure taken from [171].

gas detector) modules are arranged in two vertical columns that are offset so that the small inactive regions between modules are not aligned. The role of the MicroMegas is to amplify the signal created by the charged particles when passing through the TPCs. When charged particles pass through a TPC, they ionize the gas. The electrons released via this process drift away from the cathode toward the readout planes (anode), where they are multiplied with the MicroMegas. The MicroMegas anode is segmented into pads of 7.0×9.8 mm^2 (48 rows × 36 columns), allowing 3D track reconstruction of the traversing charged particle, where the x coordinate is given by the arrival time of the signal and the y and z by the pattern on the pad plane. The gas system was designed to maintain a stable mixture in the inner volume, a constant positive pressure with respect to the outer volume, and a constant pressure between the outer volume and the atmosphere. The inner gas mixture, Ar:CF_4:iC_4H_{10}(95:3:2) was chosen for its low diffusion and good performance with MicroMegas chambers. Each of the three TPC volumes contains 3000 L and each of the three gap volumes contains 3300 L of this gas mixture. The TPC gas system was designed for an operating flow of 10 $L/min/TPC$ (30 L/min total flow), corresponding to five TPC-volume flushes per day. To reduce gas operating

costs, the system was designed to purify and recycle roughly 90% of the TPC exhaust gas.

Particle identification (PID) is done with a truncated mean of measurements of energy loss of charged particles in the gas (Fig. 3.19). The linear charge density of the track is estimated for each cluster by taking into account the length of the track segment corresponding to a pad column. The PID has been optimized through MC simulation and test beam studies [171]. The resolution of deposited energy obtained using this method is about 7.8% for minimum ionizing particles, better than the design requirement of 10%.

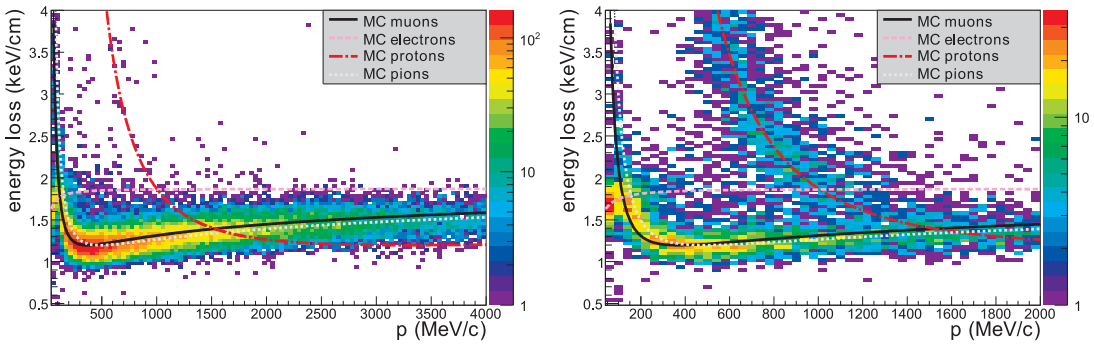

Figure 3.19. Distribution of the energy loss as a function of the momentum for negatively (left) and positively (right) charged particles produced in neutrino interactions, compared to the expected curves for muons, electrons, protons, and pions. Figure taken from [171].

The spatial resolution is estimated by comparing the transverse coordinate resulting from the global track fit to the one obtained with information from a single column of pads. The resolution is found to be typically 0.7 mm per column, in line with expectations, and degrades with increasing track angle with respect to the horizontal due to the ionization fluctuations along the track. The observed spatial resolution is sufficient to achieve the momentum resolution goals for the detectors.

3.4.7 The Fine-Grained Detector

In the inner part of the near detector, interleaved between the three TPCs, there are two FGDs whose purpose is to provide target mass for neutrino interactions as well as tracking of charged particles coming from the interaction vertex. Moreover, the design of the first FGD being made of scintillators only (in the following referred as FGD1) and the other as a sandwich of scintillator and water (in the following referred as FGD2) allows a comparison of neutrino cross sections on carbon and water, complementary to the PØD cross section.
Each FGD (Fig. 3.20) has outer dimensions of $2300\times2400\times365\ mm^3$ (width×height×depth in beam direction), and contains 1.1 tons of target material. The FGDs are constructed from $9.61\times9.61\times1864.3\ mm^3$ bars of extruded polystyrene scintillator, which are oriented perpendicular to the beam in either the x or y direction. The first FGD consists of 5760 scintillator bars, arranged into 30 layers of 192 bars each. The bars are orthogonally oriented in successive planes, such that each pair of orthogonal layers builds an XY module perpendicular to the neutrino beam. The second FGD is made of seven XY modules

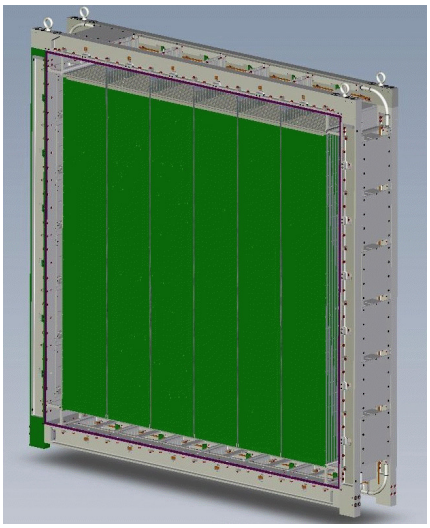

Figure 3.20. View of an FGD with the front cover removed. XY scintillator modules (green) hang perpendicular to the direction of the neutrino beam. Along the top, six mini-crates with electronics can be seen without their cooling lines, while on the right side the cooling lids covering the mini-crates are shown. Figure taken from [159].

interleaved with 2.5 *cm* thick water layers at sub-atmospheric pressure for a total of 2688 active scintillator bars and 15 *cm* total thickness of water. Each FGD is contained in a light-tight dark box that contains the scintillator, fibers, and photo- sensors, while the FGD electronics are mounted in mini-crates around the outside of the dark box. Each scintillator bar has a reflective coating containing TiO_2 and a WLS fiber going down a hole in its center. One end of each fiber is mirrored by vacuum deposition of aluminium, while the other end is attached to an MPPC and associated electronics, which digitize the light signal produced by scintillation inside the bar.

The FGD PID is performed only for the reconstructed tracks which are fully contained in the detector volume. Fully contained reconstructed tracks are due to low momentum particles, mainly protons and pions, created in neutrino interactions. Fig. 3.21 depicts the reconstructed energy versus the track length for both FGDs for different particle hypothesis. In both cases pions and muons are clustered in the same energy deposit band and cannot be distinguish. Instead, the protons discrimination from muons and pions is very clear especially in FGD1 which is fully active.

Fully contained pions can be identified tagging the Michel electron emitted by the muons which in turn are produced by the pion decay. The tagging of such electron is made by seeking a delayed time cluster following the first time cluster associated to the initial neutrino interaction. A sample of cosmic rays stopping in the FGD can be used to determine the detector capability to tag the Michel electrons by measuring the muon life time. The measured Michel detection efficiencies in FGD1 is $\sim 56\%$ while it is evaluated to be $\sim 43\%$ in FGD2, this difference is due to the presence of the water module [172].

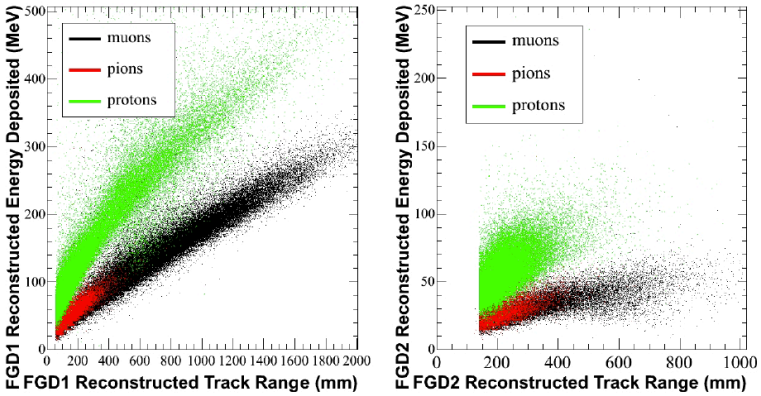

Figure 3.21. Reconstructed energy depositions as a function of the track lenght for muons, pions and protons in FGD1 (left) and FGD2 (right).

3.4.8 The Electromagnetic Calorimeter

The Electromagnetic Calorimeter (ECal) is a sampling electromagnetic calorimeter surrounding the inner detectors (PØD, TPCs, FGDs) [170]. Its main role is to complement the inner detectors in full event reconstruction. Firstly through the measurement of photon energy and direction, secondly the detection of charged particles escaping the inner detectors and the extraction of information relevant for their identification and finally the reconstruction of π^0 produced in neutrino interactions inside the inner detectors. It uses layers of plastic scintillator bars as active material with lead absorber sheets between layers, and it provides nearly-hermetic coverage for all particles exiting the inner detector volume. The ECal is made of 13 independent modules of three different types:

Barrel ECal (Br-ECal): six modules surrounding the tracker volume on its four sides parallel to the z axis. It is formed of 31 layers at each side corresponding to 9.7 X_0: 6 with 1520 mm-long scintillator bars running perpendicular to the beam direction, and 15 with 3840 mm-long bars running longitudinally, i.e. parallel to the beam direction;

Downstream ECal (Ds-ECal): one module covering the downstream exit of the tracker volume. It consists of 34 layers with 1.75 mm thick lead sheets corresponding to 10.6 X_0 ($\sim$ 1 λ_I). 50 bars of 2.04 m length form a layer, and the orientation alternates between x and y in successive layers;

PØD-ECal: six modules surrounding the PØD detector volume on its four sides parallel to the z axis. It has a reduced granularity respect to other ECal modules and is made of six scintillator planes containing 2.34 m long bars oriented in z-direction and interleaved by 4 mm of lead sheets. This because in the PØD region the photon conversion mainly happens inside, and so the PØD-ECal is used as a veto for entering particles and tag muons and gammas that escape the PØD without being reconstructed.

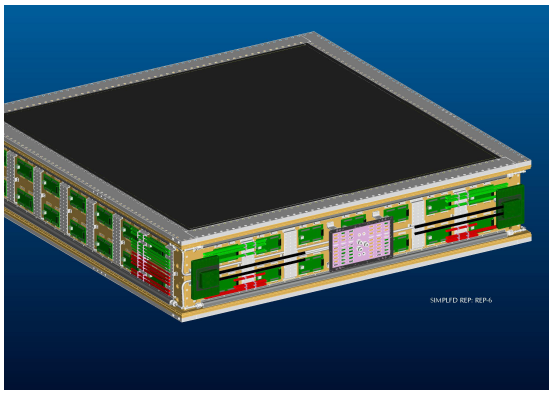

Figure 3.22. External view of one ECal module. The scintillator bars run horizontally inside the module as shown. The readout electronics, signal and power cables, and cooling pipes can be seen mounted on the aluminium plates on the sides of the module. The gray surface at the top is the carbon fiber sandwich front plate, which in the final module position is facing towards the inner subdetectors (PØD, FGDs and TPCs). Figure taken from [159].

3.5 The far detector: Super-Kamiokande

The SK water Čerenkov detector is located 295 km west of the beam source where it is used to sample the beam's flavor composition and look for $\nu_\mu \rightarrow \nu_e$ appearance and ν_μ disappearance. It is built 1 km deep (2,700 meters water equivalent) in the Kamioka mine. SK has been running since 1996 and operation time was divided in four running periods: SK-I, SK-II, SK-III, and SK-IV during which it has produced data for a number of well-known results that include world-leading limits on the proton lifetime and the measurement of flavor oscillations in atmospheric, solar and accelerator-produced neutrinos. A schematic view of detector is shown in Fig. 3.23. It is a cylindrical detector cavity whose dimensions are 41 m in height and 39 m in diameter and is filled with 50 kton of pure water. On the detector walls roughly 13,000 photomultiplier tubes (PMTs) detect neutrino interactions. The geometry of the SK detector consists of two major volumes, an inner and an outer detector which are separated by a cylindrical stainless steel structure. The inner detector (ID) is a cylindrical space 33.8 m in diameter and 36.2 m in height which currently houses along its inner walls 11129 inward-facing 50 cm diameter PMTs, representing 40% of surface coverage. The outer detector (OD) is a cylindrical space about 2 m thick radially and on the axis at both ends. The OD contains along its inner walls 1885 outward-facing 20 cm diameter PMTs and is used as an anti-counter to identify entering/exiting particles to/from the ID. The ID and OD boundaries are defined by a cylindrical structure about 50 cm wide. This structure consists of a stainless steel scaffold covered by plastic sheets which serve to optically separate the ID and OD. The wall facing into the ID is lined with a black sheet of plastic meant to absorb light and

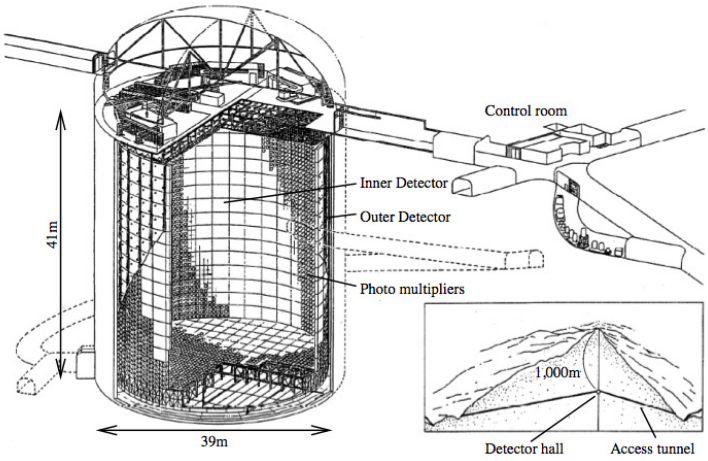

Figure 3.23. Diagram of the Super-Kamiokande Detector. It is mainly comprised of two segments, the inner and outer detectors. The boundary between the two segments is defined by a cylindrical scaffold used to mount photomultiplier tubes and optically separate the segments. Figure taken from [159].

minimize the number of photons which either scatter off of the ID wall back into the ID volume, or pass through from the ID to the OD.

The primary strategy to measure the flavor composition of the T2K neutrino beam at SK, and thereby observe the oscillation of ν_μ to ν_e is to count CCQE interactions for muon and electron neutrinos, both of which produce leptons of their respective flavor. Relativistic charged particles, produced in these neutrino interactions, travel through the detector with a speed faster than the velocity of light in water. The polarized water molecules rapidly turn back to their ground state and emit Čerenkov light, which is detected by the ID PMTs. For both ν_μ and ν_e events the starting position of the leptons is required to be fully contained in the fiducial volume, which is defined to be more than 2 m away from the ID wall for a total fiducial mass of 22.5 kton. The pulse hight and timing information of the PMTs are fitted to reconstruct the vertex, direction, energy, and particle identification of the Čerenkov rings. A typical vertex, angular and energy resolution for 1 GeV muons is 30 cm, 3° and 3%, respectively. The typical ring shape, which is obtained from fully contained charged particles with an energy above the Čerenkov threshold, allows to infer the vertex position and the momentum of the charged particles. A very good discrimination between fuzzy electron like Čerenkov rings and sharp edged rings from muons enables to separate ν_e from ν_μ interactions. The fuzzy electron like ring is due to the multiple scattering, which is more likely to occur for electrons than for muons because of the electron smaller mass, and to electromagnetic showers almost always induced at these energies. A typical rejection factor to separate muons from electrons (or vice versa) is about 100 for a single Čerenkov ring event at 1 GeV. The electrons and muons are further separated by detecting decay electrons from the μ decays. A typical detection efficiency of decay electrons from stopping cosmic muons is roughly 80%. A 4π coverage around the interaction vertex provides an efficient π^0 detection.

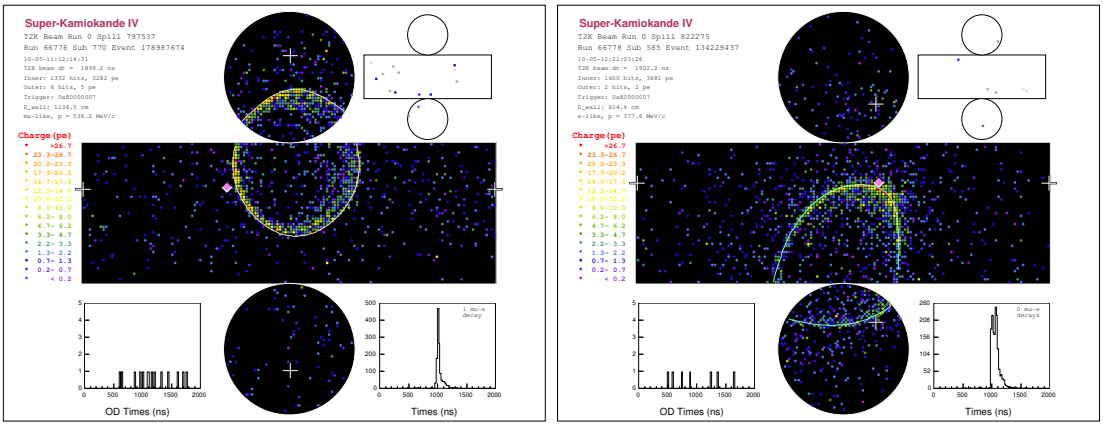

(a) muon-like event (b) electron-like event

Figure 3.24. Example of reconstructed T2K events in Super-Kamiokande for (a) a muon-like ring and (b) an electron-like ring. Each colored point represents a PMT, with the color corresponding to the amount of charge, and the reconstructed cone is shown as a white line. The second figure in the upper right corner shows the same hit map for the OD. The white crosses indicate the location of the reconstructed vertex.

Chapter 4

Measurement of the intrinsic muon neutrino component in the antineutrino beam

T2K excluded $\theta_{13} = 0$ with a significance of 7.3σ opening the possibility of the measurement of δ_{CP}, which can shed light on the matter/antimatter imbalance in the observable universe. This phase introduces a difference in the appearance probability between neutrinos and antineutrinos. A direct measurement of CP violation can then be achieved comparing $\nu_\mu \to \nu_e$ and $\bar{\nu}_\mu \to \bar{\nu}_e$ channels. The T2K experiment, after taking data with a beam predominantly composed of muon neutrinos (in the following referred as ν-mode) in order to observe the ν_μ disappearance and the ν_e appearance at the far detector [92–94, 173–175], in May 2014 switched the horn polarity and started taking data with an antineutrino beam (in the following referred also as $\bar{\nu}$-mode) in order to enhance its sensitivity to δ_{CP}.

In Fig. 4.1 is shown the predicted neutrino and antineutrino flux at ND280 and SK. In general the ν- and $\bar{\nu}$-mode fluxes are similar at low energy, although the ν_μ flux in ν-mode is $\sim$15% higher around the flux peak than the $\bar{\nu}_\mu$ flux in $\bar{\nu}$-mode. The $\bar{\nu}_\mu$ background in ν-mode is also lower (2.4% around the peak) compared to the ν_μ flux in $\bar{\nu}$-mode (3.3% around the peak), especially at high energy. These differences are due to the higher production multiplicities of positive, rather than negative, parent particles [176]. Once differences in the flux and the cross section are taken into account, the ν_μ contamination in the $\bar{\nu}$ beam is expected to be approximately 30%, while the $\bar{\nu}_\mu$ contamination in the ν beam is around 4%. SK cannot distinguish between ν and $\bar{\nu}$ interactions since the charge of the outgoing leptons cannot be reconstructed. Thus it is crucial, in order to keep low the uncertainties on δ_{CP}, to measure the ν_μ background in $\bar{\nu}$-mode at the near detector, where it is possible to distinguish between negative and positive charged particles.

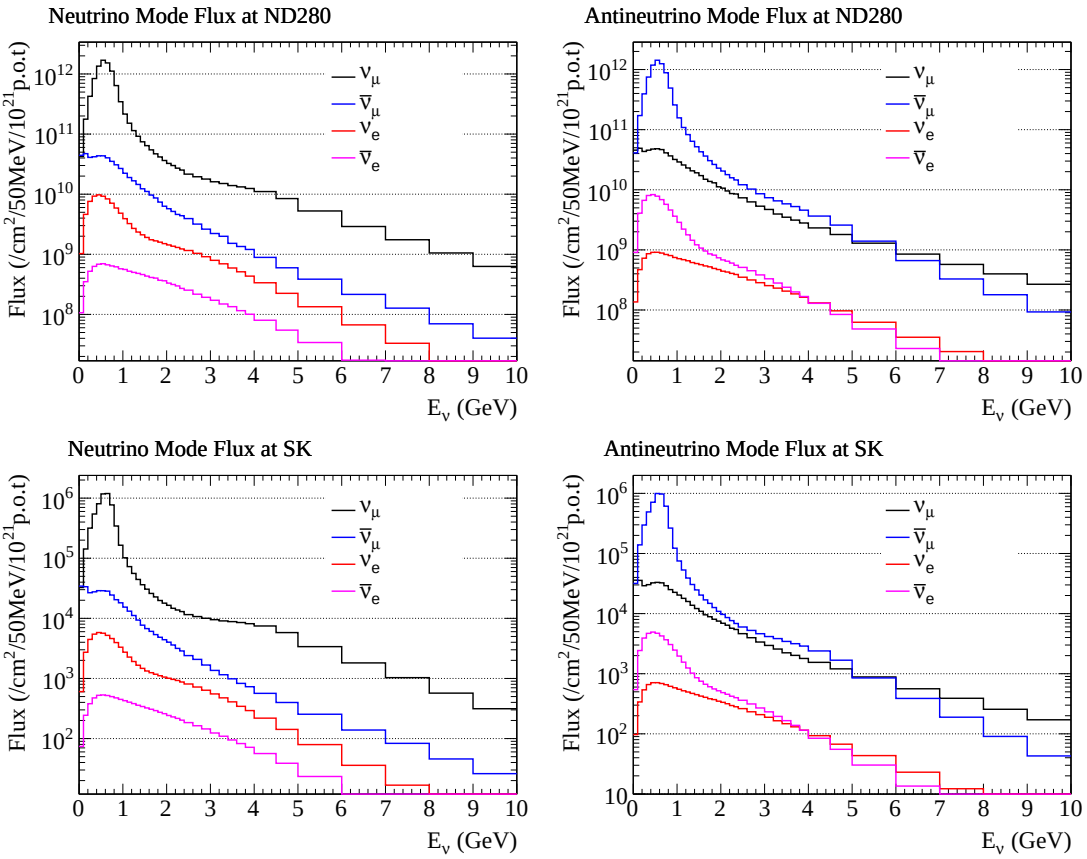

Figure 4.1. The T2K unoscillated flux prediction at ND280 (top) and SK (bottom) for neutrino (left) and antineutrino (right) modes.

In this Chapter the measurement of the ν_μ component in the $\bar{\nu}$ beam is presented. First a sample of CC events (**CC-Inclusive** sample) with vertex in one of the FGDs is selected and then it is divided in two samples according with the track multiplicity in the subsequent TPC (**Multiple track selection**). An improved selection has been developed and is here presented as well. It is based on the pion content in the CC events (**Multiple pion selection**), following the prescription discussed in Chap. 2. The impact of the detector systematic uncertainties will be discussed as well. The Multiple track selection has been used to provide the input for the latest oscillation analyses that will be presented at the end of this Chapter.

4.1 The data sets

The ν_μ selection in the antineutrino beam has been performed with the data taken from May 2014 until June 2015 which correspond to an exposure of 3.76×10^{20} protons on target (POT) collected at ND280 during two physics runs as detailed in Tab. IX. The MC samples are normalized for the data POT. Furthermore, nominal MC are corrected due to reconstruction discrepancies between data and MC studied through control sample (Sec. 4.5). All MC samples are processed using NEUT version 5.3.2 [138] which has been

already described in Sec. 2.3. In a different MC sample muon produced by $\bar{\nu}$ interactions in the wall of the pit in which is located ND280 are simulated. This sample is indicated as "MC Sand" in Tab. IX.

Run Period	**Data POT** ($\times 10^{20}$)	**MC POT** ($\times 10^{20}$)	**MC Sand POT** ($\times 10^{20}$)
Run 5	0.43	22.90	12.93
Run 6	3.40	14.86	12.93
Total	3.76	37.76	25.86

TABLE IX. T2K data-taking periods in antineutrino mode and the proton on target used in this analysis for data and MC.

4.2 ν_μ CC event selection in $\bar{\nu}$-mode

The ν_μ CC interactions can be selected identifying the μ^- in the final state. The main goals of the event selection are to:

- reject as much as possible the negative pions coming from the antineutrino interactions that can be misidentified as negative muons;
- reject the low energy electromagnetic background (e^+ and e^- pairs coming from γ conversions);
- achieve a good purity retaining a high efficiency.

In order to achieve these goals has been used the following selection criteria:

Event quality. The (anti)neutrino beam is produced impinging 8 proton bunches, which have a width of 15 ns,on a graphite target (3.2.1). Only events associated to beam trigger and compatible with one of the 8 bunches are selected. To do this selection the mean and the width of each bunch were measured and tracks in the event are accepted only if they are within 4σ from the center of one of the bunches.

Total multiplicity. Only those events where there is at least one reconstructed track crossing TPC are considered.

Track quality and fiducial. An event is selected if its reconstructed vertex is inside FGD1 (FGD2) fiducial volume (FV). The starting position of the muon is used to define the interaction vertex position. For low angle tracks, respect to the beam direction, this starting position is defined by the intersection of the fitted muon track and the XY plane at the Z position of the most upstream FGD hit of the track. However for high angle tracks, the reconstruction algorithm can use the XZ or YZ planes located at the first FGD hit. The FV has been defined in order to reduce the rate of event with vertex outside the FGD but that are reconstructed

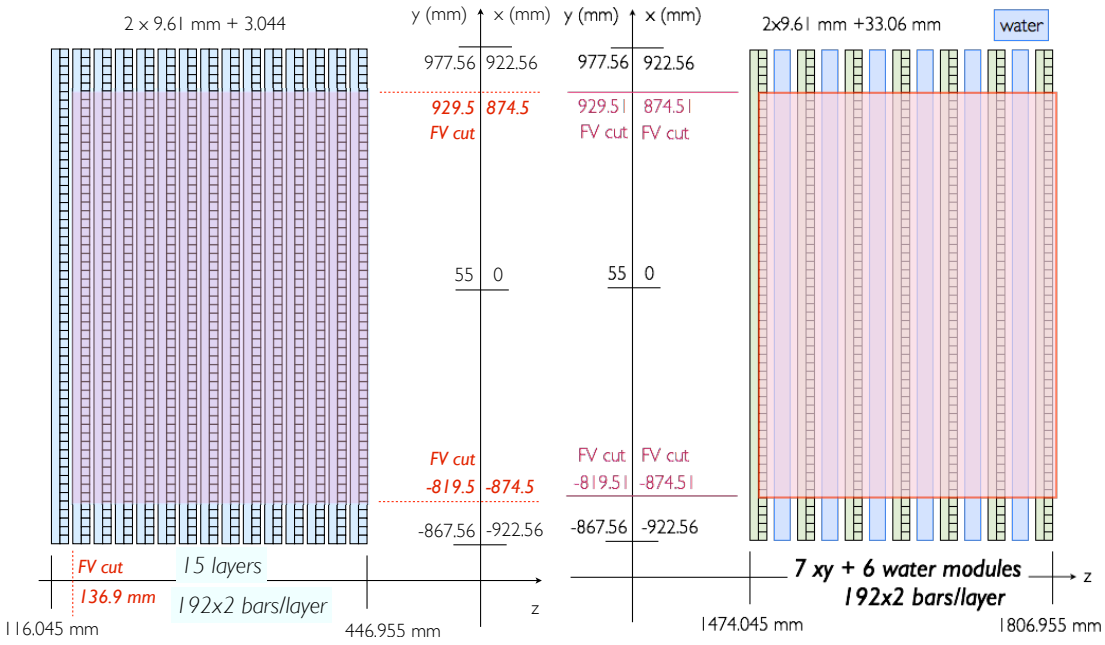

Figure 4.2. Schematic view of the FGD1 (left) and FGD2 (right) FV.

as track starting inside it. Thus in x and y direction only those interactions which have the vertex 5 scintillator bars distant from the edge of the XY module of FGD are accepted. The z cut in FV definition excludes the first most upstream XY module and includes all remaining modules of FGD1, while in FGD2 only the first scintillator bar is removed. The FV is also schematically shown in Fig. 4.2. Additionally, in order to reject short tracks for which the reconstruction in TPC is less reliable (tracks with more than 18 clusters[1]) are selected.

Negative multiplicity. Among all tracks originated in FGD1(2) FV, the highest momentum negative track (HMNT) which is also the highest momentum track (HMT) in the event is identified as the muon candidate. This cut reduce the contribution of positive muons and pions coming from $\bar{\nu}_\mu$ and CC-RES ν_μ interactions.

Upstream background veto. Reconstruction failures can lead to a muon track starting in the FGD1(2) FV even if the real muon started far upstream. For example a muon originating from the PØD and undergoing a large scattering in FGD1 may be reconstructed as two tracks instead of one. In order to exclude such events, events in which the second highest momentum track start position and the end position of the muon candidate are too close are vetoed. Additionally, for FGD2 selection, the event is vetoed if a secondary track starts in FGD1 FV.

Broken track. This cut is applied to reject events with mis-reconstructed tracks, where instead of one muon candidate track originating in FGD FV the reconstruction breaks this track into two components: one fully contained FGD track (FGD-only track) followed by second track which starts in the last layers of FGD and passes TPC. In these kind of events the second track is considered as muon candidate.

[1] A cluster is defined as a set of contiguous pads in a row or column.

Thus the event with an FGD-only track and with the start position of the muon candidate in the last two scintillator layer of the FGD are rejected.

Muon PID. For the events which satisfy the criteria described abov TPC PID procedure is applied to select them as muon candidate. In general measured energy deposit in TPC is compared with expected energy deposit under the assumption of a particle type: muon, electron and proton hypothesis. Therefore a pull value is computed as follow

$$\delta_i = \frac{C_T^{meas} - C_T^{exp}(i)}{\sigma^{exp}(i)} \tag{4.1}$$

where $i = (\mu, e, \pi, p)$, $C_T^{exp}(i)$[2] is the expected mean of the energy loss by the charged particle i crossing the TPC gas and $\sigma^{exp}(i)$ is the deposited energy resolution. The δ_i is computed for each TPC segment of the track (e.g., if the track crosses one TPC one δ_i is computed, if the track goes through two TPC two values of δ_i are computed). The following likelihood, can be defined using the δ_i distributions:

$$\mathscr{L}_i = \frac{\mathscr{P}_i}{\mathscr{P}_\mu + \mathscr{P}_e + \mathscr{P}_p + \mathscr{P}_\pi} \quad (i = \mu, e, \pi, p) \tag{4.3}$$

where the probability density functions are:

$$\mathscr{P}_i = \frac{1}{\sqrt{2\pi}\sigma(i)} \exp\left(- \sum_j^{TPC_j} \frac{\delta_j^2(i)}{2} \right) \quad (i = \mu, e, \pi, p) \tag{4.4}$$

where the sum is performed on each j-th TPC segment contained in the track. Pulls and likelihoods can be used to select tracks from a certain particle. If muons are selected correctly, the δ_μ distribution obtained will be a Gaussian centered in zero with a sigma around one. On the contrary, if the track is not a muon, the difference between the measured energy loss and the expected one will be bigger and there will be a change in the pull distribution shape. Nevertheless, μ and π are hard to distinguish because they have similar energy loss and the TPC C_T resolution is not good enough to evaluate this difference. Furthermore, in the momentum region above 800 MeV/c, where the energy loss by protons and muons are similar, protons can be mis-identified as muon. In these two cases, the TPC PID will be not efficient enough because also pions and protons will have as muons a value of δ_μ centered at zero with a sigma around one.

The TPC PID in this analysis is performed using the muon and MIP likelihoods, which is defined in the following way:

$$\mathscr{L}_{MIP} = \frac{\mathscr{L}_\mu + \mathscr{L}_\pi}{1 - \mathscr{L}_p} \tag{4.5}$$

[2]The parametrization of the expected energy loss is given is:

$$C_T^{exp}(i) = \frac{785 ADC}{\beta^{2.308}} \times 6.047 - \beta^{2.308} - \log 0.00064 + \frac{1}{(\beta\gamma)^{1.359}} \tag{4.2}$$

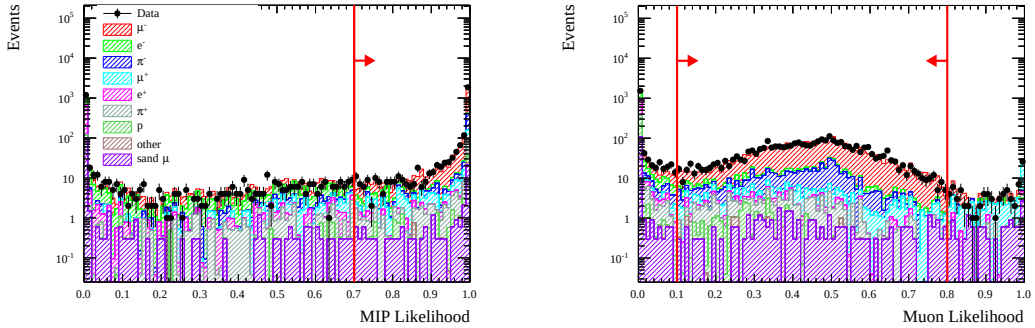

Figure 4.3. MIP likelihood on the left and muon likelihood on the right. The arrows indicate the cut used. Different colours indicate different final state particles.

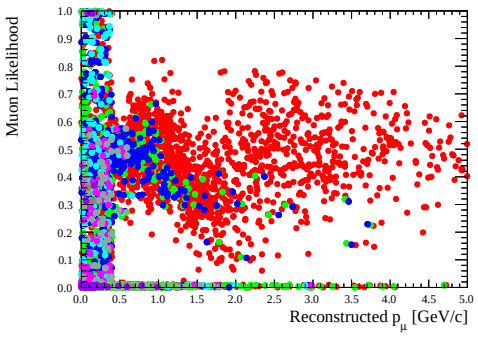

Figure 4.4. Muon likelihood versus the reconstructed muon momentum. Different colours indicate different final state particles following the same legend of Fig. 4.3.

They are shown in Fig. 4.3 in terms of the particles that can contribute to them. Asking that the MIP likelihood must be greater than 0.7 for particle with momentum less than 500 MeV the background coming from $e^{\pm}$ is rejected. Events for which the muon likelihood is less than 0.1 or greater than 0.8 are mainly μ^+ and p that are clearly mis-identified as negative tracks, therefore are rejected. This mis-identification happens when there are tracks with an opposite direction respect to the beam direction for which the reconstruction is not able to distinguish between their start and end points. It is important to mention that the PID is charge independent, thus the presence of the μ^+ rather than μ^- at $\mathscr{L}_\mu$ around 1, can be explained looking at muon likelihood versus the reconstructed muon momentum distribution shown in Fig. 4.4: at momentum lower than 0.4 GeV there is a majority of μ^+, while the μ^- are distributed at higher momentum value. It is important to notice the sizeable contamination of π^-: these particles come from the non QE $\bar{\nu}_\mu$ interactions and are not correctly identified by the TPC PID.

The distribution of events with vertex in **FGD1 FV** and **FGD2 FV** as function of the reconstructed muon momentum and scattering angle for the **CC-Inclusive** sample are shown in Figs. 4.5 and 4.6 respectively. The purity in terms of particle type, which is defined as the ratio between the number of event identified as particle i and the total number of selected events, is around 78% for muons (see Tab. XI). Therefore after the

Cut name	Cut description
Event Quality	The event must occur in defined bunch with good DQ flags
Total multiplicity	In the selected event, at least one track must cross the TPC2
Track quality & Fiducial	The HMNT in the event must have its origin in FGD1(2) FV and more than 18 TPC clusters
Negative multiplicity	The HMNT must be the HMT in the event
Upstream background veto	Veto backwards events or coming from outside the FV.
Broken track	Rejection of external background from the last two layers of FGD1(2)
TPC PID	μ^- selection using the TPC PID: $0.1 < \mathscr{L}_\mu < 0.8$ (if $p < 500$ MeV & $\mathscr{L}_{MIP} > 0.7$)

TABLE X. Summary table of the selection criteria applied in the ν_μ analysis.

TPC PID it is possible to select a sample with a rather good level of purity and a low background coming mainly from π^- misidentified as μ^-, which are produce in non QE interactions.

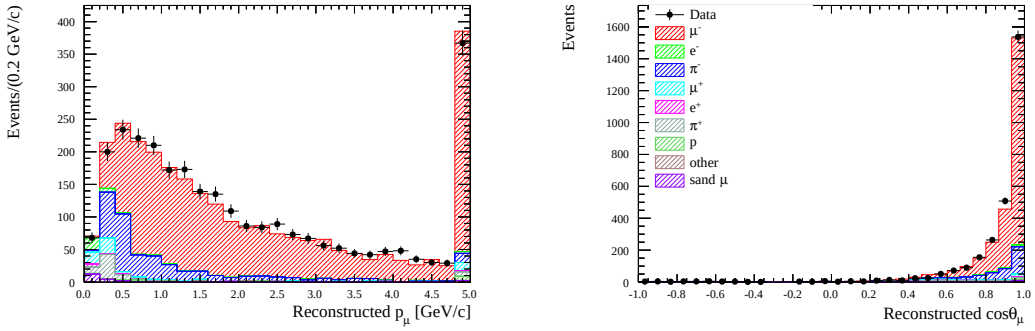

Figure 4.5. Distribution of events with vertex in **FGD1 FV** as function of the reconstructed muon momentum (left) and scattering angle (right) for the **CC-Inclusive** sample. Different colours indicate different particle. MC is scaled to POT in data.

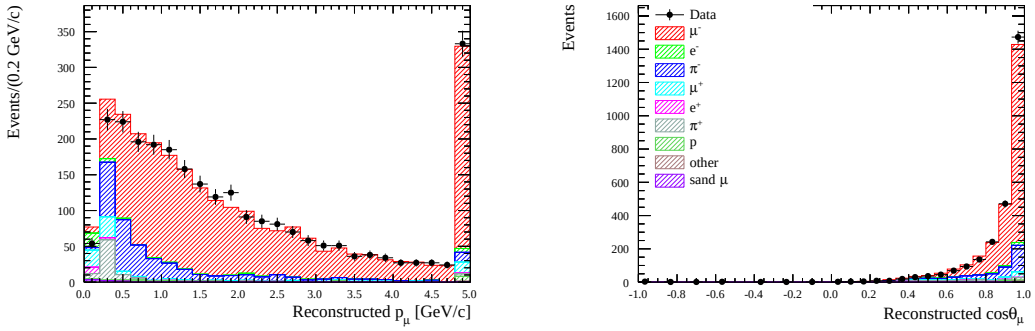

Figure 4.6. Distribution of events with vertex in **FGD2 FV** as function of the reconstructed muon momentum (left) and scattering angle (right) for the **CC-Inclusive** sample. Different colours indicate different particle. MC is scaled to POT in data.

Particle	**MC Composition (%)**	
	FGD1 FV	**FGD2 FV**
μ^-	78.2	77.1
e^-	1.4	1.6
π^-	13.2	12.9
μ^+	2.7	3.6
e^+	0.4	0.5
π^+	2.5	3.1
p	0.6	0.8
other	0.1	0.1
sand μ	0.9	0.3

TABLE XI. MC composition (in %) in term of **particles type** which contribute to the selected ν_μ CC events with reconstructed vertex in **FGD1 FV** and **FGD2 FV**.

4.3 ν_μ CC Multiple track selection in $\bar{\nu}$-mode

The CC-Inclusive sample defined above has been divided in two sub-sample according with the track multiplicity of the events:

CC-1-Track: composed of CC events with only one TPC-FGD matched track.

CC-N-Tracks: CC events with more than one TPC-FGD matched track.

The composition of the MC has been studied on the basis of the event *topology*. A *topology* is defined by the set of particles that leave the nucleus after the interaction. This choice has been driven by the analogy with the signal at SK where ν_μ or ν_e CCQE interactions are identified looking for single-ring events, since most of the other particles, except for the primary lepton, do not escape the nucleus, or are below detection threshold. The topologies used in this analysis are defined according with the number of true final state pions in the events: ν_μ CC events with one negative muon and no pions are indicated as **CC-0π** and with any number of pions are indicated as **CC-Nπ**. The other true category used are the **Background** (indicated with **BKG** in the following) which groups true $\bar{\nu}_\mu$ CC interactions, ν_e, $\bar{\nu}_e$ and NC interactions, **out FV** for events with true vertex outside the FGD FV and **sand μ** for events with true vertex outside ND280. In Figs. 4.7 (4.9) and 4.8 (4.10) are shown the distributions of events with vertex in **FGD1 FV** (**FGD2 FV**) as function of the reconstructed muon momentum and scattering angle for the **CC-1-Track** and **CC-N-Tracks** samples respectively. In Tabs. XII is reported the MC composition (in %) in term of **topologies**.

The **CC-1-Track** samples are dominated by CC-0π events to which contribute mainly CCQE, 2p2h and CC-RES for which the pion is reabsorbed in the nucleus interactions. The largest background is due to CC-Nπ events in which none of the final state pions reach the TPCs. The component indicated as "BKG" is due to $\bar{\nu}_\mu$, NC, ν_e and $\bar{\nu}_e$ interactions in which the π^- is mis-identified as μ^-. The out FV events constitute a sizeable background and are distributed at low momentum (less that 0.6 GeV/c). Those kind of events are mainly due to positive tracks mis-reconstructed as negative and with true vertex in SMRD and Br-ECal. The lowest background comes from sand μ interactions, thus is less likely that a muon generated by ν interactions outside ND280 can be mis-identified as **CC-1-Track** events.

The **CC-N-Tracks** samples are dominated by CC-Nπ events. To them contribute mainly due to a mixture of CC-RES and CC-DIS interactions. This composition explains the broader momentum distributions and the narrower distributions for the reconstructed cosine of the scattering angle, being the cross section of such processes dominant at high energy. The largest background component is due to CC-0π events in which protons produced in CCQE, 2p2h or CC-RES interactions reach the TPC. The background due to $\bar{\nu}_\mu$, NC, ν_e and $\bar{\nu}_e$ interactions is higher in this sample since there are more π^- coming from $\bar{\nu}_\mu$ CC-RES and CC-DIS that are mis-identified as μ^-. The background due to sand μ interactions is lower in this sample, since these events are characterized by one muon track that goes through ND280. The out FV events contribute less since is less likely to have an out FV events with more than one track that reach the TPC. Also in this case

they distribute at low momentum. Those kind of events are mainly due to forward-going negative tracks with true vertex in PØD or in the edges of FGDs that are not included in the FV definition. For events with reconstructed vertex in FGD2 FV, to out FV background contribute also CC-RES events with true vertex in Br-ECal.

The selection efficiency is defined as the ratio between the number of events selected as CC-0π or CC-Nπ and the generated number of events. For CC-0π events selection efficiency is around 46% and 36% for CC-Nπ, for both events with vertex in FGD1 FV or FGD2 FV. The lower value of the selection efficiency of the CC-Nπ events is related with the difficulties in selecting events with high multiplicity. The low level of purity and efficiency of the CC-0π events is a limitation of this analysis and it is related with the selection strategy that take into account only FGD-TPC matched tracks ignoring events with FGD-only segments. An example is a CC-RES interaction with a muon crossing the TPC and a pion fully contained in FGD. Furthermore for the T2K oscillation analysis is rather important a good constrain on the un-oscillated flux and the cross section model from ND280 data, thus this selection has been improved and the strategy and the results are presented in the next section.

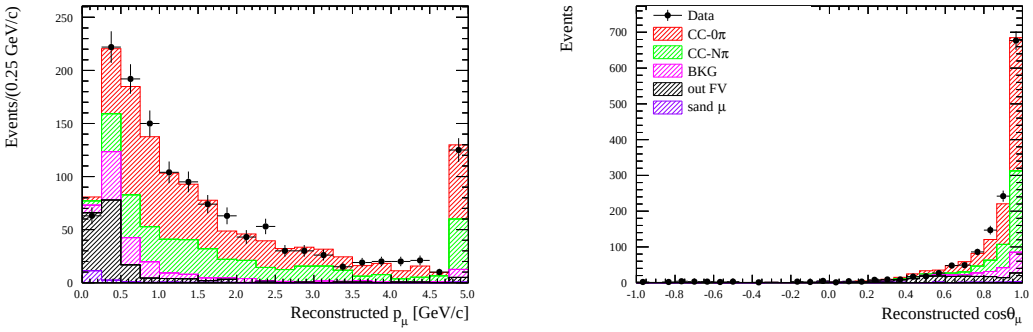

Figure 4.7. Distribution of events with vertex in **FGD1 FV** as function of the reconstructed muon momentum (left) and scattering angle (right) for the **CC-1-Track** sample. Different colours indicate different topologies. MC is scaled to POT in data.

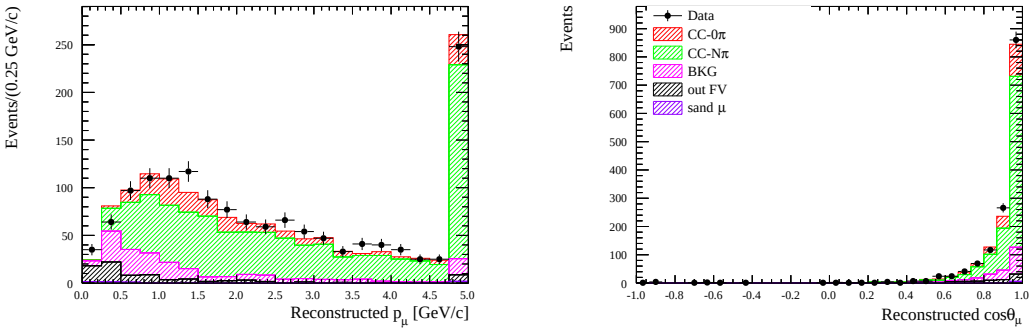

Figure 4.8. Distribution of events with vertex in **FGD1 FV** as function of the reconstructed muon momentum (left) and scattering angle (right) for the **CC-N-Tracks** sample. Different colours indicate different topologies. MC is scaled to POT in data.

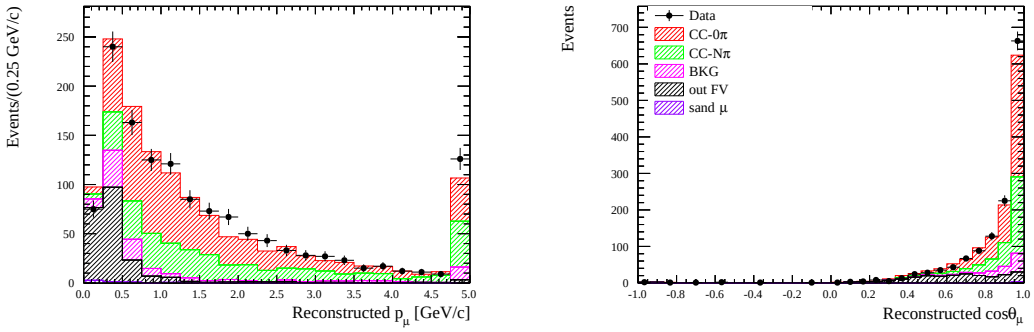

Figure 4.9. Distribution of events with vertex in **FGD2 FV** as function of the reconstructed muon momentum (left) and scattering angle (right) for the **CC-1-Track** sample. Different colours indicate different topologies. MC is scaled to POT in data.

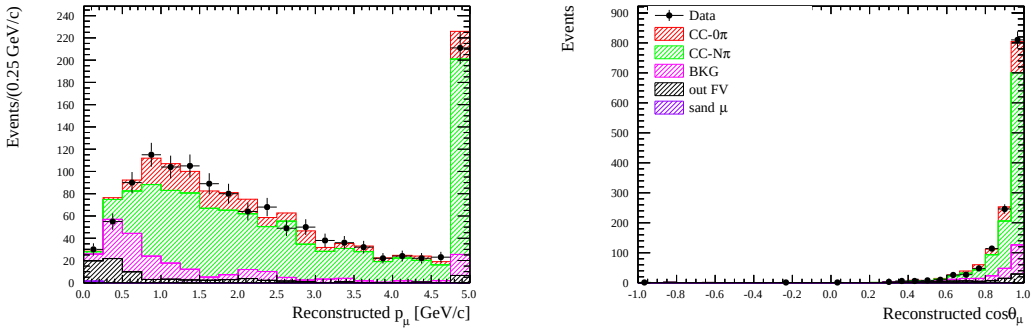

Figure 4.10. Distribution of events with vertex in **FGD2 FV** as function of the reconstructed muon momentum (left) and scattering angle (right) for the **CC-N-Tracks** sample. Different colours indicate different topologies. MC is scaled to POT in data.

Topology	**MC Composition (%)**			
	CC-1-Track		**CC-N-Tracks**	
	FGD1 FV	**FGD2 FV**	**FGD1 FV**	**FGD2 FV**
CC-0π	49.2	47.3	15.2	15.0
CC-Nπ	27.6	27.5	65.7	65.3
BKG	9.4	8.5	12.9	13.5
out FV	12.5	16.2	5.5	6.1
sand μ	1.3	0.5	0.7	0.1

TABLE XII. MC composition (in %) in term of **topologies** for the ν_μ **CC-1-Track** and **CC-N-Tracks** samples obtained selecting events with vertex in **FGD1 FV** and **FGD2 FV**.

4.4 ν_μ CC Multiple pion selection in $\bar{\nu}$-mode

Driven by the prescription discussed in Chap. 2 on the necessity to be less dependent on the cross section model, the selection described before has been improved dividing the CC-Inclusive sample into three sub-samples, defined by the number of final state pions, taking into account also FGD-only tracks. A similar selection has been already used in past oscillation analysis performed with data taken in ν-mode [175].

The sample are defined in the following way:

CC-0π-like: events with no additional TPC tracks consistent with being a pion or electron and with no additional FGD tracks consistent with being a pion, nor any time-delayed signal in the FGD which is consistent with a Michel electron.

CC-1π^+-like: events with one positive pion candidate in a TPC and no additional negative pions, electrons or positrons

CC-Other-like: CC-Inclusive events not in the CC-0π-like or CC-1π^+-like samples.

The names for these samples have the "-like" suffix to distinguish them from the topologies used for this selection that are based on truth information. They differ from the one defined above for the CC-Nπ topology which has been split in CC-1π^+ and CC-Other.

Further selection criteria based on TPC or FGD informations are applied for pions identification in order to split the CC-Inclusive sample in the three sub-sample just defined. Therefore secondary tracks different from the muon candidate must be identified. First they are required to be in the same time bunch as the muon candidate. Then they must start in the same FGD FV used for the muon candidate and if they enter one of the following TPCs they are also required to satisfy the TPC quality cut. For tracks that pass those criteria the TPC PID is performed. In case of positive tracks, three particle hypotheses are considered: pion, positron and proton. For negative tracks only the pion and electron hypotheses are considered. Thus in order to identify pions in TPC, pulls assuming particle hypotheses just mentioned are calculated, and the following cuts on the likelihoods are applied:

$$L_{MIP} = \frac{L_\mu + L_\pi}{1 - L_p} > 0.8 \quad \text{if} \quad p < 500 MeV/c \tag{4.6}$$

$$L_\pi > 0.3 \tag{4.7}$$

Neutral pions entering in TPCs are identified by the presence of positron and electron from their decay. On the other hand, if a particle does not enter the TPC, FGD informations can be combined to identify whether the secondary track is a pion. It is important to stress that this is possible only for charged pions, since electrons and positrons are not distinguished in FGDs. Here two methods of pion identification are considered depending on the length, and therefore momentum of the pion track. For pion tracks too short to leave enough hits in FGD to be reconstructed as independent tracks, the Michel electron tagging is used, while for higher momentum pions, the FGD PID is performed.

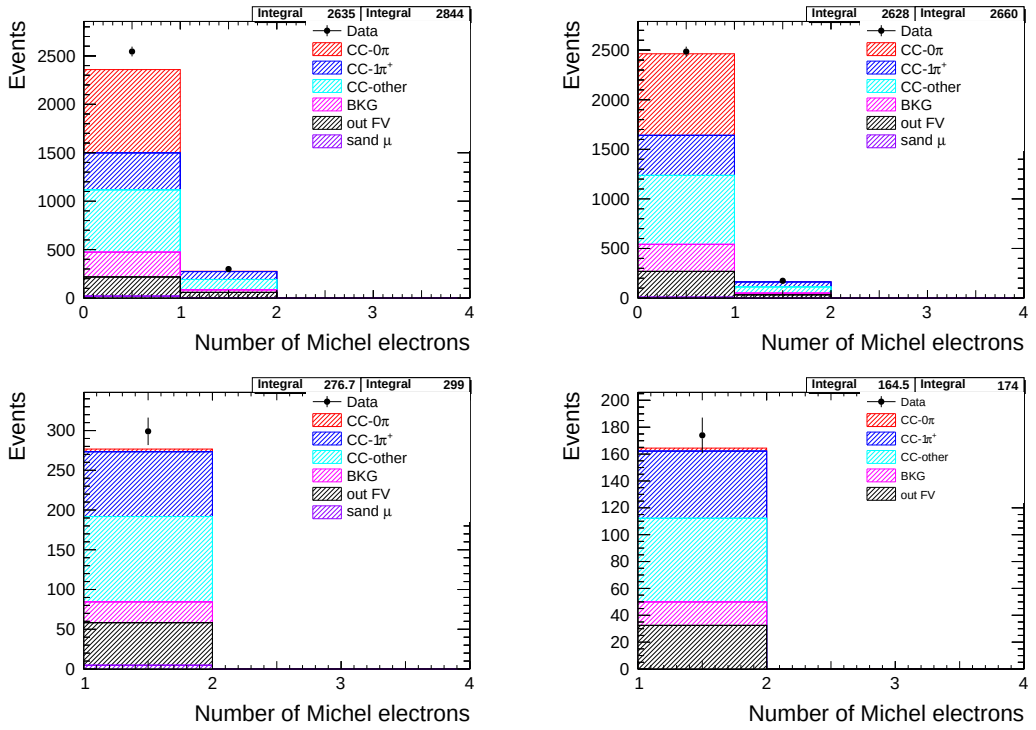

Figure 4.11. Number of Michel electron in **CC-Inclusive** sample for events with reconstructed vertex in **FGD1 FV** (top left) and **FGD2 FV** (top right). On the bottom the same figures zoomed to better display events with more than one Michel electron. Colors indicate different topologies. The MC is normalized to the POT in data.

Michel electrons come from the muons decay, which in turn have been produced by pions decay. They are identified looking for delayed signals outside the beam window in FGD, according with the μ lifetime, with at least 7 hits in FGD1 or 6 hits in FGD2. The distribution of Michel electrons associated to FGD-only tracks for events with reconstructed vertex in FGD1 FV and FGD2 FV are shown in Fig. 4.11. It is clear that most events with one reconstructed Michel electron are **CC-1π^+** events. To perform the FGD PID a pion pull is defined in order to identify charged pions based on the information of energy deposited by the particle as a function of track length. This method provides a discrimination between protons, muons and pions for tracks which start and stop inside an FGD detector and are in the same time bunch as the muon candidate. In this case, to be tagged as a pion, its pull must be $-2 < \delta_\pi < 2.5$.

Figs. 4.12 (4.15), 4.13 (4.16) and 4.14 (4.17) show distributions of events with reconstructed vertex in FGD1 FV (FGD2 FV) as function of the reconstructed muon momentum and cosine of the scattering angle for the three sub-sample after the selection criteria are applied. The MC composition according to true topology is summarized in Tab. XIII while the true reaction content is reported in Tab. XIV.

The **CC-0π-like** samples have a good purity around 50%. To them contribute mainly CCQE, 2p2h and CC-RES (the pion is reabsorbed in the nucleus) interactions. The largest background is due to CC-1π^+ and CC-Other events in which the π^- are mis-reconstructed

as μ^- and the other particles are undetected or reabsorbed in the nucleus. The events induced by $\bar{\nu}_\mu$, NC, ν_e and $\bar{\nu}_e$ have the same possibility described in the multiple track analysis to be a background. Also in this selection the out FV events constitute a sizeable background, distributed at low momentum (less that 0.6 GeV/c), and are due to positive tracks mis-reconstructed as negative coming from SMRD and Br-ECal. The sand μ contribute with the same level of contamination observed in the previous selection, since the way they mimic a CC-0π or CC-1-Track events is the same.

The **CC-1π^+-like** and **CC-Other-like** samples have a purity around 42% and 68% respectively. Most of the contamination in the CC1π^+-like sample comes from DIS events for which only one pion is detected and any other hadrons have escaped or have been lost to interactions in the surrounding material. Furthermore, positive pions can be mis-identified as muons and the event tagged as $\bar{\nu}_\mu$ CC-1π events. In the **CC-Other-like** samples the out FV events contribute less since is not likely to have an out FV events with more than one track since they are distributed at low momentum. The sand μ are negligible in both. As for the CC-Nπ, the composition in terms of reactions (Tab. XIV) for the CC-Other-like samples explains the broader momentum distributions and the narrower distributions for the reconstructed cosine of the scattering angle.

The selection efficiency is defined as the number of selected true events in a given topology divided by the total number of generated events in the FGD FV. For both CC-0π-like samples almost 60% of the interactions which have no pion in final state end up in the **CC-0π-like** sub-sample. The **CC-1π^+-like** samples is selected with an efficiency of almost 28% for interactions in FGD1 FV. The lower efficiency for the case of interaction in FGD2 FV is due to the presence of inactive water layers in FGD2, which cause the drop of the track finding efficiency for isolated FGD tracks (dominant effect) and of the Michel electron detection efficiency. The **CC-Other-like** samples are selected with almost the 23% of efficiency

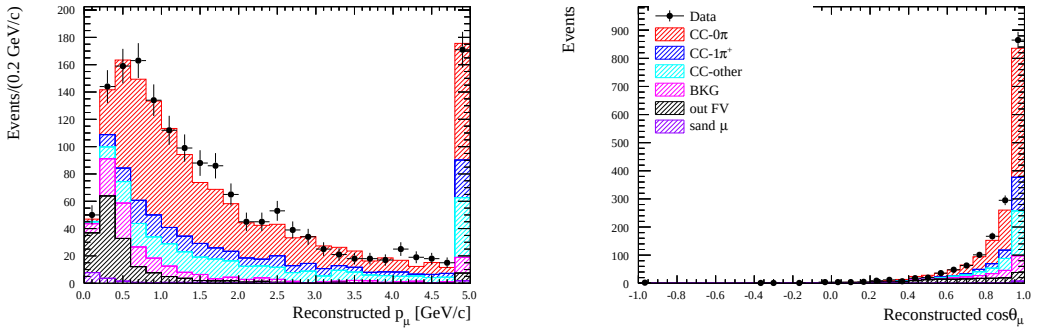

Figure 4.12. Distribution of events with vertex in **FGD1 FV** as function of the reconstructed muon momentum (left) and scattering angle (right) for the **CC-0π-like** sample. Different colours indicate different topologies. MC is scaled to POT in data.

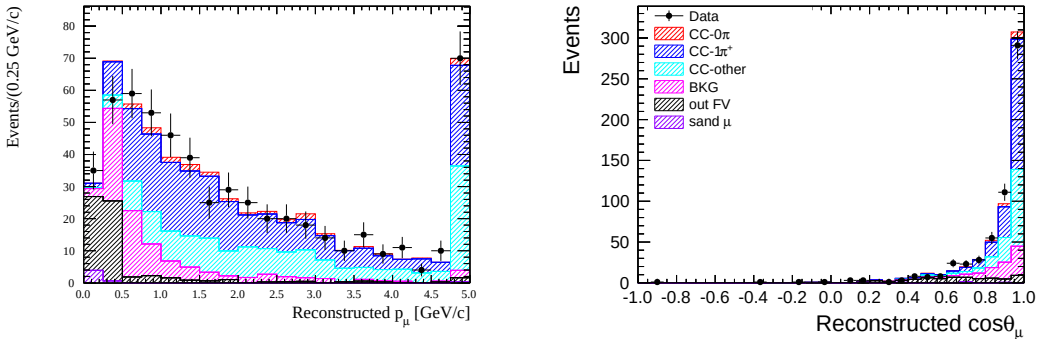

Figure 4.13. Distribution of events with vertex in **FGD1 FV** as function of the reconstructed muon momentum (left) and scattering angle (right) for the **CC-1π^+-like** sample. Different colours indicate different topologies. MC is scaled to POT in data.

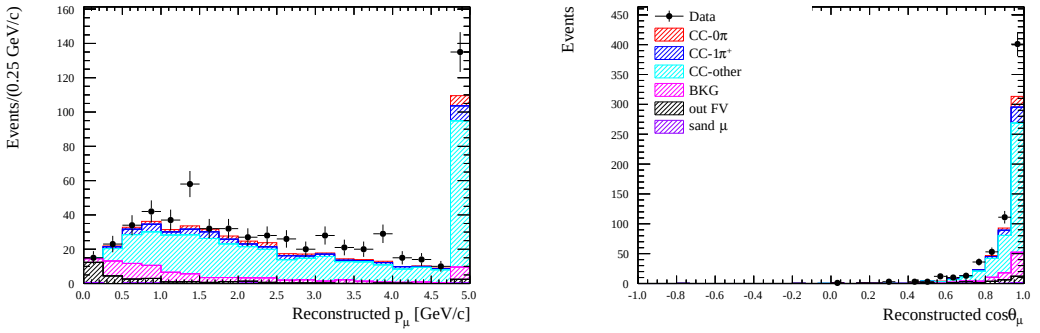

Figure 4.14. Distribution of events with vertex in **FGD1 FV** as function of the reconstructed muon momentum (left) and scattering angle (right) for the **CC-Other-like** sample. Different colours indicate different topologies. MC is scaled to POT in data.

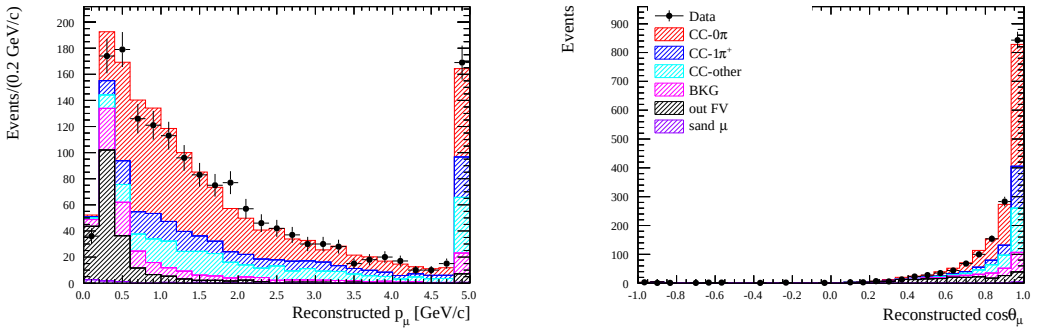

Figure 4.15. Distribution of events with vertex in **FGD2 FV** as function of the reconstructed muon momentum (left) and scattering angle (right) for the **CC-0π-like** sample. Different colours indicate different topologies. MC is scaled to POT in data.

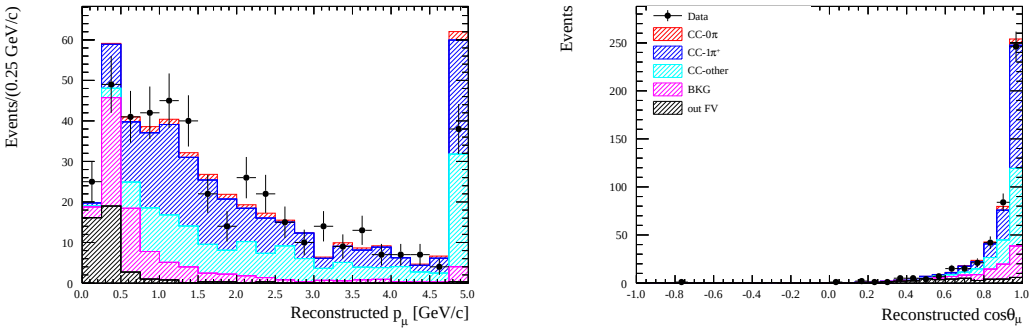

Figure 4.16. Distribution of events with vertex in **FGD2 FV** as function of the reconstructed muon momentum (left) and scattering angle (right) for the **CC-1π^+-like** sample. Different colours indicate different topologies. MC is scaled to POT in data.

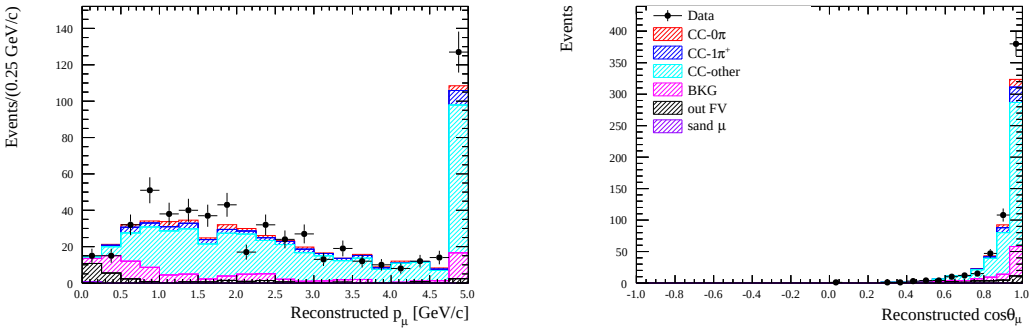

Figure 4.17. Distribution of events with vertex in **FGD2 FV** as function of the reconstructed muon momentum (left) and scattering angle (right) for the **CC-Other-like** sample. Different colours indicate different topologies. MC is scaled to POT in data.

Sample	Topology	MC Composition (%)	
		FGD1 FV	**FGD2 FV**
CC-0π-like	CC-0π	52.2	47.8
	CC-1π^+	11.7	13.6
	CC-Other	16.2	16.0
	BKG	8.4	8.6
	out FV	10.3	13.5
	sand μ	1.2	0.5
CC-1π^+-like	CC-0π	3.2	3.4
	CC-1π^+	42.4	42.2
	CC-Other	27.4	29.0
	BKG	15.5	16.5
	out FV	10.6	8.9
	sand μ	0.9	0.0
CC-Other-like	CC-0π	5.0	4.1
	CC-1π^+	8.4	7.2
	CC-Other	67.5	69.2
	BKG	12.8	14.0
	out FV	6.0	5.4
	sand μ	0.3	0.1

TABLE XIII. MC composition (in %) in term of **topologies** for the ν_μ **CC-0π-like**, **CC-1π^+-like** and **CC-Other-like** samples obtained selecting CC events with vertex in **FGD1 FV** and **FGD2 FV**.

Sample	Reaction	MC Composition (%)	
		FGD1 FV	**FGD2 FV**
CC-0π-like	CCQE	40.0	35.6
	2p2h	7.7	7.7
	RES	21.1	22.3
	DIS	10.6	10.9
	COH	0.8	0.9
	NC	2.6	2.2
	$\bar{\nu}_\mu$	5.2	5.9
	$\nu_e, \bar{\nu}_e$	0.7	0.5
	out FV	10.3	13.5
	sand μ	1.2	0.5
CC-1π$^+$-like	CCQE	3.1	3.3
	2p2h	0.6	0.4
	RES	36.0	35.4
	DIS	28.3	30.4
	COH	5.1	5.1
	NC	3.2	2.8
	$\bar{\nu}_\mu$	12.0	13.0
	$\nu_e, \bar{\nu}_e$	0.2	0.6
	out FV	10.6	9.0
	Sand μ	0.9	0.0
CC-Other-like	CCQE	3.9	3.1
	2p2h	0.7	0.7
	RES	13.3	12.8
	DIS	61.8	63.1
	COH	1.2	0.7
	NC	5.1	5.7
	$\bar{\nu}_\mu$	6.1	6.1
	$\nu_e, \bar{\nu}_e$	1.6	2.1
	out FV	6.0	5.5
	sand μ	0.3	0.1

TABLE XIV. MC composition (in %) in term of **reactions** for the ν_μ **CC-0π-like**, **CC-1π$^+$-like** and **CC-Other-like** samples obtained selecting CC events with vertex in **FGD1 FV** and **FGD2 FV**.

4.5 Detector systematics

The passage of particles through materials and the ND280 detector response are modelled using the GEANT4 toolkit [177]. Imperfections in the detectors response simulation can imply that MC poorly reproduce the detectors performance generating a systematic error. The uncertainty in the modelling of FGD and TPC responses and of neutrino interactions outside of the FGD FV are quantified through the use of control samples (dedicated data and MC samples). The differences between data and MC observed in control samples has been applied as correction factors to the nominal MC to take into account the observed discrepancies, while the error on these factors has been taken as detector systematic uncertainty.

TPC-related systematic uncertainties are divided into three classes: momentum resolution, selection efficiency and PID.
The momentum resolution is studied using sample of tracks crossing at least one FGD and two TPCs. The effect on the reconstructed momenta is evaluated when the information from one of the TPCs is removed from the analysis. The inverse momentum resolution is found to be better in simulations than in data, typically by 30%. A scaling of the difference between true and reconstructed inverse momentum is applied to the simulated data to account for this. Uncertainty in the overall magnetic field strength leads to an uncertainty on the momentum scale of 0.6%, which is confirmed using the range of cosmic ray particles that stop in the FGD.
The systematic uncertainty on selection efficiency arises in the modelling of the ionization, hit clustering and track finding and charge reconstruction. This is assessed by looking for missed track components in control samples with particles that pass through all three TPCs. The single track-finding efficiency is determined to be ($99.8^{+0.2}_{-0.4}\%$) for data and simulation for all angles, momenta and track lengths showing no dependence on the number of clusters. The same control samples are used to evaluate the charge mis-assignment systematic uncertainty. It is evaluated by comparing data and simulation of the charge mis-identification probability as a function of momentum. This is found to be less than 1% for momenta less than 5 GeV/c.
The TPC measurement of energy loss for PID is evaluated by studying high-purity control samples of electrons, muons and protons. The muon control sample has the highest statistics and is composed of particles from neutrino interactions outside the ND280 detector that pass through all the sub-detectors. For muons with momenta below 1 GeV/c, the agreement between data and MC is good, while above 1 GeV/c the resolution is better in simulation than in data.

Systematic uncertainties related to FGD are divided into three classes: track finding, tracking efficiency, PID and Michel electron tagging efficiency.
The performance for track finding in the FGD is studied separately for tracks which are connected to TPC tracks and tracks which are isolated in the FGD. The TPC-FGD matching efficiency is estimated from the fraction of through-going muons, in which the presence of a track in the TPC before and after the FGD implies that a track should be detected there. The efficiency is found to be 100%, but the control sample used only spans a limited phase-space. The matching efficiency depends also on the FGD hit efficiency,

thus it has been studied and was found to be around 96%.
The FGD PID performance is evaluated by comparing the energy deposited along the track with the expected energy deposit for a given particle type and reconstructed range in the FGD. Control samples of muons and protons passing through the first TPC (TPC1) and stopping in FGD1 are used. The pull distributions for specific particle hypotheses (proton, muon or pion) for data and simulation are fitted with Gaussian distributions.
The FGD tracking efficiency is estimated only for fully contained FGD tracks. The control sample used to asses this uncertainty is obtained with this strategy: an event with a muon candidate long tracks is selected, then in the same vertex either an FGD contained pion or proton is isotropically generated using GEANT4 particle gun, finally the FGD reconstruction is performed to check if the generated track was reconstructed. The efficiency is calculated for both data and MC as a function of the cosine of the angle between the long and short tracks and is defined as the ratio of the number of events with at least one reconstructed FGD-only track over the total number of selected events. The overall systematic uncertainties on the track efficiency is found to be less than 40% for both proton and pion.
The Michel electron tagging efficiency is studied using a sample of cosmic rays that stop in FGD1(2) for which the delayed electron is detected. The Michel electron tagging efficiency is found to be $(56.5 \pm 0.9)\%$ for simulation and $(56.4 \pm 0.2)\%$ for data in FGD1 and $(41.4 \pm 0.7)\%$ for MC and $(42.8 \pm 0.1)\%$ for data in FGD2. Particles entering from outside FGD FV can leave energy depositions that pass the Michel electron criteria causing a CC-0π event to be identified as a CC-$1\pi^+$ or CC-Other event. The external background rate for both MC and data was measured using empty beam spills to remove any products of decays from interactions in the FGDs. Additionally, the external background measurement was done separately for each run, since the measured rate differs for different beam power.

Other systematic uncertainties are: pion and proton re-interaction, out of FV, pile-up, sand μ background and FGD mass.
There is a systematic uncertainty in the modelling of pion and proton interactions travelling through the FGD. This is evaluated from differences between external interaction data [175] and the GEANT4 simulation. The external data do not cover the whole momentum range of T2K, so some extrapolation is necessary. Incorrect modelling can migrate events between the sub-samples and for some ranges of momentum this produces can lead to a large uncertainty.
To the out of FV systematic contribute both the difference in data-MC out of FV events rate and the reconstruction uncertainty. The first factor has been quantified by looking at the data-MC disagreement separately for each detector in which the out FV events occur. The systematic due to the reconstruction uncertainty is calculated by studying nine different categories of events that contribute to this background. Examples of these categories are: a high energy neutron that creates a π^- inside the FGD that is mis-identified as a muon, a backwards-going π^+ from the Br-ECal that is mis-reconstructed as a forward-going muon, and a through-going muon passing completely through the FGD and the TPC-FGD matching failed in such a way that mimics a FV event [176].
Pileup corrections are applied to account for the inefficiency due to sand muons crossing the tracker volume in coincidence with a FV event. The correction is evaluated for each

dataset separately, since it varies with the beam power, and is always below 1.3%. The systematic uncertainty arising from this correction is always below 0.28%.
The events originating from interactions outside the ND280 are simulated with a dedicated simulation. The data/MC discrepancy for $\bar{\nu}$ flux is about 30% and is included as a systematic uncertainty on the predicted number of sand muon events in the CC-Inclusive sample.
Finally, the uncertainty on the mass of FGDs is computed using the uncertainties in the size and density of the individual components and it is 0.67% for FGD1 and 0.35% for FGD2 [172, 178]. The difference between the two FGDs are explained by the correlation between the scintillator mass and water uncertainty.

The errors propagation, depending on the way they are propagated to the final number of events passing the selection criteria, can classify in three categories: normalization systematics which are treated by a single weight applied to all events, efficiency-like systematics are treated by applying a weight that depends on one or more observables (momentum, PID, etc), finally several systematics, called observable variation, are treated by adjusting the observables and re-applying the selection. Tab. XV shows the full list of base detector systematic effects considered and the way each one is treated to propagate the uncertainty.

The effect of FGD related systematic have been propagated only for the Multiple pion selection, since FGDs informations are used. The total detector systematic errors on the reconstructed number of events with vertex in **FGD1 FV** (**FGD2 FV**) for the **CC-1-Track** and **CC-N-Tracks** samples are 2.5% (1.9%) and 4.8% (4.0%). For the **CC-0π-like**, **CC-1π^+-like** and **CC-Other-like** are 5.00% (6.17%) 8.13% (9.31) and 7.17% (7.57%). The dominant source of uncertainty for both selections comes from the pion re-interaction model, used to estimate the rate of pion interactions in the FGDs. This is due to differences between the GEANT4 model, used to simulate pion re-interactions outside the nucleus, and the available experimental data. The second largest uncertainty is due to out of FV events due to the high error on the rate and reconstruction failures.

4.6 Latest T2K oscillation results

The Multiple track selection described before has been used in the last published oscillation analyses to constrain the ν_μ un-oscillated flux in $\bar{\nu}$-mode [176, 179–181].

The predicted event rates at ND280 and SK are parametrized introducing neutrino flux and interaction models parameters. These models are fit to the high statistics data collected at ND280, producing a better prediction of the SK event rate and reducing the systematic uncertainties associated with the flux and interaction models. The near detector fit uses samples of event with reconstructed vertex in FGD1 FV and FGD2 FV and from $\bar{\nu}$-mode and ν-mode data, for a total of 14 samples. Events in FGD2 FV are really important since help in constraining the cross section uncertainties relative to neutrino interactions on water, avoiding water-carbon extrapolation. In $\bar{\nu}$-mode, in addition to the ν_μ multiple track samples described in Sec. 4.3, a similar selection is performed to

Systematic error source	treatment
TPC related	
B Field distortions	Observable variation
TPC momentum resolution	Observable variation
TPC PID	Observable variation
TPC cluster efficiency	Efficiency-like
TPC tracking efficiency	Efficiency-like
TPC charge misassignment	Efficiency-like
FGD-TPC related	
TPC-FGD matching efficiency	Efficiency-like
FGD related	
FGD PID	Observable variation
FGD tracking efficiency	Efficiency-like
Michel electron efficiency	Efficiency-like
Background related	
Out FV	Normalization
Sand muon	Normalization
Pile-up	Normalization
MC modeling related	
Pion secondary interactions	Normalization
Proton secondary interactions	Normalization
FGD mass	Normalization

TABLE XV. Summary of the systematic error source and the way they are propagated.

select $\bar{\nu}_\mu$ CC interactions. In ν-mode a multiple pion selection similar to the one described above has been used. The 14 event samples are binned in muon momentum and cosine of the muon scattering angle. The ND280 likelihood, described in Ref. [175], assumes that the observed number of events in each bin follows a Poisson distribution. A penalty term is added to take into account the constrain for the flux, cross sections and detector parameters. ND280 detector systematic, flux and cross-section parameters for NC and ν_e interactions are treated as nuisance. The fitted neutrino cross-section and unoscillated SK flux parameters are passed as input to the oscillation analysis. Fig. 4.18 shows the values of the unoscillated SK flux parameters and Fig. 4.19 the cross-section parameters before and after the fit as a fraction of the nominal value, along with their prior constraints. More details on the analysis strategy and on the results of the near detector fit can be found in Refs. [175, 176].

At SK three samples are selected in ν-mode and two in $\bar{\nu}$-mode: one of ν_μ and one of ν_e CCQE interactions and another of ν_e CC-1π^+ events where an electron is produced with a charged pion, tagged from delayed clusters of PMTs hits; one of $\bar{\nu}_\mu$ and one of $\bar{\nu}_e$ CCQE interactions [176].

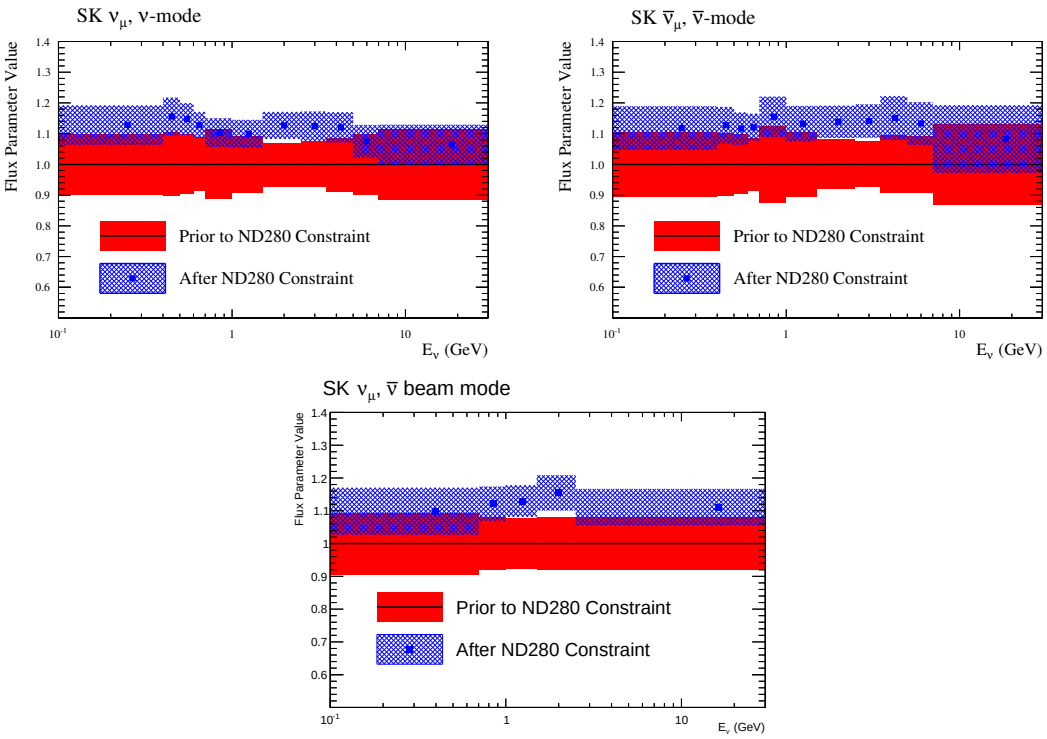

Figure 4.18. The SK flux parameters for the ν_μ (top left) in ν-mode, $\bar{\nu}_\mu$ (top right) and ν_μ (bottom) in $\bar{\nu}$-mode, shown as a fraction of the nominal value. The bands indicate the 1σ uncertainty on the parameters before (solid, red) and after (hatched, blue) the near detector fit. Figure taken from [176].

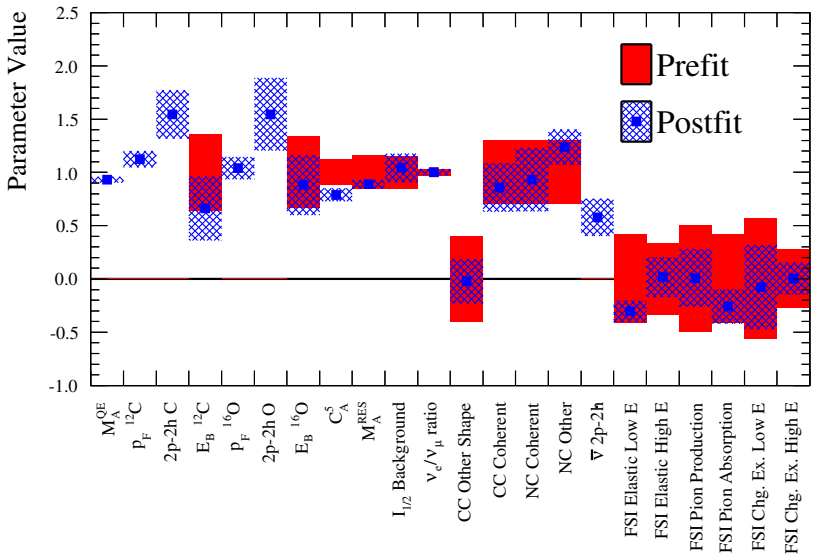

Figure 4.19. Cross-section parameters before (solid, red) and after (hatched, blue) the near detector fit, shown as a fraction of the nominal value. The colored band shows the 1σ uncertainty. Figure taken from [176].

The systematic uncertainties taken into account in oscillation analysis are grouped into

four categories: flux, cross section, and SK detector and momentum scale parameters. The flux and many of the cross-section parameters are correlated with the ND280 measurements that effectively reduce the systematic uncertainties of the measurements at SK. The effect of the systematic uncertainties on the predicted event rates of the ν- and $\bar{\nu}$-mode samples are summarized in Tabs. XVI and XVII respectively. The anti-correlations between flux and cross section parameters reduce the systematic uncertainties when both these sources are taken into account.

Source of uncertainty	ν_e CCQE-like $\delta N/N$	ν_μ $\delta N/N$	ν_e CC-1π^+ $\delta N/N$
Flux (w/ ND280 constraint)	3.7%	3.6%	3.6%
Cross section (w/ ND280 constraint)	5.1%	4.0%	4.9%
Flux+cross-section			
(w/o ND280 constraint)	11.3%	10.8%	16.4%
(w/ ND280 constraint)	4.2%	2.9%	5.0%
FSI+SI+PN at SK	2.5%	1.5%	10.5%
SK detector	2.4%	3.9%	9.3%
All			
(w/o ND280 constraint)	12.7%	12.0%	21.9%
(w/ ND280 constraint)	5.5%	5.1%	14.8%

TABLE XVI. Effect of 1σ variation of the systematic uncertainties on the predicted event rates of the ν-mode samples.

In order to stress the reduction of the systematic error due to ND280 constraints, in Fig. 4.20 is shown the effect of ND280 on the reconstructed neutrino energy spectrum for the μ-like sample in $\bar{\nu}$-mode. The systematic error is clearly reduced by ND280 measurements. In order to support the choice of a joint fit of multiple samples, the fit using ND280 data has been performed in three different configurations: consider only the neutrino or the antineutrino samples and both, but without the inclusion of the ν_μ component in $\bar{\nu}$-mode. The fractional error on the event rates at SK, in the first and second configuration, are higher than the case in which the sample are fitted together. The most interesting case is the third, where the errors are slightly larger showing the limited impact of the ν_μ component in $\bar{\nu}$-mode. On the other hand, the flux parameters related to this component are more constrained if this sample is included. In conclusion, to keep the error lower, consider this sample in the fit.

The oscillation analysis described here are based on an exposure of 7.482×10^{20} POT in ν-mode and 7.471×10^{20} POT in $\bar{\nu}$-mode collected at SK as reported in Tab. XVIII. Through combined analyses of these five samples, simultaneous measurements of four oscillation parameters, $|\Delta m^2_{32}|$, $\sin^2\theta_{23}$, $\sin^2\theta_{13}$, and δ_{CP} and of the mass ordering are made. Three oscillation analyses are performed giving frequentist (presented here) and Bayesian intervals for oscillation parameters with and without reactor constraints on $\sin^2\theta_{13}$. When combined with reactor measurements, the hypothesis of CP conservation

Source of uncertainty	$\overline{\nu}_e$ CCQE-like $\delta N/N$	$\overline{\nu}_\mu$ $\delta N/N$
Flux (w/ ND280 constraint)	3.8%	3.8%
Cross section (w/ ND280 constraint)	5.5%	4.2%
Flux+cross-section		
(w/o ND280 constraint)	12.9%	11.3%
(w/ ND280 constraint)	4.7%	3.5%
FSI+SI+PN at SK	3.0%	2.1%
SK detector	2.5%	3.4%
All		
(w/o ND280 constraint)	14.5%	12.5%
(w/ ND280 constraint)	6.5%	5.3%

TABLE XVII. Effect of 1σ variation of the systematic uncertainties on the predicted event rates of the $\bar{\nu}$- mode samples.

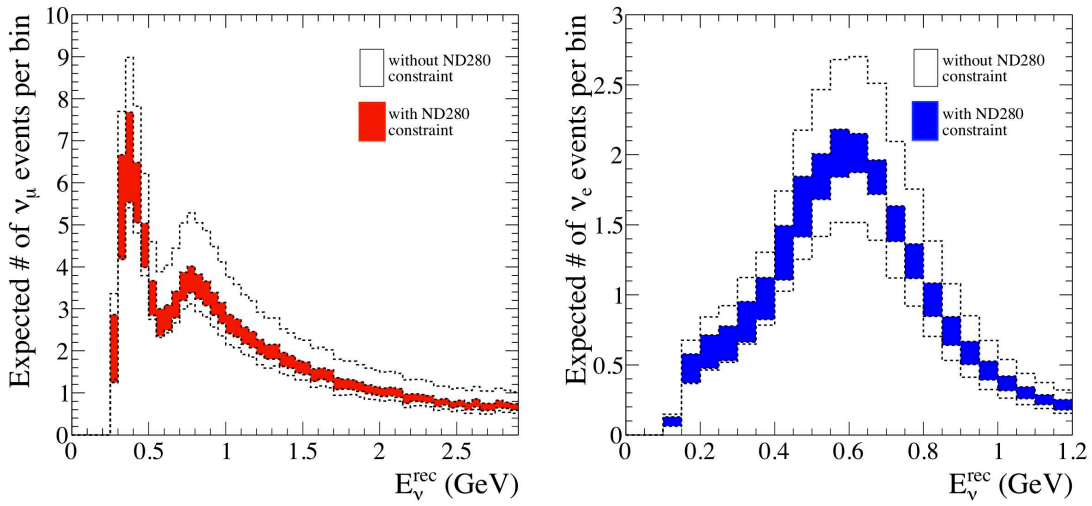

Figure 4.20. Total error envelopes for the reconstructed energy distributions of ν_μ CC (left) and ν_e CC (right) candidate events, using typical oscillation parameter values, with and without the ND280 constraint applied.

($\delta_{CP} = 0$ or π) is excluded at 90% confidence level. The 90% confidence region for δ_{CP} is [-2.95,-0.44] ([-1.47, -1.27]) for normal (inverted) ordering. The central values and 68% confidence intervals for the other oscillation parameters for normal (inverted) ordering are reported in Tab. XIX. In Fig. 4.21 is shown the comparison of the constraints in the δ_{CP}–$\sin^2\theta_{13}$ plane when appearance channels in ν-mode and in $\bar{\nu}$-mode are considered independently. Disappearance channels in both modes are used in the fits. The reactor constrain are not used in this plots. The two datasets alone prefer different values of $\sin^2\theta_{13}$, which is driven by the absolute appearance rate, since the $\bar{\nu}$-mode appearance

Run Period	ν-mode POT ($\times 10^{20}$)	$\bar{\nu}$-mode POT ($\times 10^{20}$)
Run 1	0.323	–
Run 2	1.108	–
Run 3	1.579	–
Run 4	3.560	–
Run 5	0.242	0.506
Run 6	0.190	3.505
Run 7	0.480	3.460
Total	7.482	7.471

TABLE XVIII. T2K data-taking periods and collected POT used in the last published oscillation analysis.

Parameter	Normal ordering		Inverted ordering	
	Best-fit	$\pm 1\sigma$	Best-fit	$\pm 1\sigma$
δ_{CP}	-1.728	[-2.538;-0.877]	-1.445	[-2.170;-0.768]
$\sin^2\theta_{23}$	0.550	[0.465;0.601]	0.5525	[0.470;0.601]
Δm^2_{32} (10^{-3} eV$^2/c^4$)	2.54	[2.460;2.621]	2.51	[2.429;2.588]

TABLE XIX. Best-fit results and the 68% confidence interval of the T2K data fit with the reactor constraint with normal and inverted hypotheses. Value taken from [176]

sample does not have the power to exclude a zero value of θ_{13}. In Fig. 4.22 is shown

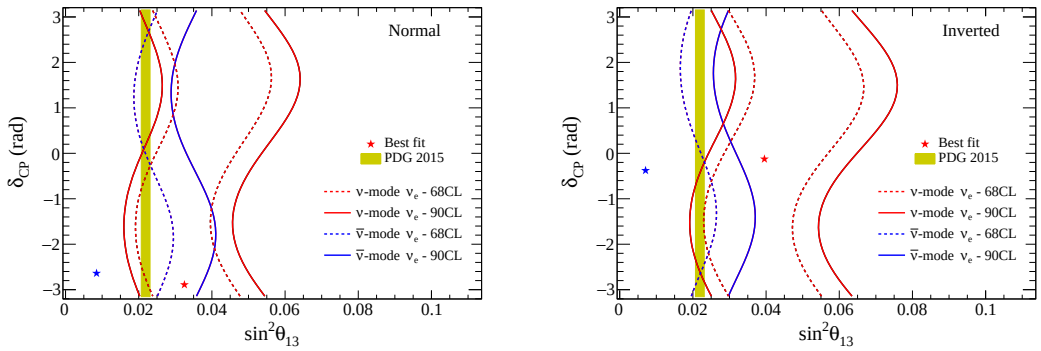

Figure 4.21. Contours in the $\sin^2\theta_{13}$–δ_{CP} plane using T2K-only data, obtained by analysing either the ν- or $\bar{\nu}$-mode appearance datasets which are compared for both orderings. The yellow band corresponds to the reactor value on $\sin^2\theta_{13}$ from the PDG 2015 [182]. Figure taken from [176].

the 2D $\sin^2\theta_{13}$–δ_{CP} confidence level contours for the fit results obtained including the reactor constrain. The results with and without the additional CC-1π^+ e-like sample are compared to demonstrate the effect of such sample. If compared to the best-fit results

obtained with the T2K-only data, the inclusion of the CC-1π^+ e-like sample results in a shift of best-fit value for the δ_{CP} phase towards $-\pi/2$. The 1D $\Delta\chi^2$ surface obtained with

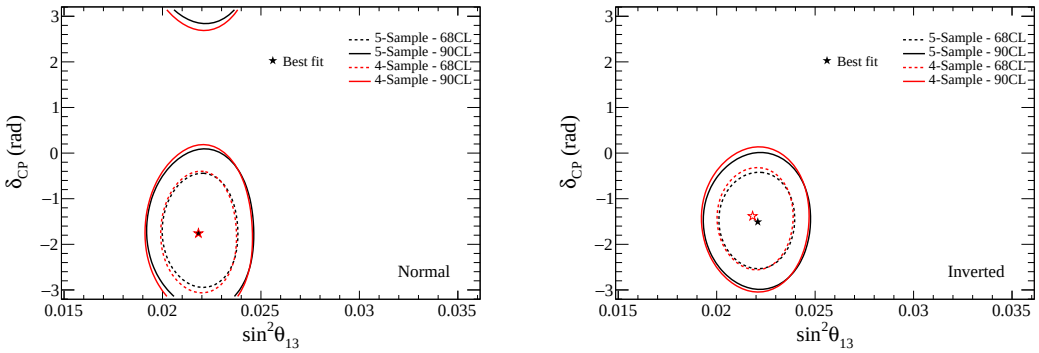

Figure 4.22. Comparison of two-dimensional constant $\Delta\chi^2$ contours in the δ_{CP}–$\sin^2\theta_{13}$ plane using T2K data with the reactor constraint, for both four-sample (red) and five-sample (black) analyses with normal (left) and inverted (right) mass ordering hypotheses. The contours are produced by marginalizing the likelihood with respect to all parameters other than the parameters of interest. Figure taken from [176].

the Feldman-Cousins approach is used to evaluate the 90% confidence intervals for δ_{CP} for both ordering cases, as shown in Fig. 4.23. CP values of $\delta_{CP} = 0,\ \pi$ are excluded at 90% and 2σ confidence levels respectively. The presented analysis has been recently

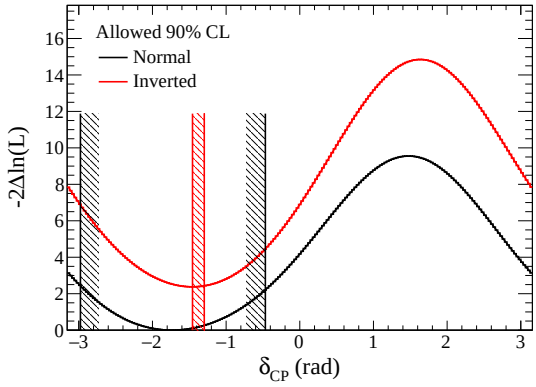

Figure 4.23. One dimensional $\Delta\chi^2$ surfaces for δ_{CP} using T2K data with the reactor constraint. The critical $\Delta\chi^2$ values obtained with the Feldman-Cousins method are used to evaluate the 90% confidence level. Figure taken from [176].

updated using the data collected in last year in ν-mode. Furthermore the selection of the SK samples has been revised in order to increase the FV for the T2K oscillation analysis. A new reconstruction algorithm allows to remove the cut on the vertex location in order to observe an increase of 20% more events, with a reduction of the background. The cross-section model has changed as well. It has been added additional parameters that help in controlling the uncertainties on short and long range correlations. In the future analysis also the samples used in the ND280 fit will be updated including the Multiple pion selection presented in Sec. 4.4.

4.7 Conclusions and future outlook

In conclusion the results of two selections has been shown and compared. It is evident that the level of purity and efficiency has been improved with the Multiple pion selection. It is important to stress that to keep low the errors on the oscillation parameter it is crucial, as already mentioned, to decrease the uncertainties on the interaction models. As already demonstrated in Ref. [175], this goal can be achieved using the samples defined by the number of final state pions, indeed this division enhance ability to constrain the CCQE and resonant single pion cross section parameters, and decrease the uncertainty they contribute to the oscillation analyses. Anyway the impact of detector systematic is higher in this case and this is mainly due to the additional FGD information needed for the identification of FGD contained tracks. Improvements are under discussion inside the T2K Collaboration. Improved reconstruction algorithms, calibration procedure and sub-detector alignment can help in this direction. The dominant uncertainty due to the pion re-interactions has been recently improved using control samples selected at ND280 with an high purity in terms of pion content. This data set has been used to constrain the poorly know GEANT4 model. Thus in future this error will be strongly reduced. In the near future a reduction of the ν_μ contamination in $\bar{\nu}$-mode by 5-10% will be possible increasing the magnetic horn pulsed current from $\pm 250\ kA$ to $\pm 320\ kA$ [183].

Chapter 5

Measurement of muon neutrino and antineutrino cross sections without pions in the final state

5.1 Introduction

Neutrino oscillations physics is entered in the precision era, imposing to the accelerator neutrino experiments a reduction of systematic errors to the level of few percent, even more in view of the measurement of the CP phase and the mass hierarchy. With a precision around 20% the neutrino-nucleus cross section, in the neutrino energy region relevant for oscillation experiments, is one of the most important source of systematic uncertainty. Information on (anti)neutrino scattering is vital for the interpretation of neutrino oscillation since it affects the key ingredients of such measurements: background estimation and neutrino energy reconstruction.

Regarding CCQE interactions on nuclear targets a complicated experimental and theoretical picture has emerged. Various measurements of CCQE cross-section noted that the kinematic distributions of the outgoing muons were not consistent with the prediction of the relativistic Fermi gas (RFG) nuclear model [142, 184–186]. The neutrino CCQE cross section measured by the MiniBooNE collaboration [184] has been compared with a prediction based on the RFG model using both the standard value of the axial mass $M_A = 1.03\,GeV/c^2$ and the larger value of $M_A = 1.35\,GeV/c^2$, which better describes the data. Many theoretical models proposed another neutrino-nucleus interaction channel where neutrinos interact with pairs of correlated nucleons and more than one nucleon is knocked-out from the nucleus (multi-nucleon component), but a consistent picture has yet to emerge [127, 187–189].

As pointed out in the Martini model [188] the multinucleon term produces a sizeable increase of the neutrino quasielastic cross section, while for antineutrino this influence is smaller (see Fig. 5.1). Thus the differences between neutrino and antineutrino cross

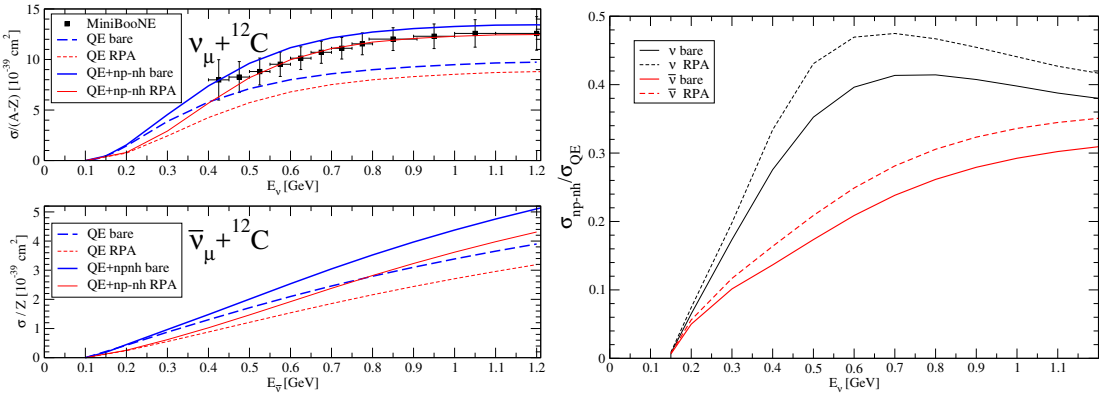

Figure 5.1. On the left: ν_μ (upper panel) and $\bar{\nu}_\mu$ (lower panel) - ^{12}C CCQE per neutron and per proton with and without the multinucleon component as a function of neutrino energy. The experimental points are taken from [184]. On the right: ratio of multinucleon component of CCQE cross section on ^{12}C to the single nucleon one for ν_μ and $\bar{\nu}_\mu$ as a function of neutrino energy. Both figures are taken from [188].

sections could be used to test the presence of the multinucleon excitations.
The same authors in Ref. [189] compared the sum and the difference of the CCQE muon neutrino [184] and antineutrino [190] cross section measured by the MiniBooNE collaboration against their model. As can be notice from Eq. 2.10 the difference contains only one term, the axial vector interference, while in the sum this term is eliminated. In conclusion the work in Ref. [189] shows the possibility to identify multinucleon component of the cross section studying the sum and the difference of the ν_μ and $\bar{\nu}_\mu$ cross section.

T2K run in $\bar{\nu}$-mode are giving the opportunity to measure cross-sections for antineutrinos at energy around 600 MeV using ND280. In this dissertation is discussed the simultaneous measurement of the flux-integrated double-differential muon neutrino and antineutrino CC cross-section on carbon without pions in the final state using the T2K off-axis near detector.
The simultaneous extraction allows to extract three measurements:

- CC-0π $\bar{\nu}_\mu$ flux-integrated double differential cross section;
- The sum and the difference of the CC-0π $\bar{\nu}_\mu$ and CC-0π ν_μ;
- The asymmetry between the two cross section, i.e. the ration between the sum and the difference, which gives a direct estimation on any possible bias due to mismodelling of neutrino interactions on the measurement of the CP violation phase in neutrino oscillation.

5.2 Analysis Strategy

5.2.1 Cross-section and signal definition

The measurement of double-differential ν_μ and $\bar{\nu}_\mu$ charged-current interactions on C_8H_8 without pions in the final state (**CC-0π**), along with the combination of them, are extracted as a function of the muon momentum and angle.
The cross-sections are measured as a function of the kinematics of the outgoing muon because other reconstructed variables, such as the neutrino energy or the transferred momentum (Q^2), relay on the nuclear model used in the MC event generator, while is important to perform a measurement highly model-independent.
For this measurement the signal has been defined in terms of the particles which exit the nucleus and can be observed in the detector, including not only CCQE events but also events where one pion is produced at the interaction point and then reabsorbed in the nuclear environment. Thus the signal is defined as CC interaction without pions in the final state, a process that match with the actual experimental signature, relying less on the MC to correct for pion re-absorption effects.
There are usually three standard ways of extracting a cross-section which are:

- the flux-unfolded cross-section:

$$\frac{d\sigma}{dx_i} = \frac{N_i^{CC0\pi}}{\epsilon_i^{MC} \int_{E_{i\nu}^{min}}^{E_{i\nu}^{max}} w_i(E_\nu)\Phi(E_\nu)dE_\nu N_{nucleons}^{FV}} \times \frac{1}{\Delta x_i} \tag{5.1}$$

  In this case the proper neutrino energy distribution in each muon kinematic bin, $w_i(E_\nu)$, need to be known. Therefore the measurement depends strongly on the particular model chosen to apply this correction, but on the other hand the result can be directly compared between different experiments, since it has been fully corrected for the flux;

- the flux averaged cross-section:

$$\frac{d\sigma}{dx_i} = \frac{N_i^{CC0\pi}}{\epsilon_i^{MC} \int_{E_{i\nu}^{min}}^{E_{i\nu}^{max}} \Phi(E_\nu)dE_\nu N_{nucleons}^{FV}} \times \frac{1}{\Delta x_i} \tag{5.2}$$

  This method produce a results which is instead experiment-dependent, since the result has not been fully unfolded for the particular neutrino flux in each muon kinematic bin, and it is also still model-dependent since an assumption on $E_{i\nu}^{min}$ and $E_{i\nu}^{max}$ for each muon kinematic bin need to be done to apply the average flux correction;

- the flux integrated cross-section:

$$\frac{d\sigma}{dx_i} = \frac{N_i^{CC0\pi}}{\epsilon_i^{MC} \Phi N_{nucleons}^{FV}} \times \frac{1}{\Delta x_i} \tag{5.3}$$

  As indicated in Eq. 5.3, the event rate is divided by the total integrated flux, in this way it is not corrected for the flux in each separated bin of muon kinematics.

In all cases ϵ_i^{MC} is the efficiency in each bin, $N_{nucleons}^{FV}$ is the number of nucleons in the fiducial volume and Δx_i is the bin width (in this analysis $\Delta x_i = \Delta p_\mu \Delta cos\theta_\mu$). The computation of that quantities and their associated uncertainty will be described in the next sections.

The last method has been chosen to perform this analysis. The results will be experiment-dependent, since no correction for the flux bin-by-bin is applied, but it is completely model-independent, i.e. no assumption needs to be made on the particular neutrino energy distribution in each muon kinematic bin. Anyway the comparison of a model with the final result can be made convoluting it with the proper flux.

5.2.2 Cross-section extraction method: binned likelihood fit

This analysis uses a binned likelihood to perform a fit to the number of selected events as a function of the muon kinematic (p_μ and $\cos\theta_\mu$) simultaneously in six signal regions (five for the neutrino sample and one for the antineutrino) and four control regions (two for each sample) to constrain the backgrounds caused by CC-RES and CC-DIS.
The number of selected events in each region and in each bin of reconstructed kinematics j is computed as

$$\begin{aligned} N_j = \sum_i^{\text{true bins}} [& c_i{}^{\nu_\mu} \left(N_i^{\text{MC } \nu_\mu \text{ CC-0}\pi} \prod_s^{\text{model}} w(s)_i^{\nu_\mu \text{CC-0}\pi} \right) + \\ & c_i{}^{\bar{\nu}_\mu} \left(N_i^{\text{MC } \bar{\nu}_\mu \text{ CC-0}\pi} \prod_s^{\text{model}} w(s)_i^{\bar{\nu}_\mu \text{CC-0}\pi} \right) + \\ & \sum_k^{\text{bkg reactions}} N_i^{\text{MC bkg } k} \prod_b^{\text{model}} w(b)_i^k] t_{ij}^{\text{det}} r_j \sum_n^{\text{E}_{\nu_\mu \text{ or } \bar{\nu}_\mu}} w_n^i f_n \end{aligned} \tag{5.4}$$

where i runs over the bins of the "true" muon kinematics before detector smearing effects, k runs over the background reactions, $c_i{}^{\nu_\mu}$ and $c_i{}^{\bar{\nu}_\mu}$ are the parameters of interest which adjust the ν_μ and $\bar{\nu}_\mu$ CC-0π number of events in Monte Carlo respectively, in order to match with the observation in data, t_{ij}^{det} is the transfer matrix from the true (i) to the reconstructed (j) muon kinematics bins, r_j represents the nuisance parameters in the fit describing the detector systematics and which are constrained by a prior covariance matrix. The last sum runs over the neutrino or antineutrino energy bins, depending on the sample, the f_n are the flux parameters and the weights w_n^i describe the neutrino energy distribution for each bin of $p_\mu^{true}, \cos\theta_\mu^{true}$. The product $\prod_{s,b}^{\text{model}}$ runs over the systematics related to the theoretical modelling of the signal (s) or the background (b). Each w is a weighting function describing how the generated muon kinematics change (in bins i for each signal or background process) as a function of the value of a particular theoretical parameter. All the parameters s and b are nuisance parameters in the fit constrained by a prior covariance matrix.
As stated before there are two sets of parameters of interest for each region. Indeed one relevant background in $\bar{\nu}_\mu$ signal regions comes from the ν_μ beam component in the antineutrino beam. Less relevant is the $\bar{\nu}_\mu$ component in neutrino beam. The simultaneous fit constrains this background component avoiding its free fluctuation. The overall number

of CC-0π events in all signal regions and control regions is obtained minimizing the following binned likelihood:

$$\begin{aligned}\chi^2 = \chi^2_{\text{stat}} + \chi^2_{\text{syst}} = &\sum_{j}^{\text{reco bins}} 2\left(N_j^{\nu_\mu} - N_j^{\nu_\mu\ \text{obs}} + N_j^{\nu_\mu\ \text{obs}} \ln \frac{N_j^{\nu_\mu\ \text{obs}}}{N_j^{\nu_\mu}}\right) \\ &+ \sum_{j}^{\text{reco bins}} 2\left(N_j^{\bar{\nu}_\mu} - N_j^{\bar{\nu}_\mu\ \text{obs}} + N_j^{\bar{\nu}_\mu\ \text{obs}} \ln \frac{N_j^{\bar{\nu}_\mu\ \text{obs}}}{N_j^{\bar{\nu}_\mu}}\right) \\ &+ \chi^2_{\text{syst}}\end{aligned} \tag{5.5}$$

where χ^2_{syst} is a penalty term for the systematics:

$$\chi^2_{\text{syst}} = \sum_{p} \left(\vec{p} - \vec{p}_{\text{prior}}\right) \left(V_{\text{cov}}^{\text{syst}}\right)^{-1} \left(\vec{p} - \vec{p}_{\text{prior}}\right) \tag{5.6}$$

where $\vec{p}$ are the parameters which describe the effect of nuisance parameters, $\vec{p}_{\text{prior}}$ are the prior values of these systematic parameters and $V_{\text{cov}}^{\text{syst}}$ is their covariance matrix which describes the confidence in the nominal parameter values as well as correlations between them. The number of ν_μ CC-0π selected events in all the signal and background regions, as a function of the "true" kinematics extracted from the fit is:

$$N_i^{\nu_\mu\text{CC-0}\pi} = \sum_{t}^{\text{regions}} \sum_{j}^{\text{reco bins}} c_i^{\nu_\mu} N_{jt}^{\text{MC}\ \nu_\mu\ \text{CC-0}\pi} t_{tij}^{\text{det}} r_{tj}^{\text{det}} \prod_{s}^{\text{model syst}} w(s)_i^{\nu_\mu\text{CC-0}\pi} \sum_{n}^{\text{E}_\nu} w_n^i f_n \tag{5.7}$$

while the number of $\bar{\nu}_\mu$ CC-0π selected events is:

$$N_i^{\bar{\nu}_\mu\text{CC-0}\pi} = \sum_{t}^{\text{regions}} \sum_{j}^{\text{reco bins}} c_i^{\bar{\nu}_\mu} N_{jt}^{\text{MC}\ \bar{\nu}_\mu\ \text{CC-0}\pi} t_{tij}^{\text{det}} r_{tj}^{\text{det}} \prod_{s}^{\text{model syst}} w(s)_i^{\bar{\nu}_\mu\text{CC-0}\pi} \sum_{n}^{\text{E}_{\bar{\nu}}} w_n^i f_n \tag{5.8}$$

Then the flux-integrated CC-0π cross-section is extracted correcting this number by the selection efficiency in each bin ϵ_i and divided by the overall integrated flux and the number of nucleons in the FGD1 FV, leading to the following formula for ν_μ:

$$\frac{\text{d}\sigma_{\nu_\mu}}{\text{d}x_i} = \frac{N_i^{\nu_\mu\text{CC-0}\pi}}{\epsilon_i^{\nu_\mu} \Phi^{\nu_\mu} N_{\text{nucleons}}^{\text{FV}}} \times \frac{1}{\Delta x_i} \tag{5.9}$$

and $\bar{\nu}_\mu$:

$$\frac{\text{d}\sigma_{\bar{\nu}_\mu}}{\text{d}x_i} = \frac{N_i^{\bar{\nu}_\mu\text{CC-0}\pi}}{\epsilon_i^{\bar{\nu}_\mu} \Phi^{\bar{\nu}_\mu} N_{\text{nucleons}}^{\text{FV}}} \times \frac{1}{\Delta x_i} \tag{5.10}$$

Accordingly the sum, the difference and the asymmetry are given by the following formulas:

$$\frac{\text{d}\sigma_{\nu_\mu}}{\text{d}x_i} \pm \frac{\text{d}\sigma_{\bar{\nu}_\mu}}{\text{d}x_i} = \left(\frac{N_i^{\nu_\mu\text{CC-0}\pi}}{\epsilon_i^{\nu_\mu} \Phi^{\nu_\mu}} \pm \frac{N_i^{\bar{\nu}_\mu\text{CC-0}\pi}}{\epsilon_i^{\bar{\nu}_\mu} \Phi^{\bar{\nu}_\mu}}\right) \times \frac{1}{N_{\text{nucleons}}^{\text{FV}} \Delta x_i} \tag{5.11}$$

$$\frac{\mathrm{d}\sigma_{\nu_\mu} - \mathrm{d}\sigma_{\bar{\nu}_\mu}}{\mathrm{d}\sigma_{\nu_\mu} + \mathrm{d}\sigma_{\bar{\nu}_\mu}} = \frac{\frac{N_i^{\nu_\mu \text{CC-0}\pi}}{\epsilon_i^{\nu_\mu}\Phi^{\nu_\mu}} - \frac{N_i^{\bar{\nu}_\mu \text{CC-0}\pi}}{\epsilon_i^{\bar{\nu}_\mu}\Phi^{\bar{\nu}_\mu}}}{\frac{N_i^{\nu_\mu \text{CC-0}\pi}}{\epsilon_i^{\nu_\mu}\Phi^{\nu_\mu}} + \frac{N_i^{\bar{\nu}_\mu \text{CC-0}\pi}}{\epsilon_i^{\bar{\nu}_\mu}\Phi^{\bar{\nu}_\mu}}} \tag{5.12}$$

MINUIT minimizer with MIGRAD strategy [191] has been used to perform the fit and particular care has been taken to have a limited number of parameters allowing the fit to converge. To this respect it is particularly important to avoid degeneracies (100% correlations between the parameters) and minimize the number of parameters, even at the expense of larger systematics errors. On one hand, the main advantage of this method with respect to other unfolding techniques is that the unsmearing process is unbiased. On the other hand, this minimization process lead to an ill-posed problem, since different sets of parameters could provide good results. In general, this would lead to a result with strong anti-correlation between nearby bins. This behaviour can be limited optimizing the binning as much as possible.

5.3 Input for the cross sections extraction

5.3.1 The data sets

In Tabs. XX and XXI is reported the statistic used in this analysis collected in ν- and $\bar{\nu}$-mode respectively. The MC samples are weighted to match the relative fraction of the different beam periods. The MC samples are normalized for the data POT. Furthermore, nominal MC are corrected due to reconstruction discrepancies between data and MC studied through control sample, as already explained in the previous Chapter. All MC samples are processed using NEUT version 5.3.2 [138] described in Sec. 2.3. It is worth to notice that, compared to the analysis presented in the previous Chapter, an additional data set has been added to the $\bar{\nu}$ data, since it became available.

Run Period	**Data POT** ($\times 10^{20}$)	**MC POT** ($\times 10^{20}$)	**MC Sand POT** ($\times 10^{20}$)
Run 2	0.79	14.53	22.34
Run 3	1.58	60.68	22.34
Run 4	3.42	51.55	22.34
Total	5.80	126.76	67.02

TABLE XX. T2K data-taking periods in ν-mode and the POT used in this analysis for data and MC.

Run Period	Data POT ($\times 10^{20}$)	MC POT ($\times 10^{20}$)	MC Sand POT ($\times 10^{20}$)
Run 5	0.43	22.90	12.93
Run 6	3.40	14.86	12.93
Run 7	2.44	10.23	12.93
Total	6.27	47.00	38.79

TABLE XXI. T2K data-taking periods in $\bar{\nu}$-mode and the POT used in this analysis for data and MC.

5.3.2 Event Selections

The selection of the signal and control regions has as main goal enlarge the phase space of the muon kinematics. In previous analysis the selection criteria has been optimised to select forward going muons originating from FGD1 and leaving more than 18 clusters in TPC2. The acceptance has been increased using all the ND280 sub-detectors and the time of flight (TOF) of the particles between different sub-detectors which gives information about the sense of the track.

For the selection of particles that enter the TPCs, the standard TPC PID is performed, while to identify particles that do not enter the TPCs, ECal PID is used if there is an associated ECal segments. ECal PID helps in the improvement of the muon purity reducing the shower-like contamination. Furthermore the ratio between the track length and the electromagnetic energy associated to the track reduce the proton contamination. Finally, the momentum in that selection is reconstructed from the total length of the track (measured by range), so it is require to stop either in ECAL or SMRD.

In both selections is used the TOF between FGD1-PØD, FGD1-BrECal and FGD1-FGD2. The first two are fundamental to tag backward going particles starting in FGD1. The other two are used to reduce the out of fiducial volume contamination in the selection of forward going tracks.
All the FGD1 thickness in the direction Z has been used for these selection in order to have a common fiducial volume between the ν_μ and $\bar{\nu}_\mu$ selection. Nonetheless at reconstructed level events starting in the first and last layer are rejected.

In the following sections are described the selection criteria of signal regions and sidebands.

Selection of the ν_μ CC-0π events

The target for the ν_μ interactions is the FGD1 which is used also as tracker along with TPC1 or TPC2, ECal and SMRD. First ν_μ charged current events are selected following the criteria described in Chap. 4. The only difference is the definition of FGD1FV: the cut along the x and y direction are the same, while all the thickness along z has been considered. These cuts has been extended to include muons which have segment only

in FGD or in FGD and in BrECAL or SMRD. Using all the ND280 sub-detectors along with the timing information between them allows the selection of backward going and high-angle muons improving the angular acceptance.
The proton selection is performed both by looking for particle reconstructed as positive track in the TPC with a vertex in the FGD1 FV which passes the TPC track quality cut and a PID criteria, and for tracks that stop in FGD and are compatible with proton hypotheses. Anyway also events without reconstructed proton are also included, thus the cross-section is fully inclusive with respect to the presence of a proton. More details about this selection can be found in [155]. The selected events are divided in five signal regions:

I region characterized by events with only one muon candidate in one of the TPCs (TPC2 if the muon is going forward and TPC1 if is going backward) and with one muon and more than one proton in FGD or TPC,

II region event with one muon candidate in one of the TPCs and one proton candidate in TPC2

III region event with one muon candidate in one of the TPCs and a proton candidate in FGD1,

IV region event with one muon candidate in FGD1 that reach the ECAL or SMRD and with one proton in TPC2 or more than one in FGD1 or TPC2,

V region event with only one muon candidate in FGD1, that reach the ECAL or SMRD or one muon plus any number of proton.

The kinematics of the muon candidate in each selection regions for the CC-0π signal and the various backgrounds are shown in Fig. 5.2. The signal regions where the muon is reconstructed in the TPC (**regions I-II-III**) have very similar momentum distributions, although events with a reconstructed proton tend to have muons at slightly larger angles, while the regions with the muon in the FGD and the proton in the TPC (**regions IV-V**) have muons with much smaller momenta and larger angles. In order to better show the contribution from the different backgrounds, the MC is broken down by the following true topologies: ν_μ CC-0π, ν_μ CC-1π^+, ν_μ CC-Other, $\bar{\nu}_\mu$ CC-0π, $\bar{\nu}_\mu$ CC-1π^-, $\bar{\nu}_\mu$ CC-Other, NC, $\nu_e, \bar{\nu}_e$, out of FV.
The ν_μ CC-0π cross section is extracted adding the contribution from all the regions, but it is important to keep separated the events with and without a proton reconstructed in the analysis because they are affected by different systematics and backgrounds.

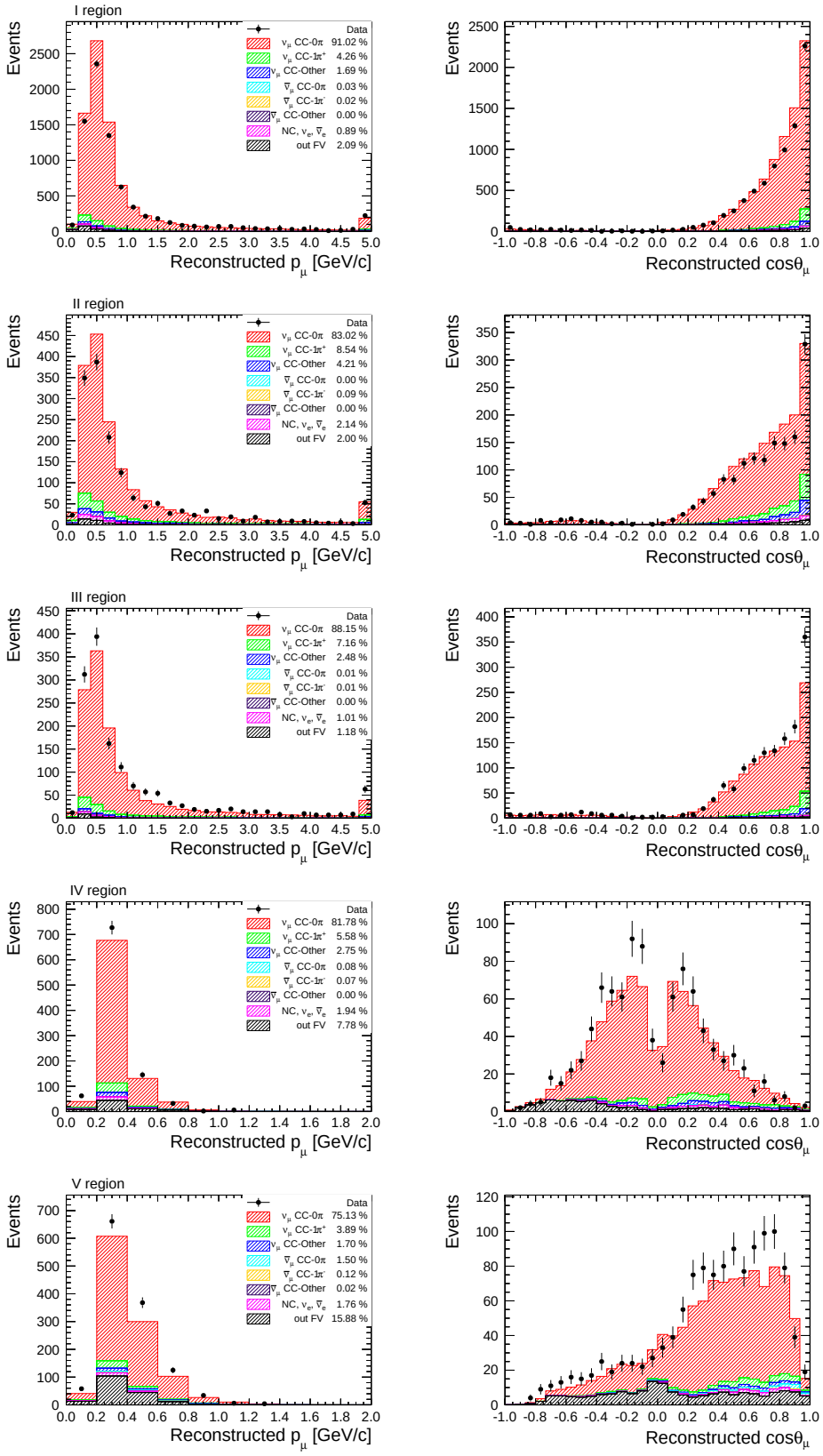

Figure 5.2. Distribution of ν_μ events in the different signal regions as function of the reconstructed muon momentum (left column) and scattering angle (right column). Different colors indicate different topologies. The legend show also the purity for each true topology.

Selection of the $\bar{\nu}_\mu$ CC-0π events

The $\bar{\nu}_\mu$ CC-0π selection has as purpose the identification of events with one positive muon and no pion in the final state, even if the experimental signature of the CCQE anti-neutrino interactions is characterized only by one positive muon since the neutron is not visible. This choice of the signal definition is supported by the goal of the model independence, since being more inclusive, also event with more that one nucleon in the final state are taken into account.

This selection is based on ν_μ charged current selection described in [192]. The main difference are the charge requirement and the TPC PID. Indeed the muon candidate is identified as the highest-momentum positively-charged track, while the PID cut is the same described in Ref. [176] and has been optimized for the $\bar{\nu}_\mu$ charged current selection. The muon candidate can be selected in one of the three following selections: forward (FWD), backward (BWD) and respectively high angle forward (HAFWD) and backward (HABWD). In the FWD/BWD selections, the muon candidate must have more than 18 clusters in TPC, while tracks with short or without TPC segment are used in the HAFWD/HABWD. The cuts are summarized in Tab. XXII.

	FWD	**BWD**	**HAFWD**	**HABWD**
Cut name	**Cut description**			
Event quality	Only good beam spills are used (see Chap.4)			
Track multiplicity	One or more FGD1 segments must exist			
Track quality	Low angle Positively-charged $N_{TPC-Cluster}$ >18 vertex in FGD1		High angle $N_{TPC-Cluster}$ $\leqslant$18 vertex in FGD1 end position in ECal or SMRD	
Track direction	$z_{start} < z_{end}$	$z_{start} > z_{end}$	$z_{start} < z_{end}$	$z_{start} > z_{end}$
Backgroud veto	$z_{veto} - z_\mu > -100\,mm$ or $p^{veto}/p^\mu < 0.8$	no cut applied	$z_{veto} - z_\mu > -150\,mm$ or $p^{veto}/p^\mu < 0.9$	no cut applied
Muon PID	$0.1 < \mathscr{L}_\mu < 0.7$ and $\mathscr{L}_{MIP}^{p<500\,MeV/c} > 0.9$ reject particles stopping in FGD2 ECal PID	$\mathscr{L}_\mu > 0.1$ and $\mathscr{L}_{MIP}^{p<500\,MeV/c} > 0.7$	ECal PID	

TABLE XXII. Summary of the selection criteria.

Compared with the selection discussed in Chap. 4, the FGD2 and ECal informations have been used. Since most of the tracks stopping in FGD2 are pions, they are rejected. ECal PID helps in the rejection of the electromagnetic and hadronic component.
Then thanks to the pion tagging developed for the ν_μ multiple pion selection described before it is possible to tag pion-less events in all the selections. The kinematics of the muon candidate for the signal regions are shown in Fig. 5.3. In the $\bar{\nu}_\mu$ sample the ν_μ contamination is not negligible in particular in the high momentum region where the ν_μ

flux is higher that the $\bar{\nu}_\mu$, as already explained in Chap. 4. Then protons and positive pions produced in ν_μ interactions can be misidentified as muon constituting an irreducible background. Moreover in HA selection the charge is not reconstructed, then also negative muons are selected. The selection of backward-going muons results in a high background due to out FV events. This happen because the veto cut is not applied to avoid rejection of muon candidate. Anyway, the $\bar{\nu}_\mu$ cross section it is very low in the backward region, for this reason the number of event is very low. This aspect will be taken under consideration in the discussion on the binning choice in Sec. 5.3.4.

In order to better show the contribution from the different backgrounds, the MC is broken down by the following true topologies: ν_μ CC-0π, ν_μ CC-1π^+, ν_μ CC-Other, $\bar{\nu}_\mu$ CC-0π, $\bar{\nu}_\mu$ CC-1π^-, $\bar{\nu}_\mu$ CC-Other, NC, $\nu_e, \bar{\nu}_e$, out of FV. As it will be shown in Sec. 5.3.5, an increment of the efficiency is achieved with this selection in high angle region, while for the selection of backward tracks is rather small. The $\bar{\nu}_\mu$ CC-0π cross section is extracted adding the contribution from all the selections.

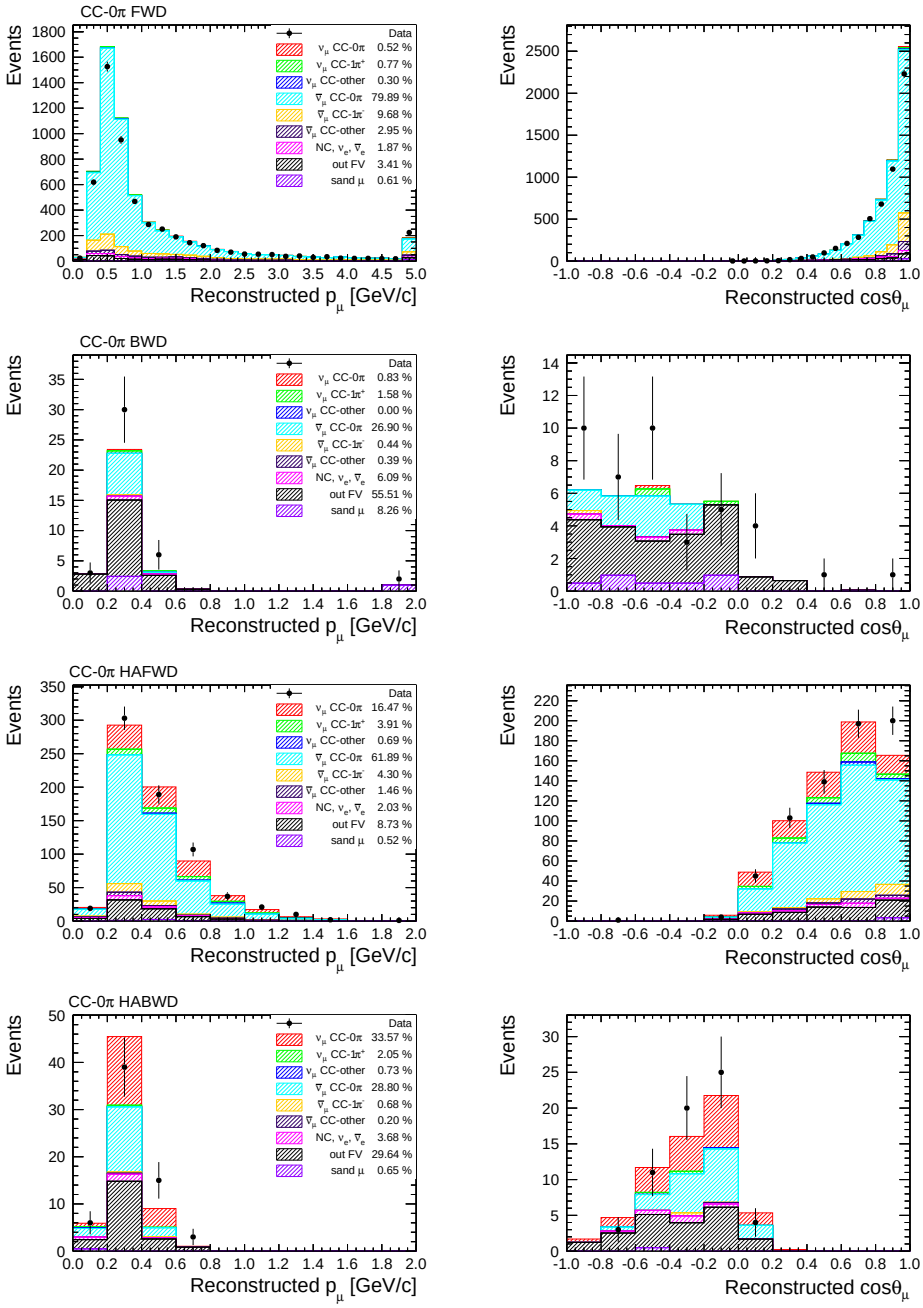

Figure 5.3. Distribution of $\bar{\nu}_\mu$ events in the different signal regions as function of the reconstructed muon momentum (left column) and scattering angle (right column). Different colors indicate different topologies. The MC is normalized for POT in data. The legend show also the purity for each true topology.

5.3.3 Sidebands

The background comes from events with one, or more true pions which are misidentified or not reconstructed, neutral current interactions (NC) and interactions that occurred outside of the fiducial volume but reconstructed inside. Additional regions are selected to constrain model parameters that affect the background prediction, pion FSI, CC-RES and CC-DIS interactions. Two regions for the ν_μ sample that fulfill the following requirements:

CC-1π^+-like events with exactly two tracks, one negative muon and one positive pion;

CC-Other-like events with more than one pion in the final state.

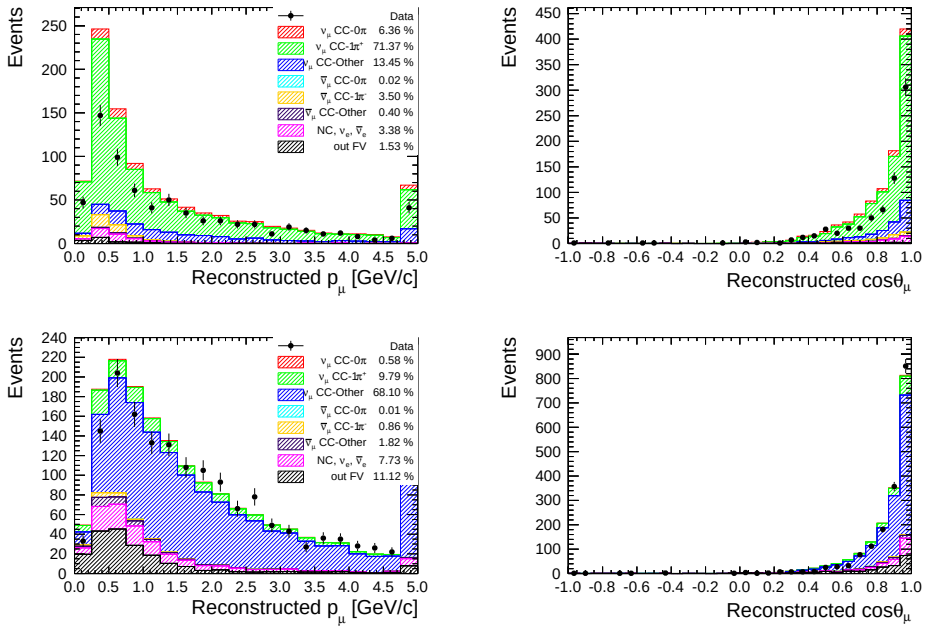

Figure 5.4. Distribution of ν_μ events in the different sideband regions as function of the reconstructed muon momentum (left column) and scattering angle (right column) for the CC-1π^+-like (top row) and CC-Other-like (bottom row) samples. Different colors indicate different topologies. The MC is normalized for POT in data. The legend show also the purity for each true topology.

The kinematic distributions of the control regions are shown in Fig. 5.4. As shown in the legend the level of the purity is rather good for both the sideband being 71% for the true CC-1π^+ and around 70% for the true CC-Other.

Other two regions are selected also for the $\bar{\nu}_\mu$ samples:

CC-1π^--like events with exactly two tracks one positive muon and one negative pion;

CC-Other-like events with more than one pion in the final state.

The kinematic distributions of the control regions are shown in Fig. 5.5. As shown in the legend the level of the purity is lower than the previous case being 48% for the true

CC-1π^- and 24% for the true CC-Other, since the positive pion generated in the ν_μ interaction are mis-identified as positive muon. This difference with the ν_μ case is related to the high ν_μ contamination in the $\bar{\nu}$ beam.

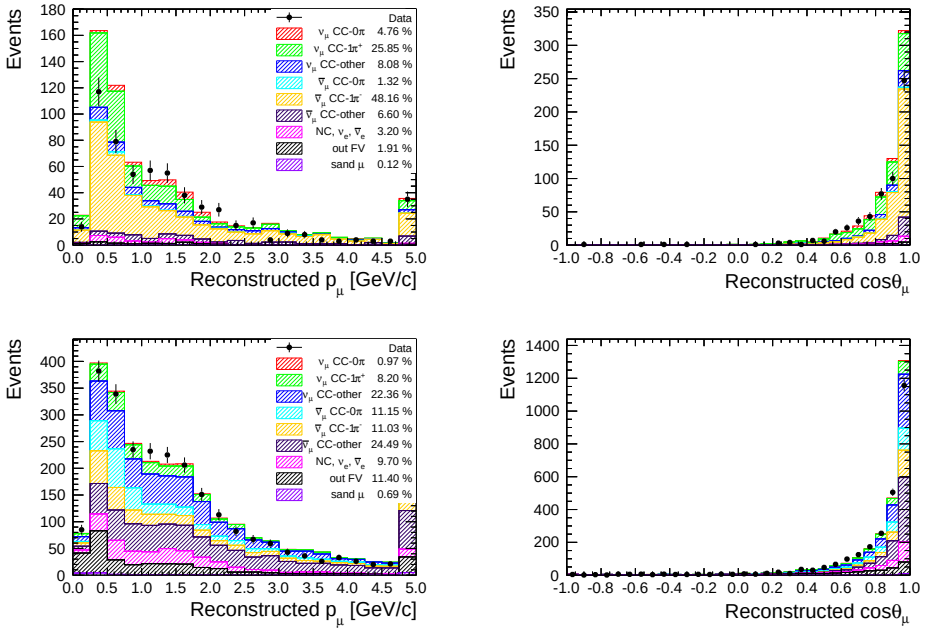

Figure 5.5. Distribution of $\bar{\nu}_\mu$ events in the different sideband regions as function of the reconstructed muon momentum (left column) and scattering angle (right column) for the CC-1π^--like (top row) and CC-Other-like (bottom row) samples. Different colors indicate different topologies. The MC is normalized for POT in data. The legend show also the purity for each true topology.

The data-MC disagreement in CC-1π^+-like and CC-1π^--like samples is consequence of a overestimation of the coherent cross section in NEUT, as pointed out by a recent work of the MINERνA Collaboration [193].

5.3.4 Analysis binning

The binning choice is a key point for a measurement as much precise as possible. If the binning is too coarse, the results does not give much information about the shape of the cross section, while on the other hand if the binning is too fine, some bins could be empty giving problem to the minimization algorithm. The best binning lies in between these extreme cases and can be found accordingly with the following general prescriptions:

- in order to avoid big fluctuations in the statistical uncertainties the number of selected events should be around 100 per bin. Therefore, starting from a fine binning, bins with small statistics should be merged;
- if a bin is surrounded by bins with larger statistics then the poissonian fluctuations of those will affect the results on the low-statistics bin giving a large statistical error, thus very narrow bins should be avoided against a more rectangular binning;
- try to have a transfer matrix diagonal as much as possible, easier with the same binning for reconstructed and true variable. Avoiding migration between reconstructed and true variables act as a regularization, since the bin-by-bin anti-correlations, artefact of the unfolding procedure, are reduced;
- the bin width must be always greater than the resolution of the variables under consideration.

In this analysis has been used the same binning for both the ν_μ and $\bar{\nu}_\mu$ cross-section since they will be combined in order to extract the sum, difference and asymmetry.
The optimization process started studying the $\cos\theta$ and later the momentum binning. The angular binning choice has been driven also by the increase of angular acceptance.

In order to follow the first point of the listed prescriptions the forward bins in cosine are narrower than the backward and high angle bins. Furthermore, there are very few backward tracks in the $\bar{\nu}_\mu$ sample since the cross-section suppresses the emission of backward muons, thus a wider bins is preferred. Anyway it is better to optimize the binning of the $\bar{\nu}_\mu$ events distribution since this sample has less statistic than the ν_μ sample.

The cosine resolution for the angular binning choice is shown in Fig. 5.6 where it is worth noting the good level of the angular resolution. The transfer matrices along with the normalized ones can be seen in Figs. 5.7 and 5.8. The matrices quantify the bin-by-bin migration which result to be very low.

After this stage the momentum bins are chosen. The momentum resolution is not as good as angular, consequently bins lower than $0.1\,GeV/c$ are not recommended. Furthermore, as can be seen in Figs. 5.9 and 5.10, it has a clear dependency on the momentum and behaves very differently in low and high angle regions since different reconstruction algorithms are used. The backward tracks are affected by vertex migration: outgoing hadrons coming in the opposite direction of the muons move over the reconstructed vertex, producing a bias in both reconstructed momentum and angle. Since the current models are not precise in the prediction of the outgoing hadron kinematic, the bias might be very different between data and simulations, thus it is better consider only one bin for the backward events. Since events with muon momentum higher than 20 GeV/c are negligible but the resolution above 10 GeV/c is poor, the momentum limit has been set

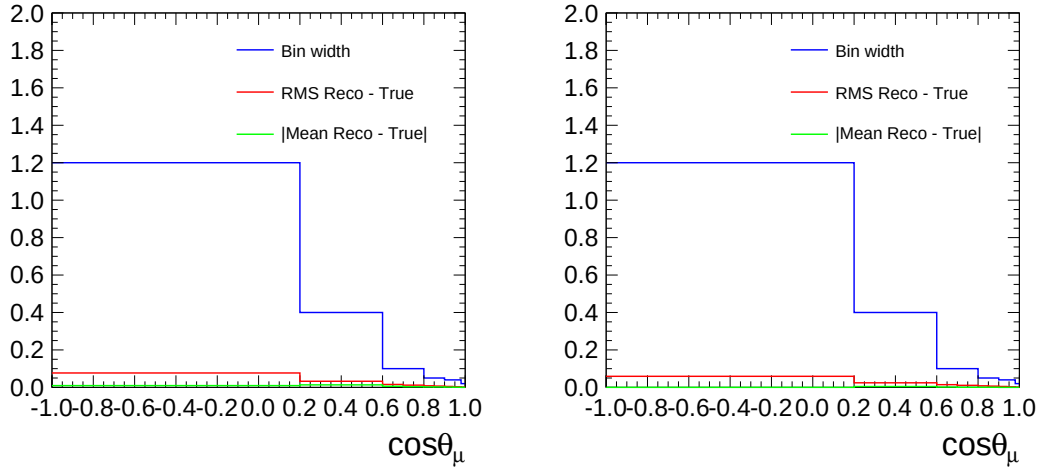

Figure 5.6. Cosine theta resolution for each bin for ν_μ (left) $\bar{\nu}_\mu$ (right) CC-0π events.

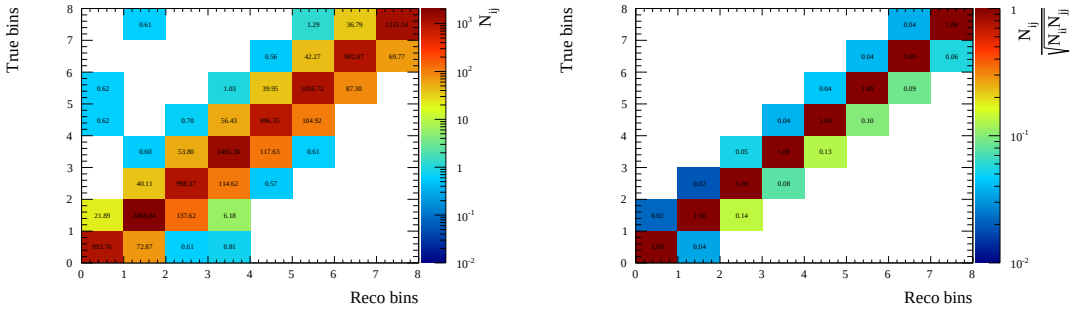

Figure 5.7. Transfer matrix (left) and normalized transfer matrix (right) for angular bins obtained from nominal MC summing the contribution from all the samples for ν_μ CC-0π events. Each row/column corresponds to an angular bin going from $0 = [-1, 0.2]$ to $7 = [0.98, 1]$.

to 30 GeV/c. The final binning chosen for this analysis is reported in Tab. XXIII.

The transfer matrices that use the optimized binning are shown in Figs. 5.11 and 5.12 where the transfer matrices along with the normalized ones quantify the level of the statistic (in particular the first) which should be around 100 events per bin and the bin-by-bin migration which result to be of the order of 11% for both ν_μ and $\bar{\nu}_\mu$. It is worth notice that for the bins close to the angular edge there are not migration because that bins correspond to last and first momentum bins. Even if a high statistics per bin is suggested, if a bin is surrounded by bins with larger statistics, then the poissonian fluctuations of those will affect the results on the low-statistics bin giving a large statistical error. This is the case especially of bins with small width. To check this kind of effects, the distributions of the true and reconstructed number of signal and background events as a function of the muon kinematics have been studied. Results are shown in Figs. 5.13 and 5.14 (without dividing by the bin width) for ν_μ and $\bar{\nu}_\mu$ respectively. The chosen binning has a good

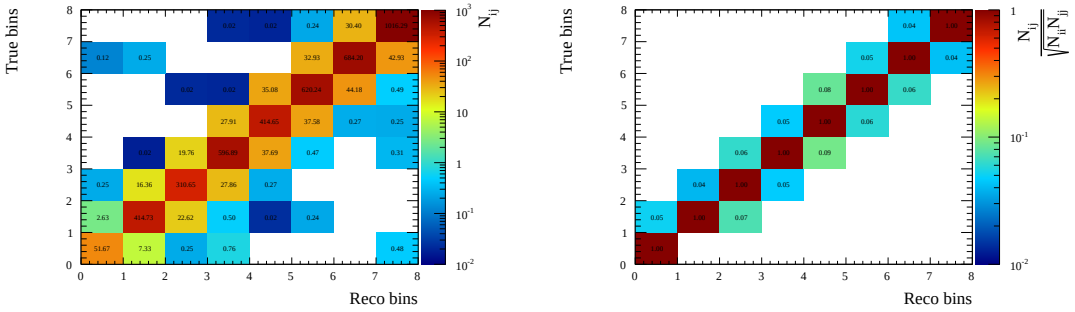

Figure 5.8. Transfer matrix (left) and normalized transfer matrix (right) for angular bins obtained from nominal MC summing the contribution from all the samples for $\bar{\nu}_\mu$ CC-0π events. Each row/column corresponds to an angular bin going from $0 = [-1, 0.2]$ to $7 = [0.98, 1]$.

$\cos\theta_\mu$	p_μ [GeV/c]
-1, 0.2	0, 30
0.2, 0.6	0, 0.3, 0.4, 0.5, 0.6, 30
0.6, 0.7	0, 0.3, 0.4, 0.5, 0.6, 0.8, 30
0.7, 0.8	0, 0.3, 0.4, 0.5, 0.6, 0.8, 30
0.8, 0.85	0, 0.3, 0.4, 0.5, 0.6, 0.8, 1.0, 30
0.85, 0.9	0, 0.3, 0.4, 0.5, 0.6, 0.8, 1.0, 1.5, 30
0.9, 0.94	0, 0.4, 0.5, 0.6, 0.8, 1.25, 2.0, 30
0.94, 0.98	0, 0.4, 0.5, 0.6, 0.8, 1.0, 1.25, 1.5, 2.0, 3.0, 30
0.98, 1.0	0, 0.5, 0.7, 0.9, 1.25, 2.0, 3.0, 5.0, 30

TABLE XXIII. Binning used for the fit to the $p_\mu, \cos\theta_\mu$ distribution and for the definition of the data/MC corrections c_i.

level of events per bin and do not show very peaked bins accordingly with the previous statement. The large disagreement in the high momentum bins, between the reconstructed and true background, is due to the migration between the sidebands: CC-Other events that are reconstructed as CC-1π^-.

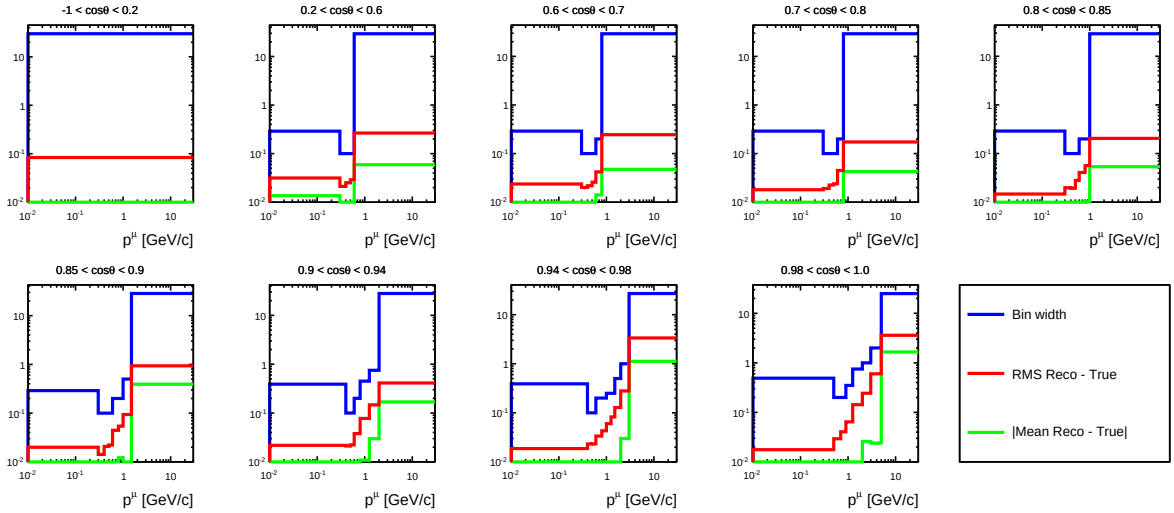

Figure 5.9. Momentum resolution for each true angular and momentum bin for ν_μ CC-0π events.

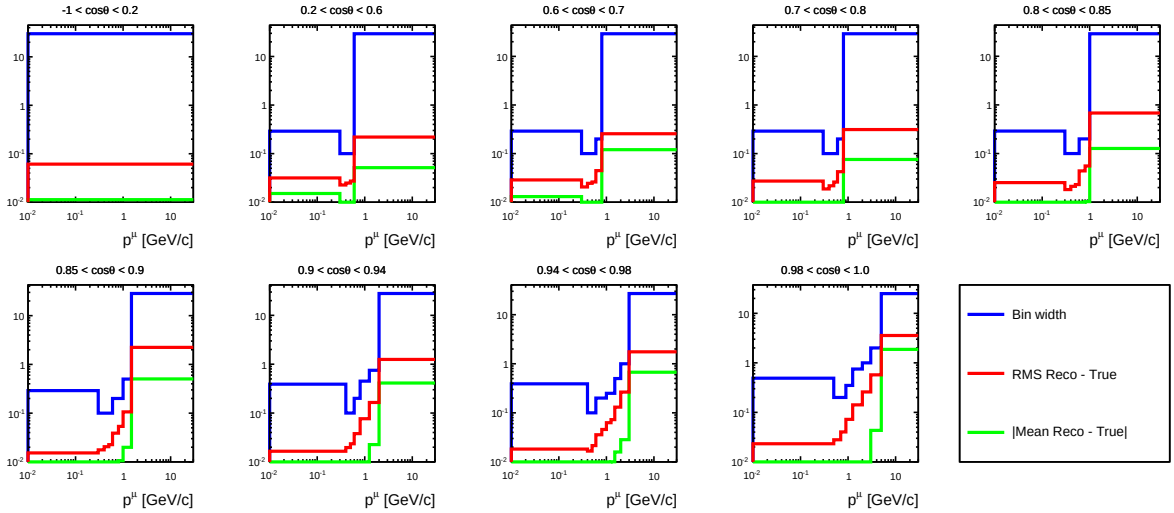

Figure 5.10. Momentum resolution for each true angular and momentum bin for $\bar{\nu}_\mu$ CC-0π events.

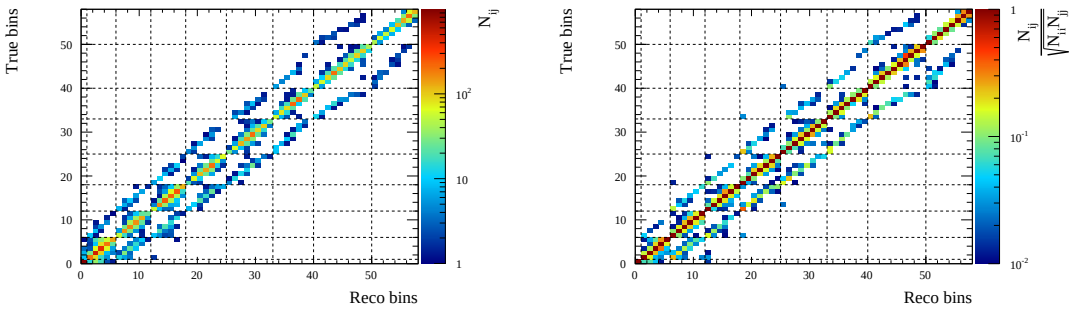

Figure 5.11. Transfer matrix (left) and normalized transfer matrix (right) for angular bins obtained from nominal MC summing the contribution from all the samples for ν_μ CC-0π events. Dashed lines indicate the angular boundaries. Each row/column corresponds to a bin going from $0 = [-1 \leqslant \cos\,\theta_\mu^{\text{true}} \leqslant 0.2,\ 0\,GeV/c \leqslant p_\mu^{\text{true}} \leqslant 30\,GeV/c]$ to $57 = [0.98 \leqslant \cos\,\theta_\mu^{\text{true}} \leqslant 1,\ 0\,GeV/c \leqslant p_\mu^{\text{true}} \leqslant 30\,GeV/c]$.

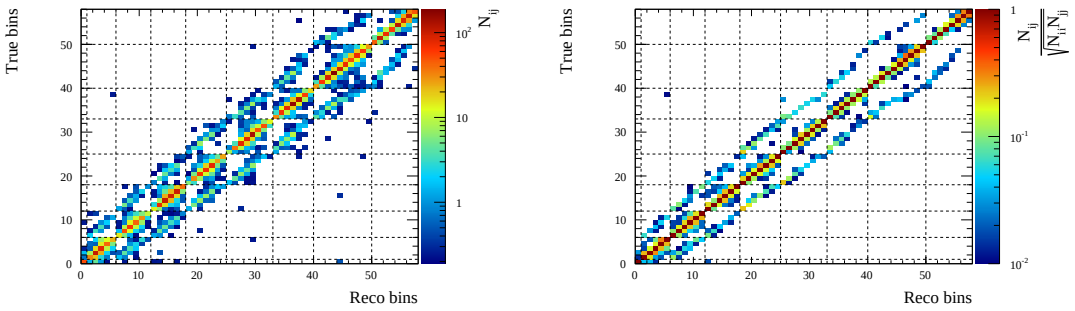

Figure 5.12. Transfer matrix (left) and normalized transfer matrix (right) for angular bins obtained from nominal MC summing the contribution from all the samples for $\bar{\nu}_\mu$ CC-0π events. Dashed lines indicate the angular boundaries. Each row/column corresponds to a bin going from $0 = [-1 \leqslant \cos\,\theta_\mu^{\text{true}} \leqslant 0.2,\ 0\,GeV/c \leqslant p_\mu^{\text{true}} \leqslant 30\,GeV/c]$ to $57 = [0.98 \leqslant \cos\,\theta_\mu^{\text{true}} \leqslant 1,\ 0\,GeV/c \leqslant p_\mu^{\text{true}} \leqslant 30\,GeV/c]$.

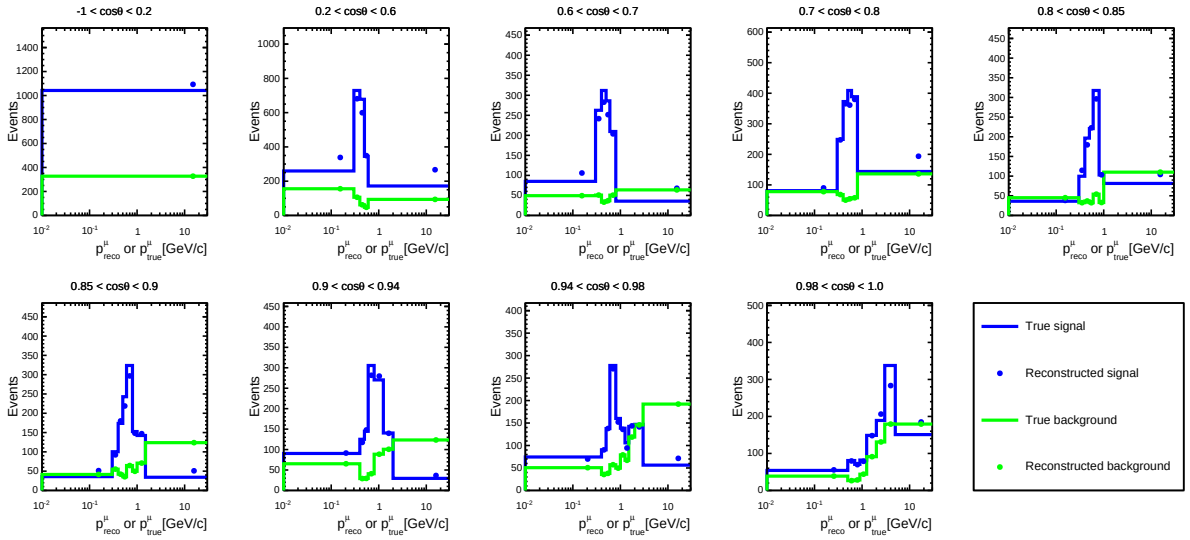

Figure 5.13. True (solid line) and reconstructed (dots) signal and background of the ν_μ sample as function of the muon kinematics using the optimized binning. The bin entries are not divided by the bin width.

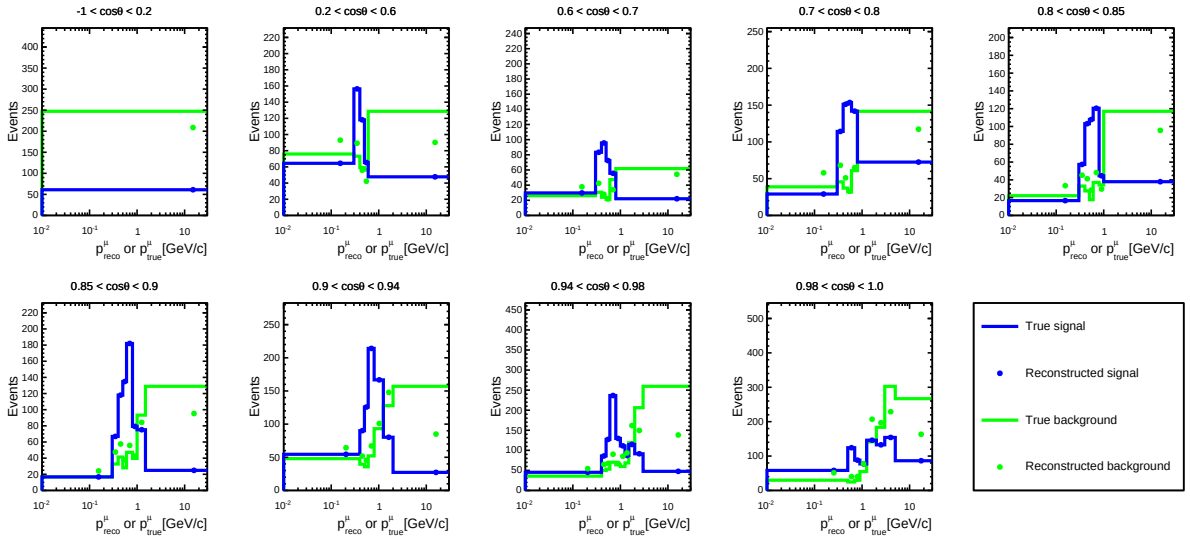

Figure 5.14. True (solid line) and reconstructed (dots) signal and background of the $\bar{\nu}_\mu$ sample as function of the muon kinematics using the optimized binning. The bin entries are not divided by the bin width.

5.3.5 Efficiency

The signal efficiency is defined as the ratio between the selected and generated CC-0π events:

$$\epsilon = \frac{N_{sel}}{N_{gen}} \tag{5.13}$$

By definition the signal efficiency is directly estimated from the MC adding model dependency to the final measurements that must be quantified with an uncertainty on the signal modelling (see Sec. 5.4.5). The efficiency versus the true momentum and cosine of the angle is shown in Figs. 5.15 and 5.16 for ν_μ and $\bar{\nu}_\mu$ CC-0π events respectively. Over all it is worth notice the increased phase space in both selections and that the efficiency is smaller for low momentum muons and/or backward going muons (in particular **region I-II-IV** for the neutrino sample and HAFWD, HABWD and BWD for antineutrino). The efficiency of the backward going muons is around 10-20% because that tracks have a very low momentum and it is very likely that they stops in the edges of the PØD or the BrECal without producing enough hits to be reconstructed. In particular in ν_μ selection the presence of the proton helps in enlarging the phase space to backward and high angle muons as well as the topology with muon in FGD1 or ECal is particularly helpful in gaining efficiency. Finally in Fig. 5.17 is shown the efficiency according to the double differential binning chosen for the cross-sections extraction. For low momentum muon the efficiency drops drastically because they do not leave the FGD, thus they are not reconstructed. The differences between ν_μ and $\bar{\nu}_\mu$ selection can explain the different efficiencies. Indeed in the ν_μ CC-0π events along with the muon also the proton is selected.

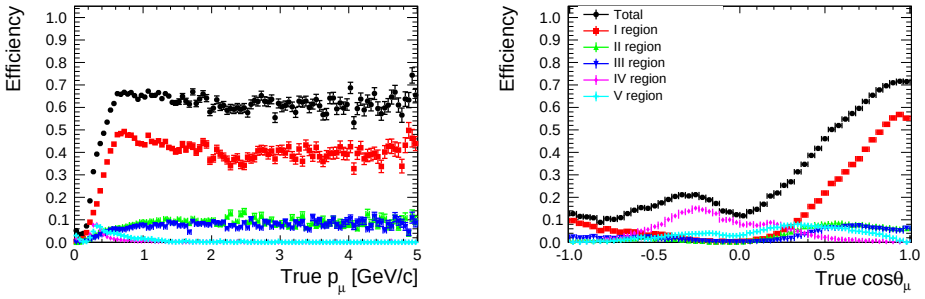

Figure 5.15. Efficiency versus the true muon momentum (left) and true muon cosine theta (right) for ν_μ CC-0π events. The different colours show the efficiency for each signal region.

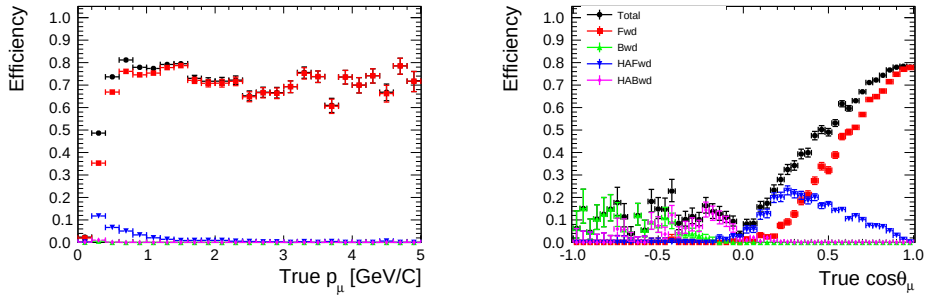

Figure 5.16. Efficiency versus the true muon momentum (left) and true muon cosine theta (right) for $\bar{\nu}_\mu$ CC-0π events. The different colours show the efficiency for each signal region.

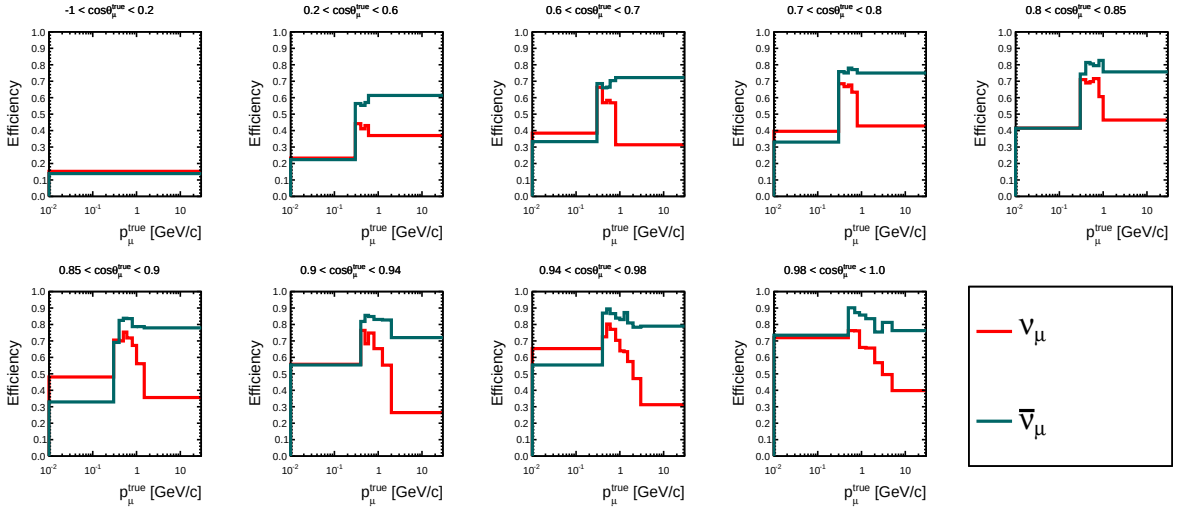

Figure 5.17. Efficiency as function of the double differential binning reported in Tab. XXIII.

5.3.6 Integrated flux

The flux prediction distinguishes between different neutrino flavours, but for the cross section evaluation only the ν_μ and $\bar{\nu}_\mu$ flux must be computed. The flux prediction available is provided for 10^{21} POT, therefore the integrated flux must be normalised to the current POT in data using the following equation:

$$\Phi^{\nu_\mu \text{ or } \bar{\nu}_\mu} = \sum_{run} POT^{run}_{DATA} \left(\frac{1}{10^{21} POT} \sum_{n}^{E_{\nu_\mu \text{ or } \bar{\nu}_\mu}} \Phi_n^{\nu_\mu \text{ or } \bar{\nu}_\mu} \right)_{run} \tag{5.14}$$

Then the integrated ν_μ flux is:

$$\Phi^{\nu_\mu} = 1.12 \times 10^{13}\, cm^{-2} \tag{5.15}$$

while the integrated $\bar{\nu}_\mu$ flux is:

$$\Phi^{\bar{\nu}_\mu} = 9.71 \times 10^{12}\, cm^{-2} \tag{5.16}$$

5.3.7 Number of Targets

The measured cross-section must be divided by the total number of nucleons inside the FGD1 fiducial volume (see Fig. 5.18) given by the following formula:

$$N^{FV}_{nucleons} = N_A \Delta X_{FV} \Delta Y_{FV} \sum_{i}^{elements} \rho_i \Delta Z_i \frac{A_i}{M_i} \tag{5.17}$$

where N_A is the Avogadro's number, ΔX_{FV} and ΔY_{FV} are the total length of the fiducial volume in X and Y axis. The index i runs over all the elements composing the FGD1 fiducial volume, A_i and M_i are the averaged number of nucleons and atomic mass per element and the product $\rho_i \Delta Z_i$ is the areal density per element in the fiducial volume, computed from the value in Tab. XXIV. The information for each element are reported in Tab. XXV and are taken from [172]. Accordingly with the quantities in Tabs. XXIV and XXV the number of nucleons inside the FGD1 fiducial volume is:

$$N^{FV}_{nucleons} = 5.9 \times 10^{29} \tag{5.18}$$

Components	$\Delta Z(mm)$	$\rho(g/cm^3)$
G10 ($\times 2$)	0.232×2	1.700
glue layer 1 ($\times 2$)	0.188×2	0.920
glue layer 2	0.19	0.920
XY module	9.61×2	1.041
air	2.0	0.00129
fibers	0.0019	1.050

TABLE XXIV. Thickness and density of each component in each layer of the FGD1.

Element	A	N_i	Natural abundance (%)	M_i	A_i	FGD1 fraction
C	12	6	98.9	6.011	12.01078	86.10%
	13	7	1.1			
O	16	8	99.762	8.00438	15.99943	3.70%
	17	9	0.038			
	18	10	0.2			
H	1	0	99.985	0.00015	1.007947	7.35%
	2	1	0.015			
Ti	46	24	8	25.98	47.8671	1.65%
	47	25	7.5			
	48	26	73.8			
	49	27	5.5			
	50	28	5.4			
Si	28	14	92.22	14.1072	28.0855	1.01%
	29	15	4.68			
	30	16	3.09			
N	14	7	99.634	7.00366	14.00672	0.14%
	15	8	0.366			

TABLE XXV. Information used to compute the total number of nucleons for each element of the FGD1 FV.

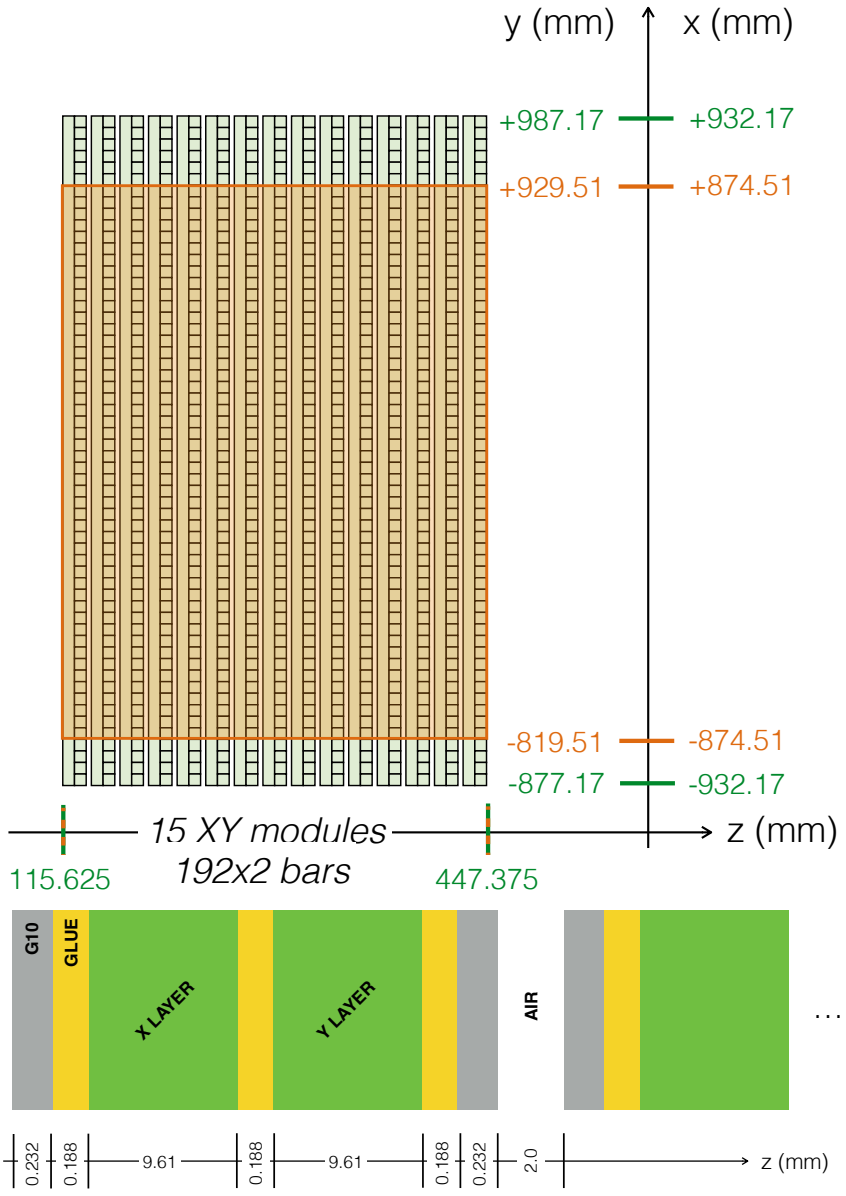

Figure 5.18. FGD1 fiducial volume definition in orange used for this analysis on the top, and scintillator layers scheme on the bottom. Picture taken from [192].

5.4 Uncertainties evaluation

The propagation of statistical and systematics uncertainties, when not possible analytically, is performed throughout MC toy experiments. The general procedure is the following:

- for the statistical uncertainty evaluation the number of reconstructed events are varied in each bin accordingly with a Poissonian distribution obtaining a 'fake' MC that will be fitted. Then the statistical error on the cross-section in each true bin i is evaluated as the standard deviation of the following distribution, obtained from the fit of a large number of toys:

$$\frac{N_i^{\text{CC-0}\pi\ Fit} - N_i^{\text{CC-0}\pi\ Nominal}}{N_i^{\text{CC-0}\pi\ Nominal}} \tag{5.19}$$

  where $N_i^{\text{CC-0}\pi\ Fit}$ is the number of CC-0π events obtained from the fit and $N_i^{\text{CC-0}\pi\ Nominal}$ is the nominal CC-0π number of events. On the sum, difference and asymmetry the statistical error in each true bin i is evaluated by combining the errors on the cross sections using the error propagation. This choice has been driven by the impossibility to define the relative error for the difference, since this quantity is expected to be around zero in the forward region, where the ν_μ and $\bar{\nu}_\mu$ cross section are similar (as explained in Chap. 2).
  The post-fit covariance matrix for the statistical uncertainties has been computed with the formula:

$$V_{ij} = \sum_{itoy}^{Ntoys} \left(\frac{d\sigma_i}{dx_i}^{Fit\ itoy} - \frac{d\sigma_i}{dx_i}^{Nominal} \right) \left(\frac{d\sigma_j}{dx_i}^{Fit\ itoy} - \frac{d\sigma_j}{dx_i}^{Nominal} \right) \tag{5.20}$$

- for the systematics uncertainty propagation the used method per each toy experiment is the following:

  1. the covariance matrix is decomposed using the Cholesky decomposition in order to generate correlated random weights Gaussianly distributed [194];
  2. using this weights a fake data sample is produced and it will be fitted using the nominal MC as prior.

  Then, as for the statistical error, the systematic uncertainty on the cross-section in each true bin i is evaluated as the standard deviation of the distribution obtained from the fit of a large number of toys, defined in the following way:

$$\frac{\frac{N_i^{\text{CC-0}\pi\ Fit}}{\Phi^{Fit}\epsilon_i^{Nominal}} - \frac{N_i^{\text{CC-0}\pi\ Thrown}}{\Phi^{Thrown}\epsilon_i^{Thrown}}}{\frac{N_i^{\text{CC-0}\pi\ Thrown}}{\Phi^{Thrown}\epsilon_i^{Thrown}}} \tag{5.21}$$

  where $N_i^{\text{CC-0}\pi\ Fit}$ is the number of CC-0π events obtained from the fit, Φ^{Fit} is the fitted flux, $\epsilon_i^{Nominal}$ is the nominal efficiency, $N_i^{\text{CC-0}\pi\ Thrown}$, Φ^{Thrown} and ϵ_i^{Thrown} are respectively the number of CC-0π events, the flux and the efficiency obtained after

each variation of the systematic parameters.
On the sum, difference and asymmetry the systematic error in each true bin i is evaluated combining the errors on the cross sections using the error propagation. The post-fit covariance matrix for the systematic uncertainties has been computed with the following formula:

$$V_{ij} = \sum_{itoy}^{Ntoys} \left(\frac{d\sigma_i}{dx_i}^{Fit\ itoy} - \frac{d\sigma_i}{dx_i}^{Thrown\ itoy} \right) \left(\frac{d\sigma_j}{dx_i}^{Fit\ itoy} - \frac{d\sigma_j}{dx_i}^{Thrown\ itoy} \right) \tag{5.22}$$

Notice that $N_i^{\text{CC-0}\pi\ Fit}$, $N_i^{\text{CC-0}\pi\ Thrown}$ are given by the number of events in the nominal MC times the parameters of interest c_i multiplied by the weight of the corresponding systematic. For the final estimation of the systematics in Sec.5.4.7 all the systematics are varied together in the toys and all the parameters are fit at once.

5.4.1 Data statistical uncertainty

To compute the data statistical uncertainty, nominal MC is normalized to the number of POT in data reported in Sec. 5.3.1. The MC is varied 100 times with poissonian distribution in each reconstructed bin, independently in each signal and control regions and the final impact on the ν_μ and $\bar{\nu}_\mu$ CC-0π cross-sections and on the sum, difference and asymmetry is evaluated as described previously.
The relative statistical uncertainty on the cross-sections are shown in Figs. 5.19. The statistical variation includes both the signal and background events, therefore it is typically larger than the simple poissonian uncertainty on the signal, especially in those bins where the background is large. Moreover the statistical variation is done in reconstructed muon kinematic bins, so the effects in each bin of generated muon kinematics may include contributions from many different reconstructed bins.

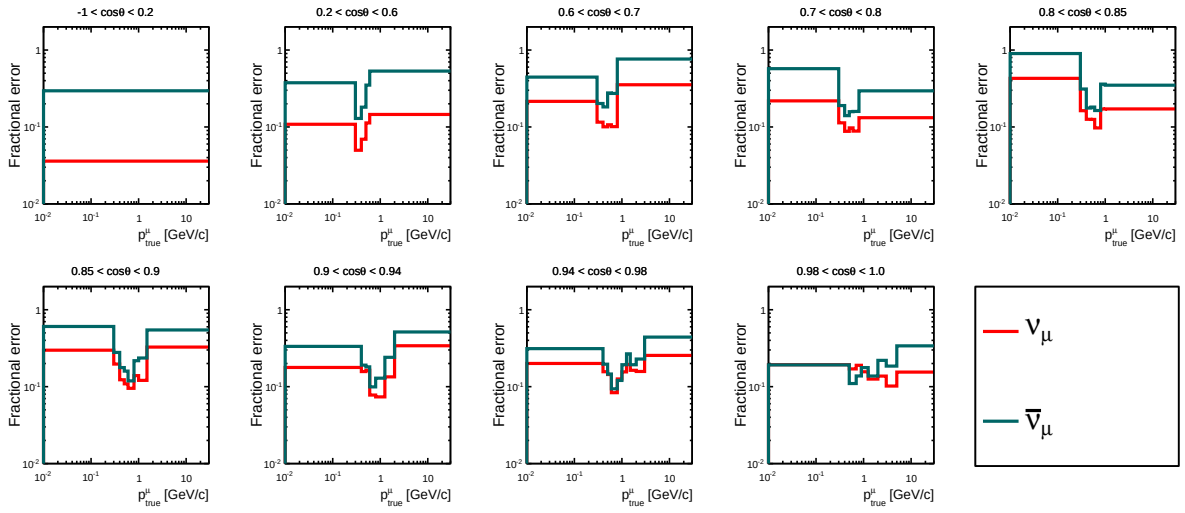

Figure 5.19. Relative uncertainty due to data statistics for ν_μ (red) and $\bar{\nu}_\mu$ (dark cyan) CC-0π cross section in bins of true muon kinematics.

5.4.2 Flux systematic uncertainty

The uncertainties associated to the flux are parametrized as a function of the neutrino flavor and energy. The several sources affecting the total error are detailed in [162]. The flux systematic uncertainty, which affects the number of selected events and the integrated flux, is propagated performing 100 fit where the MC is varied accordingly with the method described above. The flux covariance matrix considered in the penalty term for the flux systematic is reported in Fig. 5.20. Correlation between ν_μ and $\bar{\nu}_\mu$ flux has been taken into account. Furthermore also the flux uncertainty on the "wrong sign" component in each beam mode along with their correlation are taken into account, since, mainly in $\bar{\nu}$ mode, this component is not negligible. This choice lead to the presence of 32 nuisance parameters in the fit: 22 in total for ν_μ and $\bar{\nu}_\mu$ flux and 5 for each "wrong sing" component. The bin edge are reported in Tab. XXVI

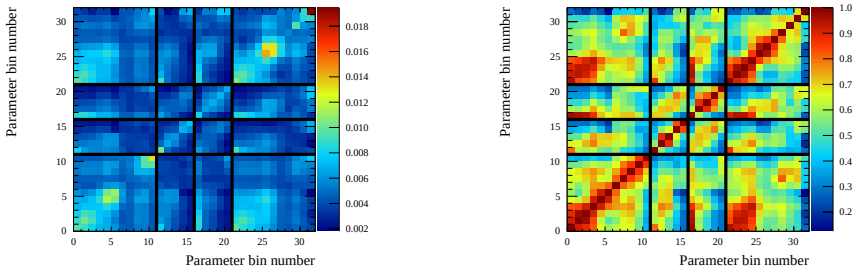

Figure 5.20. Flux covariance (left) and correlation (right) matrices. The bin number correspond to the parameter number in Tab. XXVI.

The number of ν_μ CC-0π selected events as a function of the "true" kinematics extracted from the fit and thrown accordingly with the flux covariance matrix is:

$$\begin{aligned} N_i^{\nu_\mu \text{ CC-0}\pi \, Fit} &= \sum_t^{\text{regions}} \sum_j^{\text{reco bins}} c_i^{\nu_\mu \, Fit} N_{jt}^{\text{MC } \nu_\mu \text{ CC-0}\pi} t_{tij}^{\text{det}} \sum_n^{\text{E}_\nu} w_n^i f_n^{Fit} \\ N_i^{\nu_\mu \text{ CC-0}\pi \, Thrown} &= \sum_t^{\text{regions}} \sum_j^{\text{reco bins}} N_{jt}^{\text{MC } \nu_\mu \text{ CC-0}\pi} t_{tij}^{\text{det}} \sum_n^{\text{E}_\nu} w_n^i f_n^{Thrown} \end{aligned} \tag{5.23}$$

while the number of $\bar{\nu}_\mu$ CC-0π selected events is:

$$\begin{aligned} N_i^{\bar{\nu}_\mu \text{ CC-0}\pi \, Fit} &= \sum_t^{\text{regions}} \sum_j^{\text{reco bins}} c_i^{\bar{\nu}_\mu \, Fit} N_{jt}^{\text{MC } \bar{\nu}_\mu \text{ CC-0}\pi} t_{tij}^{\text{det}} \sum_n^{\text{E}_\nu} w_n^i f_n^{Fit} \\ N_i^{\bar{\nu}_\mu \text{ CC-0}\pi \, Thrown} &= \sum_t^{\text{regions}} \sum_j^{\text{reco bins}} N_{jt}^{\text{MC } \bar{\nu}_\mu \text{ CC-0}\pi} t_{tij}^{\text{det}} \sum_n^{\text{E}_{\bar{\nu}}} w_n^i f_n^{Thrown} \end{aligned} \tag{5.24}$$

The fitted or thrown integrated fluxes are computed with this formula:

$$\Phi_{Fit \text{ or } Thrown}^{\nu_\mu \text{ or } \bar{\nu}_\mu} = \sum_n^{\text{E}_{\nu_\mu \text{ or } \bar{\nu}_\mu}} \Phi_n^{\nu_\mu \text{ or } \bar{\nu}_\mu} f_n^{Fit \text{ or } Thrown} \tag{5.25}$$

Flux Parameter	Neutrino type	Energy bin [GeV]
f_0	ν_μ	0 - 0.4
f_1	ν_μ	0.4 - 0.5
f_2	ν_μ	0.5 - 0.6
f_3	ν_μ	0.6 - 0.7
f_4	ν_μ	0.7 - 1.0
f_5	ν_μ	1.0 - 1.5
f_6	ν_μ	1.5 - 2.5
f_7	ν_μ	2.5 - 3.5
f_8	ν_μ	3.5 - 5.0
f_9	ν_μ	5.0 - 7.0
f_{10}	ν_μ	7.0 - 30
f_{11}	$\bar{\nu}_\mu$	0 - 0.7
f_{12}	$\bar{\nu}_\mu$	0.7 - 1.0
f_{13}	$\bar{\nu}_\mu$	1.0 - 1.5
f_{14}	$\bar{\nu}_\mu$	1.5 - 2.5
f_{15}	$\bar{\nu}_\mu$	2.5 - 30
f_{16}	ν_μ	0 - 0.7
f_{17}	ν_μ	0.7 - 1.0
f_{18}	ν_μ	1.0 - 1.5
f_{19}	ν_μ	1.5 - 2.5
f_{20}	ν_μ	2.5 - 30
f_{21}	$\bar{\nu}_\mu$	0 - 0.4
f_{22}	$\bar{\nu}_\mu$	0.4 - 0.5
f_{23}	$\bar{\nu}_\mu$	0.5 - 0.6
f_{24}	$\bar{\nu}_\mu$	0.6 - 0.7
f_{25}	$\bar{\nu}_\mu$	0.7 - 1.0
f_{26}	$\bar{\nu}_\mu$	1.0 - 1.5
f_{27}	$\bar{\nu}_\mu$	1.5 - 2.5
f_{28}	$\bar{\nu}_\mu$	2.5 - 3.5
f_{29}	$\bar{\nu}_\mu$	3.5 - 5.0
f_{30}	$\bar{\nu}_\mu$	5.0 - 7.0
f_{31}	$\bar{\nu}_\mu$	7.0 - 30

TABLE XXVI. Binning used for the flux.

where the flux parameters f_n are expressed in bins of E_ν and a weighted sum over the neutrino or antineutrino energy distribution inside each bin i of muon kinematic is performed. The weights w_n^i which describe the (anti)neutrino energy distribution for each bin of true kinematic are taken from MC, therefore a model dependence is introduced and the impact on the final measurement will be evaluated through 'fake' data studies

(see App. C). Anyway the flux parameter are included as nuisance and will be fitted since the fit is very powerful in constraining the flux thanks to the correlation between the two samples, enhancing our sensitivity to the final measurements. In order to justify our choice in Fig. 5.21 are compared the results when the flux parameters are fitted or not. As can be noticed the fit is very powerful in constraining the flux since the uncertainty is reduced by ∼60%.

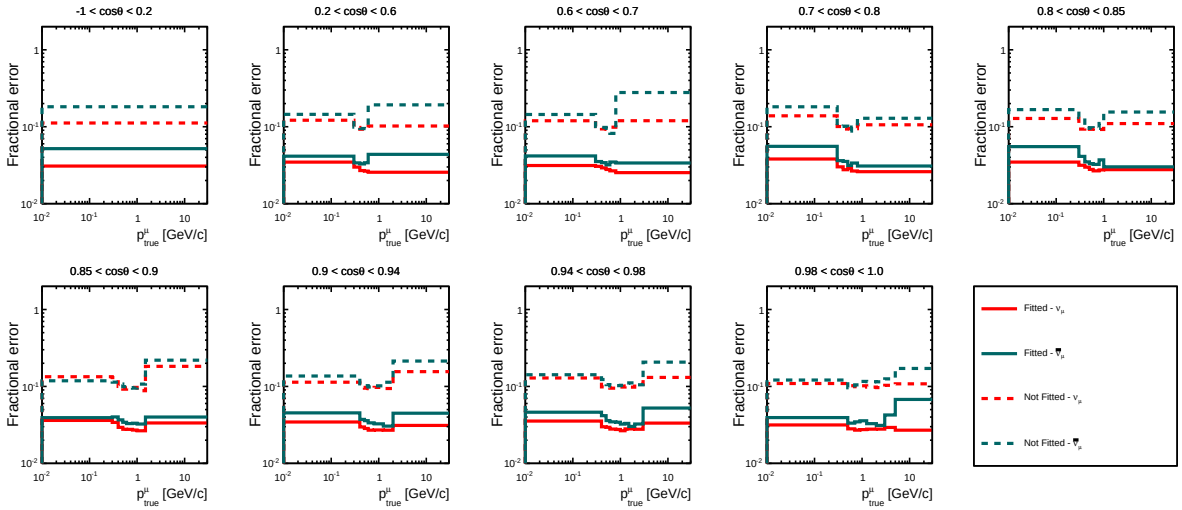

Figure 5.21. Relative uncertainty due to flux systematic for ν_μ (red) and $\bar{\nu}_\mu$ (dark cyan) CC-0π cross section in bins of true muon kinematics. Solid line show the fractional uncertainty when the detector parameter are fitted, while the dashed line when they are not fitted.

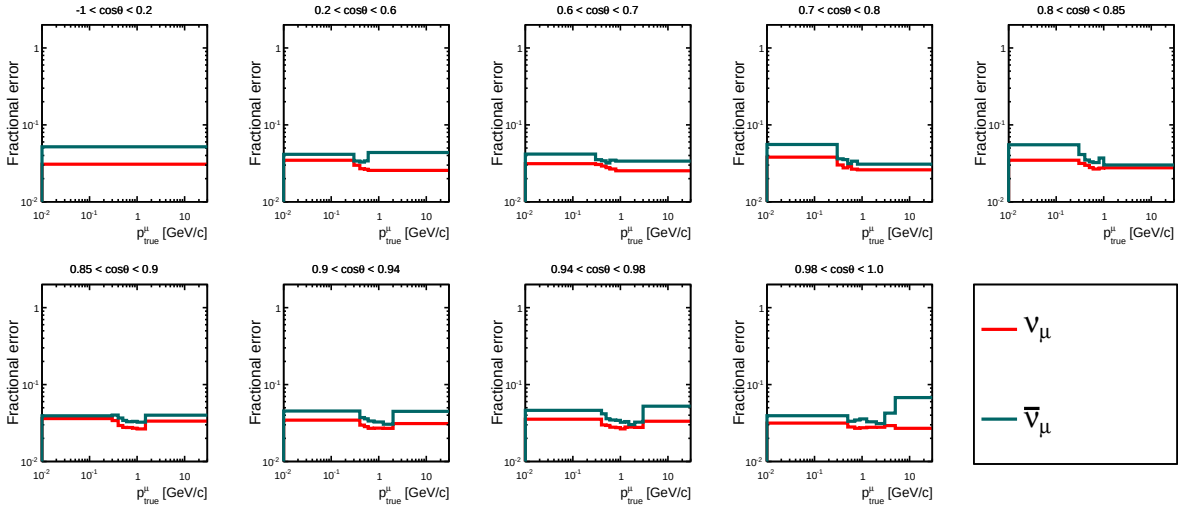

Figure 5.22. Relative uncertainty due to flux systematic for ν_μ (red) and $\bar{\nu}_\mu$ (dark cyan) CC-0π cross section in bins of true muon kinematics.

The flux systematic relative uncertainty on the cross-sections is shown in Fig. 5.22. The error on the cross section is of the order of few %. It is the same between neutrino

and antineutrino in the region around 1 GeV, while in the low and high momentum bins the uncertainty on the antineutrino cross section is higher since the pre-fit uncertainty is higher (see the flux pre-fit covariance matrix on Fig. 5.20).

5.4.3 Detector systematic uncertainty

A complete and detailed study of the detector systematics for the ν_μ and $\bar{\nu}_\mu$ selection used in this analysis is reported in Refs. [175, 178, 192, 195, 196]. The detector systematics are stored, as uncertainty on the total number of reconstructed events in each bin, in a covariance matrix corresponding to the binning of reconstructed muon momentum and angle for each regions, including the correlation between them (Fig. 5.23). In principle, for each bin of muon kinematic, a nuisance parameter to describe the detector systematics is included in the fit and constrained through the penalty term described in Eq. 5.6. In this case the total number of detector parameters would be 400, reducing the stability and compromising the convergence of the fit. To avoid this situation the covariance matrix has been reduced (Fig. 5.24) merging the ν_μ signal region in one and using larger bins, as indicated in Tab.XXVII, at the expense of larger systematics. The nuisance parameters for detector systematics are therefore constrained in the χ^2 penalty term by the reduced covariance matrix.

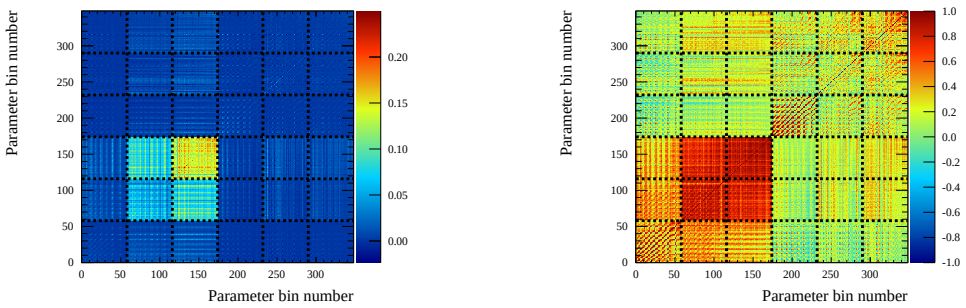

Figure 5.23. Normalized detector covariance (left) and correlation (right) matrix according to the binning used for the cross section extraction reported in Tab. XXIII. Each bin represents the relative uncertainty in the number of selected events in bins of reconstructed muon kinematics. The dotted lines divided the contribution from each samples, which is, going from left to the right: ν_μ signal region, the first and second ν_μ sideband, the $\bar{\nu}_\mu$ signal region and the two $\bar{\nu}_\mu$ sideband. The bins within each sample are ordered in increasing momentum intervals, each containing all angular bins from $0 = [-1 \leqslant \cos\theta_\mu^{\text{true}} \leqslant 0.2,\ 0\ GeV/c \leqslant p_\mu^{\text{true}} \leqslant 30\ GeV/c]$ to $57 = [0.98 \leqslant \cos\theta_\mu^{\text{true}} \leqslant 1,\ 0\ GeV/c \leqslant p_\mu^{\text{true}} \leqslant 30\ GeV/c]$.

The systematics on the final measurements are computed by repeating the fit over 100 toys. In each toy the nuisance parameters representing the detector systematics are varied using the covariance matrix obtained using the full binning, but the nuisances corresponding to the reduced one are fitted. The number of ν_μ CC-0π selected events as a function of the "true" kinematics extracted from the fit and thrown accordingly with

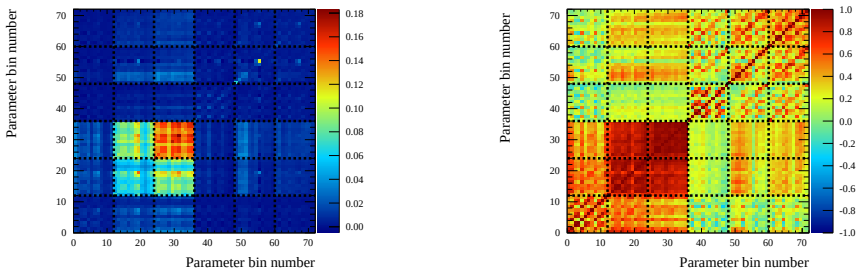

Figure 5.24. Normalized detector covariance (left) and correlation (right) matrix according to the averaged binning reported in Tab. XXVII. Each bin represents the relative uncertainty in the number of selected events in bins of reconstructed muon kinematics. The dotted lines divided the contribution from each samples, which is, going from left to the right: ν_μ signal region, the first and second ν_μ sideband, the $\bar{\nu}_\mu$ signal region and the two $\bar{\nu}_\mu$ sidebands. The bins within each sample are ordered in increasing momentum intervals, each containing all angular bins from $0 = [-1 \leqslant \cos\theta_\mu^{\text{true}} \leqslant 0.2,\ 0\,GeV/c \leqslant p_\mu^{\text{true}} \leqslant 30\,GeV/c]$ to $57 = [0.98 \leqslant \cos\theta_\mu^{\text{true}} \leqslant 1,\ 0\,GeV/c \leqslant p_\mu^{\text{true}} \leqslant 30\,GeV/c]$.

$\cos\theta_\mu$	$p_\mu(GeV)$
-1, 0.2	0, 30
0.2, 0.6	0, 0.4, 5.0, 30
0.6, 0.85	0, 0.4, 0.7, 2.0, 30
0.85, 1	0, 0.5, 0.7, 1, 30

TABLE XXVII. Binning used for the fit of the nuisance parameters correcting for the detector systematics.

the detector covariance matrix are:

$$
\begin{aligned}
N_i^{\nu_\mu \text{ CC-0}\pi\, Fit} &= \sum_t^{\text{regions}} \sum_j^{\text{reco bins}} c_i^{\nu_\mu\, Fit} N_{jt}^{\text{MC } \nu_\mu \text{ CC-0}\pi} t_{tij}^{\text{det}} \sum_s^{\text{det regions}} \sum_l^{\text{det bins}} r_{sl}^{\text{det Fit}} \\
N_i^{\nu_\mu \text{ CC-0}\pi\, Thrown} &= \sum_t^{\text{regions}} \sum_j^{\text{reco bins}} N_{jt}^{\text{MC } \nu_\mu \text{ CC-0}\pi} t_{tij}^{\text{det}} r_{tj}^{\text{det Thrown}}
\end{aligned}
\tag{5.26}
$$

while the number of $\bar{\nu}_\mu$ CC-0π selected events is:

$$
\begin{aligned}
N_i^{\bar{\nu}_\mu \text{ CC-0}\pi\, Fit} &= \sum_t^{\text{regions}} \sum_j^{\text{reco bins}} c_i^{\bar{\nu}_\mu\, Fit} N_{jt}^{\text{MC } \bar{\nu}_\mu \text{ CC-0}\pi} t_{tij}^{\text{det}} \sum_s^{\text{det regions}} \sum_l^{\text{det bins}} r_{sl}^{\text{det Fit}} \\
N_i^{\bar{\nu}_\mu \text{ CC-0}\pi\, Thrown} &= \sum_t^{\text{regions}} \sum_j^{\text{reco bins}} N_{jt}^{\text{MC } \bar{\nu}_\mu \text{ CC-0}\pi} t_{tij}^{\text{det}} r_{tj}^{\text{det Thrown}}
\end{aligned}
\tag{5.27}
$$

The last sums in the first formula in Eqs. 5.26 and 5.27 ($\sum_s^{\text{det regions}}$) stand for the reduced number of regions and the binning used to build the reduced covariance matrix.

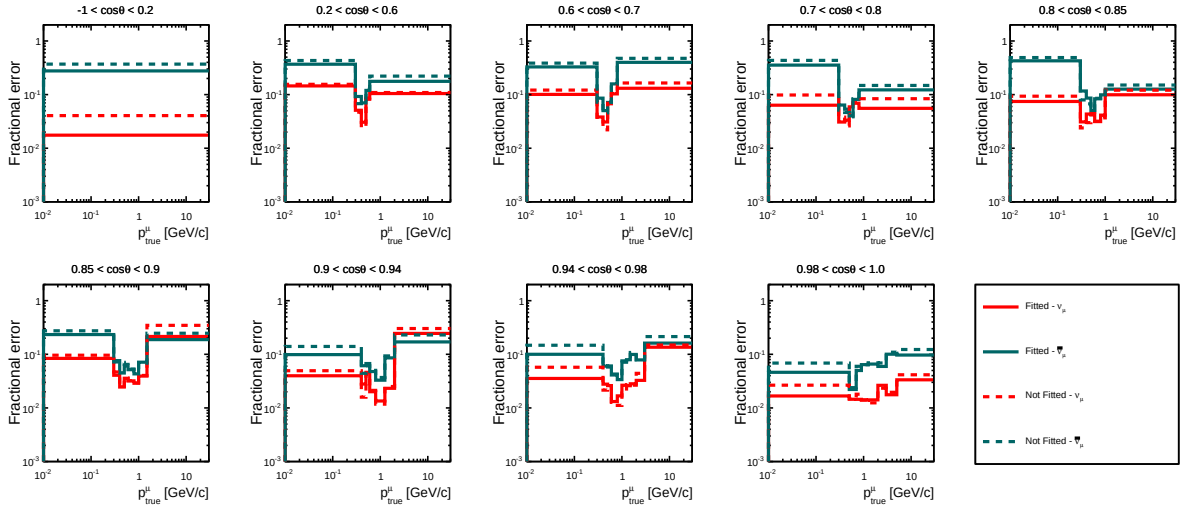

Figure 5.25. Relative uncertainty due to detector systematic for ν_μ (red) and $\bar{\nu}_\mu$ (dark cyan) CC-0π cross section in bins of true muon kinematics. Solid line show the fractional uncertainty when the detector parameter are fitted, while the dashed line when they are not fitted.

Since it is important to limit the number of parameter in the fit improving its stability and convergence, has been studied also the effect on the fitted number of events if the detector parameters are not fitted. This choice can lead to bigger error, but comparing the relative uncertainty obtained fitting or not these parameters there is not a sizeable difference as shown in Fig. 5.25. Thus in this work has been decided that the detector parameters will be not fitted.

The fractional errors on the ν_μ and $\bar{\nu}_\mu$ CC-0π cross section is shown in Fig. 5.26. The uncertainty due to detector systematics on the ν_μ CC-0π cross section is around few % in most of the relevant bins (300 MeV-1 GeV, where the signal statistics is relatively high and dominates over background) and can reach around 10% in the bins at lower and higher momenta. The situation is slightly different for the relative uncertainty on the $\bar{\nu}_\mu$ CC-0π cross section. In the most relevant bins the error is lower than 10% and always higher than the relative error on the ν_μ CC-0π cross section. For momenta greater than 1 GeV the error is always around 10%.

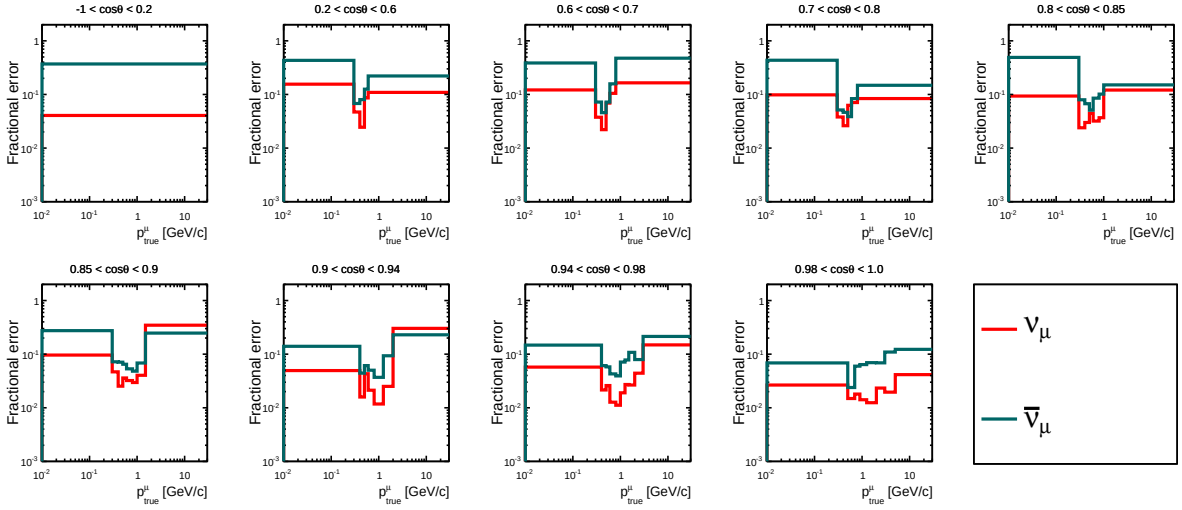

Figure 5.26. Relative uncertainty due to detector systematic for ν_μ (red) and $\bar{\nu}_\mu$ (dark cyan) CC-0π cross section in bins of true muon kinematics.

5.4.4 Systematic uncertainty on number of targets

The number of nucleons within the fiducial volume has been computed in Sec. 5.3.7. Its associated uncertainty is related to the error on the measurement of the areal density of the elements composing the FGD1. The covariance matrix of the areal density of each element with their correlation are obtained from [197] and are shown in Fig. 5.27.

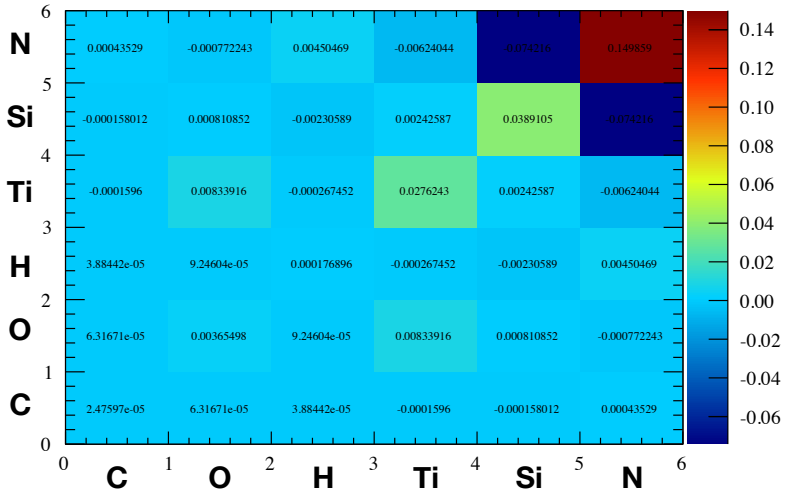

Figure 5.27. Covariance matrix of the elements composing FGD1.

In order to extract the error on the number of nucleons the procedure is the following:

1. the covariance matrix is decomposed using the Cholesky method;
2. a set of random weights is generated throwing them Gaussianly accordingly with the decomposed matrix;
3. per each throw the areal density of each element is reweighted using the thrown weights.

Therefore the number of nucleons in the FGD1 FV will vary for each toy experiment. Fig. 5.28 shows the number of targets for 10^4 toys experiments. The relative uncertainty is given by the ratio between the mean and RMS of such distribution and it is found to be 0.67%. In this case, all bins are fully correlated. It is worth notice that does not affect the asymmetry since the number of nucleon cancel out in the ratio. Furthermore the full correlation between neutrino and antineutrino ensure that the uncertainty on the cross-section is the same on sum and difference.

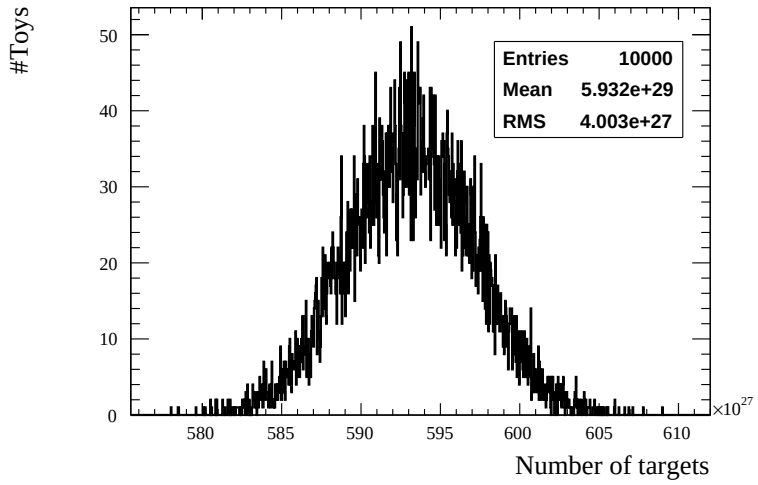

Figure 5.28. Number of targets for 10^4 toys. The distribution is produced varying the areal density of the elements composing the FGD1 fiducial volume following the covariance matrix from Fig. 5.27.

5.4.5 Signal and background modelling systematic uncertainty

Efficiency and background predictions from nominal MC have an associated uncertainty since the current cross-section models have some limitation in reproducing data. This kind of systematic are estimated with the generators re-weighting tools that, varying the neutrino cross-section parameters (defined in Chap. 2), allows the propagation of the uncertainty of each parameter to the number of events. A variation of these parameters imply a variation in the number of events, thus a relation between them is needed. Such association is performed throughout a set of so-called "response functions": $w(s)_i^{\nu_\mu \text{CC-0}\pi}$, $w(s)_i^{\bar{\nu}_\mu \text{CC-0}\pi}$ and $w(b)_i^k$ in Eq. 5.4. The response functions are evaluated for each topology and in each bin of true muon momentum and angle, using the same binning listed in Tab. XXIII. They are computed as the ratio between the number of events selected obtained varying one of the parameters with respect to the nominal MC for each sample, reaction type and true bin.
The cross-section parameters used in this analysis, along with their type, prior, error and validity range are reported in Tab. XXVIII. Requiring a parameter to be inside a particular validity range prevent unphysical weight when the value of the parameter is far from its nominal value. If any of the thrown values falls outside of the boundary, all the values will be thrown again. The signal parameter are not fitted in order to be model independent, since the extraction from the fit of these parameters relay on the correctness of the model parametrization. On the contrary the background parameters are fitted since the presence of the sidebands help in the reduction of their uncertainty.
Accordingly with the method described before, the covariance matrix of the cross-section parameters, shown in Fig. 5.29, is decomposed using the Cholesky method. In this case, the cross-section parameters are thrown following a Gaussian distribution and not directly the weight, as for flux and detector systematics, which are given by the response functions.

Parameter	Type	Prior	Error	Validity range
M_A^{QE}	Signal shape	1.2	0.3	[0,999]
p_F^C	Signal shape	217	30	[200,275]
E_B^C	Signal shape	25	9	[12,42]
2p2h ν	Signal normalization	1	1	[0,999]
2p2h $\bar{\nu}$	Signal normalization	1	1	[0,999]
$C_A^5(0)$	Background shape	1.01	0.12	[0,999]
M_A^{Res}	Background shape	0.95	0.15	[0,999]
Bkg Resonant	Background normalization	1.3	0.2	[0,999]
DIS Multiple pion	Background normalization	0.0	0.4	[-999,999]
CC Coherent on C	Background normalization	1.0	0.3	[0,999]
NC Coherent	Background normalization	1.0	0.3	[0,999]
NC Other	Background normalization	1.0	0.3	[0,999]

TABLE XXVIII. Cross-section modelling parameters used in this analysis along with their type, prior, uncertainty and validity range.

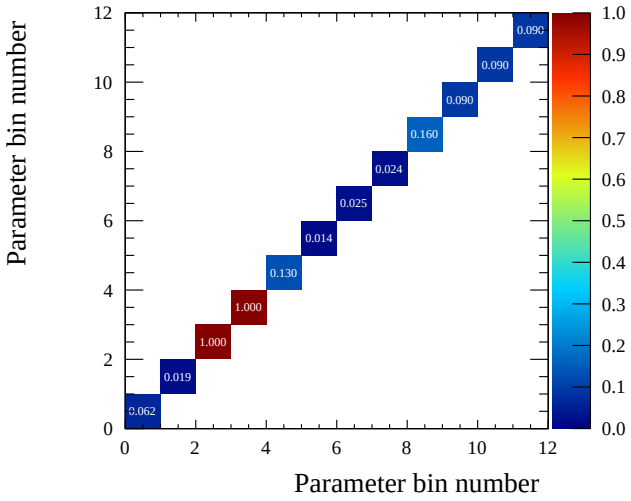

Figure 5.29. Covariance matrix of the signal and background modelling. The bin number correspond to the order in Tab. XXVIII. The displayed values are the uncertainties divided by the means.

Then the number of ν_μ CC-0π selected events as a function of the "true" kinematics extracted from the fit and thrown accordingly with the cross-section modelling covariance

matrix is:

$$N_i^{\nu_\mu \text{CC-0}\pi\, Fit} = \sum_t^{\text{regions}} \sum_j^{\text{reco bins}} c_i^{\nu_\mu\, Fit} N_{jt}^{\text{MC } \nu_\mu \text{ CC-0}\pi} t_{tij}^{\text{det}} \tag{5.28}$$

$$N_i^{\nu_\mu \text{CC-0}\pi\, Thrown} = \sum_t^{\text{regions}} \sum_j^{\text{reco bins}} N_{jt}^{\text{MC } \nu_\mu \text{ CC-0}\pi} t_{tij}^{\text{det}} \prod_s^{\text{model syst}} w(s^{Thrown})_i^{\nu_\mu \text{CC-0}\pi} \tag{5.29}$$

while the number of $\bar{\nu}_\mu$ CC-0π selected events is:

$$N_i^{\bar{\nu}_\mu \text{CC-0}\pi\, Fit} = \sum_t^{\text{regions}} \sum_j^{\text{reco bins}} c_i^{\bar{\nu}_\mu\, Fit} N_{jt}^{\text{MC } \bar{\nu}_\mu \text{ CC-0}\pi} t_{tij}^{\text{det}} \tag{5.30}$$

$$N_i^{\bar{\nu}_\mu \text{CC-0}\pi\, Thrown} = \sum_t^{\text{regions}} \sum_j^{\text{reco bins}} N_{jt}^{\text{MC } \bar{\nu}_\mu \text{ CC-0}\pi} t_{tij}^{\text{det}} \prod_s^{\text{model syst}} w(s^{Thrown})_{ij}^{\bar{\nu}_\mu \text{CC-0}\pi} \tag{5.31}$$

It is worth notice that the response functions for the background events do not enter directly in the formulas above, but only indirectly, since varying the background parameters changes the total reconstructed number of event in Eq. 5.4, thus the fitted number of events.

Anyway throwing the signal modelling parameters imply not only a variation of the CC-0π selected number of events, but also of the selection efficiency which is given by the following formulas for ν_μ and $\bar{\nu}_\mu$ respectively:

$$\begin{aligned} \epsilon_i^{\nu_\mu\, Thrown} &= \frac{N_i^{\text{Sel } \nu_\mu \text{ CC-0}\pi} \prod_s^{\text{model syst}} w(s^{Thrown})_i^{\bar{\nu}_\mu \text{CC-0}\pi}}{N_i^{\text{Gen } \nu_\mu \text{ CC-0}\pi} \prod_s^{\text{model syst}} w'(s^{Thrown})_i^{\bar{\nu}_\mu \text{CC-0}\pi}} \\ \epsilon_i^{\bar{\nu}_\mu\, Thrown} &= \frac{N_i^{\text{Sel } \bar{\nu}_\mu \text{ CC-0}\pi} \prod_s^{\text{model syst}} w(s^{Thrown})_i^{\bar{\nu}_\mu \text{CC-0}\pi}}{N_i^{\text{Gen } \bar{\nu}_\mu \text{ CC-0}\pi} \prod_s^{\text{model syst}} w'(s^{Thrown})_i^{\bar{\nu}_\mu \text{CC-0}\pi}} \end{aligned} \tag{5.32}$$

where the response function $w'(s^{Thrown})_i$ is computed as the ratio between the generated number of events obtained varying one of the parameters with respect to the nominal generated number of events for signal reaction and for each true bin.
The relative errors due to signal modelling systematic on the ν_μ and $\bar{\nu}_\mu$ CC-0π cross sections are shown in Fig. 5.30, while in Fig. 5.31 are shown the relative errors due to background modelling systematic. The uncertainty on the cross sections due to the signal modelling systematic in general is very low and is lower in the region where the background is low (see Figs. 5.13 and 5.14).

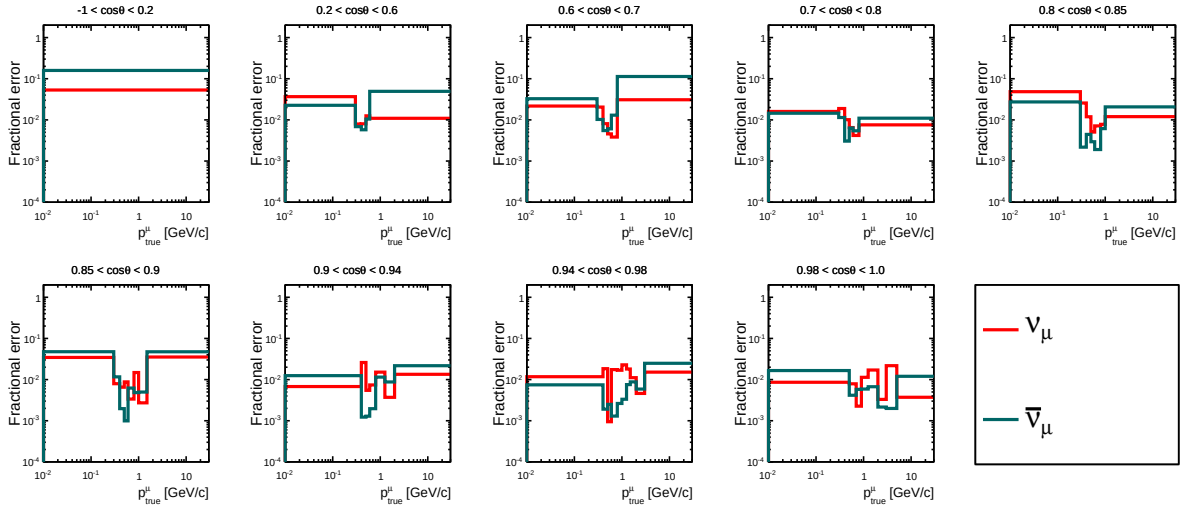

Figure 5.30. Relative uncertainty due to signal modelling systematic for ν_μ (red) and $\bar{\nu}_\mu$ (dark cyan) CC-0π cross section in bins of true muon kinematics.

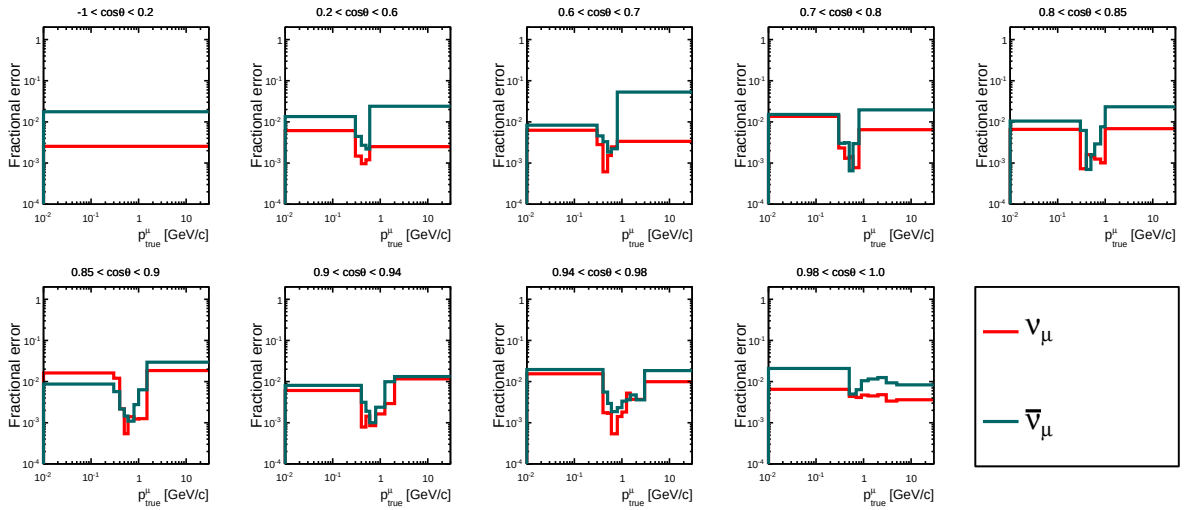

Figure 5.31. Relative uncertainty due to background modelling systematic for ν_μ (red) and $\bar{\nu}_\mu$ (dark cyan) CC-0π cross section in bins of true muon kinematics.

5.4.6 Pion final state interaction systematic uncertainty

Pion final state interactions affect pions before they leave the nuclear medium, changing their true kinematics and/or identity. In Tab. XXIX the different pion FSI parameters are shown along with their type, prior, error and validity range and in Fig. 5.32 their covariance matrix. The validity range is used, also in this case, to prevent unphysical weight when the value of the thrown parameter is far from its nominal value. If any of the thrown values falls outside of the boundary, all the values will be thrown again. The parameters in Tab. XXIX are used to re-scale the different processes that contribute to the pion FSI.

Parameter	Type	Prior	Error	Validity range
Inelastic low energy ($p_\pi < 500\ MeV/c$)	Shape	0.0	0.41	[-1.2,1.2]
Inelastic high energy ($p_\pi > 400\ MeV/c$)	Shape	0.0	0.34	[-0.9,0.9]
Pion production	Shape	0.0	0.5	[-1.5,1.5]
Pion absorption	Shape	0.0	0.41	[-1.2,1.2]
Charge exchange low energy ($p_\pi < 500\ MeV/c$)	Shape	0.0	0.57	[1.8,1.8]
Charge exchange high energy ($p_\pi > 400\ MeV/c$)	Shape	0.0	0.28	[-0.9,0.9]

TABLE XXIX. Pion FSI parameters used in this analysis along with their type, prior, uncertainty and validity range.

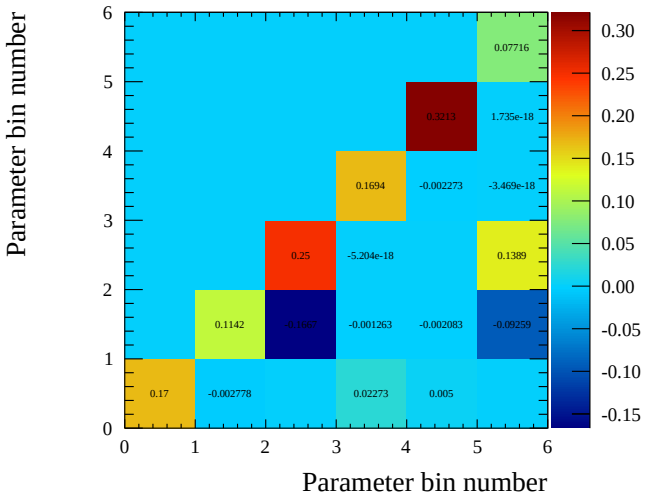

Figure 5.32. Pion FSI covariance matrix.The bin number correspond to the order in Tab. XXIX. The displayed values are the uncertainties divided by the means and the off-diagonal terms reflect the correlations between the different parameters.

The propagation of the uncertainty is similar to that described for the cross-section modelling systematic. As for the background these parameter will be fitted since the presence of the sidebands helps in the reduction of their uncertainty.

The relative error on ν_μ and $\bar{\nu}_\mu$ CC-0π cross sections is shown in Fig. 5.33. The uncertainty on the cross sections due to the pion FSI in general is very low and is lower in the region where the background is low (see Figs. 5.13 and 5.14).

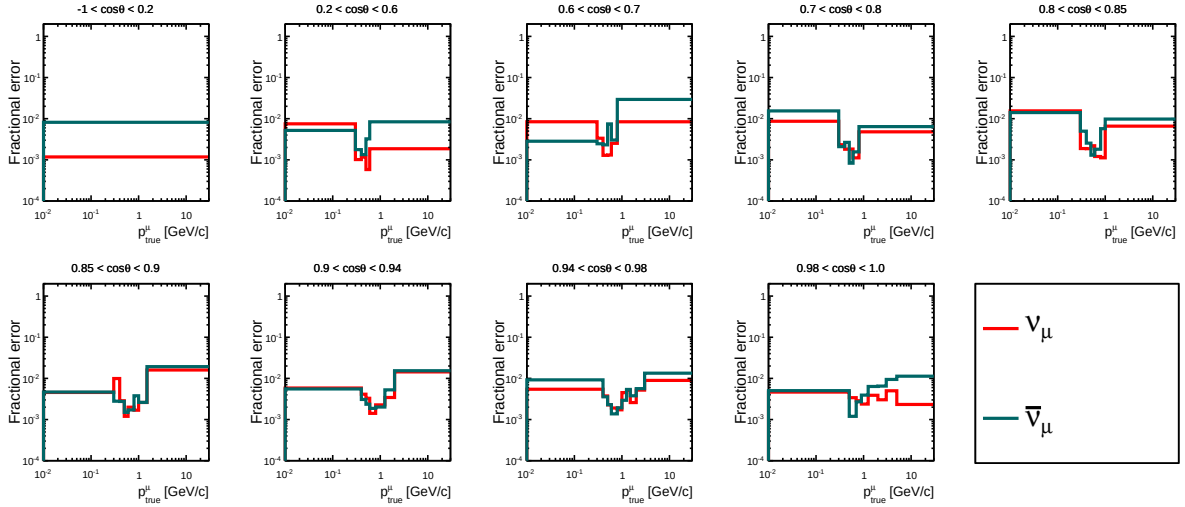

Figure 5.33. Relative uncertainty due to pion FSI modelling systematic for ν_μ (red) and $\bar{\nu}_\mu$ (dark cyan) CC-0π cross section in bins of true muon kinematics.

5.4.7 Summary of all the uncertainties

The impact of all the systematic uncertainties on ν_μ and $\bar{\nu}_\mu$ cross sections has been evaluated varied together all the systematic uncertainties. A comparison of the single and all the systematics is shown: in Figs. 5.34 and 5.35 the relative errors on ν_μ and $\bar{\nu}_\mu$ CC-0π cross sections. As expected, both for ν_μ and $\bar{\nu}_\mu$ cross sections the dominant uncertainty is the statistical, which vary from 60% in the bin where the statistic is very low, to about 10%. The detector systematics are the dominant uncertainty in most of the phase space, mainly in the high angle where the uncertainty is large since the detector resolution and efficiency is less known. The flux systematic is around few percent, then being fully correlated between all bins, it does not affect the cross-section shape but only the normalization. The background modelling and the pion FSI affect the measured cross-section mainly through their effect on the background, therefore they are larger in the forward and high momentum region where most of the background is located, but even in these regions they remain below 2% thanks to the constraints from the control regions. The systematics on the efficiency due to signal modelling are of the order of few %, except in the high angle region where the efficiency is low and therefore the extrapolation of the cross section is more MC-based.

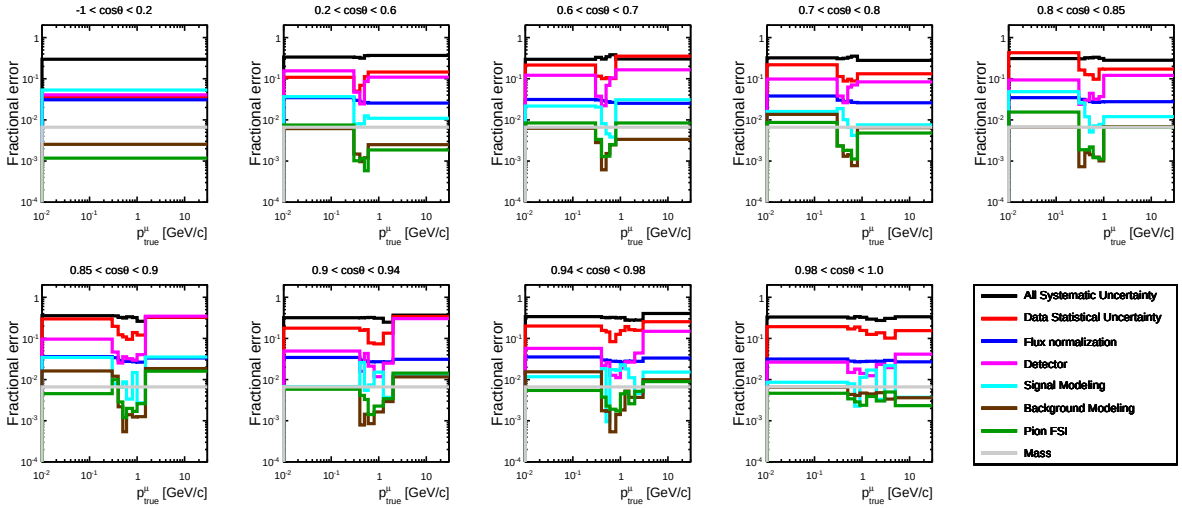

Figure 5.34. Summary of all the uncertainties on the ν_μ CC-0π cross section in bins of true muon kinematics.

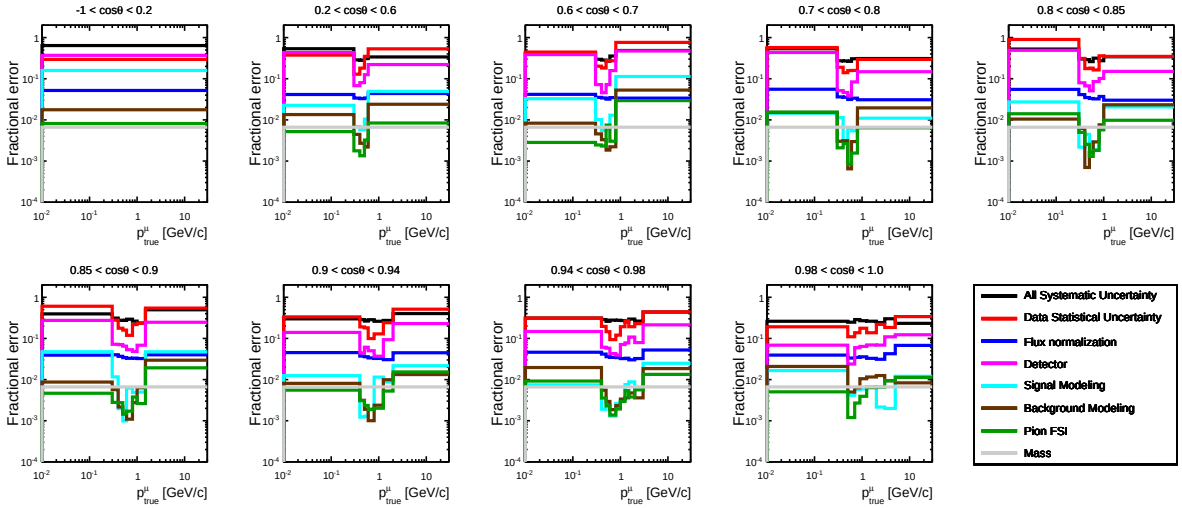

Figure 5.35. Summary of all the uncertainties on the $\bar{\nu}_\mu$ CC-0π cross section in bins of true muon kinematics.

5.5 Fit results

The fitting strategy has been carefully validated performing different studies discussed in App. C. Particular care has been taken to test the stability of the fit through fake data studies. Furthermore, in order to check the possible bias picked up fitting the flux two dedicated fake data studies has been performed: in one, the fake data set has been generated reducing the wrong sign component of a factor of 10% in the NEUT prediction used as prior in the fit, while in another the NEUT background prediction has been biased. Both the fake data studies demonstrated that there is not bias in the final results, showing the correctness of the procedure. After these checks the fit has been performed using ND280 data and the result will be discussed in this section.

5.5.1 Fit results as function of reconstructed muon kinematics

The results of the fit for the total number of events (signal plus background) as a function of the reconstructed muon kinematics can be directly compared to the data distributions, as shown in Figs. 5.36 and 5.37. The post-fit results clearly reproduce the data distributions also in the regions were the prior nominal MC is quite far from the data. In these plots the statistical error is the square root of the number of events in data and the systematics uncertainties has been computed at the reconstruction level using the strategy discussed in Sec. 5.4. It is particularly interesting that the results agree with data also in the sideband, which are dominated by backgrounds, as shown in Figs. 5.38 and 5.39. In particular in the CC-1π^- and CC-1π^+ sidebands, the fit clearly improves the background description at small angles where the pre-fit MC overestimates the background.

5.5.2 Cross section measurements

The $\bar{\nu}_\mu$ and ν_μ double-differential flux-integrated cross-sections are shown in Figs. 5.40 and 5.41, respectively. In Figs. 5.42, 5.43 and 5.44 are shown the sum, the difference and the asymmetry of the two cross sections. The systematic uncertainties and the data statistical uncertainties are summed in quadrature and shown as error bars. The uncertainty related to the flux normalization is given as a red band. The results are compared against the CC-0π cross section with and without 2p2h predicted by NEUT. Furthermore also the different contributions to the CC-0π cross section are drawn in order to show their behaviour as function of the momentum and the angle. It is clear that the 2p2h component contribute more to the ν_μ CC-0π cross section and less to the $\bar{\nu}_\mu$, and in both cases more in the region of most forward muon angles and higher muon momentum (very small transferred Q^2). Quantifying the agreement between the result of the fit and the NEUT prediction is not straightforward. In most of the bins the cross sections are in agreement inside the uncertainty with the NEUT prediction. Even if in some bin there is a disagreement, it is not currently possible to separate between the different component because of the uncertainties in the modelling of the signal and background reactions, in particular CC-1π events with the pion absorption which cannot be experimentally separated from CCQE interactions.
As already mentioned in the sum the axial vector interference is eliminated, while difference contains only this term and they could be used to test the presence of the mult-

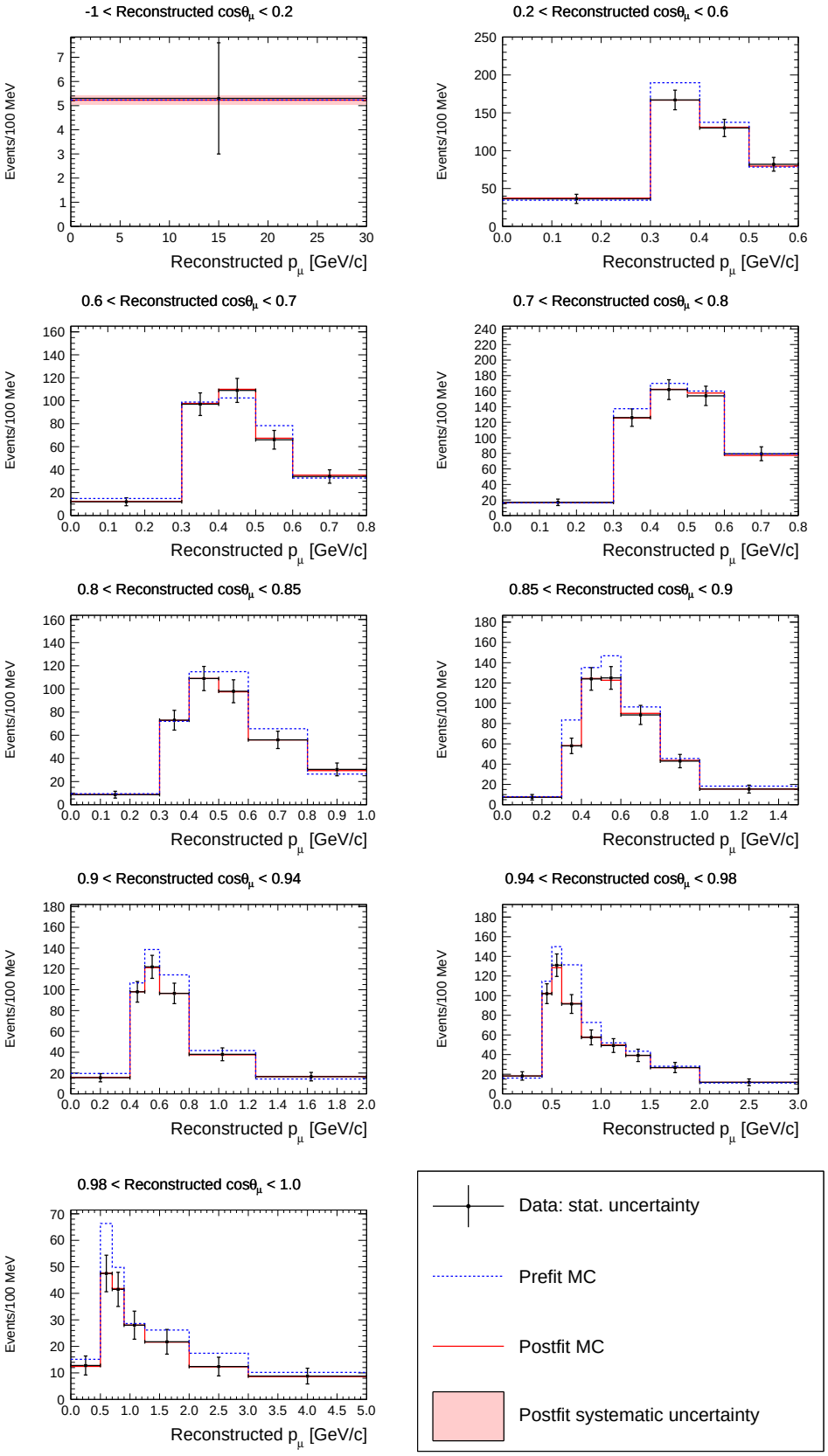

Figure 5.36. $\bar{\nu}_\mu$ CC-0π number of events as a function of reconstructed muon kinematics. The red solid lines shown the fit results with systematics uncertainties, the dots shows the data with statistical uncertainties, finally the blue dotted line show the nominal NEUT MC used as prior in the fit.

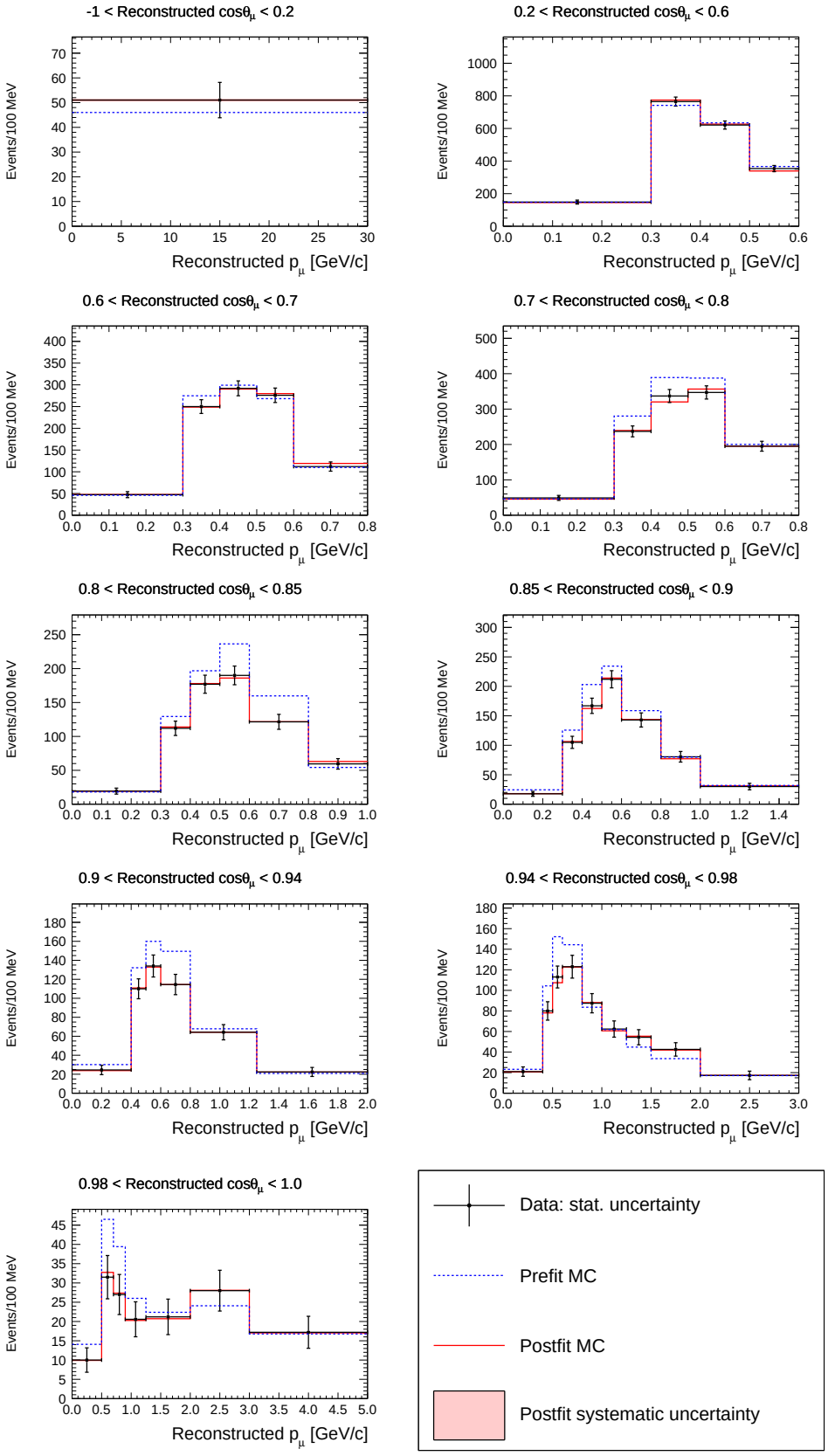

Figure 5.37. ν_μ CC-0π number of events as a function of reconstructed muon kinematics. The red solid lines shown the fit results with systematics uncertainties, the dots shows the data with statistical uncertainties, finally the blue dotted line show the nominal NEUT MC used as prior in the fit.

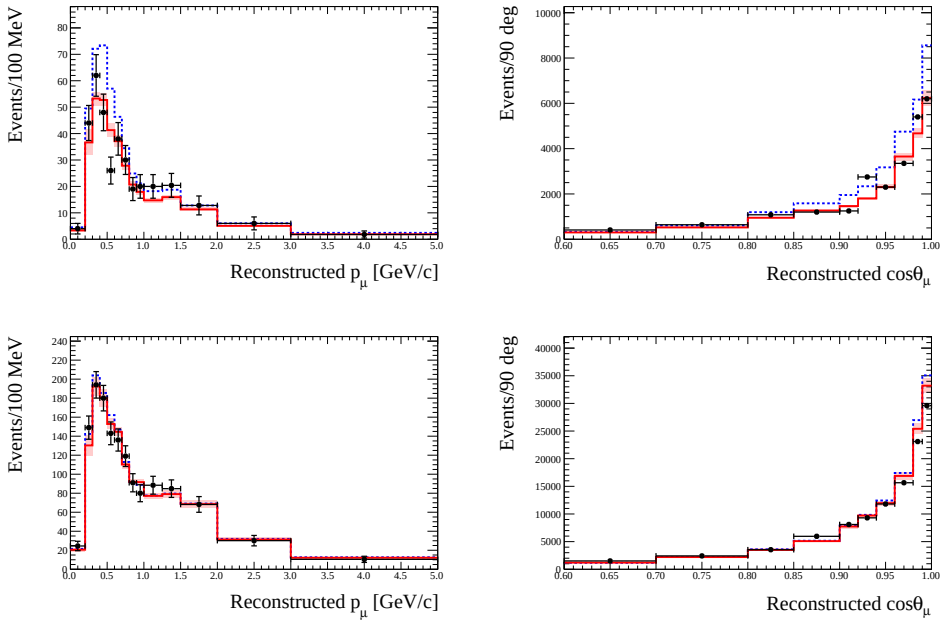

Figure 5.38. Distribution of ν_μ events in the different sideband regions as function of the reconstructed muon momentum (left column) and scattering angle (right column) for the CC-1π^+-like (top row) and CC-Other-like (bottom row) samples. The legend is the same as in Fig. 5.36: the red solid lines shown the fit results with systematics uncertainties, the dots shows the data with statistical uncertainties, finally the blue dotted line show the nominal NEUT MC used as prior in the fit.

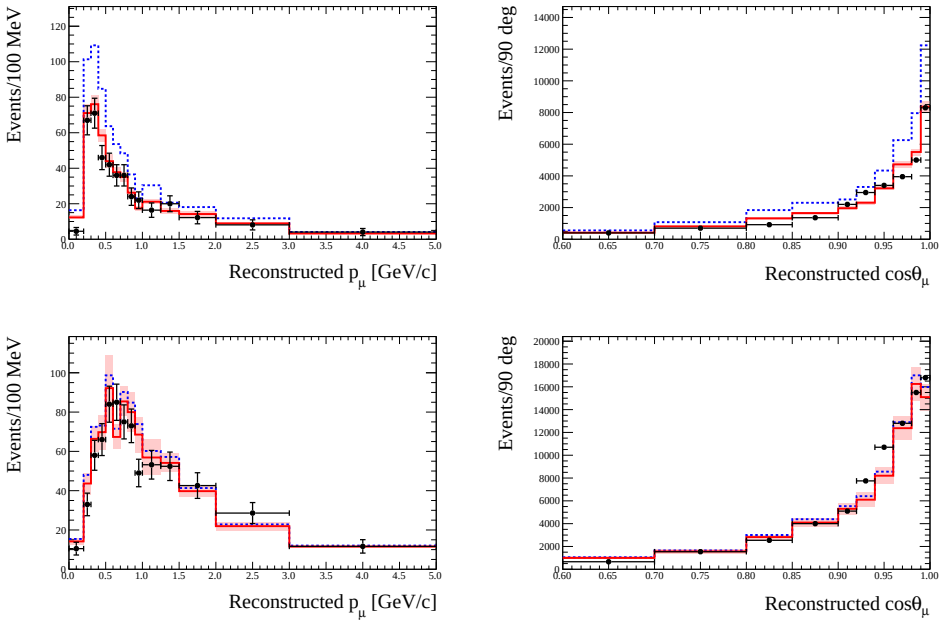

Figure 5.39. Distribution of $\bar{\nu}_\mu$ events in the different sideband regions as function of the reconstructed muon momentum (left column) and scattering angle (right column) for the CC-1π^--like (top row) and CC-Other-like (bottom row) samples. The legend is the same as in Fig. 5.36: the red solid lines shown the fit results with systematics uncertainties, the dots shows the data with statistical uncertainties, finally the blue dotted line show the nominal NEUT MC used as prior in the fit.

inucleon excitations, while the asymmetry between the two cross section gives a direct estimation on any possible bias due to mismodelling of neutrino interactions on the measurement of the CP violation phase in neutrino oscillation. The present uncertainty do not allow any conclusive statement also combing the cross sections. It is important to mention that the difference between the ν_μ and $\bar{\nu}_\mu$ cross sections is close to zero in the most forward bins, since the vector axial interference term is close to zero at low momentum transfer.

The results are compared to NEUT and GENIE (described in Sec. 2.3) in Figs. from 5.45 to 5.49. In both the generator the Llewellyn-Smith model is used to predict the CCQE interactions [104] and is used the same parametrization for the vector form factors [141]. They use a different value for the axial mass M_A^{QE} 1.21 GeV/c^2 and 0.99 GeV/c^2. The 2p2h component is modelled using an implementation of the Nieves model [127], while GENIE does not include this interaction. As nuclear model NEUT uses the SF formalism [119], while GENIE the RFG by Bodek *et al.* [148].
The uncertainties are quite large, fully dominated by statistics, but few general trends can be observed:

- in the backward region the generators are in agreement with data;
- in the high angle and low momentum region both generators slightly underestimates the data;
- in the forward regions, between 0.5-1 GeV/c NEUT and GENIE overestimates the cross-section. This region could be sensitive to the shell structure of the nucleus and to the excitations of low-lying giant resonances [198, 199], processes that are not simulated;
- in the high momentum region the agreement between generators and data is good.

In Figs. from 5.50 to 5.54 the results are compared to the Martini model [126] with and without the 2p2h contribution. It should be noted that Martini model does not include the contribution of CC-1π with pion reabsorption due to FSI and it predicts the cross section up to 3 GeV/c. Also in these comparison, despite the large uncertainties, some general trends can be observed:

- both ν_μ and $\bar{\nu}_\mu$ CC-0π cross sections results seem to prefer the Martini model with the 2p2h contribution. Only in the very forward region the model overestimate the ν_μ cross section;
- the cross sections sum seems to prefer the Martini model with the 2p2h contribution, in particular in the forward region;
- for the cross sections difference there is not a straightforward conclusion;
- the asymmetry of the cross sections, also in this case, point out that a very precise measurement is needed to disentangle the different contributions to this observable.

The ν_μ and $\bar{\nu}_\mu$ CC-0π cross-sections per nucleon integrated over all the muon kinematics phase space are:

$$\sigma_{\bar{\nu}_\mu} = 0.13 \pm 0.03\,(stat.) \pm 0.03\,(syst.) \times 10^{-38}\,\mathrm{cm}^2\mathrm{nucleon}^{-1} \quad (5.33)$$

$$\sigma_{\nu_\mu} = 0.42 \pm 0.04\,(stat.) \pm 0.06\,(syst.) \times 10^{-38}\,\mathrm{cm}^2\mathrm{nucleon}^{-1} \quad (5.34)$$

the NEUT prediction are $0.13 \times 10^{-38}\mathrm{cm}^2\mathrm{nucleon}^{-1}$ and $0.40 \times 10^{-38}\,\mathrm{cm}^2\mathrm{nucleon}^{-1}$, for $\bar{\nu}_\mu$ and ν_μ respectively.
The combination of the integrated cross-sections are:

$$\sigma_{\nu_\mu} + \sigma_{\bar{\nu}_\mu} = (0.55 \pm 0.05\,(stat.) \pm 0.07\,(syst.)) \times 10^{-38}\,\mathrm{cm}^2\mathrm{nucleon}^{-1} \quad (5.35)$$

$$\sigma_{\nu_\mu} - \sigma_{\bar{\nu}_\mu} = (0.29 \pm 0.05(stat.) \pm 0.06\,(syst.)) \times 10^{-38}\,\mathrm{cm}^2\mathrm{nucleon}^{-1} \quad (5.36)$$

$$\frac{\sigma_{\nu_\mu} - \sigma_{\bar{\nu}_\mu}}{\sigma_{\nu_\mu} + \sigma_{\bar{\nu}_\mu}} = 0.53 \pm 0.08\,(stat.) \pm 0.10\,(syst.) \quad (5.37)$$

to be compared with the NEUT prediction of $0.53 \times 10^{-38}\mathrm{cm}^2\mathrm{nucleon}^{-1}$ for the sum, $0.27 \times 10^{-38}\mathrm{cm}^2\mathrm{nucleon}^{-1}$ for the difference and 0.50 for the asymmetry.

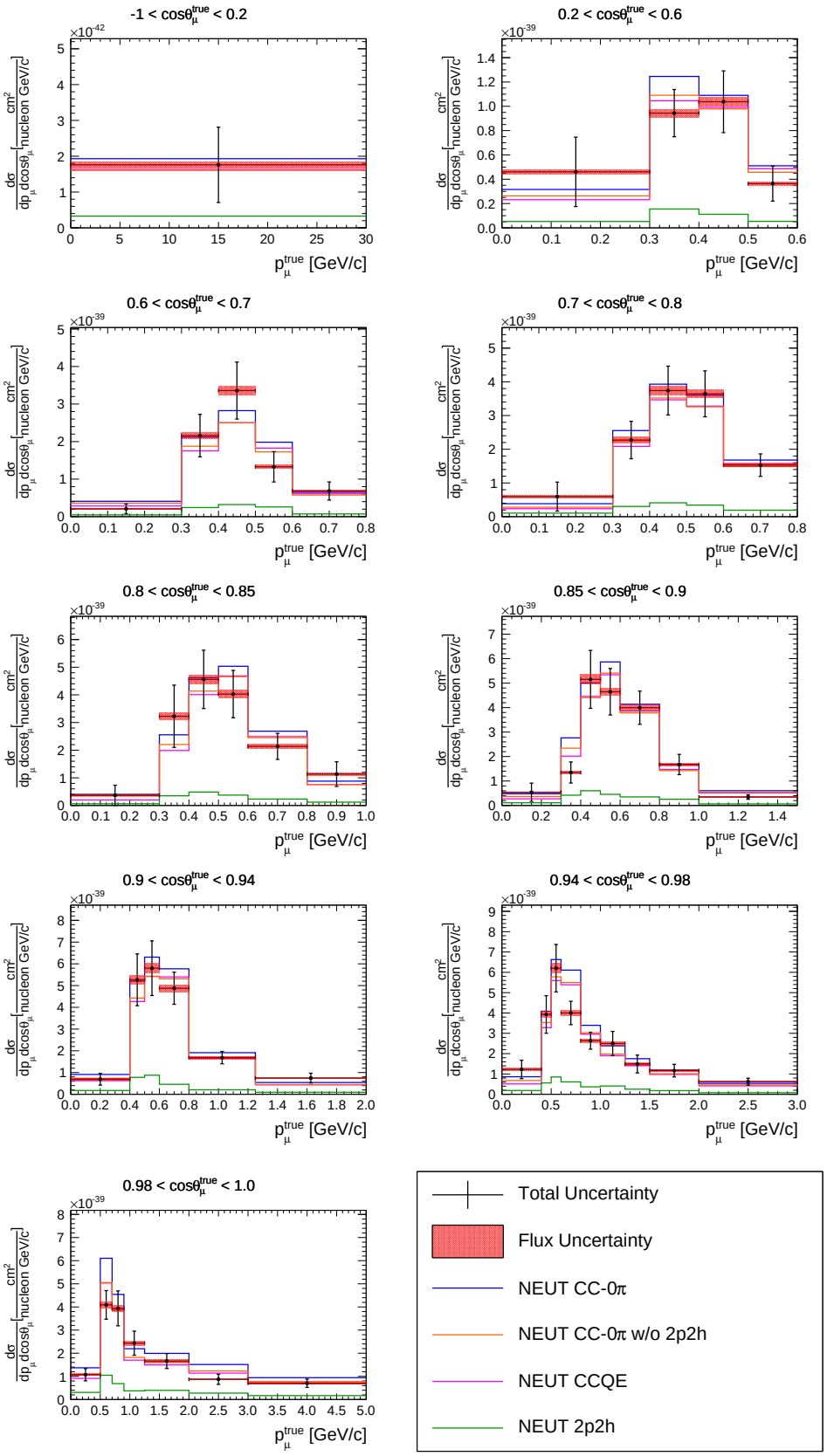

Figure 5.40. Measured $\bar{\nu}_\mu$ CC-0π cross section in bins of true muon kinematics with shape uncertainty (error band) and fully correlated normalization uncertainty (red band). The result is compared with the NEUT prediction for CC-0π (blue line), CC-0π without 2p2h (orange line), CCQE (pink line) and 2p2h (green line). The last bin, up to 30 GeV/c is not displayed.

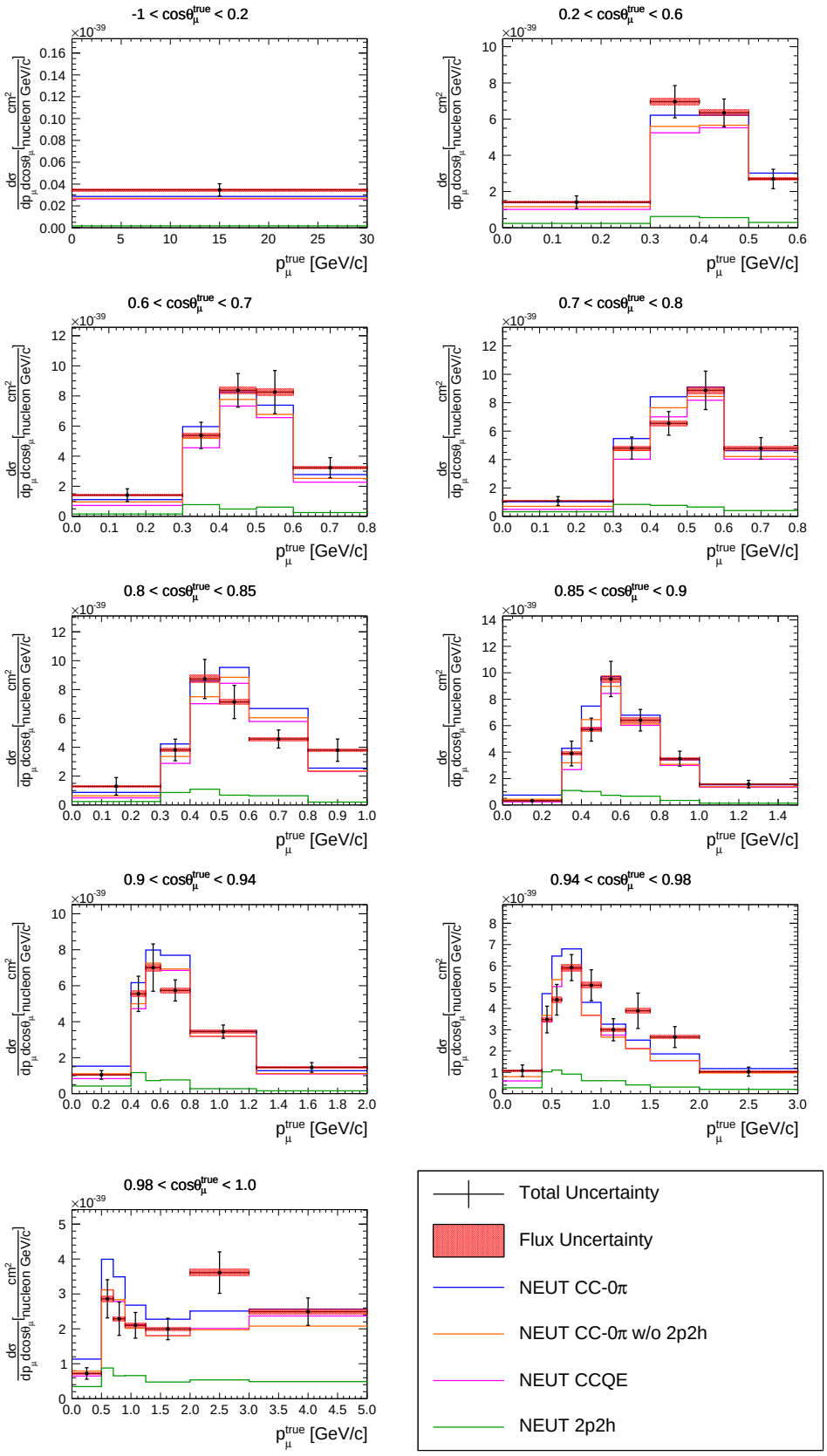

Figure 5.41. Measured ν_μ CC-0π cross section in bins of true muon kinematics with shape uncertainty (error band) and fully correlated normalization uncertainty (red band).The result is compared with the NEUT prediction for CC-0π (blue line), CC-0π without 2p2h (orange line), CCQE (pink line) and 2p2h (green line). The last bin, up to 30 GeV/c is not displayed.

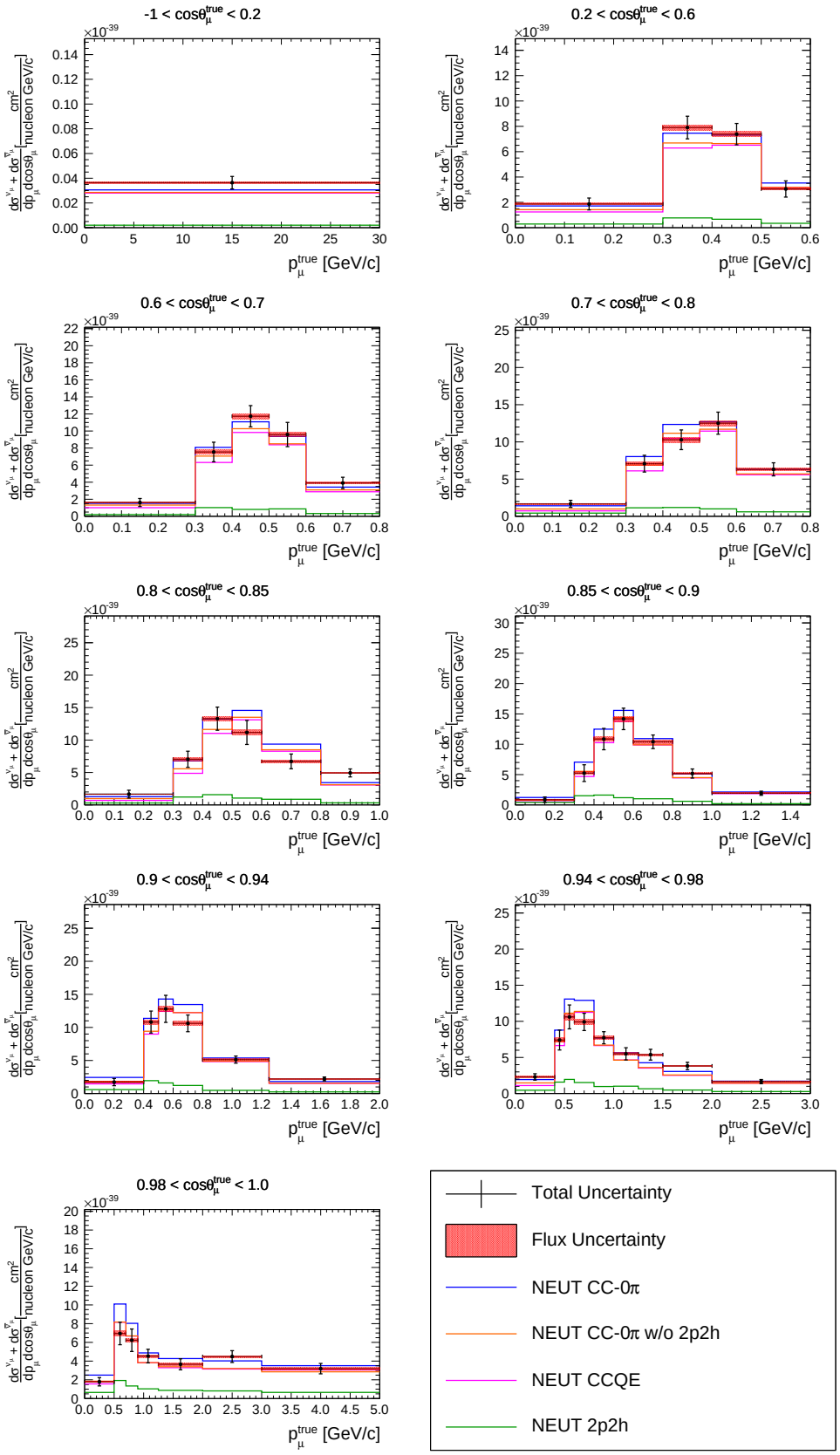

Figure 5.42. Measured cross sections sum in bins of true muon kinematics with shape uncertainty (error band) and fully correlated normalization uncertainty (red band). The result is compared with the NEUT prediction for CC-0π (blue line), CC-0π without 2p2h (orange line), CCQE (pink line) and 2p2h (green line). The last bin, up to 30 GeV/c is not displayed.

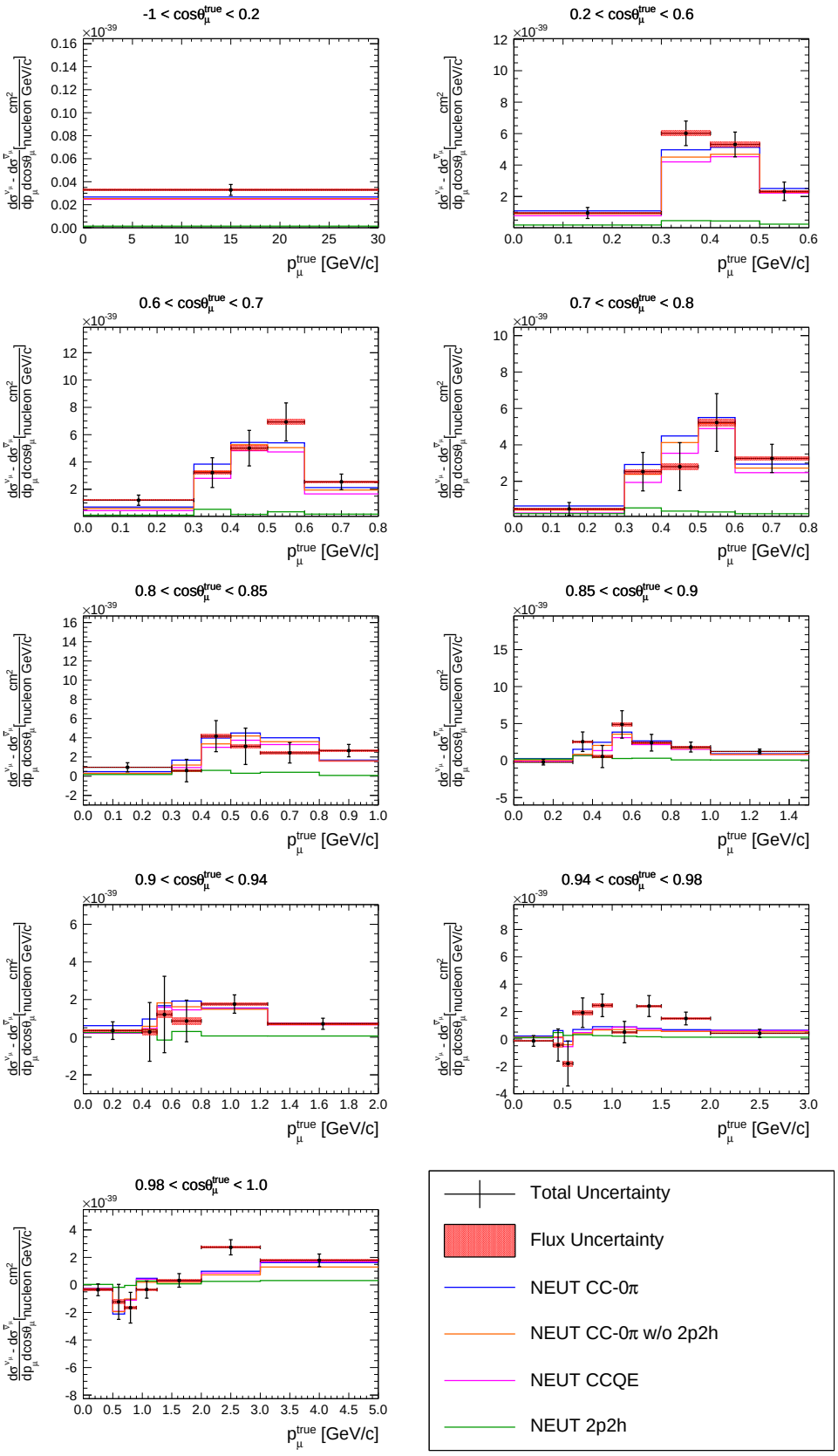

Figure 5.43. Measured cross sections difference in bins of true muon kinematics with shape uncertainty (error band) and fully correlated normalization uncertainty (red band). The result is compared with the NEUT prediction for CC-0π (blue line), CC-0π without 2p2h (orange line), CCQE (pink line) and 2p2h (green line). The last bin, up to 30 GeV/c is not displayed.

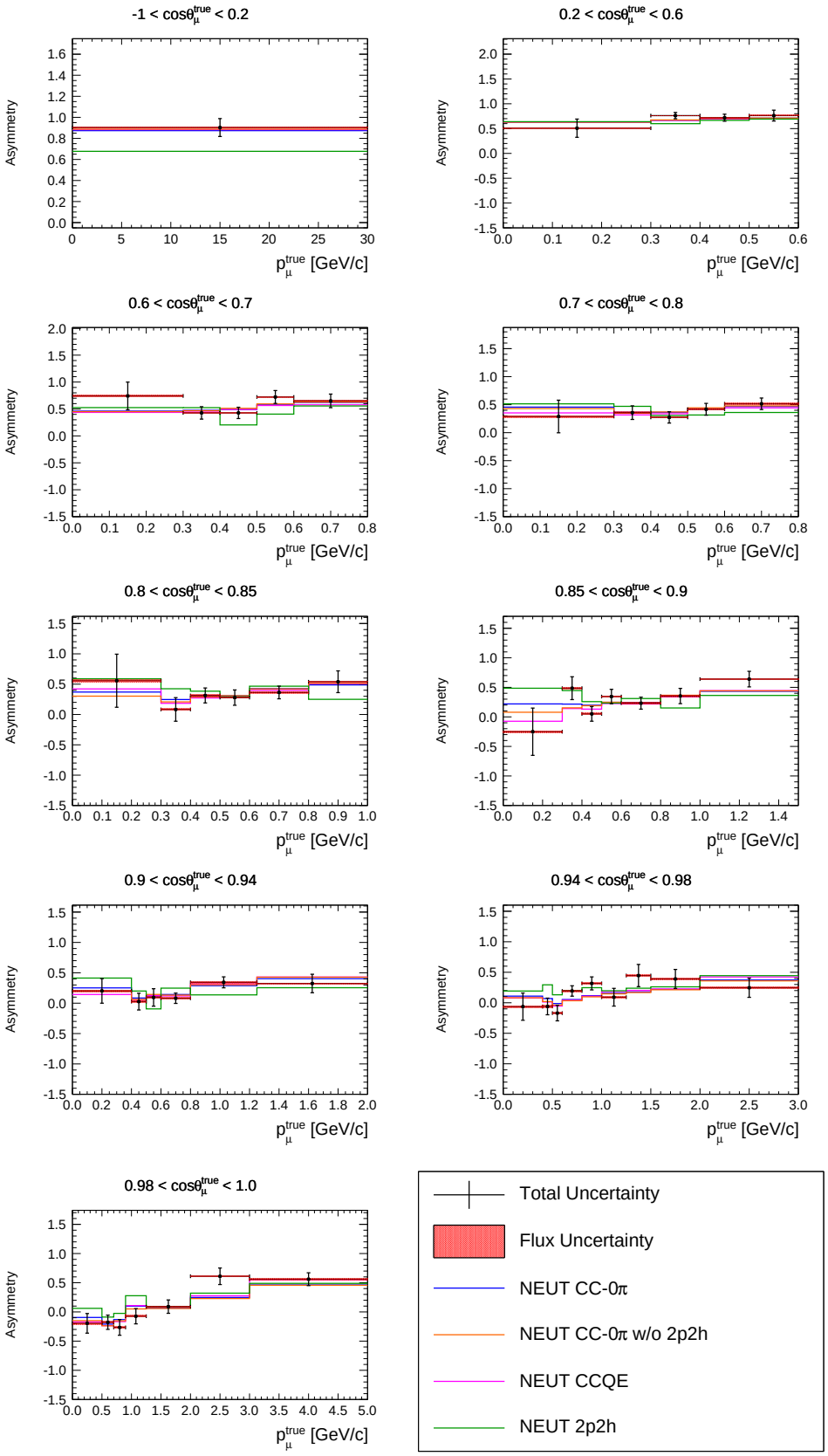

Figure 5.44. Measured cross sections asymmetry in bins of true muon kinematics with shape uncertainty (error band) and fully correlated normalization uncertainty (red band). The result is compared with the NEUT prediction for CC-0π (blue line), CC-0π without 2p2h (orange line), CCQE (pink line) and 2p2h (green line). The last bin, up to 30 GeV/c is not displayed.

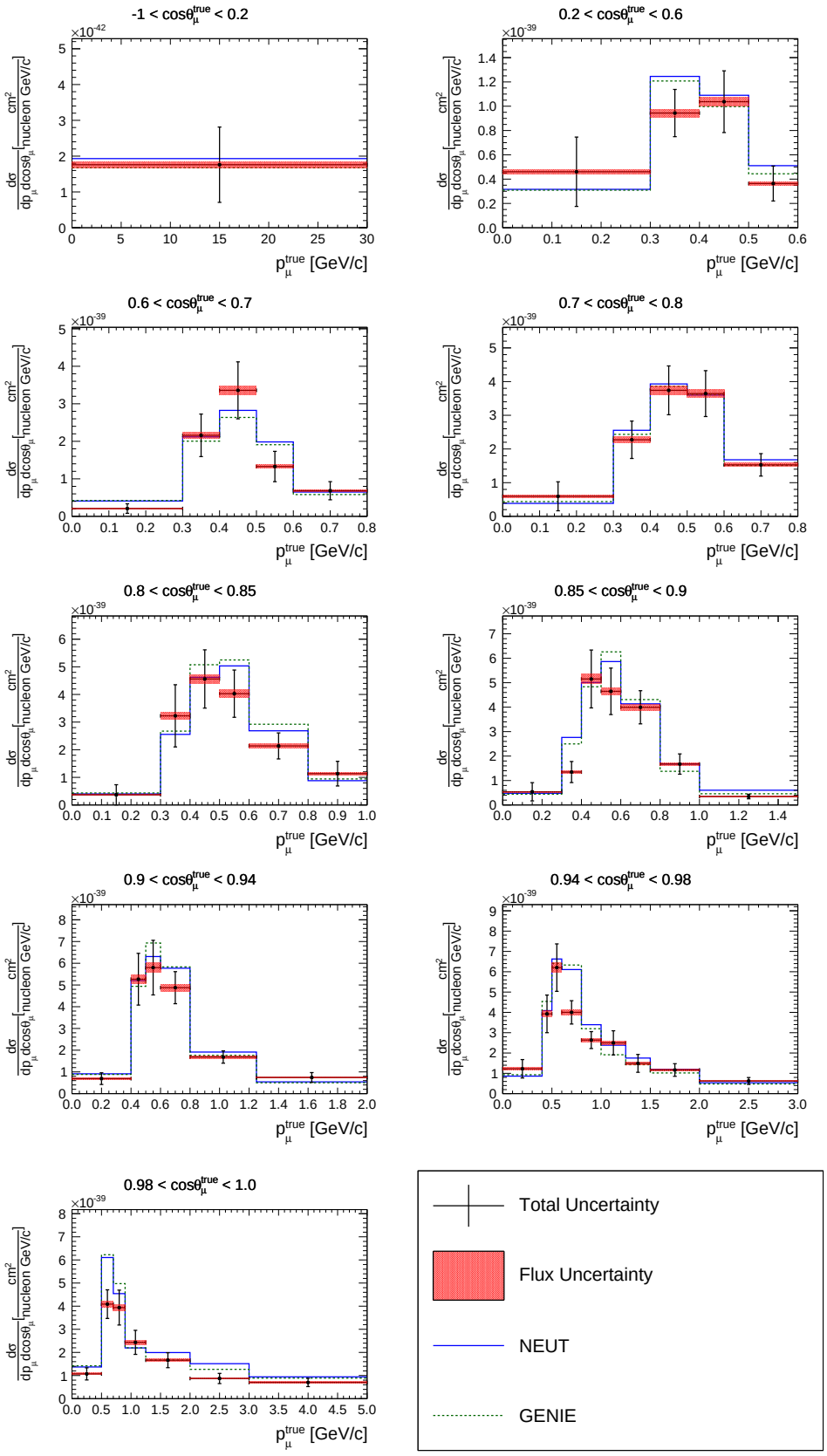

Figure 5.45. Measured $\bar{\nu}_\mu$ CC-0π cross section in bins of true muon kinematics with shape uncertainty (error band) and fully correlated normalization uncertainty (red band). The result is compared with the CC-0π NEUT (blue line) and GENIE (dotted green line) prediction. The last bin, up to 30 GeV/c is not displayed.

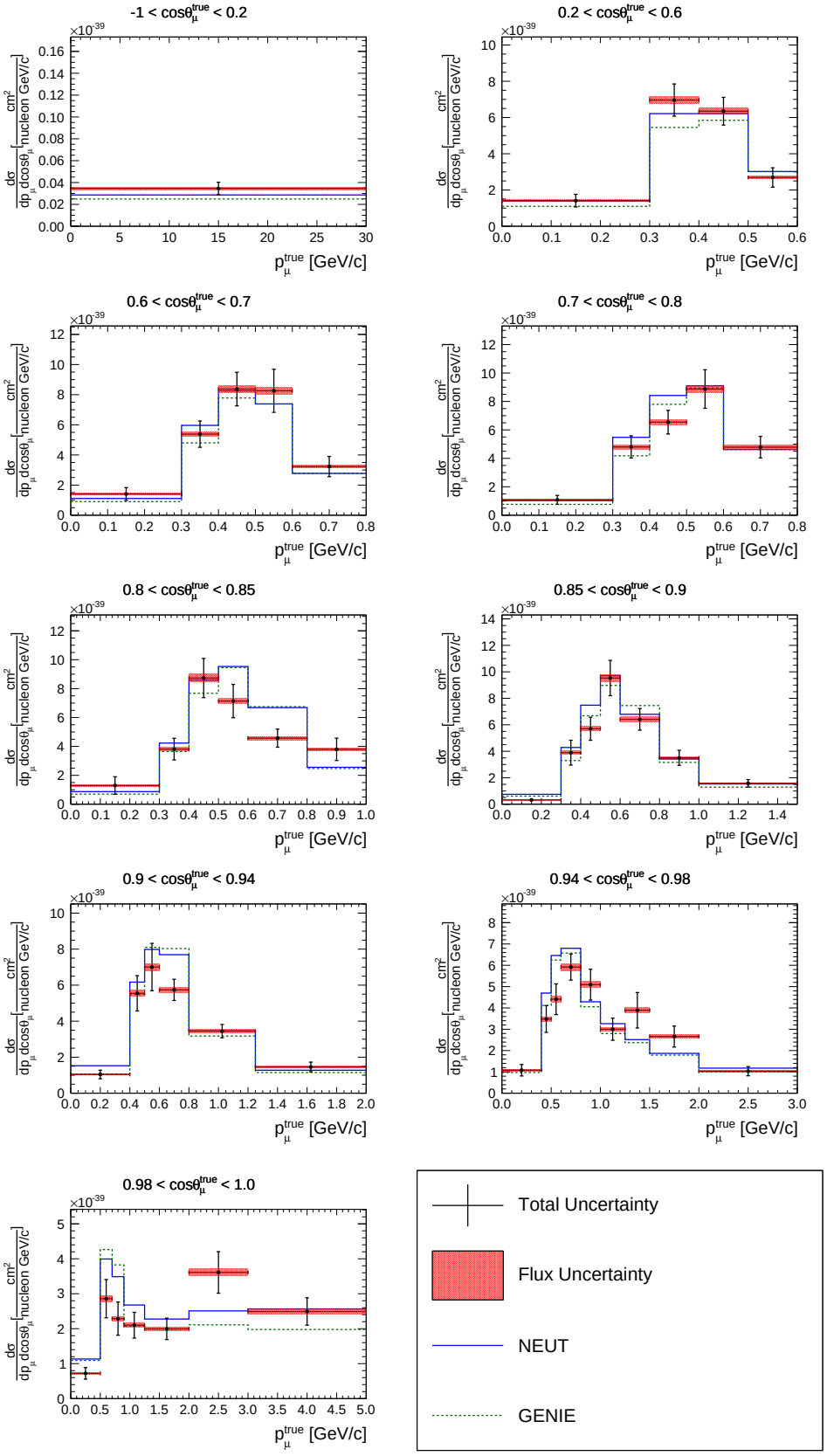

Figure 5.46. Measured ν_μ CC-0π cross section in bins of true muon kinematics with shape uncertainty (error band) and fully correlated normalization uncertainty (red band). The result is compared with the CC-0π NEUT (blue line) and GENIE (dotted green line) prediction. The last bin, up to 30 GeV/c is not displayed.

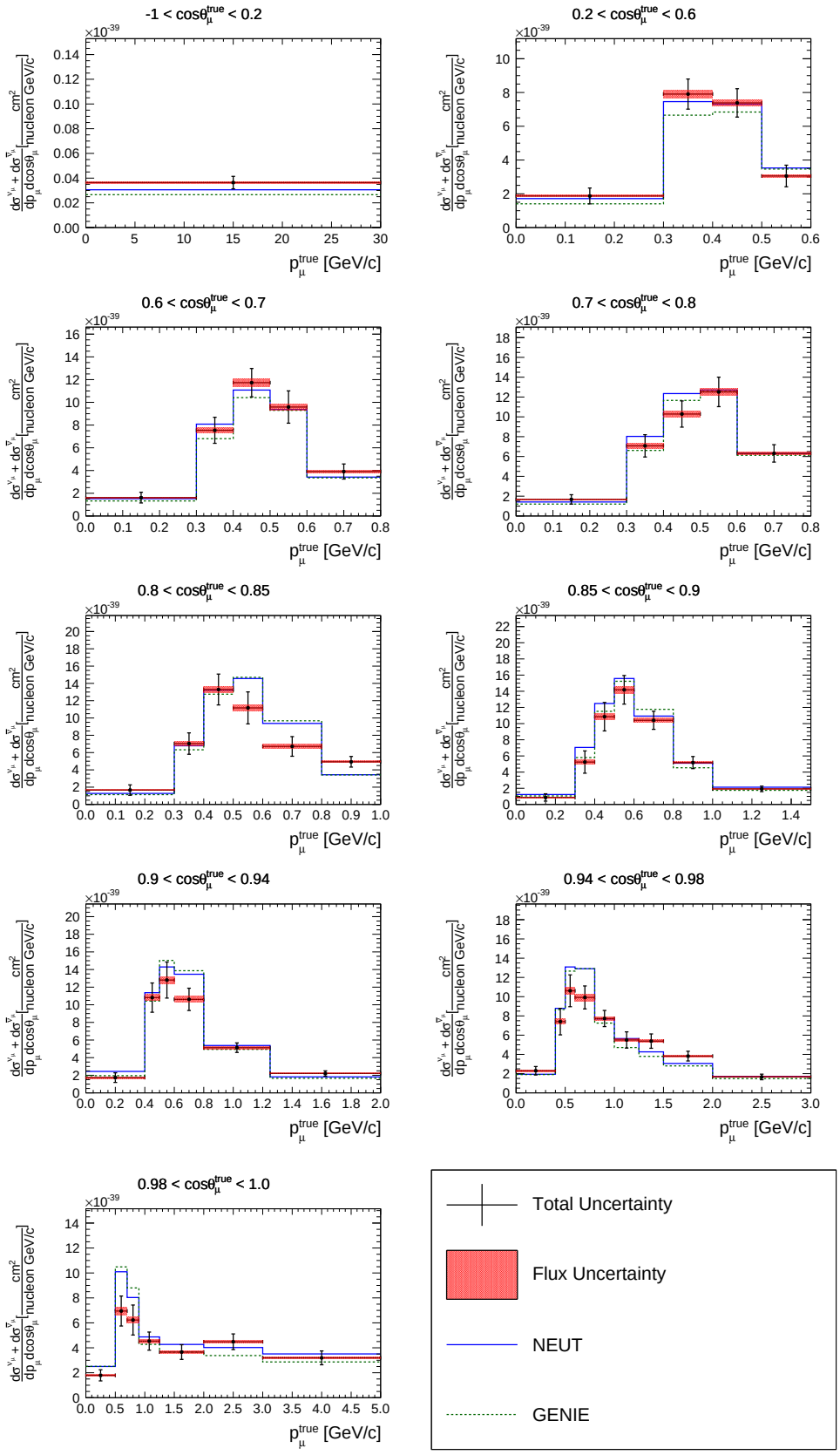

Figure 5.47. Measured cross sections sum in bins of true muon kinematics with shape uncertainty (error band) and fully correlated normalization uncertainty (red band). The result is compared with the CC-0π NEUT (blue line) and GENIE (dotted green line) prediction. The last bin, up to 30 GeV/c is not displayed.

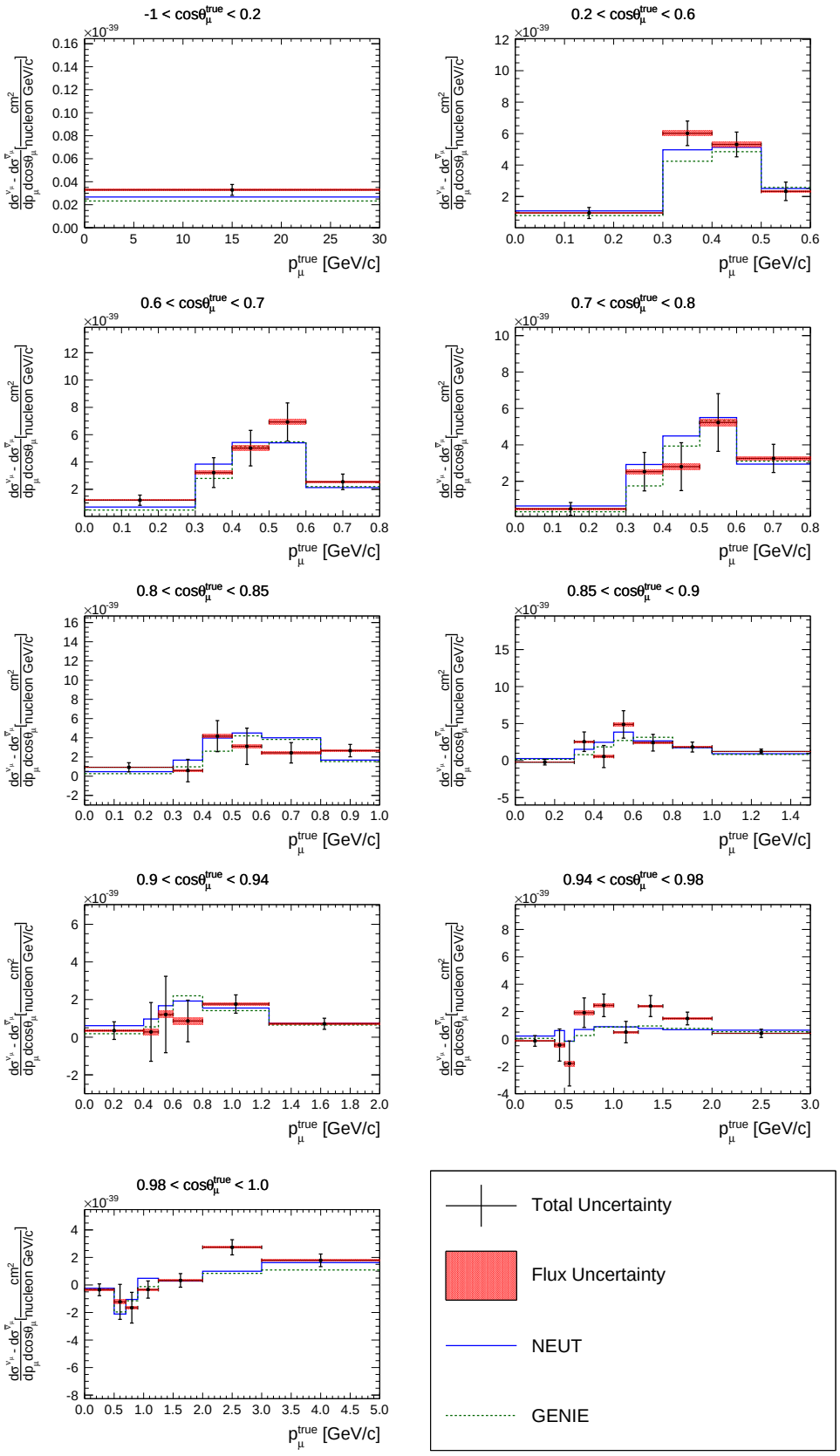

Figure 5.48. Measured cross sections difference in bins of true muon kinematics with shape uncertainty (error band) and fully correlated normalization uncertainty (red band). The result is compared with the CC-0π NEUT (blue line) and GENIE (dotted green line) prediction. The last bin, up to 30 GeV/c is not displayed.

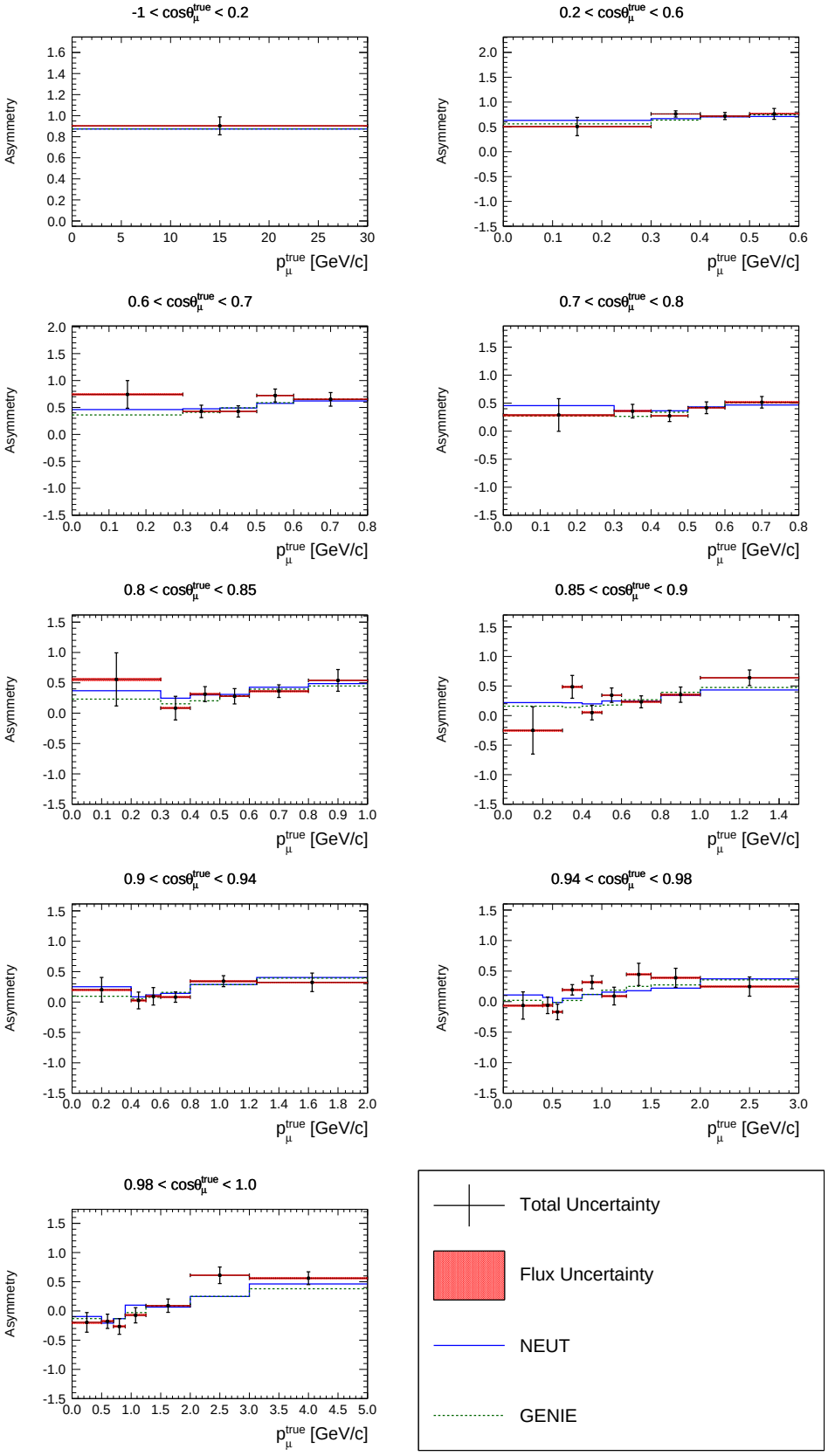

Figure 5.49. Measured cross sections asymmetry in bins of true muon kinematics with shape uncertainty (error band) and fully correlated normalization uncertainty (red band). The result is compared with the CC-0π NEUT (blue line) and GENIE (dotted green line) prediction. The last bin, up to 30 GeV/c is not displayed.

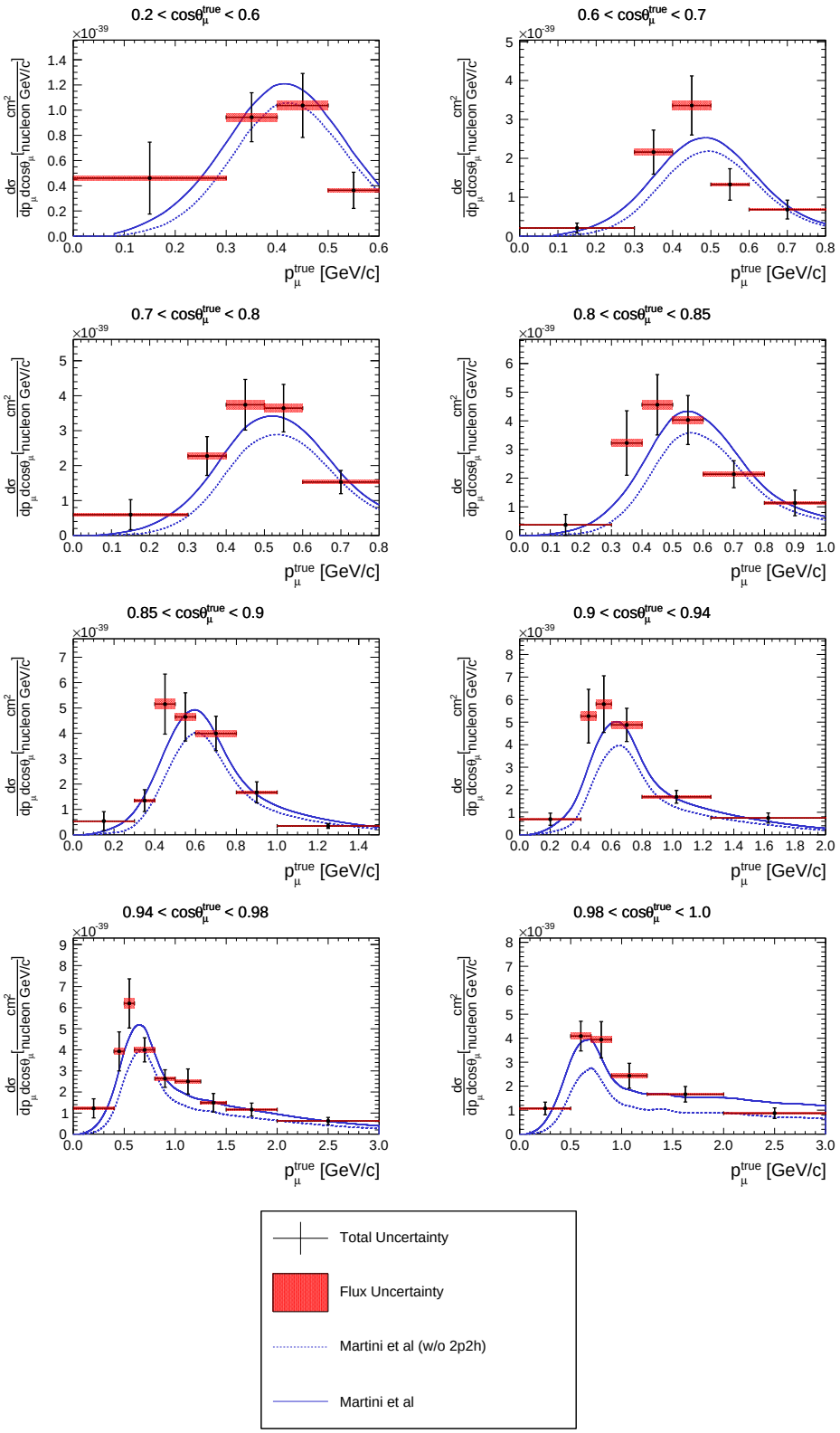

Figure 5.50. Measured $\bar{\nu}_\mu$ CC-0π cross section in bins of true muon kinematics with shape uncertainty (error band) and fully correlated normalization uncertainty (red band). The result is compared with the model by Martini et al. without (blue dotted line) and with 2p2h (solid line) prediction. The first angle bin ($-1 < \cos\theta < 0.2$) and the last bin, up to 30 GeV/c, are not displayed. In the last angle bin the momentum bin between 3.0 and 5.0 GeV/c is not displayed, since the Martini model predicts the cross section up to 3 GeV/c.

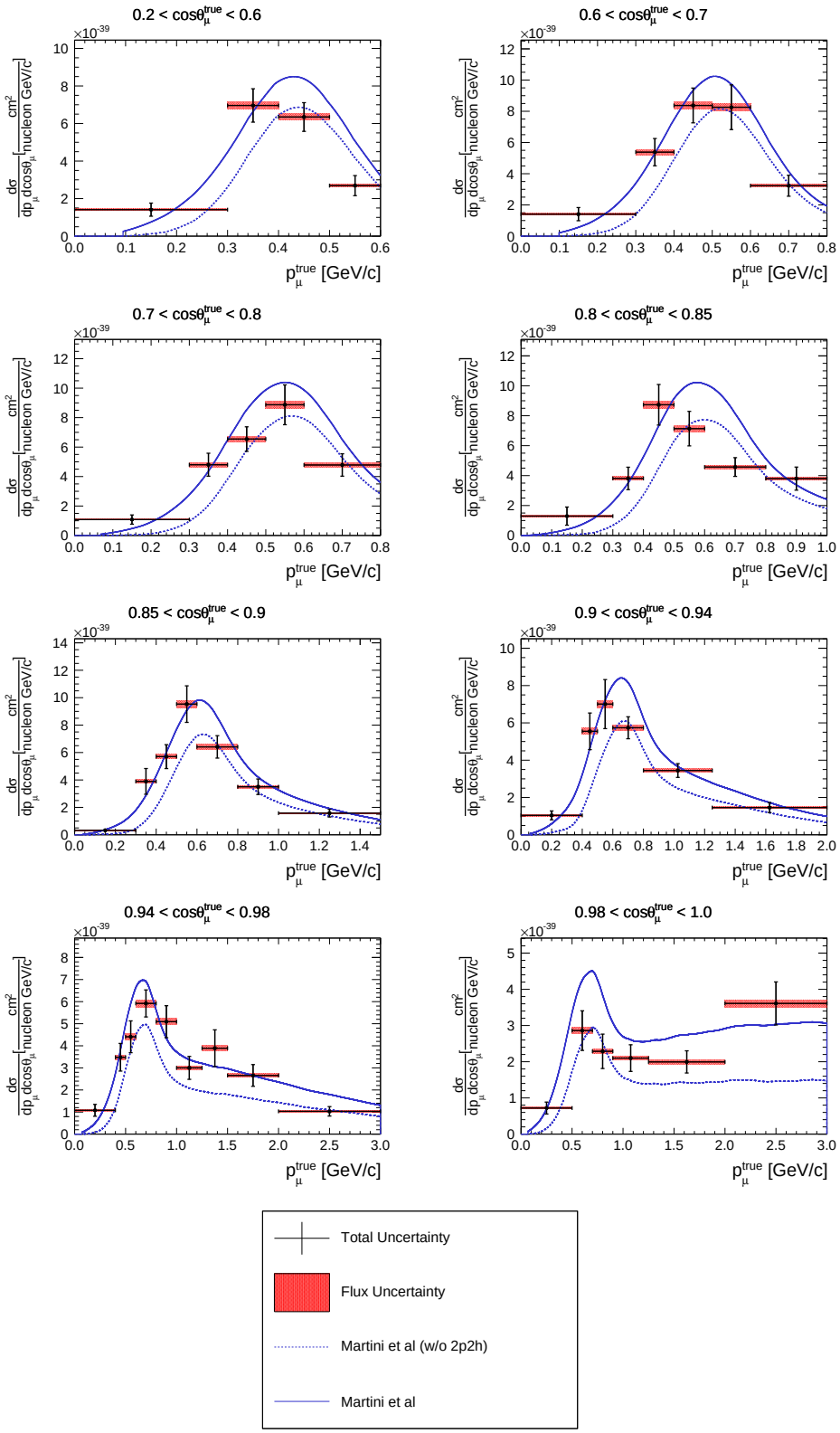

Figure 5.51. Measured ν_μ CC-0π cross section in bins of true muon kinematics with shape uncertainty (error band) and fully correlated normalization uncertainty (red band). The result is compared with the Martini model without (blue dotted line) and with 2p2h (solid line) prediction. The first angle bin ($-1 < \cos\theta < 0.2$) and the last bin, up to 30 GeV/c, are not displayed. In the last angle bin the momentum bin between 3.0 and 5.0 GeV/c is not displayed, since the Martini model predicts the cross section up to 3 GeV/c.

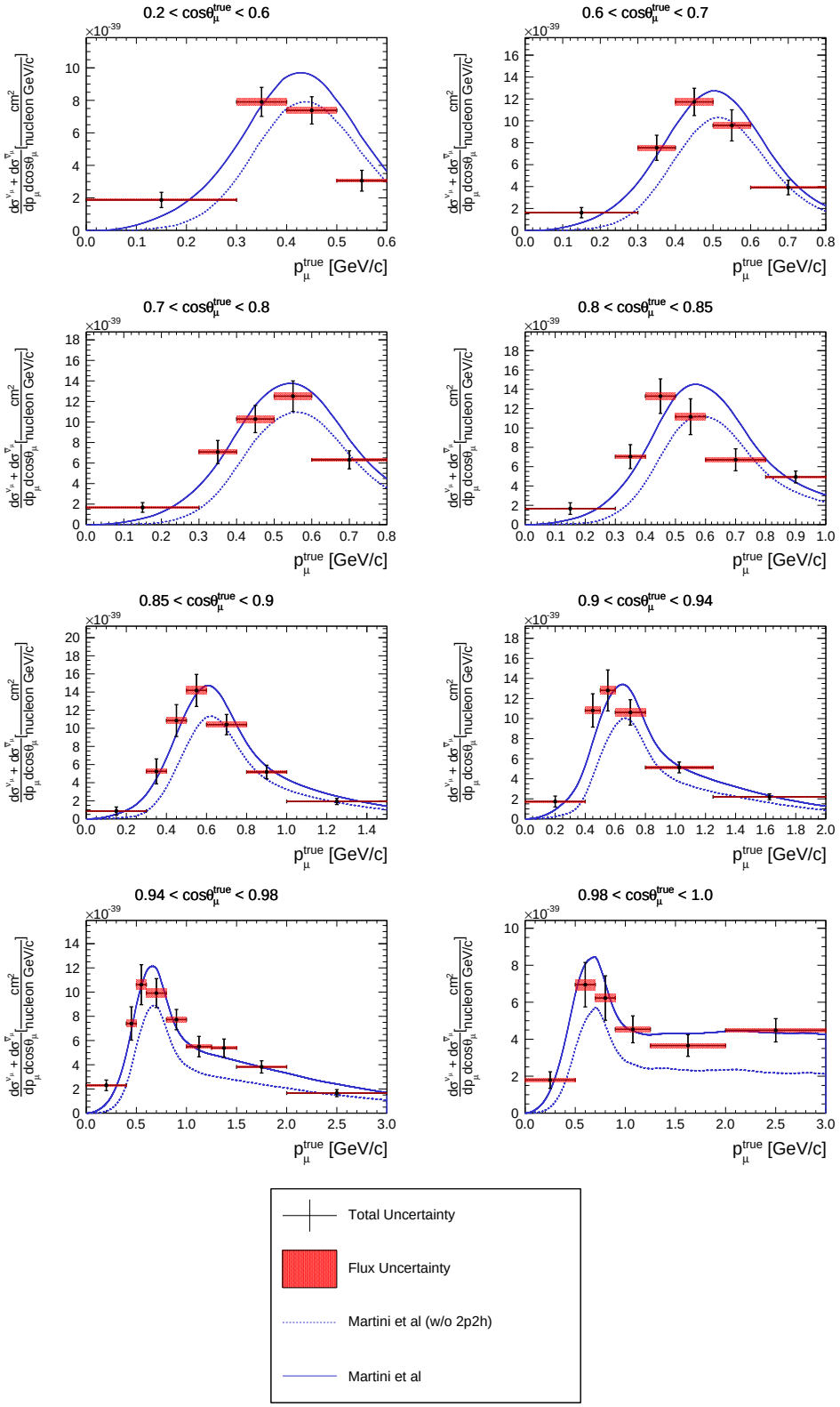

Figure 5.52. Measured cross sections sum in bins of true muon kinematics with shape uncertainty (error band) and fully correlated normalization uncertainty (red band). The result is compared with the Martini model without (blue dotted line) and with 2p2h (solid line) prediction. The first angle bin ($-1 < \cos\theta < 0.2$) and the last bin, up to 30 GeV/c, are not displayed. In the last angle bin the momentum bin between 3.0 and 5.0 GeV/c is not displayed, since the Martini model predicts the cross section momentum up to 3 GeV/c.

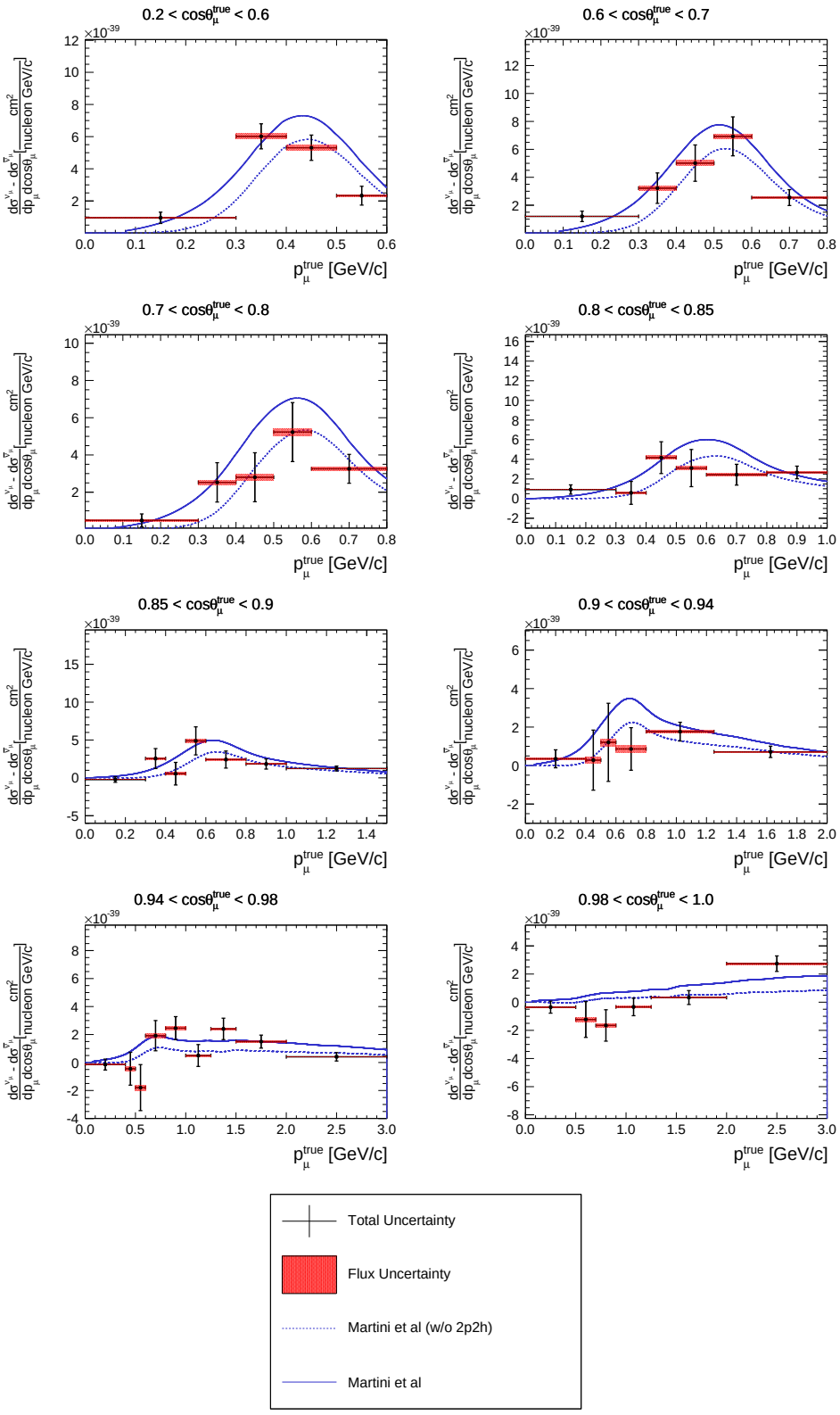

Figure 5.53. Measured cross sections difference in bins of true muon kinematics with shape uncertainty (error band) and fully correlated normalization uncertainty (red band). The result is compared with the Martini model without (blue dotted line) and with 2p2h (solid line) prediction. The first angle bin ($-1 < \cos\theta < 0.2$) and the last bin, up to 30 GeV/c, are not displayed. In the last angle bin the momentum bin between 3.0 and 5.0 GeV/c is not displayed, since the Martini model predicts the cross section up to 3 GeV/c.

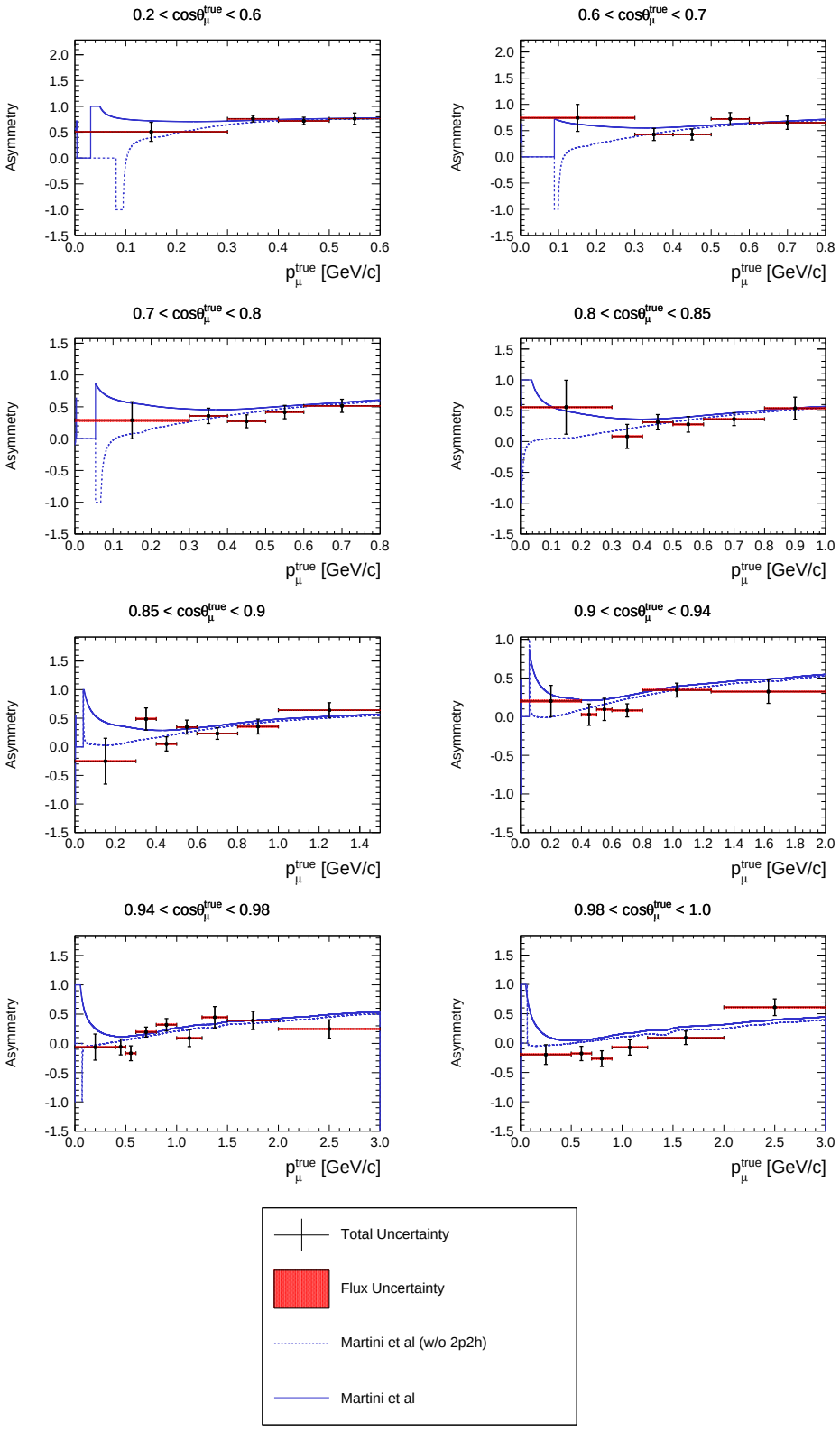

Figure 5.54. Measured cross sections asymmetry in bins of true muon kinematics with shape uncertainty (error band) and fully correlated normalization uncertainty (red band). The result is compared with the Martini model without (blue dotted line) and with 2p2h (solid line) prediction. The first angle bin ($-1 < \cos\theta < 0.2$) and the last bin, up to 30 GeV/c, are not displayed. In the last angle bin the momentum bin between 3.0 and 5.0 GeV/c is not displayed, since the Martini model predicts the cross section up to 3 GeV/c.

5.6 Conclusions and future outlook

In modern neutrino scattering and oscillation experiments, which use relatively heavy nuclear targets, CCQE cross-section measurements have been shown to contain significant contributions due to nuclear effects that are not well known and difficult to probe experimentally. In the current oscillation analyses these unknown effects introduce a not negligible uncertainty that must be reduced in order to measure the CP violation and the mass hierarchy.
The T2K off-axis beam, which has a peak energy of 0.6 GeV, could help to shed light on such nuclear effects. The measurements presented in this Chapter is a step forward compared to the ν_μ CC-0π cross section measurement discussed in Ref. [155]. In this analysis particular care has been taken in the inclusion of the backward and high angle tracks in the ν_μ and $\bar{\nu}_\mu$ events selection in order to enlarge the phase space. The proper correlation between the ν_μ and $\bar{\nu}_\mu$ samples allowed the reduction of the flux uncertainty to the level of 3% and to cancel it in the computation of the asymmetry. Furthermore, the measurements have been designed to be robust against the dependence on the signal model assumed in the analysis. The dominant uncertainty is the statistical, which vary from 60% in the bin where the statistic is very low, to about 10%. The detector systematics are the dominant uncertainty in most of the phase space, mainly in the high angle where the uncertainty is large since the detector resolution and efficiency is less known. The flux systematic is around few percent, and in some bins is higher than the detector uncertainty. The background modelling and the pion FSI are larger in the forward and high momentum region where most of the background is located, but they remain below 2%. The systematics on the efficiency due to signal modelling are of the order of few %. In conclusion the uncertainties are too large for any conclusive statement, but there is surely a lack of knowledge in the cross section modelling that must be addressed in the coming years. Furthermore these results can be compared with the different theoretical models giving a not negligible contribution in the comprehension of the underlying processes involved in neutrino-nucleus scattering. The next iteration of this analysis foresee the inclusion of the ν_μ and $\bar{\nu}_\mu$ interaction in FGD2, measuring simultaneously the ν_μ and $\bar{\nu}_\mu$ cross sections on water and carbon, giving the possibility to study the cross sections on different targets.

Chapter 6

Future perspectives: T2K-II and Hyper-Kamiokande

As discussed in the previous Chapters, the T2K experiment achieved world-leading results both on neutrino oscillation parameters and cross sections. The community born around the T2K experience is strongly active in the investigation of the future strategies. In particular the Collaboration proposed to extend the T2K run beyond 7.8×10^{21} POT, which is the current approved statistic, to 20×10^{21} POT, running until 2026. This extension will allow T2K to observe CP violation with more than 3σ significance if the oscillation parameters are close to their current values. The program also contemplate the measurement of θ_{23} and Δm^2_{32} with a precision of 1.7° and 1%, respectively [183]. To reach this goal the collaboration will upgrade the accelerator, the beamlines and the off-axis near detector. Furthermore, the addition of an intermediate water Čerenkov located ∼1-2 km far from the neutrino production point is under discussion. In 2026 is foreseen the beginning of the operation of Hyper-Kamiokande (HK). HK is the next generation large water Čerenkov detector, upgrade of SK. HK will serve as far detector of the accelerator-based neutrino program (Tokai to Hyper-Kamiokande, T2HK) allowing the observation of δ_{CP} with 5σ significance, and will also investigate a broad range of phenomena such as atmospheric neutrino oscillation studies, proton decay searches, and neutrino astrophysics with high sensitivities [100].
In this Chapter a brief overview of the second phase of T2K (T2K-II) and the HK project is given. The last part of this Chapter is dedicated to the description of the multi-PMT (mPMT) option proposed for both HK and the intermediate water Čerenkov detector. A mPMT is an optical module with about 26 PMT housed in a pressure vessel along with the read-out electronics. The mPMT can replace or be used in combination with the 20-inch PMTs increasing the granularity, the timing resolution and the safety, being the PMTs closed in a protective sphere.

6.1 T2K phase II

6.1.1 Beamline Upgrade

The J-PARC MR beam power has increased stably since the start of its operation in 2010. The power reaches 470 kW in April 2017, with 2.2×10^{14} protons-per-pulse (ppp) each 2.48 s. To achieve the design intensity of 750 kW, it is necessary a reduction of the repetition cycle to 1.3 s, possible with an upgrade of the power supplies for the MR main magnets, RF cavities, injection and extraction devices. Studies to increase the ppp are also in progress. In this scenario, the Collaboration expect to accumulate 20×10^{21} POT by 2026 as shown in Fig. 6.1.

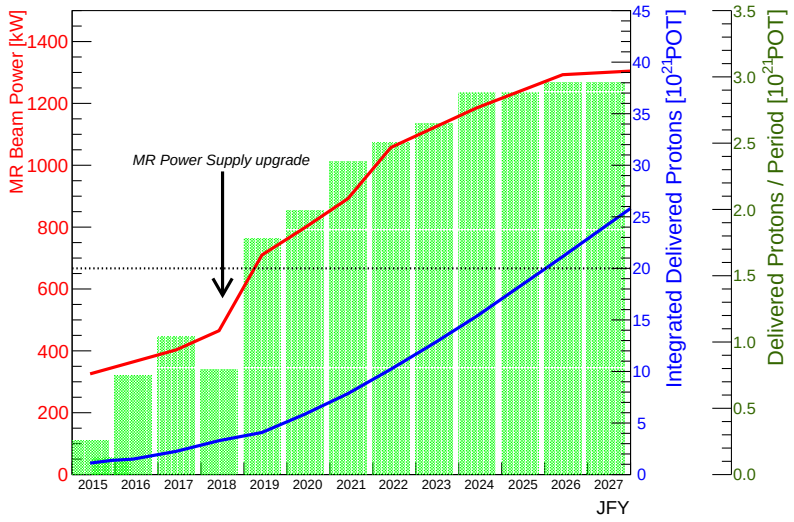

Figure 6.1. Beam power and POT accumulation plan as function of calendar year.

Based on these developments a further increase of the beam power up to 1.3 MW with 3.2×10^{14} ppp and a repetition cycle of 1.16 seconds is under study and will serve the next generation of LBL neutrino experiments in Japan.
Another important improvement will be the increase of the magnetic horn pulsed current from ±250 kA to ±320 kA. Horn operation at ±320 kA will give a 10% higher neutrino flux and will also reduce by 5-10% the $\bar{\nu}_\mu$ and ν_μ contamination in ν- and $\bar{\nu}$-mode respectively [183].

6.1.2 Near Detector plan

In Chap.4 has been shown the crucial rule of ND280 in controlling the systematic uncertainties in oscillation analysis. Therefore the reduction of the systematic uncertainties cannot disregard an upgrade of the current off-axis near detector which is currently limited by a lower angular acceptance than SK and by a low efficiency for low momentum protons. This last point in particular limits the discrimination between different neutrino-nucleus interaction models. In order to go beyond these limitations the reference design

currently under consideration is based on the replacement of the PØD with an horizontal target sandwiched by two new TPCs and, in turn, surrounded by scintillator layers which will be used as Time-of-Flight detectors, as shown in Fig. 6.2.

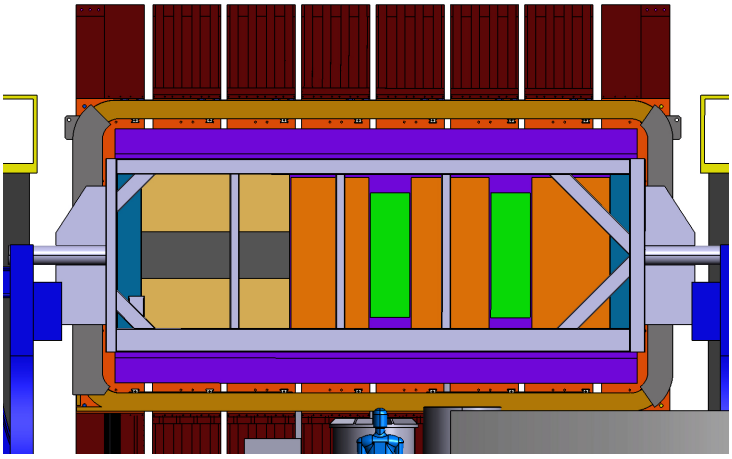

Figure 6.2. A schematic view of the upgraded ND280 detector. In place of the PØD there is a target sandwiched between two horizontal TPCs.

In this configuration the tracker region remain unchanged. For the new horizontal target it has been proposed a fully active fine grained detector with a 3D view, called SuperFGD and shown in Fig. 6.3, made of many optically independent $1{\times}1{\times}1\ cm^3$ cubes with readout on three orthogonal projections by wave-length shifting fibers [200].

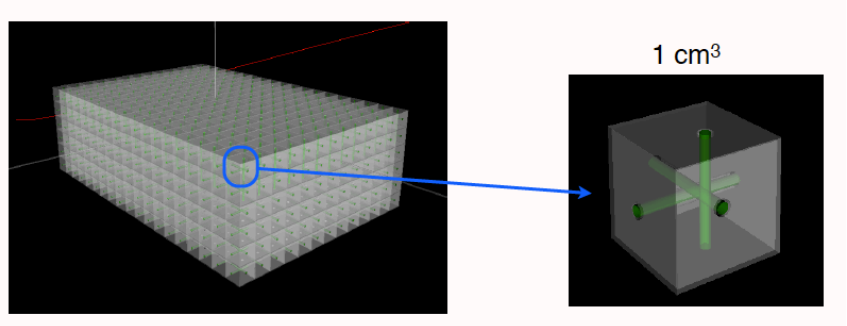

Figure 6.3. A schematic view of the SuperFGD.

The upgraded detector will keep the current Electromagnetic Calorimeter. Furthermore, in order to veto the events coming from the upstream part of the detector, the Upstream ECal of the PØD would be kept, providing in total a radiator of $\sim 5X_0$. In addition the Central ECal-P0D could also be used, providing $\sim 10X_0$. A MC simulation based on Geant4 [177] is under development to determine the best configuration. The

impact on the oscillation analysis of the larger angular acceptance and lower momentum threshold will be estimated using the same analysis framework used for the current analysis. As a second option, the concept based on a high pressure gas TPC is under investigation. This option will be able to achieve a low momentum threshold with a larger angular acceptance.

Another interesting development involve a new neutrino detector with a water target, WAGASCI (Water Grid And SCIntillator detector), which is under development to measure neutrino interactions with high precision and a large angular acceptance. It uses a 3D grid-like structure of scintillator bars, shown in Fig. 6.4, to track charged particles across the full 4π solid angle. A side muon range detector and magnetised detector will surround WAGASCI [201].

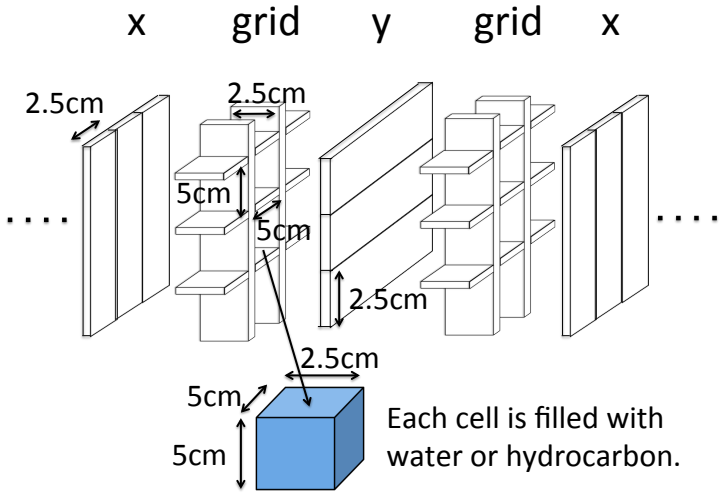

Figure 6.4. Schematic view of 3D grid-like structure of plastic scintillator bars inside the WAGASCI detector. Figure taken from [100].

The first step foresee the installation of WAGASCI in the near detector hall at J-PARC. By comparing the observed interaction rate in the two targets, the inclusive water to hydrocarbon charged current cross section ratio can be measured with better than 3% precision. This detector has been also taken into account as possible alternative to the SuperFGD.

An other challenging possibility under discussion is the addition of an intermediate water Čerenkov detector (IWCD) at ∼1-2 km. A WC near detector design should be large enough to contain muons up to the momentum of interest for measurements at the far detector and should be far enough from the neutrino production point such that there is minimal pile-up of interactions in the same beam timing bunch. The main features under discussion are:

- Realize a detector that spans an off-axis angle range of $1^\circ - 4^\circ$ to measure the final state leptonic over a wide range of neutrino spectra peaked at different energies.

Measurements at different off-axis angles can be used to address the limitation of different neutrino spectra at the near and far detectors.

- Load the water with Gd, allowing the measurement of neutron multiplicities in neutrino and antineutrino interactions. These measurements can be used for statistical separation of neutrino and antineutrino interactions as well as different interaction modes.

The intermediate distance of ∼1-2 km will allow the study of a flux much more similar to that at SK than at ND280, reducing the uncertainty in the flux extrapolation.
A first prototype of the detector will be located on the surface near the ND280 detectors at an off-axis angle of 6–12°. This surface detector is planned to start operation in 2021. In particular, the surface detector will give the opportunity to test the calibration, photosensor and Gd systems. The larger off-axis angle of the planned surface detector provides unique physics opportunities including pure electron neutrino samples, measurement of pion and kaon beam components and the possibility of a neutron multiplicity measurement. The tank will be filled with pure water and later with Gd-loaded water. The water tank will be divided into a inner detector (ID), which is cylinder of 6 m in height and $8m$ in diameter, and an outer detector (OD), which surrounds the ID with 1 m thick water layer. The photosensor technology for the prototype and the final detector will be the mPMT introduced by the KM3NeT collaboration [202]. The mPMT technology involves an array of small photosensors housed in a transparent pressure vessel along with readout electronics, calibration, and monitoring devices. Each mPMT modules encapsulate 19 inward facing and 7 outward facing 3-inch PMTs in order to look the ID and the OD.

6.1.3 T2K-II expected physics outcomes

Neutrino-nucleus cross section measurements

The future neutrino scattering program at the near detector complex involves a revisit of the published results which has a limited statistic and a new and interesting measurements.
One of these is the comparison between electron and muon neutrino cross section, which is a fundamental input to the measurements of the CP violation. The T2K electron neutrino differential cross-section, shown in Fig. 6.5, is characterized by a big statistical uncertainty in most of the bins [203]. The expected datasets achievable with the extended run of T2K-II foresee 8,000 ν_e CC and 2,000 $\bar{\nu}_e$ CC candidates, making feasible the comparison between electron and muon neutrino interactions with a good precision.

A fraction of the current ND280 is also composed of water, but also in this case the cross-section measurements on this target are statistically limited. Indeed the T2K CC-1π^+ cross section on water presented in Sec. 2.4 has a statistical error around 13%. The study of the neutrino interactions on water are crucial for the reduction of the systematic uncertainty on the oscillation analysis. Indeed a major contribution to the systematic error in the oscillation analysis is due to the different target materials of the near- and far-detectors.

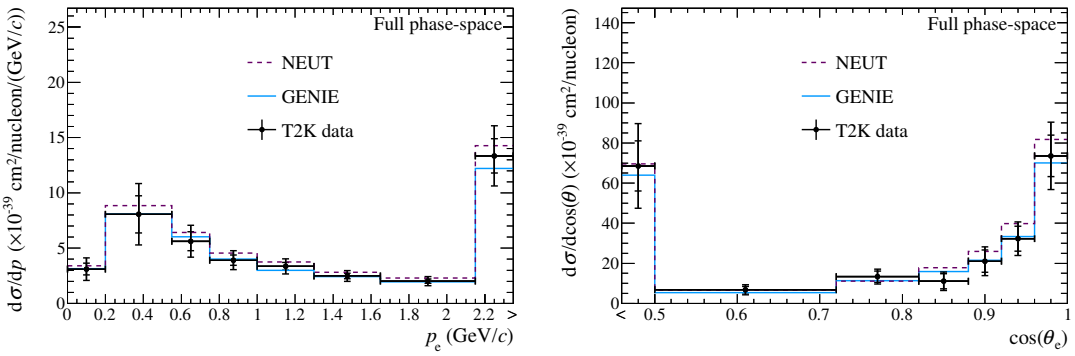

Figure 6.5. ν_e CC inclusive differential cross-sections as a function of p_e (left), $\cos\theta_e$ (right). The inner (outer) error bars show the statistical (total) uncertainty on the data. The dashed (solid) line shows the NEUT (GENIE) prediction. Overflow (underflow) bins are indicated by $>$ ($<$) labels, and are normalized to the width shown.

Further insight in understanding the nuclear effects will come from the measurement of the proton kinematics and multiplicity. T2K is actively pursuing these measurements, including the study of the energy deposited around the vertex, the usage of transverse kinematic imbalance [204, 205] and the measurement of event rates with two or more protons. In particular the number of expected events with at least two protons is limited by the available statistics, thus such a measurement will highly profit of T2K-II extended run.

Neutrino interactions in the argon gas of the TPCs is being analysed in T2K. This sample can provide unique information about proton multiplicity thanks to the very low tracking threshold of the proton in the gas of the TPC. Approximately 10,600 ν-Ar and 1,900 $\bar{\nu}$-Ar interactions are expected in T2K-II.

Strategy to reduce systematic uncertainties

The second phase of T2K will give not only the possibility to reduce the statistical error, but also to improve systematic errors that, otherwise, will limit the sensitivity to CP violation. The main source of systematic uncertainties at T2K come from the knowledge of the neutrino flux, the detector and neutrino interactions modelling.
The main reduction in the flux uncertainty will come from the use of NA61/SHINE measurements of the hadron production from a replica of the T2K target. This experiment has recently measured the pion production with initial replica target and has achieved $\sim 4\%$ precision on the measurement of $\pi^{\pm}$ spectra [206].

The largest detector modelling uncertainty at ND280 is the pion secondary interaction, which can be reduced by external measurements or by studying pion interactions within ND280 itself. Crucial to achieve this goal will be the data collected by the DUET experiment located at TRIUMF in Canada [207]. At SK, detector systematic errors are computed comparing the atmospheric neutrino data and cosmic ray muon control samples to the simulations. In future the SK detector uncertainties can be limited by the knowledge of atmospheric neutrino flux and cross-sections. To avoid this scenario an alternative method for estimating detector errors is under development. It is important to stress that

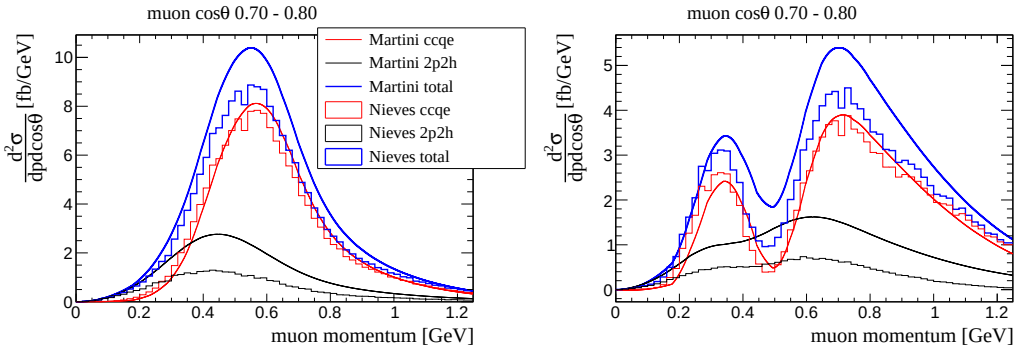

Figure 6.6. Distribution of CCQE and 2p2h contributions as a function of muon momentum in the angular range $\cos\theta = [0.7, 0.8]$ at ND280 (left) and Super-K (right) as predicted in the Martini (continuous line) and Nieves (histogram) models.

this type of uncertainty will benefit of the SK-Gd upgrade. Dissolving gadolinium sulfate into the water will improve SK ability to detect neutrons allowing a better separation of neutrino and antineutrino interactions.

There are several attempts to model neutrino-nucleus cross section by combining the neutrino-nucleon interaction correcting for the nuclear media. Anyway, the existing data on the neutrino-nucleon interaction is statistically limited. Therefore, to minimize the uncertainty it is crucial to use the neutrino-nucleus scattering data, both from the T2K and other recent experiments. These systematic uncertainties are dominated by various nuclear effects: short-range and long-range correlations and FSI. In the T2K oscillation analysis, the uncertainties in modelling these effects are constrained by the near detector, but such constraints are limited by the differences in the neutrino energy spectrum and the differences in acceptances between the near detector and SK. For instance, Fig. 6.6 shows the distribution of expected CCQE+2p2h events for $\cos\theta_\mu$ from 0.7 to 0.8 at the near and far detector for the Martini and Nieves model. The 2p2h component at ND280 is mainly an overall increase in the cross-section normalization, while at SK this component tend to bias the neutrino oscillated energy spectrum, filling the oscillation dip. There is moreover a large difference between the prediction of the two considered models which is an indication of the scale of the large uncertainties on the 2p2h modelling. In order to minimize such systematic a continuous effort to reduce the flux knowledge, enlarge the ND280 acceptance and introduce additional samples in the near detector fit has been engaged and will profit mainly of the ND280 upgrade plan.
Another important uncertainty is related to the difference between electron and muon neutrino cross-section. In the neutrino-quark interaction, the difference between the electron and muon mass has a small impact on the kinematics of the outgoing lepton: it changes the allowed value of Q^2 at fixed neutrino energy and it affects the radiative corrections to the interaction process. All these effects are calculable but uncertainties rise from their convolution with nucleon form factors and nuclear effects. An approximate calculation reported in Ref. [208] shows that the difference between ν_e and ν_μ cross-sections due to radiative corrections should be smaller than 10% (12%) for neutrino (antineutrino) at the relevant energies for T2K. The Collaboration is working to include ν_e and $\bar{\nu}_e$ samples in the near detector fit, but they are limited by statistics, thus T2K-II will certainly improve

the constraints on the ν_e cross section.

Expected sensitivity on oscillation parameters

The sensitivity studies presented here and detailed in Ref. [183], assume an equally divided exposure to neutrino and antineutrino beam. Sensitivities are calculated using the same event rates and systematics taken from the oscillation analysis reported in Chap. 4, and the effect of the statistical enhancements and systematic error reduction is implemented by a simple scaling of the event rates and covariance matrices. For the sensitivity study the value assumed for the oscillation parameters are: $\sin^2 2\theta_{13} = 0.085$, $\sin^2\theta_{23} = 0.5$, $\Delta m^2_{32} = 2.509 \times 10^{-3}$ eV^2, and normal mass hierarchy (MH). Cases in which $\sin^2\theta_{23}$ is at the edge of the 90% C.L. regions ($\sin^2\theta_{23} = 0.43,\ 0.60$) are studied as well. Furthermore the values of $\sin^2\theta_{23}$, Δm^2_{32}, and δ_{CP} are assumed to be constrained by T2K data only, while $\sin^2 2\theta_{13}$ is constrained by reactor measurements.
In Fig. 6.7 is shown a comparison of the sensitivity for resolving $\sin\delta_{CP} \neq 0$, with and without systematic errors, at various value of $\sin^2\theta_{23}$ plotted as a function of true δ_{CP} (the plot on the left) and versus the POT accumulated, for two cases: the approved T2K statistics (7.8×10^{21} POT) without an effective statistical improvement and the full T2K-II exposure (20×10^{21} POT). The fractional region for which $\sin\delta_{CP} = 0$ can be excluded at the 99% (3σ) C.L. is 49% (36%) of possible true values of δ_{CP} assuming the systematic errors are reduced to 2/3, while if it is assumed the present level of systematic errors the corresponding fractions are 42% (21%). The coverage fraction is slightly larger for the case of lower octant $\sin^2\theta_{23} = 0.43$ and slightly lower for the case of upper octant $\sin^2\theta_{23} = 0.60$.

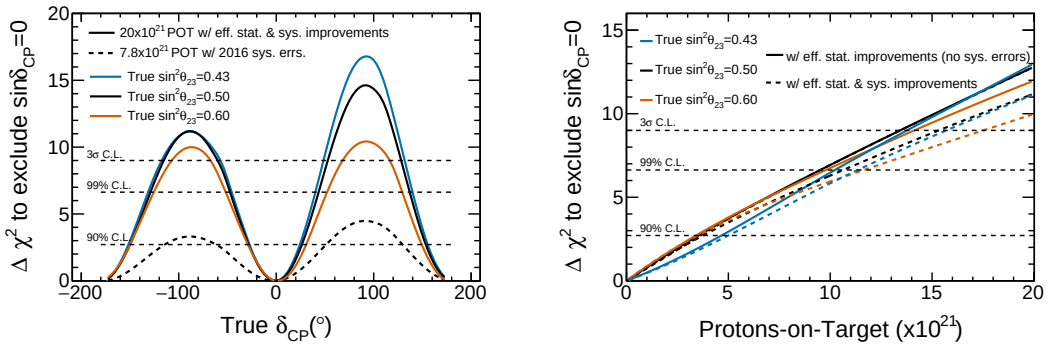

Figure 6.7. Sensitivity as a function of true δ_{CP} (left) and accumulated POT (right) with three values of $\sin^2\theta_{23}$ (0.43, 0.50, 0.60) and normal hierarchy. For the full T2K-II exposure of 20×10^{21} POT with a reduction of the systematic error to 2/3 of the present T2K uncertainties compared with the present sensitivity. Figure taken from [183].

In Fig. 6.8 is shown the expected 90% C.L. contour for Δm^2_{32} versus $\sin^2\theta_{23}$ for the full T2K-II exposure. The plots indicate that the octant degeneracy can be solved by more than 3σ if $\theta_{23} \geq 0.6$, or less if $\theta_{23} \leq 0.43$. If $\sin^2\theta_{23}$ is maximal, the expected 1σ precision of $\sin^2\theta_{23}$ is 1.7° for the case of $\sin^2\theta_{23} = 0.46$ (0.6), the uncertainty is 0.5° (0.7°). Finally Δm^2_{23} can be measured with an accuracy ∼1%.

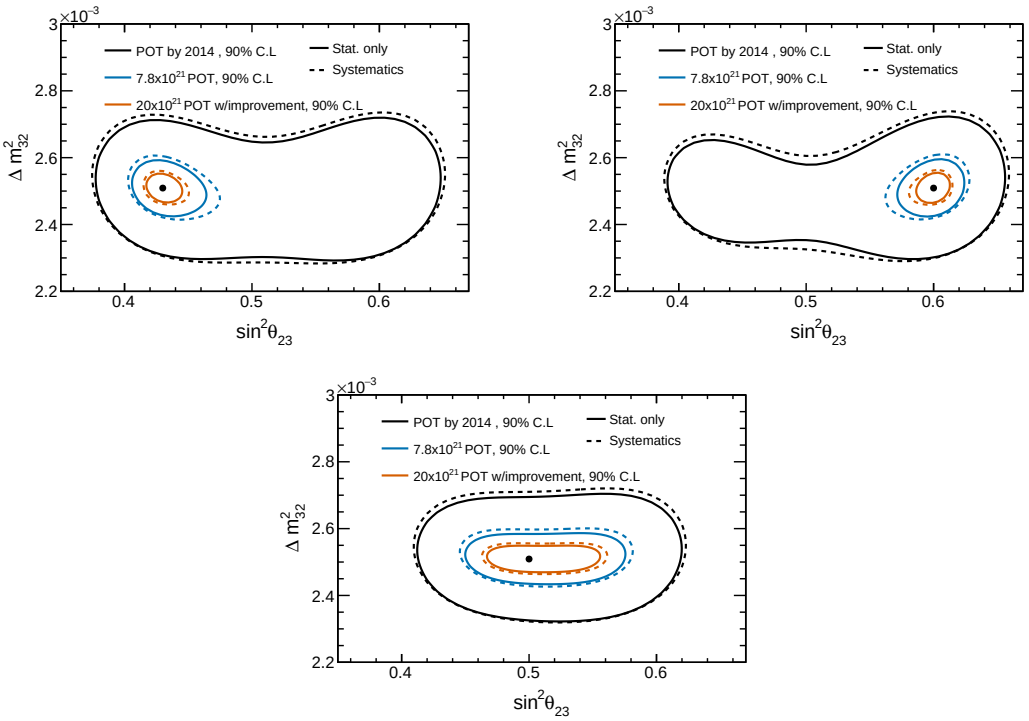

Figure 6.8. Expected 90% C.L. sensitivity to Δm^2_{32} and $\sin^2\theta_{23}$ with the current T2K systematic error. For the T2K-II exposure of 20×10^{21} POT, a 50% increase in effective statistics is assumed. Top left plot has been obtained with true $\sin^2\theta_{23} = 0.43$, top right with true $\sin^2\theta_{23} = 0.6$ and the plot on the bottom with true $\sin^2\theta_{23} = 0.5$. Figure taken from [183].

6.2 Hyper-Kamiokande

HK is a next generation underground water Čerenkov detector based on the successful SK. The detector performance will be further enhanced by an order of magnitude larger fiducial mass and higher performance photodetectors. It will have a rich physics program with high sensitivity to neutrino oscillation studies, neutrino astrophysics and proton decay searches. Assuming the construction to start in 2024, the data taking is expected to start from 2026. The current baseline design include one cylindrical detector of 60 m height and 74 m diameter, as reported in Fig. 6.9. The total (fiducial) mass of water will be 260 (190) $kton$. The proposed location for HK is about 8 km south of SK and 1,750 m water equivalent deep [100]. Recently, the HK working group start to discuss the possibility of building another tank in Korea [209].

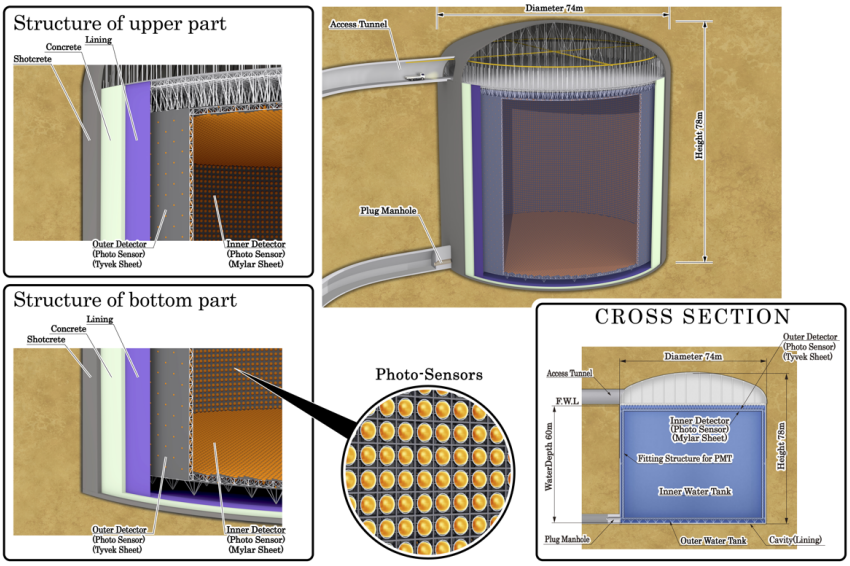

Figure 6.9. Schematic view of one HK detector. Figure take from [100].

Tab. XXX summarizes the parameters of HK compared with other previous and currently operating WC detectors. The detector mass is one of the key parameters that determines the event statistics in neutrino observations and nucleon decay searches. The detector will be filled with highly transparent purified water. A light attenuation length above 100 m can be achieved which allows to detect a large fraction of the Čerenkov light emitted near to the water volume. Radon concentration in the supplied water should be kept below 1 mBq/m^3 to control the radioactive background event rate in solar neutrino and other low energy observation. An option being investigated is to dope the water with Gd.

HK will employ newly developed high-efficiency and high-resolution PMTs which would improve the identification of neutrino interactions and proton decays. In the baseline design, the inner detector region will be instrumented with 40,000 50 cm PMTs, accounting for a 40% photo-cathode coverage, while the outer detector will be equipped with 6,700 20 cm PMTs. The photo-sensors will be located as much as 60 m underwater in the HK cavern. At this depth, the applied pressure is close to the manufacturers upper specification of the SK PMT (0.65 MPa), therefore has been developed a new vacuum

	KamiokaNDE-II	SK-IV	HK
Depth	1,000 m	1,000 m	650 m
Dimensions of water tank			
diameter	15.6 m ϕ	39 m ϕ	74 m ϕ
height	16 m	42 m	60 m
Total volume	4.5 kton	50 kton	258 kton
Fiducial volume	0.68 kton	22.5 kton	187 kton
Outer detector thickness	$\sim$ 1.5 m	$\sim$ 2 m	1 $\sim$ 2 m
Number of PMTs			
inner detector (ID)	948 (50 cm ϕ)	11,129 (50 cm ϕ)	40,000 (50 cm ϕ)
outer detector (OD)	123 (50 cm ϕ)	1,885 (20 cm ϕ)	6,700 (20 cm ϕ)
Photo-sensitive coverage	20%	40%	40%
Single-photon detection efficiency of ID PMT	unknown	12%	24%
Single-photon timing resolution of ID PMT	$\sim$ 4 nsec	2-3 nsec	1 nsec

TABLE XXX. Parameters of past (KamiokaNDE), running (SK), and future (HK) water Čerenkov detectors. Table taken form [100].

glass bulb for the PMT. Furthermore, plastic coverage will envelop each photo-sensors to avoid a potential chain reaction implosion of the glass bulb in the water. The characteristics of the baseline option are reported in Tab. XXX. Other options for the photosensors are under discussion. One of those is the mPMT optical module that will be discussed in Sec. 6.4.

6.3 Physics capabilities

The LBL program

A long baseline neutrino oscillation experiment with the J-PARC neutrino beam, called T2HK, is one of the key elements of HK physics program. In particular a precise study of CP asymmetry in the leptonic sector is one of the major goals of HK. It can also determine the mass hierarchy using atmospheric neutrinos. The sensitivities for CP violation and mass hierarchy can be further enhanced by combining accelerator and atmospheric neutrino measurements. The main goals of T2HK experiment are the measurements of $|\Delta m^2_{32}|$, $\sin^2\theta_{23}$, $\sin^2\theta_{13}$ and δ_{CP}. Precision measurements of oscillation parameters require both large statistics and well controlled systematics. Combining an intense and high quality neutrino beam from J-PARC, the huge mass and high performance of HK detector, a highly capable near/intermediate detector complex, T2HK will be the best project to probe the CP violation and new physics with neutrino oscillation.

The sensitivity study presented here is performed using the analysis framework developed within the T2K experiment [210, 211]: a binned likelihood analysis based on the

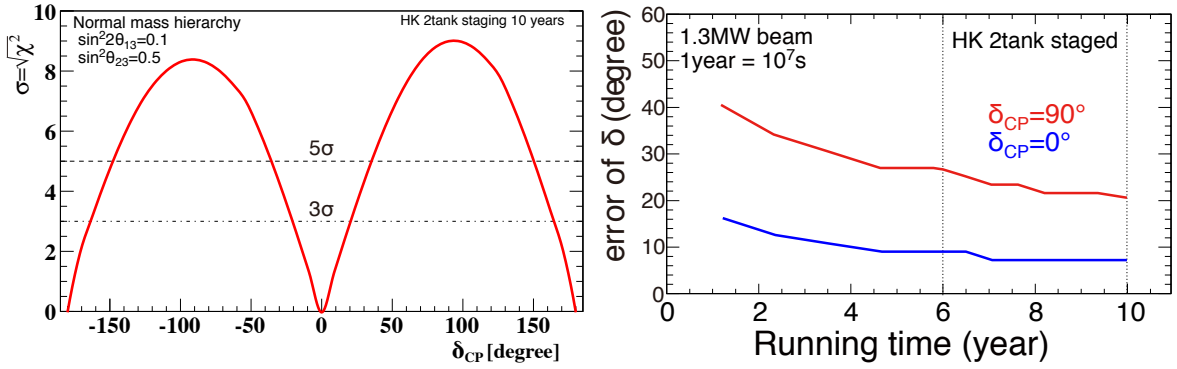

Figure 6.10. Sensitivity to exclude $\sin\delta_{CP} = 0$ for normal mass hierarchy (left) and expected 68% C.L. uncertainty of δ_{CP} as a function of running time.

reconstructed neutrino energy distribution is performed using both ν_e ($\bar{\nu}$) appearance and ν_μ ($\bar{\nu}_\mu$) disappearance samples simultaneously. Parameters to be determined with the fit are $\sin^2\theta_{13}$, $\sin^2\theta_{23}$, Δm^2_{32} and δ_{CP}. The systematic uncertainty is estimated based on the experience of T2K, with an extrapolation based on the possible improvement expected in HK era.
In Fig. 6.10, the plot on the left shows the expected significance to exclude $\sin\delta_{CP} = 0$. CP violation in the leptonic sector can be observed with more than 3 (5) σ significance for 78 (62)% of the possible values of δ_{CP}. The plot on the right shows the 68% C.L. uncertainty of δ_{CP} as a function of the year of running. The value of δ_{CP} can be determined with an uncertainty of 7.2° for $\delta_{CP} = 0°$ or 180°, and 21° for $\delta_{CP} = \pm 90°$. A joint fit performed using both ν_e appearance and ν_μ disappearance channels will enable the precise measurements of $\sin^2\theta_{23}$ and Δm^2_{32}. Expected 1σ uncertainty of $\sin^2\theta_{23}$ is 0.015 (0.006) for $\sin^2\theta_{23} = 0.5(0.45)$. The uncertainty of Δm^2_{32} is expected to reach 0.6%, while measurements by future reactor experiments are expected to achieve $< 1\%$ precision.

An alternative configuration of the T2HK experiment foresee a second HK detector in Korea, placed ∼1100 - 1300 km far from the beam target. Two detectors at different baselines improves sensitivity to leptonic CP violation, neutrino mass ordering as well as non standard neutrino interactions. There are several candidate sites in Korea at 1-3 degree off-axis angle. Thanks to larger overburden of the candidate sites in Korea, low energy physics is expected to be improved [209].

Atmospheric neutrinos

HK will have an excellent sensitivity in constraining atmospheric mixing parameters. It offers two distinct advantages: first, with its ability to distinguish between charged current ν_e and ν_μ interactions it will have improved access to the oscillation modes, $\nu_\mu \to \nu_e$ and $\bar{\nu}_\mu \to \bar{\nu}_e$. Additionally, HK will make combined beam and atmospheric neutrino oscillation measurements to yield increased sensitivity.
The measurement with atmospheric neutrino alone is expected to resolve the mass hierarchy at more than 3σ assuming both hierarchy and when $\sin^2\theta_{23} > 0.45$ after 10 years of data taking. Furthermore, the combination of the data collected by the LBL program and the atmospheric neutrinos data will enhance the sensitivity. The expected results of

such combination are reported in Fig. 6.11. On the left is shown the sensitivity for mass hierarchy while on the right for the θ_{23} octant. The mass hierarchy can be determined with more than 3(5) σ with five (ten) years of data, and the octant of θ_{23} can be resolved in ten years if $|\theta_{23} - 45| > 2.5°$.

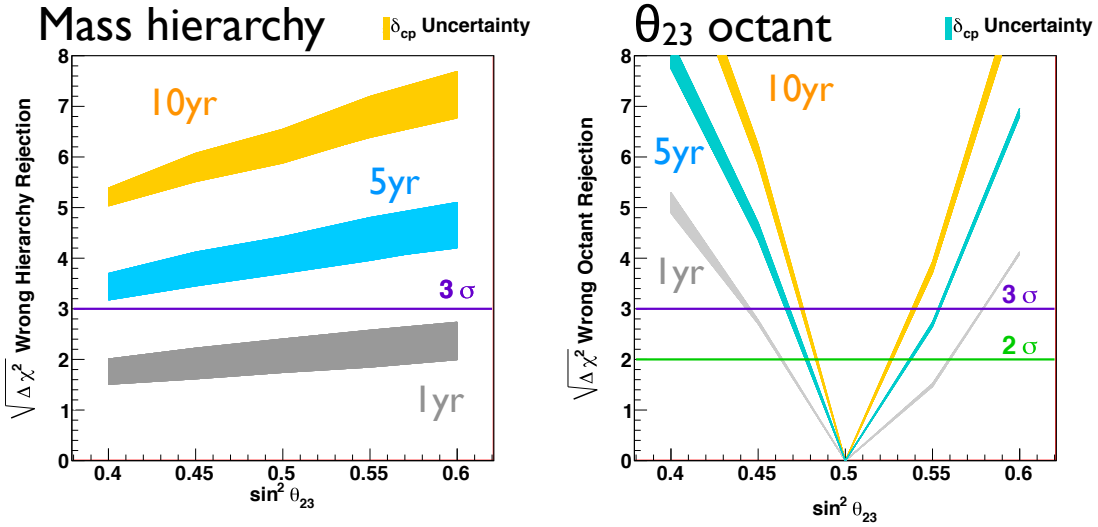

Figure 6.11. Neutrino oscillation sensitivities from combined analysis of atmospheric neutrino and accelerator data at HK. The left (middle) panel illustrates the expected hierarchy (octant) sensitivity as a function of true value of $\sin^2\theta_{23}$ for three exposures: 1 year (grey), 5 years (blue), 10 years (orange). Figure taken from [100].

Atmospheric neutrino can study additional topics, such as ν_τ cross section measurement, search for sterile neutrino, and the test of Lorentz invariance. It will also provide information on the chemical composition of Earth's outer core using matter effect, contributing to geophysics.

Solar and supernova neutrinos

The huge target mass will improve also the sensitivity to astrophysical neutrinos, i.e. solar neutrinos, supernova burst neutrinos and supernova relic neutrinos.
Solar neutrino research will test the results of the day-night asymmetry. It can be measured with larger statistics shedding light on the 2σ tension in Δm^2_{21} between solar neutrino measurements and KamLAND discussed in Ref. [55]. Moreover, many precise measurements of solar neutrino would also be possible. HK could be used for variability analyses of the Sun. Thanks to its unprecedented statistical power, could be possible to measure the solar neutrino flux over short time periods, enabling the possibility to monitor the time variability of the temperature in the solar core. The expected threshold for HK will be 4.5 MeV with a vertex resolution of 3.0 m, which could be better for higher energy events.
HK could be used to alert a supernova burst for other supernova observation experiments with its high directional sensitivity. The multi-messenger observation of supernova with neutrinos, visible light, gamma-ray, x-ray and gravitational waves will also reveal the supernova explosion system in details. Another observation is the supernova relic neutrinos

(SNR), produced by all the past supernova explosions since the beginning of the universe. SNR could provide informations of the star formation rate, energy spectrum of supernova burst neutrinos, and black hole formations.

Proton decay

The optimization for the observation and discovery of a nucleon decay signal is one of the primary design drivers of HK. In order to significantly improve sensitivity beyond SK limits, HK needs both a much larger number of nucleons and excellent reconstruction ability to extract signals and suppress backgrounds. One of the strengths of water Čerenkov detectors is their sensitivity to a wide variety of modes. Using MC and analysis techniques developed for SK, has been studied the sensitivity of HK to both the dominant proton decay modes, $p \to e^+\pi^0$ and $p \to \overline{\nu}K^+$, as well as other $\Delta(B-L)$ conserving, $\Delta B = 2$ dinucleon decays, and $\Delta(B-L) = 2$ decays [100].
Proton decay into a positron and neutral pion, $p \to e^+\pi^0$, is a dominant decay mode in many GUT models. It also has a very clean experimental signature in a water Čerenkov. After decades of search, the sensitivity is improving not only with advancement of detector technology, but also in analysis technique. An example is the background suppression with the neutron tagging. In proton decay, the probability of neutron emission is small, while in the events induced by atmospheric neutrino neutrons are often produced. Therefore, neutron tagging can provide an additional handle to suppress the background for the proton decay search improving the sensitivity. The ability to tag the 2.2 MeV photon from neutron capture on hydrogen, $n + p \to d + \gamma$, has been already demonstrated by the proton decay searches with SK-IV [212]. HK will have a better efficiency that SK for the low energy photons thanks to the higher photon detection efficiency. From the expected number of hits for 2.2 MeV γ ray, the neutron tagging efficiency in HK is assumed to be 70%. Gd doping is also under investigation as an option to further improve the neutron tagging efficiency.
Proton decay into an antineutrino and a charged kaon, $p \to \bar{\nu}K^+$, is another dominant mode. In a water Čerenkov detector, because of the Čerenkov threshold, K^+ from proton decay is not directly visible, but can be identified from its decay products. For $K^+ \to \mu^+ + \nu$, in addition to the muon, nuclear de-excitation γ ray can be used to tag the signal. Better timing resolution and detection efficiency of the new photosensor will lead to an improved efficiency of low energy γ rays. For $K^+ \to \pi^+ + \pi^0$, the π^+ has a momentum just above the Čerenkov threshold and emits only faint light. With better photon detection efficiency, also the detection of π^+ will be improved.

6.4 Multi-PMT optical module

The concept of an optical module made of a glass pressure vessel with a PMT housed inside has been developed in the last decades for neutrino telescopes in water and ice as DUMAND [213], Baikal [214], NESTOR [215, 216], ANTARES [217, 218], AMANDA [219] and IceCube [220]. In KM3NeT [221], the neutrino telescope under construction in the Mediterranean sea, a single large area phototube has been replaced by 31 7.7 cm PMTs collected in the same glass pressure vessel. The Multi-PMT (mPMT) has several advantages:

Increased granularity. This characteristic provides enhanced event reconstruction, in particular for multi-ring events, such as in proton decays and multi-GeV neutrinos which is important for mass hierarchy studies, and for events near the wall where fiducial volume is defined. Since each of the PMTs have different orientations with limited field of views, the mPMT carries information on the direction of each detected photon. This directional information effectively reduces the dark hit rate improving signal-to-noise separation for low energy events such as solar and supernova neutrinos and the neutron tagging.

Mechanically safe pressure vessel. The absence of space in the module reduces the possibility of shock waves even if an implosion takes place. Furthermore the pressure vessel contains digitization electronics and calibration sources.

Timing resolution. Better timing resolution could further reduce the dark hit background and event reconstruction.

Moreover the failure rate of small PMTs is of the order of 10^{-4}/year. Any loss of a single PMT would affect the detector performance minimally compared to the loss of one large area PMT. The design of the mPMT system both for HK and IWCD is under study. In this section will be given a general overview of the mPMT optical module and the prototype activities will be described as well.

6.4.1 The Multi-PMT Reference Design

As a reference design, has been considered a 50 *cm* size vessel. In HK, this is the same size of baseline option, so that the same mechanical support structure can be used. This would allow part of the photocathode coverage to be replaced by mPMT. Fig. 6.12 shows the 50 *cm* diameter mPMT design proposed. There are 19 7.7 *cm* PMTs looking inner detector side and 6 7.7 *cm* PMTs looking outer detector side. The 7.7 *cm* PMTs will be supported by a 3D printed structure, optically and mechanically coupled by Silicon Gel to an acrylic sphere. Reflector rings are added to each 7.7 *cm* PMT to increase the effective photocathode area by about 30%, resulting in about half of the effective photocathode area as a single 50 *cm* PMT. For the low energy events such as neutron tagging, the number of detected photons will be reduced by a factor of two, which can be compensated by the reduction of the effective dark hit rate. A back-of-the-envelope calculation shows that the neutron tagging efficiency would be similar or better than all 50 *cm* PMT, although more detailed simulation studies are required.

In a first stage, two main candidates for 7.7 *cm* PMTs, developed specifically for KM3NeT, have been considered: the Hamamatsu R12199-02 and the ET Enterprises D792KFL/9320KFL. These PMTs have been tested in detail by the KM3NeT Collaboration [222–224], resulting in a high quantum efficiency of $\sim 27\%$ at 404 *nm*, a collection efficiency more than 90%, transit time spread of about 4 *ns* at FWHM[1] and the dark rate of 200–300 *Hz*. Recently, Hamamatsu improved the transit time spread of R12199 down to 1.3 ns. In addition to Hamamatsu and ET Enterprises PMT's, HZC XP72B20 is currently reducing the dark rate and becomes a candidate. HZC has a mass production

[1]The full width half maximum is the width of a distribution corresponding to the point at which the distribution reaches half of its maximum value.

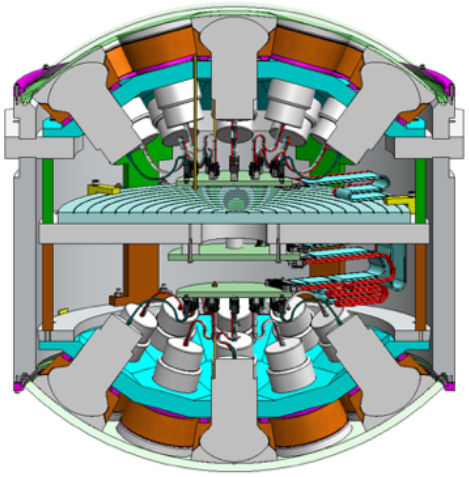

Figure 6.12. Multi-PMT conceptual drawing for IWCD with 7.7 *cm* PMTs as ID detectors and the OD detectors on the other half. Each small PMT has a reflector cone. An 50 *cm* acrylic covers on an aluminium cylinder is used as pressure vessel. Readout electronics and calibration sources are placed inside the vessel.

capability and potentiality to provide significantly lower cost. All these options are under study by the Collaboration.
The front-end electronics will be situated inside the modules. In this way it will be protected against the water pressure and infiltration. The high voltage generation for each PMT can be done on a board attached to the PMT base. Only one water-proof cable for both communication, low voltage and signal can then be connected to the whole module through a penetrator, as done in previous deep water neutrino experiments.

6.4.2 The mPMT Prototype

The design of the KM3NeT mPMT module is restricted by the size of commercially available pressure vessels. This experiment uses borosilicate glass spheres with a diameter of 33.3 *cm* and 43.5 *cm*. The glass contains radioactive contaminant emitting Rn, which is not a problem for KM3NeT where the radioactive background rate is limited by ^{40}K in the sea water. A good alternative for the future neutrino program in Japan, also in term of cost, is given by acrylics. Moreover, in KM3NeT the time over threshold (ToT) strategy has been exploited for the PMT read-out, but this is not a good solution for HK and the IWCD, since the charge must be measured.
A first prototype of a mPMT for the future experiments is under construction to demonstrate the effectiveness of a vessel system based on acrylic and to study a better solution for the PMT read-out system. Other prototypes will be built and tested when the final design of the mPMT will be defined on the basis of the optimization studies. In the following the activities on the acrylic vessel and read-out electronics, ongoing at the Instituto Nazionale di Fisica Nucleare (INFN) of Napoli laboratories, for the realization of the prototype are discussed.

The acrylic vessel. Several tests has been performed to identify the best acrylic, including optical, mechanical and thermal tests. Since the Čerenkov emission is char-

acterized by a high number of photons in the low wave-length region, from the optical point of view, the best material have to be transparent as much as possible in the ultraviolet range (UV). The UV transparency has been measured for several commercial acrylics. For some samples, the light transmittance of the acrylic has been measured also in water, resulting to be greater than 95% for a wavelength longer than 350 nm. In Fig. 6.13 the measurement of the reflectance and the transmittance of several acrylics are shown. Also optical test of the acrylic and the silicon gel used for the optical and mechanical coupling has been performed showing a good transparency.

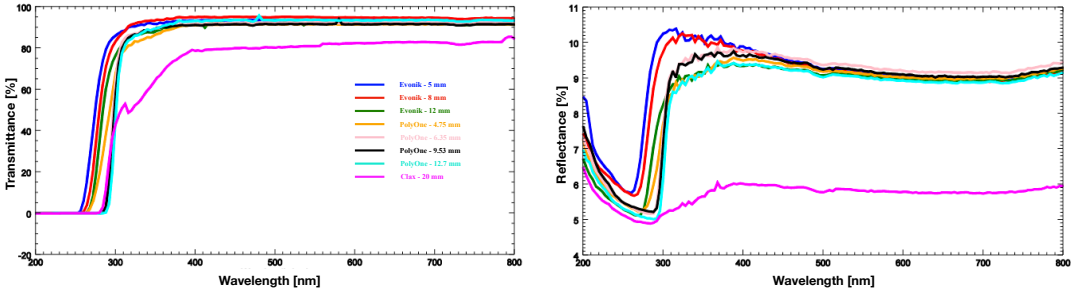

Figure 6.13. Transmittance (left) and reflectance (right) as function of the wavelength for different acrylics.

Since the pressure vessel will be realized starting from two acrylic hemispheres, they might be glued by using a specific glue for acrylics. Tests performed showed that the glue itself emit light, producing more background events for low-energy physics. A possible solution is to use the mechanical system showed in Fig. 6.14. This choice avoid fluorescence emissions, guarantees a longer endurance and simplify both the anchorage to the tank frame and the implementation of the cooling system of the mPMT.

Currently, only EVONIK UV transmitting plexiglas [2] respects the requirements and has been chosen. Anyway, pressure tests, water absorption and radioactivity contamination measurements are still needed and are planned in the near future. The pressure test foreseen the study of three vessel with thickness of 12, 15 and 18 mm. The water absorption measurement will be based on Nuclear Reaction Analysis and the radioactivity contamination measurement on the gamma spectroscopy.

mPMT electronics. A basic Cockcroft-Walton (CW) voltage multiplier circuit based on the design developed by the KM3NeT Collaboration [225] will be used to generate multiple voltages to drive the dynodes of the PMT. The CW developed at INFN of Napoli laboratories has a power consumption of 2-3 mW, well in agreement with the project requirements. The system draws less than 1.5 mA of supply current at a voltage of 3.3 V with outputs up to -1400 V_{dc}. For the readout of the PMT two options are under investigation: an integrated read-out chip and a discrete

[2] http://www.plexiglas.net

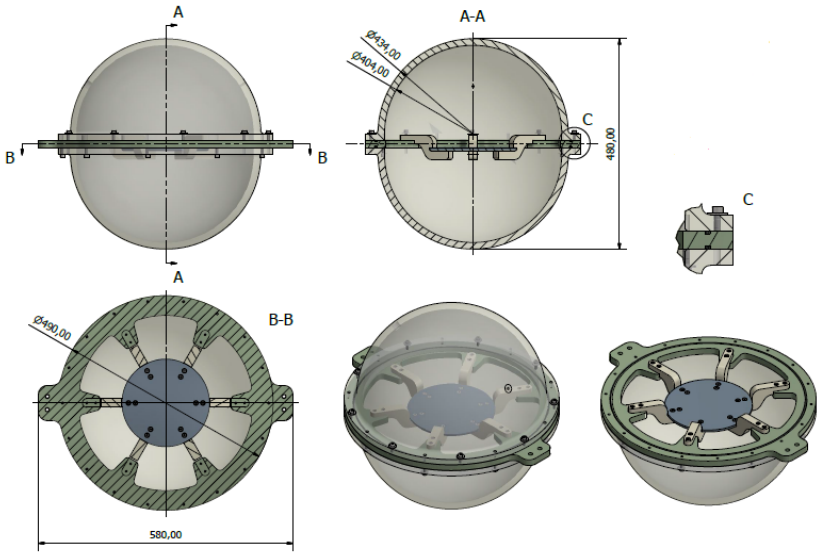

Figure 6.14. Preliminary design of the mPMT vessel with its cooling system in the equator of the sphere.

components options. Two integrated read-out chips provided by CAEN have been tested: CITIROC and PETIROC. CITIROC is a 32-channel fully-analogue front end chip dedicated to the read-out of silicon photomultipliers (SiPM) detectors, that can be adapted to the readout of the PMTs. For each channel the chip has a charge amplifier with configurable gain, fast shaping with a peaking time of 15 ns and slow shaping with configurable peaking time from 12.5 ns to 87.5 ns. Signals from the fast shaper produce a digital signals for triggering an event. These 32 signals are routed by the XILINX Spartan-6 Field Programmable Gate Array (FPGA). The analog signals for all channels can be stored in a Sample-and-Hold (S/H) circuit and multiplexed to a single analog output, which is then routed to an analogical digital converter (ADC). CITIROC has been fully tested and it does not satisfied the project requirements since the charge resolution (6% FWHM) and the power consumption resulted to be high.

A test of PETIROC integrated circuit has been realized by CAEN. This chip is similar to CITIROC, but with a lower charge resolution and power consumption The board has been tested but improvements are required in particular in terms of time resolution. Another chip, CATIROC has been proposed by CAEN and will be tested in the near future.
A board based on discrete components has been developed at INFN of Napoli. The board consists of an amplifier, a discriminator, a micro-controller unit, an integrator and an ADC. Preliminary tests demonstrated a charge resolution of 0.6% FWHM and an observed power consumption of about 60 $mW/channel$. Anyway optimization studies are ongoing.
Finally a passive cooling system, based on the heat conduction mechanism, will be present to keep the temperature of the electronics as low as possible, thus maximizing their lifetime has been designed in order to optimize the transfer of the heat

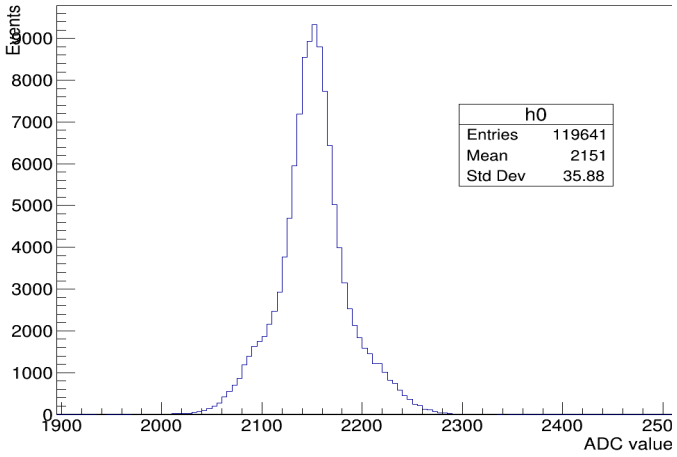

Figure 6.15. ADC output of one channel of CITIROC. Input signal of 1 Hz and voltage 5 mV.

generated by the electronics.

The first mPMT prototype will have an EVONIK UV transmitting plexiglas vessel with a diameter of 17-inch and will house 26 PMTs with a photocathode diameter of 7.7 cm: 19 PMTs will look the inner detector side and 7 PMTs will look the outer detector side. The final number of PMTs in the mPMT will be defined on the basis of simulation studies. The PMTs will be placed into a 3D printed structure and optically and mechanically coupled by Silicon Gel to an acrylic pressure sphere. For the present prototype module, Hamamatsu R12199 PMTs are used. They are arranged in 3 rings of PMTs in the hemisphere looking at the inner detector with zenith angles of 33°, 56°, 72°, respectively. In each ring 6 PMTs are spaced at 60° in azimuth and successive rings are staggered by 30°. The central PMT in the hemisphere point at a zenith angle of 0°, looking at the inner detector axis. Seven PMTs are arranged in the hemisphere looking at the outer detector. Six of them are arranged in one ring which opens a half angle of 33° with respect to the nadir.

6.5 Conclusions and future outlook

In summary the T2K Collaboration proposed to extend the T2K run to 20×10^{21} POT, running until 2026. This extension will allow the observation of δ_{CP} violation with more than 3σ significance and, θ_{23} and Δm^2_{32} with a precision of 1.7° and 1%. The cross section measurement will profit of the increased statistic shedding light on the nuclear effect in neutrino-nucleus scattering. The collaboration plan to upgrade the accelerator, the beamlines and the off-axis near detector in order to have a more intense beam and to increase its precision on the oscillation parameters and cross section measurements. Furthermore, the addition of an intermediate water Čerenkov located ∼1-2 km far from the neutrino production point is under discussion.

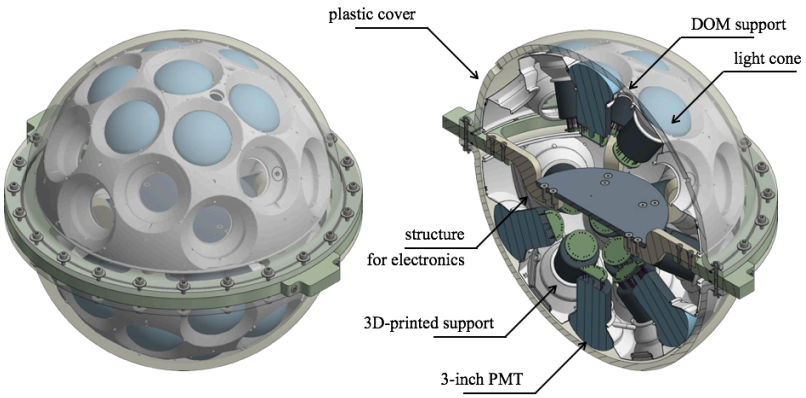

Figure 6.16. A schematic view of the Multi-PMT design.

In 2026 is foreseen the beginning of the operation of the next generation large water Čerenkov detector, HK. It will serve as far detector of the accelerator-based neutrino program (Tokai to Hyper-Kamiokande, T2HK) allowing the observation of δ_{CP} with 5σ significance. A broad rage of phenomena such as atmospheric neutrino oscillation studies, proton decay searches, and neutrino astrophysics with higher sensitivities will investigate as well. One option for the photosensors technology for both HK and the IWCD is the mPMT optical module. The first prototype is under construction and the acrylic vessel, the PMTs and the read-out electronics are under study. The proposed design foresee an optical module with 26 PMT housed in a pressure acrylic vessel along with the read-out electronics.

Conclusions

Neutrino oscillation has undergone a fast developed in the last decade and the attention around this topic is increased. T2K is one of the world-leading neutrino oscillation experiment. It found the first evidence of ν_e appearance in a neutrino beam, set the most precise limit on the atmospheric oscillation parameters and recently it excluded δ_{CP} conservation at 68% C.L.. The off-axis near detector plays an important rule in these measurements providing a better prediction of the SK event rate and reducing the systematic uncertainties associated with the flux and interaction models. In order to achieve these goals, the near detector perform a binned likelihood fit. It uses samples of event with reconstructed vertex in FGD1 FV and FGD2 FV from $\bar{\nu}$-mode and ν-mode data, for a total of 14 samples. Events in FGD2 FV are really important since help in constraining the cross section uncertainties relative to neutrino interactions on water, avoiding water-carbon extrapolation. In this framework is sat the ν_μ multiple track selection in $\bar{\nu}$-mode described in Chap. 4. It aims to select CC interactions induced by the intrinsic ν_μ component in the $\bar{\nu}$ beam. The ν_μ flux in $\bar{\nu}$-mode is 3.3% around the peak, thus is higher than the $\bar{\nu}_\mu$ background in ν-mode, which is lower (2.4% around the peak) especially at high energy. These differences are due to the higher production multiplicities of positive, rather than negative, parent particles. Once differences in the flux and the cross section are taken into account, the ν_μ contamination in the $\bar{\nu}$ beam is expected to be approximately 30%, while the $\bar{\nu}_\mu$ contamination in the ν beam is approximately 4%. Furthermore, SK cannot distinguish between ν and $\bar{\nu}$ interactions since the charge of the outgoing leptons cannot be reconstructed. Thus it is crucial to measure the ν_μ background in $\bar{\nu}$-mode at the near detector. The separation into three sub-samples based on the pion content in each event was possible with the increased statistic in $\bar{\nu}$-mode and it will be used in the next iteration of the oscillation analysis, improving the constraint on the cross section modelling and the detector systematics.

The T2K Collaboration has engaged a program of systematic error reduction through improving the modelling of the neutrino flux and developing near detector measurements to constrain the uncertainties resulting from the modelling of neutrino-nucleus interactions. Therefore, dedicated programs of neutrino-nucleus interaction studies and are also under way. Information on (anti)neutrino scattering is crucial for the interpretation of

neutrino oscillation since it affect the background prediction and energy reconstruction. Different measurements of CC cross-sections without production of pions in the final state have suggested the presence of another channel where neutrinos interact with pairs of correlated nucleons and more than one nucleon is knocked-out from the nucleus. In order to clarify the impact of nuclear effects in neutrino-nucleus scattering a simultaneous measurement of the double-differential muon neutrino and antineutrino charged-current cross-section without pions in the final state using the off-axis near detector has been performed. The neutrino and antineutrino cross-sections has been simultaneously extracted as a function of muon momentum and angle with a likelihood fit, including proper estimation of the correlations, allowing the evaluation of the sum, difference and asymmetry between the two cross-sections. For the moment the current uncertainties are too large for any conclusive statement, but with more statistic and lower systematic uncertainties a clear picture should start to come up. Anyway, already with the presented measurements, interesting comparison have been performed.

The future Japanese program on neutrino oscillation and scattering foresee an increased statistics and reduced systematics. For the second phase of T2K, in addition to extension of the running time, the Collaboration will upgrade the accelerator in order to reach the projected power, the beamlines to improve the horns current and the off-axis near detector both increasing the acceptance and to reach a lower threshold for protons. Hyper-Kamiokande will serve as far detector of the accelerator-based neutrino program (Tokai to Hyper-Kamiokande, T2HK) allowing the observation of δ_{CP} with 5σ significance, and will also investigate a broad rage of phenomena such as atmospheric neutrino oscillation studies, proton decay searches, and neutrino astrophysics with high sensitivities. One option for the photosensors is the mPMT optical module. A mPMT is a acrylic sphere filled with 26 photomultiplier tube that can improve the efficiency and the granularity of Hyper-Kamiokande. The first prototype is under construction, and in order to achieve this goal different acrylics has been tested and the read-out electronics is under development. The number of PMTs and their disposition inside the sphere will be optimized through simulation studies.

Acknowledgement

It is hard to find the correct words to express my heartfelt thanks to the all the people that made this thesis possible. I will continue this part in Italian, hoping to find more words in my own language.
Vorrei iniziare ringraziando la mia famiglia per la loro comprensione e il supporto in questi tre anni veramente intensissimi. Ringrazio i miei quattro supervisori di tesi, Gianfranca e il Prof. Palladino per il lato napoletano e Sara e Marco per il lato francese. Questa tesi non sarebbe stato possibile senza il loro aiuto. In particolare vorrei ringraziare Gianfranca e Sara per loro incredibile pazienza con me, per la disponibiltà in ogni momento e la loro infinita tenacia. Inoltre ringrazio Sara e Marco per avermi ospitato per 9 mesi a Saclay e avermi fatto sentire parte del loro gruppo. Per me è stata un'esperienza importante che ha inciso molto sulla realizzazione di questo lavoro e la mia formazione. Ringrazio i colleghi di esperimento che in questi tre anni sono diventati anche amici: Davide, Lorenzo e Francesco. Ragazzi, senza di voi i miei viaggi in Giappone sarebbero stati molto più noiosi. In particolare ringrazio Francesco per avermi accolto durante la mia permanenza a Saclay e avermi reso più semplice la vita in Francia grazie alla sua esperienza e per il continuo confronto su molti aspetti del lavoro che abbiamo portato aventi durante questi tre anni. For Alfonso and Mathieu I need to write in English, even if they should understand Italian. Alfonso, thank you for your help and discussion about many aspects of our analyses. I will never forget our weekends in Tokyo...in particular our dinners!Mathieu, there are no words to thank you for your help with French and your friendship during and after my period at Saclay. Desidero ringraziare i componenti del gruppo italiano di T2K per tutto il loro costante supporto: Gabriella, Lucio, Emilio, Vincenzo, Andrea, Gianmaria, Mauro. Un pensiero particolare va ai miei amici di sempre: Simone, Federico, Bart, Alessandro, Andrea de Lucia e Francesco Massa, i ragazzi delle aule dottorandi, Alessandro e Gennaro. Non posso non ringraziare Guido Celentano per avermi aiutato molto sulla parte burocratica del dottorato, per la tenacia con la quale ha portato aventi la mia domanda di cotutela e per gli innumerevoli consigli. Infine, ma non perché meno importante, ringrazio Roberta per il continuo conforto, la comprensione e l'affetto in questi tre anni, che senza di lei sarebbero stati vuoti.

Appendices

Appendix A

Two neutrino mixing

The simplest case is the one in which only two neutrino families exist. Here the relation between neutrino states is described by one mixing angle θ, with a value in the interval $0 \leqslant \theta \leqslant \pi/2$, and one mass difference $\Delta m^2 = m_2^2 - m_1^{21}$. Therefore, if we consider ν_α and ν_β, the unitary transformation 1.19 become:

$$\begin{pmatrix} \nu_\alpha \\ \\ \nu_\beta \end{pmatrix} = \begin{pmatrix} \cos\theta & \sin\theta \\ \\ -\sin\theta & \cos\theta \end{pmatrix} \begin{pmatrix} \nu_1 \\ \\ \nu_2 \end{pmatrix}. \tag{A.1}$$

which correspond to the following system of two equations:

$$\begin{cases} \nu_\alpha(t) = -\sin\theta\,\nu_1(t) + \cos\theta\,\nu_2(t) \\ \nu_\beta(t) = \cos\theta\,\nu_1(t) + \sin\theta\,\nu_2(t) \end{cases} \tag{A.2}$$

Since the mass eigenstates have defined mass m_j and energy $E_j = \sqrt{p^2 + m_j^2} \approx p + \frac{m_j^2}{2p}$ with $j = 1, 2$, they evolve, according to Schrödinger equation, like plane waves:

$$i\frac{\partial \nu_j(t)}{\partial t} = E_j \nu_j \Rightarrow \nu_j(t) = \nu_j(0) e^{-iE_j t} \tag{A.3}$$

Inverting relations A.2 we have

$$\begin{cases} \nu_1(t) = \cos\theta\,\nu_\beta(t) - \sin\theta\,\nu_\alpha(t) \\ \nu_2(t) = \sin\theta\,\nu_\beta(t) + \cos\theta\,\nu_\alpha(t) \end{cases} \tag{A.4}$$

[1] For convenience, we take ν_1 as the lightest neutrino, so that Δm^2 is positive.

Now, if we consider at time $t = 0$ beam composed only of ν_α with impulse p, we have

$$\nu_\alpha(0) = 1, \quad \nu_\beta(0) = 0 \tag{A.5}$$

then the system A.4 become

$$\begin{cases} \nu_1(0) = -\sin\theta \\ \nu_2(0) = \cos\theta \end{cases} \tag{A.6}$$

From this relations and from A.3

$$\begin{cases} \nu_1(t) = -\sin\theta e^{-iE_1 t} = -\sin\theta e^{-i\left(p+\frac{m_1^2}{2p}\right)} \\ \nu_2(t) = \cos\theta e^{-iE_1 t} = \cos\theta e^{-iE_2 t} = \cos\theta e^{-i\left(p+\frac{m_2^2}{2p}\right)} \end{cases} \tag{A.7}$$

Using the formulas of the previous section we get the transition probability

$$P(\nu_\alpha \to \nu_\beta) = \sin^2 2\theta \sin^2\left(\frac{\Delta m^2 L}{4E}\right) \tag{A.8}$$

This formula explicitly shows that oscillations only occur if both θ and Δm^2 are non-vanishing.
If we express Δm^2 in eV^2, L in km, E in GeV, the transition probability become

$$P(\nu_\alpha \to \nu_\beta) = \sin^2 2\theta \sin^2\left(1.27\frac{\Delta m^2 L}{E}\right) \tag{A.9}$$

In the case $\alpha = \beta$, the *survival probability* is:

$$P(\nu_\alpha \to \nu_\alpha) = 1 - P(\nu_\alpha \to \nu_\beta) = 1 - \sin^2 2\theta \sin^2\left(1.27\frac{\Delta m^2 L}{E}\right) \tag{A.10}$$

One can see from Eq. A.9 that the mixing angle dependence is expressed by $\sin^2 2\theta$, which is symmetric for $\theta = \pi/2 - \theta$. Since the allowed range of θ is $0 \leqslant \theta \leqslant \pi/2$, there is a degeneracy of the transition probability for θ and $\pi/2 - \theta$. However the two possibilities correspond to two physically different mixing: if $\theta < \pi/4$ the β neutrino is composed more of ν_1 than ν_2 and vice versa for ν_α; if $\theta > \pi/4$ the β neutrino is composed more of ν_2 than ν_1 and vice versa for ν_α.

Appendix B

Oscillation in matter

The elastic scattering of ν_e and ν_μ on electrons generates non trivial indices of refraction of the neutrinos in matter: $k(\nu_e) \neq 1$, $k(\nu_\mu) \neq 1$ and $k(\nu_e) \neq k(\nu_\mu)$. The difference between indices of refraction is determined essentially by the difference of the real parts of the forward amplitude of the elastic scattering

$$k(\nu_e) - k(\nu_\mu) = \Re[F_{\nu_e - e^-}(0)] - \Re[F_{\nu_\mu - e^-}(0)] \tag{B.1}$$

The real parts of the forward amplitude of the elastic scattering can be calculated in the SM: to leading order in the Fermi constant G_F, only the term in $F_{\nu_e - e^-}(0)$ of the diagram with exchange of a virtual W boson contributes. In the rest frame of the particle

$$k(\nu_e) - k(\nu_\mu) = \frac{2\pi}{p^2}\left(\Re[F_{\nu_e - e^-}(0)] - \Re[F_{\nu_\mu - e^-}(0)]\right) = -\frac{1}{p}\sqrt{2}G_F N_e \tag{B.2}$$

where N_e is the electron number density in matter. Given $k(\nu_e) - k(\nu_\mu)$ and indicating with $A_e(t, t_0)$ and $A_\mu(t, t_0)$ the amplitude of the probability to find ν_e or ν_μ at time t of the evolution of the system if at time $t_0 \leq t$ the neutrino ν_e or ν_μ has been produced, the system of evolution equations describing the $\nu_e \leftrightarrow \nu_\mu$ oscillations in matter is

$$i\frac{d}{dt}\begin{pmatrix} A_e(t,t_0) \\ \\ A_\mu(t,t_0) \end{pmatrix} = \begin{pmatrix} -\epsilon(t) & \epsilon' \\ \\ \epsilon' & \epsilon(t) \end{pmatrix}\begin{pmatrix} A_e(t,t_0) \\ \\ A_\mu(t,t_0) \end{pmatrix} \tag{B.3}$$

with

$$\epsilon(t) = \frac{1}{2}\left[\frac{\Delta m^2}{2E}\cos 2\theta - \sqrt{(}2)G_F N_e\right] \tag{B.4}$$

$$\epsilon' = \frac{\Delta m^2}{2E}\sin 2\theta \tag{B.5}$$

where θ is the neutrino mixing angle in vacuum. The second term in $\epsilon(t)$ is responsible for the effects of matter on neutrino oscillations. The system of evolution equations describing the oscillations of antineutrinos in matter has exactly the same form except for the matter term where it changes sign. Analyse now the case of $\nu_e \leftrightarrow \nu_\mu$ oscillation in matter with $N_e(t) = N_e = cost$. For this purpose consider the Hamiltonian

$$\mathscr{H}_{\rm m} = \mathscr{H}_0 + \mathscr{H}_{\rm int} = \frac{\Delta m^2}{4E} \begin{pmatrix} -\cos 2\theta_v & \sin 2\theta_v \\ \sin 2\theta_v & \cos 2\theta_v \end{pmatrix} + V_{CC} \begin{pmatrix} 1 & 0 \\ 0 & 0 \end{pmatrix}$$

where $V_{CC} = \sqrt{2} G_F N_e$ stand for the interaction term. Due to this term the eigenstates of the Hamiltonian of the neutrino system in vacuum, are not eigenstates of $\mathscr{H}_{\rm m}$. For the eigenstates $|\nu^m_{1,2}\rangle$ of H_m, which diagonalize the evolution matrix we have:

$$|\nu_e\rangle = |\nu^m_1\rangle \cos\theta_m + |\nu^m_2\rangle \sin\theta_m \tag{B.6}$$

$$|\nu_\mu\rangle = -|\nu^m_1\rangle \sin\theta_m + |\nu^m_2\rangle \cos\theta_m \tag{B.7}$$

here θ_m is the neutrino mixing angle in matter and

$$\sin 2\theta_m = \frac{\tan 2\theta}{\sqrt{\left(1 - \frac{N_e}{N_e^{res}}\right)^2 + \tan^2 2\theta}} \tag{B.8}$$

$$\cos 2\theta_m = \frac{1 - N_e/N_e^{res}}{\sqrt{\left(1 - \frac{N_e}{N_e^{res}}\right)^2 + \tan^2 2\theta}} \tag{B.9}$$

where the quantity

$$N_e^{res} = \frac{\Delta m^2 \cos 2\theta}{2E\sqrt{2} G_F} \simeq 6.56 \times 10^6 \frac{\Delta m^2 [eV^2]}{E[MeV]} \cos 2\theta cm^{-3} N_A \tag{B.10}$$

is called (for $\Delta m^2 2\cos\theta > 0$) "resonance density", N_A being Avogadro's number. The "adiabatic" states $|\nu^m_{1,2}\rangle$ have energies $E_{1,2}$ whose difference is given by

$$E^m_2 - E^m_1 = \frac{\Delta m^2}{2E} \sqrt{\left(\left(1 - \frac{N_e}{N_e^{res}}\right)^2 \cos^2 2\theta + \sin^2 2\theta\right)} \equiv \frac{\Delta M^2}{2E}. \tag{B.11}$$

The transition probability $\nu_e \to \nu_\mu$ in matter with $N_e = const$ has the form

$$P^{2\nu}_m(|\nu_e\rangle \to |\nu_\mu\rangle) = |A_\mu(t)|^2 = \frac{1}{2} \sin^2 2\theta_m \left[1 - \cos 2\pi \frac{L}{L_m}\right] \tag{B.12}$$

$$L_m = \frac{2\pi}{(E^m_2 - E^m_1)} \tag{B.13}$$

where L is the distance between source and detector and L_m is the oscillation length in matter. It can be seen in B.8 and B.9 the dependence of $\sin^2 2\theta_m$ on N_e has a resonant character.

Indeed, if $\cos 2\theta > 0$, for any $\sin^2 2\theta = 0$ there exists a value of N_e given by N_e^{res}, such that when $N_e = N_e^{res}$ we have $\sin^2 2\theta_m = 1$ independently of the value of $\sin^2 2\theta < 1$. This implies that the presence of matter can lead to a strong enhancement of the oscillation probability $P_m^{2\nu}(\nu_e \to \nu_\mu)$ even when the oscillations $\nu_e \to \nu_\mu$ in vacuum are suppressed due to a small value of $\sin^2 2\theta$. For obvious reasons, the resulting value

$$N_e = N_e^{res} \equiv \frac{\Delta m^2 \cos 2\theta}{2E\sqrt{2}G_F} \tag{B.14}$$

is called the "resonance condition", while the energy where Eq. B.14 holds for given N_e and $\Delta m^2 \cos 2\theta$ is referred to as the "resonance energy" (E_{res}). The oscillation length at resonance is given by $L_m^{res} = L_v/\sin 2\theta$, while the width in N_e of the resonance at half height is $\Delta N_e^{res} = 2N_e^{res} \tan 2\theta$. Thus if the mixing angle in vacuum is small, the resonance is narrow, $\Delta N_e^{res} \ll N_e^{res}$. The energy difference $E_2^m - E_1^m$ has a minimum at the resonance

$$(E_2^m - E_1^m)^{res} = min(E_2^m - E_1^m) = \frac{\Delta m^2}{2E} \sin 2\theta \tag{B.15}$$

Since the neutral current interaction of neutrinos in the SM is flavor symmetric, the formulae and results obtained are valid also for the case of $\nu_e \leftrightarrow \nu_\tau$ oscillations in matter. The case of $\nu_\mu - \nu_\tau$ mixing is different: to a relatively good precision we have $k(\nu_\mu) \simeq k(\nu_\tau)$ and this kind of oscillations in the matter of the Earth and the Sun proceed practically as in vacuum.

Consider now the oscillation of solar neutrinos. This oscillation occurs between two flavor: ν_e produced from the Sun oscillate in a state ν_x that is a linear combination of ν_μ and ν_τ. The Hamiltonian of this process is

$$\mathscr{H}_{\rm m} = \mathscr{H}_0 + \mathscr{H}_{\rm int}(r) = \frac{\Delta m^2}{4E} \begin{pmatrix} -\cos 2\theta_v & \sin 2\theta_v \\ \sin 2\theta_v & \cos 2\theta_v \end{pmatrix} + V_{CC}(r) \begin{pmatrix} 1 & 0 \\ 0 & 0 \end{pmatrix}$$

where H_0 is the Hamiltonian in the vacuum, $H_{int}(r)$ contains the matter effect and it depends from the Sun radius r, because the electron number density N_e depends on r and the angle θ_v is the solar mixing angle. From H_0 we can see that the two neutrino oscillation in vacuum cannot distinguish between a mixing angle θ_v and an angle $\theta'_v = \pi/2 - \theta_v$. But these two mixing angles represent two different physical situations: supposing $\theta_v < \pi/4$, if the mixing angle is θ_v, the lighter mass eigenstate will be more ν_e than ν_x while if it is θ'_v we will have the opposite situation. These two possibilities are discriminated by the neutrino propagation through solar matter. In fact the neutrino interaction energy $V_{CC}(r)$ has a definite, positive sign and the $\nu_e - \nu_e$ element of the solar Hamiltonian, defined by $-(\Delta m^2/4E)\cos^2\theta_v + V_{CC}(r)$ has a different value if the solution is given by θ_v (Small Mixing Angle, SMA) or θ'_v (Large Mixing Angle, LMA).

Appendix C

Fit validation

The fit procedure needs to be validated to find out any possible misbehaviour of the analysis framework and that there are no significant biases in the fit results from mis-modelled backgrounds. The closure tests performed for this analysis are:

- pull studies with and without systematics;
- bias study with and without systematics;
- fit using MC properly identified for this purpose as fake data.

C.0.1 Pull studies

Let's define with q_{Fit} the fit result for the physical quantity q, with $q_{Expected}$ the expected value and with σ_{prior} and σ_{Fit} the prior and the post-fit uncertainty on q, the pull is computed with the following formula:

$$pull = \frac{q_{Fit} - q_{Expected}}{\sigma_{Fit}} \tag{C.1}$$

when a prior knowledge on q is not present, while it becomes the following

$$pull = \frac{q_{Fit} - q_{Expected}}{\sqrt{\sigma^2_{prior} - \sigma^2_{Fit}}} \tag{C.2}$$

when an uncertainty, coming from other measurements, is available. Repeating the fit many times it is possible to build the pull distribution which should be a Gaussian with mean zero and width one if the post-fit error is correctly estimated.

For this analysis two sets of pulls are evaluated: pulls of the parameters of interest of the fit and of the nuisance parameters. For each parameter of interest the pull definition is the following:

$$pull = \frac{1 - c_{Fit}}{\sigma_{Fit}} \tag{C.3}$$

while for the nuisance parameters is:

$$pull = \frac{p_{Fit} - p_{Thrown}}{\sqrt{\sigma^2_{prior} - \sigma^2_{Fit}}} \tag{C.4}$$

where p_{Toy} is the input parameter in each toy experiment. It is worth notice that the error extracted from the fit does not affect the results of this analysis since it is not used directly to quote the uncertainty on the final measurements. Indeed, it is practically unfeasible to propagate analytically the errors on all the nuisances to the final interesting observable. It is important to show that the pull widths are compatible with one but it does not affect the analysis results.
Fig. C.1 shows the pulls means and width for the parameters of interest for a set of 100 toys in which only poissonian fluctuations are applied and the systematics are not included. The means of the pulls are correctly centered at zero inside their uncertainties and the width of the pulls is compatible with one. It is nice to show that the pull widths are compatible with 1 but it has no interest for the analysis results. The propagation of the uncertainties is indeed done through toys as discussed before.

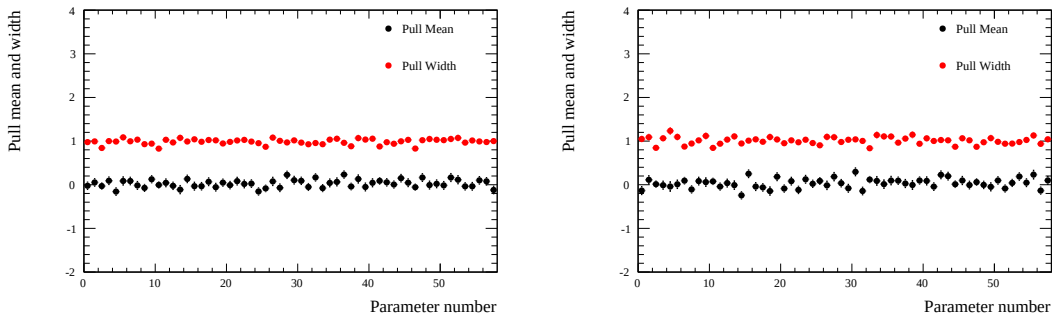

Figure C.1. Mean and width of the pulls distributions defined in Eq. C.3 for the parameters of interest for neutrino on the left and antineutrino on the right.

Fig. C.2 shows the pulls means and width for the nuisance parameters for a set of 100 toys in which they are varied separately following the corresponding covariance matrices. The means of the pulls are correctly centered at zero inside their uncertainties, but their width is not compatible with one for the neutrino sample. This is due to the underestimation of the uncertainties computed by the fitting algorithm, indeed the numerator of the Eq. C.4 is correctly centered at zero as shown in Fig C.3. Anyway, since the propagation of the uncertainties is done through toys, this result does not affect the cross-section extraction.

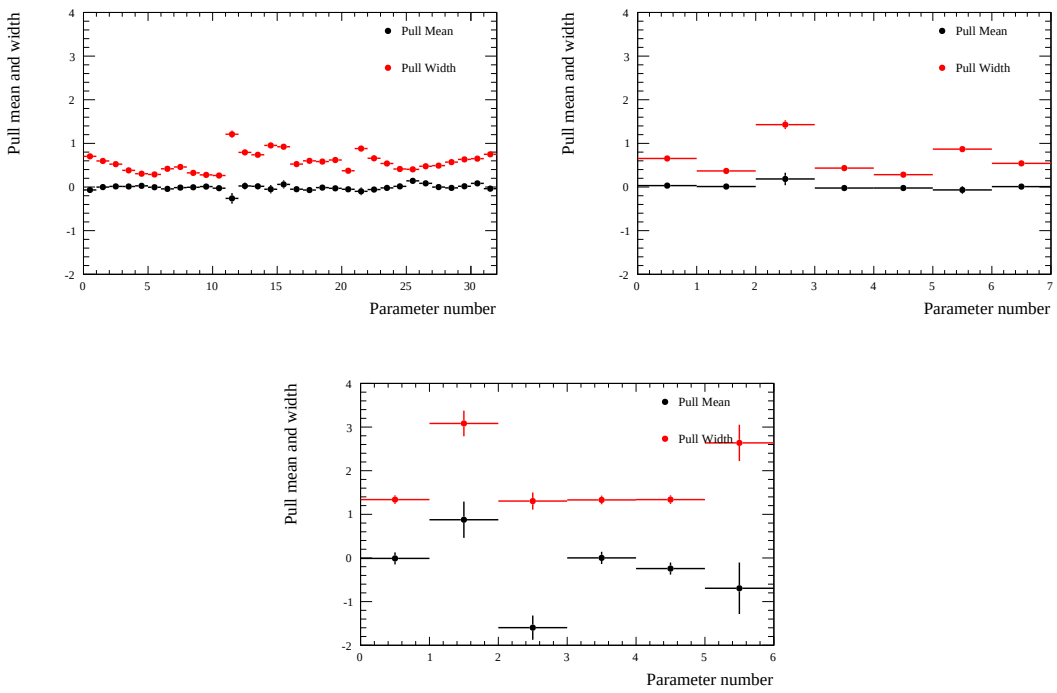

Figure C.2. Mean and width of the pulls distributions defined in Eq. C.4 for the flux (top left), background cross section modelling (top right) and pion FSI (bottom) parameters.

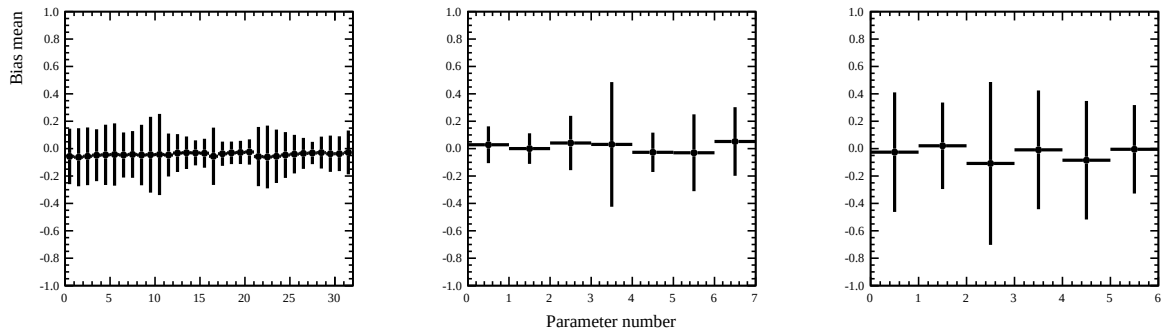

Figure C.3. Mean of the bias ($p_{Fit} - p_{Thrown}$) for the flux (left), background cross section modelling (center) and pion FSI (right) parameters.

C.0.2 Bias study

The bias study check that the average result after fitting a set of toy experiments does not deviate from the nominal MC. It is given by the mean of the following distribution:

$$N_i^{\text{CC-0}\pi\ Fit} - N_i^{\text{CC-0}\pi\ Thrown} \tag{C.5}$$

computed for each muon kinematic bin i, divided by the mean of the number of CC-0π events in each toy ($\langle N_i^{\text{CC-0}\pi\ Toy} \rangle$). Fig. C.4 shows, on the left, the bias over 100 toy experiment per each bin when statistical fluctuation and also systematic uncertainty are included, while on the right, the bias study without including the statistical variation in the toys in order to check the absence of bias at percent level. The bias study shows clearly that the minimum of the fit is really stable on average and the likelihood is symmetric.

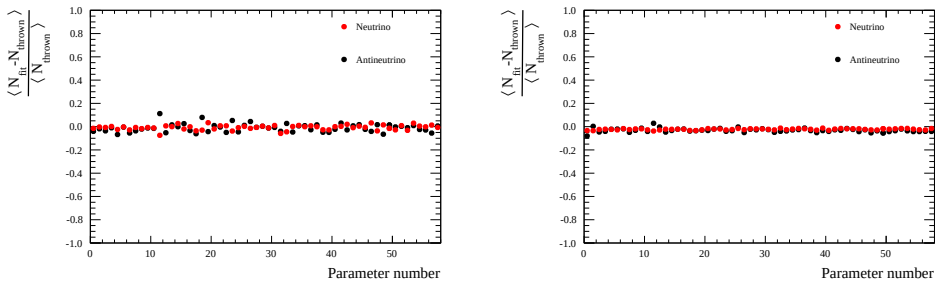

Figure C.4. Mean of the bias distribution defined in Eq. C.5 generated by applying fluctuation due to either systematic and statistical uncertainties (left) or only systematics uncertainties (right). The legend indicates if the bias is computed for the neutrino or antineutrino sample.

C.0.3 Fake data studies

The last validation test has been performed fitting several fake dataset produced either biasing nominal MC or with an alternative generator. The agreement and the sensitivity to the fake data has been assessed computing the χ^2 goodness of fit (GOF), calculated as follows:

$$\chi^2 = \sum_i \sum_j \left(\frac{d\sigma_i}{dx_i}^{Fake\ Data} - \frac{d\sigma_i}{dx_i}^{Fit} \right) \left(V_{ij}^{cov}\right)^{-1} \left(\frac{d\sigma_j}{dx_j}^{Fake\ Data} - \frac{d\sigma_j}{dx_j}^{Fit} \right) \tag{C.6}$$

where the index i and j run over the total number of bins for both ν_μ and $\bar{\nu}_\mu$. Indeed for the single cross sections the χ^2 GOF is computed considering the whole covariance matrix containing the correlation between ν_μ and $\bar{\nu}_\mu$ CC-0π cross-sections.
Anyway the χ^2 GOF gives only a global information on the result of the fit, therefore also the fractional bias from the fit to the fake data over the fake data cross section for each muon kinematic bin i has been computed in the following way:

$$\frac{\sigma_i^{Fit} - \sigma_i^{Fake\ Data}}{\sigma_i^{Fake\ Data}} \tag{C.7}$$

and the error on this quantity has been obtained propagating the error on σ^{Fit}. The bias has been extracted only for the single cross sections since the sum, difference and asymmetry are their combinations.

NEUT asimov fit

The simplest fake data study is the one in which the NEUT prediction is fitted with itself. The χ^2 GOF is reported in Tab. XXXI. As expected the χ^2 is low, confirming a good agreement of the fit result and the nominal NEUT prediction. In Fig. C.5 is reported the

Asimov Fit	χ^2
Cross section	2.60
Sum	0.36
Difference	0.23
Asymmetry	0.67

TABLE XXXI. Summary table of the χ^2 GOF computed using the total covariance matrix (statistical and systematic uncertainties).

fractional bias where is clear the agreement between the fit result and the nominal cross sections prediction. In Figs. from C.6 to C.10 are reported the ν_μ and $\bar{\nu}_\mu$ CC-0π cross sections, the sum, difference and asymmetry respectively in bins of true muon kinematics. The result is compared with the NEUT prediction for the CC-0π cross section (blue line), CCQE (pink line) and CCQE plus pion absorption(cyan line). The NEUT prediction for 2p2h is displayed as well in order to show the contribution of this component to the cross section. From the comparison is evident that the level of uncertainties does not allow a good separation between the various contributions.

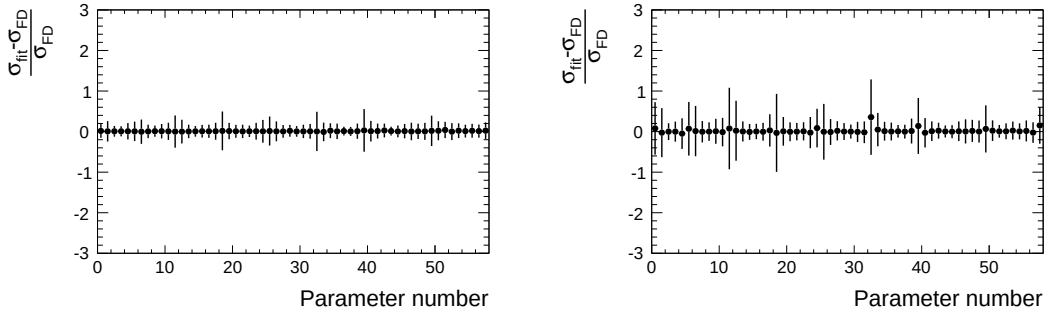

Figure C.5. Fractional bias in case of asimov fit for the ν_μ (left) and $\bar{\nu}_\mu$ CC-0π cross section (right) in bins of true muon kinematics.

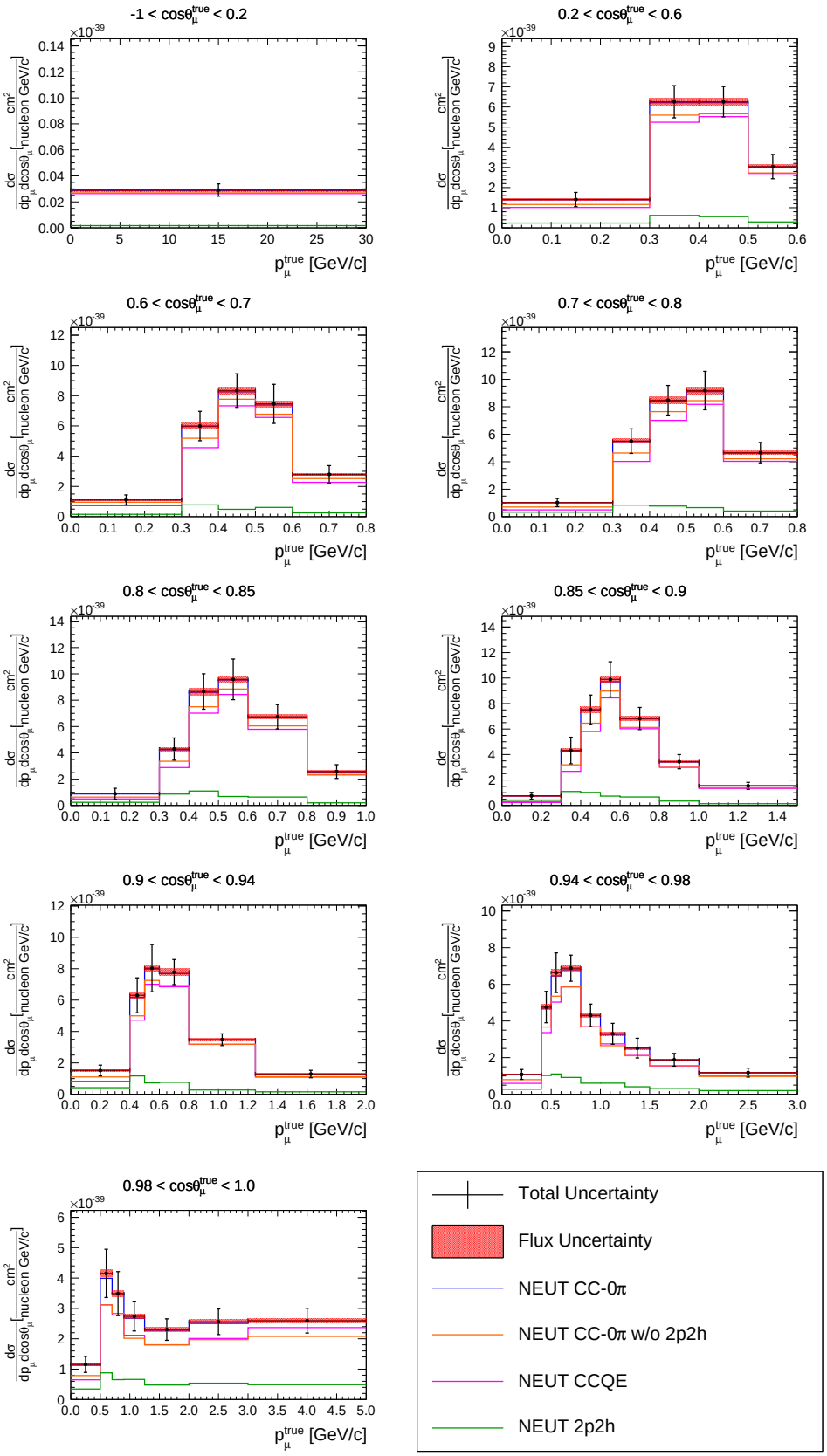

Figure C.6. ν_μ CC-0π cross section in bins of true muon kinematics obtained with an asimov fit with shape uncertainty (error band) and fully correlated normalization uncertainty (red band). The result is compared with the NEUT prediction for CC-0π (blue line), CCQE (pink line) and CCQE plus pion absorption(cyan line). The NEUT prediction for 2p2h is displayed as well. The last bin, up to 30 GeV/c, is not displayed.

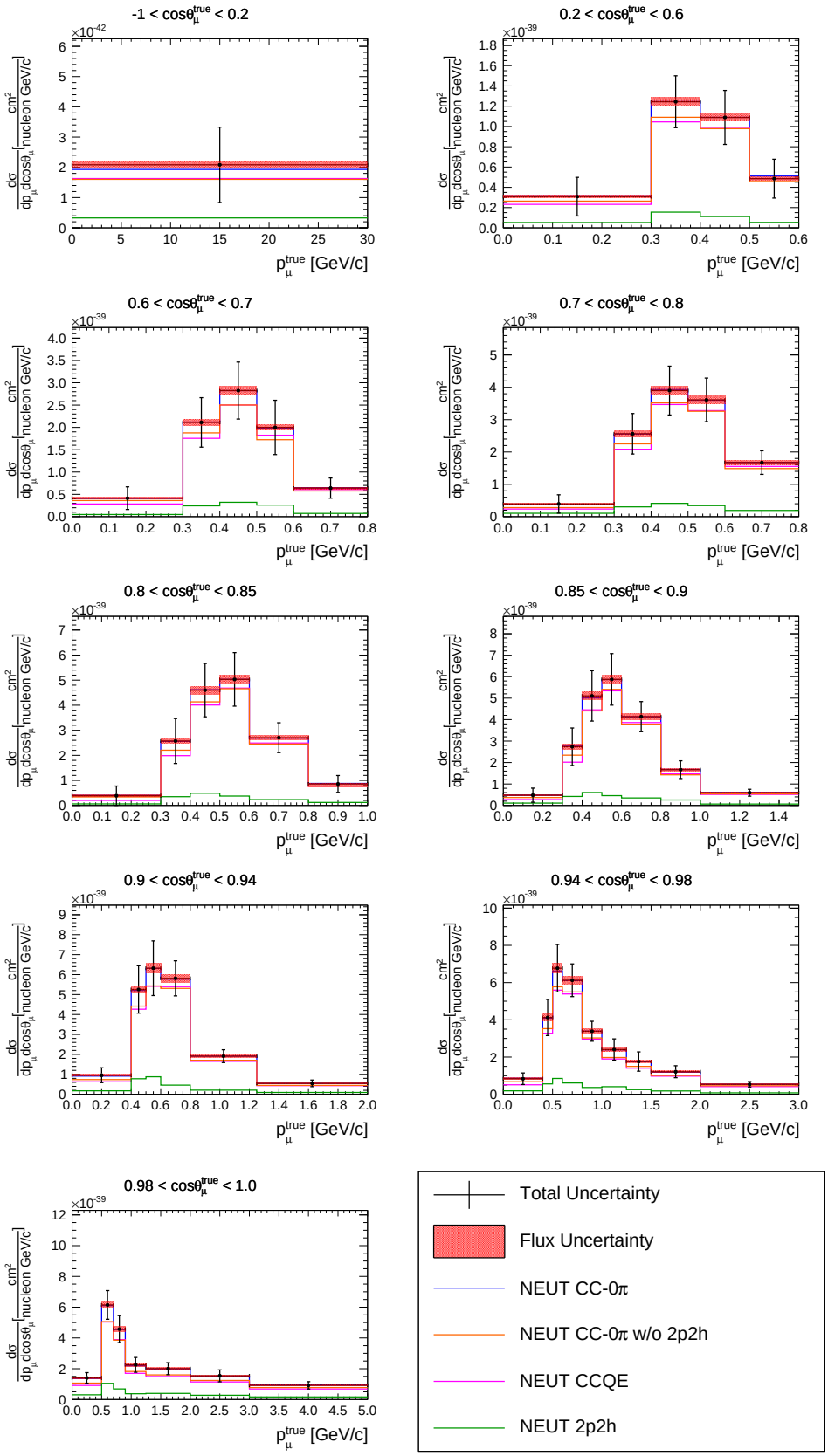

Figure C.7. $\bar{\nu}_\mu$ CC-0π cross section in bins of true muon kinematics obtained with an asimov fit with shape uncertainty (error band) and fully correlated normalization uncertainty (red band). The result is compared with the NEUT prediction for CC-0π (blue line), CCQE (pink line) and CCQE plus pion absorption(cyan line). The NEUT prediction for 2p2h is displayed as well. The last bin, up to 30 GeV/c, is not displayed.

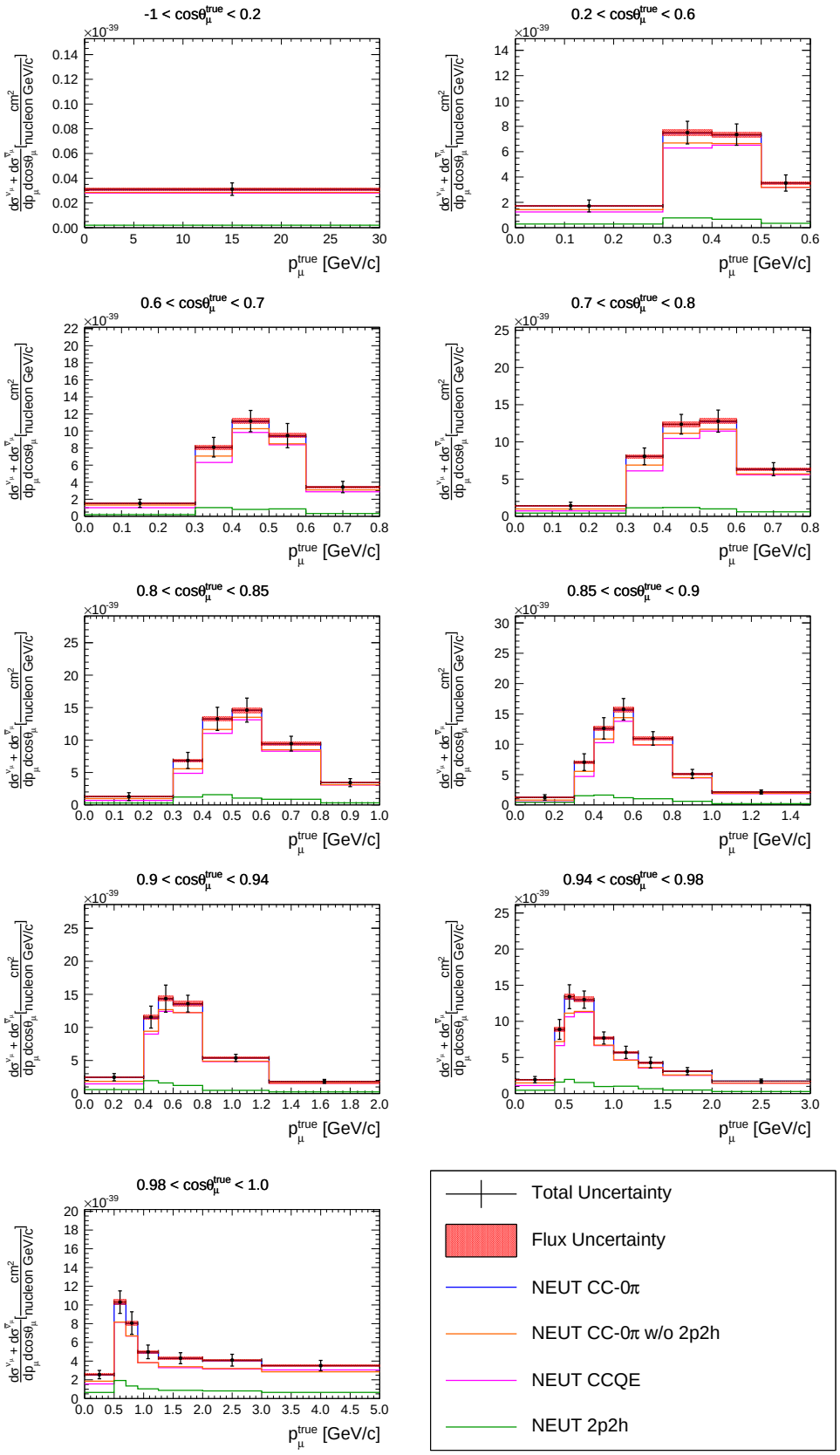

Figure C.8. Cross sections sum in bins of true muon kinematics obtained with an asimov fit with shape uncertainty (error band) and fully correlated normalization uncertainty (red band). The result is compared with the NEUT prediction for CC-0π (blue line), CCQE (pink line) and CCQE plus pion absorption(cyan line). The NEUT prediction for 2p2h is displayed as well. The last bin, up to 30 GeV/c, is not displayed.

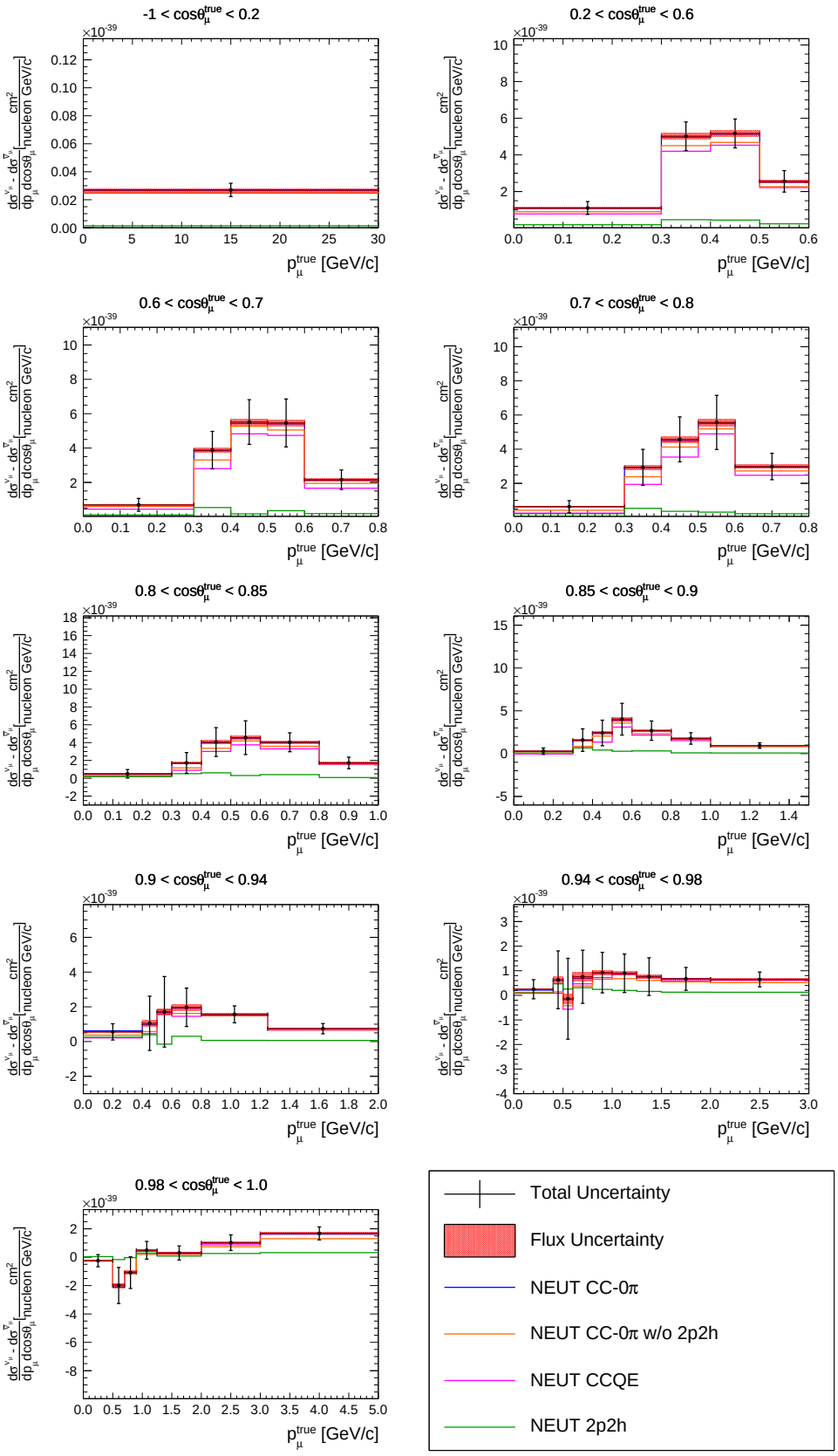

Figure C.9. Cross sections difference in bins of true muon kinematics obtained with an asimov fit with shape uncertainty (error band) and fully correlated normalization uncertainty (red band). The result is compared with the NEUT prediction for CC-0π (blue line), CCQE (pink line) and CCQE plus pion absorption(cyan line). The NEUT prediction for 2p2h is displayed as well. The last bin, up to 30 GeV/c, is not displayed.

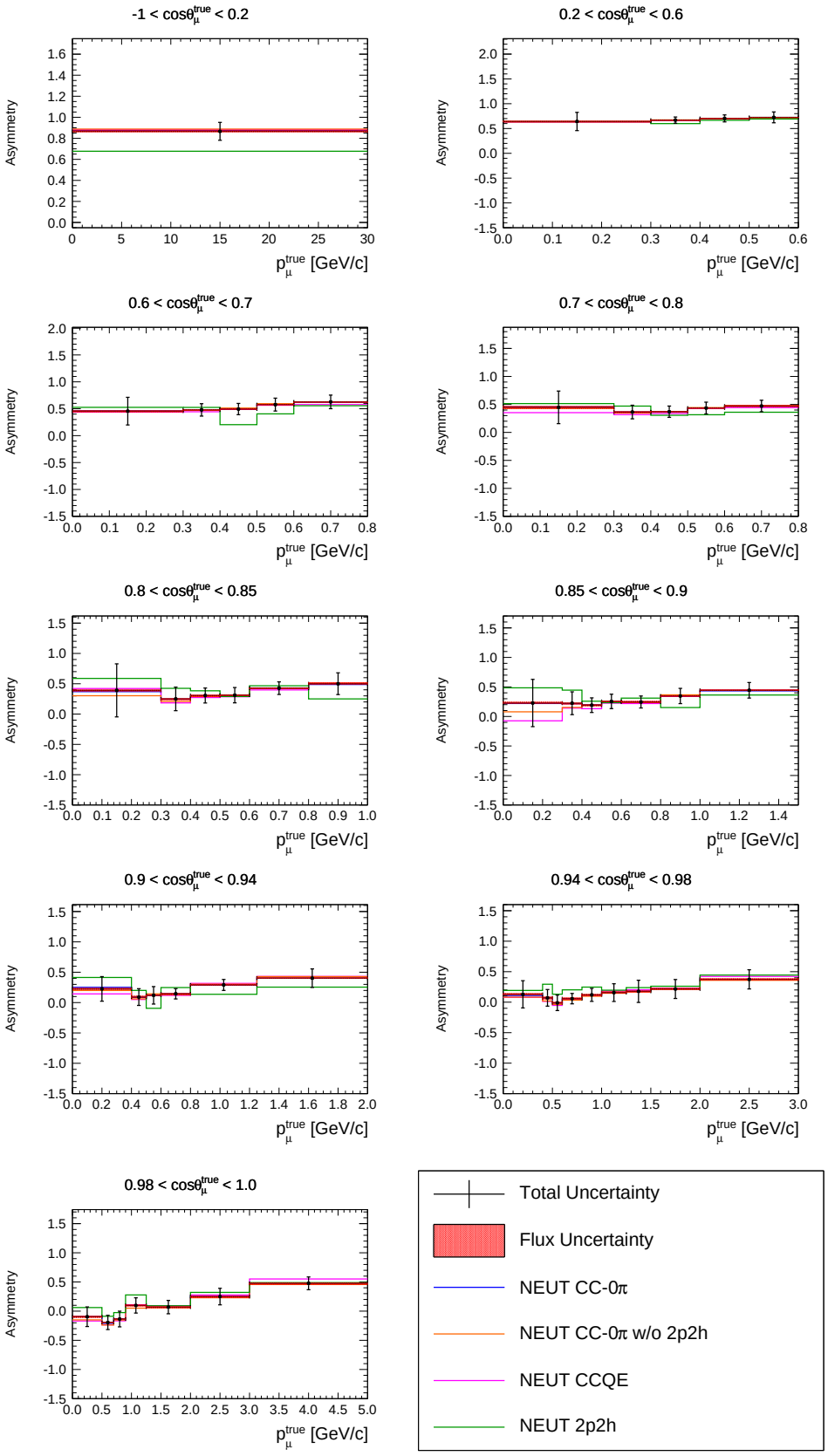

Figure C.10. Cross sections asymmetry in bins of true muon kinematics obtained with an asimov fit with shape uncertainty (error band) and fully correlated normalization uncertainty (red band). The result is compared with the NEUT prediction for CC-0π (blue line), CCQE (pink line) and CCQE plus pion absorption(cyan line). The NEUT prediction for 2p2h is displayed as well. The last bin, up to 30 GeV/c, is not displayed.

NEUT with biased CCQE and 2p2h

NEUT with biased CCQE and 2p2h has been used in order to check if the uncertainty cover any possible bias. It has been generated changing the nuclear model from SF to RFG+RPA and increasing by a factor of two the 2p2h cross section. The χ^2 GOF is reported in Tab. XXXII.

NEUT with double 2p2h	χ^2
Cross section	16.73
Sum	2.22
Difference	1.39
Asymmetry	1.60

TABLE XXXII. Summary table of the χ^2 GOF computed using the total covariance matrix (statistical plus systematic uncertainties). The fake data tested is NEUT with RFG+RPA as nuclear model and 2p2h increased by a factor of two.

In Fig. C.11 is reported the fractional bias which results compatible with zero inside the errors. In Figs. from C.12 to C.16 are reported the ν_μ and $\bar{\nu}_\mu$ CC-0π cross sections, the sum, difference and asymmetry respectively in bins of true muon kinematics.

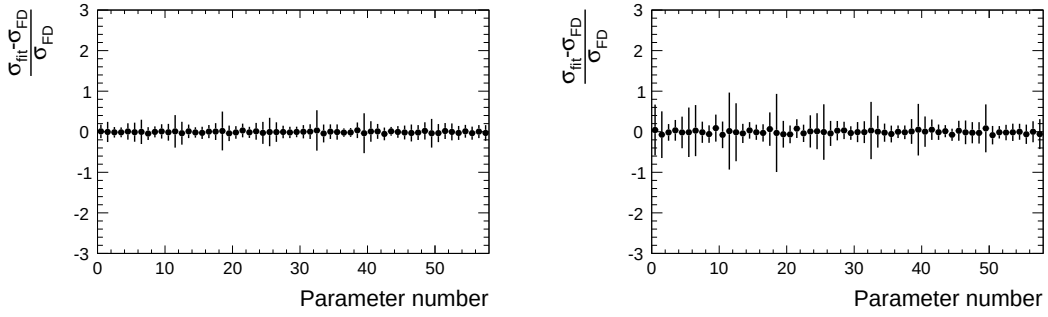

Figure C.11. Fractional bias between the result of the fit and the fake data for the ν_μ (left) and $\bar{\nu}_\mu$ CC-0π cross section (right) in bins of true muon kinematics. The fake data used is NUET with RFG+RPA as nuclear model and 2p2h increased by a factor of two.

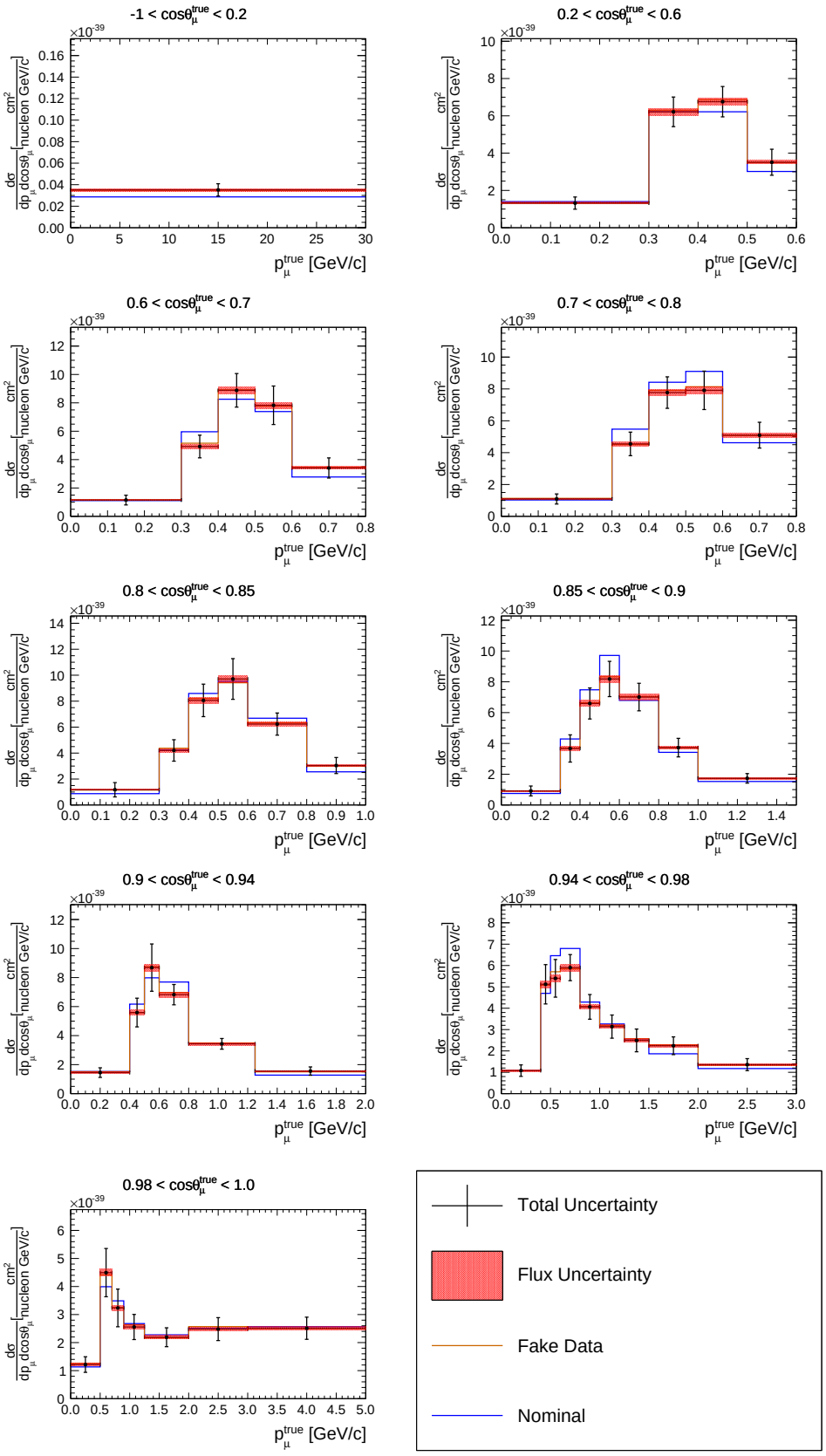

Figure C.12. $\bar{\nu}_\mu$ CC-0π cross section in bins of true muon kinematics obtained using NEUT prediction with RFG+RPA as nuclear model and 2p2h increased by a factor of two as fake data and NEUT as nominal. The result is compared with the nominal and fake data prediction. The error bars stand for the shape uncertainty while the red band are the fully correlated normalization uncertainty. The last bin, up to 30 GeV/c, is not displayed.

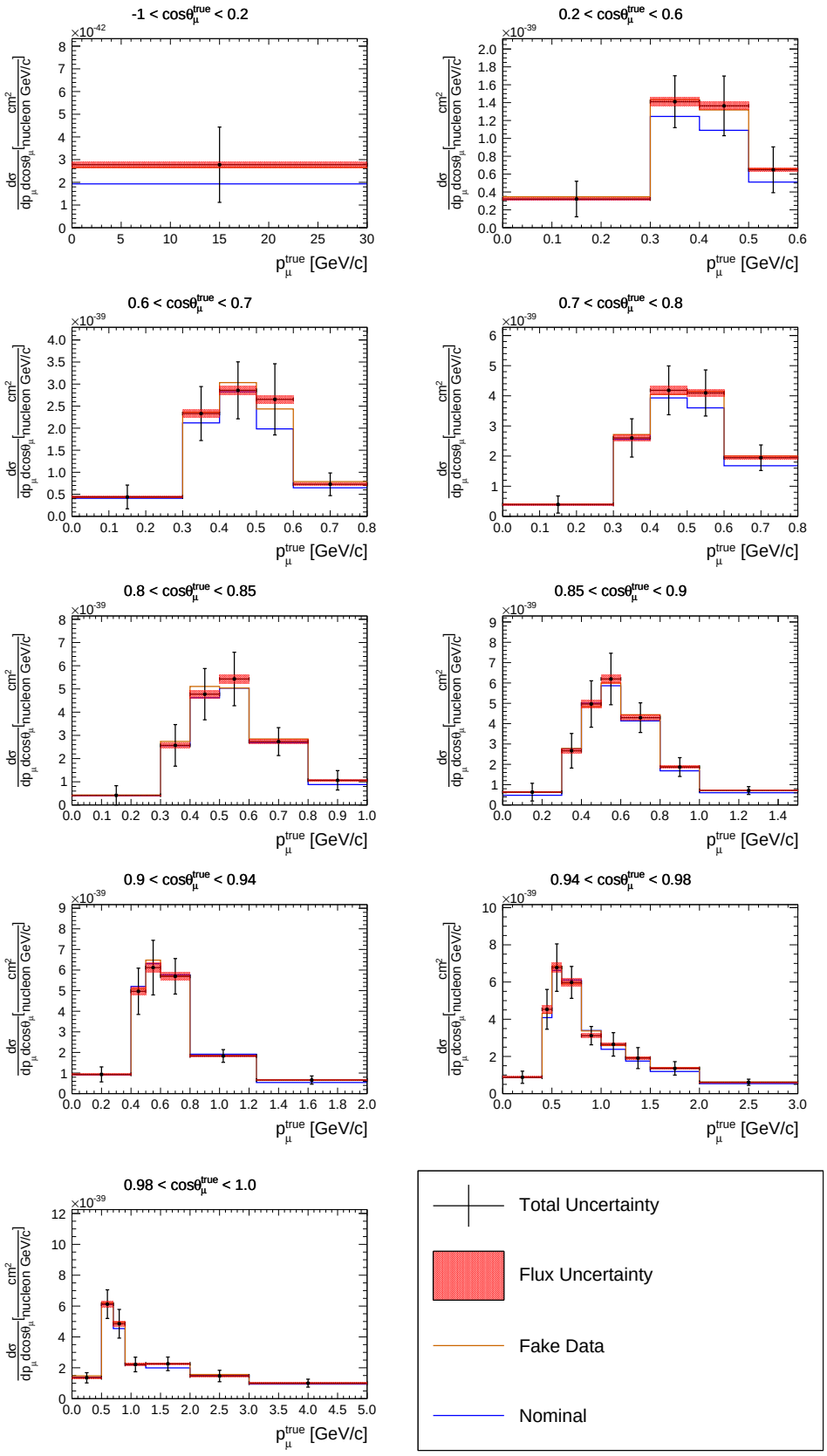

Figure C.13. $\bar{\nu}_\mu$ CC-0π cross section in bins of true muon kinematics obtained using NEUT prediction with RFG+RPA as nuclear model and 2p2h increased by a factor of two as fake data and NEUT as nominal. The result is compared with the nominal and fake data prediction. The error bars stand for the shape uncertainty while the red band are the fully correlated normalization uncertainty. The last bin, up to 30 GeV/c, is not displayed.

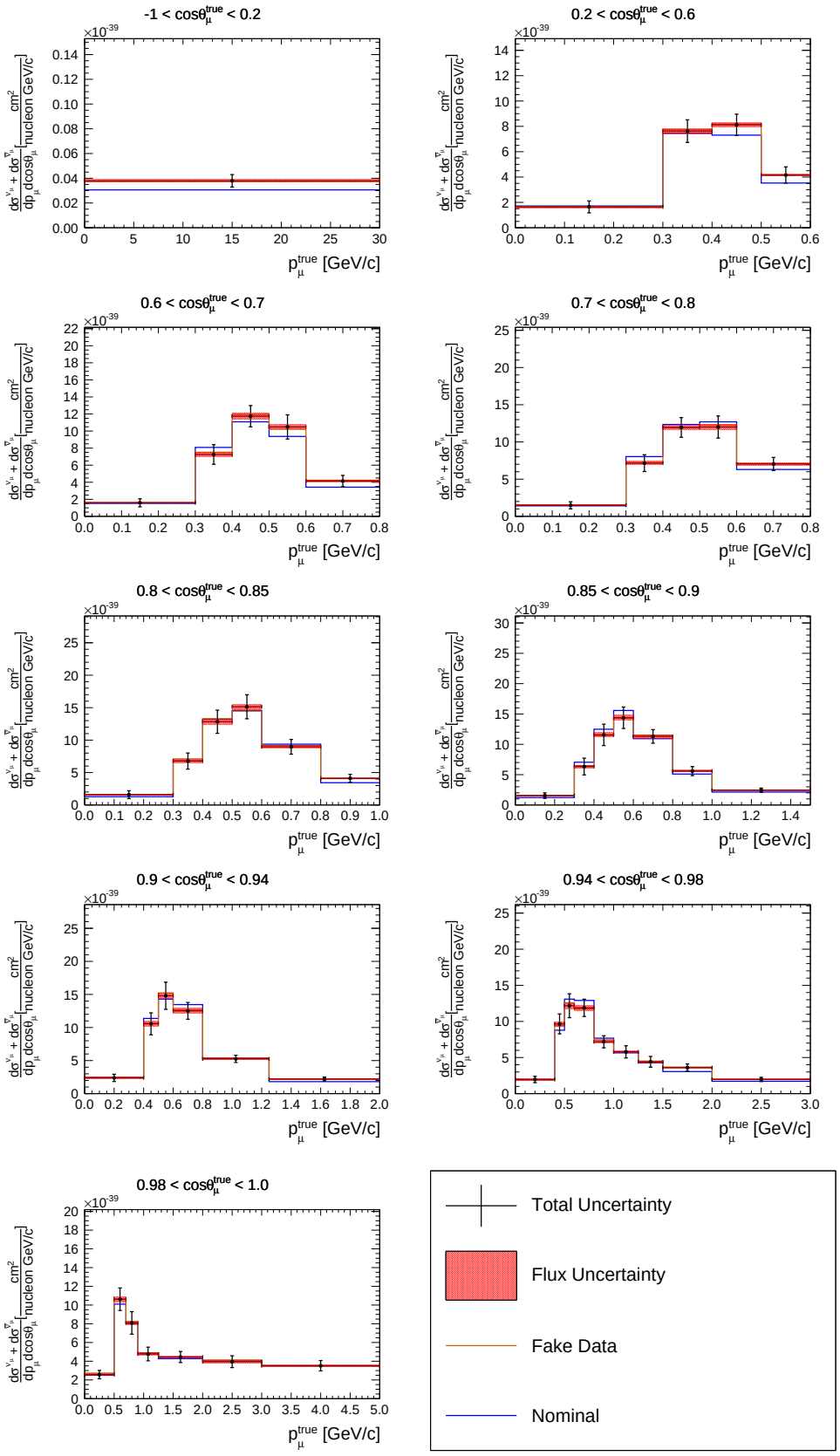

Figure C.14. Sum of the cross sections in bins of true muon kinematics obtained using NEUT prediction with RFG+RPA as nuclear model and the 2p2h component increased by a factor of two as fake data and NEUT as nominal. The result is compared with the nominal and fake data prediction. The error bars stand for the shape uncertainty while the red band are the fully correlated normalization uncertainty. The last bin, up to 30 GeV/c, is not displayed.

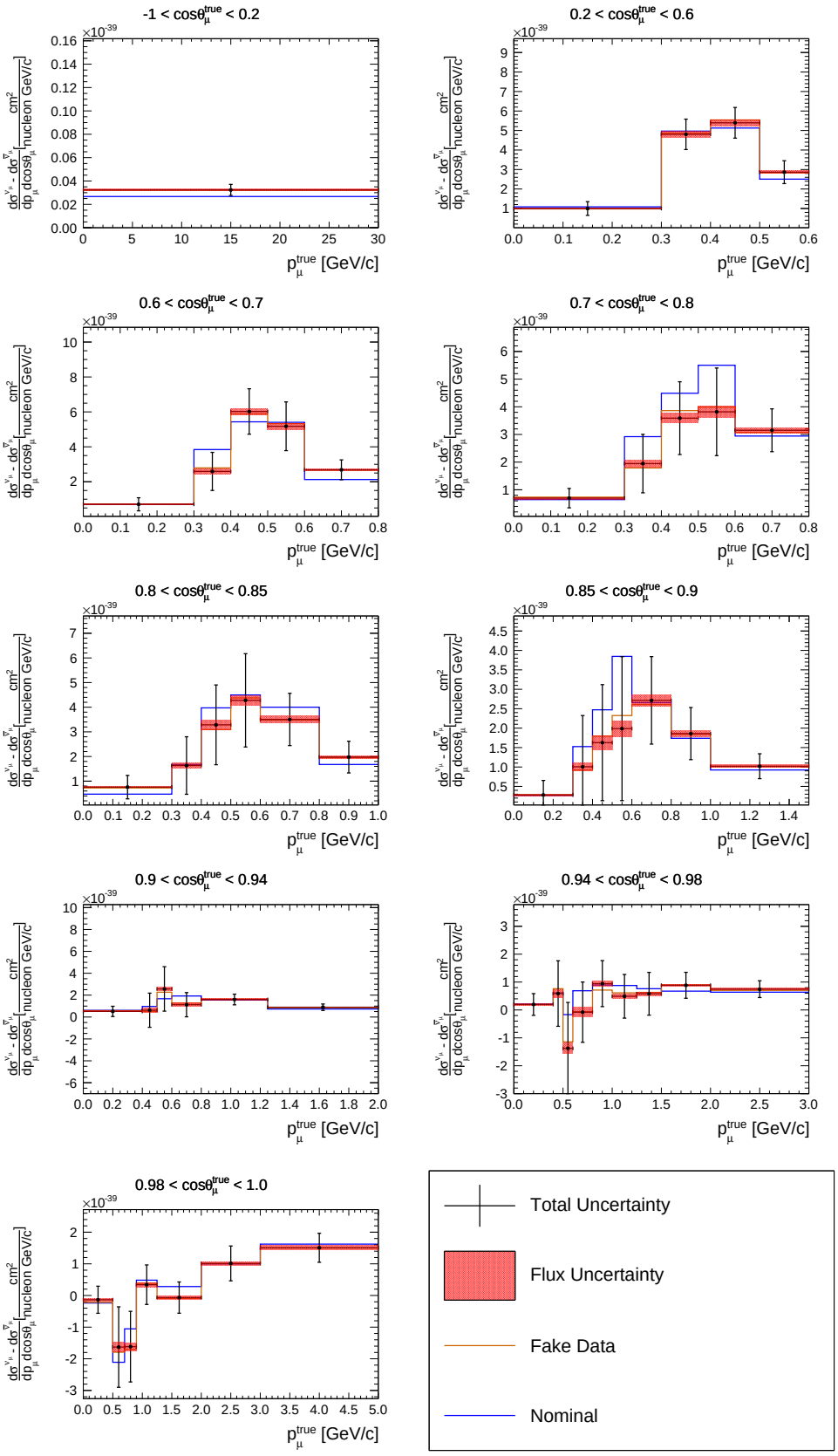

Figure C.15. Difference of the cross sections in bins of true muon kinematics obtained using NEUT prediction with RFG+RPA as nuclear model and the 2p2h component increased by a factor of two as fake data and NEUT as nominal. The result is compared with the nominal and fake data prediction. The error bars stand for the shape uncertainty while the red band are the fully correlated normalization uncertainty. The last bin, up to 30 GeV/c, is not displayed.

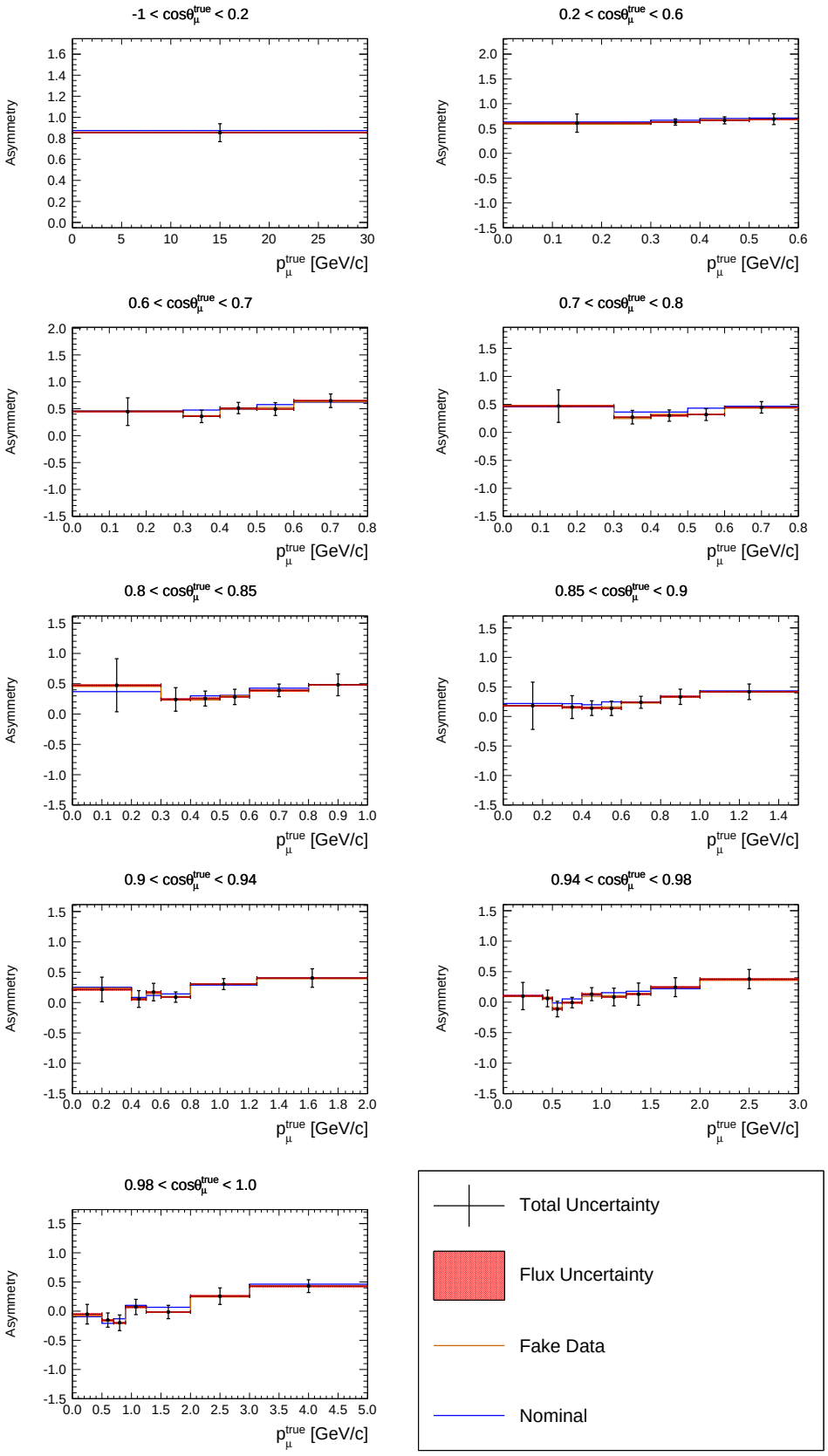

Figure C.16. Asymmetry of the cross sections in bins of true muon kinematics obtained using NEUT prediction with RFG+RPA as nuclear model and the 2p2h component increased by a factor of two as fake data and NEUT as nominal. The result is compared with the nominal and fake data prediction. The error bars stand for the shape uncertainty while the red band are the fully correlated normalization uncertainty. The last bin, up to 30 GeV/c, is not displayed.

NEUT with biased 2p2h

NEUT with SF as nuclear model (the default model used in production 6B) and with the double of 2p2h events expected or without 2p2h events have been used as fake data. The χ^2 GOF for the two cases are reported in Tabs. XXXIII and XXXIV.

NEUT with double 2p2h	χ^2
Cross section	95.65
Sum	16.25
Difference	14.78
Asymmetry	22.45

TABLE XXXIII. Summary table of the χ^2 GOF computed using the total covariance matrix (statistical plus systematic uncertainties). The fake data tested is NEUT with the double of 2p2h events.

NEUT without 2p2h	χ^2
Cross section	57.82
Sum	9.79
Difference	9.78
Asymmetry	19.63

TABLE XXXIV. Summary table of the χ^2 GOF computed using the total covariance matrix (statistical plus systematic uncertainties). The fake data tested is NEUT without 2p2h events.

In Fig. C.17 is reported the fractional bias for the fake data set obtained increasing the 2p2h component of a factor of two, while Fig. C.18 shows the fractional bias for the fake data set obtained removing the 2p2h component. In both cases the fractional bias is compatible with zero inside the errors. The fractional bias -1 for the antineutrino case correspond to the bin $0.6 < \cos\theta_\mu^{true} < 0.7$, $0.8 < p_\mu^{true} < 30\,GeV$, where the possibility to have zero events is expected. The bigger error bar in the fractional bias for antineutrino correspond to the bin $0.8 < \cos\theta_\mu^{true} < 0.85$, $0.0 < p_\mu^{true} < 0.3\,GeV$ where the statistical error is 90%. In Figs. from C.19 to C.23 are reported the ν_μ and $\bar{\nu}_\mu$ CC-0π cross sections, the sum, difference and asymmetry respectively in bins of true muon kinematics for the fake data set obtained increasing the 2p2h component of a factor of two. In Figs. from C.24 to C.28 are reported again the cross sections and their combinations but for the fake data set obtained removing the 2p2h component.

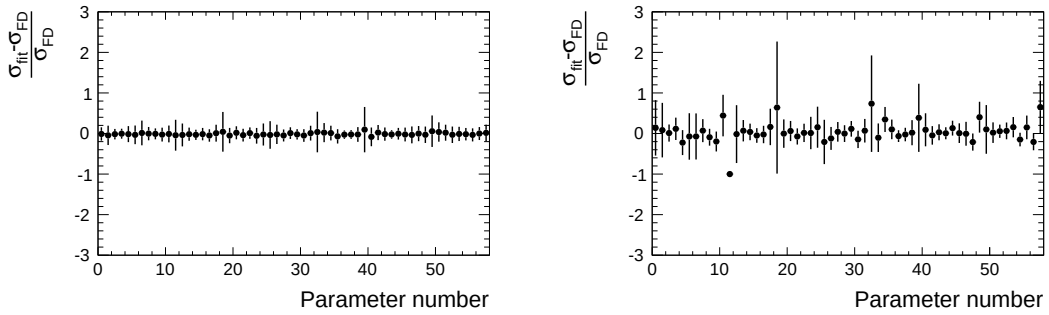

Figure C.17. Fractional bias between the result of the fit and the fake data for the ν_μ (left) and $\bar{\nu}_\mu$ CC-0π cross section (right) in bins of true muon kinematics. The fake data used is NEUT with 2p2h increased by a factor of two.

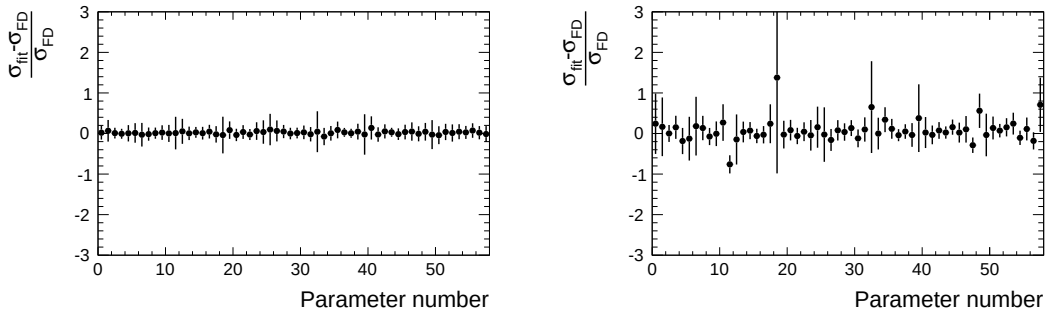

Figure C.18. Fractional bias between the result of the fit and the fake data for the ν_μ (left) and $\bar{\nu}_\mu$ CC-0π cross section (right) in bins of true muon kinematics. The fake data used is NEUT prediction without 2p2h.

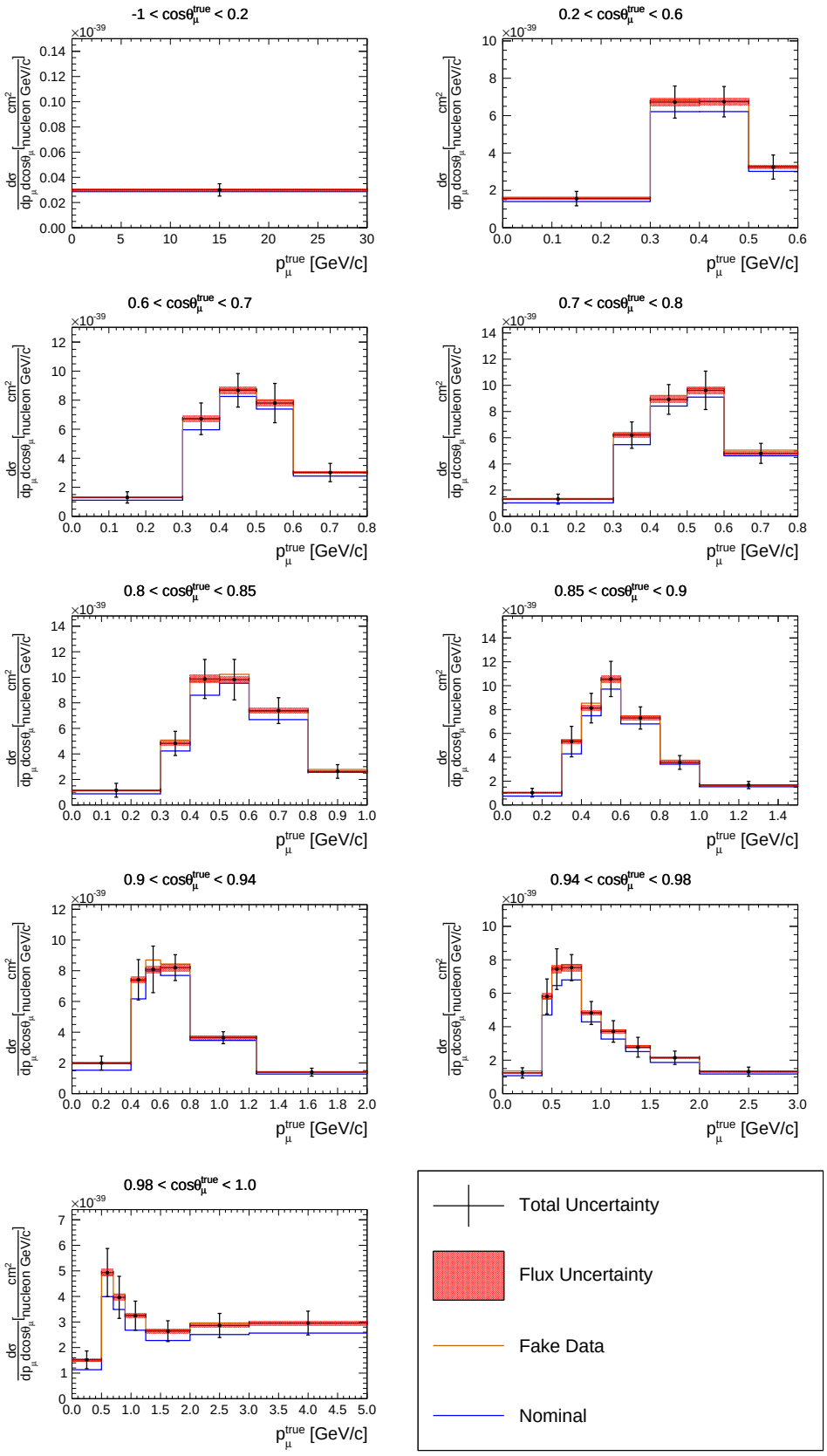

Figure C.19. ν_μ CC-0π cross section in bins of true muon kinematics obtained using NEUT prediction with 2p2h increased by a factor of two as fake data and NEUT as nominal. The result is compared with the nominal and fake data prediction. The error bars stand for the shape uncertainty while the red band are the fully correlated normalization uncertainty. The last bin, up to 30 GeV/c, is not displayed.

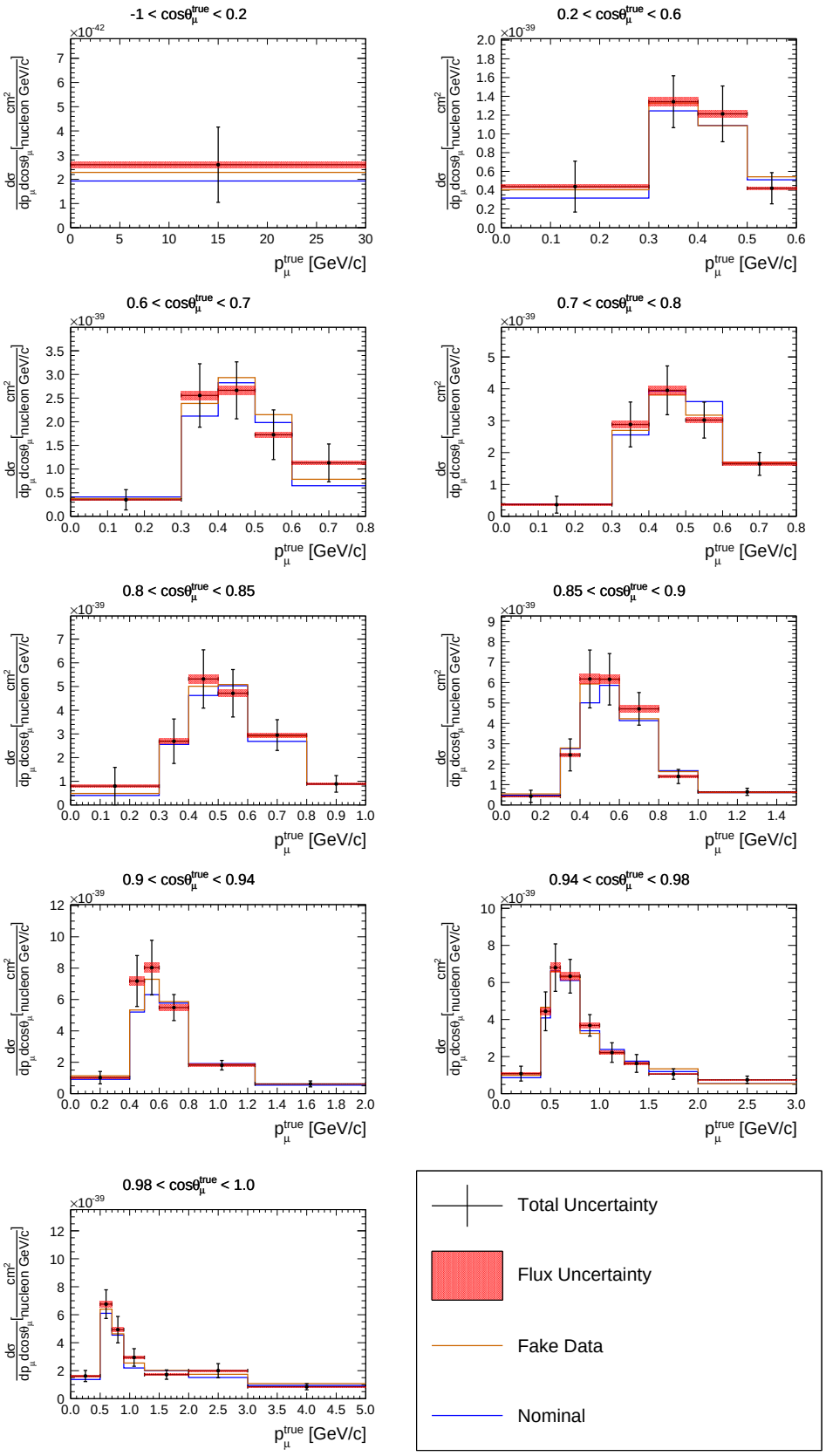

Figure C.20. $\bar{\nu}_\mu$ CC-0π cross section in bins of true muon kinematics obtained using NEUT prediction with 2p2h increased by a factor of two as fake data and NEUT as nominal. The result is compared with the nominal and fake data prediction. The error bars stand for the shape uncertainty while the red band are the fully correlated normalization uncertainty. The last bin, up to 30 GeV/c, is not displayed.

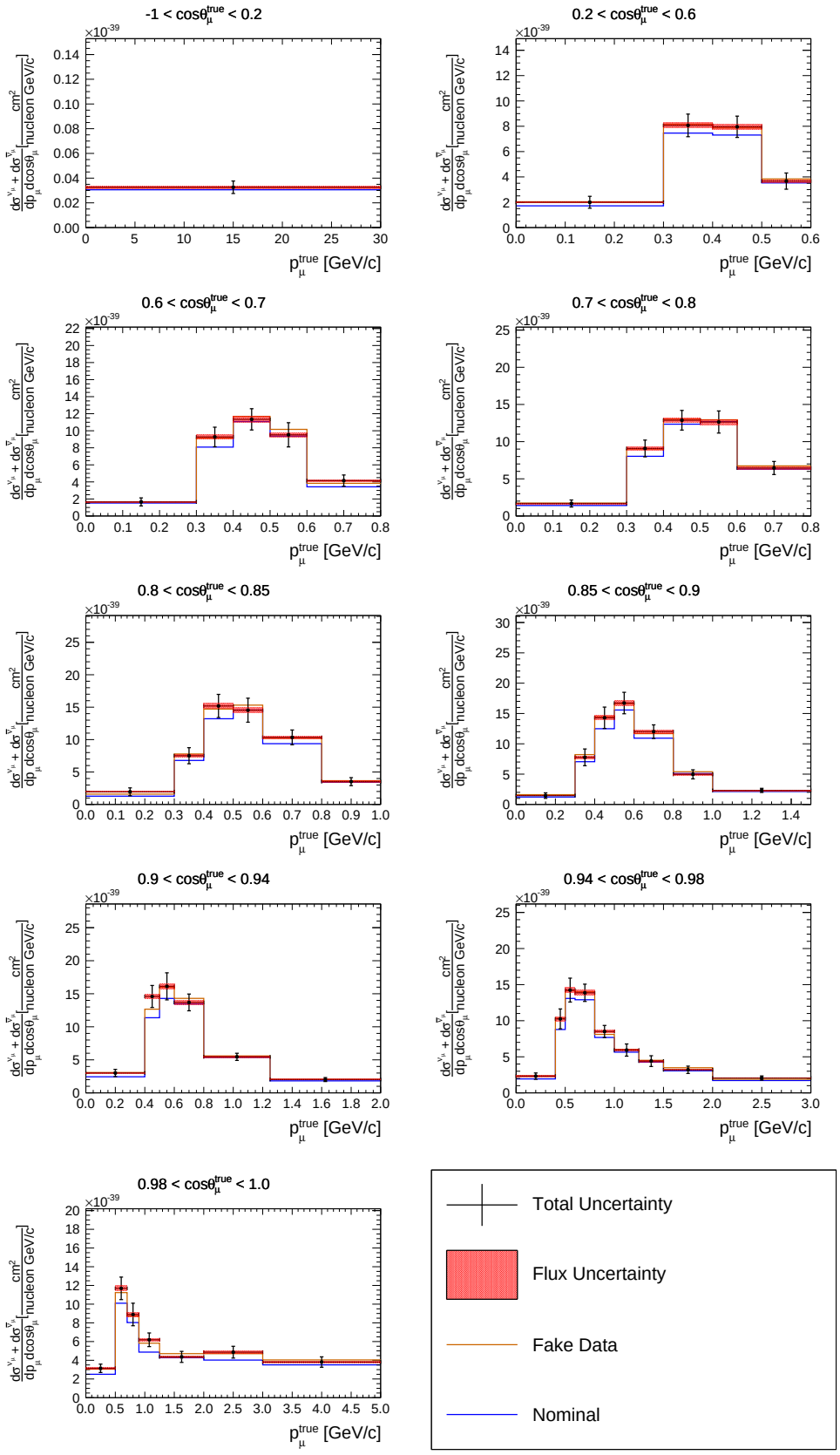

Figure C.21. Sum of the cross sections in bins of true muon kinematics obtained using NEUT prediction with 2p2h increased by a factor of two as fake data and NEUT as nominal. The result is compared with the nominal and fake data prediction. The error bars stand for the shape uncertainty while the red band are the fully correlated normalization uncertainty. The last bin, up to 30 GeV/c, is not displayed.

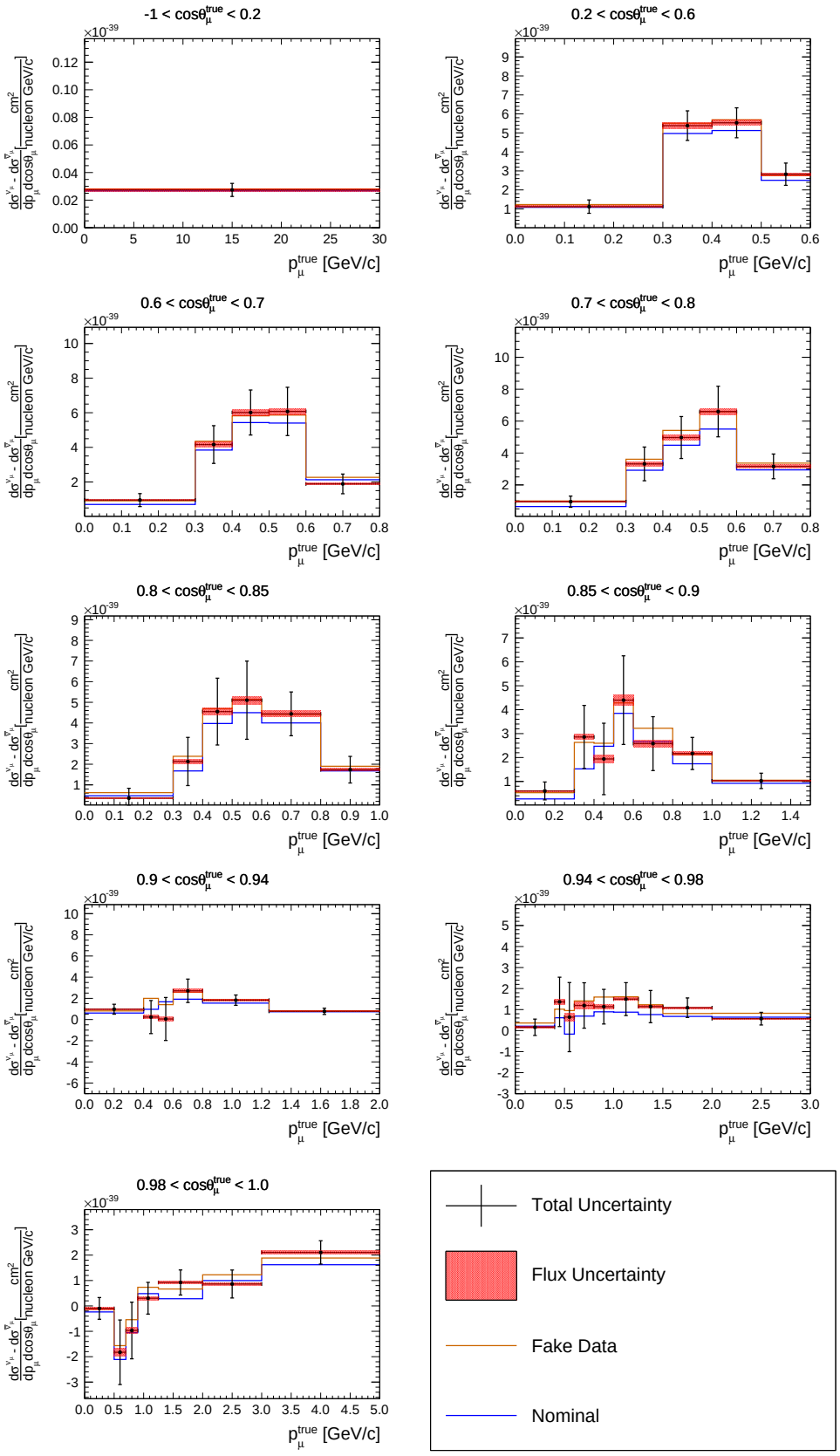

Figure C.22. Difference of the cross sections in bins of true muon kinematics obtained using NEUT prediction with 2p2h increased by a factor of two as fake data and NEUT as nominal. The result is compared with the nominal and fake data prediction. The error bars stand for the shape uncertainty while the red band are the fully correlated normalization uncertainty. The last bin, up to 30 GeV/c, is not displayed.

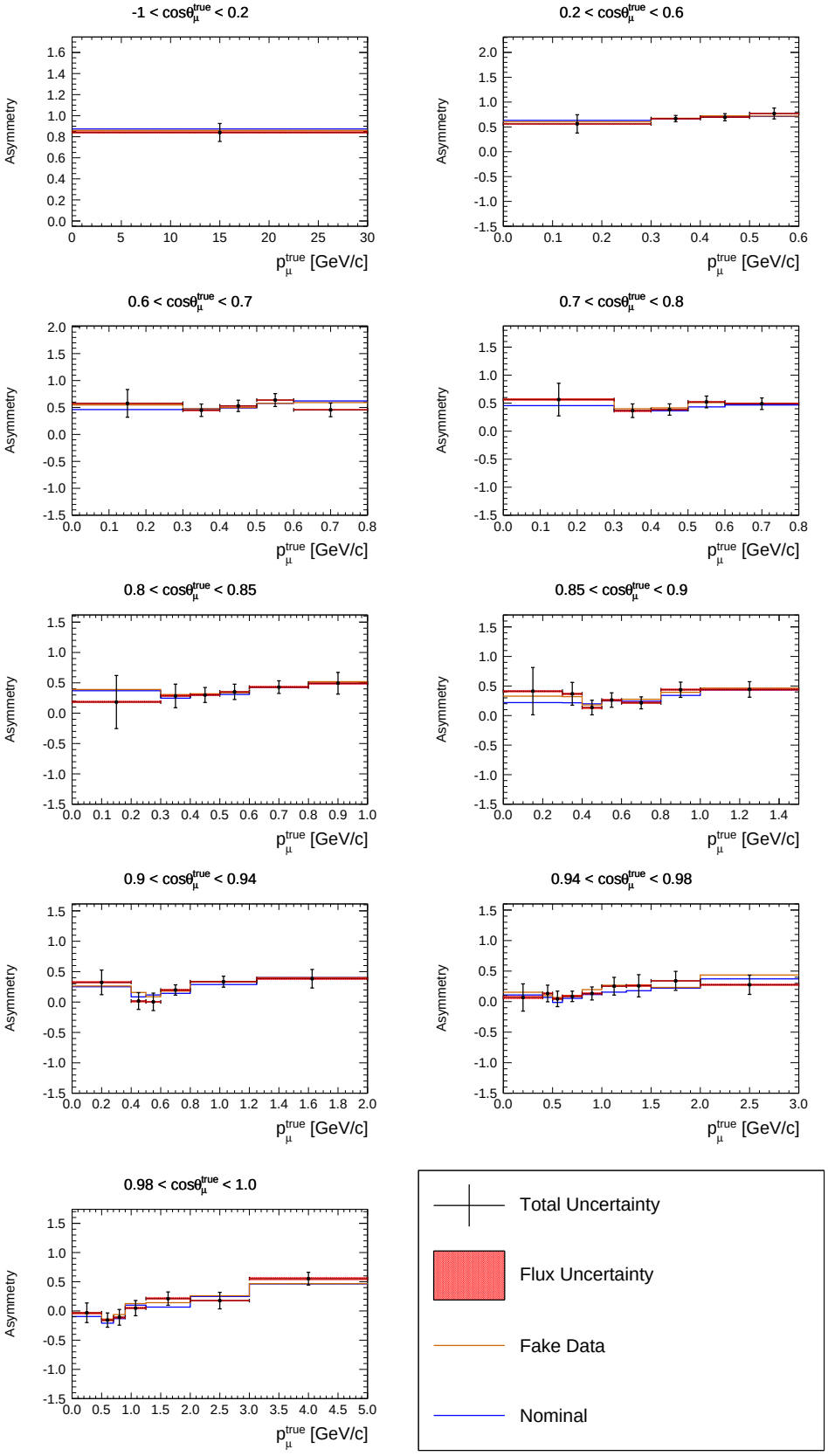

Figure C.23. Asymmetry of the cross sections in bins of true muon kinematics obtained using NEUT prediction with 2p2h increased by a factor of two as fake data and NEUT as nominal. The result is compared with the nominal and fake data prediction. The error bars stand for the shape uncertainty while the red band are the fully correlated normalization uncertainty. The last bin, up to 30 GeV/c, is not displayed.

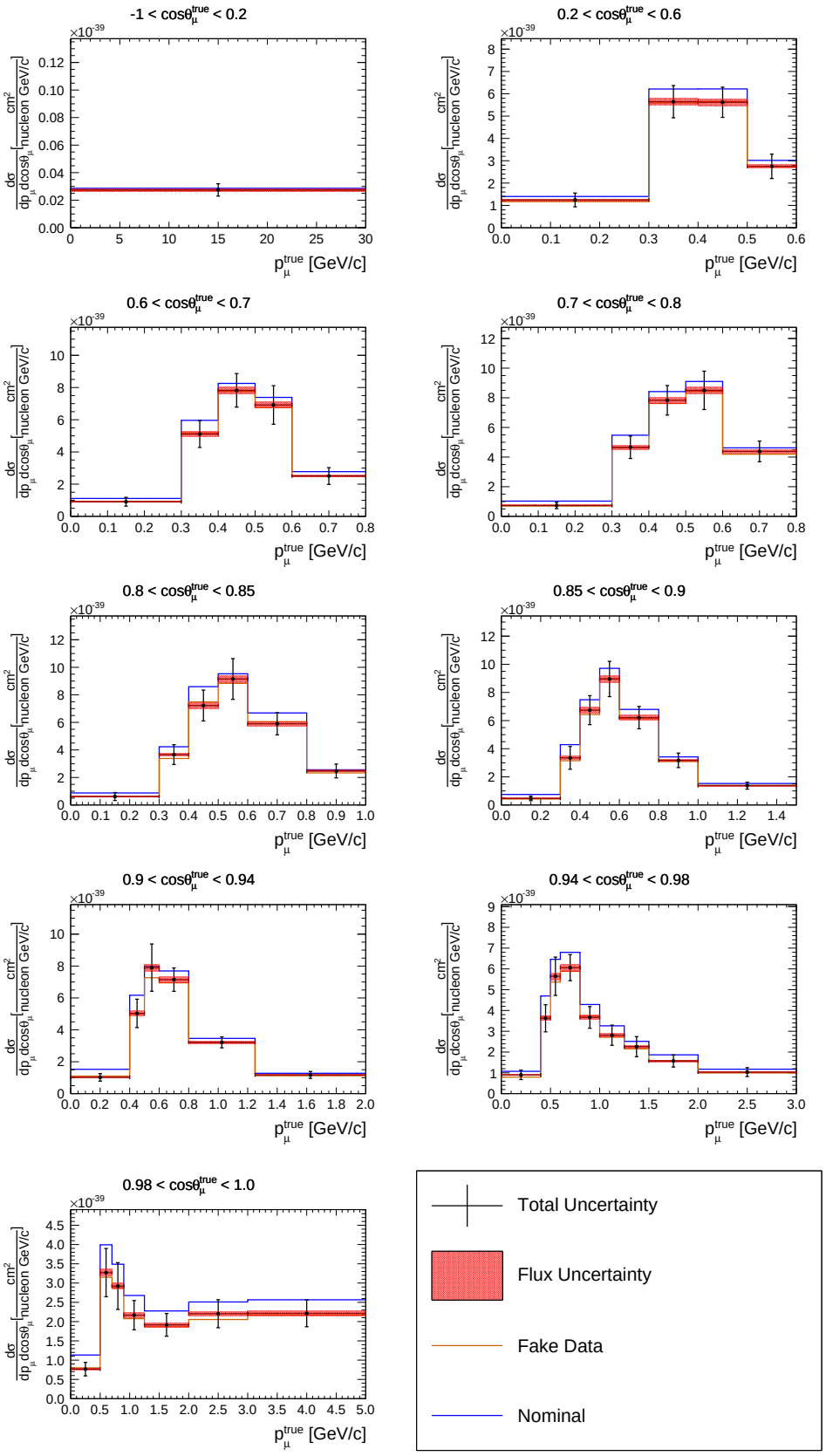

Figure C.24. ν_μ CC-0π cross section in bins of true muon kinematics obtained using NEUT prediction without 2p2h as fake data and NEUT as nominal. The result is compared with the nominal and fake data prediction. The error bars stand for the shape uncertainty while the red band are the fully correlated normalization uncertainty. The last bin, up to 30 GeV/c, is not displayed.

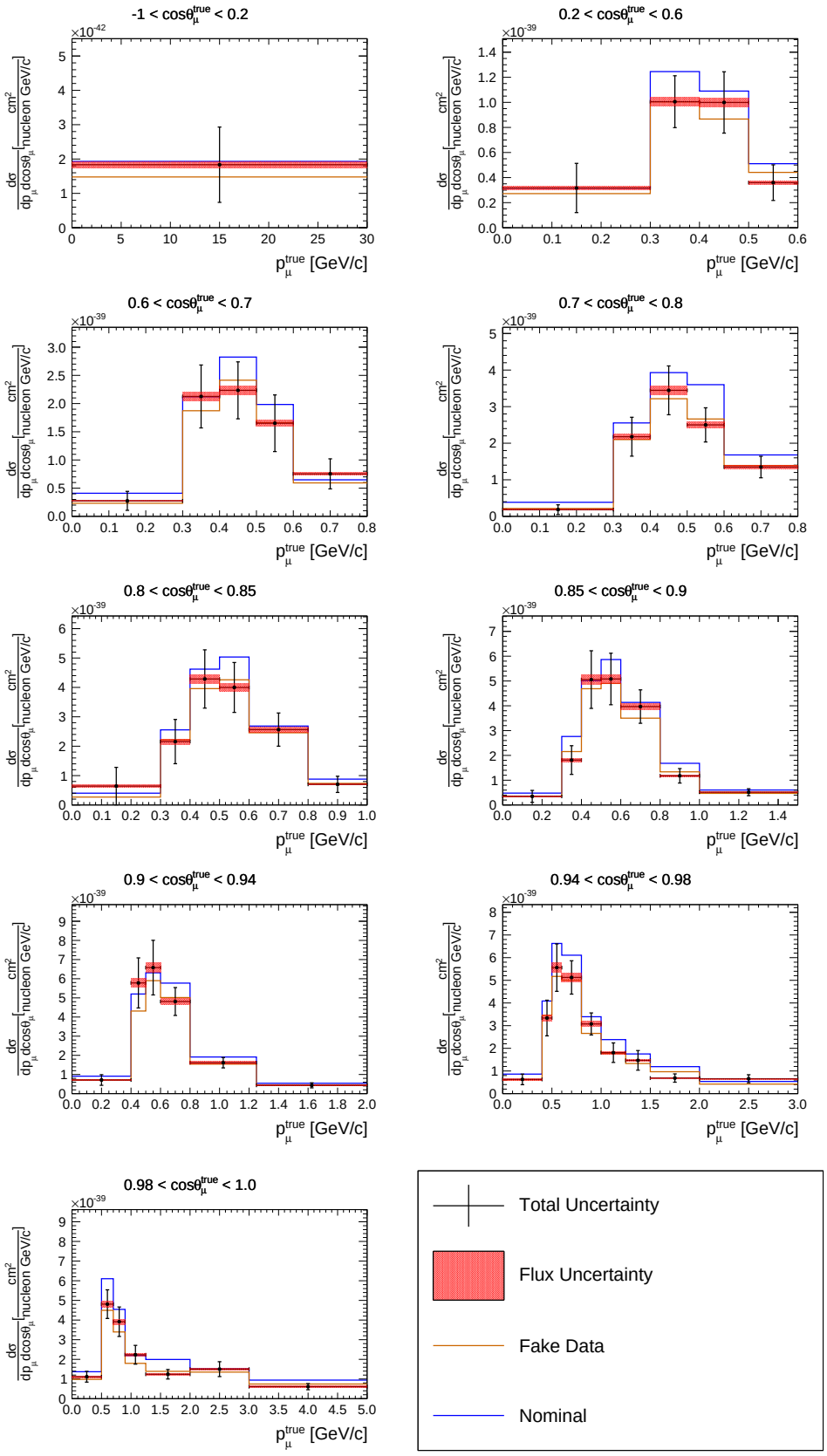

Figure C.25. $\bar{\nu}_\mu$ CC-0π cross section in bins of true muon kinematics obtained using NEUT prediction without 2p2h as fake data and NEUT as nominal. The result is compared with the nominal and fake data prediction. The error bars stand for the shape uncertainty while the red band are the fully correlated normalization uncertainty. The last bin, up to 30 GeV/c, is not displayed.

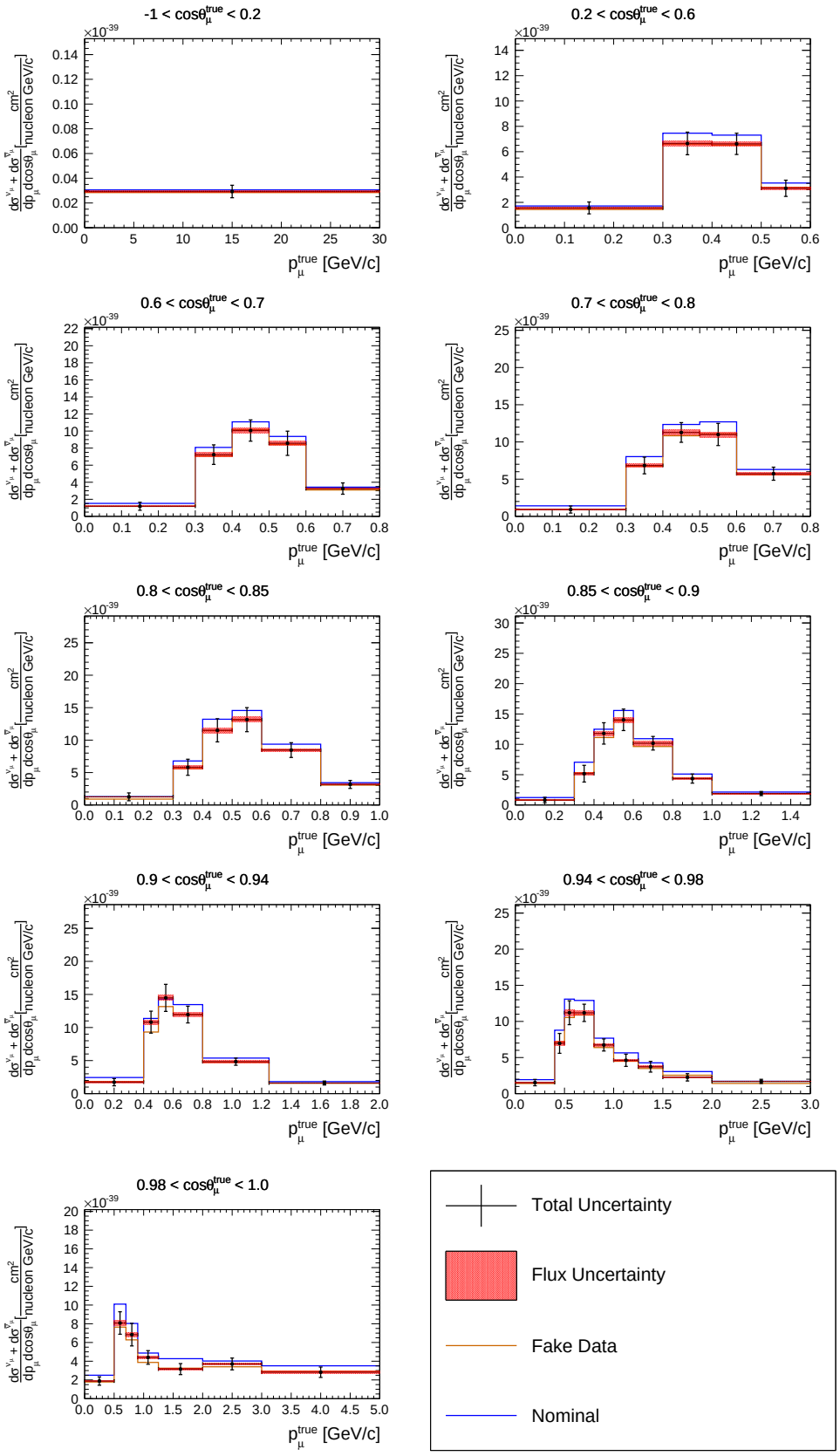

Figure C.26. Sum of the cross sections in bins of true muon kinematics obtained using NEUT prediction without 2p2h as fake data and NEUT as nominal. The result is compared with the nominal and fake data prediction. The error bars stand for the shape uncertainty while the red band are the fully correlated normalization uncertainty. The last bin, up to 30 GeV/c, is not displayed.

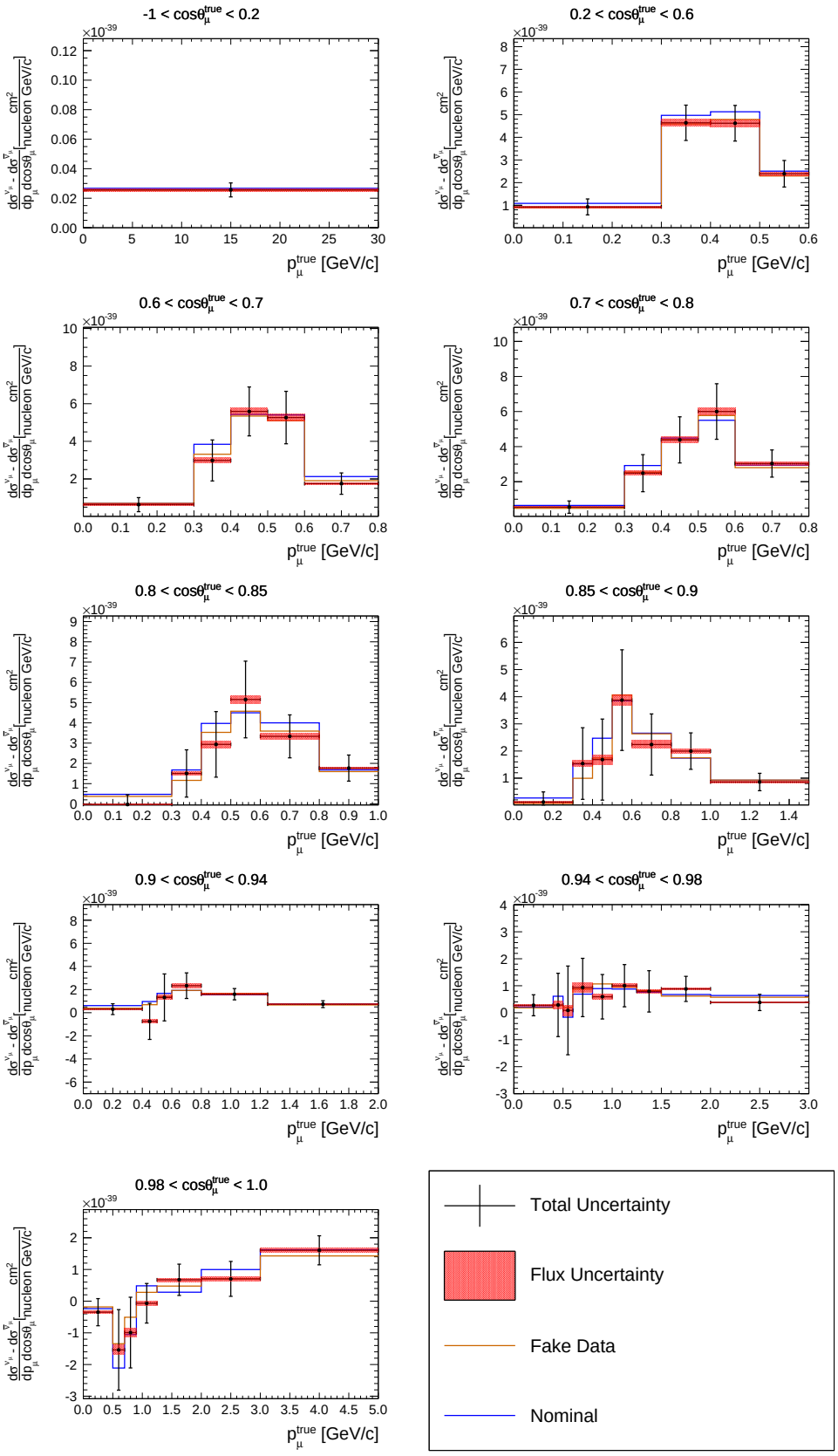

Figure C.27. Difference of the cross sections in bins of true muon kinematics obtained using NEUT prediction without 2p2h as fake data and NEUT as nominal. The result is compared with the nominal and fake data prediction. The error bars stand for the shape uncertainty while the red band are the fully correlated normalization uncertainty. The last bin, up to 30 GeV/c, is not displayed.

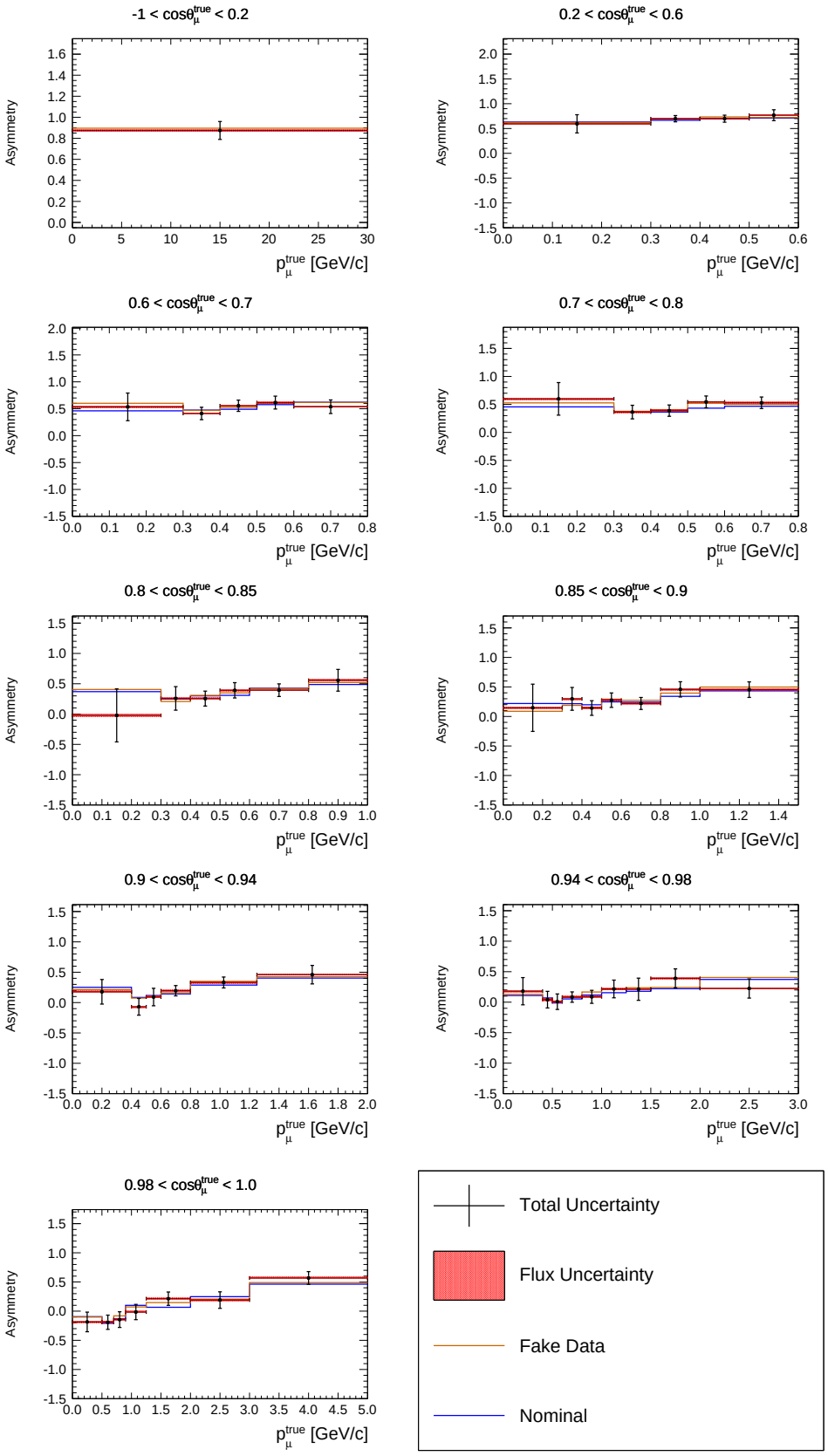

Figure C.28. Asymmetry of the cross sections in bins of true muon kinematics obtained using NEUT prediction without 2p2h as fake data and NEUT as nominal. The result is compared with the nominal and fake data prediction. The error bars stand for the shape uncertainty while the red band are the fully correlated normalization uncertainty. The last bin, up to 30 GeV/c, is not displayed.

NEUT with biased wrong sign component

This fake data set has been generated reducing the wrong sign component in each sample of a factor of 10%. The χ^2 GOF is summarized in Tab. XXXV. In Fig. C.29 is reported the fractional bias which is compatible with zero inside the errors. Also in this case the fractional bias -1 for the antineutrino case correspond to the bin $0.6 < \cos\theta_\mu^{true} < 0.7$, $0.8 < p_\mu^{true} < 30\,GeV$, where the possibility to have zero events is expected. The bigger error bar in the fractional bias for antineutrino correspond to the bin $0.8 < \cos\theta_\mu^{true} < 0.85$, $0.0 < p_\mu^{true} < 0.3\,GeV$ where the statistical error is 90%. In Figs. from C.30 to C.34 are reported the ν_μ and $\bar{\nu}_\mu$ CC-0π cross sections, the sum, difference and asymmetry in bins of true muon kinematics. Looking at the comparison between the nominal, the fake data and the fit results is clear that the effect of a reduction of 10% of the wrong sign component in the neutrino beam does not produce a visible effect since this component is low, while, for the antineutrino being the wrong sign component higher, the effect of the reduction is visible and present around 0.6 GeV/c.

	χ^2
Cross section	66.43
Sum	11.35
Difference	9.65
Asymmetry	19.20

TABLE XXXV. Summary table of the χ^2 GOF computed using the total covariance matrix (statistical plus systematic uncertainties).

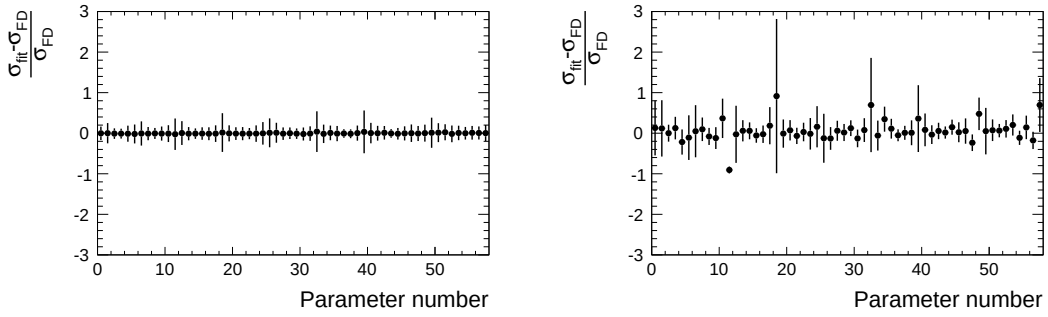

Figure C.29. Fractional bias between the result of the fit and the fake data for the ν_μ (left) and $\bar{\nu}_\mu$ CC-0π cross section (right) in bins of true muon kinematics. The fake data used is NEUT prediction with a lower "wrong sign" component in the different beams.

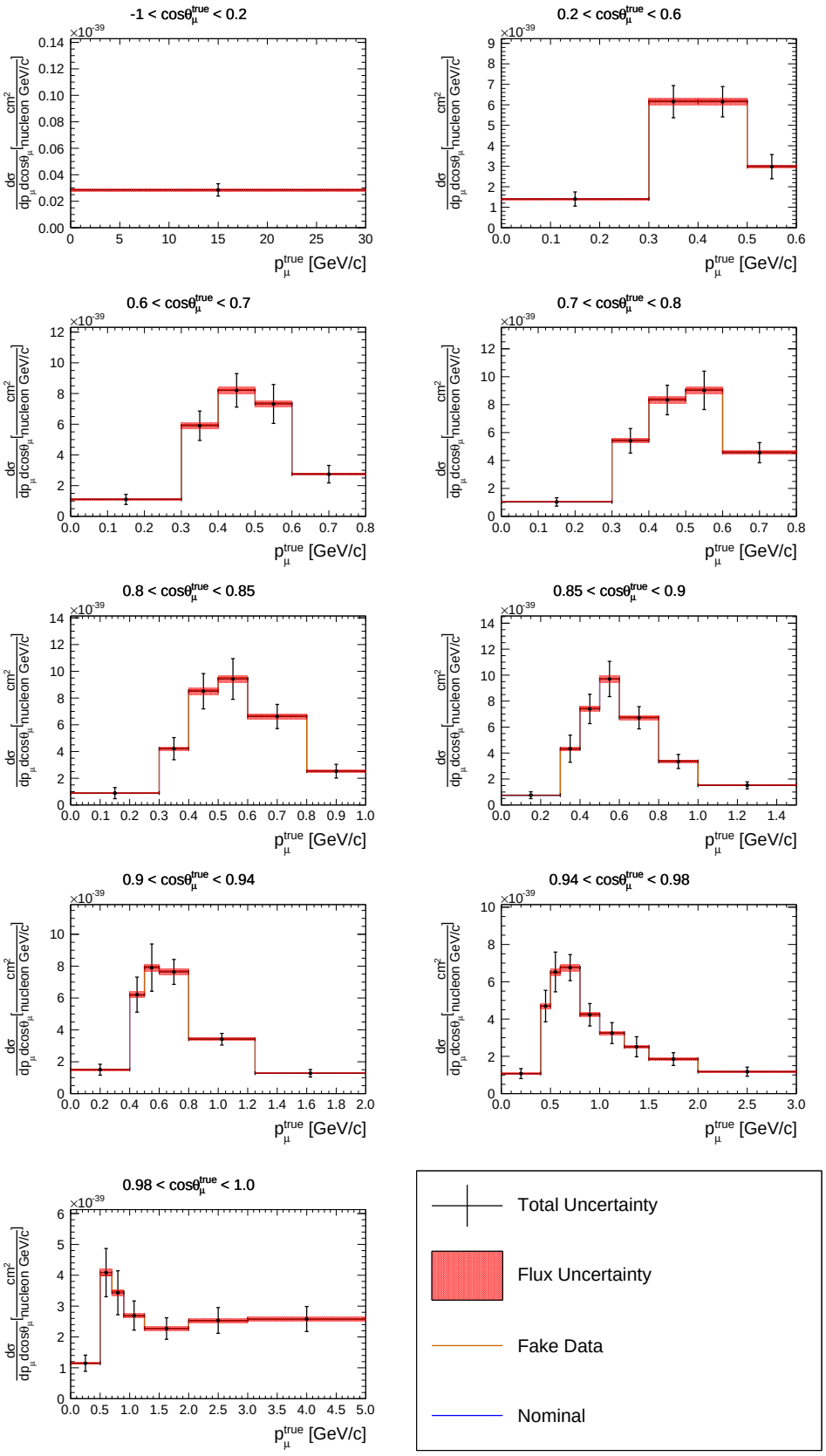

Figure C.30. ν_μ CC-0π cross section in bins of true muon kinematics obtained using NEUT prediction with a lower "wrong sign" component in the different beams as fake data and NEUT as nominal. The result is compared with the nominal and fake data prediction. The error bars stand for the shape uncertainty while the red band are the fully correlated normalization uncertainty. The last bin, up to 30 GeV/c, is not displayed.

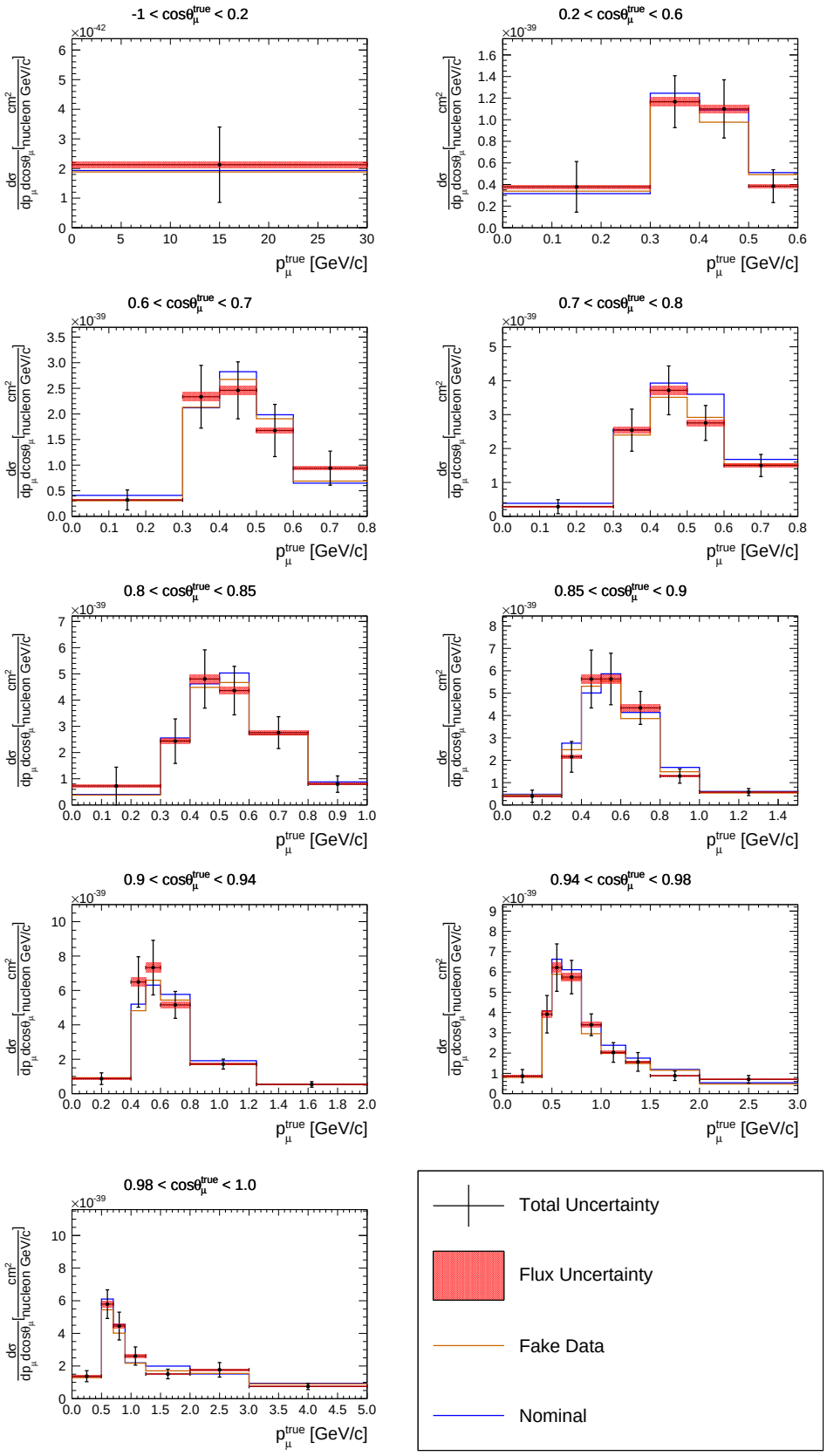

Figure C.31. $\bar{\nu}_\mu$ CC-0π cross section in bins of true muon kinematics obtained using NEUT prediction with a lower "wrong sign" component in the different beams as fake data and NEUT as nominal. The result is compared with the nominal and fake data prediction. The error bars stand for the shape uncertainty while the red band are the fully correlated normalization uncertainty. The last bin, up to 30 GeV/c, is not displayed.

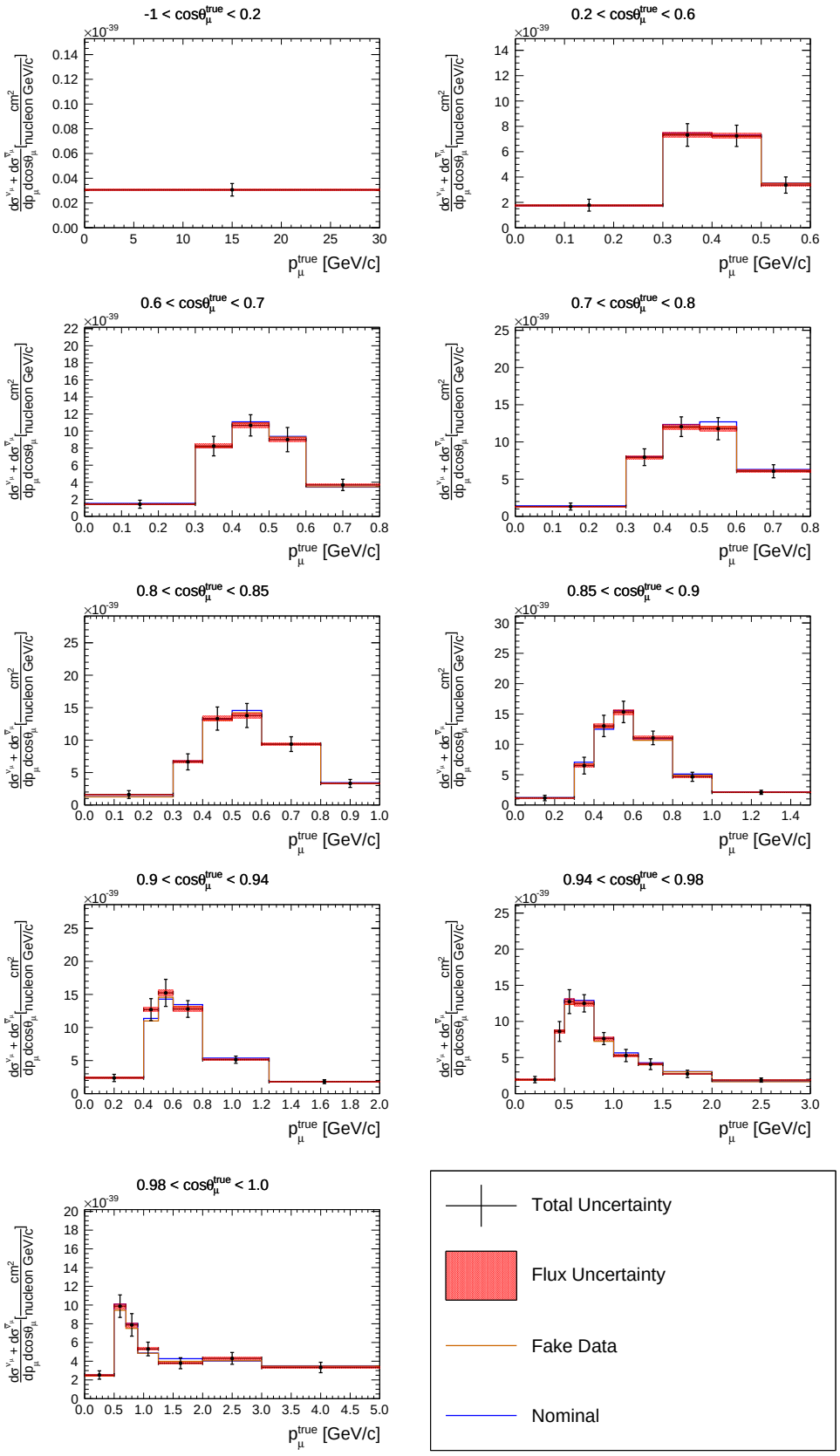

Figure C.32. Sum of the cross sections in bins of true muon kinematics obtained using NEUT prediction with a lower "wrong sign" component in the different beams as fake data and NEUT as nominal. The result is compared with the nominal and fake data prediction. The error bars stand for the shape uncertainty while the red band are the fully correlated normalization uncertainty. The last bin, up to 30 GeV/c, is not displayed.

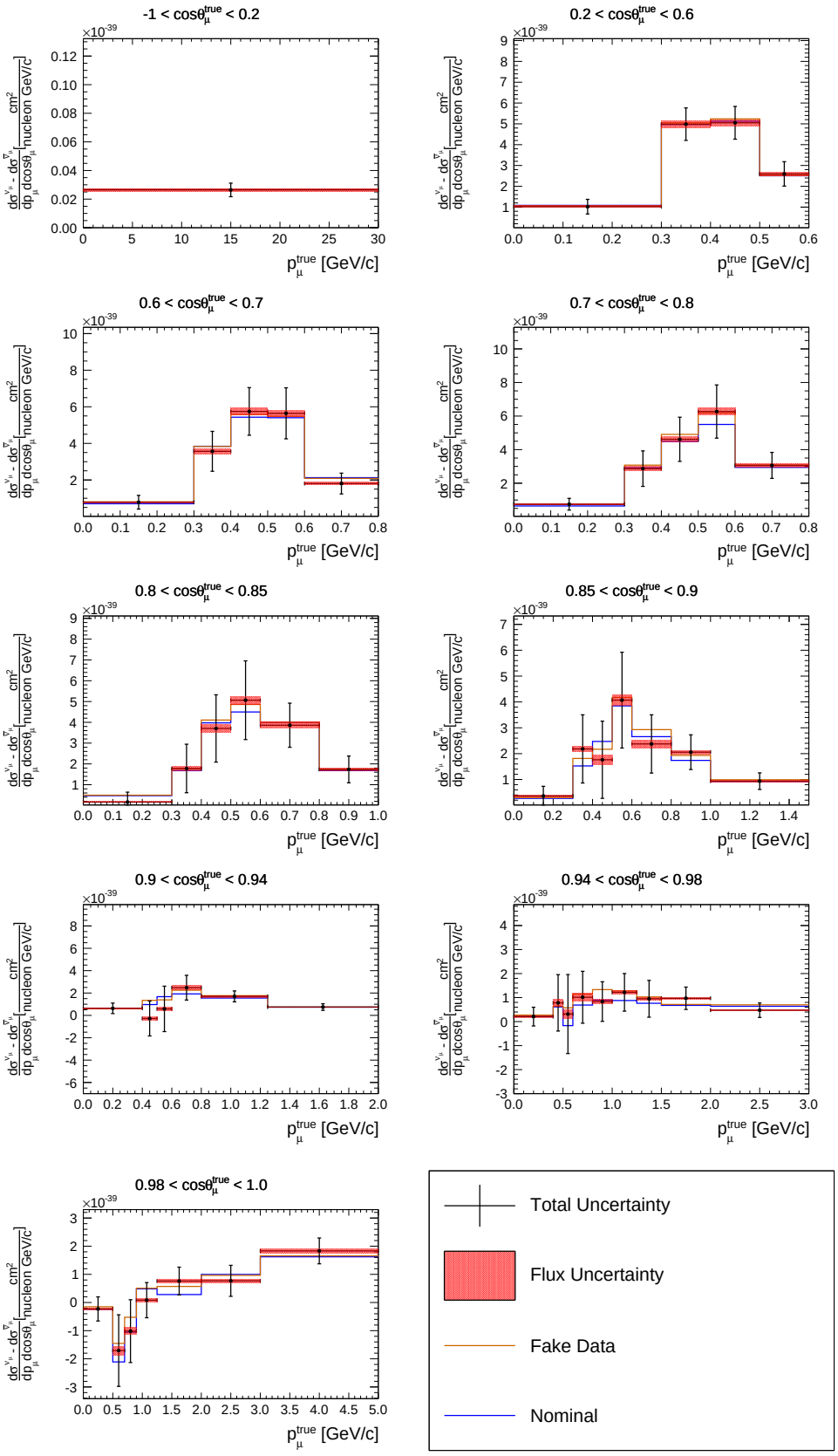

Figure C.33. Difference of the cross sections in bins of true muon kinematics obtained using NEUT prediction with a lower "wrong sign" component in the different beams as fake data and NEUT as nominal. The result is compared with the nominal and fake data prediction. The error bars stand for the shape uncertainty while the red band are the fully correlated normalization uncertainty. The last bin, up to 30 GeV/c, is not displayed.

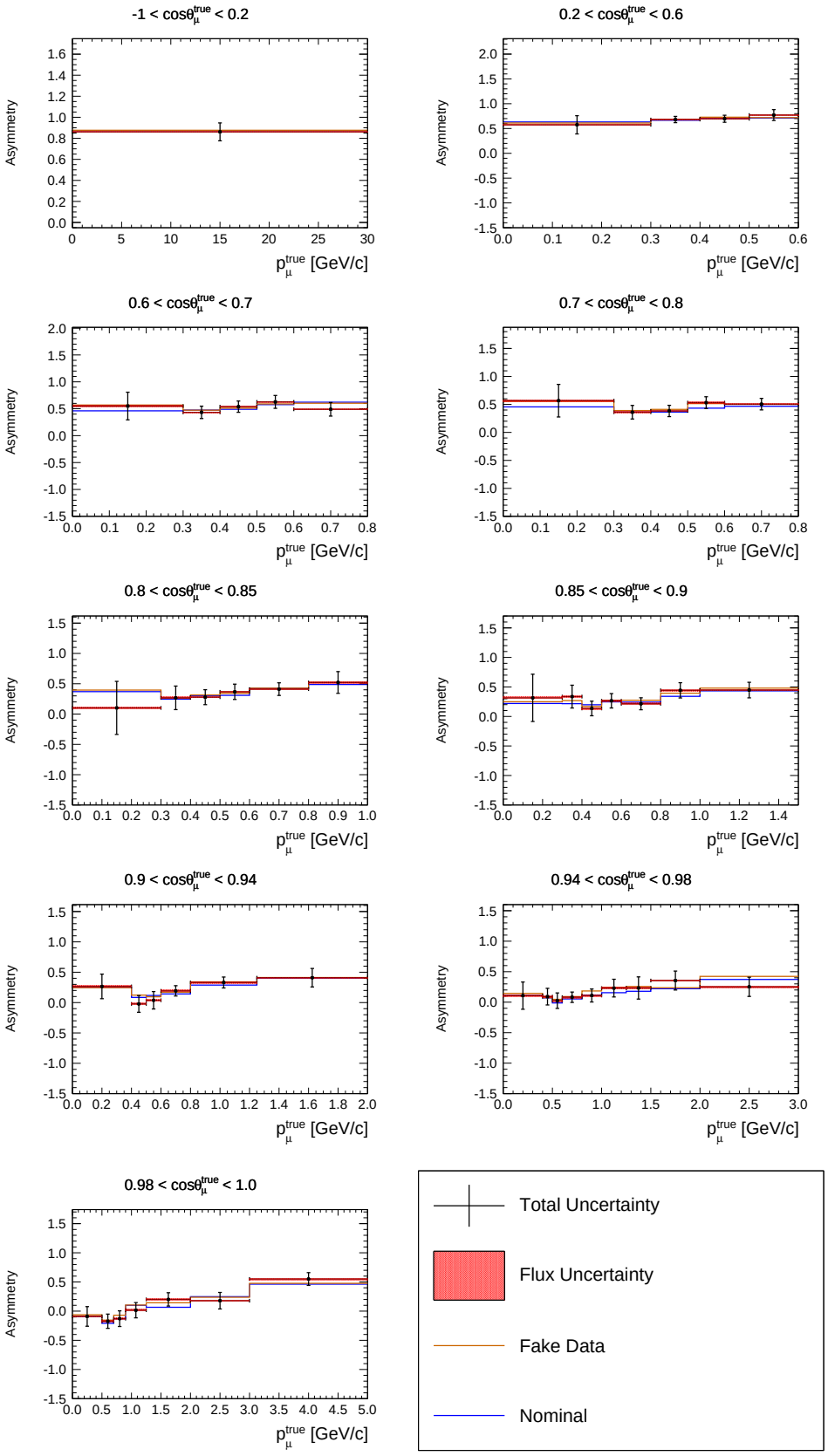

Figure C.34. Asymmetry of the cross sections in bins of true muon kinematics obtained using NEUT prediction with a lower "wrong sign" component in the different beams as fake data and NEUT as nominal. The result is compared with the nominal and fake data prediction. The error bars stand for the shape uncertainty while the red band are the fully correlated normalization uncertainty. The last bin, up to 30 GeV/c, is not displayed.

NEUT with biased background

This fake data set has been generated increasing the resonant axial mass used in NEUT from 0.95 GeV/c^2 to in 1.3 GeV/c^2. The χ^2 GOF is summarized in Tab. XXXVI. In Fig. C.35 is reported the fractional bias which is compatible with zero inside the errors. This demonstrates that fitting the flux the final results is not biased. In Figs. from C.36 to C.40 the ν_μ and $\bar{\nu}_\mu$ CC-0π cross sections, the sum, difference and asymmetry in bins of true muon kinematics are reported.

	χ^2
Cross section	71.34
Sum	11.77
Difference	9.72
Asymmetry	20.61

TABLE XXXVI. Summary table of the χ^2 GOF computed using the total covariance matrix (statistical plus systematic uncertainties).

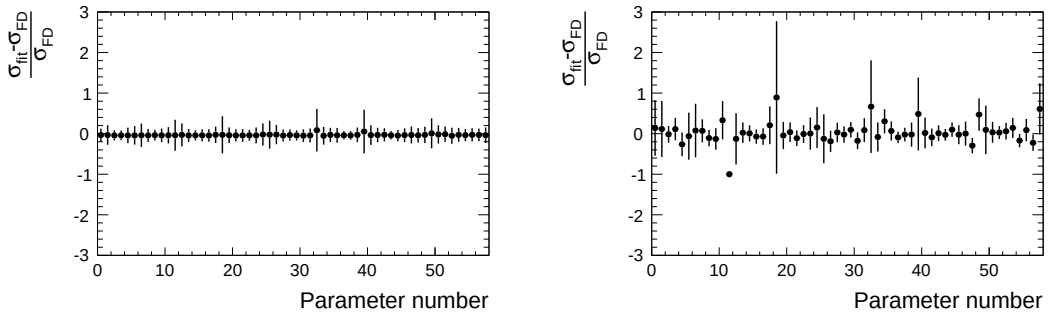

Figure C.35. Fractional bias between the result of the fit and the fake data for the ν_μ (left) and $\bar{\nu}_\mu$ CC-0π cross section (right) in bins of true muon kinematics. The fake data used is NEUT prediction with biased background.

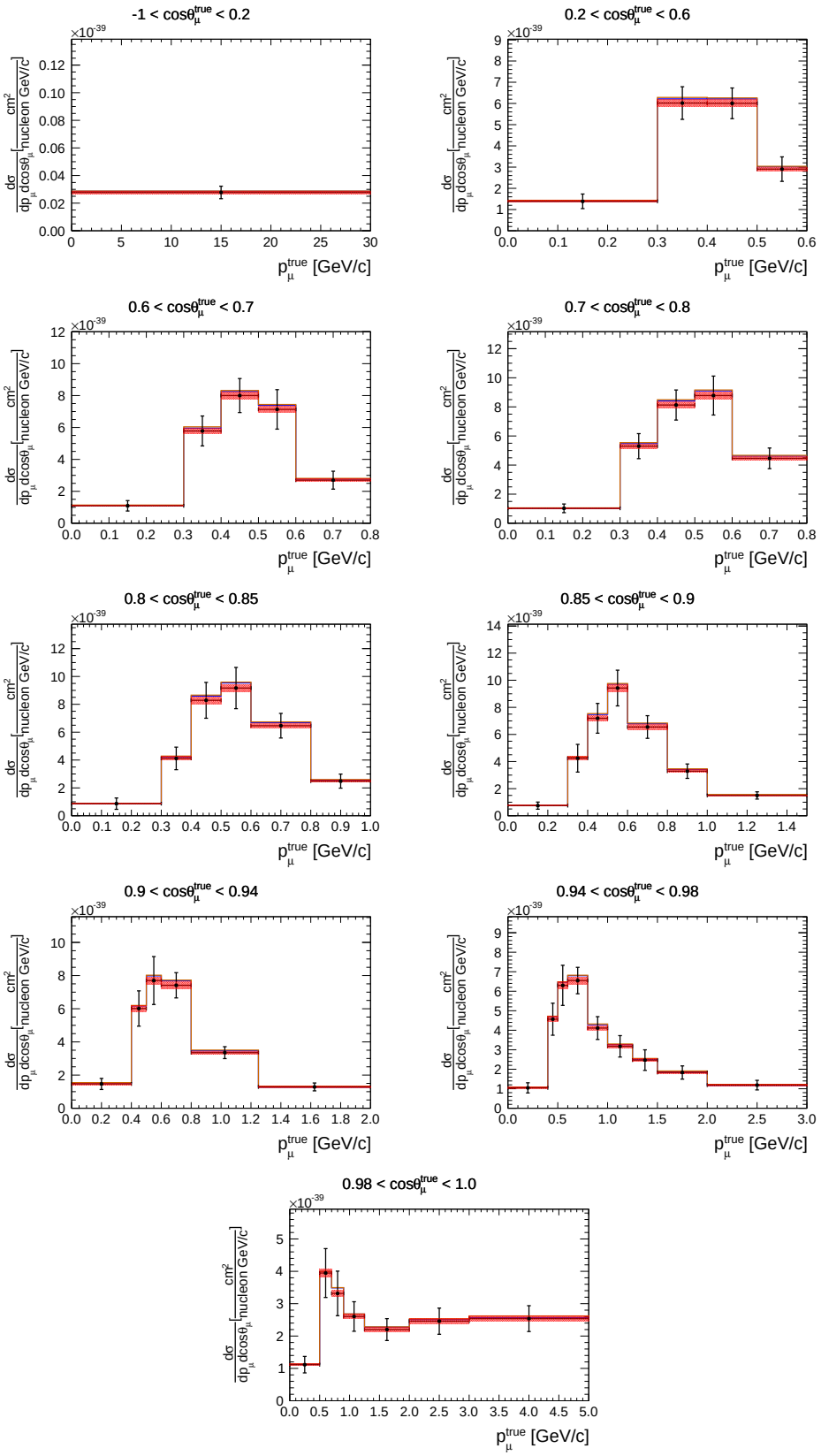

Figure C.36. ν_μ CC-0π cross section in bins of true muon kinematics obtained using NEUT prediction with biased background as fake data and NEUT as nominal. The result is compared with the nominal and fake data prediction. The error bars stand for the shape uncertainty while the red band are the fully correlated normalization uncertainty. The last bin, up to 30 GeV/c, is not displayed.

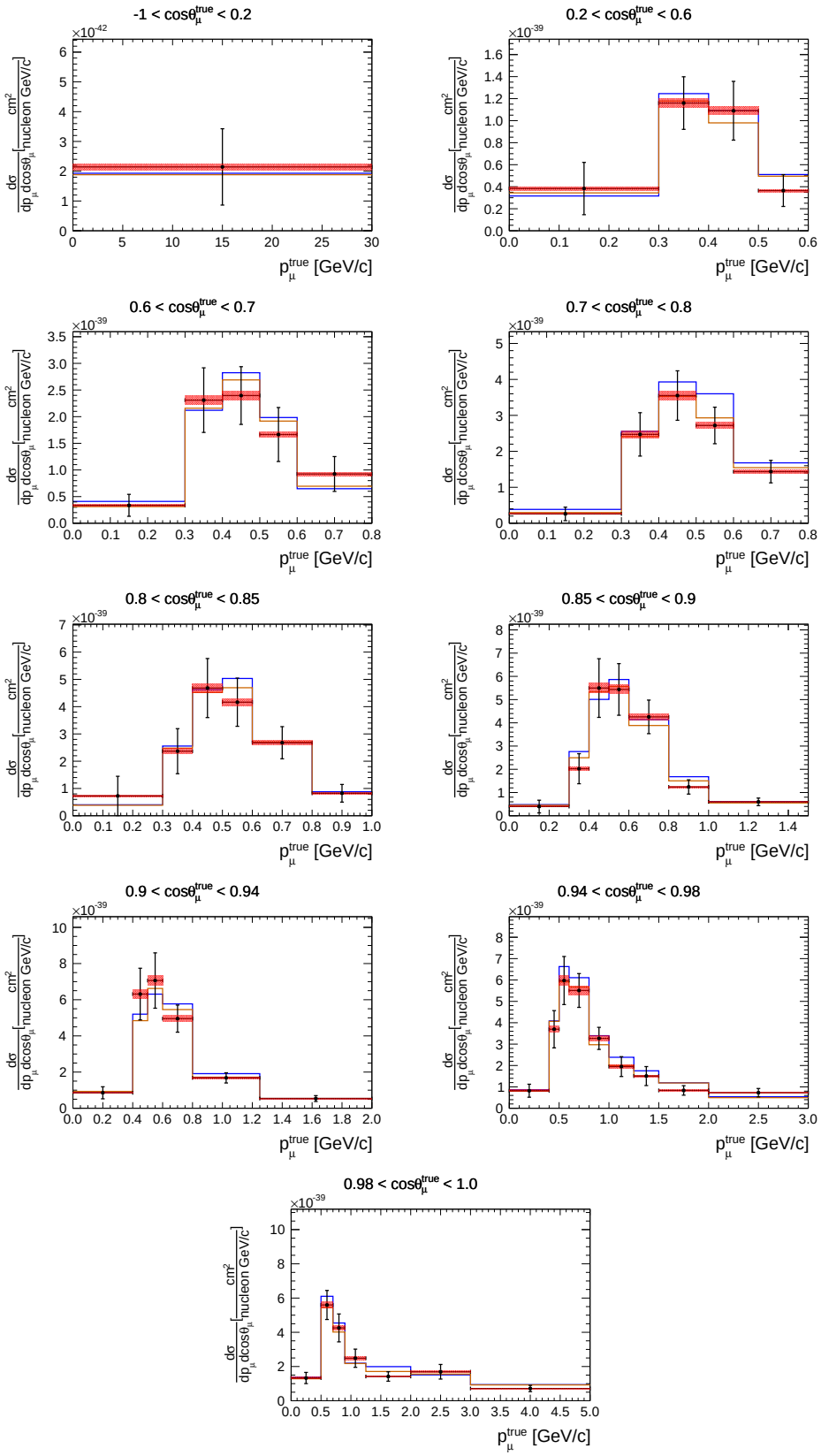

Figure C.37. $\bar{\nu}_\mu$ CC-0π cross section in bins of true muon kinematics obtained using NEUT prediction with biased background as fake data and NEUT as nominal. The result is compared with the nominal and fake data prediction. The error bars stand for the shape uncertainty while the red band are the fully correlated normalization uncertainty. The last bin, up to 30 GeV/c, is not displayed.

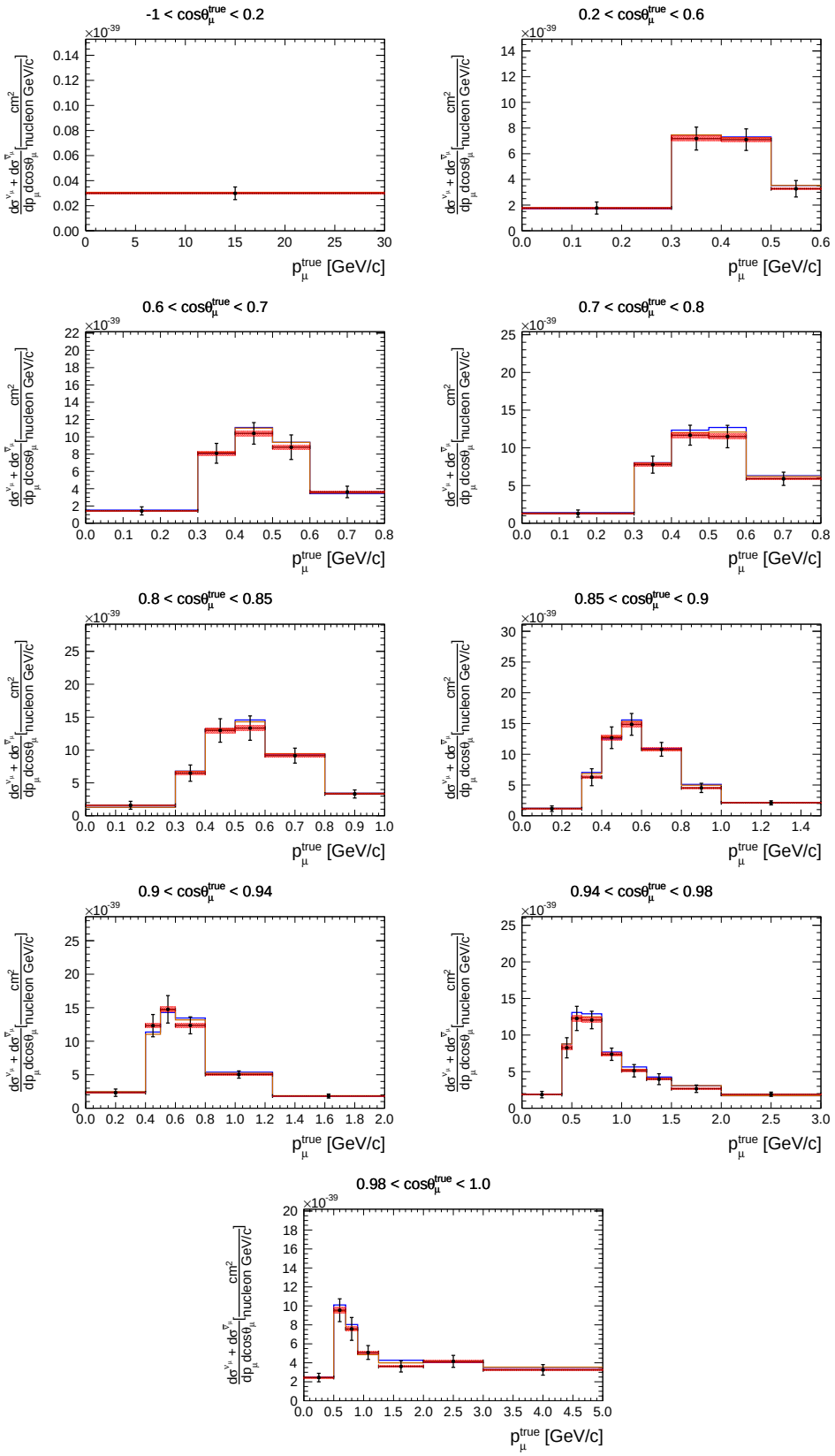

Figure C.38. Sum of the cross sections in bins of true muon kinematics obtained using NEUT prediction with biased background as fake data and NEUT as nominal. The result is compared with the nominal and fake data prediction. The error bars stand for the shape uncertainty while the red band are the fully correlated normalization uncertainty. The last bin, up to 30 GeV/c, is not displayed.

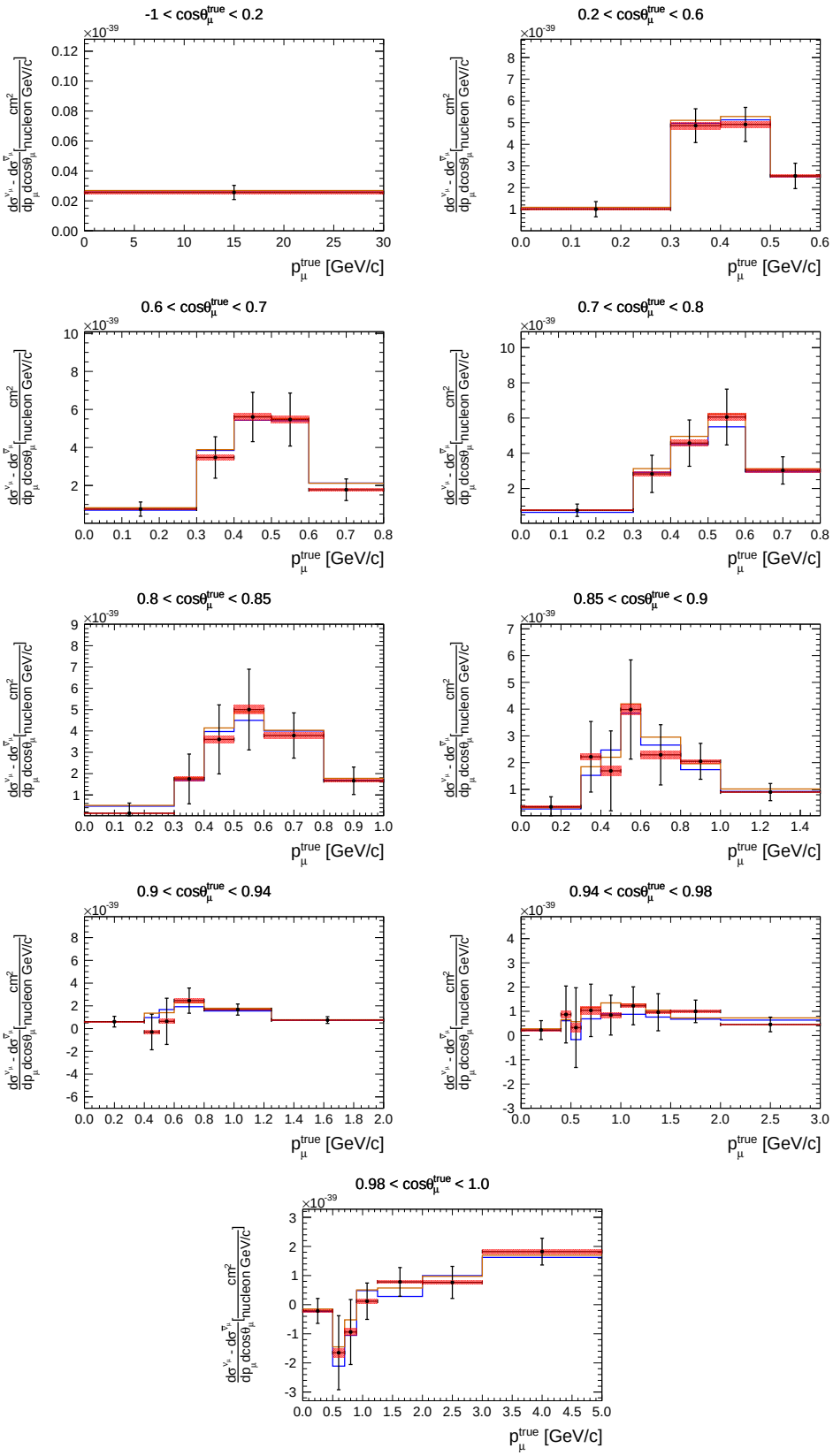

Figure C.39. Difference of the cross sections in bins of true muon kinematics obtained using NEUT prediction with biased background as fake data and NEUT as nominal. The result is compared with the nominal and fake data prediction. The error bars stand for the shape uncertainty while the red band are the fully correlated normalization uncertainty. The last bin, up to 30 GeV/c, is not displayed.

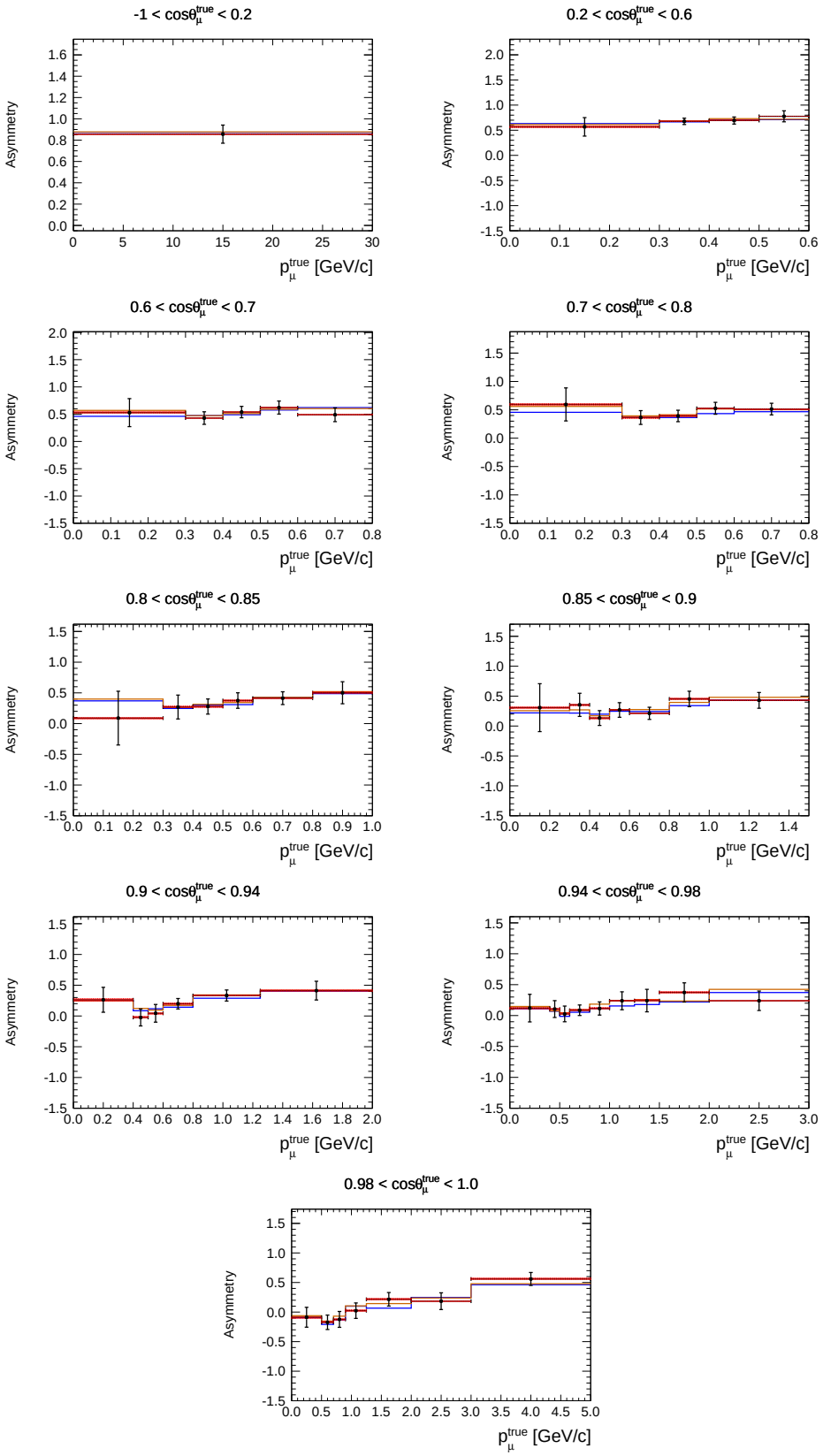

Figure C.40. Asymmetry of the cross sections in bins of true muon kinematics obtained using NEUT prediction with biased background as fake data and NEUT as nominal. The result is compared with the nominal and fake data prediction. The error bars stand for the shape uncertainty while the red band are the fully correlated normalization uncertainty. The last bin, up to 30 GeV/c, is not displayed.

Bibliography

[1] W. Pauli. "Letter to the Tübingen conference" (1930). http://www.library.ethz.ch/en/ms/Virtuelle-Ausstellungen/Wolfgang-Pauli-und-die-moderne-Physik (cit. on p. 1).

[2] J. Chadwick. "Possible Existence of a Neutron". *Nature* 129 (1932), p. 312. DOI: 10.1038/129312a0 (cit. on p. 1).

[3] C. L. Cowan et al. "Detection of the Free Neutrino: a Confirmation". *Science* 124.3212 (1956), pp. 103–104. ISSN: 0036-8075. DOI: 10.1126/science.124.3212.103. eprint: http://science.sciencemag.org/content/124/3212/103.full.pdf. URL: http://science.sciencemag.org/content/124/3212/103 (cit. on p. 1).

[4] "The Nobel Prize in Physics 1995" (1995). URL: http://www.nobelprize.org/nobel_prizes/physics/laureates/1995/ (cit. on p. 1).

[5] B. Pontecorvo. "Electron and Muon Neutrinos". *Sov. Phys. JETP* 10 (1960). [Zh. Eksp. Teor. Fiz.37,1751(1959)], pp. 1236–1240 (cit. on p. 1).

[6] G. Danby et al. "Observation of High-Energy Neutrino Reactions and the Existence of Two Kinds of Neutrinos". *Phys. Rev. Lett.* 9 (1962), pp. 36–44. DOI: 10.1103/PhysRevLett.9.36 (cit. on p. 1).

[7] "The Nobel Prize in Physics 1988" (1988). URL: http://www.nobelprize.org/nobel_prizes/physics/laureates/1988/ (cit. on p. 1).

[8] K. Kodama et al. "Observation of tau neutrino interactions". *Phys. Lett.* B504 (2001), pp. 218–224. DOI: 10.1016/S0370-2693(01)00307-0. arXiv: hep-ex/0012035 [hep-ex] (cit. on p. 1).

[9] Steven Weinberg. "A Model of Leptons". *Phys. Rev. Lett.* 19 (21 1967), pp. 1264–1266. DOI: 10.1103/PhysRevLett.19.1264. URL: https://link.aps.org/doi/10.1103/PhysRevLett.19.1264 (cit. on p. 1).

[10] Abdus Salam and J. C. Ward. "Weak and electromagnetic interactions". *Il Nuovo Cimento (1955-1965)* 11.4 (1959), pp. 568–577. ISSN: 1827-6121. DOI: 10.1007/BF02726525. URL: https://doi.org/10.1007/BF02726525 (cit. on p. 1).

[11] S. L. Glashow. "Partial Symmetries of Weak Interactions". *Nucl. Phys.* 22 (1961), pp. 579–588. DOI: 10.1016/0029-5582(61)90469-2 (cit. on p. 1).

[12] F. Englert and R. Brout. "Broken Symmetry and the Mass of Gauge Vector Mesons". *Phys. Rev. Lett.* 13 (9 1964), pp. 321–323. DOI: 10.1103/PhysRevLett.13.321. URL: https://link.aps.org/doi/10.1103/PhysRevLett.13.321 (cit. on p. 4).

[13] P.W. Higgs. "Broken symmetries, massless particles and gauge fields". *Physics Letters* 12.2 (1964), pp. 132 –133. ISSN: 0031-9163. DOI: http://dx.doi.org/10.1016/0031-9163(64)91136-9. URL: http://www.sciencedirect.com/science/article/pii/0031916364911369 (cit. on p. 4).

[14] Peter W. Higgs. "Broken Symmetries and the Masses of Gauge Bosons". *Phys. Rev. Lett.* 13 (16 1964), pp. 508–509. DOI: 10.1103/PhysRevLett.13.508. URL: https://link.aps.org/doi/10.1103/PhysRevLett.13.508 (cit. on p. 4).

[15] C. S. Wu et al. "Experimental Test of Parity Conservation in Beta Decay". *Phys. Rev.* 105 (1957), pp. 1413–1414. DOI: 10.1103/PhysRev.105.1413 (cit. on p. 4).

[16] R. L. Garwin, L. M. Lederman, and Marcel Weinrich. "Observations of the Failure of Conservation of Parity and Charge Conjugation in Meson Decays: The Magnetic Moment of the Free Muon". *Phys. Rev.* 105 (1957), pp. 1415–1417. DOI: 10.1103/PhysRev.105.1415 (cit. on p. 4).

[17] Ettore Majorana and Luciano Maiani. "A symmetric theory of electrons and positrons". *Ettore Majorana Scientific Papers: On occasion of the centenary of his birth*. Ed. by Giuseppe Franco Bassani. Berlin, Heidelberg: Springer Berlin Heidelberg, 2006, pp. 201–233. ISBN: 978-3-540-48095-2. DOI: 10.1007/978-3-540-48095-2_10. URL: https://doi.org/10.1007/978-3-540-48095-2_10 (cit. on p. 5).

[18] A. Gando et al. "Search for Majorana Neutrinos near the Inverted Mass Hierarchy region with KamLAND-Zen". *Phys. Rev. Lett.* 117 (2016), p. 082503. arXiv: 1605.02889 [hep-ex] (cit. on p. 5).

[19] C Arnaboldi et al. "CUORE: a cryogenic underground observatory for rare events". *Nuclear Instruments and Methods in Physics Research Section A: Accelerators, Spectrometers, Detectors and Associated Equipment* 518.3 (2004), pp. 775 –798. ISSN: 0168-9002. DOI: https://doi.org/10.1016/j.nima.2003.07.067. URL: http://www.sciencedirect.com/science/article/pii/S0168900203023374 (cit. on p. 5).

[20] M. Agostini et al. "Background free search for neutrinoless double beta decay with GERDA Phase II" (2017). arXiv: 1703.00570 [nucl-ex] (cit. on p. 5).

[21] B. Pontecorvo. "Mesonium and anti-mesonium". *Sov. Phys. JETP* 6 (1957). [Zh. Eksp. Teor. Fiz.33,549(1957)], p. 429 (cit. on p. 6).

[22] B. Pontecorvo. "Inverse beta processes and nonconservation of lepton charge". *Sov. Phys. JETP* 7 (1958). [Zh. Eksp. Teor. Fiz.34,247(1957)], pp. 172–173 (cit. on p. 6).

[23] Z. Maki, M. Nakagawa, and S. Sakata. "Remarks on the unified model of elementary particles". *Prog. Theor. Phys.* 28 (1962), pp. 870–880. DOI: 10.1143/PTP.28.870 (cit. on p. 6).

[24] B. Pontecorvo. "Neutrino Experiments and the Problem of Conservation of Leptonic Charge". *Sov. Phys. JETP* 26 (1968). [Zh. Eksp. Teor. Fiz.53,1717(1967)], pp. 984–988 (cit. on p. 6).

[25] Raymond Davis Jr., Don S. Harmer, and Kenneth C. Hoffman. "Search for neutrinos from the sun". *Phys. Rev. Lett.* 20 (1968), pp. 1205–1209. DOI: 10.1103/PhysRevLett.20.1205 (cit. on p. 6).

[26] Y. Fukuda et al. "Evidence for oscillation of atmospheric neutrinos". *Phys. Rev. Lett.* 81 (1998), pp. 1562–1567. DOI: 10.1103/PhysRevLett.81.1562. arXiv: hep-ex/9807003 [hep-ex] (cit. on pp. 6, 20).

[27] Q. R. Ahmad et al. "Measurement of the rate of $\nu_e + d \to p + p + e^-$ interactions produced by ^8B solar neutrinos at the Sudbury Neutrino Observatory". *Phys. Rev. Lett.* 87 (2001), p. 071301. DOI: 10.1103/PhysRevLett.87.071301. arXiv: nucl-ex/0106015 [nucl-ex] (cit. on pp. 6, 17).

[28] Q. R. Ahmad et al. "Direct evidence for neutrino flavor transformation from neutral current interactions in the Sudbury Neutrino Observatory". *Phys. Rev. Lett.* 89 (2002), p. 011301. DOI: 10.1103/PhysRevLett.89.011301. arXiv: nucl-ex/0204008 [nucl-ex] (cit. on p. 6).

[29] "The Nobel Prize in Physics 2015" (1988). URL: http://www.nobelprize.org/nobel_prizes/physics/laureates/2015/ (cit. on pp. 6, 18, 19).

[30] Arthur B. McDonald. "Nobel Lecture: The Sudbury Neutrino Observatory: Observation of flavor change for solar neutrinos". *Rev. Mod. Phys.* 88.3 (2016), p. 030502. DOI: 10.1103/RevModPhys.88.030502 (cit. on p. 6).

[31] Takaaki Kajita. "Nobel Lecture: Discovery of atmospheric neutrino oscillations". *Rev. Mod. Phys.* 88.3 (2016), p. 030501. DOI: 10.1103/RevModPhys.88.030501 (cit. on p. 6).

[32] Samoil M. Bilenky and B. Pontecorvo. "Lepton Mixing and Neutrino Oscillations". *Phys. Rept.* 41 (1978), pp. 225–261. DOI: 10.1016/0370-1573(78)90095-9 (cit. on p. 7).

[33] Samoil M. Bilenky and B. Pontecorvo. "Again on Neutrino Oscillations". *Lett. Nuovo Cim.* 17 (1976), p. 569. DOI: 10.1007/BF02746567 (cit. on p. 7).

[34] Samoil M. Bilenky and B. Pontecorvo. "The Quark-Lepton Analogy and the Muonic Charge". *Yad. Fiz.* 24 (1976). [Sov. J. Nucl. Phys.24,316(1976)], pp. 603–608 (cit. on p. 7).

[35] R. B. Patterson. "Prospects for Measurement of the Neutrino Mass Hierarchy". *Ann. Rev. Nucl. Part. Sci.* 65 (2015), pp. 177–192. DOI: 10.1146/annurev-nucl-102014-021916. arXiv: 1506.07917 [hep-ex] (cit. on p. 10).

[36] Claudio Giganti, Stéphane Lavignac, and Marco Zito. "Neutrino oscillations: the rise of the PMNS paradigm" (2017). arXiv: 1710.00715 [hep-ex] (cit. on pp. 9, 17, 50).

[37] C. Jarlskog. "A Basis Independent Formulation of the Connection Between Quark Mass Matrices, CP Violation and Experiment". *Z. Phys.* C29 (1985), pp. 491–497. DOI: 10.1007/BF01565198 (cit. on p. 9).

[38] C. Jarlskog. "Commutator of the Quark Mass Matrices in the Standard Electroweak Model and a Measure of Maximal CP Violation". *Phys. Rev. Lett.* 55 (1985), p. 1039. DOI: 10.1103/PhysRevLett.55.1039 (cit. on p. 9).

[39] L. Wolfenstein. "Neutrino Oscillations in Matter". *Phys. Rev.* D17 (1978), pp. 2369–2374. DOI: 10.1103/PhysRevD.17.2369 (cit. on p. 10).

[40] S. P. Mikheev and A. Yu. Smirnov. "Resonance Amplification of Oscillations in Matter and Spectroscopy of Solar Neutrinos". *Sov. J. Nucl. Phys.* 42 (1985). [Yad. Fiz.42,1441(1985)], pp. 913–917 (cit. on p. 10).

[41] S. P. Mikheev and A. Yu. Smirnov. "Resonant amplification of neutrino oscillations in matter and solar neutrino spectroscopy". *Nuovo Cim.* C9 (1986), pp. 17–26. DOI: 10.1007/BF02508049 (cit. on p. 10).

[42] J. N. Bahcall et al. "Solar neutrino flux". *Astrophys. J.* 137 (1963), pp. 344–346. DOI: 10.1086/147513 (cit. on p. 13).

[43] E. G. Adelberger et al. "Solar fusion cross sections II: the pp chain and CNO cycles". *Rev. Mod. Phys.* 83 (2011), p. 195. DOI: 10.1103/RevModPhys.83.195. arXiv: 1004.2318 [nucl-ex] (cit. on p. 14).

[44] W. C. Haxton, R. G. Hamish Robertson, and Aldo M. Serenelli. "Solar Neutrinos: Status and Prospects". *Ann. Rev. Astron. Astrophys.* 51 (2013), pp. 21–61. DOI: 10.1146/annurev-astro-081811-125539. arXiv: 1208.5723 [astro-ph.SR] (cit. on p. 15).

[45] Bruce T. Cleveland et al. "Measurement of the Solar Electron Neutrino Flux with the Homestake Chlorine Detector". *The Astrophysical Journal* 496.1 (1998), p. 505. URL: http://stacks.iop.org/0004-637X/496/i=1/a=505 (cit. on p. 15).

[46] B. Pontecorvo. "Inverse beta process". *Camb. Monogr. Part. Phys. Nucl. Phys. Cosmol.* 1 (1991), pp. 25–31 (cit. on p. 15).

[47] Luis W. Alvarez. "A Proposed Experimental Test of the Neutrino Theory" (1949). DOI: 10.2172/929771 (cit. on p. 15).

[48] R. Davis. "A review of the Homestake solar neutrino experiment". *Prog. Part. Nucl. Phys.* 32 (1994), pp. 13–32. DOI: 10.1016/0146-6410(94)90004-3 (cit. on p. 15).

[49] W. Hampel et al. "GALLEX solar neutrino observations: Results for GALLEX IV". *Phys. Lett.* B447 (1999), pp. 127–133. DOI: 10.1016/S0370-2693(98)01579-2 (cit. on p. 15).

[50] J. N. Abdurashitov et al. "Solar neutrino flux measurements by the Soviet-American Gallium Experiment (SAGE) for half the 22 year solar cycle". *J. Exp. Theor. Phys.* 95 (2002). [Zh. Eksp. Teor. Fiz.122,211(2002)], pp. 181–193. DOI: 10.1134/1.1506424. arXiv: astro-ph/0204245 [astro-ph] (cit. on p. 16).

[51] M. Altmann et al. "Complete results for five years of GNO solar neutrino observations". *Phys. Lett.* B616 (2005), pp. 174–190. DOI: 10.1016/j.physletb.2005.04.068. arXiv: hep-ex/0504037 [hep-ex] (cit. on p. 16).

[52] V. N. Gavrin. "The Russian-American gallium experiment SAGE". *Phys. Usp.* 54 (2011). [Usp. Fiz. Nauk181,975(2011)], pp. 941–949. DOI: 10.3367/UFNe.0181.201109g.0975 (cit. on p. 16).

[53] John N. Bahcall, M. H. Pinsonneault, and Sarbani Basu. "Solar models: Current epoch and time dependences, neutrinos, and helioseismological properties". *Astrophys. J.* 555 (2001), pp. 990–1012. DOI: 10.1086/321493. arXiv: astro-ph/0010346 [astro-ph] (cit. on p. 16).

[54] Y. Fukuda et al. "Solar neutrino data covering solar cycle 22". *Phys. Rev. Lett.* 77 (1996), pp. 1683–1686. DOI: 10.1103/PhysRevLett.77.1683 (cit. on p. 16).

[55] K. Abe et al. "Solar Neutrino Measurements in Super-Kamiokande-IV". *Phys. Rev.* D94.5 (2016), p. 052010. DOI: 10.1103/PhysRevD.94.052010. arXiv: 1606.07538 [hep-ex] (cit. on pp. 16, 177).

[56] A. Renshaw et al. "First Indication of Terrestrial Matter Effects on Solar Neutrino Oscillation". *Phys. Rev. Lett.* 112.9 (2014), p. 091805. DOI: 10.1103/PhysRevLett.112.091805. arXiv: 1312.5176 [hep-ex] (cit. on p. 17).

[57] B. Aharmim et al. "Electron energy spectra, fluxes, and day-night asymmetries of B-8 solar neutrinos from measurements with NaCl dissolved in the heavy-water detector at the Sudbury Neutrino Observatory". *Phys. Rev.* C72 (2005), p. 055502. DOI: 10.1103/PhysRevC.72.055502. arXiv: nucl-ex/0502021 [nucl-ex] (cit. on p. 17).

[58] G. Bellini et al. "Neutrinos from the primary proton–proton fusion process in the Sun". *Nature* 512.7515 (2014), pp. 383–386. DOI: 10.1038/nature13702 (cit. on p. 18).

[59] G. Bellini et al. "Precision measurement of the 7Be solar neutrino interaction rate in Borexino". *Phys. Rev. Lett.* 107 (2011), p. 141302. DOI: 10.1103/PhysRevLett.107.141302. arXiv: 1104.1816 [hep-ex] (cit. on p. 18).

[60] G. Bellini et al. "Measurement of the solar 8B neutrino rate with a liquid scintillator target and 3 MeV energy threshold in the Borexino detector". *Phys. Rev.* D82 (2010), p. 033006. DOI: 10.1103/PhysRevD.82.033006. arXiv: 0808.2868 [astro-ph] (cit. on p. 18).

[61] G. Bellini et al. "First evidence of pep solar neutrinos by direct detection in Borexino". *Phys. Rev. Lett.* 108 (2012), p. 051302. DOI: 10.1103/PhysRevLett.108.051302. arXiv: 1110.3230 [hep-ex] (cit. on p. 18).

[62] A. Gando et al. "^{7}Be Solar Neutrino Measurement with KamLAND". *Phys. Rev.* C92.5 (2015), p. 055808. DOI: 10.1103/PhysRevC.92.055808. arXiv: 1405.6190 [hep-ex] (cit. on p. 18).

[63] S. Abe et al. "Measurement of the 8B Solar Neutrino Flux with the KamLAND Liquid Scintillator Detector". *Phys. Rev.* C84 (2011), p. 035804. DOI: 10.1103/PhysRevC.84.035804. arXiv: 1106.0861 [hep-ex] (cit. on p. 18).

[64] Thomas K. Gaisser. "Atmospheric neutrino fluxes". *Phys. Scripta* T121 (2005), pp. 51–56. DOI: 10.1088/0031-8949/2005/T121/007. arXiv: astro-ph/0502380 [astro-ph] (cit. on p. 18).

[65] K. S. Hirata et al. "Experimental Study of the Atmospheric Neutrino Flux". *Phys. Lett.* B205 (1988). [,447(1988)], p. 416. DOI: 10.1016/0370-2693(88)91690-5 (cit. on p. 19).

[66] K. S. Hirata et al. "Observation of a small atmospheric muon-neutrino / electron-neutrino ratio in Kamiokande". *Phys. Lett.* B280 (1992), pp. 146–152. DOI: 10.1016/0370-2693(92)90788-6 (cit. on p. 19).

[67] Y. Fukuda et al. "Atmospheric muon-neutrino / electron-neutrino ratio in the multiGeV energy range". *Phys. Lett.* B335 (1994), pp. 237–245. DOI: 10.1016/0370-2693(94)91420-6 (cit. on p. 19).

[68] T. J. Haines et al. "Calculation of Atmospheric Neutrino Induced Backgrounds in a Nucleon Decay Search". *Phys. Rev. Lett.* 57 (1986), pp. 1986–1989. DOI: 10.1103/PhysRevLett.57.1986 (cit. on p. 19).

[69] G. Battistoni et al. "Fully Contained Events in the Mont Blanc Nucleon Decay Detector". *Phys. Lett.* 118B (1982), p. 461. DOI: 10.1016/0370-2693(82)90225-8 (cit. on p. 19).

[70] Christoph Berger et al. "Study of Atmospheric Neutrino Interactions with the Frejus Detector". *Phys. Lett.* B227 (1989), p. 489. DOI: 10.1016/0370-2693(89)90968-4 (cit. on p. 19).

[71] M. Ambrosio et al. "Measurement of the atmospheric neutrino induced upgoing muon flux using MACRO". *Phys. Lett.* B434 (1998), pp. 451–457. DOI: 10.1016/S0370-2693(98)00885-5. arXiv: hep-ex/9807005 [hep-ex] (cit. on p. 20).

[72] M. Ambrosio et al. "Atmospheric neutrino oscillations from upward through going muon multiple scattering in MACRO". *Phys. Lett.* B566 (2003), pp. 35–44. DOI: 10.1016/S0370-2693(03)00806-2. arXiv: hep-ex/0304037 [hep-ex] (cit. on p. 20).

[73] Mayly C. Sanchez et al. "Measurement of the L/E distributions of atmospheric neutrinos in Soudan 2 and their interpretation as neutrino oscillations". *Phys. Rev.* D68 (2003), p. 113004. DOI: 10.1103/PhysRevD.68.113004. arXiv: hep-ex/0307069 [hep-ex] (cit. on p. 20).

[74] S. Adrian-Martinez et al. "Measurement of Atmospheric Neutrino Oscillations with the ANTARES Neutrino Telescope". *Phys. Lett.* B714 (2012), pp. 224–230. DOI: 10.1016/j.physletb.2012.07.002. arXiv: 1206.0645 [hep-ex] (cit. on p. 20).

[75] M. G. Aartsen et al. "Determining neutrino oscillation parameters from atmospheric muon neutrino disappearance with three years of IceCube DeepCore data". *Phys. Rev.* D91.7 (2015), p. 072004. DOI: 10.1103/PhysRevD.91.072004. arXiv: 1410.7227 [hep-ex] (cit. on p. 20).

[76] M. Apollonio et al. "Search for neutrino oscillations on a long baseline at the CHOOZ nuclear power station". *Eur. Phys. J.* C27 (2003), pp. 331–374. DOI: 10.1140/epjc/s2002-01127-9. arXiv: hep-ex/0301017 [hep-ex] (cit. on p. 21).

[77] F. P. An et al. "Observation of electron-antineutrino disappearance at Daya Bay". *Phys. Rev. Lett.* 108 (2012), p. 171803. DOI: 10.1103/PhysRevLett.108.171803. arXiv: 1203.1669 [hep-ex] (cit. on p. 22).

[78] Soo-Bong Kim et al. "Observation of Reactor Electron Antineutrino Disappearance in the RENO Experiment". *Phys. Rev. Lett.* 108 (2012), p. 191802. arXiv: 1204.0626 [hep-ex] (cit. on p. 22).

[79] F. P. An et al. "New Measurement of Antineutrino Oscillation with the Full Detector Configuration at Daya Bay". *Phys. Rev. Lett.* 115.11 (2015), p. 111802. DOI: 10.1103/PhysRevLett.115.111802. arXiv: 1505.03456 [hep-ex] (cit. on p. 22).

[80] J. H. Choi et al. "Observation of Energy and Baseline Dependent Reactor Antineutrino Disappearance in the RENO Experiment". *Phys. Rev. Lett.* 116.21 (2016), p. 211801. DOI: 10.1103/PhysRevLett.116.211801. arXiv: 1511.05849 [hep-ex] (cit. on p. 22).

[81] Y. Abe et al. "Measurement of θ_{13} in Double Chooz using neutron captures on hydrogen with novel background rejection techniques". *JHEP* 01 (2016), p. 163. DOI: 10.1007/JHEP01(2016)163. arXiv: 1510.08937 [hep-ex] (cit. on p. 22).

[82] K. Eguchi et al. "First results from KamLAND: Evidence for reactor anti-neutrino disappearance". *Phys. Rev. Lett.* 90 (2003), p. 021802. DOI: 10.1103/PhysRevLett.90.021802. arXiv: hep-ex/0212021 [hep-ex] (cit. on pp. 22, 23).

[83] A. Gando et al. "Constraints on θ_{13} from A Three-Flavor Oscillation Analysis of Reactor Antineutrinos at KamLAND". *Phys. Rev.* D83 (2011), p. 052002. DOI: 10.1103/PhysRevD.83.052002. arXiv: 1009.4771 [hep-ex] (cit. on p. 22).

[84] Fengpeng An et al. "Neutrino Physics with JUNO". *J. Phys.* G43.3 (2016), p. 030401. DOI: 10.1088/0954-3899/43/3/030401. arXiv: 1507.05613 [physics.ins-det] (cit. on p. 22).

[85] A. Aguilar-Arevalo et al. "Evidence for neutrino oscillations from the observation of anti-neutrino(electron) appearance in a anti-neutrino(muon) beam". *Phys. Rev.* D64 (2001), p. 112007. DOI: 10.1103/PhysRevD.64.112007. arXiv: hep-ex/0104049 [hep-ex] (cit. on p. 24).

[86] C. Athanassopoulos et al. "Evidence for $\nu_\mu \to \nu_e$ neutrino oscillations from LSND". *Phys. Rev. Lett.* 81 (1998), pp. 1774–1777. DOI: 10.1103/PhysRevLett.81.1774. arXiv: nucl-ex/9709006 [nucl-ex] (cit. on p. 24).

[87] M. H. Ahn et al. "Measurement of neutrino oscillation by the K2K experiment". *Phys. Rev.* D74 (2006), p. 072003. arXiv: hep-ex/0606032 (cit. on p. 24).

[88] S. Yamamoto et al. "An Improved search for $\nu_\mu \to \nu_e$ oscillation in a long-baseline accelerator experiment". *Phys. Rev. Lett.* 96 (2006), p. 181801. DOI: 10.1103/PhysRevLett.96.181801. arXiv: hep-ex/0603004 [hep-ex] (cit. on p. 24).

[89] P. Adamson et al. "Combined analysis of ν_μ disappearance and $\nu_\mu \to \nu_e$ appearance in MINOS using accelerator and atmospheric neutrinos". *Phys.Rev.Lett.* 112 (2014), p. 191801. DOI: 10.1103/PhysRevLett.112.191801. arXiv: 1403.0867 [hep-ex] (cit. on p. 24).

[90] P. Adamson et al. "Measurement of Neutrino and Antineutrino Oscillations Using Beam and Atmospheric Data in MINOS". *Phys. Rev. Lett.* 110.25 (2013), p. 251801. DOI: 10.1103/PhysRevLett.110.251801. arXiv: 1304.6335 [hep-ex] (cit. on p. 24).

[91] N. Agafonova et al. "Discovery of tau neutrino appearance in the CNGS neutrino beam with the OPERA experiment". *Phys. Rev. Lett.* 115 (2015), p. 121802. arXiv: 1507.01417 [hep-ex] (cit. on p. 25).

[92] K. Abe et al. "Indication of Electron Neutrino Appearance from an Accelerator-produced Off-axis Muon Neutrino Beam". *Phys. Rev. Lett.* 107 (2011), p. 041801. DOI: 10.1103/PhysRevLett.107.041801. arXiv: 1106.2822 [hep-ex] (cit. on pp. 25, 48, 72).

[93] K. Abe et al. "Observation of Electron Neutrino Appearance in a Muon Neutrino Beam". *Phys.Rev.Lett.* 112 (2014), p. 061802. DOI: 10.1103/PhysRevLett.112.061802. arXiv: 1311.4750 [hep-ex] (cit. on pp. 25, 48, 72).

[94] K. Abe et al. "Precise Measurement of the Neutrino Mixing Parameter θ_{23} from Muon Neutrino Disappearance in an Off-Axis Beam". *Phys. Rev. Lett.* 112.18 (2014), p. 181801. DOI: 10.1103/PhysRevLett.112.181801. arXiv: 1403.1532 [hep-ex] (cit. on pp. 25, 48, 72).

[95] P. Adamson et al. "First measurement of electron neutrino appearance in NOvA". *Phys. Rev. Lett.* 116.15 (2016), p. 151806. DOI: 10.1103/PhysRevLett.116.151806. arXiv: 1601.05022 [hep-ex] (cit. on p. 25).

[96] P. Adamson et al. "First measurement of muon-neutrino disappearance in NOvA". *Phys. Rev.* D93.5 (2016), p. 051104. DOI: 10.1103/PhysRevD.93.051104. arXiv: 1601.05037 [hep-ex] (cit. on p. 25).

[97] P. Adamson et al. "Measurement of the neutrino mixing angle θ_{23} in NOvA". *Submitted to: Phys. Rev. Lett.* (2017). arXiv: 1701.05891 [hep-ex] (cit. on p. 25).

[98] P. Adamson et al. "Constraints on Oscillation Parameters from ν_e Appearance and ν_μ Disappearance in NOvA". *Phys. Rev. Lett.* 118.23 (2017), p. 231801. DOI: 10.1103/PhysRevLett.118.231801. arXiv: 1703.03328 [hep-ex] (cit. on pp. 25, 26).

[99] R. Acciarri et al. "Long-Baseline Neutrino Facility (LBNF) and Deep Underground Neutrino Experiment (DUNE)" (2015). arXiv: 1512.06148 [physics.ins-det] (cit. on p. 25).

[100] "Hyper-Kamiokande Design Report" (2016) (cit. on pp. 25, 165, 168, 174, 175, 177, 178).

[101] Francesco Capozzi et al. "Global constraints on absolute neutrino masses and their ordering". *Phys. Rev.* D95.9 (2017), p. 096014. DOI: 10.1103/PhysRevD.95.096014. arXiv: 1703.04471 [hep-ph] (cit. on pp. 27, 28).

[102] J. A. Formaggio and G. P. Zeller. "From eV to EeV: Neutrino Cross Sections Across Energy Scales". *Rev. Mod. Phys.* 84 (2012), pp. 1307–1341. DOI: 10.1103/RevModPhys.84.1307. arXiv: 1305.7513 [hep-ex] (cit. on pp. 29, 49).

[103] A.W. Thomas and W. Weise. *The Structure of the Nucleon*. Wiley, 2001. ISBN: 9783527402977. URL: https://books.google.it/books?id=ZqAsAAAAYAAJ (cit. on p. 31).

[104] C.H. Llewellyn Smith. "Neutrino reactions at accelerator energies". *Physics Reports* 3.5 (1972), pp. 261 –379. ISSN: 0370-1573. DOI: https://doi.org/10.1016/0370-1573(72)90010-5. URL: http://www.sciencedirect.com/science/article/pii/0370157372900105 (cit. on pp. 31, 43, 147).

[105] C. Patrignani et al. "Review of Particle Physics". *Chin. Phys.* C40.10 (2016), p. 100001. DOI: 10.1088/1674-1137/40/10/100001 (cit. on pp. 32, 42).

[106] Veronique Bernard, Latifa Elouadrhiri, and Ulf-G. Meissner. "Axial structure of the nucleon: Topical Review". *J. Phys.* G28 (2002), R1–R35. DOI: 10.1088/0954-3899/28/1/201. arXiv: hep-ph/0107088 [hep-ph] (cit. on p. 33).

[107] W. A. Mann et al. "Study of the reaction $\nu + n \to \mu^- + p$". *Phys. Rev. Lett.* 31 (1973), pp. 844–847. DOI: 10.1103/PhysRevLett.31.844 (cit. on p. 33).

[108] S. J. Barish et al. "Study of Neutrino Interactions in Hydrogen and Deuterium. 1. Description of the Experiment and Study of the Reaction $\nu + d \to \mu^- + p + p(s)$". *Phys. Rev.* D16 (1977), p. 3103. DOI: 10.1103/PhysRevD.16.3103 (cit. on p. 33).

[109] N. J. Baker et al. "Quasielastic Neutrino Scattering: A Measurement of the Weak Nucleon Axial Vector Form-Factor". *Phys. Rev.* D23 (1981), pp. 2499–2505. DOI: 10.1103/PhysRevD.23.2499 (cit. on p. 33).

[110] T. Kitagaki et al. "High-Energy Quasielastic $\nu_\mu + n \to \mu^- + p$ Scattering in Deuterium". *Phys. Rev.* D28 (1983), pp. 436–442. DOI: 10.1103/PhysRevD.28.436 (cit. on p. 33).

[111] Konstantin S. Kuzmin, Vladimir V. Lyubushkin, and Vadim A. Naumov. "Quasielastic axial-vector mass from experiments on neutrino-nucleus scattering". *Eur. Phys. J.* C54 (2008), pp. 517–538. DOI: 10.1140/epjc/s10052-008-0582-x. arXiv: 0712.4384 [hep-ph] (cit. on p. 33).

[112] D. Rein and Sehgal L. M. "Neutrino-excitation of baryon resonances and single pion production". *Annals of Physics* 133.1 (1981), pp. 79–153. ISSN: 0003-4916. DOI: http://dx.doi.org/10.1016/0003-4916(81)90242-6. URL: http://www.sciencedirect.com/science/article/pii/0003491681902426 (cit. on pp. 33, 43, 44).

[113] Ulrich Mosel. "Neutrino Interactions with Nucleons and Nuclei: Importance for Long-Baseline Experiments". *Ann. Rev. Nucl. Part. Sci.* 66 (2016), pp. 171–195. DOI: 10.1146/annurev-nucl-102115-044720. arXiv: 1602.00696 [nucl-th] (cit. on p. 33).

[114] L. Alvarez-Ruso, Y. Hayato, and J. Nieves. "Progress and open questions in the physics of neutrino cross sections at intermediate energies". *New J. Phys.* 16 (2014), p. 075015. DOI: 10.1088/1367-2630/16/7/075015. arXiv: 1403.2673 [hep-ph] (cit. on pp. 35, 39).

[115] A.L. Fetter and J.D. Walecka. *Quantum Theory of Many-particle Systems*. McGraw-Hill, 1980. URL: https://books.google.co.jp/books?id=tofKnQEACAAJ (cit. on p. 35).

[116] R.A. Smith and E.J. Moniz. "Neutrino reactions on nuclear targets". *Nuclear Physics B* 43.Supplement C (1972), pp. 605 –622. ISSN: 0550-3213. DOI: https://doi.org/10.1016/0550-3213(72)90040-5. URL: http://www.sciencedirect.com/science/article/pii/0550321372900405 (cit. on pp. 36, 44).

[117] E. J. Moniz et al. "Nuclear Fermi momenta from quasielastic electron scattering". *Phys. Rev. Lett.* 26 (1971), pp. 445–448. DOI: 10.1103/PhysRevLett.26.445 (cit. on p. 36).

[118] B. Povh. *Particles and Nuclei: An Introduction to the Physical Concepts*. Particles & Nuclei. Springer, 1995. ISBN: 9783540594390. URL: https://books.google.it/books?id=rMPvAAAAMAAJ (cit. on p. 36).

[119] O. Benhar et al. "Spectral function of finite nuclei and scattering of GeV electrons". *Nucl. Phys.* A579 (1994), pp. 493–517. DOI: 10.1016/0375-9474(94)90920-2 (cit. on pp. 36, 43, 44, 147).

[120] O. Benhar and A. Fabrocini. "Two nucleon spectral function in infinite nuclear matter". *Phys. Rev.* C62 (2000), p. 034304. DOI: 10.1103/PhysRevC.62.034304. arXiv: nucl-th/9909014 [nucl-th] (cit. on p. 36).

[121] C. Wilkinson et al. "Testing charged current quasi-elastic and multinucleon interaction models in the NEUT neutrino interaction generator with published datasets from the MiniBooNE and MINERνA experiments". *Phys. Rev.* D93.7 (2016), p. 072010. DOI: 10.1103/PhysRevD.93.072010. arXiv: 1601.05592 [hep-ex] (cit. on p. 37).

[122] Omar Benhar et al. "Neutrino–nucleus interactions and the determination of oscillation parameters". *Phys. Rept.* 700 (2017), pp. 1–47. DOI: 10.1016/j.physrep.2017.07.004. arXiv: 1501.06448 [nucl-th] (cit. on p. 38).

[123] David Bohm and David Pines. "A Collective Description of Electron Interactions. 1. Magnetic Interactions". *Phys. Rev.* 82 (1951), pp. 625–634. DOI: 10.1103/PhysRev.82.625 (cit. on p. 37).

[124] David Pines and David Bohm. "A Collective Description of Electron Interactions: 2. Collective vs Individual Particle Aspects of the Interactions". *Phys. Rev.* 85 (1952), pp. 338–353. DOI: 10.1103/PhysRev.85.338 (cit. on p. 37).

[125] David Bohm and David Pines. "A Collective Description of Electron Interactions: 3. Coulomb Interactions in a Degenerate Electron Gas". *Phys. Rev.* 92 (1953), pp. 609–625. DOI: 10.1103/PhysRev.92.609 (cit. on p. 37).

[126] M. Martini et al. "A Unified approach for nucleon knock-out, coherent and incoherent pion production in neutrino interactions with nuclei". *Phys. Rev.* C80 (2009), p. 065501. DOI: 10.1103/PhysRevC.80.065501. arXiv: 0910.2622 [nucl-th] (cit. on pp. 37, 39, 147).

[127] J. Nieves, I. Ruiz Simo, and M. J. Vicente Vacas. "Inclusive Charged–Current Neutrino–Nucleus Reactions". *Phys. Rev.* C83 (2011), p. 045501. DOI: 10.1103/PhysRevC.83.045501. arXiv: 1102.2777 [hep-ph] (cit. on pp. 37, 40, 43, 44, 100, 147).

[128] T. G. O'Neill et al. "A-dependence of nuclear transparency in quasielastic A (e, e-prime p) at high Q^2". *Phys. Lett.* B351 (1995), pp. 87–92. DOI: 10.1016/0370-2693(95)00362-O. arXiv: hep-ph/9408260 [hep-ph] (cit. on p. 38).

[129] Teppei Katori and Marco Martini. "Neutrino-Nucleus Cross Sections for Oscillation Experiments" (2016). arXiv: 1611.07770 [hep-ph] (cit. on p. 39).

[130] A. A. Aguilar-Arevalo et al. "First Measurement of the Muon Neutrino Charged Current Quasielastic Double Differential Cross Section". *Phys. Rev.* D81 (2010), p. 092005. DOI: 10.1103/PhysRevD.81.092005. arXiv: 1002.2680 [hep-ex] (cit. on pp. 39, 40).

[131] V. Lyubushkin et al. "A study of quasi-elastic muon neutrino and antineutrino scattering in the NOMAD experiment". *Eur. Phys. J.* C63 (2009), pp. 355–381. arXiv: 0812.4543 [hep-ex] (cit. on pp. 39, 40).

[132] L. B. Auerbach et al. "Measurements of charged current reactions of muon neutrinos on C-12". *Phys. Rev.* C66 (2002), p. 015501. DOI: 10.1103/PhysRevC.66.015501. arXiv: nucl-ex/0203011 [nucl-ex] (cit. on p. 40).

[133] J. W. Van Orden and T. W. Donnelly. "Mesonic process in deep inelastic scattering from nuclei". *Annals Phys.* 131 (1981), pp. 451–493. DOI: 10.1016/0003-4916(81)90038-5 (cit. on p. 39).

[134] W. M. Alberico, Magda Ericson, and A. Molinari. "The Role of Two Particles - Two Holes Excitations in the Spin - Isospin Nuclear Response". *Annals Phys.* 154 (1984), p. 356. DOI: 10.1016/0003-4916(84)90155-6 (cit. on p. 39).

[135] K. Gallmeister, U. Mosel, and J. Weil. "Neutrino-Induced Reactions on Nuclei". *Phys. Rev.* C94.3 (2016), p. 035502. DOI: 10.1103/PhysRevC.94.035502. arXiv: 1605.09391 [nucl-th] (cit. on p. 41).

[136] M. Martini, M. Ericson, and G. Chanfray. "Neutrino quasielastic interaction and nuclear dynamics". *Phys. Rev.* C84 (2011), p. 055502. DOI: 10.1103/PhysRevC.84.055502. arXiv: 1110.0221 [nucl-th] (cit. on p. 41).

[137] C. Andreopoulos et al. "The GENIE Neutrino Monte Carlo Generator". *Nucl. Instrum. Meth.* A614 (2010), pp. 87–104. DOI: 10.1016/j.nima.2009.12.009. arXiv: 0905.2517 [hep-ph] (cit. on p. 42).

[138] Yoshinari Hayato. "A neutrino interaction simulation program library NEUT". *Acta Phys. Polon.* B40 (2009), pp. 2477–2489 (cit. on pp. 42, 73, 105).

[139] O. Buss et al. "Transport-theoretical Description of Nuclear Reactions". *Phys. Rept.* 512 (2012), pp. 1–124. DOI: 10.1016/j.physrep.2011.12.001. arXiv: 1106.1344 [hep-ph] (cit. on p. 42).

[140] Cezary Juszczak, Jaroslaw A. Nowak, and Jan T. Sobczyk. "Simulations from a new neutrino event generator". *Nucl. Phys. Proc. Suppl.* 159 (2006). [,211(2005)], pp. 211–216. DOI: 10.1016/j.nuclphysbps.2006.08.069. arXiv: hep-ph/0512365 [hep-ph] (cit. on p. 42).

[141] R. Bradford et al. "A New Parameterization of the Nucleon Elastic Form Factors". *Nuclear Physics B - Proceedings Supplements* 159.0 (2006), pp. 127 –132. ISSN: 0920-5632. DOI: 10.1016/j.nuclphysbps.2006.08.028. URL: http://www.sciencedirect.com/science/article/pii/S0920563206005184 (cit. on pp. 43, 44, 147).

[142] R. Gran et al. "Measurement of the quasi-elastic axial vector mass in neutrino-oxygen interactions". *Phys. Rev.* D74 (2006), p. 052002. DOI: 10.1103/PhysRevD.74.052002. arXiv: hep-ex/0603034 [hep-ex] (cit. on pp. 43, 100).

[143] Jackie Schwehr, Dan Cherdack, and Rik Gran. "GENIE implementation of IFIC Valencia model for QE-like 2p2h neutrino-nucleus cross section" (2016). arXiv: 1601.02038 [hep-ph] (cit. on p. 43).

[144] Krzysztof M. Graczyk and Jan T. Sobczyk. "Form factors in the quark resonance model". *Phys. Rev. D* 77 (5 2008), p. 053001. DOI: 10.1103/PhysRevD.77.053001. URL: https://link.aps.org/doi/10.1103/PhysRevD.77.053001 (cit. on pp. 43, 44).

[145] Konstantin S. Kuzmin, Vladimir V. Lyubushkin, and Vadim A. Naumov. "Axial masses in quasielastic neutrino scattering and single-pion neutrinoproduction on nucleons and nuclei". *Acta Phys. Polon.* B37 (2006), pp. 2337–2348. arXiv: hep-ph/0606184 [hep-ph] (cit. on pp. 43, 44).

[146] D. Rein and L. M. Sehgal. "Coherent π^0 production in neutrino reactions". *Nucl. Phys.* B223 (1983), p. 29. DOI: 10.1016/0550-3213(83)90090-1 (cit. on p. 43).

[147] M. Glück, E. Reya, and A. Vogt. "Dynamical parton distributions revisited". *The European Physical Journal C - Particles and Fields* 5.3 (1998), pp. 461–470. ISSN: 1434-6052. DOI: 10.1007/s100529800978. URL: http://dx.doi.org/10.1007/s100529800978 (cit. on pp. 43, 44).

[148] A. Bodek and J. L. Ritchie. "Fermi Motion Effects in Deep Inelastic Lepton Scattering from Nuclear Targets". *Phys. Rev.* D23 (1981), p. 1070. DOI: 10.1103/PhysRevD.23.1070 (cit. on pp. 43, 44, 147).

[149] Z. Koba, H.B. Nielsen, and P. Olesen. "Scaling of multiplicity distributions in high energy hadron collisions". *Nuclear Physics B* 40.Supplement C (1972), pp. 317 –334. ISSN: 0550-3213. DOI: https://doi.org/10.1016/0550-3213(72)90551-2. URL: http://www.sciencedirect.com/science/article/pii/0550321372905512 (cit. on pp. 43, 44).

[150] T. Sjöstrand. "High-energy-physics event generation with PYTHIA 5.7 and JETSET 7.4". *Computer Physics Communications* 82.1 (1994), pp. 74 –89. ISSN: 0010-4655. DOI: http://dx.doi.org/10.1016/0010-4655(94)90132-5. URL: http://www.sciencedirect.com/science/article/pii/0010465594901325 (cit. on pp. 43, 44).

[151] T. Yang et al. "A Hadronization Model for Few-GeV Neutrino Interactions". *Eur. Phys. J.* C63 (2009), pp. 1–10. DOI: 10.1140/epjc/s10052-009-1094-z. arXiv: 0904.4043 [hep-ph] (cit. on pp. 43, 44).

[152] Roger D. Woods and David S. Saxon. "Diffuse Surface Optical Model for Nucleon-Nuclei Scattering". *Phys. Rev.* 95 (1954), pp. 577–578. DOI: 10.1103/PhysRev.95.577 (cit. on p. 44).

[153] A.Bodek and U.K. Yang. "Modeling neutrino and electron scattering cross sections in the few-GeV region with effective LO PDFs". *AIP Conf. Proc.* 670 (2003), pp. 110–117 (cit. on p. 44).

[154] P. A. Rodrigues et al. "Identification of nuclear effects in neutrino-carbon interactions at low three-momentum transfer". *Phys. Rev. Lett.* 116 (2016), p. 071802. DOI: 10.1103/PhysRevLett.116.071802. arXiv: 1511.05944 [hep-ex] (cit. on pp. 45, 46).

[155] Ko Abe et al. "Measurement of double-differential muon neutrino charged-current interactions on C_8H_8 without pions in the final state using the T2K off-axis beam". *Phys. Rev.* D93.11 (2016), p. 112012. DOI: 10.1103/PhysRevD.93.112012. arXiv: 1602.03652 [hep-ex] (cit. on pp. 45, 47, 107, 164).

[156] A. A. Aguilar-Arevalo et al. "Measurement of Neutrino-Induced Charged-Current Charged Pion Production Cross Sections on Mineral Oil at $E_\nu \sim 1$ GeV". *Phys.Rev.* D83 (2011), p. 052007. arXiv: 1011.3572 [hep-ex] (cit. on p. 46).

[157] B. Eberly et al. "Charged Pion Production in ν_μ Interactions on Hydrocarbon at $\langle E_\nu \rangle = 4.0$ GeV". *Phys. Rev.* D92 (2015), p. 092008. arXiv: 1406.6415 [hep-ex] (cit. on p. 46).

[158] K. Abe et al. "First measurement of the muon neutrino charged current single pion production cross section on water with the T2K near detector". *Phys. Rev.* D95.1 (2017), p. 012010. DOI: 10.1103/PhysRevD.95.012010. arXiv: 1605.07964 [hep-ex] (cit. on p. 47).

[159] K. Abe et al. "The T2K Experiment". *Nucl. Instrum. Meth.* A659 (2011), pp. 106–135. DOI: 10.1016/j.nima.2011.06.067. arXiv: 1106.1238 [physics.ins-det] (cit. on pp. 48, 53, 58, 60, 63, 64, 67, 69, 70).

[160] K. Abe et al. "A Long Baseline Neutrino Oscillation Experiment Using J-PARC Neutrino Beam and Hyper-Kamiokande". 2014. arXiv: 1412.4673 [physics.ins-det]. URL: http://inspirehep.net/record/1334360/files/arXiv:1412.4673.pdf (cit. on pp. 50, 51).

[161] S. Bhadra et al. "Optical Transition Radiation Monitor for the T2K Experiment". *Nucl. Instrum. Meth.* A703 (2013), pp. 45–58. DOI: 10.1016/j.nima.2012.11.044. arXiv: 1201.1922 [physics.ins-det] (cit. on p. 53).

[162] K. Abe et al. "T2K neutrino flux prediction". *Phys. Rev.* D87.1 (2013). [Addendum: Phys. Rev.D87,no.1,019902(2013)], p. 012001. DOI: 10.1103/PhysRevD.87.012001,10.1103/PhysRevD.87.019902. arXiv: 1211.0469 [hep-ex] (cit. on pp. 57, 127).

[163] A. Ferrari et al. "FLUKA: A multi-particle transport code". *CERN-2005-010, SLAC-R-773, INFN-TC-05-11* () (cit. on p. 58).

[164] R. Brun, F. Carminati, and S. Giani. *CERN-W5013* (1994) (cit. on p. 58).

[165] C. Zeitnitz and T. A. Gabriel. *Proc. of International Conference on Calorimetry in High Energy Physics* (1993) (cit. on p. 58).

[166] N Abgrall et al. "Measurements of Cross Sections and Charged Pion Spectra in Proton-Carbon Interactions at 31 GeV/c". *Phys. Rev. C* 84 (2011), p. 034604. DOI: 10.1103/PhysRevC.84.034604 (cit. on p. 58).

[167] N. Abgrall et al. "Measurement of Production Properties of Positively Charged Kaons in Proton-Carbon Interactions at 31 GeV/c". *Phys. Rev. C* 85 (2012), p. 035210. DOI: 10.1103/PhysRevC.85.035210 (cit. on p. 58).

[168] K. Abe et al. "Measurements of the T2K neutrino beam properties using the INGRID on-axis near detector". *Nucl. Instrum. Meth.* A694 (2012), pp. 211–223. DOI: 10.1016/j.nima.2012.03.023. arXiv: 1111.3119 [physics.ins-det] (cit. on p. 59).

[169] S. Aoki et al. "The T2K Side Muon Range Detector (SMRD)". *Nucl. Instrum. Meth.* A698 (2013), pp. 135–146. DOI: 10.1016/j.nima.2012.10.001. arXiv: 1206.3553 [physics.ins-det] (cit. on p. 62).

[170] S. Assylbekov et al. "The T2K ND280 Off-Axis Pi-Zero Detector". *Nucl. Instrum. Meth.* A686 (2012), pp. 48–63. DOI: 10.1016/j.nima.2012.05.028. arXiv: 1111.5030 [physics.ins-det] (cit. on pp. 64, 68).

[171] N. Abgrall et al. "Time Projection Chambers for the T2K Near Detectors". *Nucl. Instrum. Meth.* A637 (2011), pp. 25–46. DOI: 10.1016/j.nima.2011.02.036. arXiv: 1012.0865 [physics.ins-det] (cit. on pp. 65, 66).

[172] P. A. Amaudruz et al. "The T2K Fine-Grained Detectors". *Nucl. Instrum. Meth.* A696 (2012), pp. 1–31. DOI: 10.1016/j.nima.2012.08.020. arXiv: 1204.3666 [physics.ins-det] (cit. on pp. 67, 92, 122).

[173] K. Abe et al. "First Muon-Neutrino Disappearance Study with an Off-Axis Beam". *Phys. Rev.* D85 (2012), p. 031103. DOI: 10.1103/PhysRevD.85.031103. arXiv: 1201.1386 [hep-ex] (cit. on p. 72).

[174] K. Abe et al. "Evidence of Electron Neutrino Appearance in a Muon Neutrino Beam". *Phys. Rev.* D88.3 (2013), p. 032002. DOI: 10.1103/PhysRevD.88.032002. arXiv: 1304.0841 [hep-ex] (cit. on p. 72).

[175] K. Abe et al. "Measurements of neutrino oscillation in appearance and disappearance channels by the T2K experiment with 6.6E20 protons on target". *Phys.Rev.* D91 (2015), p. 072010. arXiv: 1502.01550 [hep-ex] (cit. on pp. 72, 83, 91, 93, 99, 130).

[176] K. Abe et al. "Measurement of neutrino and antineutrino oscillations by the T2K experiment including a new additional sample of ν_e interactions at the far detector". *Phys. Rev. D* 96 (9 2017), p. 092006. DOI: 10.1103/PhysRevD.96.092006. arXiv: 1707.01048 [hep-ex]. URL: https://link.aps.org/doi/10.1103/PhysRevD.96.092006 (cit. on pp. 72, 91–94, 97, 98, 109).

[177] S. Agostinelli et al. "Geant4-a simulation toolkit". *Nuclear Instruments and Methods in Physics Research Section A: Accelerators, Spectrometers, Detectors and Associated Equipment* 506.3 (2003), pp. 250 –303. ISSN: 0168-9002. DOI: https://doi.org/10.1016/S0168-9002(03)01368-8. URL: http://www.sciencedirect.com/science/article/pii/S0168900203013688 (cit. on pp. 90, 167).

[178] P. Bartet at al. "ν_μ CC event selections in the ND280 tracker using Run 2+3+4 ". *T2K-TN-212* (2015) (cit. on pp. 92, 130).

[179] K. Abe et al. "Measurement of muon anti-neutrino oscillations with an accelerator-produced off-axis beam". *Phys.Rev.Lett.* 116 (2016), p. 181801. arXiv: 1512.02495 [hep-ex] (cit. on p. 92).

[180] K. Abe et al. "Updated T2K measurements of muon neutrino and antineutrino disappearance using 1.5×10^{21} protons on target". *Phys. Rev.* D96.1 (2017), p. 011102. DOI: 10.1103/PhysRevD.96.011102. arXiv: 1704.06409 [hep-ex] (cit. on p. 92).

[181] K. Abe et al. "Combined Analysis of Neutrino and Antineutrino Oscillations at T2K". *Phys. Rev. Lett.* 118.15 (2017), p. 151801. DOI: 10.1103/PhysRevLett.118.151801. arXiv: 1701.00432 [hep-ex] (cit. on p. 92).

[182] K. A. Olive et al. "Review of Particle Physics". *Chin. Phys.* C38 ((2014) and 2015 update), p. 090001. DOI: 10.1088/1674-1137/38/9/090001 (cit. on p. 97).

[183] Ko Abe et al. "Proposal for an Extended Run of T2K to 20×10^{21} POT" (2016). arXiv: 1609.04111 [hep-ex] (cit. on pp. 99, 165, 166, 172, 173).

[184] A.A. Aguilar-Arevalo et al. "First measurement of the muon neutrino charged current quasielastic double-differential cross section". *Phys. Rev.* D81 (2010), p. 092005. DOI: 10.1103/PhysRevD.81.092005. arXiv: 1002.2680 [hep-ex] (cit. on pp. 100, 101).

[185] P. Adamson et al. "Study of quasielastic scattering using charged-current ν_μ-iron interactions in the MINOS near detector". *Phys. Rev.* D91.1 (2015), p. 012005. DOI: 10.1103/PhysRevD.91.012005. arXiv: 1410.8613 [hep-ex] (cit. on p. 100).

[186] Jose Luis Alcaraz Aunion. "Measurement of the absolute ν_μ-CCQE cross section at the SciBooNE experiment". PhD thesis. Barcelona, IFAE, 2010. URL: http://lss.fnal.gov/cgi-bin/find_paper.pl?thesis-2010-45 (cit. on p. 100).

[187] Martini, M. and Ericson, M. and Chanfray, G. and Marteau, J. "Unified approach for nucleon knock-out and coherent and incoherent pion production in neutrino interactions with nuclei". *Phys. Rev. C* 80 (6 2009), 065501. DOI: 10.1103/PhysRevC.80.065501. URL: https://link.aps.org/doi/10.1103/PhysRevC.80.065501 (cit. on p. 100).

[188] M. Martini et al. "Neutrino and antineutrino quasielastic interactions with nuclei". *Phys. Rev.* C81 (2010), p. 045502. DOI: 10.1103/PhysRevC.81.045502. arXiv: 1002.4538 [hep-ph] (cit. on pp. 100, 101).

[189] M. Ericson and M. Martini. "Neutrino versus antineutrino cross sections and CP violation". *Phys. Rev.* C91.3 (2015), p. 035501. DOI: 10.1103/PhysRevC.91.035501. arXiv: 1501.02442 [nucl-th] (cit. on pp. 100, 101).

[190] A. A. Aguilar-Arevalo et al. "First measurement of the muon antineutrino double-differential charged-current quasielastic cross ection". *Phys. Rev.* D88.3 (2013), p. 032001. DOI: 10.1103/PhysRevD.88.032001. arXiv: 1301.7067 [hep-ex] (cit. on p. 101).

[191] Fred James and Matthias Winkler. "MINUIT User's Guide" (2004) (cit. on p. 105).

[192] Alfonso Garcia. "Study of the ν_μ interactions via charged current in the T2K near detector". PhD thesis. Barcelona, Autonoma U., 2017-05-15. URL: http://www.t2k.org/docs/thesis/082/thesis (cit. on pp. 109, 124, 130).

[193] A. Higuera et al. "Measurement of Coherent Production of $\pi^\pm$ in Neutrino and Antineutrino Beams on Carbon from E_ν of 1.5 to 20 GeV". *Phys. Rev. Lett.* 113.26 (2014), p. 261802. DOI: 10.1103/PhysRevLett.113.261802. arXiv: 1409.3835 [hep-ex] (cit. on p. 113).

[194] James E. Gentle. *Numerical Linear Algebra for Applications in Statistics*. Statistics and Computing. Springer, 1998. ISBN: 9781461268420. URL: http://www.springer.com/in/book/9780387985428 (cit. on p. 125).

[195] A. Cervera et al. "CC-0π Multi-Topology Selection and Systematics in FGD1". *T2K-TN-216* (2014) (cit. on p. 130).

[196] V. Berardi at al. "CC anti-nu event selection in the ND280 tracker using Run 5c and Run 6 anti-neutrino beam data". *T2K-TN-246* (2015) (cit. on p. 130).

[197] S. Oser. "Elemental composition and masses of FGD XY modules". *T2K-TN-091* (2014) (cit. on p. 134).

[198] V. Pandey et al. "Low-energy excitations and quasielastic contribution to electron-nucleus and neutrino-nucleus scattering in the continuum random-phase approximation". *Phys. Rev.* C92.2 (2015), p. 024606. DOI: 10.1103/PhysRevC.92.024606. arXiv: 1412.4624 [nucl-th] (cit. on p. 147).

[199] M. Martini and M. Ericson. "Inclusive and pion production neutrino-nucleus cross sections". *Phys. Rev.* C90.2 (2014), p. 025501. DOI: 10.1103/PhysRevC.90.025501. arXiv: 1404.1490 [nucl-th] (cit. on p. 147).

[200] Davide Sgalaberna et al. "A fully active fine grained detector with three readout views" (2017). arXiv: 1707.01785 [physics.ins-det] (cit. on p. 167).

[201] R. Asfandiyarov et al. "Proposal for SPS beam time for the baby MIND and TASD neutrino detector prototypes" (2014). arXiv: 1405.6089 [physics.ins-det] (cit. on p. 168).

[202] S. Adrian-Martinez et al. "Letter of intent for KM3NeT 2.0". *J. Phys.* G43.8 (2016), p. 084001. DOI: 10.1088/0954-3899/43/8/084001. arXiv: 1601.07459 [astro-ph.IM] (cit. on p. 169).

[203] K. Abe et al. "Measurement of the Inclusive Electron Neutrino Charged Current Cross Section on Carbon with the T2K Near Detector". *Phys. Rev. Lett.* 113.24 (2014), p. 241803. DOI: 10.1103/PhysRevLett.113.241803. arXiv: 1407.7389 [hep-ex] (cit. on p. 169).

[204] X. G. Lu et al. "Measurement of nuclear effects in neutrino interactions with minimal dependence on neutrino energy". *Phys. Rev.* C94.1 (2016), p. 015503. DOI: 10.1103/PhysRevC.94.015503. arXiv: 1512.05748 [nucl-th] (cit. on p. 170).

[205] X. G. Lu et al. "Reconstruction of Energy Spectra of Neutrino Beams Independent of Nuclear Effects". *Phys. Rev.* D92.5 (2015), p. 051302. DOI: 10.1103/PhysRevD.92.051302. arXiv: 1507.00967 [hep-ex] (cit. on p. 170).

[206] N. Abgrall et al. "Measurements of $\pi^{\pm}$ differential yields from the surface of the T2K replica target for incoming 31 GeV/c protons with the NA61/SHINE spectrometer at the CERN SPS". *Eur. Phys. J.* C76.11 (2016), p. 617. DOI: 10.1140/epjc/s10052-016-4440-y. arXiv: 1603.06774 [hep-ex] (cit. on p. 170).

[207] E. S. Pinzon Guerra et al. "Measurement of σ_{ABS} and σ_{CX} of π^{+} on carbon by the Dual Use Experiment at TRIUMF (DUET)". *Phys. Rev.* C95.4 (2017), p. 045203. DOI: 10.1103/PhysRevC.95.045203. arXiv: 1611.05612 [hep-ex] (cit. on p. 170).

[208] Melanie Day and Kevin S. McFarland. "Differences in Quasi-Elastic Cross-Sections of Muon and Electron Neutrinos". *Phys. Rev.* D86 (2012), p. 053003. DOI: 10.1103/PhysRevD.86.053003. arXiv: 1206.6745 [hep-ph] (cit. on p. 171).

[209] K. Abe et al. "Physics Potentials with the Second Hyper-Kamiokande Detector in Korea" (2016). arXiv: 1611.06118 [hep-ex] (cit. on pp. 174, 176).

[210] K. Abe et al. "Neutrino oscillation physics potential of the T2K experiment". *PTEP* 2015.4 (2015), p. 043C01. DOI: 10.1093/ptep/ptv031. arXiv: 1409.7469 [hep-ex] (cit. on p. 175).

[211] K. Abe et al. "Physics potential of a long-baseline neutrino oscillation experiment using a J-PARC neutrino beam and Hyper-Kamiokande". *PTEP* 2015 (2015), p. 053C02. DOI: 10.1093/ptep/ptv061. arXiv: 1502.05199 [hep-ex] (cit. on p. 175).

[212] K. Abe et al. "Search for proton decay via $p \to e^{+}\pi^{0}$ and $p \to \mu^{+}\pi^{0}$ in 0.31 megaton·years exposure of the Super-Kamiokande water Cherenkov detector". *Phys. Rev.* D95.1 (2017), p. 012004. DOI: 10.1103/PhysRevD.95.012004. arXiv: 1610.03597 [hep-ex] (cit. on p. 178).

[213] J. Babson et al. "Cosmic-ray muons in the deep ocean". *Phys. Rev. D* 42 (1990), p. 3613. DOI: 10.1103/PhysRevD.42.3613 (cit. on p. 178).

[214] I. A. Belolaptikov et al. "The Baikal underwater neutrino telescope: Design, performance, and first results." *Astropart. Phys.* 7(3) (1997), pp. 263–282. DOI: 10.1016/S0927-6505(97)00022-4 (cit. on p. 178).

[215] P. Rapidis et al. "The NESTOR underwater neutrino telescope project". *Nucl. Instrum. Meth.* A602 (2009), pp. 54–57. DOI: 10.1016/j.nima.2008.12.216 (cit. on p. 178).

[216] E.G.Anassontzis et al. "The optical module for the NESTOR neutrino telescope". *Nucl. Instrum. Meth.* A479 (2002), pp. 439–455. DOI: 10.1016/S0168-9002(01)00927-5 (cit. on p. 178).

[217] M. Ageron et al. "ANTARES: the first undersea neutrino telescope". *Nucl. Instrum. Meth.* A656 (2011), pp. 11–38. DOI: 10.1016/j.nima.2011.06.103 (cit. on p. 178).

[218] P. Amram et al. "The ANTARES optical module". *Nucl. Instrum. Meth.* A484 (2002), pp. 369–383. DOI: 10.1016/S0168-9002(01)02026-5 (cit. on p. 178).

[219] E. Andres et al. "The AMANDA neutrino telescope: Principle of operation and first results". *Astropart. Phys.* 13 (2000), pp. 1–20. DOI: 10.1016/S0927-6505(99)00092-4. arXiv: astro-ph/9906203 [astro-ph] (cit. on p. 178).

[220] A. Achterberg et al. "First year performance of the IceCube neutrino telescope". *Astropart. Phys.* 26(3) (2006), pp. 155–173. DOI: 10.1016/j.astropartphys.2006.06.007 (cit. on p. 178).

[221] KM3Net Consortium. Conceptual design for a deep-sea research infrastructure incorporating a very large volume neutrino telescope in the Mediterranean Sea, http://www.km3net.org/CDR/CDR-KM3NeT.pdf; Technical design report for a deep-sea research infrastructure in the Mediterranean Sea incorporating a very large volume neutrino telescope, http://www.km3net.org/TDR/TDRKM3NeT.pdf (cit. on p. 178).

[222] S. Aiello et al. "Characterization of the 80-mm diameter Hamamatsu PMTs for the KM3NeT project". *AIP Conference Proceedings* 1630 (2014), p. 118. DOI: 10.1063/1.4902786 (cit. on p. 179).

[223] G. Bourlis et al. "Characterization of the KM3NeT photomultipliers in the Hellenic Open University". *AIP Conference Proceedings* 1630 (2014), p. 106. DOI: 10.1063/1.4902783 (cit. on p. 179).

[224] R. Bormuth et al. "Characterization of the ETEL and HZC 3-inch PMTs for the KM3NeT project". *AIP Conference Proceedings* 1630 (2014), p. 114. DOI: 10.1063/1.4902785 (cit. on p. 179).

[225] P. Timmer et al. "Very low power, high voltage base for a Photo Multiplier Tube for the KM3NeT deep sea neutrino telescope". *Journal of Instrumentation* 5 (Dec. 2010), p. C12049. DOI: 10.1088/1748-0221/5/12/C12049 (cit. on p. 181).

École Doctorale
PHENIICS
Doctoral School

Titre : Mesure du flux et de la section efficace du antineutrino dans le détecteur proche de l'expérience T2K

Mots-clés : *antineutrino, Section efficace,T2K.*
Résumé : T2K (Tokai to Kamioka) est une expérience d'oscillation de neutrinos sur une longue ligne de base, située au Japon. Elle est conçue pour mesurer le changement de saveur des neutrinos d'un faisceau produit à l'aide d'un accélérateur au laboratoire JPARC de Tokai. Les détecteurs proche et lointain sont placés légèrement hors axe par rapport au faisceau. En 2014 T2K a inversé la polarité des cornes magnétiques intervenant dans la production du faisceau, afin de produire un faisceau d'antineutrinos et d'augmenter la sensibilité de l'expérience à la violation de la charge-parité dans le secteur leptonique. Le faisceau produit est alors dominé par les antineutrinos muoniques avec une composante mesurable de neutrinos muoniques. L'analyse simultanée, dans les données prises avec le faisceau de neutrinos et le faisceau d'antineutrinos, des interactions par courant chargé dans le détecteur proche ND280, permet de réduire l'impact sur les analyses d'oscillation des incertitudes liées au flux des (anti)neutrinos et à leur section efficace d'interaction. Les données de ND280 permettent également de mesurer les sections efficaces d'interaction des antineutrinos d'énergie proche de 600 MeV. Cette thèse se compose de trois études. La première détaille la sélection des interactions de neutrinos muoniques par courant chargé dans le détecteur proche hors axe. Dans un premier temps l'échantillon de données était divisé en deux selon le nombre de traces chargées de l'événement, puis l'accumulation de davantage de données a permis la séparation de l'échantillon en trois lots selon le contenu en pions de l'événement. La seconde étude consiste en la mesure simultanée de la section efficace d'interaction des neutrinos et des antineutrinos muoniques par courant chargé, conduisant à un état final sans pion mesuré dans le détecteur ND280. Ces sections efficaces sont extraites en fonction des variables décrivant la cinématique du muon issu de l'interaction, permettant ainsi d'évaluer la somme, la différence et l'asymétrie entre les sections efficaces des neutrinos et des antineutrinos. La somme et la différence donnent des indications sur les processus à l'oeuvre dans les interactions des neutrinos. L'asymétrie permet d'estimer directement le biais éventuel sur la mesure de la violation de la charge-parité dû à la modélisation des sections efficaces. La dernière partie de la thèse étudie la proposition d'utiliser la technologie dite de multi-PMT pour le detector Hyper-Kamiokande, version à plus grande échelle de Super-Kamiokande, ainsi que la possibilité d'étudier le flux de neutrinos à 1 ou 2 km de l'origine du faisceau de neutrinos, avec un détecteur de rayonnement Čerenkov dans l'eau. Un multi-PMT est une sphère de plastique contenant 26 tubes photomultiplicateurs, qui pourrait améliorer l'efficacité et la granularité des détecteurs basés sur le rayonnement Čerenkov.

Title: Measurement of muon neutrino and antineutrino cross sections without pions in the final state

Keywords: *antineutrinos, T2K, cross-section.*
Abstract: T2K (Tokai to Kamioka) is a long-baseline neutrino oscillation experiment installed in Japan. It is designed to measure neutrino flavor oscillation using an off-axis neutrino beam produced at the J-PARC accelerator facility in Tokai. In 2014 T2K has switched its beam magnet polarities to run with an antineutrino beam to enhance its sensitivity to the charge-parity violation in the leptonic sector. The beam is dominated by muon antineutrinos and contains a sizable contamination of muon neutrinos. The analysis of both neutrino and antineutrino charged-current interactions in the off-axis near detector (ND280), provides a significant reduction of the flux and cross-section modeling uncertainties on the oscillation analysis. ND280 data also gives the opportunity to measure antineutrinos cross-sections at the energy around 600 MeV. This thesis is focused on three different arguments. First the selection of charged current interactions in the off-axis near detector of muon neutrinos in the antineutrino beam is shown. In a first iteration the selected sample has been divided into two sub-sample based on the track multiplicity, then with more statistic a separation into three sub-samples based on the pion content in each event was possible. The second argument is the simultaneous measurement of the double-differential muon neutrino and antineutrino charged-current cross-section without pions in the final state at ND280. The cross-sections will be simultaneously extracted as a function of muon kinematics, allowing the evaluation of the sum, difference and asymmetry between the two cross-sections. Sum and difference can shed light on the processes involved in neutrino interactions. The asymmetry is a direct estimation on any possible bias on the charge-parity violation measurement due to cross section mismodeling. The last topic concerns the proposal of the multi-PMT technology as detector for Hyper-Kamiokande, the upgrade of Super-Kamiokande, and the intermediate water Čerenkov proposed to study the neutrino flux at ∼1-2 km from the beam production point. A multi-PMT is a plastic sphere filled with 26 photomultiplier tube that could improve the reconstruction efficiency and the granularity of such Čerenkov detectors.

Université Paris-Saclay
Espace Technologique / Immeuble Discovery
Route de l'Orme aux Merisiers RD 128 / 91190, Saint-Aubin, France